Springer Theses
Recognizing Outstanding Ph.D. Research

Wei Wang

Archean-Mesoproterozoic Crustal Evolution and Crust-Mantle Geodynamics of Western Liaoning-Northeastern Hebei Provinces, North China Craton

Springer

Springer Theses

Recognizing Outstanding Ph.D. Research

Aims and Scope

The series "Springer Theses" brings together a selection of the very best Ph.D. theses from around the world and across the physical sciences. Nominated and endorsed by two recognized specialists, each published volume has been selected for its scientific excellence and the high impact of its contents for the pertinent field of research. For greater accessibility to non-specialists, the published versions include an extended introduction, as well as a foreword by the student's supervisor explaining the special relevance of the work for the field. As a whole, the series will provide a valuable resource both for newcomers to the research fields described, and for other scientists seeking detailed background information on special questions. Finally, it provides an accredited documentation of the valuable contributions made by today's younger generation of scientists.

Theses are accepted into the series by invited nomination only and must fulfill all of the following criteria

- They must be written in good English.
- The topic should fall within the confines of Chemistry, Physics, Earth Sciences, Engineering and related interdisciplinary fields such as Materials, Nanoscience, Chemical Engineering, Complex Systems and Biophysics.
- The work reported in the thesis must represent a significant scientific advance.
- If the thesis includes previously published material, permission to reproduce this must be gained from the respective copyright holder.
- They must have been examined and passed during the 12 months prior to nomination.
- Each thesis should include a foreword by the supervisor outlining the significance of its content.
- The theses should have a clearly defined structure including an introduction accessible to scientists not expert in that particular field.

More information about this series at http://www.springer.com/series/8790

Wei Wang

Archean-Mesoproterozoic Crustal Evolution and Crust-Mantle Geodynamics of Western Liaoning-Northeastern Hebei Provinces, North China Craton

Doctoral Thesis accepted by
Peking University,
School of Earth and Space Sciences;
Beijing, China

Springer

Author
Dr. Wei Wang
School of Earth Sciences and Resources
China University of Geosciences (Beijing)
Beijing
China

Supervisor
Prof. Shuwen Liu
School of Earth and Space Sciences
Peking University
Beijing
China

ISSN 2190-5053 ISSN 2190-5061 (electronic)
Springer Theses
ISBN 978-981-10-7921-4 ISBN 978-981-10-7922-1 (eBook)
https://doi.org/10.1007/978-981-10-7922-1

Library of Congress Control Number: 2017962983

Printed on acid-free paper

This Springer imprint is published by Springer Nature
The registered company is Springer Nature Singapore Pte Ltd.
The registered company address is: 152 Beach Road, #21-01/04 Gateway East, Singapore 189721, Singapore

To my family

Supervisor's Foreword

The North China Craton (NCC) is one of the oldest cratons in the world, recording complex Precambrian geological events dating back to ~3.8 Ga. It provides a natural laboratory to study the formation and evolution of continental crust as well as geodynamic evolution throughout almost all the Precambrian period. During the past two decades, great achievements have been obtained in terms of discovery of early Archean geological records, sequences of early Precambrian geological events, crustal growth and evolution, and reconstruction of Paleoproterozoic tectonic framework. Though it is widely accepted that this craton was consolidated by several separate blocks, the number and division of these blocks as well as timing of final amalgamation remain hotly debated. While some researchers propose that the NCC was formed by collision between the Eastern Block and Western Block along the Trans-North China Orogen at ~1.85 Ga, others advocate a ~2.5 Ga cratonization event. These controversies are largely resulted from the lack of knowledge about (1) the nature of Archean basement terranes and comparative studies of different terranes; (2) the genesis and tectonic attributes of late Paleoproterozoic to Mesoproterozoic tectono-magmatic events; and (3) the formation and evolution of Precambrian lithospheric mantle and crust-mantle interactions, which essentially controlled the crustal formation and evolution history.

The metamorphic basement terranes of Western Liaoning-Northeastern Hebei provinces are located at the northern margin of North China Craton, i.e., the northwestern part of Eastern Block. They comprise well-exposed Archean basement rocks, and late Paleoproterozoic to mid-Mesoproterozoic magmatic rocks, and are ideal to study the prolonged Precambrian evolution of continental crust and related crust-mantle geodynamic processes of NCC. These form the justification of Dr. Wei Wang's doctoral research work. Detailed geological, petrological, whole-rock geochemical, and zircon U–Pb and Lu–Hf isotopic data are provided for the Archean metavolcanic rocks of greenstone belt and granitoid gneisses in Western Liaoning, the late Paleoproterozoic Jianping diorite–monzonite–syenite suite and Pinggu K-rich volcanic rocks, and the newly discovered ~1.23 Ga mafic dyke swarms. These data are used to constrain (1) the magma source and genesis of each magmatic episode; (2) growth and evolution of continental crust, and crust-mantle interactions at each tectono-magmatic episode; and (3) the lithospheric mantle evolution and crust-mantle geodynamic evolution from Archean to Mesoproterozoic.

A series of new and innovative achievements were obtained in this doctoral thesis: (1) the ~2640–2534 Ma metavolcanic rocks in Western Liaoning show geochemical affinities to MORBs, island arc tholeiitic to calc-alkaline basalts, adakites, and high magnesium andesites, which are considered to have been formed by the partial melting of asthenospheric mantle at a mid-ocean spreading ridge and subsequent slab–mantle wedge interactions, respectively; (2) the ~2532–2506 Ma dioritic and TTG gneisses are divided into two subgroups, i.e., a high magnesium group (HMG) derived from the partial melting of descending slabs and a low magnesium group (LMG) from the partial melting of metabasaltic rocks at the arc root; (3) the ~2495 Ma potassium-rich granodioritic and monzogranitic gneisses are nearly coeval with ~2485 Ma granulite facies metamorphism, which could have been resulted from the partial melting of metamorphosed felsic volcanic and sedimentary rocks; (4) the ~1721–1696 Ma Jianping diorite–monzonite–syenite suite and ~1671–1625 Ma Pinggu K-rich volcanic rocks were derived from the partial melting of enriched subcontinental lithospheric mantle and depleted asthenospheric mantle, respectively, forming at post-collisional to post-orogenic settings following final amalgamation of NCC; and (5) the newly discovered ~1.23 Ga mafic dyke swarms cover an area of $\sim 0.6 \times 10^6$ km^2, which could have been produced by complex asthenosphere–lithospheric mantle interactions under a mantle plume setting.

Based on the above studies, the prolonged Precambrian (~2.6–1.2 Ga) lithospheric mantle evolution and crust-mantle geodynamic processes of Western Liaoning-Northeastern Hebei provinces are established for the first time, highlighting that (a) the Western Liaoning Province was evolved at an Archean accretionary orogenic system, recording subduction accretion-related crust-mantle geodynamic processes from mid-ocean ridge spreading, through initiation and maturation of an intra-oceanic arc system, to the final arc-continent accretion, which is marked by intense ~2.6–2.5 Ga crustal growth; (b) the metasomatized depleted Archean lithospheric mantle was gradually evolved to an enriched mantle through close-system evolution during Paleoproterozoic. It was further modified by late Paleoproterozoic eastward subduction between the Eastern Block and Western Block, which served as the major mantle sources of the widespread ~1780–1680 Ma magmatic rocks within the NCC; and (c) the late Paleoproterozoic enriched lithospheric mantle witnessed two major episodes of vertical accretion processes triggered by the ~1671–1625 Ma post-orogenic lithospheric delamination and ~1230 Ma global mantle plume events, which led to the final breakup of global Columbia supercontinent.

These new studies and achievements in this doctoral thesis provide critical insights into the Precambrian crustal and geodynamic evolution of not only North China Craton, but also our Planetary Earth, particularly from the viewpoint of crust-mantle interactions. Though when and how plate tectonic processes started on earth remain contentious, this doctoral thesis provides some critical lines of evidence supporting that Neoarchean lateral subduction–accretion processes could have been operated in the North China Craton. Dr. Wang's current research focus on the comparison of crust-mantle interaction processes in the late Archean subduction–accretion system along the northern margin of NCC with those of modern ones as well as early Archean pre-subduction geodynamic regimes, which open a new window into our further understanding of the early geodynamic evolution history of the Earth. Accordingly, Dr. Wang's doctoral thesis provides a leading and exemplary ways for the future Precambrian studies of both the North China Craton and other ancient cratons in the world.

Beijing, China Prof. Shuwen Liu
June 2017

Parts of this doctoral thesis have been published in the following journal articles:

1. ***Wang, W.***, Liu, S.W., Santosh, M., Wang, G.H., Bai, X., Guo, R.R., 2015a. Neoarchean intra-oceanic arc system in the Western Liaoning Province: Implications for Early Precambrian crustal evolution in the Eastern Block of the North China Craton. ***Earth-Science Reviews*** 150, 329–364. (Reproduced with permission)
2. ***Wang, W.,*** Liu, S.W., Santosh, M., et al. 2015b. Late Paleoproterozoic geodynamics of the North China Craton: Geochemical and zircon U-Pb-Hf records from a volcanic suite in the Yanliao rift. ***Gondwana Research*** 27, 300–325. (Reproduced with permission)
3. ***Wang, W.,*** Liu, S.W., Santosh, M., Zhang, L.F., Bai, X., Zhao, Y., Zhang, S.H., Guo, R.R., 2015c. 1.23 Ga mafic dykes in the North China Craton reconstruct the Columbia supercontinent. ***Gondwana Research*** 27, 1407–1418. (Reproduced with permission)
4. ***Wang, W.,*** Liu, S.W., Santosh, M., Bai, X., Li, Q.G., Yang, P.T., Guo, R.R., 2013a. Zircon U–Pb–Hf isotopes and whole-rock geochemistry of granitoid gneisses in the Jianping gneissic terrane, Western Liaoning Province: Constraints on the Neoarchean crustal evolution of the North China Craton. **P*recambrian Research*** 224, 184–221. (Reproduced with permission)
5. ***Wang. W.,*** Liu, S.W., Bai, X., et al. 2013b. Geochemistry and zircon U-Pb-Hf isotopes of the late Paleoproterozoic Jianping diorite-monzonite-syenite suite of the North China Craton: Implications for petrogenesis and geodynamic setting. ***Lithos*** 162–163, 175–194. (Reproduced with permission)
6. ***Wang, W.,*** Liu, S.W., Wilde, S.A., Li, Q.G., Zhang, J., Bai, X., Yang, P.T., Guo, R.R., 2012. Petrogenesis and geochronology of Precambrian granitoid gneisses in Western Liaoning Province: Constraints on Neoarchean to early Paleoproterozoic crustal evolution of the North China Craton. ***Precambrian Research*** 222–223, 290–311. (Reproduced with permission)
7. ***Wang, W.,*** Liu, S.W., Bai, X., Yang, P.T., Li, Q.G., Zhang, L.F., 2011. Geochemistry and zircon U-Pb-Hf isotopic systematics of the Neoarchean Yixian-Fuxin greenstone belt, northern margin of the North China Craton: Implications for petrogenesis and tectonic setting. ***Gondwana Research*** 20, 64–81. (Reproduced with permission)

Acknowledgements

I am lucky to have the opportunity to study and live in the historic campus of Peking University (namely Yanyuan in Chinese) in the past five years (2009–2014). During my Ph.D. study and preparation of this dissertation, I have received great help, support, and encouragement from many people around me, and I would like to express my sincerely appreciations to them.

Firstly and specially, I want to express my deepest appreciations to my supervisor, Prof. Shuwen Liu in the School of Earth and Space Sciences, Peking University. The dissertation could not have been successfully accomplished without his kind guidance, encouragement, and support in terms of both my life and study. His rigorous scientific attitude, profound knowledge, and hard-working style exert significant impacts on my career. In fact, this dissertation should be regarded as a synthesis and extension of seven peer-reviewed international SCI papers I have published in the past five years. Meticulous care and support from Teacher Guixin Nie, Prof. Liu's wife, are also greatly appreciated.

Many thanks are given to Prof. Lifei Zhang, Prof. Yongfeng Zhu, Prof. Haifei Zheng, and associate Profs. Yulin Liu and Qiugen Li in the School of Earth and Space Sciences, Peking University, for their kind suggestions on my research work. I also appreciate Prof. Mingguo Zhai and Prof. Jinghui Guo (Institute of Geology and Geophysics, Chinese Academy of Sciences), Prof. Guochun Zhao (the University of Hongkong), and Prof. Yusheng Wan, Prof. Yue Zhao, and Prof. Shuanhong Zhang (Chinese Academy of Geological Sciences), for their suggestion, and support during my Ph.D. study and the publication of seven SCI papers. Gratefulness is given to my colleagues from Prof. Liu's research group, including Lishuang Guo, Kai Yang, Fan Zhang, Youzhang Chen, Pengtao Yang, Xiang Bai, Rongrong Guo, Ming Yan, Boran Guo, Zhengbin Deng, and Fangyang Hu et al., for their kind help and support from field work, laboratory experiment, to the final writing of this dissertation. Special thanks are given to Xiang Bai and Rongrong Guo, as we have studied and undertaken field work together during the past five years.

Great thanks are expressed to the laboratory supports from Fang Ma, Libing Gu, Bin Yang, Debao Ni, and Qiuyue Jia in the Key Laboratory of Orogenic Belts and Crustal Evolution of Peking University; Li Chen in the SEM Laboratory of Peking University; Li Su in the Geological Lab Centre at China University of Geosciences, Beijing; and Zhaochu Hu in the State Key Laboratory of Geological Processes and Mineral Resources, China University of Geosciences in Wuhan. Their kind help and assistance during laboratory experiments and the obtained geochemical data are key foundation of this dissertation.

Finally, I would like to express my deepest appreciations to my parents (Zhaokun Wang and Huanmei Xiao) and my wife (Pei Zhang) for their selfless love and support, which encourage me to have walked through one important period in my life. They are the source of endless powers in my career and life. This book is dedicated to them and our forthcoming baby.

Beijing, China
December 2017

Wei Wang

Contents

About the Author

Dr. Wei Wang received his doctor's degree in June 2014 from the Peking University. His Ph.D. thesis was nominated as the outstanding doctoral thesis in Peking University during his graduation. He has also gained various awards and prizes for the prominent research work during his Ph.D. study, including the award of National Lisiguang Outstanding Doctoral Student (2012, four Ph.D. students per year nationwide) and the "Top Ten Academic Ph.D. students" of Peking University in 2013.

He now works at the China University of Geosciences, Beijing, as an Associate Professor (since January 2016). His research focuses on two major aspects: (1) Archean continental crust formation and evolution as well as crust-mantle geodynamic processes; and (2) Proterozoic magmatism (e.g., mafic dyke swarms and alkaline igneous suites) and crust-mantle geodynamic processes as well as supercontinent reconstruction.

Chapter 1
Introduction

Abstract In the past decade, great achievements have been obtained in terms of sequences of Precambrian geological events, crustal growth and evolution, and Paleoproterozoic tectonic framework of the North China Craton. However, some key scientific issues are still unresolved, particularly the timing and tectonic model of Archean crustal growth and evolution, Archean tectonic framework of the North China Craton (especially the Eastern Block), and late Paleoproterozoic to Mesoproterozoic geodynamic processes. It is noteworthy that crustal evolution and geodynamic processes are essentially controlled by magma convection and crust-mantle interactions at any tectonic environments. Therefore, comprehensive studies of the nature and evolution of the magma sources and crust-mantle interactions for different episodes of Precambrian mafic to felsic rocks are key to our understanding of both the late Archean to Paleoproterozoic crustal growth and evolution as well as geodynamic evolution of the North China Craton. In this dissertation, systematic studies of geology, petrology, zircon U–Pb isotopic chronology and Lu–Hf isotopes, and whole-rock major and trace elements were conducted on the Neoarchean greenstone metavolcanic rocks and granitoid gneisses in Western Liaoning, late Paleoproterozoic Jianping diorite-monzonite-syenite suite and Pinggu K-rich volcanic rocks, as well as $\sim$1.23 Ga mafic dykes in the Western Liaoning-Northeastern Hebei Provinces. All these studies are combined, aiming to (1) decipher the nature of magma sources, genesis, and crust-mantle interactions for each episode of lithological unit or assemblage; (2) establish the prolonged Neoarchean to Mesoproterozoic evolution of the lithospheric mantle and crust-mantle interactions; and (3) provide further constraints on the Precambrian crustal formation and evolution as well as geodynamic evolution of the North China Craton.

Keywords North China Craton · Western Liaoning-Northeastern Hebei Provinces Archean to Mesoproterozoic crust-mantle geodynamics · Crustal growth and evolution · Lithospheric mantle evolution

W. Wang, *Archean-Mesoproterozoic Crustal Evolution and Crust-Mantle Geodynamics of Western Liaoning-Northeastern Hebei Provinces, North China Craton*, Springer Theses, https://doi.org/10.1007/978-981-10-7922-1_1

1.1 Research Background

1.1.1 Archean Greenstone Belt and Crust-Mantle Interactions

The “Greenstone belt” was initially put forward at the meeting of North Atlantic countries hold in Canada at 1965, which are used to describe a series of supracrustal rocks preserved in the “Sea of granitoid gneisses” [15]. The greenstone belt rocks and granitoid gneisses are closely related, and they are together termed as the “Granite-greenstone belt”. Archean greenstone belts are widely distributed within nearly all ancient cratons, and the Nuvvuagittuq greenstone belt exposed in the northern Quebec, Canada, is the oldest one (~4.3–3.8 Ga) [67, 93]. They are always the focus of Precambrian research, since the record of valuable clues about early formation and evolution of both the continental crust and mantle, crust-mantle interactions, and related geodynamics, as well as the preservation of prolific ore deposits, such as Fe, Au, Cu, Pb, Zn, and Ni.

Greenstone belts are linear- to irregular-shaped, synformal supracrustal rock succesions, commonly with a width of 10–50 km and a length of 100–300 km. They are characterized by an exposed stratigraphic thickness of 10–20 km, and contain dominantly mafic to ultramafic volcanic and intrusive rocks, as well as subordinate but important intermediate to acidic volcanic rocks, pyroclastic rocks, terrigenous clastic rocks, and chemical sedimentary rocks. These rocks are commonly subjected to greenschist to amphibolite facies metamorphism, recording multiple episodes of metamorphism and deformation. In general, the greenstone volcano-sedimentary rocks show tectonic or intrusive relationship with surrounding granitoid rocks, with the latter being either younger than or served as the basement of greenstone rock sequences [15, 17, 19, 41].

Recently, increasingly more studies have been performed on the genesis of Archean greenstone belts, especially focusing on several special lithological types, e.g., komatiites, boninites, Nb-enriched basalts, and alkaline basalts, and they record apparently distinct crust-mantle geodynamic processes. Komatiites are a series of Mg-rich ultramafic to mafic volcanic rocks. Mineral assemblages are olivine and pyroxene phenocrysts (or skeleton crystals) with minor Cr-spinel, and glassy matrix, and they constitute a typical spinifex texture [95]. Geochemically, they are characterized by $MgO > 9\%$, $CaO/Al_2O_3 > 1$ and low alkalis ($K_2O < 0.9\%$), which can be subdivided into two petrochemical types, i.e., olivine komatiites ($SiO_2 < 44\%$, $MgO > 20\%$) and basaltic komatiites ($SiO_2 = 44–56\%$, $MgO = 9–20\%$). Most researchers suggest that komatiites were derived from high degrees of partial melting of deep and dry mantle sources under high temperatures, with depths of 70–270 km (2–9 Gpa) and eruption temperatures of 1400–1600 °C, which are commonly linked to a mantle plume setting [65, 91]. Komatiites usually occur interlayered with tholeiitic basalts, with the former produced by high temperature plume axial commonly with recycled oceanic crust materials, whereas the latter formed by low temperature plume annulus with local involvement of shallow lithospheric mantle materials [10, 37, 38]. Parman et al. [68] argued that komatiites may be generated by the partial melting of a shallow depleted mantle that was metasomatized by slab-derived fluids at a convergent arc setting. Nonetheless, the association of komatiites and tholeiitic basalts has been proposed to be generated at oceanic plateau, cratonic margin, or is closely intercalated with subduction-related volcanic assemblages [2, 3, 77, 83].

Boninites are water-rich and high magnesium andesitic rocks with a saturation of silica [40, 73]. They are characterized by: (1) moderate SiO_2 (>53%) and high MgO, Mg#, and compatible elements (e.g., Cr, Co, and Ni); (2) low TiO_2 (<0.5%) but high Al_2O_3/TiO_2 (>22); (3) U-shaped chondrite-normalized rare earth element (REE) patterns; and (4) strong depletion of heavy REEs (HREEs) and high field strength elements (HFSEs), low Ti/Zr and Zr/Y ratios, and enrichment of Zr and Hf relative to the neighboring middle REEs [74]. It is suggested that the genesis of boninites was probably related to high thermal gradients, mantle decompression, and the addition of water [21]. They may have experienced a two-stage genetic process: (1) high degree partial melting of a primitive mantle; and (2) the generated ultra-depleted mantle source was subsequently metasomatized by slab-derived materials, and the partial melting of this metasomatized mantle at an incipient subduction or a back-arc extension setting formed boninites [88]. Archean boninites were discovered for the first time in the Abitibi greenstone belt, Canada [39]. They are closely interlayered with komatiites-tholeiitic basalts, which may be generated by plume-arc interaction processes [118]. Recently, Archean boninites are increasing identified in Isua (Greenland), Koolyanobbing (Yilgarn), Gadwal (India), and North Chaoyang-Fuxin-Yixian (Western Liaoning of North China Craton) greenstone belts [2, 62, 78, 108]. They record probably a common crust-mantle process involving the partial melting of an ultra-depleted mantle that was previously metasomatized by slab-derived materials under a subduction-related arc setting.

Nb-enriched basalts were firstly identified in the Zamboanga Island of Philippines [82]. Compared to typical island arc magmatic rocks, they show higher TiO_2 (1–2%) and Nb (7–16 ppm) contents, and lower LILE (large ion lithophile element)/HFSE and HREE/HFSE ratios. On the primitive mantle (PM)-normalized multi-element plot, they display weakly negative Nb–Ta anomalies, with $(La/Nb)_{PM}$ ratios lower than 2. Importantly, the Nb-enriched basalts are commonly associated with adakites, implying that they may be genetically linked to the metasomatism of mantle wedge materials by slab melts [81]. Nonetheless, Castillo et al. [11, 12] argued that Nb-enriched basalts in the Jolo Island of Phillippines may be produced by mixing of depleted and enriched materials from the mantle wedge, with the enriched materials probably sourced from the nearby seamount of South China Sea. The first Archean Nb-enriched basalts were discovered by Wyman et al. [119] in the Wabigoon greenstone belt, Canada, and they were considered to be formed under a back-arc or intra-arc basin setting. Recently, increasingly more Nb-enriched basalts were documented in the Eastern Hebei of North China Craton, Wawa and Wabigoon greenstone belts of Canada, and Penakacherla terrane of India [26, 29, 31, 119]. Particularly in the Wawa greenstone belt, the close association of

Nb-enriched basalts, adakites, and high magnesian andesites indicates that they could have been produced by crust-mantle interaction processes including partial melting of subducted oceanic slabs and interactions between the slab melts and mantle wedge materials [79].

Metavolcanic rocks in the Archean greenstone belts are mostly tholeiitic to calc-alkaline in composition, with rare alkaline rocks [9]. Whether there are enriched Archean mantle sources or not is still enigmatic, since plume-related komatiites-tholeiitic basalts and arc-related volcanic rocks show dominantly depleted isotopic compositions [80]. Recently, some Archean alkaline basalts were identified in the Superior Province of Canada, Dharwar Craton of India, as well as the Eastern Hebei Province of North China Craton [26, 61, 80]. Petrogenetic studies reveal that they may record recycling of continental crust materials, reflecting Archean mantle heterogeneity and the diversification of Archean geodynamic processes [36, 75]. Notably, it is usually difficult to identify the nature and heterogeneity of Archean mantle sources due to the mobility of Sr–Pb isotopic system and elements Rb, Ba, Pb, K, and Sr in the Archean metamorphic rocks. In this case, systematic studies of whole rock major and trace elements (especially REE, HFSE and transition group elements) and Sm–Nd isotopes as well as zircon Lu–Hf isotopes are key to resolve this issue [34, 38, 61, 83].

1.1.2 Archean Plate Tectonics

When and how plate tectonics began to operate on our planetary Earth is one of the major issues of Precambrian research. It is suggested by some researchers that there are no plate tectonics during the Archean period due to high thermal gradients, and the lack of ophiolites and high pressure metamorphic rocks [5, 6, 90]. However, increasingly more lines of evidence indicate that plate tectonics could have been initiated during the Archean period [20, 64, 75, 87]: (1) ~3.8 Ga sheeted dykes and associated pillow lavas in the Isua supracrustal belt of southwest Greenland may constitute the oldest SSZ-type ophiolite in the world [20]; (2) the mineral association of garnet and albite in the ~3.2 Ga amphibolites of south Africa records a low thermal gradient (1.2–1.5 Gpa and 600–650 °C) resembling those of Phanerozoic subduction zones [64]; (3) ~2.87–2.70 Ga eclogites have been discovered in the Kola peninsula and Greenland, indicating local presence of Mesoarchean to Neoarchean low temperature and high pressure metamorphism [63, 92]; (4) the appearance of eclogite-bearing diamonds after ~3.0 Ga may also indicate the onset of plate tectonics during late Archean [86]; (5) all the ~3.8–3.0 Ga metamorphosed mafic to ultramafic rocks in the southwest Greenland show typical arc-related geochemical features, which may be produced by the interaction of subducted oceanic slabs with the mantle wedge materials during the initiation and gradual maturation of Archean subduction zones [76]. Interestingly, the intercalation of komatiites-tholeiitic basalts and calc-alkaline basaltic-andesitic-dacitic-rhyolitic rocks as well as subordinate boninites, low-Ti tholeiities, Nb-enriched basalts, high magnesium andesites, and adakites, suggest that they could have been evolved under a subduction-related arc or a plume-arc interaction environment [35, 38, 76, 80, 118].

In the Pilbara Craton of Australia, the ~3.5–3.2 Ga West Pilbara terrane is surrounded by ~3.0 Ga linear-shaped metavolcanic rocks, with the latter showing features of exotic accreted terranes and island arc complex [87]. They may be evolved under a Mesoarchean subduction-accretion process. The stratigraphic sequences of >3.8 Ga metavolcanics rocks in the Quebec area, Canada show close affinities to those produced in the modern incipient subduction environment of Izu-Bonin-Mariana system of southwest Pacific, implying probably early Archean onset of plate tectonics [69, 93].

1.2 Research Progress and Key Issues of Precambrian Geology of North China Craton

1.2.1 Summary of Precambrian Research of North China Craton

(1) Increasing discovery of ancient crustal materials

The North China Craton (NCC) is one of the oldest cratons in the world, with ~3.8 Ga granitoid gneisses developed in the Anshan area [50, 58, 97, 100]. In the Huangbaiyu area of Eastern Hebei Province, detrital zircons of ~3.86–3.13 Ga in age are preserved in the Caozhuang Complex [46, 111]. ~3.6 Ga felsic granulite xenoliths have been recognized in the Mesozoic volcanic rocks of Xinyang area, southern margin of North China Craton [137]. Recently, a ~4.17 Ga xenocrystic zircon grain is identified in the Neoarchean amphibolites of Benxi area [16]. Systematic zircon Lu–Hf isotopes reveal that there are ~3.8 Ga depleted mantle beneath the North China Craton. Some zircon grains fall below the ~4.0 Ga crustal evolution line, which together with the ~4.17 Ga zircon grain, suggesting the presence of ancient continental crust materials possibly older than 4.0 Ga in the Anshan-Benxi area [23]. ~2.7 Ga rocks are widely developed in the Western Shandong, Eastern Shandong, Hengshan, Fuping, Zhongtiao, Huoqiu, and Wuchuan areas, which represent the important geological imprints of global ~2.7 Ga crustal growth ([96] and references therein).

(2) Early Precambrian tectonic framework of North China Craton

The North China Craton has experienced two major episodes of early Precambrian tectonothermal events at ~2.7–2.5 Ga and ~2.1–1.7 Ga [126, 127, 133]. Most researchers believe that this ancient craton was formed by collision among several microcontinents, whereas the number of microcontinents and the collision timing and pattern among them remain hotly debated [27, 28, 42, 47, 53, 56, 57, 118, 126–128, 133]. It is proposed by some researchers that the North China Craton was welded by the collision between Eastern Block (EB) and Western Block (WB) along the Trans-North China Orogen (TNCO) at ~1.85 Ga [27, 28, 47, 53, 56, 57, 129, 130, 133, 136]. The Eastern Block experienced ~2.1–1.9 Ga rifting and subsequent subduction-collision events, forming the Jiao-Liao-Ji Belt, whereas the Western Block was amalgamated by the collision between the Yinshan Block in the north and the Ordos Block in the south along the E-W trending Khondalite Belt at ~1.92 Ga [128]. Zhai et al. [129] suggested that the North China Craton consists of six ancient continental nucleus, i.e., Jiaoliao, Qianhuai, Xuchang, Fuping, Jining, and Alashan blocks. The unified crystalline basement of NCC was considered to have been consolidated through late Archean continent-continent and arc-continent collision, and they experienced ~2.30–1.82 Ga rifting-subduction-accretion processes and ~1.82–1.60 Ga extension-related tectonothermal events [126–127].

(3) Early Precambrian crustal growth and geodynamic processes

Distinct from most other cratons in the world, the North China Craton is characterized by a major episode of tectonothermal event at ~2.6–2.5 Ga. On the basis of anti-clockwise metamorphic P-T-t paths of mafic granulites, large exposure region of late Neoarchean granitoid gneisses, ~2.7 Ga komatiites in Western Shandong, and the nearly coeval magmatic (>2.50 Ga) and metamorphic events (~ 2.50–2.48 Ga), some researchers propose that the Eastern Block of North China Craton was evolved under a mantle plume setting during the late Neoarchean [24, 115, 133, 136]. On the other hand, others argued that plate tectonic processes could be an important late Neoarchean crust-mantle geodynamic regime for the Eastern Block, as revealed by comprehensive geochemical, chronological, and crust-mantle interaction studies of representative lithological assemblages in the Western Liaoning, Eastern Hebei, Northern Liaoning-Southern Jilin, Fuping-Wutai, and Dantazi Complex of Northern Hebei [26, 44, 45, 48, 51–57, 102, 105, 107, 108]. Moreover, both the supracrustal metavolcanic rocks and plutonic granitoid gneisses in Eastern Hebei and Western Shandong show arc-like geochemical features as well as asymmetric distribution of lithological units with different ages, suggesting that they could have been formed at a convergent margin setting [66, 98, 99, 110].

Whole-rock Sm–Nd isotopic data reveal that the Eastern Block may have experienced two major episodes of crustal growth at ~3.6–3.2 Ga and ~3.0–2.6 Ga, respectively (Wu et al. [117]). Recently, numerous studies of zircon Lu–Hf isotopes have been performed on the basement rocks of North China Craton, and the calculated depleted mantle model ages indicate a major episode of crustal growth at ~2.8–2.7 Ga and dominantly crustal reworking during the period of 2.6–2.5 Ga [23]. Zircon Lu–Hf isotopic data of ~2.7 Ga granitoid gneisses throughout the NCC reveal that they were dominantly derived from the reworking of juvenile crustal materials, further suggesting that ~2.7 Ga is the major episode of crustal growth. Nonetheless, voluminous ~2.6–2.5 Ga metamorphosed ultramafic to mafic volcanic rocks in the NCC were sourced directly from mantle sources, and some dioritic and TTG gneisses were derived from complex crust-mantle interaction processes [26, 66, 105, 107, 108]. It is therefore suggested that ~2.6–2.5 Ga could also represent an important episode of crustal growth in the NCC [18, 48, 102, 108].

(4) Ultrahigh temperature metamorphism in the Western Block

Within the Khondalite Belt of the Western Block, Paleoproterozoic sapphirine-bearing ultrahigh temperature metamorphic events were recently reported in the Daqingshan and Ji'ning areas of Inner Mongolia [27, 70, 84]. The peak metamorphic temperature is up to 910–950 °C, and the metamorphic age is ~1.93–1.92 Ga [27]. Various models have been proposed to explain this episode of extreme metamorphism, e.g., (1) mantle upwelling in a post-collisional setting; (2) ridge subduction; or (3) emplacement of high temperature gabbronorites [27, 70, 129].

(5) Proterozoic tectono-magmatic events and supercontinent reconstruction

After consolidation of the North China Craton, the united crystalline basement experienced intense extension with the development of several rifts (e.g., Yanliao, Xiong'er, and Zha'ertai-Bayan Obo-Huade rifts), forming thick Proterozoic sedimentary covers as well as voluminous extension-related magmatism [60, 72, 103, 105, 124, 131, 132]. A ~1.78 Ga large igneous provence was established along the Trans-North China Orogen (TNCO), with the mafic dykes and Xiong'er volcanic rocks considered to have been formed by mantle plume processes [72]. Whereas some others argued that the Xiong'er volcanic rocks at the southern extent of the TNCO may be generated under active continental margin or post-collisional settings [109, 131]. Along the northern margin of the NCC, ~1.78–1.62 Ga alkaline plutonic and volcanic rocks as well as mafic dykes have been proposed to be evolved at post-collisional, continental rifting, or mantle plume settings [30, 33, 59, 103, 124].

The North China Craton could be an important component of the Paleo- to Mesoproterozoic Columbia supercontinent, since the ~1.85 Ga TNCO is coeval with global ~2.1–1.8 Ga orogenic events that assembled the supercontinent [47, 57, 129, 131–134]. However, the paleogeographic position of NCC within the Columbia supercontinent remains hotly debated, with the NCC linked variably to India, Baltica, or Siberia, respectively [13, 14, 112, 123, 134, 135].

Accordingly, although great achievements have been obtained regarding Precambrian timings of geological events, crustal evolution, and tectonic framework of the crystalline basement during the past two decades, some key scientific issues are still unresolved, e.g., timing and tectonic model of Archean crustal growth and evolution; Neoarchean tectonic framework of the North China Craton; and late Paleoproterozoic to Mesoproterozoic geodynamic processes, et al. Notably, crustal evolution and geodynamic processes are essentially controlled by mantle convection and crust-mantle interactions. The lithological assemblage and their geochemical features, the nature of their mantle sources, and crust-mantle interaction processes at diverse tectonic settings are apparently different. Thus, it is key to unravel the nature and evolution of Precambrian mantle sources as well as crust-mantle interactions so as to resolve the above issues.

1.2.2 Key Scientific Issues

(1) Nature of the Neoarchean lithospheric mantle and crust-mantle geodynamics

Recently, most studies of early Precambrian geological evolution of the North China Craton focused on the Paleoproterozoic mobile belts, whereas the Archean crystalline basement received relatively less attention. The late Neoarchean tectonic regime of the basement terranes in the Eastern Block is still hotly debated, which is largely resulted from reliance on zircon geochronology and metamorphic P-T-t paths. The large areal extent of late Neoarchean granitoid gneisses also cannot be linked to a specific tectonic regime. Importantly, the crustal evolution and geodynamic regimes are directly controlled by the thermal structure and convection of the underlying mantle. Different tectonic environments could be characterized by distinct nature and thermal structure of the mantle sources, as well as distinct lithological assemblages and geochemical features of the magmatic products. Part of the metavolcanic rocks in the Archean greenstone belt were directly derived from the mantle sources, which preserve crucial information about the nature of Archean mantle and the crust-mantle geodynamic regimes. On the other hand, voluminous Archean granitoid gneisses also record key clues of regional thermal gradients and crust-mantle interaction processes. Accordingly, combined studies of the nature of the lithospheric mantle and crust-mantle interactions recorded by the greenstone metavolcanic rocks and granitoid gneisses are important to fully unravel the late Neoarchean geodynamic regime of the Eastern Block.

(2) Paleoproterozoic changing of the lithospheric mantle sources and crust-mantle geodynamics

The nature of Paleoproterozoic geological events are key to reconstruct the tectonic framework of North China Craton. As documented above, some researchers suggest that the western margin of the Eastern Block experienced long-term subduction possibly since the late Neoarchean, which finally resulted in the collision between the Eastern Block and Western Block during the late Paleoproterozoic [129, 133, 134]. Whereas others argued that cratonization of the North China Craton occurred at the terminal Archean, and the united crystalline basement witnessed middle to late Paleoproterozoic rifting-subduction-collision processes [126, 127]. Recent studies reveal that late Neoarchean metabasaltic rocks in the North China Craton were mostly derived from a depleted mantle source, whereas late Paleoproterozoic mafic rocks were mainly produced by the partial melting of enriched lithospheric mantle sources [26, 30, 72, 108, 109, 124]. Apparently, the nature of lithospheric mantle underlying the North China Craton could have been significantly changed during the Paleoproterozoic, which is key to decipher the Precambrian tectonic evolution of the North China Craton. However, the definite crust-mantle geodynamic processes responsible for the changing lithospheric mantle remain unknown. Comparative studies of the mantle sources of the Neoarchean to late Paleoproterozoic mafic rocks throughout the North China Craton, especially the

Eastern Block, are crucial to understand the changes of lithospheric mantle, crust-mantle interactions, and geodynamic processes during Paleoproterozoic.

(3) Crust-mantle geodynamic processes responsible for the Yanliao rift

The lower boundary age of the Yanliao rift is another major debated issue regarding the Precambrian evolution of the North China Craton, and the deep geodynamic processes responsible for the onset of Yanliao rifting are still unknown [22, 43, 59, 71, 101, 103]. A series of ~1.68–1.62 Ga potassic volcanic rocks was developed within the Yanliao rift. They are not only key to unravel the nature and evolution of the lithospheric mantle as well as crust-mantle interactions during continental rifting, but also important for our understanding of the Paleoproterozoic change of the lithospheric mantle and crust-mantle geodynamic scenarios.

(4) Nature and evolution of Precambrian mantle sources and crust-mantle geodynamic evolution

The North China Craton experienced prolonged Precambrian crustal evolution and geodynamic processes, which were directly controlled by the nature and evolution of the underlying lithospheric mantle as well as crust-mantle interactions. However, rare studies have been focused on this new issue of Precambrian geology. In this doctoral thesis, the isotopic data of different episodes of Precambrian mafic rocks (~2.5–1.2 Ga) are compiled for the North China Craton, aiming to reveal the Precambrian evolution of the lithospheric mantle, which can further constrain the Precambrian crustal evolution and geodynamic processes of this ancient craton.

1.3 Objectives of this Thesis

Based on the above research achievements, it is clear that hot debates exist surrounding the late Archean and late Paleoproterozoic geodynamic setting of the North China Craton. The transition mechanism of the nature of lithospheric mantle during Paleoproterozoic remains enigmatic. Although zircon chronological and Lu–Hf isotopic data outpouring in the past decade have contributed greatly to the understanding of Precambrian sequences of geological events and crustal growth and evolution, there are some apparent limitations to use them to re-establish the Precambrian geodynamic processes. Crustal evolution and geodynamic processes are essentially controlled by and exclusively linked to a convective mantle with specific thermal structure and related crust-mantle interactions. For example, in a mantle plume setting, the mantle sources are featured by high temperature and the lack of water, the partial melting of which forming chiefly tholeiitic and alkaline basaltic rocks, with subordinate high magnesium rock series (e.g., picrites/komaiites). The underplating of mantle plume-derived magmas can trigger the partial melting of lower crust materials at a high temperature and water-poor environment, leading to the formation of mainly alkaline granitoid rocks. In comparison, the mantle wedge materials in a subduction zone setting are cool and hydrous, and the derivative arc magmas are dominantly calc-alkaline in composition with a lithological assemblage of basaltic-andesitic-dacitic-rhyolitic rocks. Mafic to ultramafic rocks were directly sourced from the hydrous mantle wedge materials, whereas felsic rocks are indirect products of mantle convection and crust-mantle interactions. Therefore, comprehensive studies of the nature and evolution of the mantle sources and crust-mantle interactions recorded by different episodes of Precambrian mafic to felsic rocks are key to our understanding of both the late Archean to Paleoproterozoic geodynamic evolution and the transition of lithospheric mantle in the North China Craton.

The Western Liaoning-Northeastern Hebei Provinces are located at the middle to east segments of the northern margin of North China Craton. In this area, prolonged Precambrian tectonothermal events are well developed, which represent a natural laboratory to study the Precambrian lithospheric mantle evolution and crust-mantle geodynamic processes: (1) Eoarchean to Neoarchean geological records, including ~3.86–3.13 Ga detrital zircons and widespread ~2.60–2.49 Ga metamorphosed volcano-sedimentary sequences and granitoid gneisses [26, 49, 51, 52, 58, 100, 102, 105]; (2) pervasive ~1.80–1.62 Ga extension-related tectono-magmatic events, forming the Jianping diorite-monzonite-syenite suite (JDMSS), Damiao anorthosite complex, Miyun rapakivi granites, and Pinggu K-rich volcanic rocks [103, 106, 124, 132]; and (3) two major episodes of Mesoproterozoic mafic dykes at ~1.33 and ~1.23 Ga ([104]; Zhang et al. [122]).

In this doctoral dissertation, systematic studies of geology, petrology, zircon U–Pb chronology and Lu–Hf isotopes, and whole-rock major and trace elements were conducted on the Neoarchean greenstone metavolcanic rocks and granitoid gneisses in the Western Liaoning, late Paleoproterozoic Jianping diorite-monzonite-syenite suite and Pinggu K-rich volcanic rocks, as well as ~1.23 Ga mafic dykes. All these studies were combined, aiming to (1) decipher the nature of magma sources, petrogenesis, and crust-mantle interactions of each episode of lithological unit or assemblage; (2) establish the prolonged late Neoarchean to Mesoproterozoic evolution of the lithospheric mantle and crust-mantle interactions; and (3) provide further constraints on the Precambrian crustal formation and evolution as well as geodynamic evolution of the North China Craton from the viewpoint of crust-mantle geodynamics.

1.4 Research Contents of this Thesis

The research contents of this doctoral thesis are summarized as follows:

(1) To study the late Neoarchean crustal growth and evolution, the nature and evolution of mantle sources, crust-mantle interactions and geodynamic processes recorded by the basement rocks in the Western Liaoning Province. This includes (I) establishing the lithological assemblages, spatial and temporal distributions,

the source characteristics and petrogenesis of different lithologies as well as the genetic relationships between the supracrustal metavolcanic rocks and granitoid gneisses; (II) reconstructing the late Neoarchean to Paleoproterozoic crustal evolution and crust-mantle interactions through comparison between the North Chaoyang-Fuxin-Yixian granite-greenstone belt and the high grade Jianping gneissic terrane; and (III) discussing the formation mechanism of late Neoarchean lithospheric mantle as well as the role of plate tectonics in the crust-mantle interaction processes in the Western Liaoning Province and adjacent terranes.

(2) To establish the precise formation ages of the late Paleoproterozoic diorite-monzonite-syenite suite and the K-rich volcanic rocks in the Tuanshanzi and Dahongyu Formations of Changcheng Group, and analyze the nature and evolution of their mantle sources, petrogenesis, and crust-mantle interaction processes. Combined with the isotopic data of voluminous ~1.78–1.68 Ga and minor ~2.4–1.8 Ga mafic rocks within the North China Craton, the transition mechanism of the Paleoperoterozic lithospheric mantle sources will be discussed.

(3) To determine the field geological characteristics, lithological assemblages, and emplacement ages of the ~1.23 Ga mafic dyke swarms in the North China Craton, and discuss the nature and evolution of Mesoproterozoic lithospheric mantle sources and related crust-mantle geodynamic processes.

(4) To summarize the crustal growth and evolution, nature of mantle sources, and crust-mantle interactions at different evolution stages from Neoarchean to Mesoproterozoic (~2.6–1.2 Ga) in the Western Liaoning-Northeastern Hebei Provinces, so as to establish the Precambrian crustal evolution, lithospheric mantle evolution, and crust-mantle geodynamic scenarios of the study area.

1.5 Methodology

Whole-rock samples were trimmed to remove the weathered surfaces, and the fresh portions were chipped and crushed to about 60–80 mesh, and then powdered in an agate mill to about 200 mesh for major and trace element analysis. Zircon grains were separated by standard density and magnetic techniques from crushed samples of 60–80 mesh, and handpicked under a binocular microscope. These zircon grains were mounted in epoxy resin discs, and polished to half the grain thickness. Prior to analyses, cathodoluminescence images were obtained using a scanning electron microscope at the SEM Laboratory of Peking University.

1.5.1 Whole-Rock Major Element Analyses

Sample powders were blended with lithium metaborate, and fused at 1100 °C in a Pt–Au crucible for 20–40 min. The melts were then cooled with resultant disks prepared for analyses. Loss on ignition (LOI) values were determined by measuring the weight loss after heating the samples at 1050 °C for 30 min. Major elements were analyzed using X-ray Fluorescence (XRF, Thermo Arl Advant XP+) at the Key Laboratory of Orogenic Belts and Crustal Evolution, Ministry of Education, Peking University, and were calibrated against standards GSR-1 (granite), GSR-2 (andesite), GSR-3 (basalt), GSR-9 (diorite), GSR-10 (gabbro), GSR-14 (granitoid gneiss), and GSR-15 (amphibolite). The analytical precision is $\leq 0.5\%$ for major element oxides [4, 107].

1.5.2 Whole-Rock Trace Element Analyses

Sample powders for trace element analyses were pre-treated at Peking University. 25 mg of the powders were placed into Savillex Teflon beakers, and then within a high-pressure bomb with a 1:1 mixture of HF–HNO_3. They were heated for 24 h at 80 °C, and then evaporated. After evaporation, 1.5 ml HNO_3, 1.5 ml HF and 0.5 ml $HClO_4$ were added, and the beakers were capped for digestion within a high-temperature oven at 180 °C for 48 h or longer until the powders were completely digested. Finally, the residue was diluted with 1% HNO_3 to 50 ml. Trace elements, including rare earth elements (REEs), were measured using an ELEMENT-I plasma mass spectrometer (Finnigan-MAT Ltd.) at the Key Laboratory of Orogenic Belts and Crustal Evolution, Peking University. Standards GSR-1 (granite), GSR-2 (andesite), GSR-3 (basalt), GSR-9 (diorite), GSR-10 (gabbro), GSR-14 (granitoid gneiss), and GSR-15 (amphibolite) were used for analytical control, and the measurement precision of trace elements was better than 5% (see Liu et al. [47, 56] for detailed analytical procedures).

1.5.3 Whole-Rock Rb–Sr Isotope Analyses

The magnetite diorite sample OCY44-1 from the ~1671–1696 Ma Jianping diorite-monzonite-syenite suite was selected to obtain whole-rock Rb–Sr isotopic data using a multi-collector VG 354 mass spectrometer in static mode at the Institute of Geology and Geophysics, Chinese Academy of Sciences (Beijing). Rb–Sr isotopic data for three samples, including one anorthosite and two mangerites from the ~1.74 Ga Damiao anorthosite complex in the central segment of the northern margin of the NCC, are cited for comparison [119]. Approximately 100–150 mg of whole-rock powder was digested in a mixture of HF–$HClO_4$ in the screw-top Teflon beakers, and Rb and Sr were separated by cation exchange columns, following the procedure of Zhang et al. [125]. Rb and Sr concentrations were determined by the isotope dilution method, using a mixed ^{87}Rb–^{84}Sr spike solution. Procedural blanks were <200 pg for Sr, and the $^{87}Sr/^{86}Sr$ ratio was normalized to $^{86}Sr/^{88}Sr = 0.1194$. During the analyses, the standard BCR-2 yielded a $^{87}Sr/^{86}Sr$ ratio of 0.705048 ± 0.000010 (2σ).

1.5.4 LA-ICPMS Zircon U–Pb Isotope Analyses

The separated zircon grains were analyzed for in situ zircon U–Pb isotopes and trace elements using a laser ablation inductively coupled plasma mass spectrometer (LA-ICP-MS) at the Geological Lab Center, China University of Geosciences, Beijing [121]. During analyses, the laser spot diameter and frequency were 36 μm and 10 Hz, respectively. Harvard zircon 91500 was used as an external standard for zircon U–Th–Pb analyses, and NIST610 as an external standard to calculate the contents of U, Th, Pb, and other trace elements in the analyzed zircon grains. The $^{207}Pb/^{206}Pb$ and $^{206}Pb/^{238}U$ ratios were calculated using GLITTER program [94], and common Pb was corrected using the method of Anderson [1]. Age calculations and concordia plots were done using Isoplot (ver. 3.0) [60]. Notably, it is common to have mixed analyses (i.e., down-hole variations) during LA-ICPMS U–Pb isotopic analyses because of intense laser ablation of the zircon grains, especially for the Archean zircon grains recording complex crustal evolution history. Nonetheless, these effects are insignificant for the chronological data in this thesis, since the isotopic signals from the analyzed zircon spots show no apparent changes of the isotopic ratios during the 35–40s' multiple analyses of any single zircon spot. These chronological data can be used with confidence to constrain the sequences of geological events in the study region.

1.5.5 SHRIMP Zircon U–Pb Isotope Analyses

The metabasaltic rock sample OFX08-5 (garnet clinopyroxene amphibolite) from the Fuxin-Yixian greenstone belt was dated using the SHIRMP II ion microprobe at the Beijing SHRIMP Center, Chinese Academy of Geological Sciences. The intensity of the Primary O^{2-} ion beam was 4–6 nA and spot sizes were ~30 μm, with each site rastered for 2–3 min prior to analysis. Five scans through the mass stations were made for each age determination. Reference zircons SL13 (U = 238 ppm [113] and TEMORA ($^{206}Pb/^{238}U$ age = 417 Ma [7] were used for elemental abundance and calibration of $^{206}Pb/^{238}U$, respectively. The common lead correction was applied using measured ^{204}Pb abundances. Data processing and assessment was carried out using the SQUID and ISOPLOT programs. $^{207}Pb/^{206}Pb$ ages are used for all data. Uncertainties for individual analyses are quoted at the 1 confidence level, whereas errors for weighted mean ages are quoted at the 95% confidence level. The analytical procedure for zircon was similar to that described by Williams [113].

1.5.6 Zircon Lu–Hf Isotope Analyses

In situ zircon Lu–Hf isotopic analyses were performed on the similar internal domains or close to the original pit used for U–Pb isotopic analyses, using a

Neptune Plus MC-ICP-MS (Thermo Fisher Scientific, Gemany) attached to a Geolas 2005 excimer ArF laser ablation system (Lambda physik, Göttingen, Germany) at the state Key Laboratory of Geological Processes and Mineral Resources, China University of Geosciences in Wuhan [32]. Beam diameter of 44 μm and repetition rate of 6 Hz were applied, and zircon 91500 and GJ-1 were used as the external standard and the unknown, respectively. During analyses, every eighth analysis of an unknown was followed by analyses of 91500 and GJ-1. The interference of ^{176}Yb and ^{176}Lu on ^{176}Hf could significantly affect the accuracy of ^{176}Hf/^{177}Hf ratios. ^{179}Hf/^{177}Hf and ^{173}Yb/^{171}Yb ratios were used to calculate the mass bias of Hf (β_{Hf}) and Yb (β_{Yb}), which were normalized to ^{179}Hf/^{177}Hf = 0.7325 and ^{173}Yb/^{171}Yb = 1.13017 [85] using an exponential correction for mass bias. Interference of ^{176}Yb on ^{176}Hf was corrected by measuring the interference-free ^{173}Yb isotope and using ^{176}Yb/^{173}Yb = 0.79381 [85] to calculate ^{176}Yb/^{177}Hf. The relatively minor interference of ^{176}Lu on ^{176}Hf was corrected by measuring the intensity of the interference-free ^{175}Lu isotope and using the recommended ^{176}Lu/^{175}Lu = 0.02656 [8] to calculate ^{176}Lu/^{177}Hf. We used the mass bias of Yb (β_{Yb}) to calculate the mass fractionation of Lu because of their similar physicochemical properties. The determined ^{176}Hf/^{177}Hf ratios for standards 91500 (0.282290 ± 0.000022) and GJ-1 (0.282011 ± 0.000021) are within error of the reported values [32, 115]. Relate formula of zircon Lu–Hf isotopes are as follows:

1. $\varepsilon Hf_{(0)} = ((^{176}Hf/^{177}Hf)_s/(^{176}Hf/^{177}Hf)_{CHUR,0} - 1) \times 1000$
2. $\varepsilon Hf_{(t)} = 10000\{[(^{176}Hf/^{177}Hf)_S - (^{176}Lu/^{177}Hf)_S \times (e^{\lambda t} - 1)]/[(^{176}Hf/^{177}Hf)_{CHUR,0} - (^{176}Lu/^{177}Hf)_{CHUR} \times (e^{\lambda t} - 1)] - 1\}$;
3. $T_{DM} = 1/\lambda \times \ln \{1 + [(^{176}Hf/^{177}Hf)_S - (^{176}Hf/^{177}Hf)_{DM}]/[(^{176}Lu/^{177}Hf)_S - (^{176}Lu/^{177}Hf)_{DM}]\}$;
4. $f_{Lu/Hf=}(^{176}Lu/^{177}Hf)_S/(^{176}Lu/^{177}Hf)_{CHUR}$-1;
   (^{176}Lu/^{177}Hf)s and (^{176}Hf/^{177}Hf)$_S$ are determined values for the zircon grain samples. The present ^{176}Hf/^{177}Hf and ^{176}Lu/^{177}Hf ratios of chondrite and depleted mantle are 0.282772 and 0.0332, and 0.28325 and 0.0384, respectively [8, 25]. $\lambda = 1.867 \times 10^{-11}$ a^{-1} [89]. f_{cc}, f_s and f_{DM} are $f_{Lu/Hf}$ values for the continental crust, zircon grain samples, and depleted mantle, respectively; $f_{cc} = -0.55$, $f_{DM} = 0.16$; t is the formation age of zircon samples.

References

1. Anderson T (2002) Correlation of common lead in U–Pb analyses that do not report 204Pb. Chem Geol 192:59–79
2. Angerer T, Kerrich R, Hagemann SG (2013) Geochemistry of a komatiitic, boninitic, and tholeiitic basalt association in the Mesoarchean Koolyanobbing greenstone belt, Southern Cross Domain, Yilgarn craton: implications for mantle sources and geodynamic setting of banded iron formation. Precambr Res 224:110–128
3. Arndt NT (2008) Komatiites. Cambridge University Press, Cambridge, p 467

4. Bai X, Liu SW, Guo RR, Zhang LF, Wang W (2014) Zircon U–Pb–Hf isotopes and geochemistry of Neoarchean dioritic-trondhjemitic gneisses, Eastern Hebei, North China Craton: constraints on petrogenesis and tectonic implications. Precambr Res 251:1–20
5. Bédard JH (2013) How many arcs can dance on the head of a plume?: A 'Comment' on: A critical assessment of Neoarchean 'plume only' geodynamics: evidence from the Superior province, by Derek Wyman, Precambrian Research, 2012. Precambr Res 229:189–197
6. Bédard JH (2006) A catalytic delamination-driven model for coupled genesis of Archaean crust and sub-continental lithospheric mantle. Geochimica et Cosmochimica Acta 70:1188–1214
7. Black LP, Kamo SL, Allen CM, Aleinikoff JN, Davis DW, Korsch RJ, Foudoulis C (2003) T TEMORA 1 a new zircon standard for Phanerozoic U–Pb geochronology. Chem Geol 200:155–170
8. Blichert-Toft J, Albarède F (1997) The Lu–Hf geochemistry of chondrites and the evolution of the mantle-crust system. Earth Planet Sci Lett 148:243–258
9. Blichert-Toft J, Arndt NT, Ludden JN (1996) Precambrian alkaline magmatism. Lithos 37:97–111
10. Campbell IH, Griffiths RW, Hill RI (1989) Melting in an Archean mantle plume: heads it's basalts, tails it's komatiites. Nature 339:697–699
11. Castillo PR, Solidum RU, Punongbayan RS (2002) Origin of high field strength element enrichment in the Sulu Arc, southern Philippines, revisited. Geology 30:707–710
12. Castillo PR, Rigby SJ, Solidum RU (2007) Origin of high field strength element enrichment in volcanic arcs: geochemical evidence from the Sulu Arc, Southern Philippines. Lithos 97:271–288
13. Chen LW, Huang BC, Yi ZY, Zhao J, Yan YG (2013) Paleomagnetism of ca. 1.35 Ga sills in northern North China Craton and implications for paleogeographic reconstruction of the Mesoproterozoic supercontinent. Precambr Res 228:36–47
14. Condie KC (2002) Breakup of a Paleoproterozoic supercontinent. Gondwana Res 5:41–43
15. Condie KC (1981) Archean greenstone belts. Elsevier, Amsterdam, pp 1–425
16. Cui PL, Sun JF, Sha DM (2013) Oldest zircon xenocryst (4.17 Ga) from the North China Craton. Int Geol Rev 55:1902–1908
17. De Wit M (2004) Archean greenstone belts do contain fragments of opholites. In: Kusky TM (ed) Precambrian ophiolites and related rocks. Elsevier, Amsterdam, pp 599–614
18. Diwu CR, Sun Y, Guo AL et al (2011) Crustal growth in the North China Craton at ~2.5 Ga: evidence from in situ zircon U–Pb ages, Hf isotopes and whole-rock geochemistry of the Dengfeng complex. Gondwana Res 20:149–170
19. Furnes H, De Wit M, Robins B (2013) A review of new interpretations of the tectonostratigraphy, geochemistry and evolution of the Onverwacht Suite, Barberton Greenstone Belt, South Africa. Gondwana Res 23:403–428
20. Furnes H, De Wit M, Staudigel H et al (2007) A vestige of Earth's oldest ophiolite. Science 315:1704–1706
21. Falloon TJ, Danyushevsky LV (2000) Melting of refractory mantle at 1.5, 2 and 2.5 GPa under anhydrous and H_2O-undersaturated conditions: implications for the petrogenesis of high-Ca boninites and the influence of subduction components on mantle melting. J Petrol 41:257–283
22. Gao LZ, Zhang CH, Yin CY, Shi XY, Wang ZQ, Liu YM, Liu PJ, Tang F, Song B (2008) SHRIMP zircon ages: basis for refining the chronostratigraphic classification of the Meso- and Neoproterozoic strata in North China old land. Acta Geoscientica Sinica 29:366–376 (in Chinese with English abstract)
23. Geng YS, Du LL, Ren LD (2012) Growth and reworking of the early Precambrian continental crust in the North China Craton: constraints from zircon Hf isotopes. Gondwana Res 21:517–529
24. Geng YS, Liu FL, Yang C (2006) Magmatic event at the end of the Archean in eastern Hebei Province and its geological implication. Acta Geol Sin (English version) 80:819–833

25. Griffin WL, Pearson NJ, Belousova E, Jackson SE, van Achterbergh E, O'Reilly SY, Shee SR (2000) The Hf isotope composition of cratonic mantle: LA-MC-ICPMS analysis of zircon megacrysts in kimberlites. Geochim Cosmochim Acta 64:133–147
26. Guo RR, Liu SW, Santosh M et al (2013) Geochemistry, zircon U–Pb geochronology and Lu–Hf isotopes of metavolcanics from eastern Hebei reveal Neoarchean subduction tectonics in the North China Craton. Gondwana Res 24:664–686
27. Guo JH, Peng P, Chen Y, Jiao SJ, Windley BF (2012) UHT sapphirine granulite metamorphism at 1.93–1.92 Ga caused by gabbronorite intrusions: implications for tectonic evolution of the northern margin of the North China Craton. Precambr Res 222–223:124–142
28. Guo JH, O'Brien PJ, Zhai MG (2002) High-pressure granulites in the Sanggan area, North China Craton: metamorphic evolution, P–T paths and geotectonic significance. J Metamorph Geol 20:741–756
29. Hollings P (2002) Archean Nb-enriched basalts in the northern Superior Province. Lithos 64:1–14
30. Han BF, Zhang L, Wang YM, Song B (2007) Enriched mantle source for Paleoproterozoic high Mg and low Ti–P mafic dykes in central part of the North China Craton: constraints from zircon Hf isotopic compositions. Acta Petrologica Sinica 23:277–284 (in Chinese with English abstract)
31. Hollings P, Kerrich R (2000) An Archean arc basalt–Nb-enriched basalt–adakite association: the 2.7 Ga Confederation assemblage of the Birch–Uchi greenstone belt, Superior Province. Contrib Miner Petrol 139:208–226
32. Hu ZC, Liu YS, Gao S, Liu WG, Zhang W, Tong XR, Lin L, Zong KQ, Li M, Chen HH, Zhou L, Yang L (2012) Improved in situ Hf isotope ratio analysis of zircon using newly designed X skimmer cone and jet sample cone in combination with the addition of nitrogen by laser ablation multiple collector ICP-MS. J Anal At Spectrom 27:1391–1399
33. Hu JL, Zhao TP, Xu YH, Chen W (2007) Geochemistry and petrogenesis of the high-K volcanic rocks in the Dahongyu Formation, North China Craton. J Miner Petrol 27:70–77 (in Chinese with English abstract)
34. Jackson MG, Dasgupta R (2008) Compositions of HIMU, EM1 and EM2 from global trends between radiogenic isotopes and major elements in ocean island basalts. Earth Planet Sci Lett 276:175–186
35. Jayananda M (2013) Geochemical constraints on komatiite volcanism from Sargur Group Nagamangala greenstone belt, Western Dharwar craton, Southern India: implications for Mesoarchean mantle evolution and continental growth. Geosci Front 4:321–340
36. Jenner FE, Bennett VC, Yaxley G (2013) Eoarchean within-plate basalts from southwest Greenland. Geology 41:327–330
37. Kerrich R, Xie QL (2002) Compositional recycling structure of an Archean super-plume: Nb-Th-U-LREE systematics of Archean komatiites and basalts revised. Contrib Miner Petrol 142:476–484
38. Kerrich R, Polat A, Wyman D, Hollings P (1999) Trace element systematics of Mg-, to Fe-tholeiitic basalt suites of the Superior Province: implications for Archean mantle reservoirs and greenstone belt genesis. Lithos 46:163–187
39. Kerrich R, Wyman D, Fan J (1998) Boninite series: low Ti-tholeiite associations from the 2.7 Ga Abitibi greenstone belt. Earth Planet Sci Lett 164:303–316
40. Kikuchi Y (1890) On pyroxenic compounds in certain volcanic rocks from Bonin Island. J Coll Sci Imp Univ Tokyo 3:67–89
41. Kröner A, Hoffmann JE, Xie HQ et al (2013) Generation of early Archean felsic greenstone volcanic rocks through crustal melting in the Kaapvaal craton, Southern Africa. Earth Planet Sci Lett 381:188–197
42. Kusky TM, Li JH (2003) Paleoproterozoic tectonic evolution of the North China Craton. J Asian Earth Sci 22:383–397

43. Li HK, Lu SN, Su WB, Xiang ZQ, Zhou HY, Zhang YQ (2013) Recent advances in the study of the Mesoproterozoic geochronology in the North China Craton. J Asian Earth Sci 72:216–227
44. Li QG, Liu SW, Wang ZQ et al (2011) Provenance and geotectonic setting of the Palaeoproterozoic Zhongtiao Group and implications for assembly of the North China Craton: whole-rock geochemistry and detrital zircon data. J Geol Soc 168:1215–1224
45. Li QG, Liu SW, Wang ZQ et al (2008) Contrasting provenance of Late Archean metasedimentary rocks from the Wutai Complex, North China Craton: detrital zircon U–Pb, whole-rocks Sm–Nd isotopic, and geochemical data. Int J Earth Sci 97:443–458
46. Liu SJ, Wan YS, Sun HY et al (2013) Paleo- to Eoarchean crustal evolution in eastern Hebei, North China Craton: New evidence from SHRIMP U–Pb dating and in situ Hf isotopic study of detrital zircons from paragneisses. J Asian Earth Sci 78:4–17
47. Liu SW, Zhang J, Li QG, Zhang LF, Wang W, Yang PT (2012) Geochemistry and U–Pb zircon ages of metamorphic volcanic rocks of the Paleoproterozoic Lüliang Complex and constraints on the evolution of the Trans-North China Orogen, North China Craton. Precambr Res 222–223:173–190
48. Liu F, Guo JH, Peng P, Qian Q (2012) Zircon U–Pb ages and geochemistry of the Huai'an TTG gneisses terrane: petrogenesis and implications for $\sim$2.5 Ga crustal growth in the North China Craton. Precambr Res 212–213:225–244
49. Liu SW, Santosh M, Wang W, Bai X, Yang PT (2011) Zircon U–Pb chronology of the Jianping Complex: implications for the Precambrian crustal evolution history of the northern margin of North China Craton. Gondwana Res 20:48–63
50. Liu DY, Wilde SA, Wan YS et al (2008) New U–Pb and Hf isotopic data confirm Anshan as the oldest preserved segment of the North China Craton. Am J Sci 308:200–231
51. Liu SW, Lü YJ, Feng YG, Zhang C, Tian W, Yan QR, Liu XM (2007) Geology and zircon U–Pb isotopic chronology of Dantazi Complex, Northern Hebei Province. Geol J China Univ 13:484–497 (in Chinese with English abstract)
52. Liu SW, Lü YJ, Feng YG, Liu XM, Yan QR, Zhang C, Tian W (2007) Zircon and monazite geochronology of the Hongqiyingzi complex, northern Hebei, China. Geol Bull China 26:1086–1100 (in Chinese with English abstract)
53. Liu SW, Zhao GC, Wilde SA, Shu GM, Sun M, Li QG, Tian W, Zhang J (2006) Th-U-Pb monazite geochronology of the Lüliang and Wutai Complexes: constraints on the tectonothermal evolution of the Trans-North China Orogen. Precambr Res 148:205–224
54. Liu SW, Tian W, Lv YJ et al (2006) Geochemistry, Nd isotopic characteristics of metamorphic complexes in Northern Hebei: implications for crustal accretion. Acta Geol Sinica (English version) 80:807–818
55. Liu SW, Pan YM, Xie QL, Zhang J, Li QG (2005) Geochemistry of the Paleoproterozoic Nanying granitic gneisses in the Fuping complex: implications for the tectonic evolution of the Central zone, North China Craton. J Asian Earth Sci 24:643–658
56. Liu SW, Pan YM, Xie QL, Zhang J, Li QG (2004) Archean geodynamics in the Central Zone, North China craton: constraints from geochemistry of two contrasting series of granitoids in the Fuping and Wutaishan complexes. Precambr Res 130:229–249
57. Liu SW, Pan YM, Li JH, Zhang J, Li QG (2002) Geological and isotopic geochemical constraints on the evolution of the Fuping Complex, North China Craton. Precambr Res 117:41–56
58. Liu DY, Nutman AP, Compston W, Wu JS, Shen QH (1992) Remmants of $\geq$3800 Ma crust in the Chinese part of the Sino-Korean Craton. Geology 20:339–342
59. Lu SN, Zhao GC, Wang HC, Hao GJ (2008) Precambrian metamorphic basement and sedimentary cover of the North China Craton: a review. Precambr Res 160:77–93
60. Ludwig KR (2003) User's Manual for Isoplot 3.00. A geochronological toolkit for Microsoft Excel. Special Publication No. 4a. Berkeley Geochronology Center, Berkeley, CA
61. Manikyamba C, Kerrich R (2011) Geochemistry of alkaline basalts and associated high-Mg basalts from the 2.7 Ga Penakacherla Terrane, Dharwar craton, India: an Archean depleted mantle-OIB array. Precambr Res 188:104–122

62. Manikyamba C, Napvi SM, Subba Rao DV et al (2005) Boninites from the Neoarchaean Gadwal Greenstone belt, Eastern Dharwar Craton, India: implications for Archaean subduction processes. Earth Planet Sci Lett 230:65–83
63. Mints MV, Belousova EA, Konilov AN et al (2010) Mesoarchean subduction processes: 2.87 Ga eclogites from the Kola Peninsula, Russia. Geology 38:739–742
64. Moyen JF, Stevens G, Kiseters A (2006) Record of mid-Archaean subduction from metamorphism in the Barberton terrain, South Africa. Nature 442:559–562
65. Nisbet EG, Cheadle M, Arndt N et al (1993) Constraining the potential temperature of the Archaean mantle: a review of the evidence from komatiites. Lithos 30:291–307
66. Nutman AP, Wan YS, Du LL, Friend CRL, Dong CY, Xie HQ, Wang W, Sun HY, Liu DY (2011) Multistage late Neoarchaean crustal evolution of the North China Craton, eastern Hebei. Precambr Res 189:43–65
67. O'Neil J, Francis D, Carlson RW (2011) Implications of the Nuvvuagittuq greenstone belt for the formation of Earth's early crust. J Petrol 52:985–1009
68. Parman SW, Grove TL, Dann JC (2001) The production of Barberton komatiites in an Archean subduction zone. Geophys Res Lett 28:2513–2516
69. Pearce JA (2014) Geochemical fingerprinting of the earth's oldest rocks. Geology 42:175–176
70. Peng P, Guo JH, Windley BF et al (2012) Petrogenesis of Late Paleoproterozoic Liangcheng charnockites and S-type granites in the central-northern margin of the North China Craton: implications for ridge subduction. Precambr Res 222:107–123
71. Peng P, Liu F, Zhai MG, Guo JH (2011) Age of the Miyun dyke swarm: constraints on the maximum depositional age of the Changcheng System. Chin Sci Bull 57:105–110 (in Chinese with English abstract)
72. Peng P, Zhai MG, Ernst RE, Guo JH, Liu F, Hu B (2008) A 1.78 Ga large igneous province in the North China craton: the Xiong'er Volcanic Province and the North China dyke swarm. Lithos 101:260–280
73. Peterson J (1891) Beitrge zur Petrographie von Sulphur Island, Peel Island, Hachijo und Mijakeshima. Jahrb Hamburg Wiss Anst 8:1–59
74. Piercey SJ, Murphy DC, Mortensen JK (2001) Boninitic magmatism in a continental margin setting. Yukon-Tanana terrane, southeastern Yukon. Can Geol 29:731–734
75. Polat A (2013) Geochemical variations in Archean volcanic rocks, southwestern Greenland: traces of diverse tectonic settings in the early Earth. Geology 41:379–380
76. Polat A, Appel PWU, Fryer BJ (2011) An overview of the geochemistry of Eoarchean to Mesoarchean ultramafic to mafic volcanic rocks, SW Greenland: Implications for mantle depletion and petrogenetic processes at subduction zones in the early Earth. Gondwana Res 20:255–283
77. Polat A, Li J, Fryer B et al (2006) Geochemical characteristics of the Neoarchean (2800–2700 Ma) Taishan greenstone belt, North China Craton: evidence for plume-craton interaction. Chem Geol 230:60–87
78. Polat A, Hofmann AW, Rosing MT (2002) Boninite-like volcanic rocks in the 3.7–3.8 Ga Isua greenstone belt, West Greenland: geochemical evidence for intra-oceanic subduction zone processes in the early Earth. Chem Geol 184:231–254
79. Polat A, Kerrich R (2001) Magnesian andesites, Nb-enriched basalt-andesites, and adakites from late-Archean 2.7 Ga Wawa greenstone belts, Superior Province, Canada: implications for late Archean subduction zone petrogenetic processes. Contrib Miner Petrol 141:36–52
80. Polat A, Kerrich R, Wyman DA (1999) Geochemical diversity in oceanic komatiites and basalts from the late Archean Wawa greenstone belts, Superior Province, Canada: trace element and Nd isotope evidence for a heterogeneous mantle. Precambr Res 94:139–173
81. Sajona FG, Maury RC, Bellon H et al (1996) High field strength element enrichment of Pliocene-Pleistocene island arc basalts, Zamboanga Peninsula, western Mindanao (Philippines). J Petrol 37:693–726
82. Sajona FG, Maury RC, Bellon H et al (1993) Initiation of subduction and the generation of slab melts in western and eastern mindanao, Philippines. Geology 21:1007–1010

83. Said N, Kerrich R (2009) Geochemistry of coexisting depleted and enriched Paringa Basalts, in the 2.7 Ga Kalgoorlie Terrane, Yilgarn Craton, Western Australia: evidence for a heterogeneous mantle plume event. Precambr Res 174:287–309
84. Santosh M, Sajeev K, Li JH (2006) Extreme crustal metamorphism during Columbia supercontinent assembly: evidence from North China Craton. Gondwana Res 10:256–266
85. Segal I, Halicz L, Platzner IT (2003) Accurate isotope ratio measurements of ytterbium by multiple collection inductively coupled plasma mass spectrometry applying erbium and hafnium in an improved double external normalization procedure. J Anal At Spectrom 18:1217–1223
86. Shirey SB, Richardson SH (2011) Start of the Wilson cycle at 3 Ga shown by diamonds from subcontinental mantle. Science 333:434–436
87. Smithies RH, Kranendonk MJ, Champion DC (2007) The Mesoarchean emergence of modern-style subduction. Gondwana Res 11:50–68
88. Smithies RH, Champion DC, Sun SS (2004) The case for Archeaen boninites. Contrib Miner Petrol 147:705–721
89. Söderlund U, Patchett PJ, Vervoort JD, Isachsen CE (2004) The ^{176}Lu decay constant determined by Lu–Hf and U–Pb isotope systematics of Precambrian mafic intrusions. Earth Planet Sci Lett 219:311–324
90. Stern R (2008) Modern-style plate tectonics bagan in Neoproterozoic time: an alternative interpretation of Earth's tectonic history. In: Condie KC, Pease V (eds), When did plate tectonics begin on planet earth? Geol Soc Am, Special paper 440:265–280
91. Stiegler MT, Lowe DR, Byerly GR (2010) The petrogenesis of volcaniclastic komatiites in the Barberton greenstone belt, South Africa: a textural and geochemical study. J Petrol 51:947–972
92. Tappe S, Smart KA, Pearson DG et al (2011) Craton formation in Late Archean subduction zones revealed by first Greenland eclogites. Geology 39:1103–1106
93. Turner S, Rushmer T, Reagan M, Moyen JF (2014) Heading down early on? Start of subduction on Earth. Geology 42:139–142
94. Van Achterbergh E, Ryan CG, Jackson SE, Griffin WL (2001) Data reduction software for LA-ICPMS. Laser-ablation-ICPMS in the Earth Sciences: Principles and applications. Mineralogical Association of Canadian (Short Course Series) 29:239–243
95. Viljoen MJ, Viljoen RP (1969) The geology and geochemistry of the lower ultramafic unit of the Onverwacht Group and a proposed new class of igneous rocks. Spec Publ Geol SOC S Afr 2:55–85
96. Wan YS, Xie SW, Yang CH, Kröner A, Ma MZ, Dong CY, Du LL, Xie HQ, Liu DY (2014) Early Neoarchean ($\sim$2.7 Ga) tectono-thermal events in the North China Craton: a synthesis. Precambrian Res. 247:45–63
97. Wan YS, Zhang YH, Williams IS, Liu DY, Dong CY, Fan RL, Shi YR, Ma MZ (2013) Extreme zircon O isotopic compositions from 3.8 to 2.5 Ga magmatic rocks from the Anshan area, North China Craton. Chem Geol 352:108–124
98. Wan YS, Liu DY, Wang SJ, Yang EX, Wang W, Dong CY, Zhou HY, Du LL, Yang YH, Diwu CR (2011) $\sim$2.7 Ga juvenile crust formation in the North China Craton (Taishan-Xintai area, western Shandong Province): further evidence of an understated event from U–Pb dating and Hf isotopic composition of zircon. Precambr Res 186:169–180
99. Wan YS, Liu DY, Wang SJ et al (2010) Juvenile magmatism and crustal recycling at the end of the Neoarchean in Western Shandong Province, North China Craton: evidence from SHRIMP zircon dating. Am J Sci 310:1503–1552
100. Wan YS, Liu DY, Dong CY, Nutman AP, Wilde SA, Wang W, Xie HQ, Yin XY, Zhou HY (2009) The oldest rocks and zircons in China. Acta Petrologica Sinica 25:1793–1807 (in Chinese with English abstract)
101. Wan YS, Zhang Q, Song T (2003) SHRIMP ages of detrital zircons from the Changcheng System in the Ming Tombs area, Beijing: constraints on the protolith nature and maximum depositional age of the Mesoproterozoic cover of the North China Craton. Chin Sci Bull 48:2500–2506

102. Wang W, Liu SW, Santosh M, Wang GH, Bai X, Guo RR (2015) Neoarchean intra-oceanic arc system in the Western Liaoning Province: Implications for Early Precambrian crustal evolution in the Eastern Block of the North China Craton. Earth Sci Rev 150:329–364
103. Wang W, Liu SW, Santosh M et al (2015) Late Paleoproterozoic geodynamics of the north China Craton: geochemical and zircon U-Pb–Hf records from a volcanic suite in the Yanliao rift. Gondwana Res 27:300–325
104. Wang W, Liu SW, Santosh M, Zhang LF, Bai X, Zhao Y, Zhang SH, Guo RR (2015) 1.23 Ga mafic dykes in the North China Craton reconstruct the Columbia supercontinent. Gondwana Res 27:1407–1418
105. Wang W, Liu SW, Bai X et al (2013) Zircon U–Pb–Hf isotopes and whole-rock geochemistry of granitoid gneisses in the Jianping gneissic terrane, Western Liaoning Province: constraints on the Neoarchean crustal evolution of the North China Craton. Precambr Res 224:184–221
106. Wang W, Liu SW, Bai X, Li QG, Yang PT, Zhao Y, Zhang SH, Guo RR (2013) Geochemistry and zircon U–Pb–Hf isotopes of the late Paleoproterozoic Jianping diorite-monzonite-syenite suites of the North China Craton: implications for petrogenesis and geodynamic setting. Lithos 162–163:175–194
107. Wang W, Liu SW, Wilde SA, Li QG, Zhang J (2012) Petrogenesis and geochronology of Precambrian granitoid gneisses in Western Liaoning Province: constraints on Neoarchean to early Paleoproterozoic crustal evolution of the North China Craton. Precambr Res 222–223:290–311
108. Wang W, Liu SW, Bai X, Yang PT, Li QG, Zhang LF (2011) Geochemistry and zircon U–Pb–Hf isotopic systematics of the Neoarchean Yixian-Fuxin greenstone belt, northern margin of the North China Craton: implications for petrogenesis and tectonic setting. Gondwana Res 20:64–81
109. Wang XL, Jiang SY, Dai BZ (2010) Melting of enriched Archean subcontinental lithospheric mantle: evidence from the ca. 1760 Ma volcanic rocks of the Xiong'er Group, southern margin of the North China Craton. Precambr Res 182:204–216
110. Wang YJ, Zhang YZ, Zhao GC, Fan WM, Xia XP, Zhang FF, Zhang AM (2009) Zircon U–Pb geochronological and geochemical constaints on the petrogenesis of the Taishan sanukitoids (Shandong): implications for Neoarchean subduction in the Eastern Block, North China Craton. Precambr Res 174:273–286
111. Wilde SA, Vallly JW, Kita NT et al (2008) SHRIMP U–Pb and CAMECA 1280 oxygen isotope results from ancient detrital zircons in the Caozhuang quartzite, Eastern Hebei, North China Craton: evidence for crustal reworking 3.8 Ga ago. Am J Sci 308:185–199
112. Wilde SA, Zhao GC, Sun M (2002) Development of the North China Craton during the late Archaean and its final amalgamation at 1.8 Ga; some speculations on its position within a global Palaeoproterozoic supercontinent. Gondwana Res 5:85–94
113. Williams IS (1998) U–Th–Pb geochronology by ion microprobe. In: Mckibben MA, Shanks III WC, Ridley WI (eds) Applications of microanalytical techniques to understanding mineralizing processes. Rev Ecol Geol. vol 7, pp 1–35
114. Wu ML, Zhao GC, Sun M, Li SZ, Bao ZA, Tam PY, Eizenhöefer PR, He YH (2014) Zircon U–Pb geochronology and Hf isotopes of major lithologies from the Jiaodong Terrane: implications for the crustal evolution of the Eastern Block of the North China Craton. Lithos 190–191:71–84
115. Wu FY, Yang YH, Xie LW, Yang JH, Xu P (2006) Hf isotopic compositions of the standard zircons and baddeleyites used in U–Pb geochronology. Chem Geol 234:105–126
116. Wu FY, Zhao GC, Wilde SA, Sun DY (2005) Nd isotopic constraints on crustal formation in the North China Craton. J Asian Earth Sci 24:523–545
117. Wu JS, Geng YS, Shen QH, Wan YS, Liu DY, Song B (1998) Archean geology characteristics and tectonic evolution of China-Korea Paleo-continent. Geological Publishing House, Beijing, pp 1–212 (in Chinese)

118. Wyman D, Kerrich R (2009) Plume and arc magmatism in the Abitibi subprovince: implications for the origin of Archean continental lithospheric mantle. Precambr Res 168:4–22
119. Wyman D, Ayer JA, Devaney JR (2000) Niobium-enriched basalts from the Wabigoon subprovince, Canada: evidence for adakitic metasomatism above an Archean subduction zone. Earth Planet Sci Letters 179:21–30
120. Xie GH (2005) Petrology and geochemistry of the Damiao Anorthosite and the Miyun Rapakivi Granite. Science Press, Beijing, pp 1–195 (in Chinese)
121. Yuan HL, Gao S, Liu XM, Li HM, Günther D, Wu FY (2004) Accurate U–Pb age and trace element determinations of zircon by laser ablation inductively coupled plasma-mass spectrometry. Geostand Geoanal Res 28:353–370
122. Zhang SH, Zhao Y, Santosh M (2012) Mid-Mesoproterozoic bimodal magmatic rocks in the northern North China Craton: implications for magmatism related to breakup of the Columbia supercontinent. Precambrian Res 222–223:339–367
123. Zhang SH, Zhao Y, Yang ZY, He ZF, Wu H (2009) The 1.35 Ga diabase sills from the northern North China Craton: implications for breakup of the Columbia (Nuna) supercontinent. Earth Planet Sci Lett 288:588–600
124. Zhang SH, Liu SW, Zhao Y, Yang JH, Song B, Liu XM (2007) The 1.75–1.68 Ga anorthosite-mangerite-alkali granitoid-rapakivi granite suite from the northern North China Craton: magmatism related to a Paleoproterozoic orogen. Precambr Res 155:287–312
125. Zhang HF, Sun M, Lu FX, Zhou XH, Zhou MF, Liu YS, Zhang GH (2001) Moderately depleted lithospheric mantle underneath the Yangtze Block: evidence from a garnet lherzolite xenolith in the Dahongshan kimberlite. Geochem J 35:315–331
126. Zhai MG, Santosh M (2011) The Early Precambrian odyssey of the North China Craton: a synoptic overview. Gondwana Res 20:6–25
127. Zhai MG, Santosh M (2013) Metallogeny of the North China Craton: link with secular changes in the evolving Earth. Gondwana Res 24:275–297
128. Zhai MG, Bian AG, Zhao TP (2000) The amalgamation of the supercontinent of North China Craton at the end of Neo-Archaean and its breakup during late Palaeoproterozoic and Mesoproterozoic. Sci China (Ser. D) 43:219–232
129. Zhao GC, Cawood PA, Li SZ, Wilde SA, Sun M, Zhang J, He YH, Yin CQ (2012) Amalgamation of the North China Craton: key issues and discussions. Precambr Res 222–223:55–76
130. Zhao GC, Wilde SA, Guo JH, Cawood PA, Sun M, Li XP (2010) Single zircon grains record two Paleoproterozoic collisional events in the North China Craton. Precambr Res 177:266–276
131. Zhao GC, He YH, Sun M (2009) The Xiong'er volcanic belt at the southern margin of the North China Craton: petrographic and geochemical evidence for its outboard position in the Paleo-Mesoproterozoic Columbia Supercontinent. Gondwana Res 16:170–181
132. Zhao TP, Chen W, Zhou MF (2009) Geochemical and Nd–Hf isotopic constraints on the origin of the ~1.74 Ga Damiao anorthosite complex. North China Craton Lithos 113:673–690
133. Zhao GC, Sun M, Wilde SA et al (2005) Late Archean to proterozoic evolution of the North China Craton: key issues revisited. Precambr Res 136:177–202
134. Zhao GC, Sun M, Wilde SA, Li SZ (2004) A Paleo-Mesoproterozoic supercontinent: assembly, growth and breakup. Earth Sci Rev 67:91–123
135. Zhao GC, Cawood PA, Wilde SA, Sun M (2002) Review of global 2.1–1.8 Ga orogens: implications for a pre-Rodinia supercontinent. Earth Sci Rev 59:125–162
136. Zhao GC, Wilde SA, Cawood PA et al (1999) Thermal evolution of two types of mafic granulites from the North China Craton: implications for both mantle plume and collisional tectonics. Geol Mag 136:223–240
137. Zheng JP, Griffin WL, O'Reilly SY (2004) 3.6 Ga lower crust in central China: new evidence on the assembly of the North China craton. Geology 32:229–232

Chapter 2
Geological Background

Abstract The North China Craton (NCC) is one of the oldest cratons in the world, and records prolonged Precambrian evolution history dating back to ~3.8 Ga. The studied area of Western Liaoning-Northeastern Hebei Provinces are major exposure regions of Archean basement terranes at the northeastern part of the NCC, i.e., the northwestern part of the Eastern Block, including the Western Liaoning, Northern Hebei, and Eastern Hebei Provinces. These basement terranes could have been cratonized during the late Neoarchean, and experienced intense rifting and extensive late Paleoproterozoic and Mesoproterozoic extension-related magmatism (e.g., alkaline plutonic rocks, K-rich volcanic rocks, and mafic dykes). Detailed regional geological background, crustal evolution history as well as recent research progresses of the Western Liaoning-Northeastern Hebei Provinces are reviewed in this chapter.

Keywords North China Craton · Western Liaoning-Northeastern Hebei Provinces Archean basement terranes · Late Paleoproterozoic extension-related magmatism Mesoproterozoic mafic dykes

2.1 Tectonic Framework of the Crystalline Basement in the North China Craton

The North China Craton (NCC) is one of oldest cratons in the world, and also the major focus of international Precambrian studies, which is bounded by the Proterozoic to Paleozoic Central Asian Orogenic Belt to the north, by the Mesozoic Paleo-Tethys tectonic domain (Qinling-Dabie-Sulu orogenic belt) to the south and east, and by the early Paleozoic Qilian orogenic belt to the west (Fig. 2.1a; [24, 30–32, 70, 72, 75, 77, 78, 80]).

It is suggested by early researchers that the NCC consists of unified Archean to Paleoproterozoic crystalline basement and Proterozoic to Mesozoic unmetamorphosed

W. Wang, *Archean-Mesoproterozoic Crustal Evolution and Crust-Mantle Geodynamics of Western Liaoning-Northeastern Hebei Provinces, North China Craton*, Springer Theses, https://doi.org/10.1007/978-981-10-7922-1_2

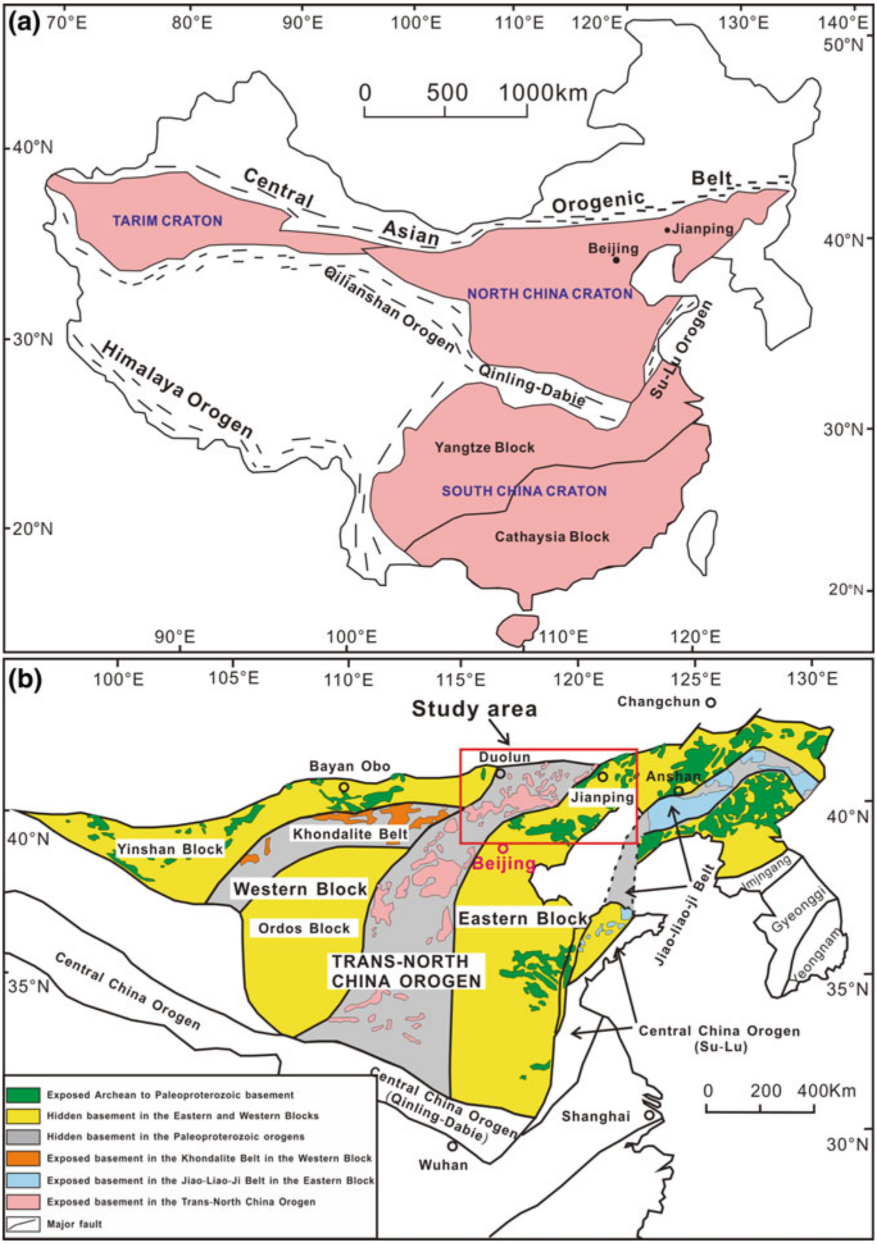

Fig. 2.1 Simplified tectonic map showing cratonic blocks and orogenic belts of China (**a**) and tectonic subdivision of the Precambrian basement of North China Craton (**b**; after [75])

sedimentary covers [35]. Though combined studies of lithological assemblages, metamorphism, and geochronology revealed that this ancient craton was amalgamated by subduction-accretion among several microcontinents, the division of these microcontinents is still hotly debated [14, 60, 69–72, 77]. For example, Wu et al. [60] subdivided the NCC into five microcontinents, i.e., Jiaoliao, Qianhuai, Jinji, Yuwan, and Mengshan; Zhai and Santosh [70] proposed that there are six microcontinents, i.e., Jiaoliao, Qianhuai, Fuping, Xuchang, Jining, and Alashan; and Zhang et al. [69] suggested a model including fifteen microcontinents. Nonetheless, Prof. Guochun Zhao and coauthors proposed that the NCC was amalgamated by the collision between the Eastern Block and the Western Block along the Trans-North China Orogen at ~1.85 Ga [23, 77]. Later, they further refined the tectonic model, suggesting that the Western Block was formed by the collision between the Yinshan Block to the north and the Ordos Block to the south along the E-W trending Khondalite belt at ~1.92 Ga, and that the Eastern Block experienced ~2.1–1.9 Ga rifting-subduction-collision processes forming the Jiao-Liao-Ji Belt [72, 75]. Kusky and Li [14] advocated a similar threefold division model, but argued that the final cratonization of the NCC occurred at the end of Archean. According to Zhao et al.'s [75] tectonic model, the study area of this doctoral thesis is located along the northwestern part of the Eastern Block, and details of regional geological background will be described as follows.

The crystalline basement in the Eastern Block exposed mainly in the Eastern Hebei, Northern Hebei, Western Liaoning, Eastern Liaoning, Southern Jilin, Western Shandong, and Eastern Shandong (Fig. 2.1b). They occur as either high grade gneissic terrane or low- to medium-grade granite-greenstone terrane, with the former located mainly in Santunying-Taipingzhai-Jinchangyu of Eastern Hebei, Jianping of Western Liaoning, Hunnan of Northern Liaoning, and Longgang Block of Southern Jilin, whereas the latter situated mainly in the Qingyuan of Northern Liaoning, Jiapigou of Southern Jilin, North Chaoyang-Fuxin-Yixian of Western Liaoning, and Yanlingguan of Western Shandong [3, 5, 24, 47, 52, 55, 75]. Neoarchean granitoid gneisses constitute at least 80% of the exposure region of basement in the Eastern Block, and the supracrustal rocks include low- to high grade metamorphosed volcano-sedimentary sequences, with local preservation of komatiites [41, 72, 74]. Sporadic Eoarchean to Mesoarchean rocks and detrital zircons as well as some ~2.7 Ga supracrustal rocks and granitoid gneisses are developed in the Anshan-Benxi complex, Eastern Hebei, Western Shandong, Eastern Shandong, and Southern Jilin areas [10, 26, 43, 45, 57]. All the above lithologies were subjected to regional ~2.50–2.48 Ga granulite to greenschist facies metamorphism, with the formation of coeval potassic granitoids and some charnockites [3–5, 24, 44, 49, 52, 54, 55]. Notably, most mafic granulites in the Eastern Block record anti-clockwise metamorphic P-T-t paths with an isobaric cooling (IBC) retrograde process [34, 58, 59, 77].

2.2 Geological Background of the Western Liaoning-Northeastern Hebei Provinces

The Western Liaoning-Northeastern Hebei Provinces are important exposure regions of Precambrian crystalline basement along the middle to eastern segments of the northern margin of NCC (Fig. 2.2). The study region is comprised of Precambrian Western Liaoning, Eastern Hebei, and Northern Hebei Provinces, which are covered by thick Proterozoic sedimentary rocks and experienced extensive late Paleoproterozoic magmatism forming alkaline plutonic rocks (e.g., Damiao anorthosite complex) and volcanic rock series (e.g., Pinggu volcanic rocks) [50]. Then, the study region witnessed prolonged Precambrian tectonic quiescence, with some ~1.33 Ga and ~1.23 Ga mafic dykes recognized [51, 66]. During the Phanerozoic, the Western Liaoning-Northeastern Hebei Provinces were located at the superimposed area of the Paleo-Asian and Paleo-Pacific tectonic domains, recording intense tectono-magmatic events and large-scale pull-apart basins [61].

2.2.1 Precambrian Crystalline Basement

Western Liaoning Province The Western Liaoning Province is located in the northeastern part of the study region (Fig. 2.3). It consists of the Jianping high grade gneissic terrane (JPGT) in the southwest and the North Chaoyang-Fuxin-Yixian granite-greenstone belt (NCFY-GGB) in the northeast, and they are separated by Proterozoic to Mesozoic unmetamorphosed volcano-sedimentary rock sequences [19, 24, 55]. The JPGT is a NE-trending fault-block, and exposes around the Hu'nuerlu mountain region. Granitoid gneisses are the major components of the JPGT, with compositions ranging from diorite, through tonalite and granodiorite, to monzogranite [52]. They show intrusive relationships with the metamorphosed supracrustal rocks, and carry supracrustal xenoliths of various dimensions. In the southwestern and central segments of the JPGT, the supracrustal lithologies are dominated by garnet two pyroxene granulites, garnet clinopyroxene amphibolites, felsic gneisses, garnet quartzites, and banded iron formations (BIFs) that were metamorphosed under granulite facies. In the northeastern segment, the supracrustal lithologies are mainly garnet amphibolites, garnet- and pyroxene-bearing amphibolites, magnetite quartzites, marbles, felsic schists, and gneisses, all of which were subjected to metamorphism under amphibolite to greenschist facies. Based on the reaction relationships of metamorphic minerals, the JPGT could have experienced a four-stage metamorphic evolution history, in turn showing mineral assemblages of hornblende + plagioclase ± quartz ± biotite, orthopyroxene + plagioclase + quartz ± clinopyroxene ± biotite ± K-feldspar ± hornblende, clinopyroxene + garnet ± plagioclase ± hornblende ± quartz, and hornblende + plagioclase ± garnet ± quartz ± biotite, respectively. They record an anti-clockwise metamorphic P-T-t path,

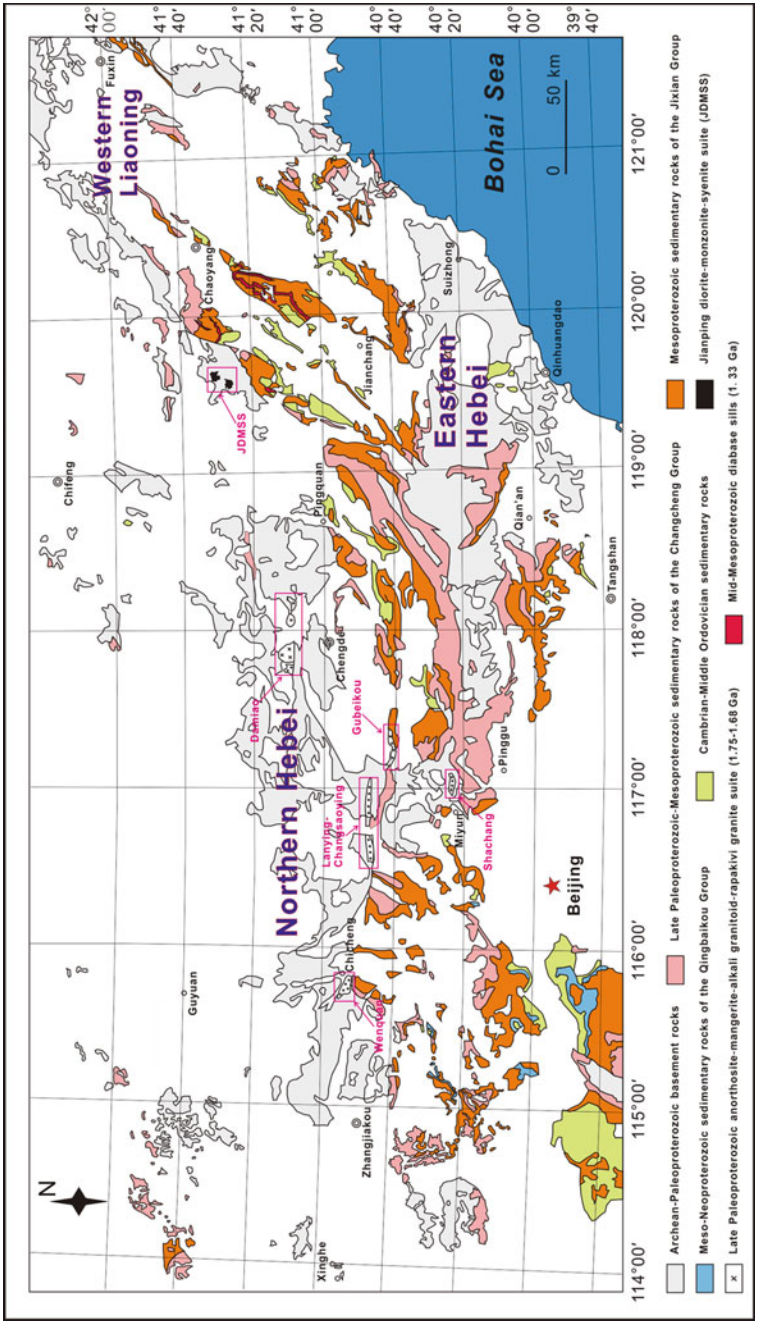

Fig. 2.2 Regional geological map of the Western Liaoning-Northeastern Hebei Provinces showing Archean basement terranes as well as Paleo- to Mesoproterozoic plutonic and volcanic rocks (after [67])

showing a peak metamorphic P–T condition of T = 785–820 °C and P = 1.05–1.17 Gpa [19, 24].

Early single zircon ages dated by Pb–Pb evaporation method reveal that supracrustal rocks of the JPGT were formed at 2551–2522 Ma, which were emplaced by 2522–2500 Ma TTG gneisses. Then, the above lithologies were together subjected to ~2490 Ma regional granulite facie metamorphism, with the generation of nearly coeval charnockites and later ~2472 Ma post-tectonic granites [13]. Liu et al. [24] further dated the basement rocks in the JPGT using LA-ICPMS in situ zircon U–Pb isotopic dating method, suggesting that the protoliths of metavolcanic rocks were erupted at ~2555–2550 Ma, and possibly up to 2615 Ma. During ~2538–2498 Ma, voluminous granitoid rocks were emplaced, forming the protoliths of dioritic and TTG gneisses. They all underwent regional ~2485 Ma granulite facies metamorphism and subsequent ~2450–2400 Ma retrograde metamorphism.

The NCFY-GGB is a typical Archean granite-greenstone belt (Fig. 2.3), showing lithological assemblages of hornblendites (with <10% plagioclase), amphibolites, hornblende plagioclase gneisses, biotite plagioclase gneisses, marbles, and banded iron formations (BIFs). They were emplaced by dioritic, TTG, and monzogranitic gneisses, and subjected to mostly amphibolite to greenschist facies metamorphism [19, 49, 54, 55]. Early 1:200000 regional geological mapping subdivided the Archean supracrustal volcano-sedimentary sequences into three units, i.e., from bottom to top the Xiaotazigou Formation, Dayingzi Formation and

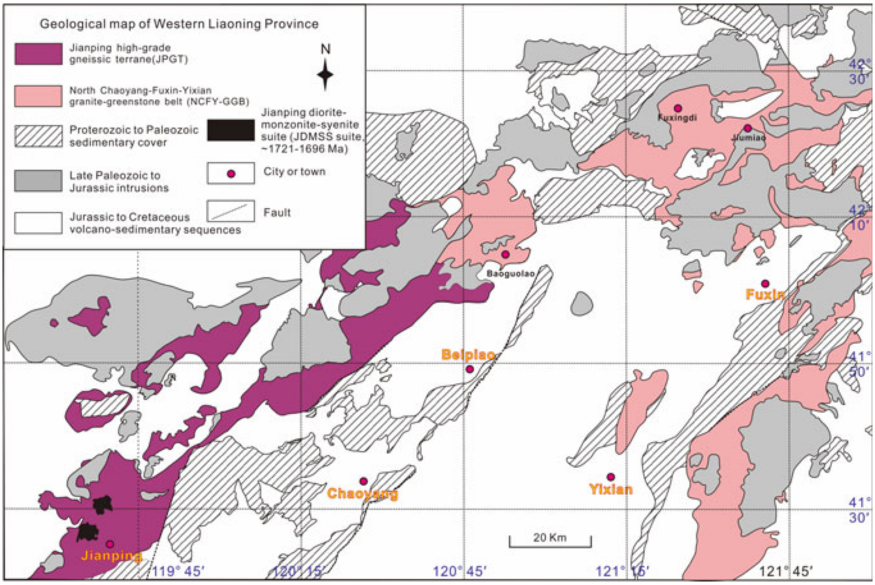

Fig. 2.3 Simplified geological map of the Western Liaoning Province, including the North Chaoyang-Fuxin-Yixian granite-greenstone belt (NCFY-GGB) in the northeast and the high grade Jianping gneissic terrane (JPGT) in the southwest (after [52])

Waziyu Formation. The Xiaotazigou Formation is composed chiefly of ultramafic to mafic clinopyroxene amphibolites, amphibolites, and minor BIFs and felsic gneisses. The Dayingzi Formation is dominated by hornblende plagioclase gneisses, biotite plagioclase gneisses and biotite two feldspar gneisses, with minor mafic rocks, BIFs and metamorphosed clastic sedimentary rocks. The uppermost Waziyu Formation consists of two mica quartz schists with interlayered magnetite quartzites and felsic metavolcanic rocks [19]. LA-ICPMS zircon U–Pb isotopic dating data indicate that voluminous late Neoarchean mafic volcanic rocks erupted in the North Chaoyang area, which were subjected to ~2460–2350 Ma high garde metamorphism with coeval plutonic magmatism [22]. Bai et al. [1] reported a series of Permian (259–251 Ma) mafic to felsic plutons within the basement rocks of NCFY-GGB, implying that part of basement rocks in the original Dayingzi Formation should be disassembled.

The crystalline basement of Western Liaoning Province experienced multiple episodes of deformation, with a NEE-SWW trending. At least three episodes of deformation were identified: the oldest deformation event (D_1) is characterized by F_1 folds, which is recorded merely in the magnetite quartzite and the original structural elements were disturbed by subsequent deformation; the second episode of deformation (D_2) resulted from the NEE-SWW trending faults (F_2) and synchronous shear deformation, which represents the regional principal deformation; and the latest episode of deformation is characterized by NE-SW trending faults (F_3), which further complicated the above major structure patterns [19].

Eastern Hebei Province The Eastern Hebei Province is mainly located in the Zunhua-Qinglong areas, i.e., to the southwest of Western Liaoning Province (Fig. 2.2), which is a classic Precambrian research area in the NCC. Voluminous early Archean to Paleoproterozoic basement rocks are exposed in this area, and they were covered by thick late Paleoproterozoic to Phanerozoic unmetamorphosed sedimentary rock sequences, and emplaced by extensive Mesozoic granitoids (Fig. 2.4). Early researchers subdivided the basement rocks of Eastern Hebei into

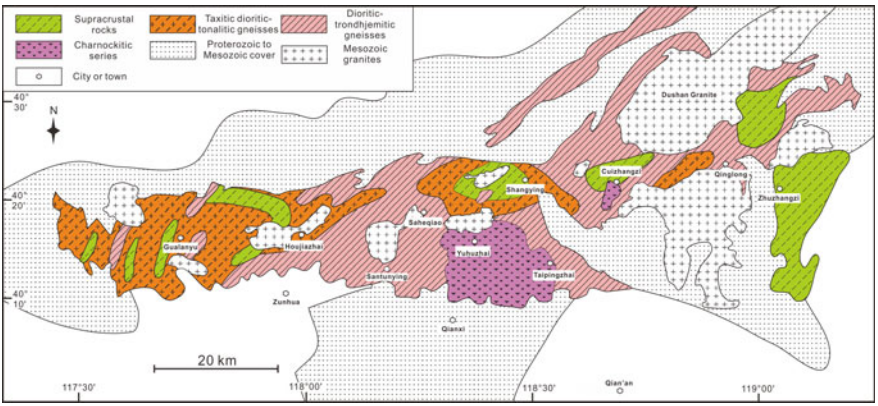

Fig. 2.4 Geological map of the Eastern Hebei Province in the southern part of the Western Liaoning-Northeastern Hebei Provinces (after [5])

different groups: i.e., Archean Qian'xi and Badaohe Groups and Paleoproterozoic Shuangshanzi and Qinglonghe Groups; or Archean Qian'xi and Luanxian Groups and Paleoproterozoic Dantazi and Zhuzhangzi Groups [5]. Later, large volumes of plutonic gneisses were recognized in the above stratigraphic sequences, including dioritic, TTG, and monzogranitic gneisses, whereas the supracrustal rocks occur as either large-scale intercalated volcano-sedimentary sequences or small-scale xenoliths in the granitoid gneisses [3, 39, 62].

Early Archean rocks and detrital zircons are mainly discovered in the Caozhuang-Huangbaiyu areas, including the famous fuchsite quartzites containing ~3.8 Ga detrital zircons [46]. The Caozhuang complex consists mainly of amphibolites, hornblende gneisses, (fuchsite) quartzites, sillimanite-bearing felsic gneisses, marbles, and garnet biotite gneisses, with intercalated BIFs [21]. Whole-rock Sm–Nd isochron dating data yield a ~3.5 Ga age for the amphibolites in the Qian'xi complex, implying possibly early Archean rocks around Huangbaiyu area [11]. Later SHRIMP U–Pb isotopic dating data reveal that detrital zircons in the fuchsite quartzites of Caozhuang Complex show an age range of 3860–3135 Ma, with the former being the oldest zircon in Eastern Hebei [33]. These zircon grains display slightly higher $\delta^{18}O$ values (an average value of 6.6‰), suggesting early Archean crustal recycling and low temperature hydrothermal alteration processes [57]. Liu et al. [21] further identified some ~3838–3343 Ma zircon grains in the hornblende gneisses and garnet biotite gneisses of the Caozhuang Complex. Some ~3287–2940 Ma granitoid gneisses were also reported [37].

The Eastern Hebei Province is dominated by late Neoarchean to early Paleoproterozoic rocks. Lin et al. [20] classified the orthogneisses in Eastern Hebei into granitoid rock series of Opx-bearing granodioritic gneisses, Opx-bearing granitic gneisses, tonalitic-trondhjemitic gneisses, granodioritic-monzogranitic gneisses, monzogranitic-alkali granitic gneisses, and leucogranites. Recent geological survey indicates that supracrustal metavolcanic rocks are widespread in Gualanyu, Houjiazhai, Saheqiao, Shangying, Cuizhangzi, North Qinglong, and Zhuzhangzi areas [5]. Geng et al. [3] reported a series of zircon U–Pb isotopic ages for the granitoid gneisses of Eastern Hebei, i.e., ~2550 Ma of Yuhuzhai gneisses, ~2515 Ma Qiuhuayu gneisses, ~2495 Ma Xiaoguanzhuang gneisses, and ~2492 Ma Cuizhangzi gneisses, and suggested that they were generated by intense underplating of mantle-derived magmas under a mantle plume setting. Protoliths of the Anziling granitoid gneisses in the Qinhuangdao area were emplaced at ~2526–2515 Ma, which were metamorphosed during ~2500–2440 Ma, and they were considered to be formed by magma mixing processes under a mantle plume setting [62]. However, basement rocks in the Eastern Hebei Province were formed during three magmatic episodes of ~2550–2535 Ma, ~2530–2520 Ma, and ~2500–2490 Ma, showing clear asymmetric distribution [39]. Combined with the island arc geochemical features of mafic to ultramafic rocks, it is suggested that the Eastern Hebei Province was evolved under an active continental margin setting. The metavolcanic rocks in the Saheqiao area show geochemical features analogous to those of N-MORBs, Nb-enriched basalts, tholeiitic to calc-alkaline basaltic to andesitic rocks, respectively [5]. These volcanic rocks were erupted during ~2614–2518 Ma, and experienced ~2450–2370 Ma multi-episode of metamorphism, which could have been generated under a subduction-related arc setting. ~2511–2503 Ma bimodal volcanic rocks in the Qinglong area were considered to have been formed at an intracontinental rift setting [37], whereas ~2.5 Ga ultramafic to mafic and syenitic dykes around Huangbaiyu area may indicate the final cratonization of NCC at the terminal Archean [16].

Northern Hebei Province. The Northern Hebei Province is located in the northwestern part of the Western Liaoning-Northeastern Hebei Provinces, which also belongs to the northern extent of the Paleoproterozoic Trans-North China Orogen (Fig. 2.2; [75]). The crystalline basement was subdivided into the Hongqiyingzi complex to the north and the Dantazi complex to the south, separated by the Chicheng-Longhua Fault (Fig. 2.5; [9]).

The Dantazi complex comprises mainly granulite-facies metavolcanic rocks in the lower formation, and metasedimentary rocks with minor interlayered metavolcanic rocks in the upper formation [56]. The garnet-bearing granulites in the lower formation are classified as high pressure granulites, which together with those in the Sanggan and Hengshan areas, forming a N-S trending high-pressure granulite belt [6, 79]. They could mark the collisional belt between the Eastern Block and Western Block [75]. Recent studies indicate that the original Dantazi Complex consists chiefly of granitoid gneisses, with some relicts of supracrustal rocks including mafic granulites, felsic leptynites, and marbles [27, 28]. The granitoid

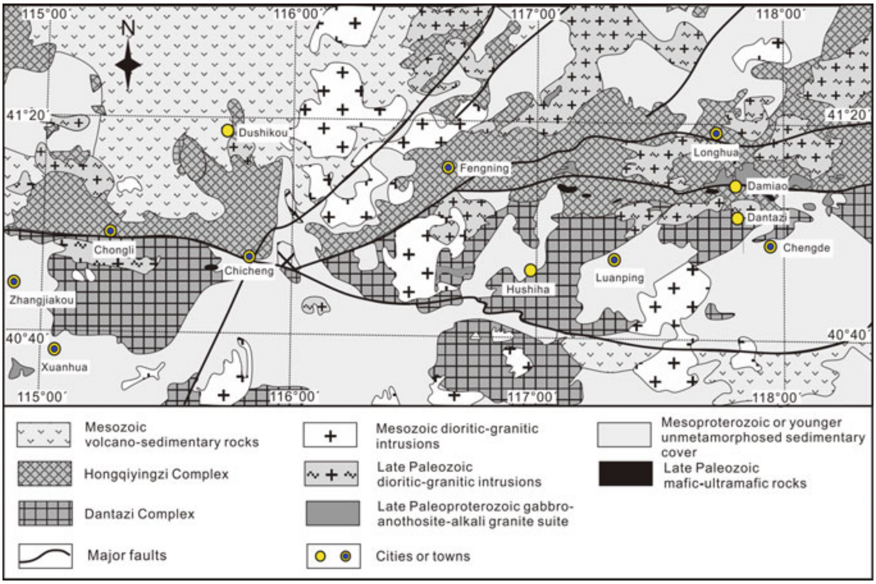

Fig. 2.5 Geological map of the Northern Hebei Province in the northwestern part of the Western Liaoning-Northeastern Hebei Provinces (after Liu et al. [24, 25])

gneisses distribute mainly in the Chengde-Sanchakou-Hushiha areas, showing lithological assemblages of two pyroxene quartz dioritic gneisses, diopsite or two pyroxene tonalitic gneisses, biotite trondhjemitic gneisses, pyroxene-bearing hornblende biotite granodioritic gneisses, and some monzogranitic gneisses. Supracrustal rocks of the Dantazi Complex include: (1) the association of garnet biotite plagioclase leptynites, chlorite hornblende plagioclase gneisses, hornblende schists, garnet diopsite hornblendites, garnet hornblende two-pyroxene granulites, and magnetite quartzites, which belongs to the original Yanwopu Formation mainly in the south Damiao-Yanwopu areas; and (2) garnet leptynites, garnet sillimanite schists, marbles, and graphite leptynites, dominantly in the Hongqizhen-Chaolianggou-Fenghuangzui areas [38]. LA-ICPMS zircon U–Pb isotopic dating data of the Dantazi Complex reveal six episodes of tectonothermal events, forming respectively: (1) ~2600–2530 Ma mafic volcanic rocks; (2) ~2517–2473 Ma quartz dioritic and monzogranitic rocks; (3) early granulite facies metamorphism and anatexis at ~2427–2404 Ma; (4) mafic plutonic rocks at ~1859 Ma; (5) intense late granulite facies metamorphism at ~1834–1793 Ma; and (6) late fluid activity at ~1730 Ma leading to the modification of zircon grains [27]. These data suggest that the Dantazi complex were not subjected to the effects of Paleozoic tectonothermal events. Petrogenetic studies indicate that granitoid gneisses of the Dantazi Complex were mainly derived from the partial melting of mixed basaltic and greywacke sources, forming probably in an active continental margin to back-arc extensional setting [25].

The typical section of Hongqiyingzi complex is located to the north of Chongli, showing lithological assemblages of biotite plagioclase gneisses, hornblende biotite plagioclase gneisses, biotite leptynites, sillimanite biotite leptynites, garnet biotite plagioclase gneisses, garnet biotite schist, and marbles. Whereas in the Fengning area, granitoid gneisses, porphyraceous granites, biotite monzogranites, and two-mica granitoid gneisses are the dominant lithologies. According to the lithological assemblages and geochemical and geochronological features, the upper subgroup of the original Dantazi complex was re-grouped into the Hongqiyingzi complex [27, 28]. LA-ICPMS zircon U–Pb isotopic dating data reveal that (1) the hornblende biotite granodioritic gneisses in the Chicheng-Chongli terrane formed at ~2535–2480 Ma, followed by the generation of garnet-bearing tonalitic gneisses and garnet biotite plagioclase leptynites at ~1871 and ~1841 Ma, respectively; (2) the quartz dioritic gneisses and garnet biotite monzogranitic gneisses were generated at ~2484 and ~2180 Ma, respectively, and the fine-grained monzogranitic gneisses at ~413 Ma; and (3) the mylonitized potassium-rich granitoid gneisses, hornblende biotite quartz dioritic gneisses, and biotite monzogranites were generated at ~1876, ~1838, and ~1810 Ma, respectively [28]. Therefore, both Archean to Paleoproterozoic and Paleozoic terranes are preserved in the Hongqiyingzi Complex. They were commonly subjected to Paleozoic metamorphic and deformational events, including high pressure metamorphism, probably related to the subduction-accretion, collisional, and post-collisional processes of the Paleo-Asian orogenic belt [29].

2.2.2 Yanliao Rift and Late Paleoproterozoic Magmatism

The Yanliao rift is located at the middle to eastern segments of the northern margin of North China Craton, extending from Zhangjiakou in the west through the northern coastline of Bohai to Jinzhou-Fuxin areas. It overlaps roughly with the study area of Western Liaoning-Northeastern Hebei Provinces in this thesis (Fig. 2.2). Following amalgamation of the crystalline basement of North China Craton at ~1.85 Ga, an intracontinental rift basin, i.e., Yanliao aulacogen was developed at its northern part, which is bounded by deep extensional faults with an E-W trending [35, 64].

From the bottom upward, sedimentary sequences in the Yanliao rift can be subdivided into the Changcheng, Jixian and Qingbaikou groups with a total thickness of ca. 9000 m (Fig. 2.6). Among these, the Jixian section represents one of the best late Paleoproterozoic to Neoproterozoic stratigraphic sections in the world [2, 35]. The lowermost Changcheng Group consists of four formations: Changzhougou, Chuanlinggou, Tuanshanzi and Dahongyu. Unconformably overlying the Archean to Paleoproterozoic crystalline basement, the Changzhougou Formation is composed mainly of sandstones with minor conglomerates and pebble-bearing sandstones, and these rocks are in turn conformably overlain by shales of the Chuanlinggou Formation. The two formations show a total thickness of ~1740 m (860 and 880 m, respectively). Notably, there are no syn-depositional magmatic records in the lower two formations. Conformably overlying the Chuanlinggou Formation, the Tuanshanzi Formation is dominated by thick dolostones with subordinate thin silty shales and minor sandstones (total thickness of 520 m). In the Dahuashan, Maoshan and Taipingzhuang areas, minor volcanic rocks were recognized in the upper sequence of this formation, representing the oldest volcanism in the Yanliao rift [18, 50]. The Dahongyu Formation is the uppermost unit of the Changcheng Group with a thickness of ca. 410 m, and is well known for the preservation of voluminous K-rich volcanic rocks [8, 35, 36]. Stratigraphically, three distinct units can be recognized within this formation from base upward, with the lower two members dominated by sandstones and intercalated shales, whereas dolostones with minor sandstones are the main lithologies in the upper unit.

Long-term field geological and geochronological studies have been conducted to resolve the lowest boundary age of the Changcheng Group. SHRIMP U–Pb isotopic dating data of detrital zircons from sandstones of the Changzhougou Formation reveal that late Archean to early Paleoproterozoic (~2.60–2.35 Ga) continental materials dominate the provenance area, with subordinate contribution from ~2.3–2.1 Ga and ~1.9–1.8 Ga rocks [48]. This provides a maximum age of ~1.8 Ga for the Changcheng Group as well as the onset of Yanliao rift [35]. A granitic porphyritic vein was recently discovered in the Shachang area of Miyun, Beijing, which emplaced into the Archean amphibolites of the Miyun Group and was unconformably overlain by the pebble-bearing sandstone of the Changzhougou Formation [15]. This granitic vein was dated at ~1673 Ma, implying that the

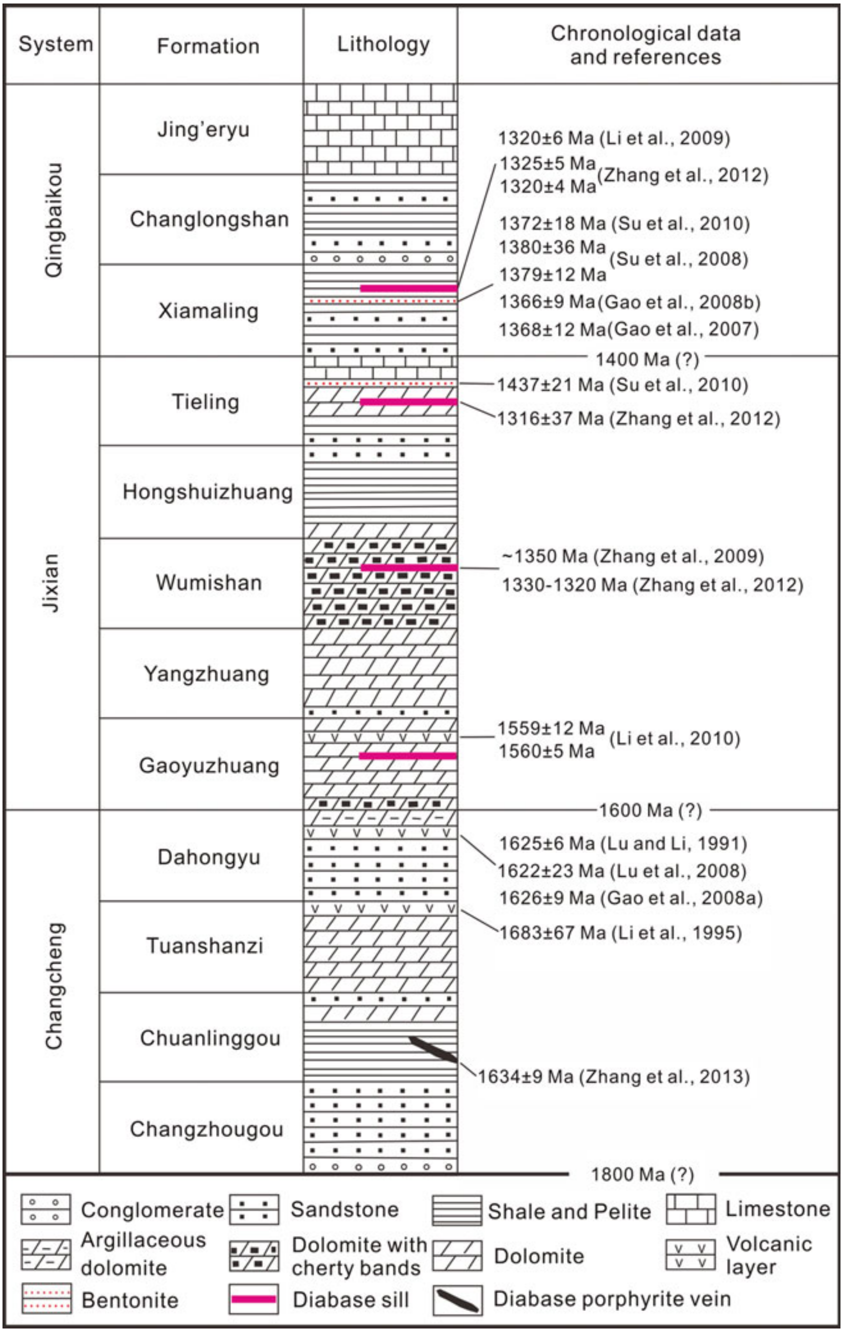

Fig. 2.6 Subdivision and geochronological constraints on the Mesoproterozoic strata along the middle to eastern segments of the northern margin of North China Craton (from [65])

lowest boundary age of the Changcheng Group could be younger, possibly at ~1650 Ma. Nonetheless, Wang et al. [50] carried out systematic LA-ICPMS zircon U–Pb isotopic chronological studies of the K-rich volcanic rocks in the Tuanshanzi and Dahongyu formations, and suggested ~1680 Ma as the lowest boundary age of the Changcheng Group.

Except for the above K-rich volcanic rocks, the Western Liaoning-Northeastern Hebei Provinces also witnessed intense late Paleoproterozoic (~1.75–1.68 Ga) plutonic magmatism, forming the Damiao anorthosite complex, Miyun rapakivi granites, and the Jianping diorite-monzonite-syenite suites (JDMSS; [53]). The main mafic lithologies include norites, anorthosites, magnetite diorites, and mafic dykes, whereas mangerites, clinopyroxene monzonites, (quartz) syenites, potassium-rich granites, and rapakivi granites are the dominant felsic rocks [12, 40, 53, 68]. All the above lithologies intrude into the Archean crystalline basement, but don't show intrusive relationship with the sedimentary cover of the Changcheng Group in the Yanliao rift. They show massive structure without any metamorphic or deformational imprints. The Damiao anorthosite complex is located to the north of Chengde in the Northern Hebei Province, which is the only Proterozoic massif-type anorthosites in China and contains prolific V–Ti magnetite and apatite deposits [76]. Spatially, they are closely related to regional alkaline granites and rapakivi granites, constituting typical anorthosite-mangerite-charnockite-rapakivi granite suites (AMGRS, [68]). The Damiao anorthosite complex was precisely dated at ~1.74 Ga [73], and the parental magmas could have been derived from the partial melting of EM-I type lithospheric mantle, possibly under a post-collisional setting [68]. The Miyun rapakivi granites are composed mainly of hornblende and biotite-bearing rapakivi granites and porphyritic biotite granites. The rapakivi granites distributed chiefly at the western part of the pluton, and they contain voluminous K-feldspar phencrysts, with ~30% containing plagioclase rims, forming typical rapakivi texture [63]. Zircon U–Pb isotopic dating data reveal that these granitic rocks were generated at ~1680 Ma [2]. In summary, the intense late Paleoproterozoic magmatism of NCC occurred coevally with the anorthosites, rapakivi granites, and mafic dykes in Laurentia (including North America and Greenland) and Baltica, possibly marking the initial breakup of the global Paleo- to Mesoproterozoic Columbia supercontinent [7, 53].

2.2.3 Mesoproterozoic Mafic Dykes

Following the late Paleoproterozoic tectono-magmatic events, the North China Craton entered a long period of tectonic quiescence, with only sporadic tectonothermal events reported [35]. Recently, Li et al. [17] reported volcanic tuffs within the Gaoyuzhuang Formation, and they yield a SHRIMP zircon U–Pb isotopic age of ~1560 Ma, which is taken as the lowest boundary age of the Jixian Group. A series of thin K-bentonite layer was documented within the Xiamaling Formation of the Qingbaikou Group, yielding SHRIMP zircon U–Pb isotopic ages of ~1380–1368 Ma [42]. Notably, the actual sources of these volcanic tuffs and the K-bentonites (commonly altered from volcanic tuffs) are always questionable, since they can transport for several hundred kilometers before sedimentation [67].

Zhang et al. [66, 67] reported a series of diabase sills within the Xiamaling, Tieling, and Wumishan Formations in Pingquan, Xiabancheng, Lingyuan, and Kuancheng areas. Zircon and baddeleyite U–Pb isotopic dating data suggest a formation age of ~1.33 Ga for these diabase sills, and they could have been generated by the partial melting of a depleted asthenospheric mantle source with some crustal contamination under a mantle plume setting [66]. Recently, large volumes of ~1.23 Ga gabbroic diabase dykes were documented by Wang et al. [51] for the first time in the North China Craton, i.e., Jianping of Western Liaoning, Qinglong of Eastern Hebei, and Qingyuan of Northern Liaoning. They are nearly contemporaneous with the famous ~1.27 Ga Mackenzie and ~1.23 Ga Sudbury mafic dyke swarms of North America, signifying probably the final breakup of Columbia supercontinent. These newly identified Mesoproterozoic mafic dykes or sills in the study region have the potential to provide key information for global stratigraphic correlation and supercontinent reconstruction.

References

1. Bai X, Liu SW, Wang W et al (2013) U–Pb geochronology and Lu–Hf isotopes of zircons from newly identified Permian-Early Triassic plutons in western Liaoning province along the northern margin of the North China Craton: constraints on petrogenesis and tectonic setting. Int J Earth Sci 102:671–685
2. Gao LZ, Zhang CH, Yin CY, Shi XY, Wang ZQ, Liu YM, Liu PJ, Tang F, Song B (2008) SHRIMP zircon ages: basis for refining the chronostratigraphic classification of the Meso- and Neoproterozoic strata in North China Old land. Acta Geoscientica Sinica 29:366–376 (in Chinese with English abstract)
3. Geng YS, Liu FL, Yang C (2006) Magmatic event at the end of the Archean in eastern Hebei Province and its geological implication. Acta Geol Sin (English version) 80:819–833
4. Grant ML, Wilde SA, Wu FY, Yang JH (2009) The application of zircon cathodoluminescence imaging, Th–U–Pb chemistry and U–Pb ages in interpreting discrete magmatic and high-grade metamorphic events in the North China Craton at the Archean/Proterozoic boundary. Chem Geol 261:155–171
5. Guo RR, Liu SW, Santosh M et al (2013) Geochemistry, zircon U–Pb geochronology and Lu–Hf isotopes of metavolcanics from eastern Hebei reveal Neoarchean subduction tectonics in the North China Craton. Gondwana Res 24:664–686
6. Guo JH, O'Brien PJ, Zhai MG (2002) High-pressure granulites in the Sanggan area, North China craton: metamorphic evolution, P–T paths and geotectonic significance. J Metamorph Geol 20:741–756
7. Hou GT, Li JH, Yang MH, Yao WH, Wang CC, Wang YX (2008) Geochemical constraints on the tectonic environment of the late Paleoproterozoic mafic dyke swarms in the North China Craton. Gondwana Res 13:103–116
8. Hu JL, Zhao TP, Xu YH, Chen W (2007) Geochemistry and petrogenesis of the high-K volcanic rocks in the Dahongyu Formation, North China Craton. J Miner Petrol 27:70–77 (in Chinese with English abstract)
9. Hu XW, Zhang JM, Quan H (1996) The isotopic ages of the Hongqiyingzi Group in northern Hebei and its age assignment. Reg Geol China 2:186–192 (in Chinese with English abstract)

10. Jahn BM, Liu DY, Wan YS, Song B, Wu JS (2008) New U–Pb and Hf isotopic data confirm Anshan as the oldest preserved segment of the North China Craton. Am J Sci 308:232–269
11. Jahn BM, Auvary B, Cornichet J, Bai YL, Shen QH, Liu DY (1987) 3.5 Ga old amphibolites from eastern Hebei Province, China: field occurrence, petrography, Sm–Nd isochron age and REE geochemistry. Precambr Res 34:311–346
12. Jiang N, Guo JH, Zhai MG (2011) Nature and origin of the Wenquan granite: implications for the provenance of Proterozoic A-type granites in the North China Craton. J Asian Earth Sci 42:76–82
13. Kröner A, Cui WY, Wang SQ, Wang CQ, Nemchin AA (1998) Single zircon ages from high-grade rocks of the Jianping Complex, Liaoning Province, NE China. J Asian Earth Sci 16:519–532
14. Kusky TM, Li JH (2003) Paleoproterozoic tectonic evolution of the North China Craton. J Asian Earth Sci 22:383–397
15. Li HK, Lu SN, Su WB, Xiang ZQ, Zhou HY, Zhang YQ (2013) Recent advances in the study of the Mesoproterozoic geochronology in the North China Craton. J Asian Earth Sci 72:216–227
16. Li TS, Zhai MG, Peng P, Chen L, Guo JH (2010) Ca. 2.5 billion year old coeval ultramafic-mafic and syenitic dykes in Eastern Hebei: implications for cratonization of the North China Craton. Precambr Res 180:143–155
17. Li HK, Zhu SX, Xiang ZQ, Su WB, Lu SN, Zhou HY, Geng JZ, Li S, Yang FJ (2010) Zircon U–Pb dating on tuff bed from Gaoyuzhuang formation in Yanqing, Beijing: further constraints on the new subdivision of the Mesoproterozoic stratigraphy in the northern North China Craton. Acta Petrologica Sinica 26:2131–2140 (in Chinese with English abstract)
18. Li HK, Li HM, Lu SN (1995) Grain zircon U–Pb ages for volcanic rocks from Tuanshanzi Formation of Changcheng System and their geological implications. Geochimica 24:43–48 (in Chinese)
19. Lin BQ, Cui WY, Wang SQ, Shen ES (1997) The Archean geology and gold deposits in Western Liaoning Province. Seismological Press, Beijing, pp 1–130 (in Chinese)
20. Lin Q, Wu FY, Liu SW, Ge WC, Sun JG, Yin JZ (1992) Archean granites in the East of North China platform. Science Publishing House, Beijing (in Chinese with English abstract)
21. Liu SJ, Wan YS, Sun HY et al (2013) Paleo- to Eoarchean crustal evolution in eastern Hebei, North China Craton: New evidence from SHRIMP U–Pb dating and in-situ Hf isotopic study of detrital zircons from paragneisses. J Asian Earth Sci 78:4–17
22. Liu SW, Wang W, Bai X, Zhang F (2010) Geological events of early Precambrian complex in North Chaoyang area, Liaoning Province. Acta Petrologica Sinica 26:1993–2004 (In Chinese with English abstract)
23. Liu SW, Zhang J, Li QG, Zhang LF, Wang W, Yang PT (2012) Geochemistry and U–Pb zircon ages of metamorphic volcanic rocks of the Paleoproterozoic Lüliang Complex and constraints on the evolution of the Trans-North China Orogen, North China Craton. Precambr Res 222–223:173–190
24. Liu SW, Santosh M, Wang W, Bai X, Yang PT (2011) Zircon U–Pb chronology of the Jianping Complex: implications for the Precambrian crustal evolution history of the northern margin of North China Craton. Gondwana Res 20:48–63
25. Liu SW, Lv YJ, Wang W, Yang PT, Bai X, Feng YG (2011) Petrogenesis of the Neoarchean granitoid gneisses in northern Hebei Province. Acta Petrologica Sinica 27:909–921 (in Chinese with English abstract)
26. Liu DY, Wilde SA, Wan YS et al (2008) New U–Pb and Hf isotopic data confirm Anshan as the oldest preserved segment of the North China Craton. Am J Sci 308:200–231
27. Liu SW, Lü YJ, Feng YG, Zhang C, Tian W, Yan QR, Liu XM (2007) Geology and zircon U–Pb isotopic chronology of Dantazi Complex, Northern Hebei Province. Geol J China Univ 13:484–497 (in Chinese with English abstract)
28. Liu SW, Lü YJ, Feng YG, Liu XM, Yan QR, Zhang C, Tian W (2007) Zircon and monazite geochronology of the Hongqiyingzi complex, northern Hebei, China. Geol Bull China 26:1086–1100 (in Chinese with English abstract)

29. Liu SW, Tian W, Lv YJ et al (2006) Geochemistry, Nd isotopic characteristics of metamorphic complexes in Northern Hebei: implications for crustal accretion. Acta Geol Sin (English version) 80:807–818
30. Liu SW, Pan YM, Xie QL, Zhang J, Li QG (2005) Geochemistry of the Paleoproterozoic Nanying granitic gneisses in the Fuping complex: implications for the tectonic evolution of the Central zone, North China Craton. J Asian Earth Sci 24:643–658
31. Liu SW, Pan YM, Xie QL, Zhang J, Li QG (2004) Archean geodynamics in the Central Zone, North China craton: constraints from geochemistry of two contrasting series of granitoids in the Fuping and Wutaishan complexes. Precambr Res 130:229–249
32. Liu SW, Pan YM, Li JH, Zhang J, Li QG (2002) Geological and isotopic geochemical constraints on the evolution of the Fuping Complex, North China Craton. Precambr Res 117:41–56
33. Liu DY, Nutman AP, Compston W, Wu JS, Shen QH (1992) Remmants of $\geq$3800 Ma crust in the Chinese part of the Sino-Korean Craton. Geology 20:339–342
34. Liu SW, Lin Q, Cao L (1991) The P-T-t trajectory recorded by the compositional zonations of amphibole in Eastern Hebei Province. J Changchun Univ Earth Sci 21:129–142 (in Chinese with English abstract)
35. Lu SN, Zhao GC, Wang HC, Hao GJ (2008) Precambrian metamorphic basement and sedimentary cover of the North China Craton: a review. Precambr Res 160:77–93
36. Lu SN, Li HM (1991) A precise U–Pb single zircon age determination for the volcanics of the Dahongyu Formation, Changcheng System in Jinxian. Bull Chin Acad Geol Sci 22:137–145 (in Chinese with English abstract)
37. Lv B, Zhai MG, Li TS, Peng P (2012) Zircon U–Pb ages and geochemistry of the Qinglong volcano-sedimentary rock series in Eastern Hebei: implication for 2500 Ma intra-continental rifting in the North China. Precambr Res 208–211:145–160
38. Mao DB, Zhong CT, Chen ZH, Lin YX, Li HM, Hu XD (1999) The isotope ages and their geological implications of high-pressure basic granulites in north region to Chengde, Hebei Province, China. Acta Petrologica Sinica 15:524–531 (in Chinese with English abstract)
39. Nutman AP, Wan YS, Du LL, Friend CRL, Dong CY, Xie HQ, Wang W, Sun HY, Liu DY (2011) Multistage late Neoarchaean crustal evolution of the North China Craton, eastern Hebei. Precambr Res 189:43–65
40. Peng P, Liu F, Zhai MG, Guo JH (2011) Age of the Miyun dyke swarm: constraints on the maximum depositional age of the Changcheng System. Chin Sci Bull 57:105–110 (in Chinese with English abstract)
41. Polat A, Li J, Fryer B et al (2006) Geochemical characteristics of the Neoarchean (2800–2700 Ma) Taishan greenstone belt, North China Craton: evidence for plume-craton interaction. Chem Geol 230:60–87
42. Su W, Zhang S, Huff WD, Li H, Ettensohn FR, Chen X, Yang H, Han Y, Song B, Santosh M (2008) SHRIMP U–Pb ages of K-bentonite beds in the Xiamaling Formation: implications for revised subdivision of the Meso- to Neoproterozoic history of the North China Craton. Gondwana Res 14:543–553
43. Wan YS, Xie SW, Yang CH, Kröner A, Ma MZ, Dong CY, Du LL, Xie HQ, Liu DY (2014) Early Neoarchean ($\sim$2.7 Ga) tectono-thermal events in the North China Craton: a synthesis. Precambr Res 247:45–63
44. Wan YS, Dong CY, Liu DY, Kröner A, Yang CH, Wang W, Du LL, Xie HQ, Ma MZ (2012) Zircon ages and geochemistry of late Neoarchean syenogranites in the North China Craton: a review. Precambr Res 222–223:265–289
45. Wan YS, Liu DY, Wang SJ, Yang EX, Wang W, Dong CY, Zhou HY, Du LL, Yang YH, Diwu CR (2011) $\sim$2.7 Ga juvenile crust formation in the North China Craton (Taishan-Xintai area, western Shandong Province): further evidence of an understated event from U–Pb dating and Hf isotopic composition of zircon. Precambr Res 186:169–180
46. Wan YS, Liu DY, Dong CY, Nutman AP, Wilde SA, Wang W, Xie HQ, Yin XY, Zhou HY (2009) The oldest rocks and zircons in China. Acta Petrologica Sinica 25:1793–1807 (in Chinese with English abstract)

47. Wan YS, Song B, Geng YS, Liu DY (2005) Geochemical characteristics of Archean basement in the Fushun-Qingyuan area, Northern Liaoning Province and its geological significance. Geol Rev 51:128–137 (in Chinese with English abstract)
48. Wan YS, Zhang Q, Song T (2003) SHRIMP ages of detrital zircons from the Changcheng System in the Ming Tombs area, Beijing: constraints on the protolith nature and maximum depositional age of the Mesoproterozoic cover of the North China Craton. Chin Sci Bull 48:2500–2506
49. Wang W, Liu SW, Santosh M, Wang GH, Bai X, Guo RR (2015) Neoarchean intra-oceanic arc system in the Western Liaoning Province: Implications for Early Precambrian crustal evolution in the Eastern Block of the North China Craton. Earth Sci Rev 150:329–364
50. Wang W, Liu SW, Santosh M et al (2015) Late Paleoproterozoic geodynamics of the north China Craton: Geochemical and zircon U–Pb–Hf records from a volcanic suite in the Yanliao rift. Gondwana Res 27:300–325
51. Wang W, Liu SW, Santosh M, Zhang LF, Bai X, Zhao Y, Zhang SH, Guo RR (2015) 1.23 Ga mafic dykes in the North China Craton reconstruct the Columbia supercontinent. Gondwana Res 27:1407–1418
52. Wang W, Liu SW, Bai X et al (2013) Zircon U–Pb–Hf isotopes and whole-rock geochemistry of granitoid gneisses in the Jianping gneissic terrane, Western Liaoning Province: constraints on the Neoarchean crustal evolution of the North China Craton. Precambr Res 224:184–221
53. Wang W, Liu SW, Bai X, Li QG, Yang PT, Zhao Y, Zhang SH, Guo RR (2013) Geochemistry and zircon U–Pb–Hf isotopes of the late Paleoproterozoic Jianping diorite-monzonite-syenite suites of the North China Craton: implications for petrogenesis and geodynamic setting. Lithos 162–163:175–194
54. Wang W, Liu SW, Wilde SA, Li QG, Zhang J (2012) Petrogenesis and geochronology of Precambrian granitoid gneisses in Western Liaoning Province: constraints on Neoarchean to early Paleoproterozoic crustal evolution of the North China Craton. Precambr Res 222–223:290–311
55. Wang W, Liu SW, Bai X, Yang PT, Li QG, Zhang LF (2011) Geochemistry and zircon U–Pb–Hf isotopic systematics of the Neoarchean Yixian-Fuxin greenstone belt, northern margin of the North China Craton: implications for petrogenesis and tectonic setting. Gondwana Res 20:64–81
56. Wang QC (1992) On the age of Hongqiyingzi Group and geological thermal events in undergone. Scientia Geologica Sinica (Suppl):17–24 (in Chinese)
57. Wilde SA, Vallly JW, Kita NT et al (2008) SHRIMP U–Pb and CAMECA 1280 oxygen isotope results from ancient detrital zircons in the Caozhuang quartzite, Eastern Hebei, North China Craton: Evidence for crustal reworking 3.8 Ga ago. Am J Sci 308:185–199
58. Wu ML, Zhao GC, Sun M, Li SZ, He YH, Bao ZA (2013) Zircon U–Pb geochronology and Hf isotopes of major lithologies from the Yishui Terrane: implications for the crustal evolution of the Eastern Block, North China Craton. Lithos 170–171:164–178
59. Wu ML, Zhao GC, Sun M, Yin CQ, Li SZ, Tam PY (2012) Petrology and P–T path of the Yishui mafic granulites: Implications for tectonothermal evolution of the Western Shandong Complex in the Eastern Block of the North China Craton. Precambr Res 222–223:312–324
60. Wu JS, Geng YS, Shen QH, Wan YS, Liu DY, Song B (1998) Archean geology characteristics and tectonic evolution of China-Korea Paleo-continent. Geological Publishing House, Beijing, pp 1–212 (in Chinese)
61. Xu B, Charvet J, Chen Y, Zhao P, Shi GZ (2013) Middle Paleozoic convergent orogenic belts in western Inner Mongolia (China): framework, kinematics, geochronology and implications for tectonic evolution of the Central Asian Orogenic Belt. Gondwana Res 23:1342–1364
62. Yang JH, Wu FY, Wilde SA, Zhao GC (2008) Petrogenesis and geodynamics of late Archean magmatism in eastern Hebei, eastern North China Craton: Geochronological, geochemical and Nd–Hf isotopic evidence. Precambr Res 167:125–149
63. Yang JH, Wu FY, Liu XM, Xie LW (2005) Zircon U–Pb ages and Hf isotopes and their geological significance of the Miyun rapakivi granites from Beijing, China. Acta Petrologica Sinica 21:1633–1644 (in Chinese with English abstract)

64. Yu JH, Fu HQ, Zhang FL, Wan FX (1994) Petrogenesis of potassic alkaline volcanism and plutonism in a Proterozoic rift trough near Beijing. Regional Geology of China 2:115–122 (in Chinese with English abstract)
65. Zhang SH, Zhao Y, Ye H, Hu JM, Wu F (2013) New constraints on ages of the Chuanlinggou and Tuanshanzi formations of the Changcheng System in the Yanliao area in the northern North China Craton. Acta Petrologica Sinica 29:2481–2490 (in Chinese with English abstract)
66. Zhang SH, Zhao Y, Santosh M (2012) Mid-Mesoproterozoic bimodal magmatic rocks in the northern North China Craton: implications for magmatism related to breakup of the Columbia supercontinent. Precambr Res 222–223:339–367
67. Zhang SH, Zhao Y, Yang ZY, He ZF, Wu H (2009) The 1.35 Ga diabase sills from the northern North China Craton: implications for breakup of the Columbia (Nuna) supercontinent. Earth Planet Sci Lett 288:588–600
68. Zhang SH, Liu SW, Zhao Y, Yang JH, Song B, Liu XM (2007) The 1.75–1.68 Ga anorthosite-mangerite-alkali granitoid-rapakivi granite suite from the northern North China Craton: magmatism related to a Paleoproterozoic orogen. Precambr Res 155:287–312
69. Zhang FQ, Zhong LJ, Ouyang ZY (1998) Greenstone petro-tectonic framework of cratonic basement, North China. Acta Geophysica Sinica 41:99–107
70. Zhai MG, Santosh M (2011) The Early Precambrian odyssey of the North China Craton: a synoptic overview. Gondwana Res 20:6–25
71. Zhao GC, Zhai MG (2013) Lithotectonic elements of Precambrian basement in the North China Craton: review and tectonic implications. Gondwana Res 23:1207–1240
72. Zhao GC, Cawood PA, Li SZ, Wilde SA, Sun M, Zhang J, He YH, Yin CQ (2012) Amalgamation of the North China Craton: key issues and discussions. Precambr Res 222–223:55–76
73. Zhao TP, Chen W, Zhou MF (2009) Geochemical and Nd–Hf isotopic constraints on the origin of the 1.74 Ga Damiao anorthosite complex, North China Craton. Lithos 113:673–690
74. Zhao GC (2009) Metamorphic evolution of major tectonic units in the basement of the North China Craton: key issues and discussion. Acta Petrologica Sinica 25:1772–1792
75. Zhao GC, Sun M, Wilde SA et al (2005) Late Archean to Proterozoic evolution of the North China Craton: key issues revisited. Precambr Res 136:177–202
76. Zhao TP, Chen FK, Zhai MG, Xia B (2004) Single zircon U–Pb ages and their geological significance of the Damiao anorthosite complex, Hebei Province, China. Acta Petrologica Sinica 20:685–690 (in Chinese with English abstract)
77. Zhao GC, Wilde SA, Cawood PA, Lu LZ (1998) Thermal evolution of the Archaean basement rocks from the eastern part of the North China Craton and its bearing on tectonic setting. Int Geol Rev 40:706–721
78. Zheng YF, Xiao WJ, Zhao GC (2013) Introduction to tectonics of China. Gondwana Res 23:1189–1206
79. Zhong CT, Mao DB, Zhao FQ, Chen ZH, Hu XD (2001) Rock units of the high-pressure granulite belt in northern Hebei Province, North China: their properties, isotopic and evolution. Prog Precambr Res 24:175–183 (in Chinese with English abstract)
80. Zhu RX, Xu YG, Zhu G et al (2012) Destruction of the North China Craton. Sci China (Earth Sci) 55:1565–1587

Chapter 3
Neoarchean Basement Rock Assemblage, Crustal Evolution and Crust-Mantle Interactions of Western Liaoning Province

Abstract The formation and evolution of Archean continental crust as well as related crust-mantle geodynamic evolution history are the major focus of Precambrian studies. As one of the oldest cratons in the world, the North China Craton is dominated by late Neoarchean (~2.6–2.5 Ga) geological events. However, it is still hotly debated about the nature of these major episodes of tectonothermal processes, i.e., whether they represent crustal growth or reworking, and how about the geodynamic regimes (plate tectonics or mantle plume setting)? Systematic studies of lithological assemblage of the basement rocks, petrogenesis, and crust-mantle interactions are key to resolve the above issues. In this chapter, we provide geological, petrological, whole-rock geochemical, and zircon U–Pb and Lu–Hf isotopic data for representative late Neoarchean greenstone metavolcanic rocks and granitoid gneisses in the Western Liaoning Province (WLP) along the northern margin of Eastern Block. It is suggested that magmatic precursors of the metavolcanic rocks in the Fuxin greenstone belt were erupted during ~2640–2534 Ma, and they show dominantly positive zircon $\varepsilon Hf(t_2)$ values of +2.7 to +9.7. These metavolcanic rocks show chemical affinities to Mid-ocean ridge basalts (MORBs), island arc tholeiitic to calc-alkaline basalts, adakite-like and high magnesium andesites, respectively, and they were considered to have been generated by the partial melting of upwelling asthenospheric mantle beneath an Archean spreading ridge and complex interactions between the depleted mantle wedge lithospheric mantle and slab-derived fluids and melts, respectively. Dioritic to TTG gneisses are the major lithologies in the WLP. They were emplaced during ~2532–2506 Ma, and show intrusive relationships with the metavolcanic rocks, with chiefly positive zircon $\varepsilon Hf(t_2)$ values of +1.2 to +8.4. Based on mineral assemblages and chemical features, these granitoid gneisses were subdivided into a high magnesium group (HMG) and a low magnesium group (LMG), which could have been derived from the partial melting of descending oceanic slabs and metabasaltic rocks at the arc root, respectively. Some volume of potassium-rich granitoid gneisses, including granodioritic and monzogranitic rocks with weakly gneissic to massive structures, intruded both the supracrustal metavolcanic rocks and the strongly deformed dioritic to TTG gneisses. They were formed at ~2495 Ma with zircon $\varepsilon Hf(t_2)$ values of +0.9 to +7.6, which were suggested to

W. Wang, *Archean-Mesoproterozoic Crustal Evolution and Crust-Mantle Geodynamics of Western Liaoning-Northeastern Hebei Provinces, North China Craton*, Springer Theses, https://doi.org/10.1007/978-981-10-7922-1_3

have been produced by the partial melting of metamorphosed felsic to sedimentary rocks under an extensional setting. Most of the above lithologies were subjected to ~2485 Ma regional peak granulite facies and ~2450–2401 Ma retrograde metamorphism. ~2.4–1.7 Ga metamorphic imprints could be ascribed to the middle to late Paleoproterozoic tectonothermal events prevailed along the northern margin of NCC. Accordingly, the Western Liaoning Province experienced complex late Neoarchean subduction-accretion processes from mid-ocean ridge spreading, through initiation and maturation of an intra-oceanic arc system, to the final arc-continent accretion. It records intense ~2.6–2.5 Ga subduction-related crustal growth, and the Archean lithospheric mantle sources beneath the northern margin of NCC could have been transformed from juvenile oceanic lithospheric mantle that was initially formed under the oceanic spreading ridge, and they were subjected to gradual metasomatism by slab-derived fluids and melts. All the above data indicate that intra-oceanic subduction and arc-continent accretion within an accretionary orogen could have been an important mechanism of continental growth along the northwestern margin of Eastern Block in the Neoarchean.

Keywords Metavolcanic rocks of greenstone belt · TTG and potassium-rich granitoids · Late Neoarchean crustal growth and formation of lithospheric mantle Archean subduction-accretion processes · Western Liaoning Province North China Craton

3.1 Metavolcanic Rocks in the Fuxin-Yixian Greenstone Belt

The Fuxin-Yixian greenstone belt is located at the eastern segment of the northern margin of the North China Craton (Fig. 3.1). Voluminous metamorphosed supracrustal rocks were developed in this area, with prolific iron, copper, and gold deposits [36, 43, 89–91, 93]. Whole-rock major and trace elements as well as zircon U–Pb and Lu–Hf isotopes were provided for the metavolcanic rocks of the Fuxin-Yixian greenstone belt, aiming to (1) determine their formation ages; (2) analyze the source characteristics and petrogenesis of different lithologies; and (3) decipher the crust-mantle geodynamic processes responsible for the formation of this greenstone belt, which can provide crucial constraints on the early Precambrian crustal formation and evolution of North China Craton.

3.1.1 Geological and Petrographic Features and Sampling

Metavolcanic rocks in the Fuxin-Yixian greenstone belt consist of amphibolites, garnet amphibolites, and hornblende plagioclase gneisses, with subordinate

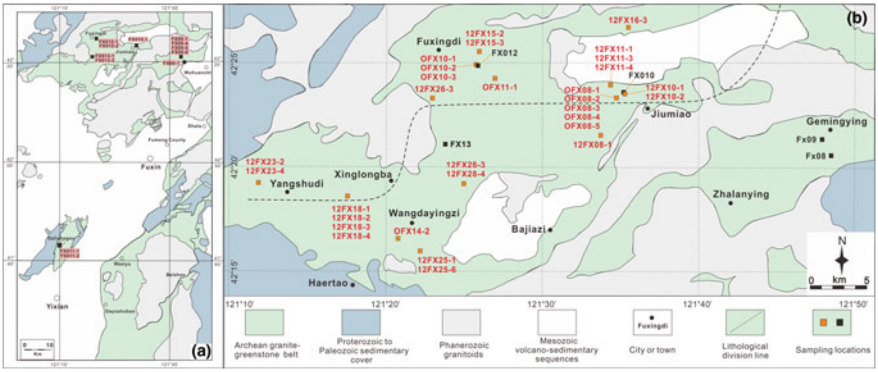

Fig. 3.1 Regional geological map of the Fuxin-Yixian granite-greenstone belt (the left panel), with an amplified map of the basement terrane to the north of Fuxin (the right pannel)

metasedimentary rocks of carbonates and magnetite quartzites. These metavolcanic rocks are intercalated among each other and also with magnetite quartzites and two biotite quartzites on scales from several centimeters to several meters (Fig. 3.2a–d). Metavolcanic rocks occur as xenoliths or roof pendants of variable dimensions within the granitoid gneisses, indicating an intrusive relationship (Fig. 3.2e). These rocks were subjected to intense shear deformation with local mylonitization (Fig. 3.2f).

A total of forty-two representative samples of metavolcanic rocks were collected for geochemical analyses (Fig. 3.1), including twenty-one amphibolites, two garnet clinopyroxene plagioclase gneisses, two garnet clinopyroxene amphibolites, thirteen hornblende plagioclase gneisses, and three metabasaltic and one metaandesitic rocks with palimpsest volcanic textures (Table 3.1). The amphibolites show medium- to fine-grained texture and gneissic structure, with a dominant mineral assemblage of hornblende (43–56%) and plagioclase (44–54%), along with minor magnetite and quartz (Fig. 3.3a). Some garnet- or clinopyroxene-bearing amphibolites show mineral assemblages of hornblende (55–58%) + plagioclase (25–28%) + garnet (8–12%) or hornblende (33–36%) + plagioclase (48–52%) + clinopyroxene (5–8%), with subordinate quartz (3–5%). Zircon, apatite, epidote, and zoisite are the main accessory minerals. Chloritization of hornblende and clinopyroxene, as well as sericitization and kaolinization of plagioclase, are common (Fig. 3.3b). The garnet clinopyroxene plagioclase gneisses (samples 12FX18-2 and 12FX18-3) display fine-grained texture and massive structure, and are composed dominantly of plagioclase (42–46%), clinopyroxene (28–33%), garnet (15–18%), and quartz (3–6%), with minor hornblende and accessory magnetite, zircon, apatite, and zoisite (Fig. 3.3c). The mineral assemblage of garnet + clinopyroxene + plagioclase + quartz indicates possibly high pressure granulite facies metamorphism. The presence of quartz and absence of plutonic rocks and other typical skarn-type minerals (e.g., scapolite and idocrase) in the surrounding areas suggest that these rocks form part of the regional metamorphic

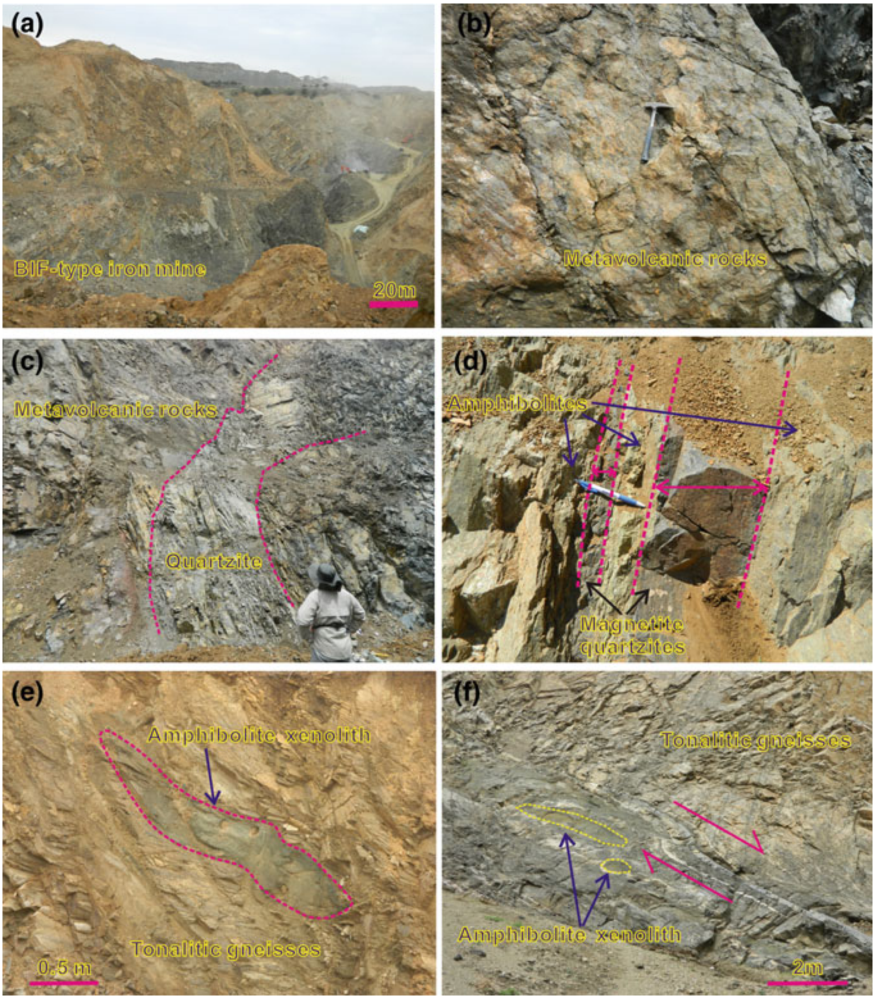

Fig. 3.2 Field geological features of the metamorphosed supracrustal rocks in the Fuxin-Yixian greenstone belt

belt but are not skarn-related. The two garnet clinopyroxene amphibolites (samples OFX08-5 and 12FX10-2; i.e., retrograded granulites) also exhibit fine-grained texture and massive structure. They show mineral association of garnet + clinopyroxene + plagioclase surrounded by rims of hornblende and plagioclase, with a mineral assemblage of plagioclase (40–42%) + clinopyroxene (16–18%) + garnet (24–26%) + hornblende (12–14%) and minor quartz. The accessory minerals are zircon, magnetite, and apatite. Notably, the metabasaltic rock samples 12FX10-1, 12FX11-4, and 12FX26-3 preserve fine-grained porphyritic texture with clinopyroxene phenocrysts (~ 8–12%, with grain size in the range of 0.2–0.5 mm),

Table 3.1 LA-ICPMS zircon U–Pb isotopic dating data for representative metavolcanics from Fuxin-Yixian greenstone belt, Western Liaoning Province

Samples and analytical numbers	Th (ppm)	U (ppm)	Th/U	Isotopic ratios						Apparent ages (Ma)					
				$^{207}Pb/^{206}Pb$	±1σ	$^{207}Pb/^{235}U$	±1σ	$^{206}Pb/^{238}U$	±1σ	$^{207}Pb/^{206}Pb$	±σ	$^{207}Pb/^{235}U$	±σ	$^{206}Pb/^{238}U$	±σ
FX09-1-01	53	92	0.57	0.1767	0.0037	12.0885	0.2295	0.4982	0.0083	2633	35	2611	18	2606	36
FX09-1-02	72	119	0.61	0.1260	0.0016	6.6529	0.1161	0.3806	0.0044	2043	22	2066	15	2079	21
FX09-1-03	314	757	0.42	0.1646	0.0007	10.7652	0.1207	0.4720	0.0052	2503	6	2503	10	2492	23
FX09-1-04	122	216	0.56	0.1680	0.0028	11.2900	0.2354	0.4868	0.0084	2539	27	2547	19	2557	36
FX09-1-05	31	191	0.16	0.1633	0.0016	10.6480	0.1160	0.4722	0.0051	2490	16	2493	10	2493	22
FX09-1-06	42	87	0.48	0.1669	0.0021	10.9714	0.1952	0.4778	0.0078	2528	21	2521	17	2518	34
FX09-1-07	95	149	0.64	0.1660	0.0013	10.9884	0.1344	0.4786	0.0054	2518	13	2522	11	2521	23
FX09-1-08	22	68	0.33	0.1519	0.0022	9.3537	0.2046	0.4456	0.0078	2369	25	2373	20	2376	35
FX09-1-09	78	114	0.68	0.1623	0.0016	10.5361	0.1658	0.4699	0.0064	2480	17	2483	15	2483	28
FX09-1-11	61	140	0.44	0.1629	0.0013	10.7047	0.1510	0.4755	0.0065	2487	13	2498	13	2508	28
FX09-1-12	48	121	0.39	0.1637	0.0043	10.9532	0.3792	0.4866	0.0156	2495	44	2519	32	2556	68
FX09-1-13	57	104	0.55	0.1630	0.0025	10.5285	0.1708	0.4691	0.0079	2487	26	2482	15	2480	35
FX09-1-14	211	1535	0.14	0.1631	0.0005	10.5286	0.1160	0.4658	0.0046	2489	6	2482	10	2465	20
FX09-1-15	52	131	0.40	0.1686	0.0061	11.0029	0.4560	0.4789	0.0189	2544	60	2523	39	2522	82
FX09-1-16	53	100	0.53	0.1608	0.0023	10.2928	0.1737	0.4655	0.0068	2464	25	2461	16	2464	30
FX09-1-17	42	77	0.55	0.1688	0.0021	11.4079	0.1708	0.4885	0.0060	2545	21	2557	14	2564	26
FX09-1-18	42	123	0.34	0.1640	0.0011	10.7013	0.1111	0.4704	0.0033	2498	11	2498	10	2486	14
FX09-1-19	71	158	0.45	0.1578	0.0011	10.0473	0.1188	0.4598	0.0047	2432	12	2439	11	2438	21
FX09-1-21	204	1471	0.14	0.1664	0.0005	11.0306	0.0496	0.4792	0.0021	2521	5	2526	4	2524	9
FX09-1-22	95	153	0.62	0.1656	0.0020	11.0061	0.1393	0.4836	0.0063	2514	53	2524	12	2543	27
FX09-1-23	63	120	0.53	0.1700	0.0023	11.4134	0.2284	0.4872	0.0093	2558	23	2558	19	2558	40
FX09-1-24	202	1678	0.12	0.1668	0.0004	11.0142	0.1306	0.4773	0.0055	2528	5	2524	11	2516	24
FX09-1-26	25	145	0.17	0.1283	0.0015	6.6738	0.1100	0.3763	0.0049	2076	20	2069	15	2059	23
FX09-1-28	142	902	0.16	0.1637	0.0005	10.7838	0.0593	0.4764	0.0022	2494	5	2505	5	2511	9

(continued)

Table 3.1 (continued)

Samples and analytical numbers	Th (ppm)	U (ppm)	Th/U	Isotopic ratios						Apparent ages (Ma)					
				$^{207}Pb/^{206}Pb$	±1σ	$^{207}Pb/^{235}U$	±1σ	$^{206}Pb/^{238}U$	±1σ	$^{207}Pb/^{206}Pb$	±σ	$^{207}Pb/^{235}U$	±σ	$^{206}Pb/^{238}U$	±σ
FX09-1-29	74	1887	0.04	0.1618	0.0005	10.4456	0.1109	0.4666	0.0044	2476	6	2475	10	2468	19
FX09-1-30	214	1642	0.13	0.1635	0.0004	10.7290	0.0614	0.4739	0.0024	2492	5	2500	5	2501	11
FX09-1-31	159	1177	0.13	0.1609	0.0009	10.2239	0.1192	0.459	0.0049	2465	10	2455	11	2435	22
FX09-1-32	285	773	0.37	0.1639	0.0014	10.7704	0.0934	0.4749	0.0028	2498	14	2504	8	2505	12
FX09-1-33	1684	1712	0.98	0.1623	0.0006	10.4414	0.1021	0.464	0.0041	2480	6	2475	9	2457	18
FX09-1-34	49	229	0.21	0.1681	0.0021	11.1132	0.1569	0.4789	0.0059	2539	22	2533	13	2522	26
FX09-1-35	826	1320	0.63	0.1613	0.0005	10.5394	0.1872	0.4703	0.0076	2470	6	2483	16	2485	33
FX09-1-36	158	1376	0.11	0.1619	0.0007	10.4148	0.1114	0.4648	0.0052	2475	3	2472	10	2461	23
FX09-1-37	392	576	0.68	0.1627	0.0018	10.6074	0.0885	0.4714	0.0045	2484	19	2489	8	2490	20
FX09-1-38	46	152	0.30	0.1720	0.0039	10.9600	0.2182	0.4727	0.0096	2577	38	2520	19	2495	42
12FX18-2-01	39	109	0.35	0.1815	0.0048	12.7880	0.3290	0.5115	0.0106	2666	19	2664	24	2663	45
12FX18-2-02	36	151	0.24	0.1582	0.0043	9.9569	0.2600	0.4569	0.0095	2436	20	2431	24	2426	42
12FX18-2-03	21	64	0.33	0.1760	0.0055	12.0682	0.3720	0.4976	0.0118	2616	24	2610	29	2604	51
12FX18-2-05	91	163	0.56	0.1680	0.0044	11.1382	0.2843	0.4813	0.0098	2538	20	2535	24	2533	43
12FX18-2-06	6	21	0.31	0.1772	0.0071	11.3780	0.4557	0.4661	0.0122	2627	34	2555	37	2467	54
12FX18-2-07	5	41	0.11	0.1577	0.0054	9.9703	0.3389	0.4589	0.0112	2431	28	2432	31	2435	49
12FX18-2-08	3	51	0.06	0.1655	0.0050	10.8714	0.3238	0.4767	0.0109	2513	23	2512	28	2513	47
12FX18-2-09	17	72	0.24	0.1580	0.0048	9.9664	0.2944	0.4578	0.0100	2435	24	2432	27	2430	44
12FX18-2-10	5	14	0.31	0.1426	0.0093	8.0559	0.5237	0.4100	0.0135	2259	67	2237	59	2215	62
12FX18-2-11	81	120	0.68	0.1667	0.0047	10.3249	0.2810	0.4497	0.0094	2524	21	2464	25	2394	42
12FX18-2-12	43	109	0.39	0.1764	0.0048	11.2517	0.2980	0.4630	0.0096	2619	20	2544	25	2453	42
12FX18-2-13	17	43	0.38	0.1436	0.0052	7.6739	0.2717	0.3880	0.0091	2270	31	2194	32	2114	42
12FX18-2-14	2	95	0.02	0.1672	0.0049	11.1277	0.3161	0.4830	0.0104	2530	22	2534	26	2540	45
12FX18-2-15	18	114	0.16	0.1656	0.0047	10.8817	0.3038	0.4769	0.0101	2514	22	2513	26	2514	44

(continued)

Table 3.1 (continued)

Samples and analytical numbers	Th (ppm)	U (ppm)	Th/U	Isotopic ratios						Apparent ages (Ma)					
				$^{207}Pb/^{206}Pb$	±1σ	$^{207}Pb/^{235}U$	±1σ	$^{206}Pb/^{238}U$	±1σ	$^{207}Pb/^{206}Pb$	±σ	$^{207}Pb/^{235}U$	±σ	$^{206}Pb/^{238}U$	±σ
12FX18-2-16	18	100	0.18	0.1667	0.0050	10.5204	0.3081	0.4581	0.0099	2525	23	2482	27	2431	44
12FX18-2-17	28	95	0.29	0.1815	0.0052	12.7268	0.3568	0.5088	0.0108	2667	22	2660	26	2652	46
12FX18-2-18	9	109	0.08	0.1440	0.0043	7.7314	0.2235	0.3896	0.0082	2276	24	2200	26	2121	38
12FX18-2-19	32	131	0.25	0.1650	0.0051	10.8274	0.3295	0.4763	0.0106	2508	24	2508	28	2511	46
12FX18-2-20	3	36	0.09	0.1652	0.0061	10.6286	0.3920	0.4669	0.0126	2510	30	2491	34	2470	55
12FX18-2-21	48	210	0.23	0.1593	0.0046	9.9845	0.2810	0.4549	0.0094	2448	23	2433	26	2417	42
12FX18-2-22	15	126	0.12	0.1593	0.0048	10.0897	0.2952	0.4597	0.0096	2448	24	2443	27	2438	42
12FX18-2-23	0	9	0.05	0.1688	0.0099	11.2393	0.6601	0.4833	0.0168	2546	54	2543	55	2541	73
12FX18-2-24	6	64	0.10	0.1658	0.0055	10.8681	0.3584	0.4757	0.0108	2516	28	2512	31	2508	47
12FX18-2-25	5	15	0.32	0.1758	0.0103	11.6856	0.6931	0.4823	0.0162	2614	56	2580	55	2537	70
12FX18-2-26	2	32	0.05	0.1667	0.0084	11.0161	0.5604	0.4797	0.0150	2524	45	2524	47	2526	66
12FX18-2-27	30	152	0.20	0.1659	0.0052	10.5674	0.3267	0.4623	0.0102	2517	25	2486	29	2450	45
12FX18-2-28	5	107	0.05	0.1585	0.0060	10.0742	0.3753	0.4612	0.0110	2440	33	2442	34	2445	49
12FX18-2-29	5	65	0.08	0.1056	0.0050	4.5316	0.2127	0.3115	0.0080	1725	49	1737	39	1748	40
12FX18-2-30	2	12	0.14	0.1765	0.0085	10.6538	0.5316	0.4381	0.0171	2620	38	2493	46	2342	77
12FX25-6-01	282	118	2.39	0.1510	0.0043	9.2430	0.2551	0.4441	0.0097	2357	22	2362	25	2369	43
12FX25-6-02	97	72	1.34	0.1404	0.0041	7.9701	0.2306	0.4119	0.0090	2232	24	2228	26	2224	41
12FX25-6-03	121	93	1.31	0.1555	0.0046	9.7271	0.2806	0.4539	0.0102	2407	23	2409	27	2413	45
12FX25-6-04	524	221	2.37	0.1555	0.0040	9.6015	0.2411	0.4481	0.0094	2407	19	2397	23	2387	42
12FX25-6-05	1043	708	1.47	0.1613	0.0040	10.4043	0.2568	0.4679	0.0097	2469	19	2471	23	2474	43
12FX25-6-06	150	185	0.81	0.1552	0.0040	9.3308	0.2393	0.4360	0.0091	2404	20	2371	24	2333	41
12FX25-6-07	411	365	1.13	0.1618	0.0041	10.4424	0.2598	0.4682	0.0097	2475	19	2475	23	2475	43
12FX25-6-08	427	882	0.48	0.1482	0.0037	8.8581	0.2185	0.4335	0.0089	2326	19	2323	23	2321	40
12FX25-6-09	234	201	1.16	0.1551	0.0041	9.7079	0.2525	0.4539	0.0096	2403	20	2407	24	2413	42

(continued)

Table 3.1 (continued)

Samples and analytical numbers	Th (ppm)	U (ppm)	Th/U	Isotopic ratios						Apparent ages (Ma)					
				$^{207}Pb/^{206}Pb$	±1σ	$^{207}Pb/^{235}U$	±1σ	$^{206}Pb/^{238}U$	±1σ	$^{207}Pb/^{206}Pb$	±σ	$^{207}Pb/^{235}U$	±σ	$^{206}Pb/^{238}U$	±σ
12FX25-6-10	345	158	2.18	0.1551	0.0041	9.3135	0.2416	0.4356	0.0091	2403	20	2369	24	2331	41
12FX25-6-11	82	78	1.05	0.1522	0.0044	9.3704	0.2639	0.4465	0.0096	2371	22	2375	26	2380	43
12FX25-6-12	2	7	0.23	0.1410	0.0118	8.0474	0.6509	0.4141	0.0157	2239	88	2236	73	2234	71
12FX25-6-13	129	94	1.38	0.1614	0.0048	10.3420	0.3011	0.4647	0.0104	2471	23	2466	27	2460	46
12FX25-6-14	1228	525	2.34	0.1689	0.0044	11.2108	0.2866	0.4816	0.0100	2546	19	2541	24	2534	43
12FX25-6-15	198	162	1.22	0.1244	0.0099	6.1201	0.4605	0.3568	0.0091	2020	145	1993	66	1967	43
12FX28-3-01	25	50	0.51	0.1677	0.0054	10.8566	0.3411	0.4698	0.0107	2534	25	2511	29	2482	47
12FX28-3-02	41	44	0.92	0.1676	0.0052	11.1027	0.3347	0.4805	0.0109	2534	24	2532	28	2529	47
12FX28-3-03	90	79	1.14	0.1624	0.0047	10.1773	0.2869	0.4547	0.0098	2480	22	2451	26	2416	43
12FX28-3-04	176	308	0.57	0.1686	0.0046	11.2171	0.2998	0.4825	0.0101	2544	21	2541	25	2538	44
12FX28-3-05	58	79	0.74	0.1616	0.0048	10.4137	0.3019	0.4674	0.0102	2473	23	2472	27	2472	45
12FX28-3-06	41	47	0.85	0.1620	0.0053	10.18070	0.3281	0.4559	0.0101	2476	27	2451	30	2422	45
12FX28-3-07	40	48	0.84	0.1611	0.0051	10.3451	0.3238	0.4659	0.0103	2467	26	2466	29	2466	45
12FX28-3-08	77	77	0.99	0.1497	0.0044	8.5465	0.2486	0.4141	0.0089	2343	24	2291	26	2234	40
12FX28-3-09	30	42	0.71	0.1531	0.0048	9.4279	0.2888	0.4467	0.0098	2381	25	2381	28	2381	44
12FX28-3-10	62	87	0.71	0.1575	0.0050	9.9534	0.3064	0.4584	0.0101	2429	25	2430	28	2433	45
12FX28-3-11	61	93	0.66	0.1615	0.0049	10.4256	0.3088	0.4682	0.0101	2472	24	2473	27	2476	44
12FX28-3-12	111	152	0.73	0.1622	0.0049	10.2034	0.3031	0.4562	0.0098	2479	24	2453	27	2423	43
12FX28-3-13	57	73	0.79	0.1714	0.0058	11.6442	0.3839	0.4927	0.0114	2572	27	2576	31	2583	49
12FX28-3-14	94	142	0.66	0.1668	0.0051	11.0602	0.3312	0.4810	0.0103	2526	24	2528	28	2531	45
12FX28-3-15	33	43	0.77	0.1666	0.0057	10.3855	0.3467	0.4521	0.0103	2524	28	2470	31	2405	46
12FX28-3-16	29	34	0.84	0.1576	0.0066	9.9273	0.4037	0.4571	0.0108	2430	38	2428	38	2427	48
12FX28-3-17	41	101	0.41	0.1622	0.0053	9.9597	0.3173	0.4455	0.0096	2479	27	2431	29	2375	43
12FX28-3-18	38	52	0.72	0.1625	0.0054	10.2090	0.3338	0.4558	0.0101	2482	28	2454	30	2421	45

(continued)

Table 3.1 (continued)

Samples and analytical numbers	Th (ppm)	U (ppm)	Th/U	Isotopic ratios						Apparent ages (Ma)					
				$^{207}Pb/^{206}Pb$	±1σ	$^{207}Pb/^{235}U$	±1σ	$^{206}Pb/^{238}U$	±1σ	$^{207}Pb/^{206}Pb$	±σ	$^{207}Pb/^{235}U$	±σ	$^{206}Pb/^{238}U$	±σ
12FX28-3-19	290	249	1.16	0.1618	0.0052	10.1363	0.3201	0.4545	0.0097	2474	27	2447	29	2415	43
12FX28-3-20	55	71	0.78	0.1615	0.0057	9.7603	0.3334	0.4385	0.0099	2471	29	2412	31	2344	44
12FX28-3-21	136	221	0.61	0.1683	0.0056	11.1857	0.3639	0.4821	0.0104	2541	28	2539	30	2536	45
12FX28-3-22	90	120	0.75	0.1693	0.0059	10.5505	0.3582	0.4520	0.0101	2551	29	2484	31	2404	45
12FX28-3-23	250	309	0.81	0.1622	0.0055	9.9438	0.3302	0.4449	0.0096	2478	29	2430	31	2372	43
12FX28-3-24	45	62	0.72	0.1619	0.0061	9.8406	0.3619	0.4411	0.0100	2475	33	2420	34	2356	45
12FX28-3-25	341	287	1.19	0.1680	0.0057	10.6531	0.3522	0.4601	0.0099	2537	29	2493	31	2440	43

Note ^{204}Pb has been corrected using the method of [2]

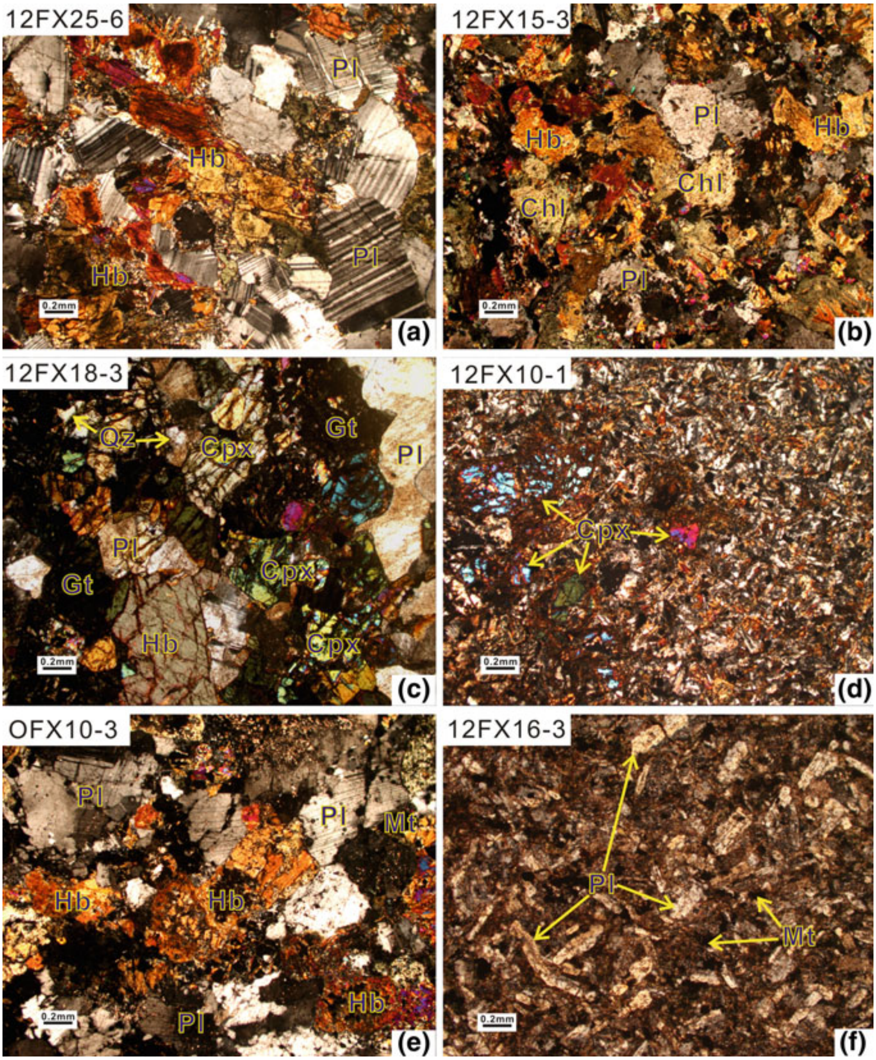

Fig. 3.3 Microphotographs of representative **a** amphibolite, **b** chloritized amphibolite, **c** garnet clinopyroxene plagioclase gneiss, **d** palimpsest basalt, **e** hornblende plagioclase gneisses and **f** palimpsest andesite of the Fuxin-Yixian greenstone belt. (+): cross-polarized light; (-): plane-polarized light. *Mineral abbreviations* Cpx—clinopyroxene; Hb—hornblende; Chl—chlorite; Mt—magnetite; Pl—plagioclase; Qz—quartz

and plagioclase, magnetite, and clinopyroxene in the groundmass constitute a typical intersertal texture (Fig. 3.3d). The hornblende plagioclase gneisses exhibit medium- to fine-grained texture and gneissic structure, and are composed of more plagioclase (54–63%) and less hornblende (32–42%) than the metabasaltic rocks, with minor magnetite, quartz, and biotite (Fig. 3.3e). Zircon, apatite, and zoisite are the major accessory minerals. The mafic minerals were commonly subjected to chloritization or zoisitization, whereas plagioclase grains were locally altered to sericite or kaolinite. Sample 12FX16-3 preserves fine-grained andesitic texture, with mafic minerals (generally altered to biotite and magnetite) and plagioclase crystals in the groundmass showing crude alignment (Fig. 3.3f). It is noteworthy that the basaltic and andesitic rocks subjected to low-grade metamorphism occur dominantly along the northern margin of Fuxin greenstone belt, and are locally intercalated with amphibolites or retrograded granulites (Fig. 3.1).

3.1.2 Zircon U–Pb and Lu–Hf Isotopes

3.1.2.1 Sample FX09-1 (Metaandesitic Rocks)

The hornblende plagioclase gneiss sample FX09-1 was collected near Gemingying village (Fig. 3.1). Zircon grains separated from this rock show oval to stubby shapes, with lengths and length/width ratios of 100–300 μm and 1:1–2:1, respectively. Cathodoluminescence (CL) images reveal core-rim structures, showing oscillatory and blurred zoned (e.g., spots #17 and #38) or structureless (e.g., spots #6 and #32) cores surrounded by bright or dark rims (e.g., spot #36; Fig. 3.4a). Locally, dark seams are preserved between the oscillatory cores and bright rims, representing metamorphic recrystallization and overgrowth [19]. A total of thirty-four analyses were conducted on thirty-four zircon grains, and all the data plot on or close to the concordia, yielding apparent $^{207}Pb/^{206}Pb$ ages ranging between 2633 ± 35 Ma and 2076 ± 20 Ma (Fig. 3.4b). Th/U ratios are generally >0.11. Two analyses (spots #12 and #15) with large errors are rejected from the age calculation (Table 3.1). Chondrite-normalized REE patterns of the analyzed zircon grains show mostly positive Ce and negative Eu anomalies with fractionated heavy REE patterns, indicating that they are originally magmatic zircons but were subjected to subsequent Pb loss triggered by metamictization or metamorphic recrystallization [89]. On the probability density plot (not shown), the analyses constitute two major age peaks and several small peaks, which are divided into three groups as followed.

(1) Eleven analyses form the oldest age peak, among which seven analyses on oscillatory zoned cores yield a concordia age of 2534 ± 6 Ma (MSWD = 0.05), and are considered to be close to the crystallization age of the magmatic precursor (Fig. 3.4b).
(2) Sixteen analyses, mostly on the structureless cores or rims, define the second age peak. They yield an upper intercept age of 2482 ± 5 Ma (MSWD = 1.9; Fig. 3.4b). This age, when combined with ages of the four youngest analyses (spots #2, #8, #19, and #26 with apparent $^{207}Pb/^{206}Pb$ ages of 2432 ± 12 Ma to 2043 ± 22 Ma), represent the effects of multiple Paleoproterozoic tectonothermal events on the magmatic precursor of sample FX09-1.

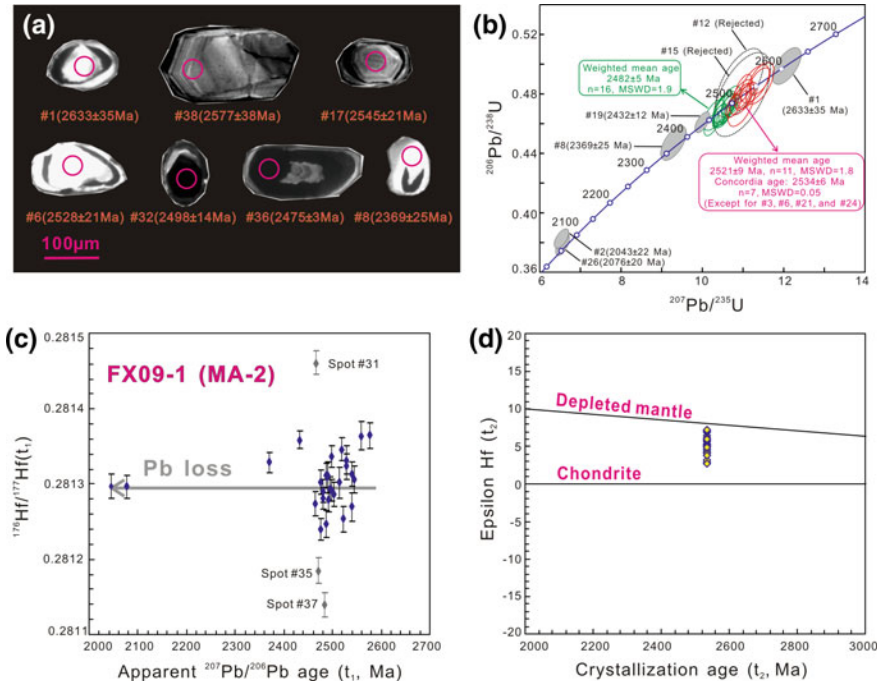

Fig. 3.4 Internal structures and U–Pb and Lu–Hf isotopic data of zircons from the hornblende plagioclase gneiss sample FX09-1. **a** CL images of representative zircon grains showing internal structures and analyzed locations. Numbers are spot locations in Table 3.1. **b** Concordia diagram showing all analyzed spots. **c** $^{176}Hf/^{177}Hf(t_1)$ isotopic ratios versus apparent $^{207}Pb/^{206}Pb$ ages (t_1) diagram. The defined horizontal line (except three analyses #1, #12, and #15) points to the dominant effects of Pb loss. **d** εHf(t_2) versus crystallization age (t_2, 2534 Ma) of sample FX09-1. The $^{176}Lu/^{177}Hf$ isotopic ratios of the depleted mantle and chondrite are 0.0384 and 0.0332, respectively, after Blichert-Toft and Albarède [6] and Griffin et al. [20]

(3) Analysis of spot #1 on a blurred zoned core shows an older apparent $^{207}Pb/^{206}Pb$ age of 2633 ± 35 Ma. This age is within error of the crystallization ages of the magmatic precursors for samples OFX08-5 and 12FX18-2 (Figs. 3.5 and 3.6), which is therefore taken as the age of xenocrystic zircon grains.

A total of thirty-one dated spots were further analyzed for Lu–Hf isotopes (excluding spots #1, #12, and #15; Table 3.2). When calculated at the apparent $^{207}Pb/^{206}Pb$ ages (t_1), most of them yield nearly consistent $^{176}Hf/^{177}Hf(t_1)$ ratios of 0.281240–0.281365 (Fig. 3.4c). This implies that the zircon grains were originally crystallized from the same magmatic event, but were subjected to different degrees of Pb loss [89, 100, 101]. When recalculated at the crystallization age of the rock (2534 Ma of t_2, except for the three anomalous spots #31, #35, and #37), the data

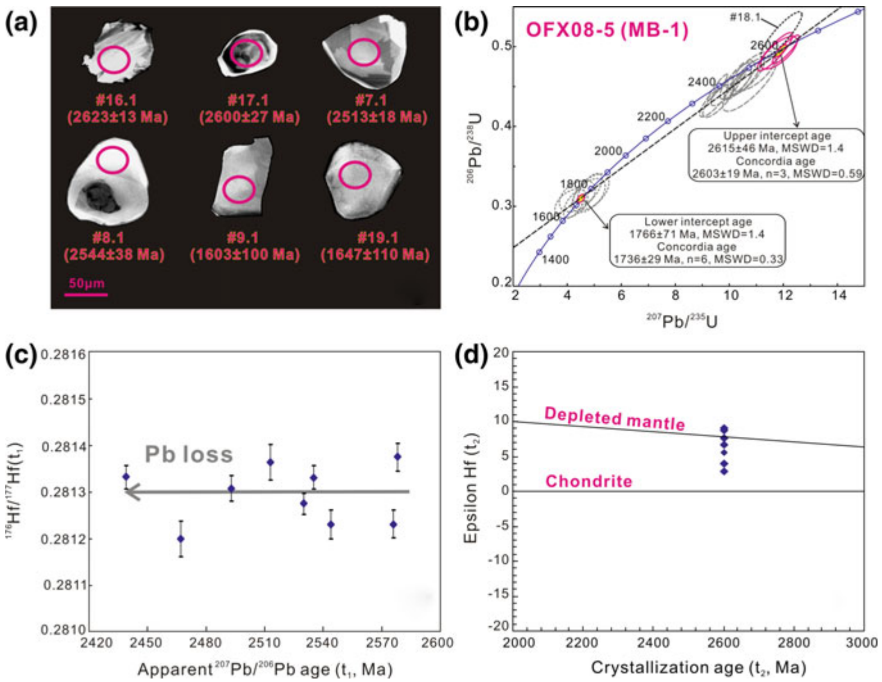

Fig. 3.5 Internal structures and U–Pb and Lu–Hf isotopic data of zircons from the garnet clinopyroxene plagioclase gneiss sample OFX08-5. **a** CL images of representative zircon grains showing internal structures and analyzed locations. Numbers are spot locations in Table 3.3. **b** Concordia diagram showing all analyzed spots. **c** The $^{176}Hf/^{177}Hf(t_1)$ isotopic ratios versus apparent $^{207}Pb/^{206}Pb$ ages (t_1) diagram. The nearly consistent $^{176}Hf/^{177}Hf(t_1)$ isotopic ratios define a horizontal line, pointing to the dominant effects of Pb loss. **d** $\varepsilon Hf(t_2)$ versus the crystallization age (t_2, 2603 Ma) of sample OFX08-5

show $\varepsilon Hf(t_2)$ and $T_{DM}(Hf)$ values of +2.7 to +7.2 and 2733–2567 Ma, respectively (Fig. 3.4d).

3.1.2.2 Sample 12FX08-5 (Metabasaltic Rocks)

Sample OFX08-5 is a garnet clinopyroxene amphibolite (retrograded granulite) from the northwest of Jiumiao which has been retrograded under amphibolite facies (Fig. 3.1). Zircon grains separated from this sample show stubby or oval shapes, with lengths and length/width ratios of 50–80 μm and 1:1–1.5:1, respectively (Fig. 3.5a). On the cathodoluminescence images, some zircon grains show oscillatory or blurred zoned structures (spots #16.1 and #17.1), whereas others display fir-tree zonings (spot #7.1) or bright homogenous domains without internal structures (spots #8.1 and #9.1). A total of twenty-one analyses were conducted on twenty-one zircon grains using SHRIMP U-Pb isotopic dating method, and the

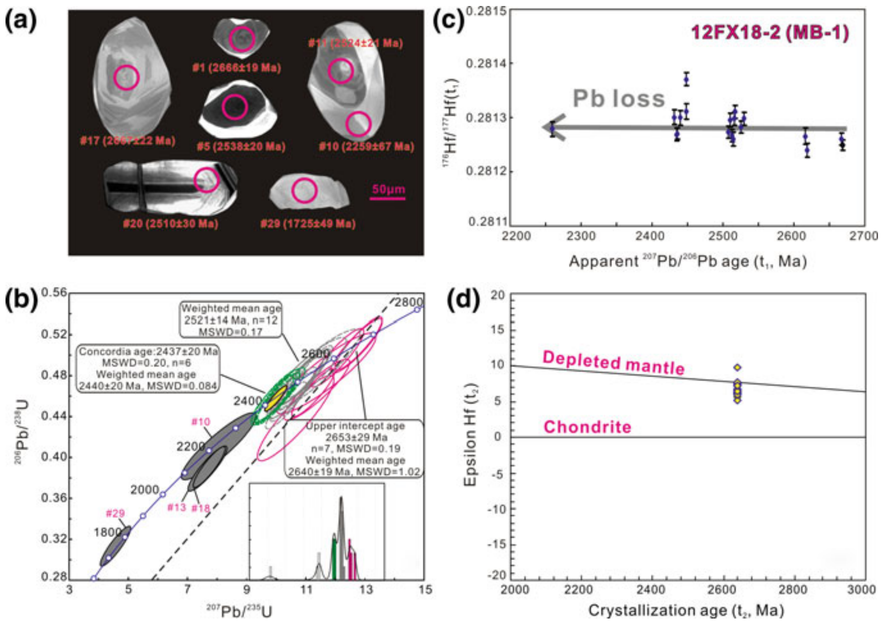

Fig. 3.6 Internal structures and U–Pb and Lu–Hf isotopic data of zircons from the garnet clinopyroxene plagioclase gneiss sample 12FX18-2. **a** CL images of representative zircon grains showing internal structures and analytized locations. Numbers are spot locations in Table 3.1. **b** Concordia diagram showing all analyzed spots, with a histogram of the apparent $^{207}Pb/^{206}Pb$ ages as an inset. **c** $^{176}Hf/^{177}Hf$ (t_1) versus apparent $^{207}Pb/^{206}Pb$ age (t_1) diagram. **d** εHf(t_2) versus crystallization age (t_2, 2640 Ma) diagram

results show apparent $^{207}Pb/^{206}Pb$ ages between 2623 ± 13 Ma and 1603 ± 100 Ma (Table 3.3). Th and U contents range from 1–19 ppm and 9–129 ppm, respectively, with Th/U ratios of mostly >0.10 (except for spots #4.1 and #15.1 with lower values of 0.06–0.09). The isotopic ratios of spot #18.1 are plotted above the concordia, which is excluded from the age calculation (Fig. 3.5b). The remaining twenty analyses define a discordia, yielding an upper intercept age of 2615 ± 46 Ma and a lower intercept age of 1766 ± 71 Ma (MSWD = 1.4). Among these, three analyses with oscillatory or blurred zonings plot close to the upper intercept (spots #10.1, #16.1, and #17.1), and yield a concordia age of 2603 ± 19 Ma (MSWD = 0.59). In the lower intercept, six analyses (spots #2.1, #9.1, #13.1, #14.1, #19.1, and #21.1), mostly on bright structureless zircon grains, give a younger concordia age of 1736 ± 29 Ma (MSWD = 0.33).

Nine Lu–Hf isotopic data were obtained from the dated magmatic zircon domains (with isotopic ratios close to the upper intercept, Fig. 3.5d and Table 3.2). As shown on the CL images, the zircon grains with isotopic ratios close to the lower intercept are generally metamorphic overgrowths [72]. Lu–Hf isotopic analyses were not performed on these grains as they do not represent composition of the original magmas [100, 101]. When calculated at the apparent $^{207}Pb/^{206}Pb$ ages (t_1),

Table 3.2 Zircon Lu–Hf isotopic data for the dated spots of representative metavolcanics from Fuxin-Yixian greenstone belt, Western Liaoning Province

Samples and analytical numbers	t_1 (Ma)	$^{176}Yb/^{177}Hf$	$^{176}Lu/^{177}Hf$	$^{176}Hf/^{177}Hf$	2σ	$(^{176}Hf/^{177}Hf)t_1$	2σ	t_2 (Ma)	$\varepsilon_{Hf}(0)$	$\varepsilon_{Hf}(t_2)$	T_{DM} (Ma)	$f_{Lu/Hf}$
FX09-1-01	2633	0.020257	0.000634	0.281331	0.000017	0.281299	0.000017	–	−50.9	–	–	−0.98
FX09-1-02	2043	0.027261	0.000858	0.281331	0.000016	0.281298	0.000016	2534	−51.0	4.5	2670	−0.97
FX09-1-03	2503	0.010749	0.000356	0.281303	0.000016	0.281286	0.000016	2534	−52.0	4.3	2674	−0.99
FX09-1-04	2539	0.036878	0.001157	0.281369	0.000016	0.281313	0.000016	2534	−49.6	5.3	2639	−0.97
FX09-1-05	2490	0.012226	0.000374	0.281326	0.000021	0.281309	0.000021	2534	−51.1	5.1	2643	−0.99
FX09-1-06	2528	0.017435	0.000547	0.281351	0.000017	0.281324	0.000017	2534	−50.3	5.7	2622	−0.98
FX09-1-07	2518	0.017810	0.000552	0.281372	0.000015	0.281346	0.000015	2534	−49.5	6.5	2593	−0.98
FX09-1-08	2369	0.019323	0.000603	0.281356	0.000014	0.281329	0.000014	2534	−50.1	5.8	2619	−0.98
FX09-1-09	2480	0.026059	0.000809	0.281330	0.000016	0.281291	0.000016	2534	−51.0	4.5	2668	−0.98
FX09-1-11	2487	0.020023	0.000556	0.281273	0.000018	0.281247	0.000018	2534	−53.0	2.9	2727	−0.98
FX09-1-12	2495	0.011828	0.000372	0.281319	0.000015	0.281301	0.000015	2534	−51.4	4.9	2653	−0.99
FX09-1-13	2487	0.014825	0.000457	0.281334	0.000016	0.281312	0.000016	2534	−50.9	5.3	2639	−0.99
FX09-1-14	2489	0.017580	0.000531	0.281338	0.000017	0.281312	0.000017	2534	−50.7	5.3	2639	−0.98
FX09-1-15	2544	0.016494	0.000460	0.281353	0.000014	0.281330	0.000014	2534	−50.2	5.9	2614	−0.99
FX09-1-16	2464	0.028122	0.000797	0.281312	0.000016	0.281274	0.000016	2534	−51.6	3.9	2692	−0.98
FX09-1-17	2545	0.016685	0.000519	0.281333	0.000018	0.281307	0.000018	2534	−50.9	5.1	2645	−0.98
FX09-1-18	2498	0.015831	0.000541	0.281363	0.000014	0.281337	0.000014	2534	−49.8	6.1	2606	−0.98
FX09-1-19	2432	0.015504	0.000459	0.281380	0.000012	0.281359	0.000012	2534	−49.2	6.9	2577	−0.99
FX09-1-21	2521	0.010838	0.000353	0.281271	0.000017	0.281254	0.000017	2534	−53.1	3.2	2716	−0.99
FX09-1-22	2514	0.027900	0.000884	0.281345	0.000020	0.281302	0.000020	2534	−50.5	4.9	2654	−0.97
FX09-1-23	2558	0.024145	0.000696	0.281398	0.000019	0.281364	0.000019	2534	−48.6	7.2	2568	−0.98
FX09-1-24	2528	0.014155	0.000457	0.281354	0.000019	0.281332	0.000019	2534	−50.1	6.0	2611	−0.99
FX09-1-26	2076	0.012397	0.000386	0.281312	0.000015	0.281297	0.000015	2534	−51.6	4.6	2663	−0.99

(continued)

Table 3.2 (continued)

Samples and analytical numbers	t_1 (Ma)	$^{176}Yb/^{177}Hf$	$^{176}Lu/^{177}Hf$	$^{176}Hf/^{177}Hf$	2σ	$(^{176}Hf/^{177}Hf)t_1$	2σ	t_2 (Ma)	$\varepsilon_{Hf}(0)$	$\varepsilon_{Hf}(t_2)$	T_{DM} (Ma)	$f_{Lu/Hf}$
FX09-1-28	2494	0.013990	0.000436	0.281315	0.000016	0.281294	0.000016	2534	−51.5	4.6	2663	−0.99
FX09-1-29	2476	0.000407	0.000008	0.281240	0.000015	0.281240	0.000015	2534	−54.2	2.7	2733	−1.00
FX09-1-30	2492	0.012824	0.000425	0.281300	0.000016	0.281280	0.000016	2534	−52.1	4.1	2682	−0.99
FX09-1-31	2465	0.009845	0.000271	0.281474	0.000015	0.281461	0.000015	–	−45.9	–	–	−0.99
FX09-1-32	2498	0.009214	0.000297	0.281307	0.000014	0.281292	0.000014	2534	−51.8	4.6	2665	−0.99
FX09-1-33	2480	0.017405	0.000490	0.281305	0.000015	0.281281	0.000015	2534	−51.9	4.2	2680	−0.99
FX09-1-34	2539	0.015974	0.000465	0.281292	0.000019	0.281270	0.000019	2534	−52.3	3.8	2695	−0.99
FX09-1-35	2470	0.053830	0.001508	0.281256	0.000017	0.281185	0.000017	–	−53.6	–	–	−0.95
FX09-1-36	2475	0.013953	0.000437	0.281323	0.000016	0.281302	0.000016	2534	−51.3	4.9	2652	−0.99
FX09-1-37	2484	0.024412	0.000762	0.281175	0.000016	0.281139	0.000016	–	−56.5	–	–	−0.98
FX09-1-38	2577	0.021163	0.000698	0.281399	0.000017	0.281365	0.000017	2534	−48.6	7.2	2567	−0.98
OFX08-5-01	2530	0.013515	0.000338	0.281292	0.000023	0.281276	0.000023	2603	−52.3	5.6	2687	−0.99
OFX08-5-03	2535	0.013980	0.000356	0.281349	0.000024	0.281332	0.000024	2603	−50.3	7.6	2612	−0.99
OFX08-5-04	2578	0.014995	0.000398	0.281395	0.000029	0.281375	0.000029	2603	−48.7	9.1	2553	−0.99
OFX08-5-05	2439	0.016270	0.000472	0.281354	0.000024	0.281332	0.000024	2603	−50.1	7.5	2612	−0.99
OFX08-5-06	2493	0.011676	0.000331	0.281323	0.000028	0.281307	0.000028	2603	−51.2	6.7	2645	−0.99
OFX08-5-07	2513	0.018489	0.000667	0.281397	0.000038	0.281365	0.000038	2603	−48.6	8.7	2568	−0.98
OFX08-5-08	2544	0.006624	0.000139	0.281238	0.000031	0.281231	0.000031	2603	−54.3	4.0	2745	−1.00
OFX08-5-10	2576	0.015509	0.000666	0.281265	0.000031	0.281232	0.000031	2603	−53.3	4.0	2746	−0.98
OFX08-5-11	2467	0.016535	0.000703	0.281233	0.000038	0.281200	0.000038	2603	−54.4	2.8	2792	−0.98
12FX18-2-01	2669	0.006717	0.000224	0.281261	0.000009	0.281249	0.000009	2640	−53.4	5.5	2721	−0.99
12FX18-2-02	2436	0.017031	0.000541	0.281296	0.000011	0.281271	0.000011	2640	−52.2	6.2	2696	−0.98
12FX18-2-03	2616	0.008239	0.000287	0.281280	0.000015	0.281265	0.000015	2640	−52.8	6.1	2700	−0.99

(continued)

Table 3.2 (continued)

Samples and analytical numbers	t_1 (Ma)	$^{176}Yb/^{177}Hf$	$^{176}Lu/^{177}Hf$	$^{176}Hf/^{177}Hf$	2σ	$(^{176}Hf/^{177}Hf)t_1$	2σ	t_2 (Ma)	$\varepsilon_{Hf}(0)$	$\varepsilon_{Hf}(t_2)$	T_{DM} (Ma)	$f_{Lu/Hf}$
12FX18-2-04	2431	0.031184	0.000948	0.281344	0.000013	0.281300	0.000013	2640	−50.5	7.2	2659	−0.97
12FX18-2-05	2513	0.015176	0.000489	0.281290	0.000011	0.281267	0.000011	2640	−52.4	6.1	2700	−0.99
12FX18-2-06	2435	0.020743	0.000617	0.281298	0.000012	0.281269	0.000012	2640	−52.1	6.1	2699	−0.98
12FX18-2-07	2259	0.006646	0.000200	0.281288	0.000013	0.281279	0.000013	2640	−52.5	6.5	2683	−0.99
12FX18-2-08	2619	0.005241	0.000154	0.281247	0.000013	0.281240	0.000013	2640	−53.9	5.2	2734	−1.00
12FX18-2-09	2530	0.001953	0.000046	0.281300	0.000012	0.281298	0.000012	2640	−52.1	7.2	2656	−1.00
12FX18-2-10	2514	0.016882	0.000548	0.281287	0.000013	0.281260	0.000013	2640	−52.5	5.8	2709	−0.98
12FX18-2-11	2525	0.024243	0.000682	0.281316	0.000011	0.281283	0.000011	2640	−51.5	6.6	2679	−0.98
12FX18-2-12	2667	0.003258	0.000100	0.281265	0.000011	0.281260	0.000011	2640	−53.3	5.9	2707	−1.00
12FX18-2-13	2508	0.021771	0.000613	0.281302	0.000011	0.281273	0.000011	2640	−52.0	6.3	2692	−0.98
12FX18-2-14	2510	0.019876	0.000664	0.281327	0.000013	0.281295	0.000013	2640	−51.1	7.1	2662	−0.98
12FX18-2-15	2448	0.056359	0.001611	0.281386	0.000014	0.281311	0.000014	2640	−49.0	7.5	2647	−0.95
12FX18-2-16	2448	0.013487	0.000437	0.281391	0.000012	0.281370	0.000012	2640	−48.8	9.7	2561	−0.99
12FX18-2-17	2516	0.015762	0.000477	0.281321	0.000011	0.281298	0.000011	2640	−51.3	7.2	2658	−0.99
12FX18-2-18	2517	0.029281	0.000926	0.281355	0.000012	0.281310	0.000012	2640	−50.1	7.6	2642	−0.97
12FX18-2-19	2440	0.017637	0.000522	0.281324	0.000013	0.281299	0.000013	2640	−51.2	7.2	2657	−0.98
12FX25-6-01	2357	0.067904	0.002125	0.281387	0.000015	0.281291	0.000015	2546	−49.0	4.5	2683	−0.94
12FX25-6-02	2232	0.065461	0.001917	0.281406	0.000014	0.281324	0.000014	2546	−48.3	5.6	2642	−0.94
12FX25-6-03	2407	0.060478	0.001782	0.281400	0.000014	0.281318	0.000014	2546	−48.5	5.6	2640	−0.95
12FX25-6-04	2407	0.056743	0.001580	0.281397	0.000018	0.281325	0.000018	2546	−48.6	5.9	2629	−0.95
12FX25-6-05	2469	0.058691	0.001477	0.281369	0.000013	0.281299	0.000013	2546	−49.6	5.0	2661	−0.96
12FX25-6-06	2475	0.019055	0.000507	0.281344	0.000011	0.281320	0.000011	2546	−50.5	5.8	2629	−0.98
12FX25-6-07	2404	0.061174	0.001953	0.281396	0.000010	0.281306	0.000010	2546	−48.7	5.2	2658	−0.94

(continued)

Table 3.2 (continued)

Samples and analytical numbers	t_1 (Ma)	$^{176}Yb/^{177}Hf$	$^{176}Lu/^{177}Hf$	$^{176}Hf/^{177}Hf$	2σ	$(^{176}Hf/^{177}Hf)t_1$	2σ	t_2 (Ma)	$\varepsilon_{Hf}(0)$	$\varepsilon_{Hf}(t_2)$	T_{DM} (Ma)	$f_{Lu/Hf}$
12FX25-6-08	2326	0.073369	0.002306	0.281454	0.000023	0.281352	0.000023	2546	−46.6	6.6	2601	−0.93
12FX25-6-09	2371	0.031904	0.000954	0.281414	0.000015	0.281370	0.000015	2546	−48.0	7.5	2564	−0.97
12FX25-6-10	2239	0.045160	0.001259	0.281381	0.000014	0.281328	0.000014	2546	−49.2	5.8	2629	−0.96
12FX25-6-11	2471	0.048195	0.001318	0.281394	0.000013	0.281332	0.000013	2546	−48.7	6.2	2616	−0.96
12FX25-6-12	2403	0.096894	0.002597	0.281457	0.000014	0.281338	0.000014	2546	−46.5	6.2	2617	−0.92
12FX25-6-13	2546	0.070465	0.001906	0.281424	0.000015	0.281331	0.000015	2546	−47.7	6.2	2615	−0.94
12FX25-6-14	2020	0.069696	0.002122	0.281450	0.000025	0.281369	0.000025	2546	−46.7	6.8	2593	−0.94
12FX28-3-01	2537	0.050144	0.001483	0.281408	0.000014	0.281336	0.000014	2540	−48.2	6.3	2608	−0.96
12FX28-3-02	2475	0.012015	0.000353	0.281280	0.000010	0.281263	0.000010	2540	−52.8	3.7	2704	−0.99
12FX28-3-03	2478	0.016944	0.000466	0.281299	0.000008	0.281277	0.000008	2540	−52.1	4.2	2686	−0.99
12FX28-3-04	2551	0.064605	0.001870	0.281432	0.000013	0.281341	0.000013	2540	−47.4	6.5	2602	−0.94
12FX28-3-05	2541	0.053643	0.001585	0.281393	0.000014	0.281316	0.000014	2540	−48.8	5.6	2635	−0.95
12FX28-3-06	2474	0.015487	0.000421	0.281297	0.000009	0.281277	0.000009	2540	−52.2	4.2	2685	−0.99
12FX28-3-07	2471	0.009124	0.000255	0.281282	0.000010	0.281270	0.000010	2540	−52.7	3.9	2694	−0.99
12FX28-3-08	2482	0.016469	0.000499	0.281276	0.000013	0.281252	0.000013	2540	−52.9	3.3	2720	−0.98
12FX28-3-09	2479	0.018265	0.000577	0.281366	0.000012	0.281338	0.000012	2540	−49.7	6.3	2604	−0.98
12FX28-3-10	2430	0.009633	0.000282	0.281288	0.000011	0.281274	0.000011	2540	−52.5	4.1	2689	−0.99
12FX28-3-11	2524	0.008775	0.000244	0.281290	0.000010	0.281278	0.000010	2540	−52.4	4.2	2683	−0.99
12FX28-3-12	2526	0.022926	0.000789	0.281359	0.000011	0.281321	0.000011	2540	−50.0	5.7	2627	−0.98
12FX28-3-13	2572	0.019448	0.000585	0.281313	0.000010	0.281284	0.000010	2540	−51.6	4.4	2676	−0.98
12FX28-3-14	2479	0.016995	0.000496	0.281299	0.000009	0.281275	0.000009	2540	−52.1	4.1	2689	−0.99
12FX28-3-15	2472	0.015775	0.000455	0.281289	0.000010	0.281268	0.000010	2540	−52.4	3.8	2699	−0.99
12FX28-3-16	2429	0.016210	0.000483	0.281298	0.000010	0.281276	0.000010	2540	−52.1	4.1	2689	−0.99

(continued)

Table 3.2 (continued)

Samples and analytical numbers	t_1 (Ma)	$^{176}Yb/^{177}Hf$	$^{176}Lu/^{177}Hf$	$^{176}Hf/^{177}Hf$	2σ	$(^{176}Hf/^{177}Hf)t_1$	2σ	t_2 (Ma)	$\varepsilon_{Hf}(0)$	$\varepsilon_{Hf}(t_2)$	T_{DM} (Ma)	$f_{Lu/Hf}$
12FX28-3-17	2381	0.007747	0.000217	0.281271	0.000012	0.281261	0.000012	2540	−53.1	3.6	2707	−0.99
12FX28-3-18	2476	0.042369	0.001292	0.281341	0.000013	0.281280	0.000013	2540	−50.6	4.2	2687	−0.96
12FX28-3-19	2480	0.013316	0.000371	0.281280	0.000011	0.281263	0.000011	2540	−52.8	3.7	2705	−0.99
12FX28-3-20	2534	0.016892	0.000547	0.281349	0.000010	0.281323	0.000010	2540	−50.3	5.8	2624	−0.98

Note t_1, apparent $^{207}Pb/^{206}Pb$ ages; t_2, crystallizaiton ages. "—" in the analytical data indicate that the values were not calculated because they are analyzed on the inherited/xenocrystic zircon domains

Table 3.3 SHRIMP zircon U–Pb isotopic dating data for metavolcanic rock sample OFX08-5 from Fuxin-Yixian greenstone belt, Western Liaoning Province

Analyzed spot number	U (ppm)	Th (ppm)	Th/U	$^{206}Pb^*$ (ppm)	$^{207}Pb^*/^{206}Pb^*$	± %	$^{207}Pb^*/^{235}U$	± %	$^{206}Pb^*/^{238}U$	± %	err Corr	$^{206}Pb/^{238}U$ Age		$^{207}Pb/^{206}Pb$ Age		Discordance (%)
OFX08-5-1.1	27	11	0.43	10.7	0.1673	1.4	10.67	2.4	0.463	2.0	0.81	2451	±40	2530	±24	3.1
OFX08-5-2.1	11	1	0.11	3.1	0.1113	4.8	4.86	5.6	0.317	2.9	0.52	1774	±45	1821	±86	2.6
OFX08-5-3.1	37	11	0.31	14.6	0.1677	1.0	10.63	2.0	0.460	1.8	0.86	2438	±36	2535	±17	3.8
OFX08-5-4.1	9	1	0.06	3.6	0.1720	2.2	10.75	3.8	0.453	3.1	0.81	2410	±63	2578	±37	6.5
OFX08-5-5.1	30	9	0.32	11.1	0.1584	1.3	9.43	2.3	0.432	1.9	0.83	2314	±37	2439	±22	5.1
OFX08-5-6.1	24	8	0.36	9.3	0.1635	1.5	10.31	2.6	0.457	2.1	0.80	2428	±42	2493	±26	2.6
OFX08-5-7.1	40	12	0.31	15.4	0.1655	1.1	10.31	2.0	0.452	1.7	0.85	2403	±34	2513	±18	4.4
OFX08-5-8.1	21	7	0.36	8.5	0.1686	2.3	10.90	3.1	0.469	2.2	0.69	2479	±44	2544	±38	2.6
OFX08-5-9.1	16	2	0.13	4.1	0.0989	5.6	4.12	6.1	0.302	2.5	0.41	1702	±37	1603	±100	−6.2
OFX08-5-10.1	25	9	0.39	10.5	0.1719	1.1	11.69	2.3	0.494	2.0	0.87	2586	±42	2576	±19	−0.4
OFX08-5-11.1	25	8	0.32	9.2	0.1610	1.5	9.60	2.5	0.432	2.0	0.80	2316	±39	2467	±25	6.1
OFX08-5-12.1	30	4	0.14	11.6	0.1607	1.3	9.87	2.3	0.445	1.8	0.81	2375	±37	2463	±22	3.6
OFX08-5-13.1	11	1	0.11	3.0	0.1107	4.5	4.77	5.3	0.312	2.8	0.52	1753	±43	1811	±82	3.2
OFX08-5-14.1	15	2	0.14	4.2	0.1088	3.1	4.81	3.9	0.321	2.5	0.63	1792	±39	1780	±56	−0.7
OFX08-5-15.1	129	11	0.09	50.0	0.1544	0.6	9.56	1.6	0.449	1.5	0.94	2391	±31	2395	±9.3	0.2
OFX08-5-16.1	49	19	0.40	21.1	0.1768	0.8	12.10	1.7	0.497	1.5	0.89	2599	±32	2623	±13	0.9
OFX08-5-17.1	34	15	0.44	14.5	0.1744	1.6	11.84	2.3	0.492	1.7	0.72	2581	±36	2600	±27	0.7
OFX08-5-18.1	20	6	0.32	8.8	0.1680	1.2	11.93	2.6	0.515	2.3	0.88	2678	±49	2538	±20	−5.5
OFX08-5-19.1	11	1	0.10	3.1	0.1012	5.7	4.35	6.3	0.312	2.6	0.42	1749	±40	1647	±110	−6.2
OFX08-5-20.1	38	15	0.41	15.3	0.1615	1.0	10.37	1.9	0.466	1.6	0.85	2465	±33	2471	±17	0.3
OFX08-5-21.1	13	2	0.12	3.5	0.1018	3.0	4.24	3.9	0.302	2.4	0.63	1700	±37	1658	±55	−2.5

Note Common lead corrected using ^{204}Pb; $^{206}Pb_C$(%) is the amount of common ^{206}Pb in total ^{206}Pb, $^{206}Pb^*$ is the total ^{206}Pb; discordance (%) is defined as $[1 - (^{206}Pb/^{238}U \text{ age})/(^{207}Pb/^{206}Pb \text{ age})] \times 100$

these zircon grains show nearly constant $^{176}Hf/^{177}Hf(t_1)$ ratios (0.281200–0.281375, with a weighted mean value of 0.281300 ± 0.000043), forming a horizontal line in the $^{176}Hf/^{177}Hf$ (t_1)-t_1 binary diagram (Fig. 3.5c). This implies that these zircon grains were crystallized from the same magmatic event, but subjected to different degrees of Pb loss during subsequent metamorphism, with the original Lu–Hf isotopic composition preserved [10, 100]. In this case, age of the oldest zircons can be regarded as the best estimate of the crystallization age for the magmatic precursor. The oldest zircon group is unlikely xenocrystic grains as there are no ~2603 Ma magmatic records in the study region, except for the data from sample OFX08-5. Combined with the magmatic zircon-like internal structures and generally high Th/U ratios of the three analyses close to the upper intercept, the age of 2603 ± 19 Ma is considered as the crystallization age of this sample. The younger concordia age of 1736 ± 29 Ma is within error of the formation age of the nearby Jianping diorite-monzonite-syenite suite (~1721–1696 Ma), and reflects the effect of late Paleoproterozoic tectonothermal events [92].

The Lu–Hf isotopic data were further calculated at the crystallization age of 2603 Ma (t_2), and they show high $\varepsilon Hf(t_2)$ values of +2.8 to +9.1, with Hf depleted mantle model ages (T_{DM}(Hf)) ranging from 2792 to 2553 Ma (Fig. 3.5d and Table 3.2).

3.1.2.3 Sample 12FX28-2 (Metabasaltic Rocks)

Sample 12FX18-2 is a garnet clinopyroxene plagioclase gneiss, collected to the north of Haertao town (Fig. 3.1). Zircon grains from this sample have elongated to oval shapes (e.g., spots #17 and #20), showing lengths and length/width ratios of 50–200 μm and 1:1–2:1, respectively (Fig. 3.6a). Cathodoluminescence images reveal blurred/banded zoned (e.g., spots #1 and #17) or dark structureless domains (e.g., spot #5), surrounded by bright structureless rims in some cases (e.g., spots #5 and #10). These complex internal structures indicate that most zircon grains were modified by post-magmatic alteration. A total of twenty-nine analyses were conducted on twenty-seven zircon grains using LA-ICPMS U-Pb isotopic dating method (Table 3.1). All the isotopic data plot on or close to the concordia, showing apparent $^{207}Pb/^{206}Pb$ ages ranging from 2667 ± 22 Ma to 1725 ± 49 Ma (Fig. 3.6b). Th and U contents vary from 1–91 ppm and 8–220 ppm, respectively, with Th/U ratios of mostly >0.10. On the probability density plot, the analyses can be subdivided into four groups, as discussed below (the inset in Fig. 3.6b). The oldest age group is composed of seven analyses (spots #1, #3, #6, #12, #17, #25, and #30), most of which were collected from blurred oscillatory zoned domains, with Th/U ratios of >0.10 (0.14–0.39; Fig. 3.6a). The apparent $^{207}Pb/^{206}Pb$ ages range from 2667 ± 22 Ma to 2614 ± 56 Ma, and they yield a weighted mean $^{207}Pb/^{206}Pb$ age of 2640 ± 19 Ma (MSWD = 1.02), which is within error of the upper intercept age of 2653 ± 29 Ma (MSWD = 0.19) (Fig. 3.6b). The second age group is composed of twelve analyses mostly from the dark cores or blurred zoned domains (spots #5, #8, #11, #14, #15, #16, #19, #20, #23, #24, #26, and #27), with Th/U ratios of 0.02–0.68 (Fig. 3.6a). These data show apparent $^{207}Pb/^{206}Pb$ ages ranging from 2546 ± 54 Ma to 2508 ± 24 Ma, yielding a weighted mean age of 2521 ± 14 Ma (MSWD = 0.17; Fig. 3.6b). The third age group consists of six analyses (spots #2, #7, #9, #21, #22, and #28) conducted on the banded zoned domains or dark cores (Fig. 3.6a). These six analyses show apparent $^{207}Pb/^{206}Pb$ ages and Th/U ratios of 2448 ± 24 Ma to 2431 ± 28 Ma and 0.05–0.24, respectively, and they yield a concordia age of 2437 ± 20 Ma (MSWD = 0.20) and a weighted mean age of 2440 ± 20 Ma (MSWD = 0.084), which are within error consistent with each other (Fig. 3.6b). Four scattered analyses conducted mainly on the bright structureless domains or rims (spots #10, #13, #18, and #29) constitute the youngest age group (Fig. 3.6a). They have Th/U ratios of 0.08-0.38, and the apparent $^{207}Pb/^{206}Pb$ ages range widely from 2276 ± 24 Ma to 1725 ± 49 Ma (Fig. 3.6b).

A total of nineteen dated zircon domains were analyzed for Lu–Hf isotopes (Table 3.2). When calculated at the apparent $^{207}Pb/^{206}Pb$ ages (t_1), they show nearly consistent $^{176}Hf/^{177}Hf(t_1)$ ratios of 0.281240–0.281370 (weighted mean value of 0.281282 ± 0.000014), with decreasing apparent ages (Fig. 3.6c). These data suggest that the zircon grains were likely formed during the same magmatic event, and were then subjected to different degrees of Pb loss during subsequent metamorphism [100, 101]. Considering the absence of ~2640 Ma magmatic events in the study region, except for sample 12FX18-2 dated in this study, a xenocrystic origin of the oldest zircon group can be excluded. Given the internal structures and high Th/U ratios of zircon grains from the oldest age group, the weighted mean age of 2640 ± 19 Ma is taken as the best estimate of the crystallization age of the magmatic precursor. The calculated younger ages of 2521 ± 14 Ma, 2437 ± 20 Ma, and 2276 ± 24 to 1725 ± 49 Ma suggest later tectonothermal events, and correlate well with regional late Archean granitoid magmatism (2532–2495 Ma) and multiple Paleoproterozoic tectonothermal events [21, 43, 89–91].

The Lu–Hf isotopic data, calculated at the crystallization age of 2640 Ma (t_2), show high $\varepsilon Hf(t_2)$ values of +5.2 to +9.7 (mostly of +5.2 to +7.6), with $T_{DM}(Hf)$ ages ranging between 2734 Ma and 2561 Ma (mostly in the range of 2734–2642 Ma) (Fig. 3.6d).

3.1.2.4 Sample 12FX25-6 (Metabasaltic Rocks)

The amphibolite sample 12FX25-6 was collected to the south of Wangdayingzi village (Fig. 3.1). Zircon grains are rare in this sample, with only oval to elongated small crystals, and the lengths and length/width ratios are 50–80 μm and 1:1–2:1, respectively (Fig. 3.7a). In the cathodoluminescence images, most of them show dark banded zoned (e.g., spot #14) or homogenous internal structures (e.g., spot #11), similar to magmatic zircon grains which were subjected to different degrees of Pb loss [13, 44]. A total of fifteen analyses were conducted on fifteen zircon grains using LA-ICPMS U-Pb isotopic dating method (Table 3.1). The data plot on or close to the concordia, with apparent $^{207}Pb/^{206}Pb$ ages ranging between 2546 ± 19 Ma and 2020 ± 145 Ma (Fig. 3.7b). Th and U contents are in the range of 2–1228 ppm and 7–882 ppm, respectively, with generally high Th/U ratios of 0.23–2.39. Most zircon domains show consistent chondrite-normalized REE patterns, with positive Ce and negative Eu anomalies as well as steep HREE patterns, suggesting that they are typical magmatic zircons. One analysis (spot #12) yields exceptionally low REE contents, possibly resulting from element mobilization triggered by local recrystallization of the magmatic zircon grains [96]. Fourteen dated zircon spots were analyzed for Lu–Hf isotopic data (Table 3.2). When calculated at the apparent $^{207}Pb/^{206}Pb$ ages, the zircon grains show nearly consistent $^{176}Hf/^{177}Hf(t_1)$ values of 0.281291–0.281370 (weighted mean value of 0.281323 ± 0.000012), defining a horizontal line in the $^{176}Hf/^{177}Hf(t_1)$-t_1 binary diagram (Fig. 3.7c). Considering the magmatic zircon-like internal structures, REE patterns, and high Th/U ratios, the oldest apparent $^{207}Pb/^{206}Pb$ age of 2546 ± 19 Ma is considered as the lower limit of crystallization age for the magmatic precursor, with the younger ages ascribed to different degrees of Pb loss [100, 101]. The Lu–Hf isotopic data, calculated at the age of 2546 Ma (t_2), yield high εHf(t_2) values of +4.5 to +7.5, with T_{DM}(Hf) values ranging between 2683 and 2564 Ma (Fig. 3.7d and Table 3.2).

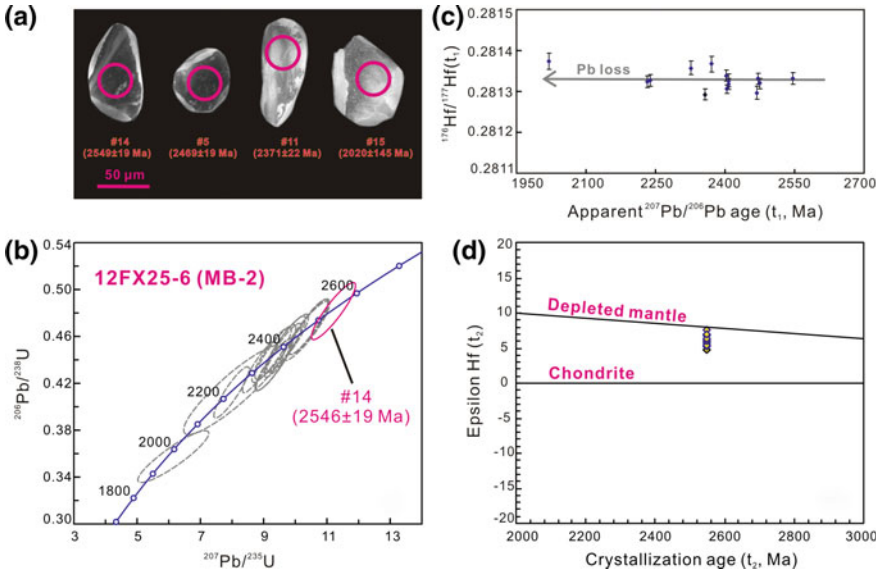

Fig. 3.7 Internal structures and U–Pb and Lu–Hf isotopic data of zircon grains from the amphibolite sample 12FX25-6. **a** CL images of representative zircon grains showing internal structures and analyzed locations. Numbers are spot locations in Table 3.1. **b** Concordia diagram showing all the analyzed spots. **c** $^{176}Hf/^{177}Hf$ (t_1) versus apparent $^{207}Pb/^{206}Pb$ age (t_1) diagram. **d** εHf(t_2) versus crystallization age (t_2, 2546 Ma) diagram

3.1.2.5 Sample 12FX28-3 (Metaandesitic Rocks)

The clinopyroxene amphibolite sample 12FX28-3 was collected east of the Xinglongba village (Fig. 3.1), and most zircon grains from this sample show elongated to stubby shapes (e.g., spots #1 and #14), with a minor population exhibiting oval shapes (e.g., spot #11; Fig. 3.8a). The lengths and length/width ratios range from 50–120 μm and 1:1–2.5:1, respectively, and most of them display core-rim structures. The oscillatory zoned cores are generally surrounded by thin bright or dark rims (Fig. 3.8a). Some cores are prismatic and euhedral crystals (e.g., spot #1), whereas others have been eroded as irregular crystals (e.g., spots #4 and #14), which are typical magmatic zircon grains [13]. Some zircon grains show dark or bright structureless domains (e.g., spots #9 and #11). A total of twenty-five analyses were conducted on twenty-five zircon grains using LA-ICPMS U-Pb isotopic dating method, and the data plot on or close to the concordia (Fig. 3.8b and Table 3.1). These analyses yield apparent ^{207}Pb/^{206}Pb ages ranging between 2572 ± 27 Ma and 2343 ± 24 Ma. Th and U contents are 25–341 ppm and 34–309 ppm, respectively, with generally high Th/U ratios of 0.41–1.89. Based on the internal structures of the dated zircon grains, the analyzed data can be divided into two groups. The older age group is composed of nine analyses on oscillatory zoned zircon domains (i.e., spots #1, #2, #4, #13, #14, #15, #21, #22, and #25), and they have relatively older apparent ^{207}Pb/^{206}Pb ages of 2572 ± 27 Ma to 2524 ± 24 Ma. These grains yield an upper intercept age of 2542 ± 21 Ma (MSWD = 0.32) and a weighted mean age of 2540 ± 17 Ma (MSWD = 0.30), which are within error consistent with each other (Fig. 3.8b). These zircon grains show magmatic zircon-like internal structures and high Th/U ratios (0.51–1.19), and the weighted mean age of 2540 ± 17 Ma is therefore taken as the crystallization age of the magmatic precursor. The second age group consists of sixteen analyses mostly on the structureless domains. Except for spots #8 and #9, which have much younger apparent ^{207}Pb/^{206}Pb ages (2343 ± 24 Ma and 2381 ± 25 Ma, respectively), the other fourteen analyses yield apparent ^{207}Pb/^{206}Pb ages ranging from 2482 ± 28 Ma to 2429 ± 25 Ma, and a weighted mean age of 2470 ± 14 Ma (MSWD = 0.36) (Fig. 3.8b). These ages are consistent with the thermal events associated with regional ~2485 Ma granulite facies metamorphism and subsequent multiple tectonothermal events [21, 43, 89, 93]. A total of twenty dated spots were analyzed for Lu–Hf isotopes (Table 3.2). When calculated at the apparent ^{207}Pb/^{206}Pb ages (t_1), the data define a horizontal line in the ^{176}Hf/^{177}Hf (t_1)-t_1 binary diagram, with ^{176}Hf/^{177}Hf(t_1) ratios ranging from 0.281252 to 0.281341 (Fig. 3.8c). These data indicate that the zircon grains were crystallized from the same magmatic event, and the structureless zircon grains were subjected to different degrees of Pb loss triggered by later tectonothermal events [100, 101]. When the Lu–Hf isotopic data are calculated at the crystallization age of 2540 Ma (t_2), they yield εHf(t_2) and T_{DM}(Hf) values of +3.3 to +6.5 and 2720 and 2602 Ma, respectively (Fig. 3.8d and Table 3.2).

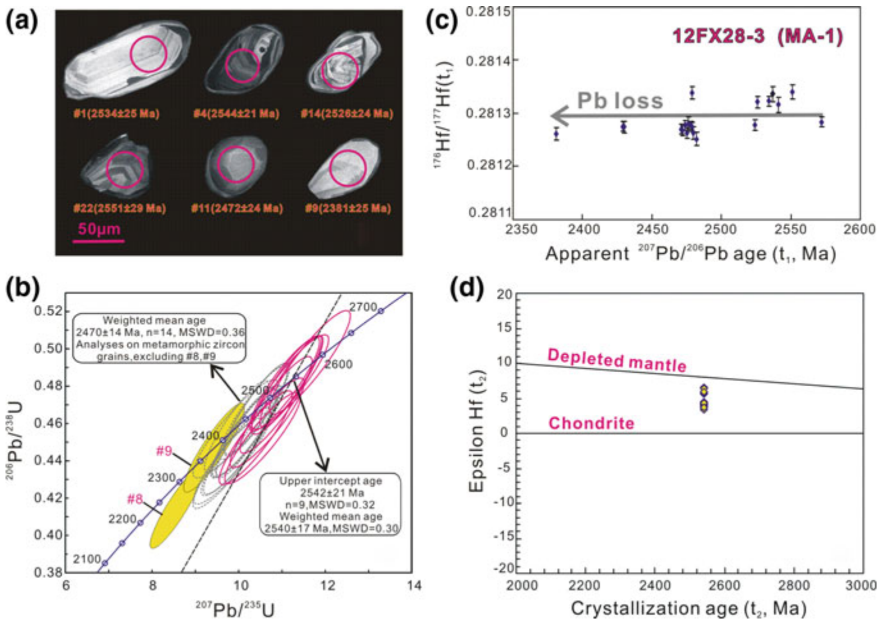

Fig. 3.8 Internal structures and U–Pb and Lu–Hf isotopic data of zircons from the clinopyroxene amphibolite sample 12FX28-3. **a** CL images of representative zircon grains showing internal structures and analytized locations. Numbers are spot locations in Table 3.1. **b** Concordia diagram showing all analyzed spots. **c** $^{176}Hf/^{177}Hf$ (t_1) versus apparent $^{207}Pb/^{206}Pb$ age (t_1) diagram. **d** εHf (t_2) versus crystallization age (t_2, 2540 Ma) diagram

3.1.3 Whole-Rock Geochemistry and Classification

Since most samples were subjected to amphibolite facies metamorphism, discrimination diagrams using immobile elements (Zr/TiO_2*0.0001 vs. Nb/Y diagram) are applied in this study. Despite large variations of mineral assemblages of the metavolcanic rocks (Fig. 3.3), the analyzed forty-two samples fall mostly within the fields of basaltic (twenty-seven samples) and andesitic (fifteen samples) rocks (Fig. 3.9a) [97]. On the La-Yb binary diagram (Fig. 3.9b), most basaltic rocks belong to the tholeiitic to transitional rock series, whereas three palimpsest basalts (12FX10-1, 12FX11-4, and 12FX26-3) and all the metaandesitic rocks fall into the field of calc-alkaline rock series. Combined with the normalized trace element patterns, particularly $(La/Yb)_N$ and $(Nb/La)_{PM}$ ratios, the analyzed samples can be subdivided into the following three metabasaltic groups (MB-1, MB-2, and MB-3) and two metaandesitic groups (MA-1 and MA-2) (Table 3.4).

The Group MB-1 comprises five amphibolites, three garnet amphibolites, two garnet clinopyroxene plagioclase gneisses, two garnet clinopyroxene amphibolites, and one clinopyroxene amphibolite (Table 3.4). They are characterized by low SiO_2 of mostly 44.34–48.88 wt% (sample 12FX10-2 has a higher value of 52.48 wt%),

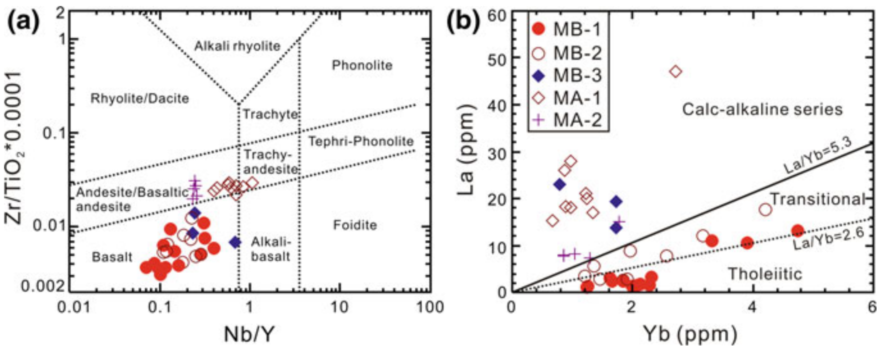

Fig. 3.9 Petrochemical classification diagrams: **a** Zr/TiO_2*0.0001-Nb/Y binary diagram [97]; **b** La–Yb binary diagram [71], with calc-alkaline, tholeiitic and transitional series marked by La/Yb ratios of >5.3, <2.6, and between 5.3 and 2.6, respectively

high MgO of 4.54–8.19 wt%, Mg# (100 Mg/(Mg + Fe^{2+}) atomic ratios) of 36.63–65.85, the highest $(Nb/La)_{PM}$ ratios (0.87–1.59), and the lowest $(La/Sm)_N$ ratios (0.55–1.58). These samples fall in the field of tholeiitic rock series (Fig. 3.9b) [71]. In the chondrite-normalized rare earth element (REE) diagram (Fig. 3.10a), most samples in Group MB-1, except for samples 12FX10-2, 12FX15-2, 12FX15-3, and 12FX23-4, display flat to slight LREE-depleted patterns without significant Eu anomalies (Eu_N/Eu_N^* = 1.04–1.19). They show $(La/Sm)_N$ and $(La/Yb)_N$ values of 0.55–0.97 and 0.52–1.05, respectively. These values are similar to those of N-MORBs [78]. In the primitive mantle-normalized multi-element spider diagram (Fig. 3.10b), they exhibit nearly flat patterns without significant Nb, Ta, and Ti anomalies, showing high $(Nb/La)_{PM}$ ratios of 0.87–1.21. In comparison, the other four samples show slightly right-declined REE patterns, with $(La/Sm)_N$ and $(La/Yb)_N$ ratios of 1.08–1.58 and 1.37–2.39, respectively, and absence of significant Eu anomaly (Eu_N/Eu_N^* = 0.76–1.27) (Table 3.4). They exhibit positive Nb anomalies characterized by $(Nb/La)_{PM}$ ratios of 1.09–1.59. The normalized trace element patterns straddle those of enriched mid-ocean ridge basalts (E-MORBs) and ocean island basalts (OIBs) (Fig. 3.10a, b) [78].

Group MB-2 is composed of eleven samples, including nine amphibolites and two garnet amphibolites (Table 3.4). SiO_2 and MgO contents vary from 45.09 to 51.90 wt% and 3.92 to 14.51 wt% (mostly of 3.92–8.06 wt%), respectively, with Mg# values of 38.39–70.25 (mostly of 38.39–56.97). They show lower $(Nb/La)_{PM}$ ratios (0.19–0.79, mostly of 0.51–0.72) and slightly higher $(La/Sm)_N$ ratios (1.00–3.60), falling into the fields of tholeiitic to transitional rock series (Fig. 3.9b). In the chondrite-normalized REE diagram (Fig. 3.10c), these rocks have flat to moderately fractionated REE patterns without significant Eu anomalies, showing $(La/Yb)_N$ and Eu_N/Eu_N^* values of 0.97–7.44 (mostly of 0.97–3.23) and 0.93–1.42, respectively. In the primitive mantle-normalized multi-element spider diagram (Fig. 3.10d), they display moderately negative Nb, Ta, and Ti anomalies with lower $(Nb/La)_{PM}$ ratios, distinct from those of Group MB-1 samples (Fig. 3.10b).

Table 3.4 Major (wt.%) and trace element (ppm) compositions of metavolcanic rocks from the Fuxin-Yixian greenstone belt, Western Liaoning Province

Sample	MB-1												
	FX010-1	FX012-1	OFX08-1	OFX08-2	OFX08-4	OFX08-5	OFX10-1	12FX10-2	12FX15-2	12FX15-3	12FX18-2	12FX18-3	12FX23-4
Lithology	Clinopyroxnene amphibolite	Garnet amphibolite (Gt-Amp)	Gt-Amp	Amphibolite (Amp)	Amp	Garnet clinopyroxene amphibolite (Gt-Cpx Amp)	Gt-Amp	Gt-Cpx Amp	Amp	Amp	Gt-Cpx Amp	Gt-Cpx Amp	Amp
SiO_2	47.43	48.32	44.81	45.35	46.74	46.07	48.72	52.48	47.30	44.34	48.88	47.29	45.53
Al_2O_3	15.56	14.46	15.06	14.53	13.50	15.31	11.94	14.99	12.67	11.36	13.64	13.55	11.78
Fe_2O_3T	12.66	13.13	13.29	13.27	12.89	13.28	12.68	9.48	13.84	18.53	14.37	14.03	18.30
CaO	12.52	10.83	10.61	11.94	15.17	12.22	10.16	7.77	12.29	12.14	11.42	12.94	11.72
MgO	7.84	7.93	8.12	8.19	6.98	6.39	6.92	7.84	6.56	5.13	5.97	6.23	4.54
K_2O	0.43	0.72	0.68	0.58	0.42	0.55	5.19	1.34	1.34	0.52	0.60	1.17	0.67
Na_2O	1.69	1.84	1.59	1.53	1.54	1.57	0.92	2.55	2.69	2.59	3.07	2.46	3.61
MnO	0.21	0.18	0.20	0.24	0.21	0.22	0.17	0.11	0.19	0.30	0.24	0.19	0.25
TiO_2	0.65	0.72	0.79	0.87	0.82	0.91	0.79	1.32	0.92	2.62	1.18	1.04	1.99
P_2O_5	0.05	0.07	0.04	0.05	0.04	<0.05	0.05	0.27	0.06	0.37	0.08	0.05	0.22
LOI	0.85	1.70	4.67	3.34	1.57	2.65	2.31	1.63	2.02	1.93	0.44	0.91	1.27
Total	99.91	99.88	99.85	99.87	99.87	99.16	99.84	99.80	99.87	99.84	99.89	99.85	99.88
Mg#	55.10	54.50	54.75	55.00	51.75	48.81	51.96	62.11	48.43	35.43	45.16	46.80	32.94
Al_2O_3/TiO_2	23.94	20.08	19.14	16.79	16.46	16.84	15.19	11.32	13.82	4.33	11.55	13.02	5.91
V	151	154	242	249	235	304	224	372	266	207	268	238	298
Cr	395	237	237	261	259	—	155	25	139	34	97	179	65
Co	33	28	63	50	47	—	50	38	38	34	50	39	47
Ni	210	113	158	140	141	—	106	18	97	58	75	123	55
Rb	4.07	5.36	22	19.0	11.1	16.7	279	36	19.0	7.62	2.82	7.76	10.8
Sr	96	134	215	172	139	186	181	422	376	364	255	414	229
Y	9.84	10.3	18.7	19.0	18.2	16.6	16.4	44	18.1	47	25	19.0	35
Nb	1.270	1.110	1.618	1.833	1.278	1.693	2.40	13.5	5.10	14.7	2.90	3.04	13.9
Ba	49	112	92	61	54	86	411	256	247	233	97	166	210
La	1.380	1.200	1.596	1.671	1.402	1.652	2.38	10.6	3.10	13.1	3.21	2.41	11.0
Ce	3.38	3.33	5.25	5.51	4.67	5.13	6.42	27	8.20	37	9.97	7.29	27

(continued)

Table 3.4 (continued)

Sample	MB-1												
	FX010-1	FX012-1	OFX08-1	OFX08-2	OFX08-4	OFX08-5	OFX10-1	12FX10-2	12FX15-2	12FX15-3	12FX18-2	12FX18-3	12FX23-4
Lithology	Clinopyroxnene amphibolite	Garnet amphibolite (Gt-Amp)	Gt-Amp	Amphibolite (Amp)	Amp	Garnet clinopyroxene amphibolite (Gt-Cpx Amp)	Gt-Amp	Gt-Cpx Amp	Amp	Amp	Gt-Cpx Amp	Gt-Cpx Amp	Amp
Pr	0.530	0.530	0.929	0.977	0.865	0.916	1.036	3.89	1.240	5.73	1.625	1.176	3.76
Nd	2.73	2.96	4.93	5.24	4.75	5.41	5.30	16.9	5.59	27	7.55	5.67	16.3
Sm	0.920	1.010	1.672	1.771	1.648	1.947	1.690	5.02	1.849	6.99	2.45	1.968	4.50
Eu	0.370	0.390	0.701	0.756	0.668	0.820	0.771	1.827	0.844	1.873	0.978	0.842	1.772
Gd	1.170	1.240	2.37	2.48	2.35	2.64	2.31	5.89	2.24	8.14	2.98	2.41	5.15
Tb	0.250	0.260	0.481	0.500	0.475	0.523	0.448	1.148	0.453	1.449	0.616	0.497	0.968
Dy	1.710	1.770	3.17	3.27	3.11	3.60	2.88	7.01	2.82	8.70	3.91	3.09	5.76
Ho	0.360	0.390	0.722	0.740	0.702	0.766	0.643	1.533	0.623	1.857	0.863	0.670	1.250
Er	1.170	1.220	2.08	2.13	2.01	2.35	1.827	4.30	1.771	5.13	2.46	1.864	3.50
Tm	0.200	0.200	0.334	0.339	0.320	0.333	0.295	0.615	0.254	0.786	0.359	0.265	0.514
Yb	1.250	1.230	2.08	2.12	1.993	2.28	1.840	3.90	1.617	4.75	2.31	1.656	3.31
Lu	0.200	0.210	0.332	0.334	0.316	0.338	0.293	0.606	0.250	0.737	0.356	0.248	0.511
Ta	0.080	0.090	0.198	0.098	0.084	0.115	0.319	1.150	0.642	0.795	0.446	0.605	1.300
Th	0.210	0.090	0.021	0.017	0.010	0.073	0.188	0.277	0.851	0.372	0.059	0.117	0.809
U	0.160	0.060	0.045	0.072	0.022	0.068	0.152	0.269	0.232	0.256	0.039	0.243	0.220
Zr	60	45	32	31	30	28	43	141	46	193	43	40	116
Hf	1.450	1.310	1.052	1.113	1.094	1.158	1.328	3.59	1.298	5.16	1.200	1.146	2.91
TREE	15.6	15.9	27	28	25	29	28	90	31	123	40	30	86
$(La/Sm)_N$	0.97	0.77	0.62	0.61	0.55	0.55	0.91	1.37	1.08	1.21	0.84	0.79	1.58
$(Gd/Yb)_N$	0.77	0.83	0.94	0.97	0.97	1.04	1.25	1.15	1.42	1.07	1.20	1.29	0.88
$(La/Yb)_N$	0.79	0.70	0.55	0.57	0.50	0.52	0.93	1.95	1.37	1.97	1.00	1.05	2.39
Eu_N/Eu_N^*	1.09	1.07	1.08	1.10	1.04	1.10	1.19	1.03	1.27	0.76	1.11	1.18	1.13
Nb/Y	0.13	0.11	0.09	0.10	0.07	0.10	0.15	0.31	0.28	0.31	0.12	0.16	0.39
$(Nb/La)_{PM}$	0.89	0.89	0.98	1.06	0.88	0.99	0.97	1.23	1.59	1.09	0.87	1.21	1.22

(continued)

Table 3.4 (continued)

Sample	MB-2											MB-3		
	YX011-1	FX09-4	FX13-1	OFX08-3	OFX11-1	12FX08-1	12FX18-1	12FX18-4	12FX23-2	12FX25-1	12FX25-6	12FX10-1	12FX11-4	12FX26-3
Lithology	Amp	Amp	Amp	Amp	Amp	Amp	Amp	Gt-Amp	Gt-Amp	Amp	Amp	Palimpsest basalts		
SiO_2	49.63	45.09	48.42	46.98	49.05	49.86	47.91	51.90	48.34	50.25	48.17	52.67	56.94	53.39
Al_2O_3	15.41	13.80	14.32	13.41	15.35	12.67	13.47	14.51	15.60	12.55	19.34	14.56	14.84	12.31
Fe_2O_3T	12.43	12.17	12.96	12.71	11.46	15.96	12.06	10.09	13.29	14.55	8.71	9.57	7.43	11.66
CaO	10.04	8.32	10.55	11.19	12.05	9.80	13.01	13.61	8.65	10.48	12.15	7.79	5.38	10.37
MgO	7.19	14.51	7.52	7.73	6.84	5.02	8.06	3.92	6.30	5.88	4.65	4.55	2.47	6.45
K_2O	1.00	1.78	0.54	0.65	0.57	0.81	0.95	0.10	1.30	0.82	1.37	1.29	2.25	0.55
Na_2O	1.74	0.44	3.03	2.88	2.24	2.91	2.72	3.36	3.32	2.77	3.41	2.52	4.02	3.30
MnO	0.19	0.17	0.21	0.18	0.21	0.22	0.19	0.14	0.16	0.22	0.11	0.11	0.06	0.19
TiO_2	0.65	0.52	0.64	0.82	0.72	1.75	0.80	0.88	1.61	1.26	0.58	1.34	0.58	0.73
P_2O_5	0.06	0.22	0.06	0.05	<0.05	0.19	0.05	0.05	0.46	0.11	0.05	0.28	0.30	0.04
LOI	1.56	2.77	1.63	3.30	1.39	0.69	0.66	1.32	0.72	0.96	1.33	5.11	5.50	0.89
Total	99.91	99.79	99.87	99.89	99.87	99.87	99.86	99.87	99.74	99.87	99.89	99.80	99.78	99.88
Mg#	53.40	70.20	53.50	54.63	54.18	38.39	56.95	43.51	48.44	44.44	51.37	48.48	39.68	52.30
Al_2O_3/TiO_2	23.71	26.54	22.38	16.33	21.42	7.26	16.91	16.58	9.71	9.93	33.20	10.85	25.41	16.85
V	138	67	146	227	230	303	210	211	348	277	146	145	102	190
Cr	208	372	570	242	—	51	344	79	50	43	166	388	208	156
Co	30	32	32	39	—	37	50	27	50	51	30	40	23	39
Ni	119	240	320	137	—	52	142	61	38	34	68	198	96	75
Rb	18.8	21	3.86	11.2	5.42	20	5.49	1.325	32	19.0	23	34	40	11.8
Sr	102	83.9	187	139	229	248	282	1195	333	320	260	598	630	370
Y	11.3	6.69	10.4	17.4	14.3	36	15.0	26	48	22	15.5	23	9.57	17.7
Nb	1.240	1.590	1.900	1.881	1.689	7.93	2.66	6.43	10.9	6.28	1.883	5.52	6.52	4.08
Ba	53	267	85	63	115	299	131	44	377	217	262	459	871	85
La	1.660	8.19	3.57	2.64	2.88	12.0	5.58	7.85	17.6	8.81	2.73	19.4	23	13.8
Ce	4.23	17.4	9.55	6.94	6.96	30	13.1	18.1	45	21	6.64	43	47	31
Pr	0.610	2.16	1.250	1.079	1.023	4.23	1.644	2.34	6.29	2.71	1.079	5.83	5.43	3.71

(continued)

Table 3.4 (continued)

Sample	MB-2											MB-3		
	YX011-1	FX09-4	FX13-1	OFX08-3	OFX11-1	12FX08-1	12FX18-1	12FX18-4	12FX23-2	12FX25-1	12FX25-6	12FX10-1	12FX11-4	12FX26-3
Lithology	Amp	Amp	Amp	Amp	Amp	Amp	Amp	Gt-Amp	Gt-Amp	Amp	Amp	Palimpsest basalts		
Nd	3.31	9.04	5.57	5.26	5.31	17.9	6.47	9.19	27	11.2	5.04	22	18.9	13.3
Sm	1.020	1.470	1.330	1.705	1.711	4.89	1.807	2.50	7.02	2.97	1.610	4.99	3.24	2.64
Eu	0.420	0.440	0.480	0.676	0.740	1.758	0.769	1.272	2.26	1.183	0.765	1.761	1.446	0.906
Gd	1.310	1.390	1.440	2.35	2.31	5.47	2.14	3.02	7.70	3.36	1.95	4.94	3.10	2.90
Tb	0.280	0.220	0.280	0.468	0.450	1.011	0.405	0.599	1.399	0.609	0.393	0.754	0.368	0.491
Dy	1.800	1.250	1.780	2.99	3.03	5.92	2.44	3.84	8.05	3.58	2.45	3.89	1.656	2.85
Ho	0.390	0.240	0.360	0.673	0.653	1.261	0.528	0.881	1.719	0.771	0.542	0.777	0.326	0.624
Er	1.240	0.760	1.110	1.904	1.955	3.47	1.466	2.60	4.71	2.12	1.521	2.05	0.858	1.761
Tm	0.200	0.120	0.190	0.301	0.284	0.500	0.211	0.392	0.672	0.309	0.229	0.281	0.120	0.267
Yb	1.230	0.790	1.200	1.845	1.915	3.16	1.349	2.56	4.20	1.955	1.458	1.730	0.780	1.721
Lu	0.200	0.120	0.200	0.286	0.282	0.484	0.208	0.396	0.648	0.297	0.227	0.262	0.119	0.271
Ta	0.080	0.080	0.120	0.133	0.125	0.530	0.250	0.583	0.835	0.520	0.253	0.428	0.327	0.784
Th	0.200	0.280	0.070	0.187	0.329	1.506	0.133	0.101	2.31	1.458	0.152	3.35	0.547	0.317
U	0.090	0.080	0.180	0.077	0.100	0.310	0.109	0.186	0.457	0.402	0.075	0.887	0.149	0.117
Zr	56	60	52	43	39	126	33	42	196	63	37	184	39	61
Hf	1.300	1.110	1.380	1.318	1.318	3.18	0.970	1.373	5.10	1.764	0.998	3.88	0.918	1.594
TREE	17.9	44	28	29	30	92	38	55	134	61	27	112	107	77
$(La/Sm)_N$	1.05	3.60	1.73	1.00	1.09	1.59	1.99	2.02	1.62	1.92	1.09	2.51	4.63	3.38
$(Gd/Yb)_N$	0.88	1.46	0.99	1.05	1.00	1.43	1.31	0.98	1.52	1.42	1.11	2.36	3.28	1.40
$(La/Yb)_N$	0.97	7.44	2.13	1.03	1.08	2.74	2.97	2.20	3.01	3.23	1.34	8.03	21.34	5.76
Eu_N/Eu_N^*	1.11	0.94	1.06	1.03	1.14	1.04	1.20	1.42	0.94	1.15	1.32	1.08	1.40	1.00
Nb/Y	0.11	0.24	0.18	0.11	0.12	0.22	0.18	0.25	0.23	0.29	0.12	0.24	0.68	0.23
$(Nb/La)_{PM}$	0.72	0.19	0.51	0.69	0.56	0.63	0.46	0.79	0.60	0.69	0.66	0.27	0.27	0.28

(continued)

Table 3.4 (continued)

Sample	MA-1										MA-2				
	YX011-2	FX09-5	OFX10-2	OFX10-3	OFX14-2	12FX11-1	12FX11-3	12FX16-3	12FX28-3	12FX28-4	FX08-1	FX09-1	FX09-6	FX12-2	FX13-2
Lithology	Amp	Hornblende Plagioclase Gneiss (Hb-Pl gneiss)	Hb-Pl gneiss	Hb-Pl gneiss	Hb-Pl gneiss	Hb-Pl gneiss	Hb-Pl gneiss	Palimpsest andesite	Cpx-Amp	Hb-Pl gneiss	Hb-Pl gneiss				
SiO_2	63.39	54.89	59.83	63.78	62.31	59.94	60.01	55.42	55.39	58.07	55.17	52.94	57.53	50.77	53.27
Al_2O_3	17.44	16.84	14.14	12.80	13.83	15.25	13.63	16.18	16.80	15.13	14.61	14.47	15.10	14.69	17.97
Fe_2O_3T	4.67	12.60	8.25	6.13	6.88	7.30	7.66	7.45	8.84	7.59	7.31	10.77	6.15	8.61	9.57
CaO	4.38	3.35	5.01	3.36	3.51	4.97	4.47	3.52	5.75	4.19	5.92	7.72	5.96	7.46	9.06
MgO	1.81	3.56	3.75	2.86	3.40	3.55	2.95	2.21	5.19	1.85	7.96	5.98	6.24	10.52	3.47
K_2O	2.19	3.48	2.77	2.10	2.07	1.89	1.41	3.25	1.67	2.66	2.28	3.00	1.89	0.48	0.28
Na_2O	3.97	2.88	3.53	4.83	3.94	3.98	4.86	5.36	4.61	3.51	2.99	2.67	4.47	3.35	3.49
MnO	0.06	0.12	0.09	0.07	0.08	0.08	0.10	0.06	0.09	0.11	0.10	0.12	0.09	0.15	0.14
TiO_2	0.41	1.01	0.67	0.54	0.64	0.62	0.53	0.99	0.68	0.79	0.61	0.63	0.56	0.80	0.99
P_2O_5	0.19	0.32	0.25	0.19	0.06	0.26	0.16	0.61	0.21	0.25	0.15	0.27	0.14	0.17	0.14
LOI	1.33	0.79	1.35	3.13	3.33	1.97	4.03	4.74	0.59	5.63	2.71	1.19	1.69	2.75	1.47
Total	99.84	99.84	99.64	99.79	100.05	99.81	99.82	99.79	99.82	99.78	99.81	99.78	99.83	99.75	99.84
Mg#	43.50	35.90	47.41	48.05	49.49	49.06	43.32	37.02	53.79	32.52	68.30	52.40	66.80	70.80	41.80
Al_2O_3/TiO_2	42.54	16.67	21.18	23.80	21.52	24.76	25.53	16.33	24.71	19.18	23.95	22.97	26.96	18.36	18.15
V	43	79	104	79	115	94	71	64	111	131	69	99	62	87	118
Cr	—	—	280	213	—	193	152	—	281	381	352	362	286	376	198
Co	24	33	21	16.0	—	17.0	18.0	12.0	22	18.0	20	23	18.4	26	20
Ni	—	—	75	70	—	64	64	—	75	44	163	148	162	177	112
Rb	29	68	56	47	48	50	26	85	54	59	25	38	27	2.69	4.84
Sr	331	181	787	550	508	655	596	511	819	659	288	260	277	249	304
Y	6.70	9.42	13.7	9.13	9.54	15.7	7.03	34	10.9	10.8	8.55	17.0	8.39	10.1	12.0
Nb	3.49	9.8	5.83	5.35	5.87	6.15	4.93	19.4	9.20	7.58	2.02	4.25	2.03	2.33	3.06
Ba	465	550	981	813	925	762	665	1326	398	740	248	409	278	560	104
La	20	18.3	21	26	17.1	20	15.4	47	28	18.0	8.04	15.0	7.72	8.17	7.35
Ce	39	38	46	48	42	43	30	99	55	35	16.6	39	16.7	16.6	16.5
Pr	4.20	4.40	6.06	5.40	4.89	5.27	3.25	11.7	6.07	4.03	2.01	5.28	2.07	2.10	2.20

(continued)

Table 3.4 (continued)

Sample	MA-1										MA-2				
	YX011-2	FX09-5	OFX10-2	OFX10-3	OFX14-2	12FX11-1	12FX11-3	12FX16-3	12FX28-3	12FX28-4	FX08-1	FX09-1	FX09-6	FX12-2	FX13-2
Lithology	Amp	Hornblende Plagioclase Gneiss (Hb-Pl gneiss)	Hb-Pl gneiss	Hb-Pl gneiss	Hb-Pl gneiss	Hb-Pl gneiss	Hb-Pl gneiss	Palimpsest andesite	Cpx-Amp	Hb-Pl gneiss	Hb-Pl gneiss				
Nd	15.6	17.9	24	19.9	21	19.7	10.9	42	22	15.0	8.31	24	8.84	9.04	10.6
Sm	2.49	3.02	4.43	3.26	3.67	4.07	1.943	7.96	3.65	2.85	1.710	4.47	1.840	1.870	2.23
Eu	0.780	0.840	1.320	1.258	1.523	1.473	1.293	2.98	1.549	1.702	0.550	0.780	0.550	0.630	0.820
Gd	1.990	2.52	3.99	2.97	3.70	3.85	1.959	7.80	3.52	2.85	1.650	3.59	1.680	1.880	2.13
Tb	0.260	0.370	0.527	0.370	0.463	0.539	0.242	1.114	0.433	0.395	0.270	0.580	0.290	0.310	0.380
Dy	1.320	1.980	2.64	1.774	2.34	2.65	1.154	5.64	1.981	1.946	1.510	3.11	1.620	1.830	2.24
Ho	0.220	0.330	0.518	0.351	0.444	0.531	0.238	1.142	0.393	0.404	0.290	0.580	0.310	0.36	0.44
Er	0.660	0.990	1.380	0.920	1.320	1.413	0.664	3.07	1.050	1.079	0.880	1.860	0.880	1.11	1.35
Tm	0.100	0.140	0.202	0.143	0.190	0.197	0.097	0.433	0.152	0.152	0.130	0.270	0.130	0.160	0.200
Yb	0.640	0.880	1.226	0.869	1.345	1.230	0.669	2.71	0.972	0.964	0.850	1.770	0.850	1.040	1.280
Lu	0.100	0.140	0.189	0.138	0.205	0.192	0.107	0.422	0.154	0.153	0.130	0.270	0.140	0.170	0.210
Ta	0.190	0.450	0.443	0.274	0.274	0.347	0.265	1.259	0.485	0.213	0.150	0.160	0.160	0.170	0.210
Th	3.34	2.18	0.160	0.355	0.657	0.290	0.275	7.08	0.880	0.588	2.65	0.350	2.35	2.31	0.070
U	0.220	0.400	0.208	0.264	0.422	0.444	0.421	1.217	0.333	0.213	0.600	0.200	0.950	0.690	0.090
Zr	143	295	173	156	164	149	144	273	179	172	151	169	169	157	208
Hf	2.88	5.99	4.30	4.04	4.71	3.56	3.24	6.10	4.12	4.08	3.16	3.57	3.74	3.17	3.72
TREE	88	90	113	111	99	104	68	233	124	85	43	101	44	45	48
$(La/Sm)_N$	5.24	3.91	3.01	5.21	3.00	3.25	5.10	3.84	4.92	4.08	3.04	2.17	2.71	2.82	2.13
$(Gd/Yb)_N$	2.57	2.37	2.69	2.83	2.28	2.59	2.42	2.38	3.00	2.45	1.61	1.68	1.64	1.50	1.38
$(La/Yb)_N$	22.64	14.92	12.07	21.69	9.10	11.93	16.48	12.55	20.49	13.40	6.78	6.08	6.51	5.63	4.12
Eu_N/Eu_N^*	1.07	0.93	0.96	1.24	1.26	1.14	2.03	1.16	1.32	1.82	1.00	0.60	0.96	1.03	1.15
Nb/Y	0.52	1.04	0.43	0.59	0.61	0.39	0.70	0.57	0.85	0.70	0.24	0.25	0.24	0.23	0.26
$(Nb/La)_{PM}$	0.17	0.52	0.27	0.20	0.33	0.29	0.31	0.39	0.32	0.41	0.24	0.27	0.25	0.27	0.40

Note: *LOI* loss on ignition; Mg#=100Mg/(Mg+Fe_{total}) in atomic ratio; *TREE* total rare earth elements;
$Eu_N/Eu_N^*=Eu_N/SQRT(Sm_N*Gd_N)$; subscript N-chondrite normalized value; subscript PM-primitive mantle normalized value
Data marked by "—" are those not analyzed or below the dection line

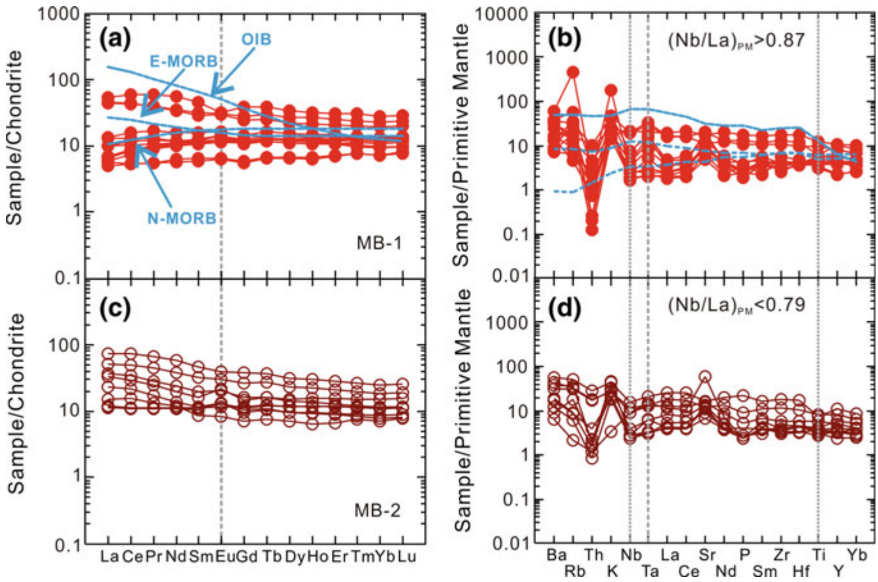

Fig. 3.10 Chondrite-normalized REE patterns and primitive mantle-normalized multi-element spider diagrams for tholeiitic metabasaltic rocks of Group MB-1 (**a** and **b**), and Group MB-2 (**c** and **d**). Symbols are the same as Fig. 3.9, and the values for chondrite, primitive mantle, N-MORB, E-MORB, and OIB are after Sun and McDonough [78]

Three metabasaltic samples with palimpsest volcanic textures (samples 12FX10-1, 12FX11-4, and 12FX26-3) belong to Group MB-3 (Fig. 3.3d). They show slightly higher SiO_2 of 52.67–56.94 wt%, with MgO and Mg# of 2.47–6.45 wt% and 39.68–52.30, respectively (Table 3.4). Compared with the other two metabasaltic groups, they are distinguished by the highest $(La/Sm)_N$ ratios (2.51–4.63) and the lowest $(Nb/La)_{PM}$ ratios (0.27–0.28). They plot in the field of calc-alkaline rock series (Fig. 3.9b). The Group MB-3 samples display strongly fractionated chondrite-normalized REE patterns, with $(La/Yb)_N$ and Eu_N/Eu_N^* ratios of 5.76–21.34 and 1.00–1.40, respectively. They show evidently negative Nb, Ta, and Ti anomalies in the primitive mantle-normalized multi-element spider diagram (Fig. 3.11a, b). The nearly consistent normalized REE and trace element patterns indicate that the primordial compositions of most immobile elements [i.e., REEs and high field strength elements (HFSEs)] are preserved.

Fifteen samples of metaandesitic rocks (Table 3.4) are characterized by low $(Nb/La)_{PM}$ ratios (0.17–0.52) and high $(La/Sm)_N$ ratios (2.13–5.24), and plot in the field of calc-alkaline rock series, similar to the Group MB-3 metabasaltic samples (Fig. 3.11c–f). The andesitic samples can be subdivided into Groups MA-1 and MA-2, with the former characterized by higher $(La/Sm)_N$ ratios (3.00–5.24) and $(La/Yb)_N$ ratios (9.10–22.64), and the latter showing lower $(La/Sm)_N$ ratios (2.13–3.04) and $(La/Yb)_N$ ratios (4.12–6.78) (Table 3.4). Ten samples constitute Group MA-1, including eight hornblende plagioclase gneisses, one clinopyroxene

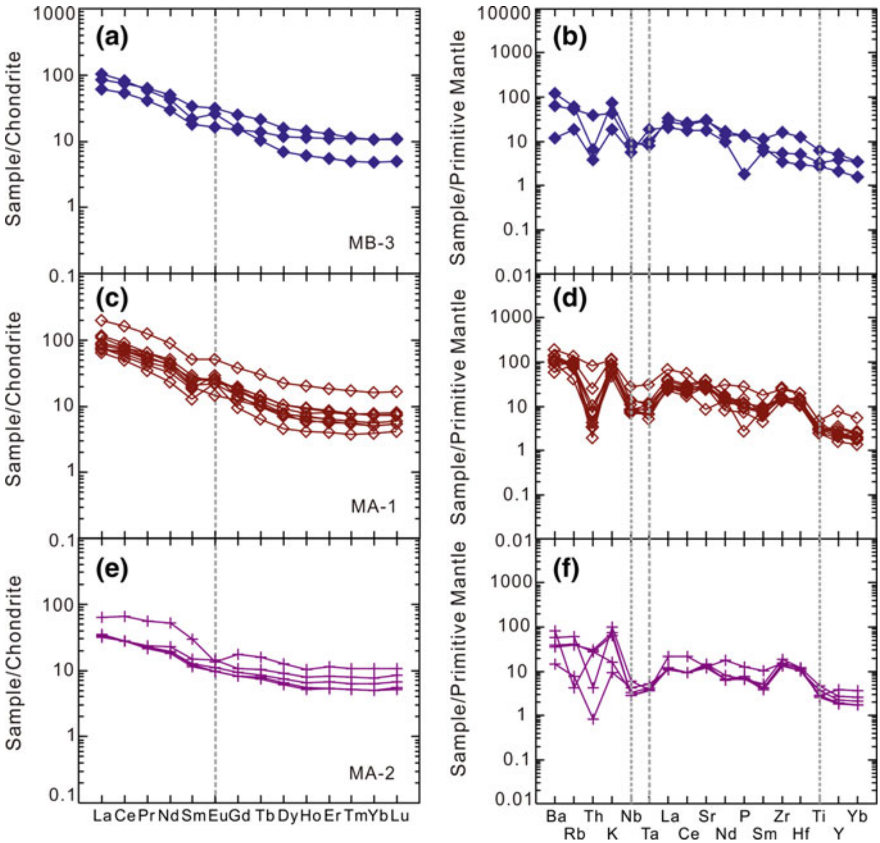

Fig. 3.11 Chondrite-normalized REE patterns and primitive mantle-normalized spider diagrams for calc-alkaline rock samples: i.e., metabasaltic rocks of Group MB-3 (**a** and **b**), metaandesitic rocks of Group MA-1 (**c** and **d**) and Group MA-2 (**e** and **f**). Sample symbols and normalized values are the same as Fig. 3.10

amphibolite (sample 12FX16-3), and one metaandesitic sample with palimpsest volcanic texture (sample 12FX28-3). They have high SiO_2 of 54.89–63.78 wt%, and MgO contents vary from 1.81 to 5.19 wt%, with Mg# values of 32.52–53.79 (Table 3.4). Group MA-2 is composed of five hornblende plagioclase gneiss samples (Table 3.4), with SiO_2 mostly in the range of 52.94–57.53 wt% (sample FX12-2 has a lower value of 50.77 wt%). The MgO contents (3.47–10.52 wt%) are generally higher than those of Group MA-1 samples, and the Mg# values are generally higher (mostly of 52.40–70.80, except for a lower value of 41.80 for sample FX13-2). In the chondrite-normalized REE diagrams (Fig. 3.11c, e), the Group MA-1 samples display strongly fractionated patterns with moderately positive Eu anomalies (Eu_N/Eu_N^* = 0.93–2.03), whereas the Group MA-2 samples show less fractionated patterns without significant Eu anomalies (Eu_N/Eu_N^* = 0.60–1.15). In the primitive mantle-normalized multi-element spider diagrams (Fig. 3.11d, f), negative Nb, Ta, and Ti anomalies and positive Zr and Hf anomalies are shown by all the andesitic samples.

3.1.4 Discussion

3.1.4.1 Assessment of Element Mobility

Metavolcanic rocks of the Fuxin-Yixian greenstone belt were generally subjected to amphibolite facies metamorphism, with some showing upper amphibolite to granulite facies (e.g., samples FX12-1, 12FX18-2, and 12FX18-4 of Groups MB-1 and MB-2; Table 3.4 and Fig. 3.3). It is therefore necessary to assess the effects of alteration on element compositions before evaluating their petrogenesis. In general, most samples have low loss on ignition (LOI) values (<3.50 wt%), with only a few samples (e.g., 12FX10-1, 12FX11-4, and 12FX28-4) showing higher LOI values (5.11–5.63 wt%). These are consistent with the absence of significant Ce anomalies ($Ce^* = Ce_N/Sqrt(La_N * Pr_N)$, mostly of 0.90–1.10) (Fig. 3.10), as rocks with Ce* values between 0.9 and 1.1 are generally considered as unaltered [63, 67, 89]. On the chondrite-normalized REE and primitive mantle-normalized multi-element spider diagrams (Figs. 3.10 and 3.11), samples of each group show coherent REE and high field strength element (HFSE) patterns, indicating general preservation of their original magmatic compositions. The interlaced HREE patterns for Group MB-3 samples might reflect different degrees of partial melting or diverse melting pressures as discussed below (Fig. 3.11a). On the other hand, two samples of Group MB-3 plotting within the basaltic field have higher silica contents (53.39–56.94 wt% of samples 12FX11-4 and 12FX26-3), and some Group MA-2 samples falling into the andesitic domain show lower SiO_2 contents (50.57–52.94 wt% of samples FX09-1 and FX12-2). The original silica contents of these metavolcanic rocks may have been mobilized during post-magmatic alteration, and therefore cannot be used for rock classification. Similar cases have been reported in the Dharwar craton by Manikyamba et al. [48]. Large variations of Ba, Rb, K, and Sr suggest that these elements have already been mobilized (Figs. 3.10 and 3.11). Large variation of Th contents in the normalized trace element patterns also points to their post-magmatic mobility. Moreover, high temperature and high pressure experiments revealed that only ~5–10% melts were produced during the partial melting of metabasalts at 1000–1025 °C and 0.8–1.6 Gpa [68]. In comparison, the peak metamorphic P-T condition of Western Liaoning basement rocks is much lower at T = 785–820 °C and P = 1.05–1.17 Gpa [36]. In this case, minor volume of anatexis melts may have been preserved at the mineral boundaries instead of gathering as independent magmas [3], and whole-rock geochemical data of the garnet amphibolites and garnet clinopyroxene plagioclase gneisses in Groups MB-1 and MB-2 can still represent the original igneous compositions (except for Rb, Ba, and Th). Accordingly, the following petrogenetic discussions will largely rely on rare earth elements (e.g., La, Sm, and Yb), and high field strength elements (e.g., Nb, Ta, Zr, and Hf).

3.1.4.2 Petrogenesis

Group MB-1

Group MB-1 samples have geochemical features analogous to those of N-MORBs and E-MORBs (with high $(Nb/La)_{PM}$ ratios of 0.90 and 1.27, respectively) [78]. In the $(Nb/La)_{PM}$ versus $(La/Sm)_N$ diagram (Fig. 3.12a), the Group MB-1 samples cluster around the N-MORB and E-MORB fields, showing no contamination by the continental crust materials [81]. The lack of negative correlation between $(Nb/La)_{PM}$ and $(La/Sm)_N$ ratios and generally low Ce/Yb ratios imply that their parental magmas erupted in an oceanic setting (Fig. 3.12a, b) [22]. For a basaltic magma system, Ni is preferentially partitioned into the crystallizing olivine and clinopyroxene (partition coefficients (Kd) of 5.9–29 and 1.5–14, respectively), whereas Cr is likely bound in clinopyroxene rather than olivine (Kd of 34 and 0.7, respectively). In comparison, V is more compatible in hornblende (Kd of 3.4, compared

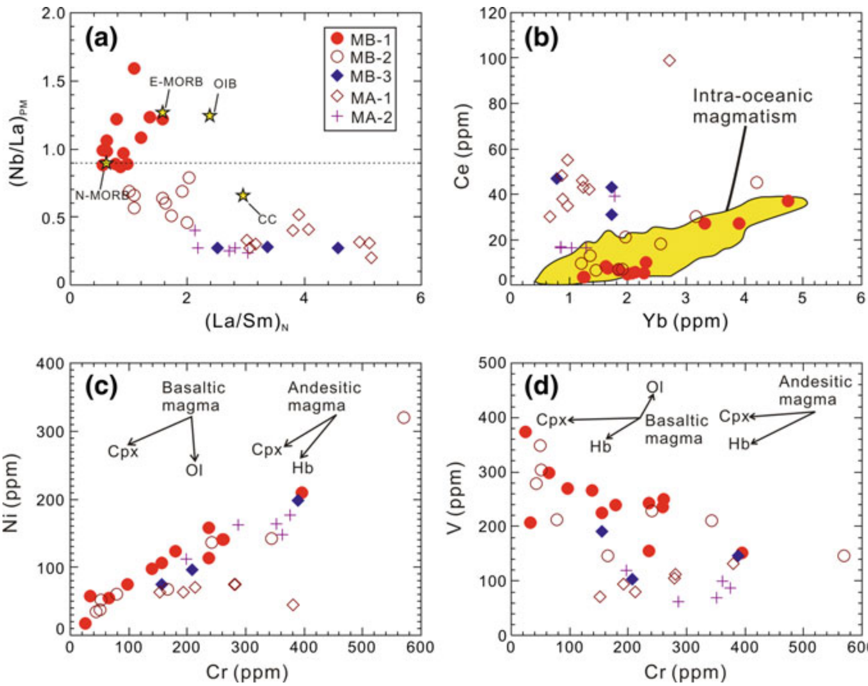

Fig. 3.12 $(Nb/La)_{PM}$ versus $(La/Sm)_N$ **a** [78], Ce versus Yb **b** [22], Ni versus Cr (**c**), and V versus Cr **d** [70] diagrams for metavolcanics from Fuxin-Yixian greenstone belt, Western Liaoning Province. The arrows in **c** and **d** represent mineral fractional crystallization trajectories from basaltic or andesitic parental magmas. The E-MORB, N-MORB, and OIB values are cited from Sun and McDonough [78]; continental crust (CC) values from Taylor and McLennan [81]. *Abbreviations* Ol—olivine; Cpx—clinopyroxene; Hb—hornblende

with generally >1.35 for olivine and clinopyroxene) [70]. The positive correlation between Ni and Cr, and negative correlation between V and Cr for the Group MB-1 samples are consistent with fractionation of olivine and clinopyroxene from the magma system (Fig. 3.12c, d). In the La/Yb versus Nb/Yb and Nd/Yb versus Nb/Yb diagrams (Fig. 3.13a, b), all the MB-1 samples plot within the MORB-OIB array, extending from the N-MORB to E-MORB fields. This is consistent with the generally high $(Nb/La)_N$ and chondrite-like $(Hf/Sm)_N$ ratios, further demonstrating that the mantle sources were unaffected by subduction-related or carbonate metasomatism (Fig. 3.13c) [33, 59]. The slightly higher $(Hf/Sm)_N$ ratios of samples FX10-1 and FX12-1 (1.86–2.26) might indicate the involvement of some residual slab components (SRC) in the mantle source [30]. The two dated samples (OFX08-5 and 12FX18-2) have N-MORB-like geochemical features (LREE-depleted REE patterns but without negative Nb, Ta, and Ti anomalies (higher $(Nb/La)_{PM}$ ratios), Figs. 3.10a, b and 3.12a), and they show high zircon εHf (t_2) values close to the coeval depleted mantle values (Figs. 3.5 and 3.6). Therefore, the Group MB-1 samples with LREE-depleted patterns could have been derived

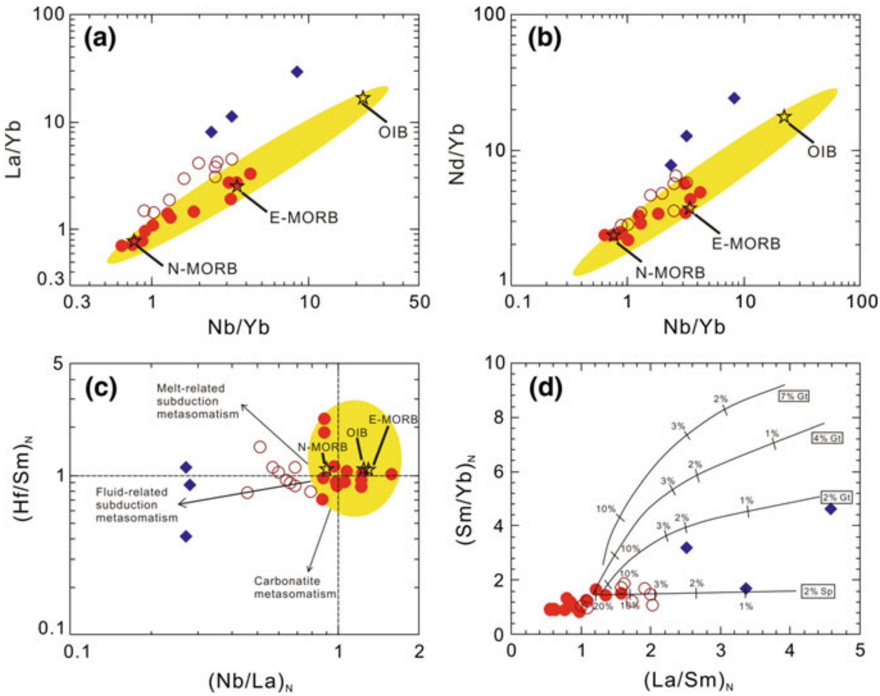

Fig. 3.13 Mantle source characteristics and petrogenesis of metabasaltic rocks from the Fuxin-Yixian greenstone belt: **a** La/Yb versus Nb/Yb diagram; **b** Nd/Yb versus Nb/Yb diagram; **c** $(Hf/Sm)_N$ versus $(Nb/La)_N$ diagram (after LaFlèche et al. [33]); and **d** $(Sm/Yb)_N$ versus $(La/Sm)_N$ diagram (after Jourdan et al. [26]). Element ratios for N-MORB, E-MORB, and OIB are after [78]. Gt—Garnet; Sp—Spinel

from the partial melting of a depleted mantle source. The four samples with LREE-enriched patterns show higher $(Nb/La)_{PM}$, La/Yb, Nb/Yb, and Nd/Yb ratios (Fig. 3.13), indicating their derivation from a relatively enriched mantle source. Similar mantle heterogeneities were documented in the Wawa greenstone belt of Superior Province and Penakacherla greenstone belt of eastern Dharwar craton [46, 66]. The $(Sm/Yb)_N$ versus $(La/Sm)_N$ diagram shows that Group MB-1 samples can be modeled by high degree ($\sim$10–20%) partial melting of lherzolites with $\sim$2% spinel (Fig. 3.13d) [26]. Accordingly, the parental magmas of Group MB-1 metabasaltic rocks are considered to have been generated by the partial melting of depleted to slightly enriched mantle sources that were not modified by subduction-related metasomatism.

Group MB-2

Similar to Group MB-1 samples, the metamorphosed tholeiitic to transitional samples of Group MB-2 show nearly flat chondrite-normalized REE patterns (Fig. 3.10c). However, they display weakly to evidently negative Nb–Ta–Ti anomalies, with lower $(Nb/La)_{PM}$ ratios mostly of 0.46–0.79 (Fig. 3.12a). These geochemical features are clearly distinct from those of MORB-like rocks, but resemble those of island arc tholeiites (IATs) in both the Phanerozoic Izu-Bonin-Mariana subduction system and early Archean Nuvvuagittuq greenstone belt of northern Quebec [69, 84]. Except for the much lower $(Nb/La)_{PM}$ ratios, the Group MB-2 samples have negative Ti anomalies, in contrast to the slightly negative to strongly positive Ti anomalies for Group MB-1 samples. Given the increasing V contents with decreasing Cr contents, the negative Ti anomalies cannot be ascribed to fractionation of Fe–Ti oxides (e.g., magnetite), which will result in simultaneous decrease in V, Cr, and TiO_2 contents [70]. Moreover, Group MB-2 samples show Nb and TiO_2 contents slightly lower than those of Group MB-1 samples (Nb: 1.240–10.9 ppm vs. 1.110–14.7 ppm; TiO_2: 0.52–1.75 wt% vs. 0.65–2.62 wt%). In the $(Nb/La)_{PM}$ versus $(La/Sm)_N$ diagram (Fig. 3.12a), Group MB-2 samples fall below the MORB and OIB fields, but lack of evident correlation between $(Nb/La)_{PM}$ and $(La/Sm)_N$ ratios. Considering the generally low Ce/Yb ratios (albeit slightly higher than those of Group MB-1 samples), significant crustal contamination can be precluded (Fig. 3.12b). This is further corroborated by the high zircon $\varepsilon Hf(t_2)$ values of +4.5 to +7.5, suggesting that Group MB-2 samples might have erupted in an oceanic setting (Fig. 3.7d) [58]. The positive correlation between Cr and Ni, and negative correlation between V and Cr, suggest the parental magmas have experienced olivine and clinopyroxene fractionation (Fig. 3.12c, d). Though Group MB-2 samples display higher La/Yb ratios, their Nb/Yb ratios are nearly consistent with those of Group MB-1 samples, and the two sample groups overlap within the MORB-OIB array in the Nd/Yb versus Nb/Yb diagram (Fig. 3.13a, b). Moreover, the dated Group MB-2 sample 12FX25-6 yields comparable zircon $\varepsilon Hf(t_2)$ values with those of Group MB-1 MORB-like samples (Figs. 3.5d, 3.6d and 3.7d). These lines of evidence indicate that the depletion degrees of mantle sources for both the two group samples are comparable. On the other hand, the Group MB-2 samples fall above the MORB-OIB array in the La/Yb versus Nb/Yb diagram (Fig. 3.13a) [59]. They exhibit chondrite-like $(Hf/Sm)_N$ ratios but lower $(Nb/La)_N$ ratios, and show negative normalized Nb–Ta–Ti anomalies [33]; Figs. 3.10d and 3.13c). Given that crustal contamination has been excluded, the mantle sources for the Group MB-2 samples could have been metasomatized mainly by slab-derived fluids before partial melting. The depleted zircon $\varepsilon Hf(t_2)$ values are also in conflict with any involvement of sedimentary components in the source. Accordingly, partial melting of a fluid-metasomatized sub-arc mantle wedge formed the magmatic precursor of Group MB-2 samples [62]. These metabasaltic samples can be modeled by ~3–20% (mostly of ~3–10%) partial melting of lherzolites with ~2% spinel (Fig. 3.13d) [26].

Group MB-3

The metabasaltic rock samples of Group MB-3 show calc-alkaline affinities, with fractionated normalized REE patterns and evidently negative normalized Nb-Ta anomalies (Figs. 3.11a, b). These chemical features are analogous to those of typical calc-alkaline basalts (CABs) in a mature subduction system [60, 84]. Previous studies noted that negative Nb anomalies in basaltic rocks could have been derived from different mechanisms in addition to subduction processes (e.g., element mobility, crustal contamination, or melting of a subduction-modified lithospheric mantle) [60, 80]. Although Group MB-3 samples exhibit slightly higher LOI values (0.89–5.50 wt%), they show roughly parallel LREE and HFSE patterns (Fig. 3.11a, b), suggesting negligible mobility of these elements. This is consistent with the preservation of primordial palimpsest volcanic textures (Fig. 3.3d). In the $(Nb/La)_{PM}$ versus $(La/Sm)_N$ diagram (Fig. 3.12a), they plot below the field of average continental crust, showing lower $(Nb/La)_{PM}$ values of 0.27–0.28. Despite higher Ce/Yb ratios, the absence of negative correlation between $(Nb/La)_{PM}$ and $(La/Sm)_N$ ratios, the generally mafic whole-rock compositions and significantly negative Nb–Ta anomalies, suggest insignificant crustal contamination (Figs. 3.11b and 3.12a, b). The positive correlation between Cr and Ni and lack of correlation between V and Cr are consistent with clinopyroxene as the major fractionation phase (Fig. 3.12c, d) [70]. In the La/Yb versus Nb/Yb and Nd/Yb versus Nb/Yb diagrams (Fig. 3.13a, b), these metabasaltic rock samples plot above the MORB-OIB array. They have Nb contents of 4.08–6.52 ppm, similar to those of tholeiitic to calc-alkaline basalts in the Phanerozoic Izu-Bonin arc (typically <7 ppm, from GEOROC data). These are much lower than those of Nb-enriched basalts or high-Nb basalts (Nb >7 ppm, and up to >20 ppm), with the latter derived from the partial melting of slab melt-metasomatized mantle wedge materials [21, 73]. Given the generally lower $(Nb/La)_N$ and moderate $(Hf/Sm)_N$ ratios, it is suggested that the Group MB-3 samples were formed by the partial melting of a mantle source that was significantly metasomatized by subduction-derived fluids (Fig. 3.13c) [33]. Sample 12FX26-3 shows high zircon $\varepsilon Hf(t_2)$ values close to the coeval depleted mantle value (+3.5 to +9.3) [93], further excluding the involvement of crustal contamination. Importantly, the subduction-related metasomatic process could have been immediately followed by the partial melting event, as evidenced by the lack of deviation of the isotopic system from those of the depleted mantle. In other words, the parental magmas of Group MB-3 samples are products of arc magmatism, and the negative Nb–Ta anomalies were not inherited from earlier subduction processes. Accordingly, the parental magmas of Group MB-3 samples were generated by the partial melting of a sub-arc depleted mantle source that was significantly metasomatized by subduction-derived fluids. They could have been generated by low degrees ($\sim$1–3%) of partial melting of lherzolites with $\sim$2% spinel or $\sim$2% garnet, which is consistent with their interlaced HREE patterns (Figs. 3.11a and 3.13d).

Group MA-1

The metaandesitic rock samples of Group MA-1 display strongly fractionated normalized REE patterns, showing higher $(La/Yb)_N$ and Sr/Y ratios, and generally positive Eu anomalies (Table 3.4). These geochemical features are comparable with those of adakitic rocks from modern island arcs or metavolcanic rocks of Archean greenstone belt [14, 47, 89]. Notably, the so-called "adakitic signature" is complex, which could be derived from fractional crystallization, high pressure melting, magma mixing, or classic "slab melting" processes [8, 52]. Since both samples from Group MB-3 and Group MA-1 belong to calc-alkaline rock series, with the latter showing higher degrees of REE fractionation, it is possible that they were derived from a common parental magma (Figs. 3.9b, 3.11a, c). However, samples of the two groups have nearly consistent $(Nb/La)_{PM}$ ratios with no positive correlation between $(Nb/La)_{PM}$ and MgO (not shown), implying that they cannot be linked by shallow-level crustal contamination [44]. In addition, the La/Sm ratios increase steadily with increasing La contents (except for sample 12FX16-3), further excluding a fractional crystallization link between Groups MA-1 and MA-2 [74]. In the La/Sm versus La and La versus La/V diagrams (Fig. 3.14a, b), most samples of Group MA-1 (except for sample 12FX16-3) define positive correlation, suggesting that the compositional variations are chiefly controlled by a partial melting process, though higher La content and La/V ratio of sample 12FX16-3 might have resulted from fractional crystallization (Fig. 3.14b) [74]. On the other hand, the dated sample 12FX28-3 does not contain inherited zircon grains, and it gives higher zircon $\varepsilon Hf(t_2)$ values close to the coeval depleted mantle value (+3.3 to +6.5; Fig. 3.8d). These features argue against significant contamination by ancient crustal materials. The higher MgO contents (1.81–5.19 wt%) of Group MA-1 samples are also distinct from those of adakitic rocks derived solely from the partial melting of thickened mafic crust [50]. Alternatively, these rocks might have been generated by the partial melting of a peridotitic mantle wedge modified by slab-melts [50]. However, this latter case is contradictory with the generally low TiO_2 contents (0.41–1.01 wt%) of Group MA-1 samples, since higher TiO_2 contents (usually >1.0 wt%) are implicit in the partial melts derived from slab melt-metasomatized mantle materials [51]. Therefore, the slightly lower SiO_2 and higher MgO in these rocks can be ascribed to a larger degree of contamination by

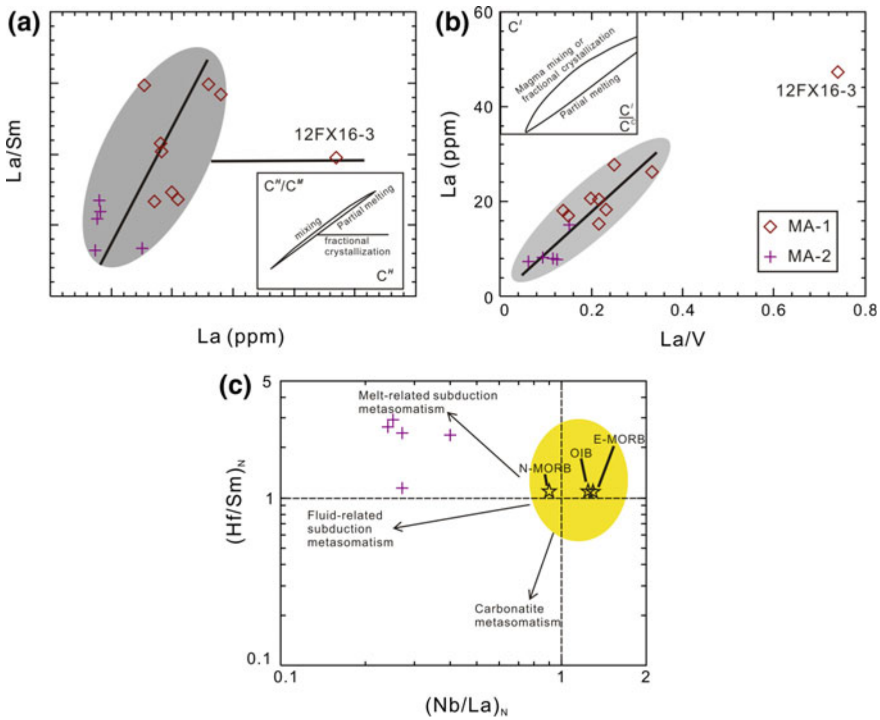

Fig. 3.14 Petrogenesis and mantle source characteristics for metaandesitic rocks (MA-1 and MA-2) from the Fuxin-Yixian greenstone belt. **a** La/Sm versus La diagram [83]; **b** La versus La/V diagram [74]; **c** $(Hf/Sm)_N$ versus $(Nb/La)_N$ diagram (after LaFlèche et al. [33]). The insets in (**a**) and (**b**) are cited from Schiano et al. [74]; and values for N-MORB, E-MORB, and OIB are after Sun and McDonough [78]

the mantle wedge materials during ascent of the slab melts. Since magma mixing has been excluded by geochemical modeling (Fig. 3.14a, b), the high zircon εHf(t_2) values and Na_2O contents (mostly of >3.50 wt%) indicate that the Group MA-1 samples resemble those of typical Phanerozoic adakites, which could have been produced by the partial melting of subducted oceanic slabs [14]. The high MgO contents suggest that the slab melts could have been contaminated by the mantle wedge materials during their ascent, which is supported by the generally high Ni and Cr contents (44–75 and 152–381 ppm, respectively) (Table 3.4). The positive Eu anomalies and somewhat concave upward REE patterns suggest that garnet and hornblende, but not plagioclase, constitute the major residue phases in the source. This is compatible with the high $(La/Yb)_N$ and Zr/Sm ratios (Fig. 3.11c and Table 3.4) [16, 70, 91].

Group MA-2

The Group MA-2 is composed of calc-alkaline metaandesitic rocks (Table 3.4). Compared to the adakite-like rocks in Group MA-1, they have much higher MgO, Ni, and Cr contents (3.47–10.52 wt%, 112–177 ppm, and 198–376 ppm, respectively), less-fractionated chondrite-normalized REE patterns, and are characterized by lower $(La/Yb)_N$ ratios of 4.12–6.78 (Fig. 3.11e). The Group MA-2 rocks show chemical affinities to Phanerozoic and Archean high magnesium andesites [29, 65]. Mg# values (mostly of 56.41–74.01), Cr, and Ni contents are higher than those of crustal-derived melts, precluding derivation from a single crustal source [50, 68]. In the La/Sm versus La and La versus La/V diagrams (Fig. 3.14a, b), most of the metaandesitic samples (with the exception of sample FX09-1) define two roughly positive correlation lines, though little variation of La contents. Therefore, the compositional variation of Group MA-2 samples was mainly controlled by partial melting but not magma mixing or fractional crystallization [74]. Their Mg# values are close to those of primitive mantle magmas (Mg# of 63–72), suggesting that they were likely derived from a mantle source [17]. This also argues against the involvement of magma mixing or fractional crystallization processes, which will result in lower Mg# values. The uniform $(Nb/La)_{PM}$ (0.24–0.40) and high zircon $\varepsilon Hf(t_2)$ of +2.7 to +7.2 suggest insignificant crustal contamination (Figs. 3.4d and 3.12a). Since a magma mixing process has been excluded, the high MgO, Mg#, Cr, Ni, $(La/Sm)_N$, and zircon $\varepsilon Hf(t_2)$ values, as well as low $(Nb/La)_{PM}$ ratios, are assumed to have stemmed from a subduction-modified depleted mantle source [28, 88]. The low $(Nb/La)_N$ and high $(Hf/Sm)_N$ values of most Group MA-2 samples suggest that the mantle source was metasomatized mainly by slab melts (Fig. 3.14c) [33]. In contrast, the slightly low $(Hf/Sm)_N$ value of sample FX09-1 may be derived from a mantle source metasomatized by slab-derived fluids. Nonetheless, the injection of slab melts into the magma sources of Group MA-2 samples is consistent with the generally high Zr/Sm ratios (mostly of 83.96–93.27 vs. chondrite value of ~25) [78], pointing to transformation of the subducted slab basalts to amphibolites before partial melting ($D_{Zr}/D_{Sm} < 1$ for low Mg amphibole) [16]. Moreover, Group MA-2 samples have Nb contents (2.03–4.25 ppm) higher than those of andesitic rocks in the Phanerozoic Izu-Bonin arc system (typically <2 ppm, from GEOROC data), further demonstrating the involvement of slab melts in the mantle source [50]. In the $(Sm/Yb)_N$ versus $(La/Sm)_N$ diagram, these metaandesitic samples can be modeled by low degrees (<3%) of partial melting of lherzolites with ~2% spinel or garnet (figures not shown). Accordingly, it is suggested that the magmatic precursor of Group MA-2 samples was generated by low degrees of partial melting of a depleted mantle source metasomatized chiefly by slab-derived melts.

3.1.4.3 Geodynamic Setting

According to the above discussion, metavolcanic rocks in the Fuxin-Yixian greenstone belt consist of five petrogenetic types. Group MB-1 samples show chemical affinities to N-MORBs or E-MORBs, which were generated by adiabatic decompression melting of depleted to slightly enriched mantle sources under an Archean spreading ridge. On the La/Nb-La and Y/15-La/10-Nb/8 plots (Fig. 3.15a,

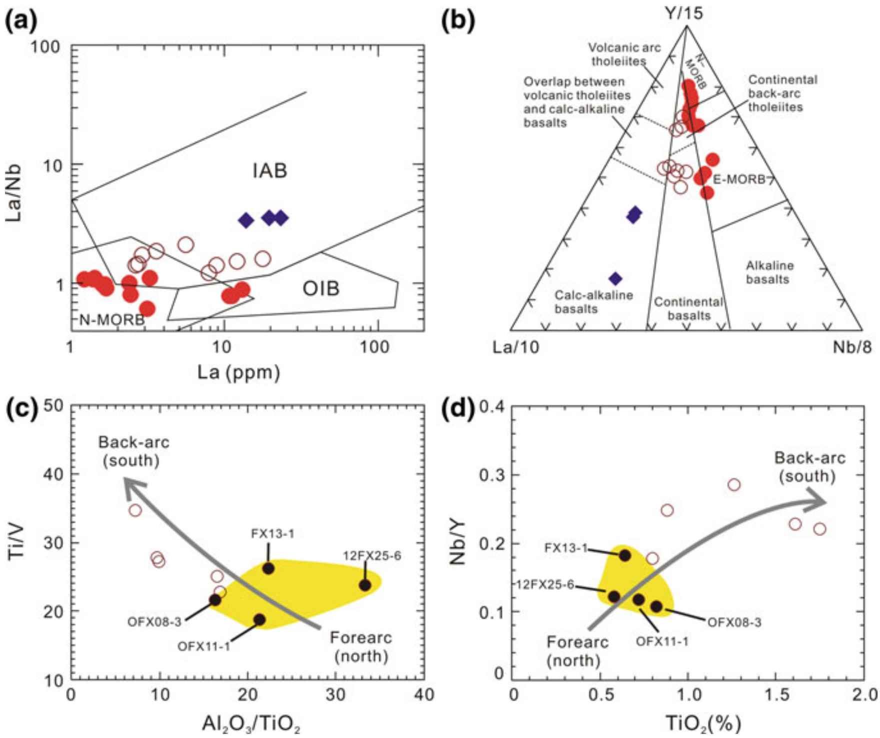

Fig. 3.15 Tectonic discrimination diagrams of the metavolcanics from Fuxin-Yixian greenstone belt. **a** La/Nb versus La diagram (after Li [35]); **b** Y/15–La/10–Nb/8 discrimination diagram (after Cabanis and Lecolle [7]); **c** Ti/V versus Al_2O_3/TiO_2 diagram; **d** Nb/Y versus TiO_2 diagram. The decrease in Al_2O_3/TiO_2 and increase in Ti/V, Nb/Yb, and TiO_2 from north (samples in the shaded areas) to south of the Fuxin greenstone belt is similar to the patterns observed from the forearc to back-arc environments in the Neoproterozoic Eritrean oceanic arc system [82]. Symbols are the same as Fig. 3.9

b), they fall into the fields of either N-MORBs or E-MORBs. Group MB-2 samples are analogous to those of island arc tholeiitic basalts, and were produced by the partial melting of a depleted to slightly enriched mantle source that were moderately metasomatized by slab-derived fluids. They could have been formed in a subduction-related arc setting (Fig. 3.15a, b). The calc-alkaline metabasaltic rocks in Group MB-3 samples were formed by the partial melting of a depleted mantle source that was significantly metasomatized by subduction-derived fluids. They fall into the field of island arc calc-alkaline basalts (Fig. 3.15a, b). The metaandesitic rocks of Group MA-1 show chemical features similar to those of Phenerozoic adakites, which could have been generated by the partial melting of descending slabs, with the melts contaminated by the mantle wedge materials. In comparison, the metaandesitic rocks of Group MA-2 resemble high magnesium andesites as those developed in Superior and Dharwar, which together with the closely associated adakite-like rocks, indicating that they could have been formed under a convergent arc setting [56, 64]. Accordingly, the above lithological assemblages indicate an Archean subduction-accretion regime for the formation and evolution of the Fuxin-Yixian greenstone belt.

The island arc tholeiitic metabasaltic rocks in Group MB-2 show increase in TiO_2 contents and Ti/V and Nb/Y ratios, but decrease in Al_2O_3/TiO_2 ratios, from north to south, suggesting a southward subduction polarity as reported in the Neoproterozoic Eritrean oceanic arc system (Fig. 3.15c, d) [59, 82]. Spatially, the MORB-like rocks of Group MB-1 cluster generally to the north of the Yangshudi-Xinglongba-Jiumiao line, whereas arc-related volcanic rocks of Groups MB-2, MB-3, MA-1, and MA-2 are distributed mostly to the south side of this line (Fig. 3.1). Accordingly, a late Neoarchean suture zone may exist roughly along the Yangshudi-Xinglongba-Jiumiao line, and the Fuxin-Yixian greenstone belt of Western Liaoning could record complex subduction-accretion-related geodynamic processes including mid-ocean ridge spreading, and initiation and maturation of a subduction zone, marked by a southward subduction polarity [93].

3.2 Neoarchean Dioritic and TTG Gneisses in the Western Liaoning Province

Tonalite-trondhjemite-granodiorite (TTG) gneisses are the major constituents of Archean basement terranes [25, 54]. Chemical modeling and experimental petrology reveal that TTG gneisses were mainly derived from the partial melting of metabasaltic rocks, whereas the geodynamic environments where they were formed remain hotly debated ([54] and references therein).

In this part, systematic geological, petrological, whole-rock geochemical, and zircon U–Pb and Lu–Hf isotopic data are provided for the TTG and minor dioritic gneisses in the Western Liaoning Province, aiming to determine the lithological assemblage, formation timing, petrogenesis and geodynamic setting.

3.2.1 Geological and Petrographic Characteristics

3.2.1.1 Granitoid Gneisses in the North Chaoyang-Fuxin-Yixian Granite-Greenstone Belt

The North Chaoyang-Fuxin-Yixian granite-greenstone belt (NCFY-GGB) is located in the northeastern part of Western Liaoning Province, and granitoid gneisses are mainly developed in Waziyu, Fuxingdi, Baoguolao-Loujiadian and Xiguanying areas (Fig. 3.16). Dioritic and TTG (DTTG) gneisses are the major lithological

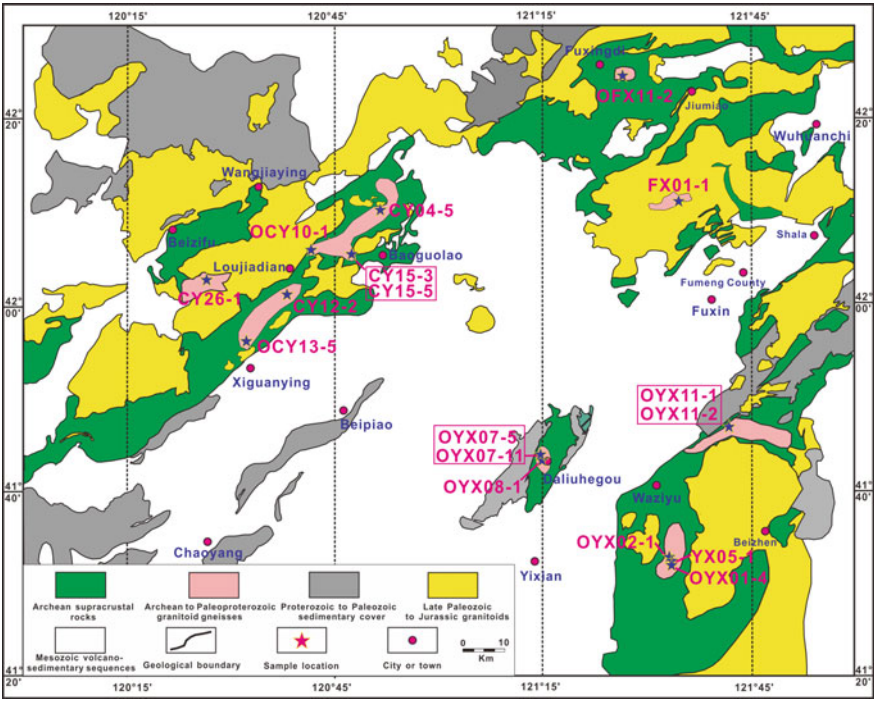

Fig. 3.16 Regional geological map and sampling locations of Archean granitoid gneisses in the North Chaoyang-Fuxin-Yixian granite-greenstone belt (NCFY-GGB) of Western Liaoning Province (after Wang et al. [89]). Note that most granitoid gneisses are dioritic to TTG in composition, whereas samples YX05-1, OYX02-1, CY12-2, and OYX11-1 are granodioritic to monzogranitic gneisses (see Part 3.3)

types, and they show intense gneissosity and intrude into the supracrustal rocks (Fig. 3.17a–c). This is further indicated by the volumes of xenoliths or roof pendants within the supracrustal rocks (Fig. 3.17d).

A total of thirteen representative samples were analyzed, including one dioritic, seven tonalitic, one trondhjemitic, and four granodioritic gneisses (Table 3.5). The mineral assemblages of most TTG gneisses are plagioclase (40–65%), quartz (10–25%), amphibole (10–20%), and a subordinate amount of K-feldspar (<15%) and biotite (<5%) (Fig. 3.17e, f). Some TTG gneisses show more quartz (25–30%) and less mafic mineral content (biotite of ~2–13%) (Fig. 3.17g, h). The dioritic gneiss (CY26-1) has a mineral assemblage of plagioclase (60%), hornblende (28%), biotite (5%), and minor quartz. These rocks were metamorphosed under greenschist to amphibolite facies, with the mafic minerals altered to chlorite and actinolite.

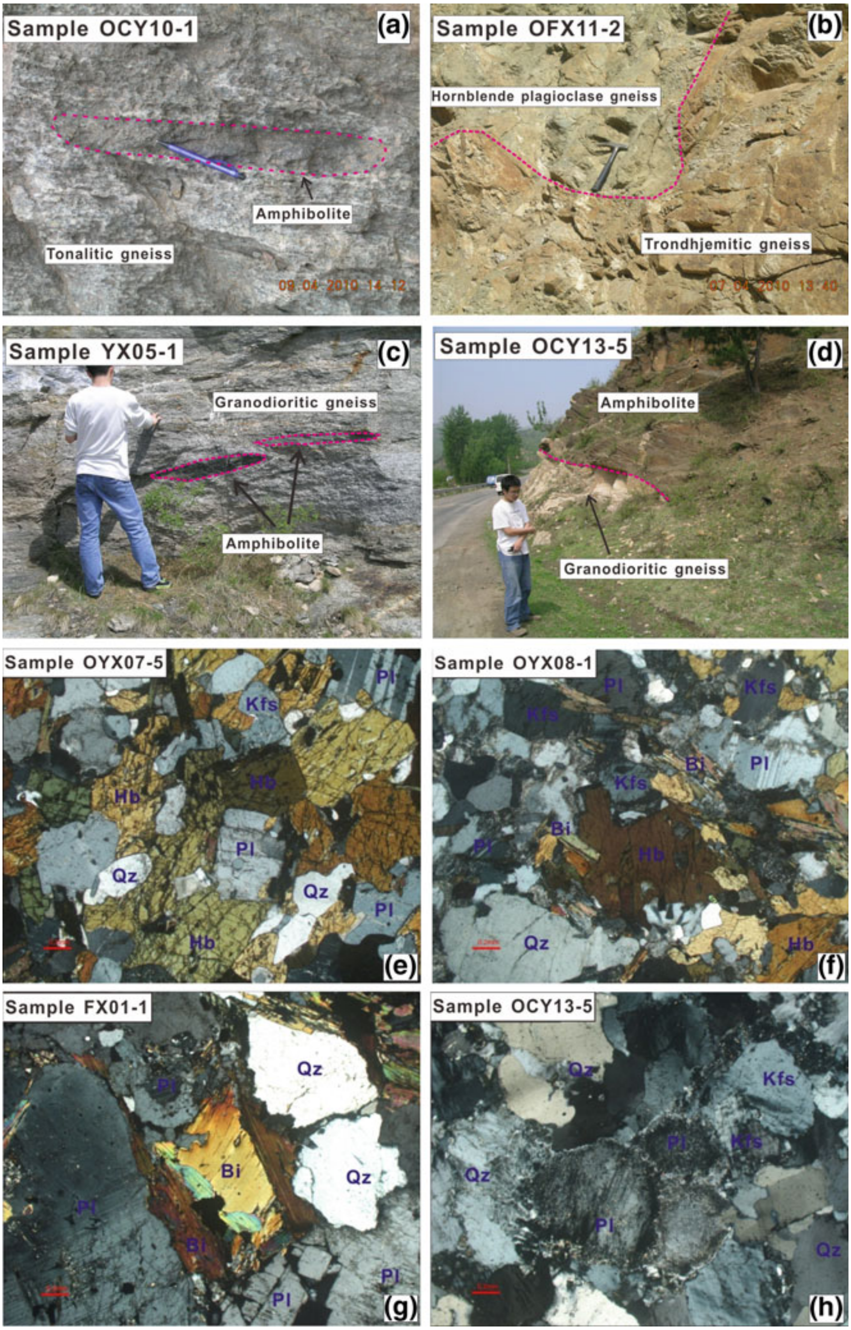

Fig. 3.17 Field geological characteristics (**a**–**d**) and petrographic features (**e**–**h**) of Archean dioritic to TTG gneisses from the North Chaoyang-Fuxin-Yixian granite-greenstone belt, Western Liaoning Province

Table 3.5 Analytical results of major (wt%) and trace elements (ppm) for late Archean granitoid gneisses from the Western Liaoning Province

Granitoid gneisses from the North Chaoyang-Fuxin-Yixian granite-greenstone belt	High magnesium group (HMG)									Low magnesium group (LMG)			
	CY15-3	CY15-5	OYX07-5	OYX07-11	OCY10-1	OYX01-4	OYX08-1	OYX11-2	CY26-1	FX01-1	CY04-5	OCY13-5	OFX11-2
	TO	TO	TO	TO	TO	GRD	GRD	GRD	DIO	TO	TO	GRD	TRON
SiO_2	60.64	58.25	59.65	61.48	62.84	65.76	61.07	62.40	55.90	63.02	67.37	72.68	73.29
TiO_2	0.13	0.34	0.61	0.65	0.23	0.44	0.71	0.55	0.56	0.88	0.25	0.06	0.18
Al_2O_3	16.37	16.28	15.86	16.14	16.69	14.69	16.45	14.91	16.23	15.72	15.68	15.74	15.37
FeOT	4.81	5.65	7.04	5.56	4.82	4.80	5.04	5.23	6.28	5.45	3.66	0.44	1.11
MnO	0.09	0.10	0.11	0.09	0.06	0.07	0.08	0.09	0.11	0.10	0.05	0	0.01
MgO	4.36	5.06	3.12	2.53	3.16	2.53	2.84	3.25	4.34	2.10	1.02	0.13	0.40
CaO	4.89	5.66	5.54	4.78	4.37	2.84	4.83	4.08	5.90	4.43	4.15	2.31	1.44
Na_2O	4.67	4.80	3.94	4.08	4.91	3.93	4.27	4.24	4.38	3.70	4.73	4.38	5.40
K_2O	2.41	2.36	1.95	2.18	1.46	2.97	2.91	3.22	2.63	2.19	1.68	3.61	1.91
P_2O_5	0.11	0.28	0.17	0.22	0.17	0.11	0.32	0.22	0.25	0.53	0.05	<0.05	<0.05
LOI	1.01	0.75	1.09	1.23	1.16	1.26	0.88	1.26	2.10	1.02	0.75	0.76	1.15
Total	99.49	99.54	99.11	98.93	99.87	99.40	99.38	99.45	98.68	99.13	99.39	100.10	100.28
Mg#	61.74	61.52	44.16	44.79	53.88	48.47	50.09	52.52	55.18	40.70	33.15	33.87	39.14
K_2O/Na_2O	0.52	0.49	0.50	0.54	0.30	0.75	0.68	0.76	0.60	0.59	0.36	0.83	0.35
A/CNK	0.85	0.78	0.85	0.91	0.95	0.99	0.87	0.83	0.78	0.95	0.91	1.03	1.13
Sc	5.01	13.6	19.6	10.1	7.30	7.87	10.2	12.5	9.04	2.93	0.11	0.42	0.73
V	37	99	134	84	37	68	85	91	51	67	21	39	10
Rb	36	78	73	61	48	112	74	91	40	115	19	68	15
Sr	311	544	479	569	574	410	633	501	507	631	241	509	504
Y	5.21	12	13.8	15.6	7.46	12.2	14.1	13.8	6.92	5.62	0.82	0.75	1.28
Nb	0.89	3.39	5.56	6.19	2.84	7.82	7.75	11.1	2.99	6.7	1.39	8.27	1.14
Cs	0.52	0.79	1.94	0.45	3.16	0.93	0.58	1.2	1.35	9.4	0.42	0.28	0.55
Ba	256	458	816	817	334	543	1113	940	816	656	234	1211	813

(continued)

Table 3.5 (continued)

Granitoid gneisses from the North Chaoyang-Fuxin-Yixian granite-greenstone belt	High magnesium group (HMG)									Low magnesium group (LMG)			
	CY15-3	CY15-5	OYX07-5	OYX07-11	OCY10-1	OYX01-4	OYX08-1	OYX11-2	CY26-1	FX01-1	CY04-5	OCY13-5	OFX11-2
	TO	TO	TO	TO	TO	GRD	GRD	GRD	DIO	TO	TO	GRD	TRON
La	11.6	22	30	48	27	72	33	33	14	22	5.03	12	10.5
Ce	21	46	62	96	52	133	67	72	29	44	7.68	15.3	16.9
Pr	2.38	5.35	7.11	10.6	5.36	12.8	7.49	7.76	3.46	5.44	0.68	1.27	1.88
Nd	9.72	22	29	42	21	42	30	31	15.2	23	2.15	3.67	6.76
Sm	1.67	4.22	5.37	7.07	3.09	5.29	5.45	5.41	2.17	3.37	0.25	0.34	0.87
Eu	0.5	1.43	1.87	2.34	1.2	1.31	2.2	1.97	0.67	0.96	0.47	1.93	1.15
Gd	1.13	4.08	5.29	7.01	3.25	6.09	5.35	5.56	1.78	2.32	0.24	0.5	0.92
Tb	0.19	0.53	0.65	0.8	0.36	0.6	0.66	0.66	0.25	0.3	0.03	0.03	0.07
Dy	0.97	2.67	3.17	3.65	1.67	2.64	3.14	3.22	1.22	1.3	0.16	0.1	0.24
Ho	0.18	0.51	0.61	0.67	0.31	0.51	0.58	0.6	0.23	0.19	0.03	0.02	0.04
Er	0.57	1.46	1.7	1.82	0.91	1.46	1.61	1.8	0.7	0.5	0.08	0.08	0.12
Tm	0.09	0.21	0.24	0.25	0.13	0.21	0.22	0.25	0.1	0.06	0.01	0.02	0.02
Yb	0.56	1.39	1.58	1.66	0.9	1.38	1.43	1.8	0.64	0.39	0.12	0.15	0.12
Lu	0.07	0.21	0.23	0.24	0.13	0.2	0.2	0.27	0.1	0.06	0.02	0.03	0.02
Ta	0.03	0.2	0.58	0.48	0.19	0.43	0.32	0.52	0.12	0.35	0.04	0.12	0.06
Th	0.12	0.27	5.93	7.5	2.04	5.39	2.86	12.1	0.09	1.55	0.23	0.25	0.06
U	0.05	0.04	0.91	0.5	0.37	0.54	0.27	0.56	0.05	0.32	0.17	0.89	0.1
Zr	46	88	133	178	78	131	160	152	68	82	23	42	53
Hf	1.39	2.02	3.63	4.92	2.15	3.55	5.17	4.7	2.35	2.17	2.41	5.61	3.48
Eu_N/Eu_N^*	1.11	1.06	1.07	1.02	1.16	0.71	1.25	1.1	1.04	1.05	5.89	14.2	3.92
$(La/Yb)_N$	15	11.6	13.8	21	21	38	16.6	13.1	15.6	41	31	58	61
TREE	50	113	150	222	116	279	158	165	69	104	16.9	35	40

(continued)

Table 3.5 (continued)

Granitoid gneisses from the North Chaoyang-Fuxin-Yixian granite-greenstone belt	High magnesium group (HMG)									Low magnesium group (LMG)			
	CY15-3	CY15-5	OYX07-5	OYX07-11	OCY10-1	OYX01-4	OYX08-1	OYX11-2	CY26-1	FX01-1	CY04-5	OCY13-5	OFX11-2
	TO	TO	TO	TO	TO	GRD	GRD	GRD	DIO	TO	TO	GRD	TRON
Sr/Y	60	45	35	37	77	34	45	36	73	112	294	680	394
Nb/La	0.08	0.15	0.18	0.13	0.11	0.11	0.23	0.34	0.21	0.30	0.28	0.69	0.11
Dy/Yb	1.74	1.91	2.01	2.20	1.86	1.92	2.19	1.79	1.89	3.34	1.32	0.65	1.98
Rb/Sr	0.12	0.14	0.15	0.11	0.08	0.27	0.12	0.18	0.08	0.18	0.08	0.13	0.03

Note LOI, loss on ignition; A/CNK = molar $Al_2O_3/(CaO + Na_2O + K_2O)$; TREE, total rare earth elements

Mg# = 100 $Mg/(Mg + Fe_{total})$ in atomic ratio, $Eu_N/Eu_N^* = Eu_N/SQRT(Sm_N \times Gd_N)$, subscript N-chondrite normalized value

<0.05 wt% for P_2O_5 means values below the detection limit

DIO—dioritic gneiss; TO—tonalitic gneiss; TRON—trondhjemitic gneiss; GRD—granodioritic gneiss

3.2.1.2 Granitoid Gneisses in the High Grade Jianping Gneissic Terrane

The Jianping gneissic terrane (JPGT) is exposed in the southwest part of Western Liaoning Province (Figs. 2.3 and 3.18). This Precambrian complex, together with the Precambrian Fengning-Chengde Complex in the west and the Precambrian North Chaoyang-Fuxin-Yixian granite-greenstone belt in the northeast, constructs a large basement uplift belt crossing the TNCO and the EB along the northern margin

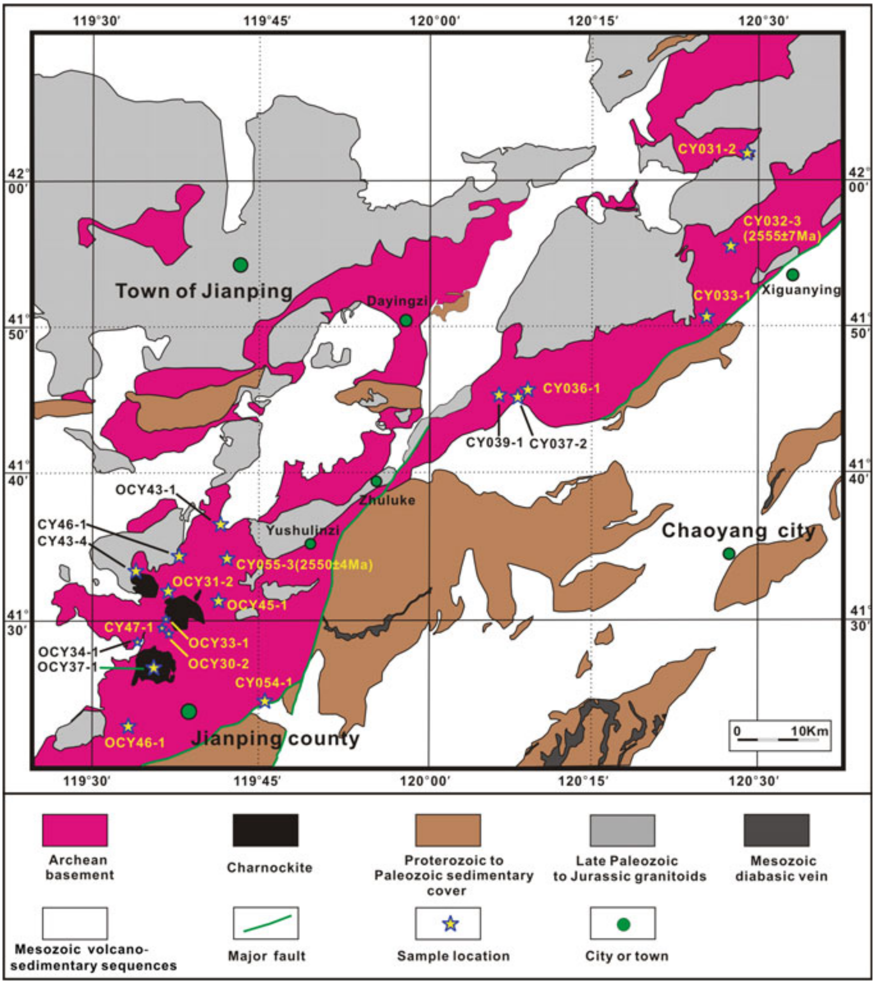

Fig. 3.18 Regional geological map and sampling locations of Archean granitoid gneisses from the Jianping high-grade gneissic terrane (JPTG) in the Western Liaoning Province (after Wang et al. [90])

of North China Craton [43]. Most lithologies of the JPGT were subjected to upper amphibolite to granulite facies metamorphism, with local greenschist to lower amphibolite facies metamorphic rocks. These rocks show volcanic cycles ranging from mafic rocks (e.g., garnet two pyroxene granulites or amphibolites) to felsic gneisses, which are interlayered with metasedimentary rocks, such as (garnet) magnetite quartzites, garnet quartzites, and carbonatites (Fig. 3.19a, b). Plutonic gneisses are the major lithologies of JPGT, including mainly dioritic, tonalitic and granodioritic gneisses (Fig. 3.19c–f). Locally, they show intrusive relationship with the metamorphosed supracrustal volcano-sedimentary rock sequences, and are characterized by intense gneissosity (Fig. 3.19d, e).

Thirteen representative samples were analyzed, including two dioritic, nine tonalitic, and two granodioritic gneisses (Table 3.5). On the basis of modal quartz contents, they can be classified into two groups: a low silica group (LSG, Qz < 20%) and a high silica group (HSG, Qz > 20%). the LSG consists of two dioritic (OCY45-1 and CY47-1), five tonalitic (CY37-2, CY46-1, CY31-2, OCY31-2 and OCY34-1) and one granodioritic gneisses (OCY33-1). The biotite two-pyroxene dioritic granulites show fine-grained texture and gneissic structure, and are composed of plagioclase (Pl), clinopyroxene (Cpx), K-feldspar (Kfs), orthopyroxene (Opx), biotite (Bi) and quartz (Qz) with accessory zircon, apatite and ilmenite (Fig. 3.20a). The peak metamorphic mineral assemblage of Cpx + Opx + Pl + Qz indicates that the rocks were subjected to granulite facies metamorphism. The other six samples are granulites (OCY31-2 and OCY33-1) or retrograde granulites (CY37-2, CY46-1, CY31-2 and OCY34-1), and show a major mineral assemblage of Pl + hornblende (Hb) + Qz + garnet (Gt) + Opx + Cpx + Bi + Kfs with accessory zircon, apatite and magnetite. They display fine-grained texture and gneissic structure (Fig. 3.20b). The association of Cpx + Opx + Pl ± Gt represents the peak metamorphic assemblage. Reaction rims of Hb + Pl and locally chlorite (CY31-2) indicate retrograde metamorphic evolution from granulite through amphibolite to greenschist facies.

The HSG comprises one granodioritic (OCY37-1) and four tonalitic (OCY46-1, CY43-4, OCY30-2 and OCY43-1). Among these, sample OCY46-1 is a two-pyroxene tonalitic granulite, with a mineral assemblage of Pl + Qz + Kfs + Cpx + Opx and minor Hb (Fig. 3.20c). The accessory minerals are zircon and magnetite. In contrast, the other three tonalitic and one granodioritic gneisses show dominant mineral assemblage of Hb + Bi + Pl + Qz with minor Kfs and only traces of Cpx and Opx (Fig. 3.20d), suggesting that the original granulite facies metamorphic mineral assemblage may have been obliterated by retrograde metamorphism. Accessory mineral assemblages are zircon, apatite, magnetite, zoisite and epidote. Sample OCY37-1 has been subjected to intense greenschist facies metamorphism, with hornblende altered to chlorite (Fig. 3.20d). In general, the HSG gneisses show fine-grained texture and clearly gneissic structure, similar to the LSG samples.

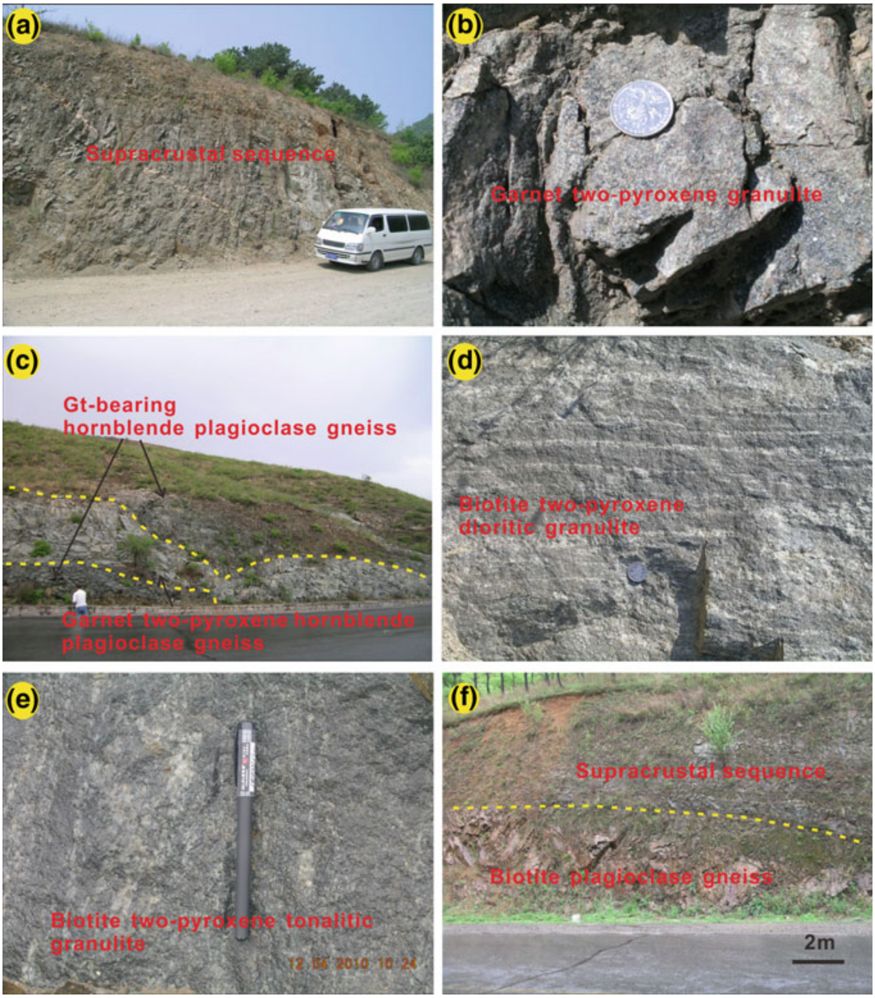

Fig. 3.19 Field photographs of granitoid gneisses from the JPGT: **a** interbedded mafic (garnet two-pyroxene granulites or amphibolites), intermediate and acidic gneisses of the supracrustal rock sequences (SRS). The car as scale bar is 5 m in length; **b** garnet two-pyroxene granulites of the SRS. The coin is 1 cm in diameter; **c** tonalitic gneisses (garnet two-pyroxene hornblende plagioclase gneisses) intruding into the SRS (garnet-bearing hornblende plagioclase gneisses). **d**–**e** Strongly gneissic structures of the dioritic (biotite two pyroxene granulites) and tonalitic (biotite two pyroxene granulites) gneisses; the pen is 10 cm long. **f** biotite plagioclase tonalitic gneisses that emplaced into the SRS

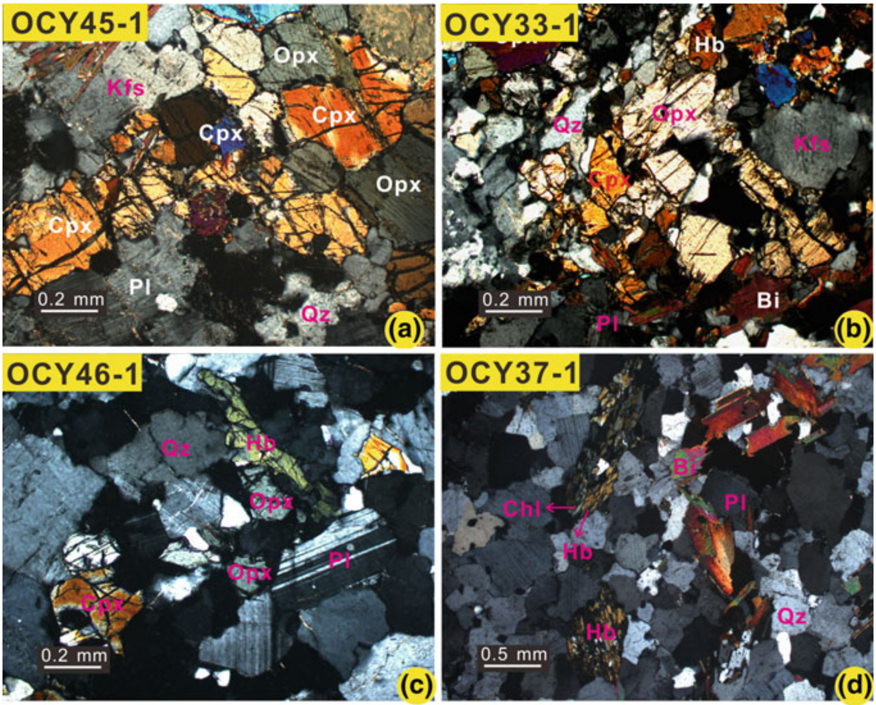

Fig. 3.20 Photomicrographs of representative samples from the JPGT showing mineral assemblages: **a** granodioritic granulite (OCY45-1, HMG); **b** granodioritic granulite (OCY33-1, HMG); **c** tonalitic granulite (OCY46-1, LMG); **d** granodioritic gneiss (OCY37-1, LMG). Mineral abbreviations: Opx—orthopyroxene, Cpx—clinopyroxene, Hb—hornblende, Bi—biotite, Chl—chlorite, Gt—garnet, Pl—plagioclase, Kfs—potassic feldspar, Qz—quartz

3.2.2 Geochemical Features

Twenty-six DTTG gneisses of Western Liaoning were analyzed for whole-rock chemical data (Table 3.5) [90, 91]. In the An-Ab-Or diagram (Fig. 3.21a), most samples (including the dioritic gneisses) plot in the tonalitic and granodioritic fields, with only sample OFX11-2 falling into the trondhjemitic domain. On the basis of MgO contents, these granitoid gneisses are divided into two major groups: (1) a high-magnesium group (HMG) with high MgO (2.37–5.31 wt%) and low SiO_2 (55.90–65.76 wt%), including the low silica group (LSG) samples of JPGT and one dioritic (CY26-1), five tonalitic (OYX07-5, OYX07-11, OCY10-1, CY15-3 and CY15-5), and three granodioritic (OYX01-4, OYX08-1, and OYX11-2) gneisses of the NCFY-GGB; and (2) a low-magnesium group (LMG) with low MgO (0.13–2.10 wt%) and high SiO_2 (63.02–73.29 wt%) contents, comprising the high silica group (HSG) samples of JPGT and one granodioritic (OCY13-5), and one trondhjemitic (OFX11-2) and two tonalitic (FX01-1 and CY04-5) gneisses of the NCFX-GGB.

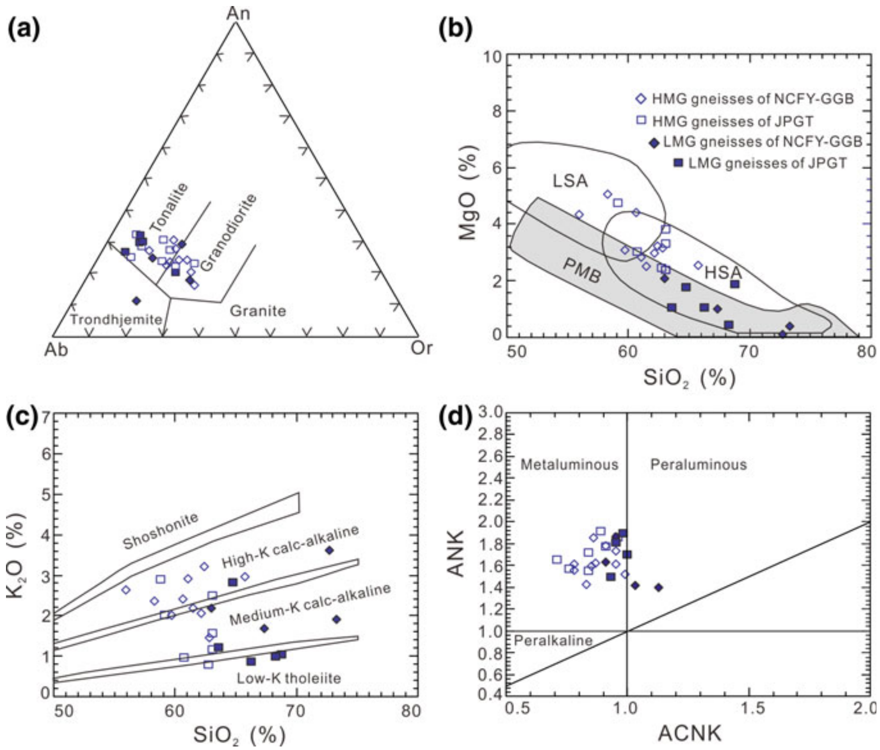

Fig. 3.21 Major element compositions of granitoid gneisses from both the NCFY-GGB and JPGT of Western Liaoning Province: **a** An-Ab-Or diagram [5]; **b** MgO versus SiO_2 diagram (PMB: experimental partial melts from metabasalts (e.g., amphibolites); LSA: low silica adakite; HSA: high silica adakite, after Martin et al. [50]); **c** K_2O versus SiO_2 classification diagram (after Rollinson [70]); **d** ANK [molar $Al_2O_3/(Na_2O + K_2O)$] versus ACNK [molar $Al_2O_3/(CaO + Na_2O + K_2O)$] (after Maniar and Piccolli [45]). Symbols: open diamond—high-Mg gneissic samples (HMG) of NCFY-GGB, solid diamond—low-Mg gneissic samples (LMG) of NCFY-GGB; open square—high-Mg gneissic samples (HMG) of JPGT, and solid square—low-Mg gneissic samples (LMG) of JPGT

3.2.2.1 Major Element Compositions

The HMG samples are characterized by low SiO_2, and high MgO and Mg# values (100 Mg/(Mg + Fe_{total}) atomic ratios; 44.16–61.74), with low TiO_2 (0.13–0.71 wt%). All of them plot in the fields of either low silica adakites (LSA) or high silica adakites (HSA), i.e., above the range of experimentally-derived partial melts from metabasaltic rocks (Fig. 3.21b) [50]. These rocks have low K_2O (0.78–3.32 wt%) and high Na_2O contents (3.65–4.94 wt%), yielding low K_2O/Na_2O ratios (0.16–0.79, with a mean value of $\sim$0.50), and they belong to the medium- to high-K calc-alkaline rock series (Fig. 3.21c). All the samples show metaluminous feature with low A/CNK values (molar Al_2O_3/($CaO + Na_2O + K_2O$) ratios) of 0.71–0.99 and Al_2O_3 contents varying of 14.30–16.69 wt% (Fig. 3.21d) [45].

In comparison, the LMG samples show high SiO_2, and low MgO and Mg# values (33.15–51.46). These features are similar to those of experimentally-derived partial melts from metabasaltic rocks (Fig. 3.21b) [50]. The rocks have high Na_2O (3.70–6.13 wt%) and Al_2O_3 (15.30–19.51 wt%). The tonalitic and trondhjemitic gneiss samples CY04-5, OFX11-2, OCY46-1, CY43-4, OCY30-2, and OCY43-1 have lower K_2O (0.85–1.91 wt%) and K_2O/Na_2O (0.19–0.36), and most of them show metaluminous features (A/CNK values of 0.91–1.00, with sample OFX11-2 exhibiting a higher value of 1.13), falling into the fields of low-K tholeiitic to medium-K calc-alkaline rock series (Fig. 3.21c, d). Whereas the tonalitic and granodioritic gneiss samples FX01-1, OCY13-5, and OCY37-1 have higher K_2O (2.09–3.61 wt%) and K_2O/Na_2O (0.59–0.83). They are metaluminous to weakly peraluminous (A/CNK = 0.93–1.03), straddling the fields between medium- and high-K calc-alkaline rock series (Fig. 3.21c, d).

3.2.2.2 Rare Earth Element Compositions

The HMG samples have total REE (TREE) contents ranging of 22–279 ppm. In the chondrite-normalized REE diagram (Fig. 3.22a, c), they display fractionated REE patterns characterized by high $(La/Yb)_N$ ratios of 8.37–38 (mostly of >10) and weakly negative to strongly positive Eu anomalies (Eu^*/Eu_N^* ratios of 0.71–2.25) (Table 3.5). The LMG samples also show large variable TREE contents (16.9–203 ppm). Distinct from the HMG samples, most LMG samples are characterized by concave-upward normalized REE patterns with weakly to strongly positive Eu anomalies (high $(La/Yb)_N$ and Eu_N/Eu_N^* ratios of 16.0–86 and 1.46–14.2, respectively; Fig. 3.22b, d). The tonalitic gneiss sample FX01-1 has no apparent Eu anomaly (Eu_N/Eu_N^* ratio of 1.05; Fig. 3.22b). With increasing SiO_2 contents, no systematic changes of TREE and $(La/Yb)_N$ are observed (Table 3.5).

3.2.2.3 Other Trace Element Compositions

In the primitive mantle-normalized multi-element spider diagrams (Fig. 3.23), all the granitoid gneisses are characterized by enrichment of Ba, Rb, K, Zr, and Hf but depletion of Nb, Ta, Ti, and Th. They have low Y (0.75–17.0 ppm) and Yb (0.07–1.85 ppm) and high Sr (241–648 ppm, and mostly of >400 ppm), yielding high Sr/Y of 32.28–837.44. Some samples are enriched in Sr, and are weakly depleted in P. The strongly negative Th anomalies may have been resulted from element mobility during granulite facies metamorphism [93].

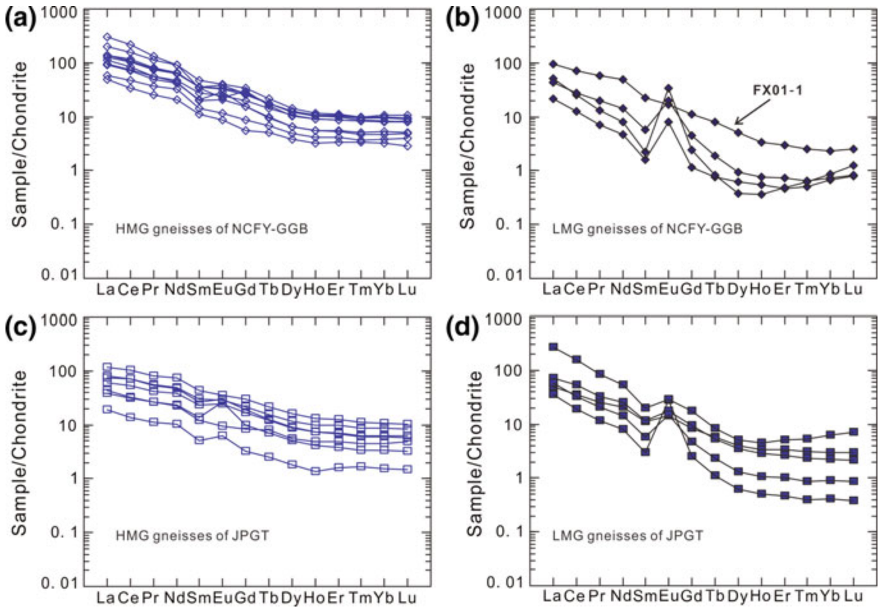

Fig. 3.22 Chondrite-normalized REE patterns for the late Neoarchean HMG and LMG granitoid gneisses in the NCFY-GGB (**a** and **b**) and the JPGT (**c** and **d**), Western Liaoning Province. Symbols are the same as Fig. 3.21, and the chondrite normalized values are after Sun and McDonough [78]

3.2.3 Zircon U–Pb and Lu–Hf Isotopes

3.2.3.1 Granitoid Gneisses in the NCFY-GGB

The tonalitic (OCY10-1) and granodioritic (OYX01-4) gneiss samples of HMG and the trondhjemitic (OFX11-2) gneiss sample of LMG from the NCFY-GGB were analyzed for zircon U–Pb isotopes and trace elements. Zircon Lu–Hf isotopes of the previously dated dioritic gneiss sample CY26-1 were also provided (crystallization age of the magmatic precursor is 2515 Ma) [43]. All the data are presented in Tables 3.6, 3.7 and 3.8.

Sample OCY10-1 (HMG)

Zircon grains from the tonalitic gneiss sample OCY10-1 display prismatic or oval shapes with lengths and length/width ratios of 100–200 μm and 1:1–2:1, respectively (Fig. 3.24a). Cathodoluminescence images reveal that most zircon grains display core-rim structures. The cores are generally euhedral with bright banded zonings, which are enveloped by dark thin rims (e.g., spots #7 and #8). Some cores underwent local or complete metamictization, and are dark structureless (e.g., spots #2 and #3; Fig. 3.24a). There are also some grains with dark oscillatory zoned cores

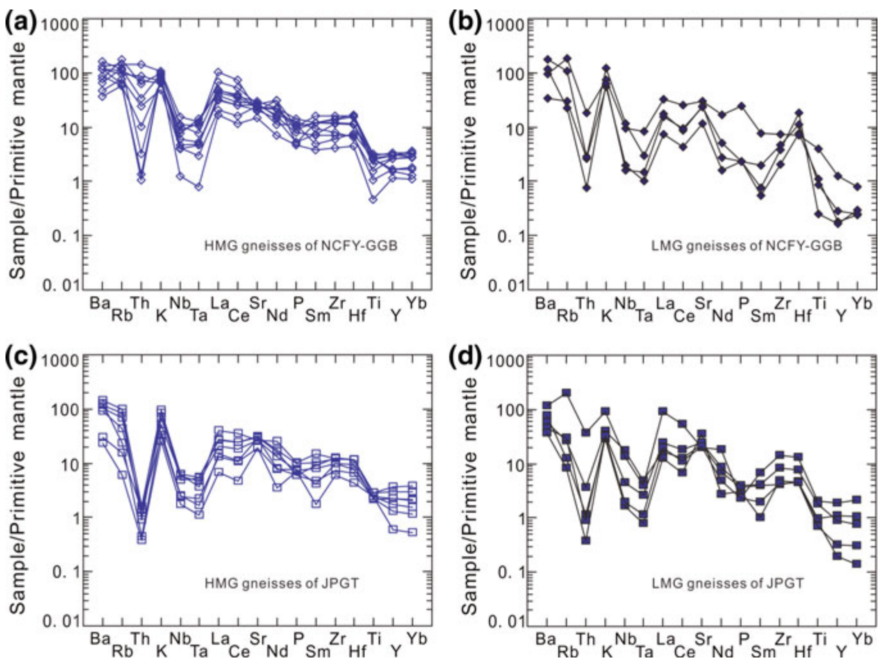

Fig. 3.23 Primitive mantle-normalized multi-element patterns for the late Neoarchean HMG and LMG granitoid gneisses from the NCFY-GGB (**a** and **b**) and the JPGT (**c** and **d**), Western Liaoning Province. Symbols are the same as Fig. 3.21, and primitive mantle values are after Sun and McDonough [78]

surrounded by thin bright rims (e.g., spot #27). Thirty-six spots were analyzed on thirty-two grains, and all of them are plotted on or close to the concordia, yielding apparent $^{207}Pb/^{206}Pb$ ages ranging from 2579 to 2269 Ma (Fig. 3.24b and Table 3.6). Th and U contents vary from 9.78 to 142.23 ppm and 12.94 to 661.24 ppm, respectively, yielding Th/U ratios mostly higher than 0.16, except for spot #12 showing a low ratio of 0.06. All the spots show consistent chondrite-normalized REE patterns with positive Ce anomalies, moderately negative Eu anomalies and steep HREE patterns (Fig. 3.24c and Table 3.7), indicating the original generation during magma crystallization [68]. On the probability density plot, these analyses constitute one major age peak and several small peaks (Fig. 3.24d), and they are subdivided into the following three groups.

The first age group is composed of three analyses on dark oscillatory zoned or structureless cores (spots #2, #9, and #27), which constructs the first small age peak (Fig. 3.24d, e). They have apparent $^{207}Pb/^{206}Pb$ ages of 2579 ± 13 Ma to 2560 ± 13 Ma, and yield a weighted mean age of 2570 ± 17 Ma (MSWD = 0.55), which is nearly consistent with the magmatic crystallization age of one hornblende plagioclase gneiss from Fuxin-Yixian greenstone belt (2567 ± 7 Ma of sample YX011-1) [89]. Considering that the tonalitic gneiss

Table 3.6 LA-ICPMS zircon U-Pb isotopic dating data for granitoid gneiss samples OCY10-1, OYX01-4 and OFX11-2 from the NCFY-GGB

Samples and analyzed spots	Th (ppm)	U (ppm)	Th/U	Isotopic ratios						Apparent ages (Ma)					
				$^{207}Pb/^{206}Pb$	±1σ	$^{207}Pb/^{235}U$	±1σ	$^{206}Pb/^{238}U$	±1σ	$^{207}Pb/^{206}Pb$	±1σ	$^{207}Pb/^{235}U$	±1σ	$^{206}Pb/^{238}U$	±1σ
OCY10-1-01	45	38	1.17	0.1386	0.0015	10.7927	0.1804	0.4754	0.0063	2504	13	2505	16	2507	27
OCY10-1-02	10	26	0.38	0.1382	0.0021	11.6745	0.1984	0.4915	0.0066	2579	13	2579	16	2577	28
OCY10-1-03	69	60	1.15	0.1193	0.0014	8.3284	0.1505	0.4210	0.0057	2269	15	2267	16	2265	26
OCY10-1-04	15	14	1.06	0.1329	0.0020	9.8045	0.2121	0.4547	0.0066	2416	18	2417	20	2416	29
OCY10-1-05	23	18	1.23	0.1380	0.0017	10.7881	0.2049	0.4743	0.0066	2507	15	2505	18	2502	29
OCY10-1-06	18	16	1.18	0.1359	0.0021	10.7667	0.2358	0.4747	0.0070	2502	19	2503	20	2504	31
OCY10-1-07	18	15	1.19	0.1371	0.0021	10.7521	0.2340	0.4743	0.0070	2501	18	2502	20	2502	31
OCY10-1-08	14	13	1.11	0.1441	0.0034	10.8086	0.3418	0.4758	0.0086	2504	30	2507	29	2509	38
OCY10-1-09	15	13	1.11	0.1410	0.0026	11.5995	0.2925	0.4900	0.0078	2574	22	2573	24	2571	34
OCY10-1-10	20	16	1.24	0.1327	0.0023	11.1477	0.2697	0.4816	0.0075	2536	21	2536	23	2534	33
OCY10-1-11	20	18	1.11	0.1384	0.0024	10.8064	0.2611	0.4747	0.0074	2508	21	2507	22	2504	32
OCY10-1-12	38	661	0.06	0.1355	0.0016	10.3005	0.1548	0.4650	0.0060	2462	11	2462	14	2462	26
OCY10-1-13	20	17	1.20	0.1410	0.0032	11.2006	0.3517	0.4822	0.0088	2542	29	2540	29	2537	38
OCY10-1-14	18	15	1.19	0.1334	0.0027	10.7432	0.2962	0.4729	0.0079	2504	25	2501	26	2496	34
OCY10-1-15	22	18	1.22	0.1340	0.0019	10.1280	0.2118	0.4621	0.0067	2444	18	2447	19	2449	29
OCY10-1-16	26	21	1.23	0.1340	0.0018	10.7768	0.2111	0.4751	0.0067	2502	16	2504	18	2506	29
OCY10-1-17	20	16	1.20	0.1327	0.0021	10.4112	0.2337	0.4674	0.0070	2471	19	2472	21	2472	31
OCY10-1-18	22	21	1.00	0.1327	0.0018	10.3036	0.1970	0.4653	0.0065	2461	16	2462	18	2463	28
OCY10-1-19	23	18	1.27	0.1298	0.0019	10.2182	0.2192	0.4635	0.0068	2454	18	2455	20	2455	30
OCY10-1-20	25	20	1.25	0.1298	0.0018	9.8478	0.2026	0.4559	0.0065	2419	17	2421	19	2421	29
OCY10-1-21	21	17	1.19	0.1377	0.0023	10.7014	0.2570	0.4733	0.0073	2497	21	2498	22	2498	32
OCY10-1-22	23	18	1.24	0.1352	0.0019	10.8451	0.2258	0.4759	0.0069	2510	17	2510	19	2510	30
OCY10-1-23	97	77	1.27	0.1346	0.0014	11.2086	0.1879	0.4830	0.0064	2540	13	2541	16	2540	28
OCY10-1-24	76	212	0.36	0.1294	0.0019	10.8215	0.1853	0.4749	0.0063	2510	13	2508	16	2505	28
OCY10-1-25	66	318	0.21	0.1283	0.0016	9.6603	0.1531	0.4521	0.0059	2401	12	2403	15	2404	26

(continued)

Table 3.6 (continued)

Samples and analyzed spots	Th (ppm)	U (ppm)	Th/U	Isotopic ratios						Apparent ages (Ma)					
				$^{207}Pb/^{206}Pb$	±1σ	$^{207}Pb/^{235}U$	±1σ	$^{206}Pb/^{238}U$	±1σ	$^{207}Pb/^{206}Pb$	±1σ	$^{207}Pb/^{235}U$	±1σ	$^{206}Pb/^{238}U$	±1σ
OCY10-1-26	19	16	1.17	0.1378	0.0022	10.9259	0.2452	0.4775	0.0071	2517	19	2517	21	2516	31
OCY10-1-27	55	73	0.76	0.1370	0.0016	11.4654	0.1949	0.4883	0.0065	2560	13	2562	16	2563	28
OCY10-1-28	45	39	1.14	0.1382	0.0016	10.7700	0.1940	0.4740	0.0064	2505	14	2503	17	2501	28
OCY10-1-29	98	511	0.19	0.1309	0.0015	9.9253	0.1550	0.4575	0.0059	2427	12	2428	14	2428	26
OCY10-1-30	142	231	0.61	0.1370	0.0014	10.7507	0.1693	0.4743	0.0062	2501	12	2502	15	2502	27
OCY10-1-31	19	16	1.19	0.1339	0.0019	10.9837	0.2273	0.4784	0.0069	2522	17	2522	19	2520	30
OCY10-1-32	18	16	1.15	0.1306	0.0021	10.7229	0.2388	0.4736	0.0070	2499	19	2499	21	2499	31
OCY10-1-33	23	18	1.27	0.1315	0.0019	10.8904	0.2352	0.4766	0.0070	2515	18	2514	20	2512	31
OCY10-1-34	85	262	0.32	0.1357	0.0015	10.8952	0.1721	0.4769	0.0062	2514	12	2514	15	2514	27
OCY10-1-35	103	650	0.16	0.1345	0.0014	10.7579	0.1676	0.4739	0.0061	2504	12	2502	14	2500	27
OCY10-1-36	55	45	1.23	0.1295	0.0016	10.4520	0.1910	0.4682	0.0064	2475	15	2476	17	2476	28
OYX01-4-01	95	693	0.14	0.1620	0.0032	7.4468	0.1171	0.3335	0.0039	2476	34	2167	14	1855	19
OYX01-4-02	88	68	1.30	0.1599	0.0028	5.0707	0.0902	0.2300	0.0029	2455	15	1831	15	1334	15
OYX01-4-03	120	373	0.32	0.1607	0.0034	8.8140	0.1532	0.3979	0.0048	2463	37	2319	16	2159	22
OYX01-4-04	66	54	1.22	0.1663	0.0027	10.8335	0.1837	0.4725	0.0058	2521	14	2509	16	2494	26
OYX01-4-05	36	113	0.32	0.1665	0.0026	11.0774	0.1801	0.4827	0.0059	2522	13	2530	15	2539	25
OYX01-4-06	32	122	0.26	0.1668	0.0026	10.5651	0.1726	0.4596	0.0056	2525	13	2486	15	2438	25
OYX01-4-07	234	170	1.37	0.1734	0.0026	10.9760	0.1753	0.4592	0.0055	2591	13	2521	15	2436	24
OYX01-4-08	50	180	0.28	0.1647	0.0035	9.6537	0.1673	0.4252	0.0052	2504	36	2402	16	2284	23
OYX01-4-09	281	335	0.84	0.1531	0.0041	3.9746	0.0932	0.1883	0.0025	2381	47	1629	19	1112	13
OYX01-4-10	68	117	0.58	0.1442	0.0038	5.0633	0.1154	0.2546	0.0033	2278	46	1830	19	1462	17
OYX01-4-11	43	66	0.66	0.1664	0.0028	10.7634	0.1860	0.4691	0.0058	2522	14	2503	16	2480	26
OYX01-4-12	60	62	0.98	0.1614	0.0048	9.7722	0.2539	0.4391	0.0061	2470	51	2414	24	2347	27
OYX01-4-13	52	208	0.25	0.1630	0.0035	7.6376	0.1343	0.3399	0.0042	2487	37	2189	16	1886	20
OYX01-4-14	84	70	1.20	0.1680	0.0027	11.1836	0.1892	0.4829	0.0060	2538	14	2539	16	2540	26

(continued)

Table 3.6 (continued)

Samples and analyzed spots	Th (ppm)	U (ppm)	Th/U	Isotopic ratios						Apparent ages (Ma)					
				$^{207}Pb/^{206}Pb$	±1σ	$^{207}Pb/^{235}U$	±1σ	$^{206}Pb/^{238}U$	±1σ	$^{207}Pb/^{206}Pb$	±1σ	$^{207}Pb/^{235}U$	±1σ	$^{206}Pb/^{238}U$	±1σ
OYX01-4-15	66	94	0.70	0.1650	0.0026	10.4644	0.1749	0.4599	0.0056	2508	13	2477	15	2439	25
OYX01-4-16	173	331	0.52	0.1666	0.0025	10.3842	0.1666	0.4520	0.0055	2524	13	2470	15	2404	24
OYX01-4-17	127	160	0.79	0.1633	0.0042	9.1596	0.2044	0.4068	0.0053	2490	45	2354	20	2200	24
OYX01-4-18	53	48	1.10	0.1671	0.0028	10.3319	0.1823	0.4484	0.0056	2529	14	2465	16	2388	25
OYX01-4-19	239	891	0.27	0.1614	0.0034	8.5980	0.1473	0.3865	0.0047	2470	36	2296	16	2106	22
OYX01-4-20	92	310	0.30	0.1578	0.0035	6.3398	0.1147	0.2914	0.0036	2432	38	2024	16	1648	18
OYX01-4-21	223	334	0.67	0.1644	0.0040	9.8986	0.2058	0.4366	0.0056	2502	42	2425	19	2336	25
OYX01-4-22	53	89	0.60	0.1292	0.0042	4.5918	0.1335	0.2579	0.0035	2086	58	1748	24	1479	18
OYX01-4-23	80	174	0.46	0.1480	0.0037	6.5189	0.1398	0.3195	0.0041	2323	44	2048	19	1787	20
OYX01-4-24	46	46	1.02	0.1677	0.0031	10.3087	0.1967	0.4458	0.0058	2535	16	2463	18	2377	26
OYX01-4-25	48	85	0.57	0.1666	0.0027	10.1662	0.1752	0.4427	0.0055	2523	14	2450	16	2363	24
OYX01-4-26	57	731	0.08	0.1608	0.0032	8.6986	0.1382	0.3923	0.0046	2464	34	2307	14	2133	21
OYX01-4-27	70	421	0.17	0.1608	0.0033	8.2197	0.1375	0.3709	0.0045	2464	36	2256	15	2033	21
OYX01-4-28	62	84	0.74	0.1652	0.0027	10.8863	0.1863	0.4779	0.0059	2510	14	2513	16	2518	26
OYX01-4-29	81	160	0.51	0.1651	0.0026	9.8609	0.1658	0.4333	0.0053	2508	14	2422	15	2321	24
OFX11-2-01	11	261	0.04	0.1669	0.0021	11.0349	0.1617	0.4796	0.0061	2526	11	2526	14	2525	26
OFX11-2-02	10	219	0.04	0.1671	0.0032	10.5518	0.1543	0.4581	0.0057	2528	33	2484	14	2431	25
OFX11-2-03	43	532	0.08	0.1663	0.0021	10.8757	0.1590	0.4744	0.0060	2520	11	2513	14	2503	26
OFX11-2-04	72	843	0.09	0.1587	0.0020	10.0787	0.1456	0.4604	0.0058	2442	11	2442	13	2441	26
OFX11-2-05	97	59	1.63	0.1641	0.0027	10.7080	0.1881	0.4732	0.0064	2498	14	2498	16	2498	28
OFX11-2-06	84	218	0.39	0.1780	0.0023	12.4018	0.1815	0.5053	0.0064	2634	11	2635	14	2636	27
OFX11-2-07	16	34	0.46	0.1797	0.0034	12.6697	0.2496	0.5113	0.0073	2650	16	2655	19	2662	31
OFX11-2-08	8	128	0.07	0.1682	0.0024	11.2125	0.1760	0.4834	0.0063	2540	12	2541	15	2542	27
OFX11-2-09	16	58	0.27	0.1631	0.0024	10.6096	0.1732	0.4718	0.0062	2488	13	2490	15	2491	27
OFX11-2-10	8	301	0.03	0.1672	0.0021	11.0514	0.1611	0.4793	0.0061	2530	11	2527	14	2524	26

(continued)

Table 3.6 (continued)

Samples and analyzed spots	Th (ppm)	U (ppm)	Th/U	Isotopic ratios						Apparent ages (Ma)					
				$^{207}Pb/^{206}Pb$	±1σ	$^{207}Pb/^{235}U$	±1σ	$^{206}Pb/^{238}U$	±1σ	$^{207}Pb/^{206}Pb$	±1σ	$^{207}Pb/^{235}U$	±1σ	$^{206}Pb/^{238}U$	±1σ
OFX11-2-11	69	27	2.61	0.1652	0.0025	11.6310	0.1947	0.5105	0.0068	2510	13	2575	16	2659	29
OFX11-2-12	48	351	0.14	0.1733	0.0022	11.7976	0.1729	0.4938	0.0063	2589	11	2588	14	2587	27
OFX11-2-13	50	78	0.63	0.1728	0.0025	11.7336	0.1894	0.4925	0.0064	2584	12	2583	15	2582	28
OFX11-2-14	12	298	0.04	0.1739	0.0023	11.8908	0.1800	0.4958	0.0064	2596	11	2596	14	2596	27
OFX11-2-15	18	569	0.03	0.1651	0.0021	10.8582	0.1600	0.4770	0.0061	2508	11	2511	14	2514	26
OFX11-2-16	68	36	1.88	0.1701	0.0029	11.4442	0.2058	0.4880	0.0066	2558	14	2560	17	2562	29
OFX11-2-17	47	500	0.09	0.1664	0.0033	9.2977	0.1390	0.4052	0.0051	2522	34	2368	14	2193	23
OFX11-2-18	359	941	0.38	0.1706	0.0021	11.4916	0.1666	0.4884	0.0062	2563	11	2564	14	2564	27
OFX11-2-19	60	13	4.45	0.1657	0.0033	10.8870	0.2260	0.4764	0.0069	2515	17	2514	19	2511	30
OFX11-2-20	51	913	0.06	0.1681	0.0021	11.1845	0.1630	0.4826	0.0061	2538	11	2539	14	2538	27
OFX11-2-21	73	118	0.62	0.1814	0.0024	12.8167	0.1953	0.5123	0.0066	2666	11	2666	14	2666	28
OFX11-2-22	144	286	0.50	0.1816	0.0025	12.8513	0.1987	0.5130	0.0066	2668	12	2669	15	2669	28
OFX11-2-23	42	85	0.49	0.1816	0.0025	12.8192	0.1979	0.5119	0.0066	2667	12	2666	15	2665	28
OFX11-2-24	54	35	1.55	0.1514	0.0027	9.2201	0.1767	0.4416	0.0061	2362	16	2360	18	2358	27
OFX11-2-25	64	255	0.25	0.1691	0.0022	11.3131	0.1688	0.4851	0.0062	2549	11	2549	14	2549	27
OFX11-2-26	44	170	0.26	0.1639	0.0023	10.6693	0.1662	0.4720	0.0061	2496	12	2495	14	2492	27
OFX11-2-27	91	66	1.38	0.1552	0.0023	9.7432	0.1597	0.4551	0.0060	2404	13	2411	15	2418	26
OFX11-2-28	88	128	0.69	0.1552	0.0022	9.6544	0.1553	0.4510	0.0059	2404	12	2402	15	2400	26
OFX11-2-29	145	331	0.44	0.1729	0.0023	11.7739	0.1770	0.4936	0.0063	2586	11	2587	14	2586	27
OFX11-2-30	80	38	2.14	0.1728	0.0028	11.7498	0.2059	0.4932	0.0067	2584	14	2585	16	2584	29
OFX11-2-31	34	483	0.07	0.1719	0.0022	11.6575	0.1731	0.4919	0.0063	2576	11	2577	14	2579	27
OFX11-2-32	81	313	0.26	0.1776	0.0023	12.3645	0.1847	0.5049	0.0065	2630	11	2632	14	2635	28
OFX11-2-33	81	57	1.42	0.1633	0.0027	10.6058	0.1890	0.4710	0.0064	2490	14	2489	17	2488	28
OFX11-2-34	54	25	2.13	0.1719	0.0031	11.6394	0.2204	0.4911	0.0068	2576	15	2576	18	2575	30

Note ^{204}Pb has been corrected using the method of [2]

Table 3.7 Trace element data (ppm) for representative zircon domains from samples OCY10-1, OYX01-4 and OFX11-2

Samples and analyzed spots	La	Ce	Pr	Nd	Sm	Eu	Gd	Tb	Dy	Ho	Er	Tm	Yb	Lu
OCY10-1-01	0.01	26	0.04	0.89	2.05	0.26	9.25	3.40	43	16.5	76	20	236	47
OCY10-1-02	0.01	2.93	0.04	0.85	2.22	1.20	10.7	3.55	42	15.1	65	16.0	181	37
OCY10-1-03	0.04	23	0.05	1.01	2.61	0.41	12.0	4.28	55	21.6	100	25	282	56
OCY10-1-04	0.01	16.0	0.03	0.64	1.51	0.26	6.98	2.34	30	11.0	49	12.2	141	27
OCY10-1-05	0.01	15.9	0.03	0.56	1.74	0.27	7.49	2.61	32	12.0	54	13.4	155	30
OCY10-1-06	0.01	18.5	0.04	0.87	2.19	0.31	9.72	3.45	41	15.6	69	17.1	193	37
OCY10-1-07	0.01	17.7	0.04	1.01	2.35	0.37	9.35	3.34	41	15.2	69	17.0	196	37
OCY10-1-08	0.01	15.2	0.03	0.65	1.51	0.22	6.60	2.26	27	9.90	44	11.5	127	25
OCY10-1-09	0.01	16.6	0.04	0.67	1.44	0.27	7.41	2.46	31	10.8	48	12.2	133	26
OCY10-1-10	0.01	16.6	0.05	0.93	2.42	0.35	10.2	3.65	45	16.8	76	18.7	210	41
OCY10-1-11	0.01	17.7	0.03	0.93	2.24	0.39	9.93	3.67	44	16.5	73	17.9	204	40
OCY10-1-12	0.01	4.37	0.01	0.18	0.60	0.34	3.03	1.07	13. 8	5.35	27	7.54	100	23
OCY10-1-13	0.01	16.6	0.04	0.92	2.06	0.37	10.8	3.70	45	17.1	77	18.5	209	42
OCY10-1-14	0.01	17.0	0.07	0.88	2.19	0.39	9.56	3.47	40	15.5	71	17.3	196	39
OCY10-1-15	0.01	18.4	0.05	0.85	2.45	0.50	11.4	4.03	50	19.4	86	21	238	46
OCY10-1-16	0.01	18.1	0.05	0.88	2.44	0.44	11.0	3.84	48	18.3	81	20	227	44
OCY10-1-17	0.01	18.3	0.05	1.02	2.32	0.37	11.2	3.90	47	17.6	79	19.3	221	43
OCY10-1-18	0.05	18.1	0.06	1.07	2.30	0.39	10.5	3.70	46	17.4	79	19.3	215	42
OCY10-1-19	0.01	18.9	0.05	1.03	2.60	0.41	11.8	4.34	53	20	90	22	243	48
OCY10-1-20	0.01	21	0.05	1.08	2.65	0.41	13.0	4.59	58	22	99	24	264	52
OCY10-1-21	0.01	18.2	0.05	0.81	2.21	0.36	9.84	3.51	43	16.7	76	18.5	208	40
OCY10-1-22	0.01	19.1	0.05	0.95	2.56	0.39	11.7	4.25	52	19.9	89	22	242	47
OCY10-1-23	0.01	28	0.04	0.85	2.55	0.32	11.4	4.09	51	19.1	87	22	254	49
OCY10-1-24	0.02	12.8	0.03	0.48	1.44	0.27	7.40	2.49	30	11.4	54	13.2	155	34

(continued)

Table 3.7 (continued)

Samples and analyzed spots	La	Ce	Pr	Nd	Sm	Eu	Gd	Tb	Dy	Ho	Er	Tm	Yb	Lu
OCY10-1-25	0.02	6.22	0.01	0.31	0.51	0.19	2.75	1.06	12.8	4.85	22	5.70	70	15.5
OCY10-1-26	0.01	18.1	0.04	0.88	2.17	0.34	9.67	3.56	43	16.1	73	18.1	205	40
OCY10-1-27	0.04	13.4	0.07	1.16	2.77	0.66	12.8	4.51	53	19.6	87	21	237	46
OCY10-1-28	0.01	19.6	0.03	0.71	1.86	0.30	8.16	2.99	37	13.6	63	16.0	179	35
OCY10-1-29	0.01	7.33	0.02	0.32	0.97	0.27	3.90	1.31	14.8	5.01	22	5.86	67	14.0
OCY10-1-30	0.16	30	0.16	2.77	4.85	1.66	19.6	6.18	72	27	124	32	397	84
OCY10-1-31	0.01	18.9	0.04	0.75	1.83	0.33	8.86	3.14	39	14.3	65	16.1	176	35
OCY10-1-32	0.01	17.4	0.04	0.69	1.59	0.27	7.75	2.74	32	12.2	55	13.2	1457	30
OCY10-1-33	0.01	17.3	0.03	0.97	2.15	0.42	10.8	3.94	48	18.1	81	19.7	2197	43
OCY10-1-34	0.02	10.5	0.09	0.86	1.27	0.32	5.05	1.78	22	8.41	39	10.5	1257	27
OCY10-1-35	0.01	7.28	0.04	0.57	1.33	0.39	6.17	1.88	22	7.71	34	8.51	97	21
OCY10-1-36	0.02	23	0.04	0.92	2.08	0.32	10.1	3.68	45	17.0	79	19.7	229	44
OYX01-4-01	0.03	2.65	0.04	0.61	1.17	0.28	6.08	2.40	32	12.7	61	15.5	183	38
OYX01-4-02	0.01	29	0.05	1.22	2.90	0.34	13.8	4.91	60	23	100	24	269	53
OYX01-4-03	0.02	9.45	0.04	0.63	1.25	0.33	6.30	2.38	32	13.0	66	18.5	237	53
OYX01-4-04	0.01	23	0.05	0.94	2.42	0.26	12.1	4.19	52	20	93	23	258	52
OYX01-4-05	0.01	5.28	0.04	0.68	1.30	0.33	5.66	1.72	21	7.89	37	9.92	124	29
OYX01-4-06	0.01	3.78	0.01	0.27	0.64	0.17	3.14	1.04	13.8	5.73	30	8.37	109	29
OYX01-4-07	0.13	36	0.24	3.92	7.06	1.87	27	7.51	77	25	97	22	239	48
OYX01-4-08	0.05	6.27	0.13	2.51	4.47	0.78	18.5	5.91	71	27	119	29	355	74
OYX01-4-09	0.14	33	0.17	2.24	3.62	1.18	13.9	4.44	54	21	97	26	317	70
OYX01-4-10	0.02	17.7	0.05	0.65	1.72	0.36	8.51	3.23	42	15.8	74	19.3	228	45
OYX01-4-11	0.01	12.6	0.02	0.32	0.91	0.14	4.25	1.59	21	8.65	44	12.3	154	34
OYX01-4-12	0.01	17.8	0.03	0.59	1.40	0.18	6.95	2.54	33	12.8	61	15.7	190	39

(continued)

Table 3.7 (continued)

Samples and analyzed spots	La	Ce	Pr	Nd	Sm	Eu	Gd	Tb	Dy	Ho	Er	Tm	Yb	Lu
OYX01-4-13	0.04	8.56	0.04	0.47	1.03	0.17	4.46	1.80	23	9.43	50	15.0	201	47
OYX01-4-14	0.02	14.8	0.08	1.37	2.43	0.97	9.69	2.89	33	12.3	56	14.3	171	38
OYX01-4-15	0.01	14.7	0.02	0.52	1.12	0.16	5.21	1.91	24	9.82	49	13.4	164	36
OYX01-4-16	0.03	15.8	0.07	1.44	3.83	0.33	20	7.34	91	34	151	36	387	76
OYX01-4-17	0.09	17.3	0.18	2.85	4.90	1.19	20	6.32	76	29	130	31	355	73
OYX01-4-18	0.01	21	0.03	0.86	1.86	0.21	9.18	3.41	43	16.4	77	19.1	216	43
OYX01-4-19	0.02	8.67	0.04	0.76	1.96	0.31	8.93	3.21	40	16.1	77	21	262	55
OYX01-4-20	0.01	8.32	0.02	0.46	1.06	0.27	4.78	1.87	26	11.0	57	15.9	206	45
OYX01-4-21	0.29	25	0.28	3.61	5.04	1.26	19.6	6.38	77	29	135	34	400	83
OYX01-4-22	0.01	16.2	0.04	0.49	1.11	0.17	5.62	1.97	26	10.8	55	15.3	196	45
OYX01-4-23	0.01	12.7	0.03	0.48	1.28	0.25	6.42	2.41	32	12.7	64	17.6	218	48
OYX01-4-24	0.01	19.8	0.03	0.68	1.52	0.18	6.63	2.48	33	12.7	62	15.8	183	38
OYX01-4-25	0.01	13.2	0.02	0.45	0.90	0.14	4.04	1.52	21	8.23	43	11.9	154	34
OYX01-4-26	0.08	2.82	0.07	0.77	1.41	0.44	7.78	2.73	30	9.37	35	7.90	84	16.4
OYX01-4-27	0.07	4.19	0.07	0.62	0.85	0.26	4.09	1.46	20	8.65	46	13.6	178	41
OYX01-4-28	0.01	16.3	0.03	0.60	1.42	0.16	6.59	2.39	31	12.0	56	14.6	171	35
OYX01-4-29	0.01	16.6	0.04	0.56	1.55	0.23	7.14	2.76	37	15.3	77	22	269	60
OFX11-2-01	0.05	6.41	0.08	0.32	4.67	4.48	22	52	98	167	257	429	746	1016
OFX11-2-02	0.09	5.88	0.15	0.26	5.67	5.67	23	48	90	150	231	400	744	1034
OFX11-2-03	1.90	10.5	3.64	5.70	14.9	27	52	109	191	318	489	818	1453	1972
OFX11-2-05	0.04	43	0.74	3.96	31	8.07	94	150	215	302	423	649	1075	1498
OFX11-2-08	0.06	5.72	0.11	0.22	4.56	4.83	18	37	67	110	165	290	544	716
OFX11-2-09	0.12	15.7	0.35	1.39	10.33	3.05	33	52	77	109	153	235	424	562
OFX11-2-10	0.18	6.03	0.15	0.43	3.63	5.84	15.9	35	63	105	166	272	489	668

(continued)

Table 3.7 (continued)

Samples and analyzed spots	La	Ce	Pr	Nd	Sm	Eu	Gd	Tb	Dy	Ho	Er	Tm	Yb	Lu
OFX11-2-11	0.03	31	0.59	3.08	22	4.34	62	97	138	194	254	398	663	911
OFX11-2-15	0.29	7.66	0.96	1.91	6.08	5.14	29	68	150	254	435	820	1566	1891
OFX11-2-17	42	115	124	182	156	374	131	173	264	417	600	973	1759	2186
OFX11-2-19	0.03	23	0.67	2.72	19.1	4.41	52	75	94	126	156	211	349	490
OFX11-2-20	33	51	60	79	69	144	103	184	318	524	810	1377	2486	3110
OFX11-2-25	0.93	25	6.00	12.0	36	38	126	244	412	613	827	1195	1849	2246
OFX11-2-26	0.06	22	0.31	1.23	13.0	4.74	52	101	160	248	358	580	1012	1430
OFX11-2-33	0.03	39	0.42	3.10	28	5.91	89	148	228	324	437	654	1114	1536

Table 3.8 Zircon Lu–Hf isotopic data for sample CY26-1 from the North Chaoyang-Fuxin-Yixian granite-greenstone belt

Sample and analyzed spots	$^{207}Pb/^{206}Pb$ apparent ages (t_1)	$^{176}Yb/^{177}Hf$	$^{176}Lu/^{177}Hf$	$^{176}Hf/^{177}Hf$	±2σ	$(^{176}Hf/^{177}Hf)_{t1}$	εHf (0)	εHf (t_1)	T_{DM}	$f_{Lu/Hf}$	Crystallization age of the dated sample (t_2)	εHf (t_2)
CY26-1-01	2473	0.008412	0.000300	0.281369	0.000021	0.281354	−49.6	5.4	2582	−0.99	2512	6.3
CY26-1-03	2513	0.010734	0.000376	0.281328	0.000024	0.281310	−51.0	4.7	2641	−0.99	2512	4.7
CY26-1-04	2484	0.008054	0.000270	0.281309	0.000027	0.281296	−51.8	3.5	2660	−0.99	2512	4.2
CY26-1-05	2488	0.011219	0.000371	0.281314	0.000028	0.281296	−51.6	3.7	2660	−0.99	2512	4.2
CY26-1-06	2469	0.010009	0.000332	0.281356	0.000021	0.281340	−50.1	4.8	2601	−0.99	2512	5.8
CY26-1-07	2483	0.010347	0.000358	0.281355	0.000023	0.281338	−50.1	5.0	2604	−0.99	2512	5.7
CY26-1-08	2506	0.030600	0.000945	0.281336	0.000024	0.281291	−50.8	3.9	2669	−0.97	2512	4.0
CY26-1-09	2432	0.015603	0.000476	0.281373	0.000026	0.281351	−49.5	4.3	2588	−0.99	2512	6.1
CY26-1-10	2444	0.015421	0.000519	0.281315	0.000027	0.281291	−51.5	2.4	2669	−0.98	2512	4.0
CY26-1-11	2418	0.015985	0.000550	0.281341	0.000022	0.281315	−50.6	2.7	2636	−0.98	2512	4.9
CY26-1-12	2509	0.021022	0.000682	0.281346	0.000023	0.281314	−50.4	4.8	2637	−0.98	2512	4.8
CY26-1-13	2418	0.020036	0.000663	0.281386	0.000027	0.281356	−49.0	4.2	2582	−0.98	2512	6.3
CY26-1-14	2443	0.017956	0.000600	0.281298	0.000027	0.281270	−52.1	1.7	2697	−0.98	2512	3.3
CY26-1-15	2572	0.013620	0.000424	0.281358	0.000019	0.281337	−50.0	7.1	2604	−0.99	2512	5.7
CY26-1-16	2410	0.021919	0.000660	0.281330	0.000024	0.281300	−51.0	2.0	2657	−0.98	2512	4.3
CY26-1-17	2517	0.014002	0.000471	0.281344	0.000025	0.281322	−50.5	5.2	2626	−0.99	2512	5.1
CY26-1-18	2481	0.015257	0.000511	0.281337	0.000023	0.281313	−50.7	4.1	2638	−0.98	2512	4.8
CY26-1-19	2444	0.008023	0.000257	0.281319	0.000020	0.281307	−51.4	3.0	2646	−0.99	2512	4.6
CY26-1-20	2522	0.016974	0.000520	0.281326	0.000021	0.281301	−51.1	4.6	2653	−0.98	2512	4.4
CY26-1-22	2502	0.033337	0.000978	0.281390	0.000030	0.281344	−48.9	5.7	2598	−0.97	2512	5.9
CY26-1-23	2408	0.015847	0.000471	0.281342	0.000026	0.281320	−50.6	2.7	2629	−0.99	2512	5.0

(continued)

Table 3.8 (continued)

Sample and analyzed spots	$^{207}Pb/^{206}Pb$ apparent ages (t_1)	$^{176}Yb/^{177}Hf$	$^{176}Lu/^{177}Hf$	$^{176}Hf/^{177}Hf$	±2σ	$(^{176}Hf/^{177}Hf)_{t1}$	εHf (0)	εHf (t_1)	T_{DM}	$f_{Lu/Hf}$	Crystallization age of the dated sample (t_2)	εHf (t_2)
CY26-1-24	2474	0.014533	0.000472	0.281256	0.000029	0.281234	−53.6	1.1	2744	−0.99	2512	2.0
CY26-1-25	2448	0.006454	0.000220	0.281330	0.000023	0.281320	−51.0	3.6	2628	−0.99	2512	5.0
CY26-1-26	2520	0.021979	0.000673	0.281339	0.000027	0.281307	−50.7	4.8	2646	−0.98	2512	4.6
CY26-1-27	2443	0.011473	0.000393	0.281336	0.000030	0.281318	−50.8	3.4	2631	−0.99	2512	5.0
CY26-1-28	2488	0.017388	0.000508	0.281322	0.000025	0.281298	−51.3	3.7	2658	−0.98	2512	4.3
CY26-1-29	2501	0.009695	0.000326	0.281312	0.000026	0.281296	−51.6	4.0	2659	−0.99	2512	4.2
CY26-1-30	2516	0.012890	0.000398	0.281334	0.000026	0.281315	−50.8	5.0	2634	−0.99	2512	4.9
CY26-1-31	2420	0.014404	0.000463	0.281331	0.000030	0.281310	−50.9	2.6	2642	−0.99	2512	4.7
CY26-1-33	2522	0.039238	0.001056	0.281318	0.000026	0.281268	−51.4	3.4	2701	−0.97	2512	3.2
CY26-1-34	2472	0.016088	0.000494	0.281304	0.000031	0.281280	−51.9	2.7	2682	−0.99	2512	3.6
CY26-1-35	2410	0.014554	0.000437	0.281330	0.000031	0.281310	−51.0	2.3	2643	−0.99	2512	4.7

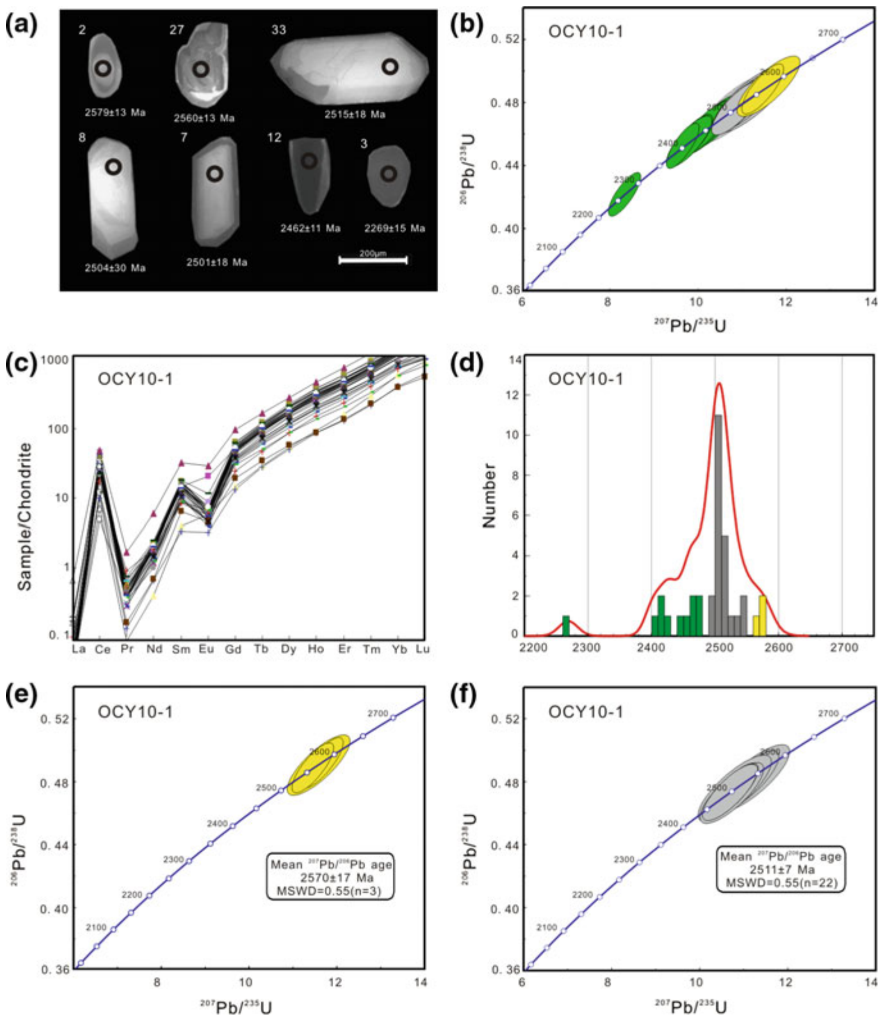

Fig. 3.24 Internal structures, LA-ICPMS U-Pb isotopic dating data, and trace element composition of zircon grains for the tonalitic gneiss sample OCY10-1. **a** CL images of representative zircon grains showing internal structures and analyzed locations. Numbers are spot locations in Table 3.7; **b** concordia diagram showing all analytical spots; **c** zircon REE patterns of all analyzed spots; **d** a histogram of the apparent ^{207}Pb/^{206}Pb ages; **e** and **f** concordia diagrams for analyses defining the oldest age peak (yellow collor) and the main age peak (grey collor), respectively

OCY10-1 intruded into the supracrustal rocks of greenstone belt, the age of 2570 ± 17 Ma could be the age of xenocrystic zircons.

Twenty-two analyses of mostly euhedral and banded zoned cores constitute the highest age peak (Fig. 3.24d). They show apparent ^{207}Pb/^{206}Pb ages of 2542 ± 29 Ma to 2497 ± 21 Ma, yielding a weighted mean age of 2511 ± 7 Ma (MSWD = 0.55) (Fig. 3.24f). Integrated with the banded zoned structure, magmatic zircon-like REE patterns and high Th/U ratios, the age of 2511 ± 7 Ma is considered as the crystallization age of the magmatic precursor.

The third age group comprises eleven analyses, and they were mostly analyzed on dark structureless cores (e.g., spots #3 and #12), yielding apparent $^{207}Pb/^{206}Pb$ ages of 2475 ± 15 Ma to 2269 ± 15 Ma (Fig. 3.24a, b). The magmatic zircon-like REE patterns (Fig. 3.24c) and high Th/U ratios suggest that they were originally crystallized from a magma system, and the large variation of the apparent ages implies different degrees of Pb loss. As noted by previous studies, granulite facies metamorphism associated with the emplacement of charnockitic rocks in the Jianping gneissic terrane occurred at ~2485 Ma, followed by the intrusion of post-tectonic granitoids at 2472 Ma [32, 43]. Subsequently, retrograde metamorphism at amphibolite facies and synchronous plutonism occurred at early Paleoproterozoic (2460–2350 Ma) in the Chaoyang area. Supracrustal sequences of the Fuxin-Yixian greenstone belt were also subjected to ~2485 Ma regional metamorphism, and record multiple episodes of younger thermal events at 2460–2043 Ma [42, 43, 89]. Accordingly, the younger ages of the third age group in sample OCY10-1 could represent the effects induced by the above Paleoproterozoic tectonothermal events.

Sample OYX01-4 (HMG)

Zircon grains separated from sample OYX01-4 display prismatic or oval shapes ranging in length between 50 and 150 μm with length/width ratios of 1:1–3:1. Cathodoluminescence images show that these zircon grains have core-rim structures. The cores show either oscillatory zonings (e.g., spots #14 and #16) or are bright structureless (e.g., spot #15) with irregular shapes, indicating that they were subjected to post-magmatic metamictization and recrystallization [13]. The cores are surrounded by dark (spot #19) or bright structureless rims (Spot #10; Fig. 3.25a). Twenty-nine analyses were conducted on twenty-six zircon grains, and these analyses show wide ranges in Th (32–281 ppm) and U (46–891 ppm) concentrations (Table 3.6). However, most Th/U ratios are higher than 0.1, and range from 0.14 to 1.37, except for one analysis (spot #26) at a dark metamicted rim showing a low Th/U ratio of 0.08. Rare earth elements of all the analyzed zircon domains show consistent chondrite-normalized patterns with positive Ce anomalies, moderate negative Eu anomalies and fractionated HREE patterns (Fig. 3.25b and Table 3.7), indicating that they were originally formed by magma crystallization [72]. All the analyses show apparent $^{207}Pb/^{206}Pb$ ages ranging from 2591 to 2086 Ma (Table 3.6), and they define a discordia with an upper intercept age of 2530 ± 22 Ma (MSWD = 5.4) (Fig. 3.25c). These imply that the analyzed zircon domains could have undergone different degrees of Pb loss. Eight analyses mostly on oscillatory zoned domains (spots #04, #05, #06, #11, #14, #15, #16 and #28) are plotted on or close to the concordia. They yield a weighted mean $^{207}Pb/^{206}Pb$ age of 2521 ± 9 Ma (MSWD = 0.46) and an upper intercept age of 2523 ± 22 Ma (MSWD = 0.18) (Fig. 3.25d). Therefore, the age of 2521 ± 9 Ma is considered to be close to the crystallization age of the magmatic precursor for sample OYX01-4.

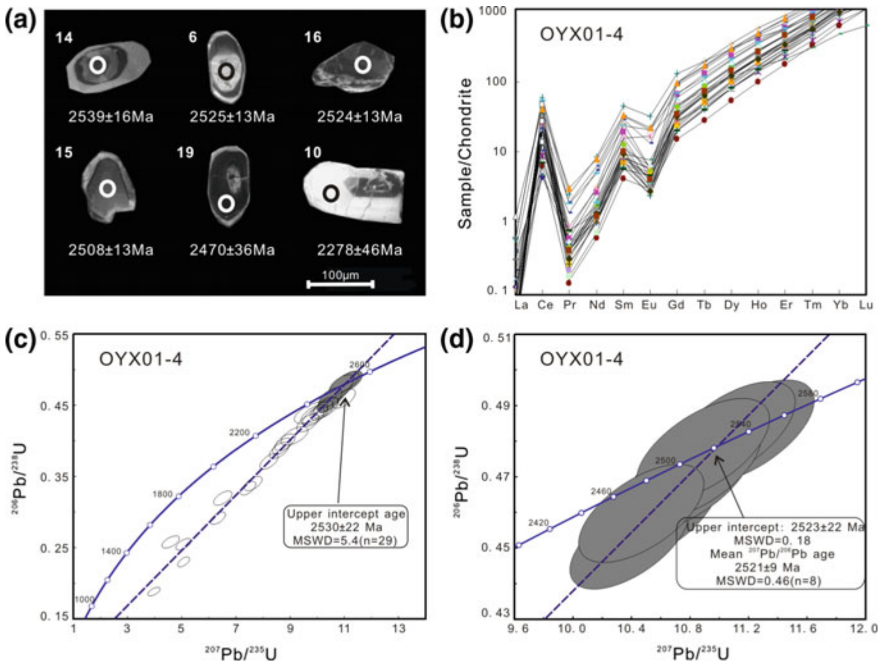

Fig. 3.25 Internal structures, LA-ICPMS U-Pb isotopic dating data, and trace element composition of zircon grains for the granodioritic gneiss sample OYX01-4. **a** CL images of representative zircon grains showing internal structures and analyzed locations. Numbers are spot locations in Table 3.7; **b** zircon REE patterns for all analyzed spots; **c** concordia diagram of all the analyzed spots; and **d** concordia diagram of the analyses (95–105% concordance level) used to calculate the crystallization age of the magmatic precursor

Sample OFX11-2 (LMG)

Most zircon grains from sample OFX11-2 exhibit long prismatic or stubby shapes with lengths and length/width ratios ranging from 100 to 200 μm and 1:1 to 3:1, respectively. Cathodoluminescence images show that they have core-rim structures. The dark elongated or bright stubby cores show oscillatory (spots #6 and #19) or banded (spot #11) zonings, indicating typical magmatic zircons. Small dark or bright zircon crystals occur as irregular shapes in the core, representing unconsumed inherited or xenocrystic zircons. This is further confirmed by their older apparent ages (e.g., 2666 ± 11 Ma of spot #21). The cores are enveloped by bright structureless rims (e.g., spot #27; Fig. 3.26a).

A total of thirty-four analyses were carried out on twenty-eight zircon grains (Table 3.6). Most of them are plotted on or close to the concordia (except for spots #11 and #17), and the apparent $^{207}Pb/^{206}Pb$ ages range from 2668 ± 12 Ma to 2362 ± 16 Ma (Fig. 3.26b). As shown in the probability density plot, six analyses at either dark prismatic cores (spots #6, #22, #23 and #32) or bright stubby cores (spots #7 and #21) yield older apparent $^{207}Pb/^{206}Pb$ ages between 2668 ± 12 Ma

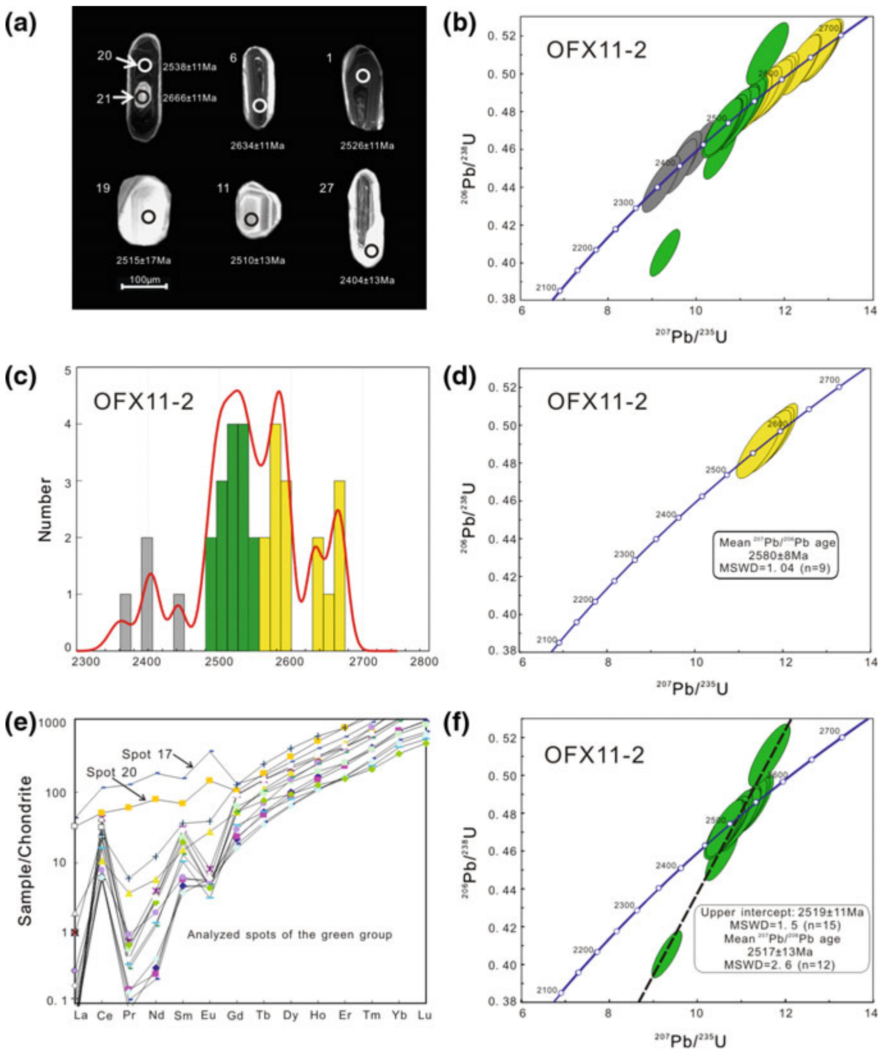

Fig. 3.26 Internal structures, LA-ICPMS U–Pb isotopic dating data, and trace element composition of zircon grains for the trondhjemitic gneiss sample OFX11-2. **a** CL images of representative zircon grains showing internal structures and analyzed locations. Numbers are spot locations in Table 3.7; **b** concordia diagram showing all analyzed spots; **c** a histogram of the apparent $^{207}Pb/^{206}Pb$ ages; **d** concordia diagram for analyses defining the first main age peak on the probability density plot (yellow color); **e** chondrite-normalized REE patterns of zircons; and **f** concordia diagram for analyses of the second main age peak (magmatic zircons; green color)

and 2630 ± 11 Ma (Fig. 3.26c), and have Th and U contents of 16–114 ppm and 34–313 ppm, respectively, yielding high Th/U ratios from 0.26 to 0.62. The ages of these zircons deviate from the main age group, but are coeval with those of the regionally oldest metavolcanic rocks (∼2640 Ma) [89, 93]. Therefore, these ages are considered as those of inherited or xenocrystic zircons. Nine analyses (spots #12, #13, #14, #16, #18, #29, #30, #31 and #34) constructing the first main age peak were analyzed mostly on dark oscillatory zoned cores, and show apparent $^{207}Pb/^{206}Pb$ ages of 2596 ± 11 Ma to 2558 ± 14 Ma. Th and U contents range from 12 to 359 ppm and 25 to 941 ppm, respectively, and Th/U ratios are mostly higher than 0.14 (except for spots #14 and #31 with Th/U values of 0.04–0.07). A weighted mean $^{207}Pb/^{206}Pb$ age of 2580 ± 8 Ma (MSWD = 1.04) is given by these analyses (Fig. 3.26d), which is within error of the crystallization age of a hornblende plagioclase gneiss from the metavolcanic rocks in Fuxin area (2589 ± 16 Ma of sample FX013-2, [89]. Since the trondhjemitic gneiss sample OFX11-2 shows intrusive contact with the supracrustal rocks (Fig. 3.19), the age of 2580 ± 8 Ma is considered as the age of inherited or xenocrystic zircons.

The second main age peak is constructed by fifteen analyses at bright stubby (e.g., spot #19) or dark elongated (e.g., spot #20) cores with oscillatory or banded zonings (Fig. 3.26a). They have Th from 8 to 97 ppm and U of 13 to 913 ppm. Eight analyses (spots #1, #2, #3, #8, #10, #15, #17 and #25) have high U contents (128–913 ppm), yielding Th/U ratios lower than 0.1 (0.03–0.09), and the other seven analyses (spots #5, #9, #11, #19, #26, #25 and #33) show low U contents between 13 and 255 ppm with Th/U values higher than 0.25. Most of them show consistent chondrite-normalized REE patterns with positive Ce anomalies, moderate negative Eu anomalies and fractionated HREE patterns (Fig. 3.26e and Table 3.7), indicative of typical magmatic zircons [72]. Two analyses (spots #17 and #20 with low Th/U of 0.06 and 0.09) have higher LREE contents without negative Eu anomalies. This could be ascribed to the mobility of incompatible elements (LREE, Th and U) resulting from local metamorphic recrystallization [96]. The fifteen analyses construct a discordia and yield an upper intercept age of 2519 ± 11 Ma (MSWD = 1.5), whereas twelve analyses, except for spots #11 (plotting away from the concordia), #17 and #20, give a weighted mean age of 2517 ± 13 Ma (MSWD = 2.6; Fig. 3.26f). Therefore, the upper intercept age of 2519 ± 11 Ma could be close to the crystallization age of the magmatic precursor of sample OFX11-2.

Four analyses at bright structureless rims (spots #4, #24, #27 and #28) have younger apparent $^{207}Pb/^{206}Pb$ ages between 2442 ± 11 Ma and 2362 ± 16 Ma, and Th and U contents of 54–91 ppm and 35–843 ppm, respectively, yielding Th/U ratios from 0.09 to 1.55. Similar to those of sample OCY10-1, they could reflect the effects of regional Paleoproterozoic multiple episodes of tectonothermal events [42, 43, 89].

Sample CY26-1 (HMG)

Zircon U–Pb isotopic dating data of the dioritic gneiss CY26-1 yield a weighted mean $^{207}Pb/^{206}Pb$ age of 2512 ± 15 Ma (MSWD = 0.09), which is interpreted as the crystallization age of the magmatic precursor [43]. Zircon Lu–Hf isotopes were analyzed for the thirty-two dated spots, except for one rejected (spot #21) and two inherited (spots #2 and #32) zircon domains (Table 3.8). When calculated at the

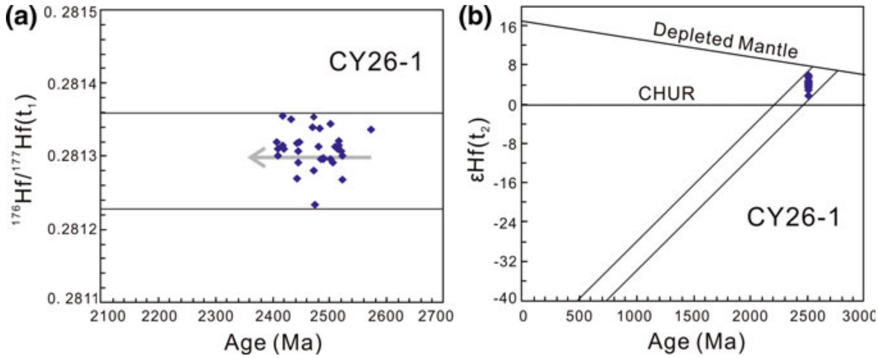

Fig. 3.27 Lu–Hf isotopic analyses of the dated zircon grains for dioritic sample CY26-1: **a** $^{176}Hf/^{177}Hf(t_1)$ versus apparent $^{207}Pb/^{206}Pb$ ages (t_1) and **b** εHf(t_2) versus crystallization age (t_2) diagrams. The $^{176}Lu/^{177}Hf$ isotopic ratios of the depleted mantle and chondrite are 0.0384 and 0.0332, respectively, after Blichert-Toft and Albarède [6] and Griffin et al. [20]

apparent $^{207}Pb/^{206}Pb$ ages (t_1), they show nearly consistent $^{176}Hf/^{177}Hf$ (t_1) ratios from 0.281234 to 0.281356 (Fig. 3.27a), suggesting that these zircon grains were crystallized from the same magmatic event and subjected to subsequent Pb loss [101]. We further calculated the Hf isotopic data at the crystallization age (t_2), and all the data show positive εHf(t_2) values from +2.0 to +6.3, with Hf depleted mantle model ages (T_{DM}(Hf)) of 2.74–2.58 Ga (Fig. 3.27b). Notably, the youngest T_{DM}(Hf) age (~2.58 Ga) is within error of the formation age of metavolcanic rocks from the Chaoyang-Fuxin-Yixian greenstone belt [43, 89].

3.2.3.2 Granitoid Gneisses in the JPGT

A total of six samples were analyzed for zircon U–Pb and Lu–Hf isotopes and trace elements, including the tonalitic gneiss samples OCY31-2, CY31-2, and CY46-1, and granodioritic gneiss sample OCY33-1 of the HMG, and the tonalitic gneiss sample OCY46-1 and granodioritic gneiss sample OCY37-1 of the LMG. Notably, zircon U–Pb isotopic dating data of samples CY31-1 and CY46-1 were documented by Liu et al. [43], and in situ Lu–Hf isotopes of these two samples were further analyzed in this study. All the data are listed in Tables 3.9, 3.10 and 3.11.

Sample OCY31-2 (HMG)

Zircon grains from the tonalitic gneiss sample OCY31-2 display elongated shapes with lengths and length/width ratios of 150–200 μm and 1.5:1–2.5:1 (Fig. 3.28a). These grains display core-rim structures with the cores showing either oscillatory zonings (e.g., spots #12, and #32) or weakly zonings (e.g., spots #8 and #4) on the cathodoluminescence images. These cores are surrounded by dark (e.g., spot 12) or bright (e.g., spots #31 and #11) thin and structureless rims. Thirty-two analyses were conducted on thirty-two zircon grains and all of them plot on or close to the

Table 3.9 Zircon U-Pb isotopic dating data for representative granitoid gneisses of the Jianping gneissic terrane (JPGT)

Samples and analyzed spots	Th (ppm)	U (ppm)	Th/U	Isotopic ratios						Apparent ages (Ma)					
				$^{207}Pb/^{206}Pb$	±1σ	$^{207}Pb/^{235}U$	±1σ	$^{206}Pb/^{238}U$	±1σ	$^{207}Pb/^{206}Pb$	±1σ	$^{207}Pb/^{235}U$	±1σ	$^{206}Pb/^{238}U$	±1σ
OCY31-2-1	94	226	0.42	0.1663	0.0023	10.9969	0.1685	0.4794	0.0061	2521	12	2523	14	2525	27
OCY31-2-2	146	157	0.93	0.1670	0.0023	11.0192	0.1705	0.4786	0.0061	2527	12	2525	14	2521	27
OCY31-2-3	75	379	0.20	0.1654	0.0022	10.8888	0.1658	0.4773	0.0061	2512	12	2514	14	2516	26
OCY31-2-4	99	234	0.42	0.1556	0.0022	9.7294	0.1522	0.4533	0.0058	2409	12	2409	14	2410	26
OCY31-2-5	59	196	0.30	0.1653	0.0023	10.8666	0.1677	0.4767	0.0061	2511	12	2512	14	2513	27
OCY31-2-6	237	184	1.29	0.1651	0.0023	10.8393	0.1688	0.4759	0.0061	2509	12	2509	14	2509	27
OCY31-2-7	609	984	0.62	0.1656	0.0024	10.8691	0.1735	0.4759	0.0061	2514	12	2512	15	2509	27
OCY31-2-8	68	282	0.24	0.1640	0.0022	10.6768	0.1644	0.4720	0.0060	2497	12	2495	14	2492	26
OCY31-2-9	324	243	1.34	0.1662	0.0023	10.9657	0.1706	0.4785	0.0061	2519	12	2520	14	2521	27
OCY31-2-10	92	381	0.24	0.1593	0.0022	10.1529	0.1579	0.4622	0.0059	2448	12	2449	14	2449	26
OCY31-2-11	179	201	0.89	0.1589	0.0022	10.1222	0.1580	0.4618	0.0059	2444	12	2446	14	2448	26
OCY31-2-12	111	146	0.76	0.1670	0.0025	11.0630	0.1806	0.4805	0.0062	2527	13	2528	15	2529	27
OCY31-2-13	237	225	1.05	0.1666	0.0024	11.0134	0.1754	0.4792	0.0062	2524	12	2524	15	2524	27
OCY31-2-14	195	191	1.02	0.1640	0.0023	10.6680	0.1675	0.4717	0.0060	2497	12	2495	15	2491	26
OCY31-2-15	188	278	0.68	0.1650	0.0023	10.8187	0.1692	0.4755	0.0061	2507	12	2508	15	2507	27
OCY31-2-16	142	111	1.27	0.1636	0.0024	10.6468	0.1716	0.4720	0.0061	2493	12	2493	15	2492	27
OCY31-2-17	105	473	0.22	0.1660	0.0023	10.9258	0.1707	0.4772	0.0061	2518	12	2517	15	2515	27
OCY31-2-18	19	40	0.49	0.1695	0.0027	11.3121	0.1957	0.4841	0.0064	2552	14	2549	16	2545	28
OCY31-2-19	81	272	0.30	0.1623	0.0023	10.4845	0.1664	0.4685	0.0060	2479	12	2479	15	2477	26
OCY31-2-20	173	141	1.23	0.1632	0.0024	10.5993	0.1736	0.4710	0.0061	2489	13	2489	15	2488	27
OCY31-2-21	69	89	0.78	0.1692	0.0026	11.3091	0.1913	0.4847	0.0064	2549	13	2549	16	2548	28
OCY31-2-22	82	98	0.84	0.1758	0.0027	12.2667	0.2080	0.5060	0.0066	2614	13	2625	16	2639	28
OCY31-2-23	161	194	0.83	0.1651	0.0027	10.8149	0.1912	0.4751	0.0063	2508	14	2507	16	2506	28
OCY31-2-24	186	537	0.35	0.1619	0.0023	10.4571	0.1681	0.4684	0.0060	2475	12	2476	15	2477	26
OCY31-2-25	105	195	0.54	0.1662	0.0026	10.9489	0.1865	0.4777	0.0063	2520	13	2519	16	2517	27

(continued)

Table 3.9 (continued)

Samples and analyzed spots	Th (ppm)	U (ppm)	Th/U	Isotopic ratios						Apparent ages (Ma)					
				$^{207}Pb/^{206}Pb$	±1σ	$^{207}Pb/^{235}U$	±1σ	$^{206}Pb/^{238}U$	±1σ	$^{207}Pb/^{206}Pb$	±1σ	$^{207}Pb/^{235}U$	±1σ	$^{206}Pb/^{238}U$	±1σ
OCY31-2-26	142	117	1.21	0.1622	0.0025	10.4776	0.1761	0.4683	0.0061	2479	13	2478	16	2476	27
OCY31-2-27	124	150	0.83	0.1651	0.0025	10.8303	0.1789	0.4757	0.0062	2508	13	2509	15	2509	27
OCY31-2-28	141	198	0.71	0.1642	0.0024	10.7223	0.1736	0.4735	0.0061	2500	13	2499	15	2499	27
OCY31-2-29	142	82	1.72	0.1625	0.0026	10.5053	0.1829	0.4688	0.0062	2482	14	2480	16	2478	27
OCY31-2-30	98	206	0.48	0.1609	0.0024	10.3140	0.1696	0.4649	0.0060	2465	13	2463	15	2461	26
OCY31-2-31	96	195	0.49	0.1728	0.0026	11.7680	0.1929	0.4938	0.0064	2585	13	2586	15	2587	27
OCY31-2-32	332	375	0.89	0.1662	0.0025	10.9436	0.1790	0.4775	0.0061	2520	13	2518	15	2516	27
OCY33-1-1	16	39	0.39	0.1569	0.0034	9.9310	0.2238	0.4589	0.0067	2423	20	2428	21	2435	30
OCY33-1-2	97	74	1.30	0.1672	0.0026	11.0895	0.1876	0.4809	0.0063	2530	13	2531	16	2531	27
OCY33-1-3	80	44	1.81	0.1646	0.0027	10.7661	0.1894	0.4743	0.0063	2504	14	2503	16	2502	27
OCY33-1-4	138	261	0.53	0.1544	0.0024	9.5794	0.1603	0.4498	0.0058	2396	13	2395	15	2394	26
OCY33-1-5	28	29	0.96	0.1398	0.0025	7.9248	0.1517	0.4112	0.0056	2224	16	2223	17	2220	25
OCY33-1-6	94	180	0.52	0.1687	0.0026	11.2734	0.1887	0.4846	0.0063	2545	13	2546	16	2547	27
OCY33-1-7	70	240	0.29	0.1591	0.0025	10.0973	0.1714	0.4604	0.0060	2446	13	2444	16	2441	26
OCY33-1-8	75	34	2.22	0.1593	0.0029	10.1556	0.1971	0.4623	0.0063	2448	16	2449	18	2450	28
OCY33-1-9	130	88	1.48	0.1614	0.0026	10.3941	0.1828	0.4670	0.0061	2470	14	2471	16	2470	27
OCY33-1-10	31	18	1.67	0.1662	0.0034	10.9466	0.2311	0.4777	0.0068	2519	18	2519	20	2517	30
OCY33-1-11	129	61	2.11	0.1587	0.0028	10.0833	0.1910	0.4609	0.0062	2441	16	2442	18	2443	27
OCY33-1-12	355	390	0.91	0.1679	0.0026	11.1741	0.1879	0.4827	0.0062	2537	13	2538	16	2539	27
OCY33-1-13	22	56	0.40	0.1639	0.0028	10.6924	0.1949	0.4730	0.0063	2497	15	2497	17	2497	27
OCY33-1-14	51	116	0.44	0.1656	0.0027	10.9080	0.1936	0.4776	0.0063	2514	14	2515	17	2517	27
OCY33-1-15	28	26	1.07	0.1605	0.0034	10.2727	0.2235	0.4643	0.0067	2461	19	2460	20	2458	29
OCY33-1-16	124	74	1.69	0.1660	0.0035	10.8549	0.2376	0.4743	0.0068	2518	19	2511	20	2502	30
OCY33-1-17	28	23	1.21	0.1634	0.0032	10.6280	0.2175	0.4716	0.0066	2492	17	2491	19	2490	29
OCY33-1-18	19	15	1.22	0.1600	0.0039	10.2019	0.2504	0.4624	0.0070	2456	22	2453	23	2450	31

(continued)

Table 3.9 (continued)

Samples and analyzed spots	Th (ppm)	U (ppm)	Th/U	Isotopic ratios						Apparent ages (Ma)					
				$^{207}Pb/^{206}Pb$	±1σ	$^{207}Pb/^{235}U$	±1σ	$^{206}Pb/^{238}U$	±1σ	$^{207}Pb/^{206}Pb$	±1σ	$^{207}Pb/^{235}U$	±1σ	$^{206}Pb/^{238}U$	±1σ
OCY33-1-19	76	30	2.52	0.1603	0.0036	10.2628	0.2345	0.4644	0.0068	2459	20	2459	21	2459	30
OCY33-1-20	965	500	1.93	0.1616	0.0026	10.4244	0.1797	0.4677	0.0061	2473	14	2473	16	2473	27
OCY33-1-21	132	66	1.99	0.1629	0.0028	10.5779	0.1954	0.4708	0.0063	2486	15	2487	17	2487	27
OCY33-1-22	15	15	1.00	0.1574	0.0044	9.9147	0.2770	0.4570	0.0075	2427	26	2427	26	2426	33
OCY33-1-23	40	29	1.39	0.1644	0.0033	10.7698	0.2235	0.4750	0.0066	2502	18	2503	19	2506	29
OCY33-1-24	154	248	0.62	0.1610	0.0026	10.3398	0.1818	0.4659	0.0061	2466	14	2466	16	2466	27
OCY33-1-25	109	82	1.34	0.1654	0.0032	10.8850	0.2186	0.4772	0.0066	2512	17	2513	19	2515	29
OCY33-1-26	118	186	0.64	0.1585	0.0027	10.0476	0.1815	0.4598	0.0060	2440	15	2439	17	2439	27
OCY33-1-27	183	749	0.24	0.1535	0.0026	9.4646	0.1706	0.4472	0.0059	2385	15	2384	17	2383	26
OCY33-1-28	127	1434	0.09	0.1605	0.0026	10.2971	0.1815	0.4654	0.0060	2460	14	2462	16	2464	27
OCY33-1-29	10	21	0.48	0.1607	0.0040	10.3160	0.2586	0.4654	0.0071	2463	23	2464	23	2463	31
OCY33-1-30	73	27	2.70	0.1598	0.0031	10.1866	0.2075	0.4625	0.0064	2453	17	2452	19	2450	28
OCY33-1-31	81	226	0.36	0.1641	0.0027	10.7109	0.1923	0.4735	0.0062	2498	15	2498	17	2499	27
OCY33-1-32	186	257	0.72	0.1588	0.0027	10.0806	0.1837	0.4603	0.0060	2443	15	2442	17	2441	27
OCY33-1-33	19	24	0.77	0.1593	0.0034	10.1288	0.2207	0.4610	0.0065	2449	19	2447	20	2444	29
OCY33-1-34	74	72	1.03	0.1645	0.0030	10.7869	0.2110	0.4755	0.0064	2503	16	2505	18	2508	28
OCY33-1-35	74	173	0.43	0.1582	0.0028	10.0312	0.1902	0.4600	0.0061	2436	16	2438	18	2440	27
OCY33-1-36	57	29	1.96	0.1614	0.0032	10.3941	0.2142	0.4671	0.0064	2470	18	2471	19	2471	28
OCY33-1-37	120	107	1.12	0.1728	0.0030	11.7540	0.2170	0.4932	0.0065	2585	15	2585	17	2585	28
OCY33-1-38	70	34	2.06	0.1608	0.0031	10.2925	0.2093	0.4644	0.0064	2464	17	2461	19	2459	28
OCY37-1-1	69	703	0.10	0.1584	0.0037	10.1290	0.2436	0.4639	0.0063	2438	23	2447	22	2457	28
OCY37-1-2	86	87	0.98	0.1678	0.0041	11.0274	0.2736	0.4768	0.0066	2535	24	2525	23	2513	29
OCY37-1-3	103	92	1.13	0.1681	0.0041	11.0323	0.2751	0.4760	0.0066	2539	24	2526	23	2510	29
OCY37-1-4	126	712	0.18	0.1621	0.0038	10.3686	0.2516	0.4639	0.0063	2478	23	2468	22	2457	28
OCY37-1-5	17	236	0.07	0.1744	0.0042	12.4169	0.3046	0.5163	0.0070	2601	23	2636	23	2684	30

(continued)

Table 3.9 (continued)

Samples and analyzed spots	Th (ppm)	U (ppm)	Th/U	Isotopic ratios						Apparent ages (Ma)					
				$^{207}Pb/^{206}Pb$	±1σ	$^{207}Pb/^{235}U$	±1σ	$^{206}Pb/^{238}U$	±1σ	$^{207}Pb/^{206}Pb$	±1σ	$^{207}Pb/^{235}U$	±1σ	$^{206}Pb/^{238}U$	±1σ
OCY37-1-6	240	190	1.26	0.1695	0.0041	11.4095	0.2836	0.4882	0.0067	2553	24	2557	23	2563	29
OCY37-1-7	120	97	1.24	0.1774	0.0044	14.7662	0.3730	0.6037	0.0083	2629	24	2800	24	3045	34
OCY37-1-8	171	190	0.90	0.1699	0.0042	12.1886	0.3058	0.5202	0.0071	2557	24	2619	24	2700	30
OCY37-1-9	159	210	0.76	0.1705	0.0042	11.2839	0.2834	0.4801	0.0066	2562	24	2547	23	2527	29
OCY37-1-10	235	1400	0.17	0.1552	0.0038	10.2408	0.2550	0.4786	0.0065	2404	24	2457	23	2521	28
OCY37-1-11	110	142	0.77	0.1562	0.0040	9.7913	0.2538	0.4546	0.0063	2415	26	2415	24	2416	28
OCY37-1-12	165	715	0.23	0.1558	0.0039	9.7351	0.2470	0.4531	0.0062	2411	25	2410	23	2409	27
OCY37-1-13	144	167	0.87	0.1654	0.0042	10.8620	0.2798	0.4764	0.0066	2511	25	2511	24	2512	29
OCY37-1-14	105	138	0.76	0.1664	0.0042	11.0076	0.2859	0.4798	0.0066	2522	25	2524	24	2526	29
OCY37-1-15	115	173	0.67	0.1666	0.0042	10.9967	0.2866	0.4788	0.0066	2524	26	2523	24	2522	29
OCY37-1-16	41	58	0.72	0.1725	0.0048	11.7166	0.3326	0.4928	0.0073	2582	28	2582	27	2583	31
OCY37-1-17	62	77	0.81	0.1685	0.0044	11.2506	0.3026	0.4842	0.0068	2543	27	2544	25	2545	30
OCY37-1-18	141	168	0.84	0.1731	0.0045	11.7593	0.3104	0.4927	0.0068	2588	26	2585	25	2582	29
OCY37-1-19	61	104	0.59	0.1743	0.0047	11.9530	0.3264	0.4974	0.0071	2599	27	2601	26	2602	30
OCY37-1-20	182	270	0.67	0.1665	0.0043	11.0102	0.2903	0.4797	0.0066	2523	26	2524	25	2526	29
OCY37-1-21	212	175	1.22	0.1655	0.0044	10.8608	0.2932	0.4761	0.0066	2512	27	2511	25	2510	29
OCY37-1-22	71	86	0.82	0.1734	0.0047	11.8009	0.3250	0.4936	0.0070	2591	27	2589	26	2586	30
OCY37-1-23	89	518	0.17	0.1733	0.0046	11.8016	0.3171	0.4940	0.0068	2590	27	2589	25	2588	29
OCY37-1-24	137	1160	0.12	0.1543	0.0040	9.5564	0.2554	0.4491	0.0062	2394	27	2393	25	2391	27
OCY37-1-25	321	325	0.99	0.1660	0.0044	10.9259	0.2963	0.4773	0.0066	2518	27	2517	25	2515	29
OCY37-1-26	201	221	0.91	0.1694	0.0046	11.3309	0.3105	0.4852	0.0067	2551	28	2551	26	2550	29
OCY37-1-27	483	567	0.85	0.1264	0.0064	5.7302	0.2772	0.3288	0.0052	2049	92	1936	42	1832	25
OCY37-1-28	120	293	0.41	0.1651	0.0048	10.8216	0.3156	0.4754	0.0069	2508	30	2508	27	2507	30
OCY37-1-29	80	138	0.58	0.1644	0.0046	10.7345	0.3020	0.4736	0.0067	2501	29	2500	26	2499	29
OCY37-1-30	92	31	2.97	0.1602	0.0048	10.2465	0.3073	0.4641	0.0069	2457	31	2457	28	2458	30

(continued)

Table 3.9 (continued)

Samples and analyzed spots	Th (ppm)	U (ppm)	Th/U	Isotopic ratios						Apparent ages (Ma)					
				$^{207}Pb/^{206}Pb$	±1σ	$^{207}Pb/^{235}U$	±1σ	$^{206}Pb/^{238}U$	±1σ	$^{207}Pb/^{206}Pb$	±1σ	$^{207}Pb/^{235}U$	±1σ	$^{206}Pb/^{238}U$	±1σ
OCY46-1-1	94	84	1.11	0.1697	0.0031	11.3826	0.2182	0.4866	0.0064	2555	16	2555	18	2556	28
OCY46-1-2	95	122	0.78	0.1668	0.0030	11.0092	0.2106	0.4787	0.0063	2526	16	2524	18	2522	28
OCY46-1-3	78	107	0.73	0.1665	0.0030	10.9930	0.2079	0.4790	0.0063	2522	16	2523	18	2523	27
OCY46-1-4	94	111	0.84	0.1688	0.0031	11.2661	0.2178	0.4842	0.0064	2545	16	2545	18	2546	28
OCY46-1-5	51	64	0.80	0.1670	0.0031	11.0563	0.2157	0.4803	0.0064	2528	16	2528	18	2528	28
OCY46-1-6	91	118	0.77	0.1621	0.0050	10.0085	0.2710	0.4478	0.0065	2478	53	2436	25	2385	29
OCY46-1-7	109	122	0.89	0.1609	0.0050	9.6584	0.2647	0.4355	0.0063	2465	54	2403	25	2330	28
OCY46-1-8	53	62	0.85	0.1675	0.0032	11.0906	0.2258	0.4803	0.0065	2533	17	2531	19	2529	28
OCY46-1-9	59	62	0.96	0.1657	0.0032	10.8986	0.2194	0.4772	0.0064	2514	17	2515	19	2515	28
OCY46-1-10	63	80	0.78	0.1677	0.0031	11.1304	0.2186	0.4814	0.0064	2535	17	2534	18	2533	28
OCY46-1-11	84	105	0.80	0.1679	0.0031	11.1462	0.2184	0.4817	0.0064	2536	17	2535	18	2535	28
OCY46-1-12	67	90	0.74	0.1644	0.0032	10.7541	0.2178	0.4744	0.0064	2502	17	2502	19	2503	28
OCY46-1-14	376	339	1.11	0.1601	0.0030	6.4232	0.1282	0.2910	0.0039	2457	17	2035	18	1647	19
OCY46-1-15	63	73	0.85	0.1677	0.0033	11.1278	0.2303	0.4814	0.0065	2535	18	2534	19	2533	28
OCY46-1-16	58	81	0.72	0.1669	0.0034	10.4363	0.2198	0.4536	0.0062	2526	18	2474	20	2411	27
OCY46-1-17	93	89	1.05	0.1681	0.0033	11.1779	0.2316	0.4822	0.0065	2539	18	2538	19	2537	28
OCY46-1-18	69	185	0.38	0.1555	0.0042	8.1221	0.1864	0.3789	0.0052	2407	46	2245	21	2071	24
OCY46-1-19	61	66	0.92	0.1694	0.0033	11.3384	0.2325	0.4856	0.0065	2551	18	2551	19	2552	28
OCY46-1-20	74	99	0.75	0.1662	0.0033	10.9551	0.2274	0.4782	0.0064	2520	18	2519	19	2519	28
OCY46-1-21	62	78	0.80	0.1689	0.0033	11.2712	0.2313	0.4840	0.0065	2547	18	2546	19	2545	28
OCY46-1-22	47	63	0.75	0.1686	0.0033	11.2316	0.2319	0.4833	0.0065	2543	18	2543	19	2542	28
OCY46-1-23	58	71	0.81	0.1678	0.0035	11.0714	0.2429	0.4787	0.0066	2536	19	2529	20	2521	29
OCY46-1-24	60	106	0.57	0.1612	0.0033	10.3146	0.2220	0.4641	0.0063	2468	19	2463	20	2458	28
OCY46-1-25	95	200	0.48	0.1658	0.0044	9.4148	0.2171	0.4117	0.0056	2516	46	2379	21	2223	26
OCY46-1-26	185	197	0.94	0.1674	0.0032	10.0467	0.2044	0.4352	0.0057	2532	18	2439	19	2329	26

(continued)

Table 3.9 (continued)

Samples and analyzed spots	Th (ppm)	U (ppm)	Th/U	Isotopic ratios						Apparent ages (Ma)					
				$^{207}Pb/^{206}Pb$	±1σ	$^{207}Pb/^{235}U$	±1σ	$^{206}Pb/^{238}U$	±1σ	$^{207}Pb/^{206}Pb$	±1σ	$^{207}Pb/^{235}U$	±1σ	$^{206}Pb/^{238}U$	±1σ
OCY46-1-27	68	95	0.71	0.1676	0.0033	11.1455	0.2323	0.4822	0.0064	2534	18	2535	19	2537	28
OCY46-1-28	88	125	0.71	0.1664	0.0032	10.9784	0.2251	0.4787	0.0063	2521	18	2521	19	2521	28
OCY46-1-29	160	168	0.96	0.1670	0.0033	11.0373	0.2283	0.4795	0.0064	2527	18	2526	19	2525	28

Note ^{204}Pb has been corrected using the method of [2]

Table 3.10 Trace element data (ppm) for the dated zircon grains of samples OCY31-2, OCY33-1, and OCY46-1 from the JPGT

Samples and analyzed spots	La	Ce	Pr	Nd	Sm	Eu	Gd	Tb	Dy	Ho	Er	Tm	Yb	Lu
OCY31-2-1	0.01	9.04	0.03	0.70	1.86	0.28	10.4	4.16	54	22	101	26	309	62
OCY31-2-2	0.01	14.7	0.04	0.90	2.31	0.29	10.7	4.04	51	18.8	84	21	228	44
OCY31-2-3	0.01	8.84	0.02	0.50	1.87	0.25	11.2	4.84	69	27	135	36	433	86
OCY31-2-4	0.01	10.3	0.02	0.63	1.93	0.28	10.8	4.19	53	21	97	25	304	59
OCY31-2-5	0.01	15.6	0.04	0.78	2.01	0.55	8.64	3.12	39	15.0	73	19.5	239	49
OCY31-2-6	0.01	15.4	0.06	1.15	3.34	0.50	17.2	6.13	72	27	115	27	293	54
OCY31-2-7	0.03	46	0.20	3.19	4.52	1.50	17.3	5.06	64	25	128	39	590	144
OCY31-2-8	3.39	23	1.21	7.21	4.26	0.80	18.2	6.72	86	34	157	40	455	90
OCY31-2-9	0.11	20	0.73	10.4	13.9	1.84	49	14.4	151	51	208	47	495	93
OCY31-2-10	0.02	10.6	0.04	0.77	2.17	0.32	11.2	4.51	60	24	110	29	344	67
OCY31-2-11	0.02	16.0	0.06	1.14	2.81	0.35	13.4	5.04	63	23	104	26	288	55
OCY31-2-12	0.01	27	0.04	0.98	1.94	0.72	9.06	3.40	40	16.2	77	21	278	58
OCY31-2-13	0.14	12.7	0.65	7.84	9.66	1.68	31	9.11	102	36	151	36	399	74
OCY31-2-14	0.07	31	0.15	2.61	4.53	1.59	17.0	5.09	57	21	93	24	300	64
OCY31-2-15	0.01	15.7	0.05	1.27	3.34	0.50	16.2	5.49	66	24	106	25	275	53
OCY31-2-16	0.01	14.4	0.06	1.04	2.94	0.37	13.4	4.97	61	23	101	25	284	53
OCY31-2-17	0.04	9.91	0.05	0.92	2.16	0.40	12.7	5.02	67	27	134	37	444	90
OCY31-2-18	0.01	9.43	0.01	0.26	0.71	0.22	3.55	1.38	18.0	7.59	39	11.4	154	34
OCY31-2-19	0.32	9.10	0.08	0.89	1.81	0.29	9.50	3.63	46	18.3	89	24	293	60
OCY31-2-20	4.28	55	1.47	11.6	7.58	2.41	23.7	7.47	85	31	139	35	416	83
OCY31-2-21	0.01	10.2	0.13	2.61	6.96	1.07	38	14.0	166	60	245	55	589	104
OCY31-2-22	0.04	16.7	0.09	1.43	2.96	1.26	14.3	5.24	69	28	136	37	469	105
OCY31-2-23	0.01	15.8	0.05	1.06	2.90	0.40	14.3	5.32	66	25	110	27	325	57

(continued)

Table 3.10 (continued)

Samples and analyzed spots	La	Ce	Pr	Nd	Sm	Eu	Gd	Tb	Dy	Ho	Er	Tm	Yb	Lu
OCY31-2-24	0.05	16.3	0.09	1.37	3.58	0.48	16.5	6.14	77	28	127	31	348	63
OCY31-2-25	0.01	13.5	0.07	1.21	3.01	1.18	13.0	4.31	55	21	101	28	343	72
OCY31-2-26	0.01	14.0	0.05	1.14	2.70	0.38	13.1	4.79	59	22	98	24	269	51
OCY31-2-27	0.01	13.2	0.04	0.84	2.11	0.27	11.1	3.98	48	18.0	79	20	224	43
OCY31-2-28	0.01	14.4	0.06	1.17	2.87	0.43	14.1	5.17	63	23	98	23	252	48
OCY31-2-29	0.01	11.5	0.05	0.98	2.51	0.32	12.6	4.63	56	21	92	23	257	50
OCY31-2-30	0.01	11.6	0.04	0.73	1.84	0.25	8.40	3.42	42	15.7	71	18.1	206	39
OCY31-2-31	0.02	12.3	0.08	1.62	3.48	1.59	17.9	6.47	78	31	144	37	449	97
OCY31-2-32	0.06	47	0.13	2.45	5.24	1.18	23	7.59	92	33	155	39	438	88
OCY33-1-1	0.01	16.6	0.03	0.54	1.32	0.29	6.46	2.35	28	10.2	47	12.0	150	28
OCY33-1-2	0.03	22	0.33	5.10	7.57	2.32	25	6.83	70	23	92	21	237	45
OCY33-1-3	0.01	24	0.06	1.29	2.92	0.63	12.6	4.54	54	21	95	25	289	57
OCY33-1-4	0.04	12.0	0.03	0.54	0.84	0.43	3.72	1.20	15.0	5.75	28	7.59	99	23
OCY33-1-5	0.30	17.1	0.14	1.32	1.71	0.38	6.68	2.21	27	9.80	46	12.2	150	30
OCY33-1-6	0.06	23	0.06	0.82	1.22	0.35	5.13	1.63	20	7.63	38	10.9	142	30
OCY33-1-7	0.04	16.5	0.07	1.34	2.13	0.57	9.18	3.22	40	15.9	77	20	256	56
OCY33-1-8	0.04	15.8	0.04	0.59	1.43	0.36	5.63	1.99	24	9.53	44	12.3	157	33
OCY33-1-9	0.01	17.0	0.04	0.62	1.30	0.48	6.25	2.03	26	9.79	48	13.2	177	38
OCY33-1-10	0.01	17.7	0.04	0.80	1.87	0.39	8.34	2.80	33	12.7	59	15.5	189	38
OCY33-1-11	0.01	19.4	0.03	0.84	1.44	0.48	6.78	2.42	29	11.2	53	14.7	193	40
OCY33-1-12	0.02	27	0.16	2.86	4.11	1.49	16.8	5.47	67	26	125	33	409	88
OCY33-1-13	0.01	5.94	0.01	0.21	0.43	0.19	1.93	0.68	8.65	3.26	16.0	4.59	64	14.8
OCY33-1-14	0.02	13.4	0.08	1.67	3.31	0.49	14.6	5.10	63	24	108	28	329	65

(continued)

Table 3.10 (continued)

Samples and analyzed spots	La	Ce	Pr	Nd	Sm	Eu	Gd	Tb	Dy	Ho	Er	Tm	Yb	Lu
OCY33-1-15	0.01	21	0.06	0.98	2.27	0.37	9.17	2.91	35	12.8	59	15.4	185	36
OCY33-1-16	0.01	19.4	0.04	0.81	1.95	0.52	8.01	3.08	35	14.0	65	18.0	214	45
OCY33-1-17	0.01	20	0.03	0.80	2.08	0.43	8.82	2.96	35	13.1	61	15.9	189	37
OCY33-1-18	0.01	19.7	0.06	1.07	2.19	0.42	9.97	3.47	41	15.0	68	17.8	215	41
OCY33-1-19	0.01	17.5	0.03	0.53	1.33	0.45	6.37	2.26	27	10.3	49	12.9	167	35
OCY33-1-20	0.10	128	0.45	7.44	14.9	5.27	52	14.2	145	46	189	44	487	93
OCY33-1-21	0.01	18.2	0.03	0.59	1.20	0.36	5.50	1.83	22	8.53	40	11.4	145	31
OCY33-1-22	0.01	27	0.06	1.09	2.64	0.46	11.5	3.88	45	16.6	76	19.3	228	43
OCY33-1-23	0.01	18.7	0.05	0.93	1.83	0.43	7.97	2.92	35	13.1	62	16.2	197	39
OCY33-1-24	0.13	27	0.12	2.24	4.03	1.85	17.2	5.44	63	24	108	28	346	73
OCY33-1-25	0.01	17.2	0.29	5.42	9.88	1.51	29	8.06	80	26	104	24	262	47
OCY33-1-26	0.01	12.5	0.02	0.35	0.85	0.17	4.45	1.83	26	10.8	56	16.5	220	47
OCY33-1-27	0.08	15.1	0.12	1.05	1.46	0.55	4.94	1.77	21	8.14	40	11.5	154	32
OCY33-1-28	0.01	10.5	0.02	0.53	1.02	0.56	6.29	2.12	26	10.3	53	15.5	207	44
OCY33-1-29	0.01	16.3	0.07	1.15	2.42	0.37	10.6	3.45	40	13.9	60	14.4	159	29
OCY33-1-30	0.02	18.7	0.04	0.69	1.48	0.43	6.27	2.29	27	10.4	50	13.5	170	36
OCY33-1-31	0.01	8.24	0.02	0.25	0.54	0.29	2.48	0.99	13.2	5.64	30	8.72	122	30
OCY33-1-32	0.03	17.0	0.04	0.62	1.45	0.46	6.22	2.18	25	9.75	49	13.6	175	38
OCY33-1-33	0.01	28	0.07	1.20	3.29	0.52	13.5	4.39	52	18.6	83	21	241	46
OCY33-1-34	0.01	17.1	0.07	1.43	3.23	0.79	12.5	3.85	42	15.0	63	15.5	174	33
OCY33-1-35	0.03	12.8	0.04	0.48	1.24	0.27	5.63	1.90	24	9.50	46	12.9	161	34
OCY33-1-36	0.01	21	0.06	0.87	2.21	0.47	9.74	3.40	41	15.2	72	18.7	227	46
OCY33-1-37	0.04	28	0.34	5.99	9.64	2.68	36	10.5	109	36	148	35	389	75

(continued)

Table 3.10 (continued)

Samples and analyzed spots	La	Ce	Pr	Nd	Sm	Eu	Gd	Tb	Dy	Ho	Er	Tm	Yb	Lu
OCY33-1-38	0.02	13.5	0.02	0.49	0.85	0.25	3.47	1.26	15.1	5.95	29	7.85	105	22
OCY46-1-01	0.01	15.6	0.15	2.92	5.82	1.24	23	6.78	74	25	103	24	263	50
OCY46-1-02	0.11	16.3	0.12	1.54	2.52	0.36	9.61	3.06	36	13.5	59	14.5	166	33
OCY46-1-03	0.05	15.3	0.07	1.23	2.29	0.50	10.0	3.26	39	14.3	65	16.3	187	38
OCY46-1-04	0.02	16.1	0.06	1.54	2.83	0.57	11.3	3.72	44	16.0	74	18.0	207	42
OCY46-1-05	0.25	13.4	0.11	1.19	2.33	0.35	8.54	2.78	32	11.4	49	12.2	139	27
OCY46-1-06	0.01	13.5	0.22	3.76	5.45	1.15	19.8	5.91	67	23	98	23	270	51
OCY46-1-07	0.11	19.6	0.15	2.34	4.69	0.86	19.0	5.92	68	24	104	25	281	53
OCY46-1-08	0.01	13.0	0.06	1.36	2.62	0.50	10.1	3.41	39	13.5	58	14.6	164	32
OCY46-1-09	0.01	13.5	0.13	2.04	3.74	0.67	13.7	4.11	46	15.7	64	15.6	176	33
OCY46-1-10	0.02	11.7	0.12	1.88	3.44	0.73	13.9	4.20	48	17.5	77	19.3	216	43
OCY46-1-11	1.50	17.6	0.64	4.46	4.79	0.78	16.9	5.18	60	21	93	23	258	51
OCY46-1-12	2.49	21.7	1.12	6.67	3.21	0.45	8.87	2.93	35	12.4	55	13.5	152	31
OCY46-1-14	37	135	14.7	73	26	4.59	51	13.3	135	46	190	46	522	101
OCY46-1-15	0.01	14.2	0.05	1.31	2.53	0.58	11.2	3.40	39	13.9	60	14.5	162	31
OCY46-1-16	0.15	12.2	0.12	1.25	2.67	0.52	10.5	3.39	40	15.3	67	17.0	201	41
OCY46-1-17	0.02	14.6	0.22	3.46	5.79	1.23	21	6.17	66	23	96	23	247	49
OCY46-1-18	0.06	14.0	0.05	0.79	1.21	0.25	4.44	1.63	20	7.92	36	9.61	116	25
OCY46-1-19	0.02	13.2	0.14	2.27	3.87	0.86	14.4	4.29	47	16.4	70	16.8	185	37
OCY46-1-20	0.02	16.9	0.10	1.65	3.14	0.47	12.5	3.86	45	16.7	75	18.8	216	43
OCY46-1-21	0.01	14.3	0.05	1.25	2.42	0.57	10.4	3.28	39	13.8	61	15.3	173	35
OCY46-1-22	0.01	12.6	0.04	0.73	1.72	0.39	7.76	2.55	30	11.1	51	12.6	146	29
OCY46-1-23	0.01	13.6	0.08	1.21	2.36	0.32	10.7	3.16	39	13.9	59	14.9	168	32

(continued)

Table 3.10 (continued)

Samples and analyzed spots	La	Ce	Pr	Nd	Sm	Eu	Gd	Tb	Dy	Ho	Er	Tm	Yb	Lu
OCY46-1-24	0.01	13.6	0.04	0.64	1.38	0.34	6.82	2.10	26	9.48	43	10.9	126	27
OCY46-1-25	0.01	15.4	0.02	0.51	1.10	0.26	4.65	1.74	22	8.63	41	11.0	135	28
OCY46-1-26	0.01	20	0.08	1.53	3.36	0.68	14.0	4.72	56	21	95	24	268	54
OCY46-1-27	0.13	15.9	0.09	1.02	1.98	0.40	8.93	2.90	37	13.8	64	15.8	184	38
OCY46-1-28	0.03	18.7	0.06	1.17	2.43	0.44	11.1	3.52	42	15.7	70	17.5	205	41
OCY46-1-29	15.6	60	6.20	31	9.22	1.67	18.7	5.67	67	25	111	27	307	62

Table 3.11 Zircon Lu–Hf isotopic data for the dated granitoid gneisses of the Jianping gneissic terrane

Samples and analyzed spots	Apparent $^{207}Pb/^{206}Pb$ ages (t_1)	$^{176}Yb/^{177}Hf$	$^{176}Lu/^{177}Hf$	$^{176}Hf/^{177}Hf$	±2σ	$(^{176}Hf/^{177}Hf)_{t1}$	εHf (0)	εHf (t_1)	T_{DM}	T_{DM}^{C} (t_1)	$f_{Lu/Hf}$	Crystallization ages (t_2)	εHf (t_2)
OCY31-2-1	2521	0.041433	0.000720	0.281341	0.000015	0.281306	–50.6	4.8	2647	2734	−0.98	2516	4.7
OCY31-2-2	2527	0.027436	0.000468	0.281331	0.000014	0.281308	−51.0	5.0	2643	2725	−0.99	2516	4.7
OCY31-2-3	2512	0.054026	0.000963	0.281377	0.000014	0.281331	−49.3	5.4	2615	2684	−0.97	2516	5.5
OCY31-2-4	2409	0.046058	0.000836	0.281344	0.000018	0.281305	−50.5	2.2	2651	2815	−0.97	2516	4.6
OCY31-2-7	2514	0.054998	0.001039	0.281358	0.000017	0.281309	−50.0	4.7	2645	2734	−0.97	2516	4.7
OCY31-2-8	2497	0.064793	0.001135	0.281360	0.000018	0.281305	−49.9	4.2	2650	2753	−0.97	2516	4.6
OCY31-2-10	2448	0.049079	0.000845	0.281373	0.000015	0.281334	−49.5	4.1	2612	2723	−0.97	2516	5.6
OCY31-2-12	2527	0.036736	0.000650	0.281354	0.000018	0.281323	−50.1	5.5	2625	2692	−0.98	2516	5.3
OCY31-2-13	2524	0.044321	0.000712	0.281373	0.000017	0.281339	−49.5	6.0	2603	2657	−0.98	2516	5.8
OCY31-2-14	2497	0.038036	0.000696	0.281284	0.000018	0.281251	−52.6	2.2	2723	2877	−0.98	2516	2.7
OCY31-2-18	2552	0.038828	0.000673	0.281353	0.000019	0.281320	−50.2	6.0	2628	2680	−0.98	2552	6.0
OCY31-2-20	2489	0.059010	0.001094	0.281303	0.000017	0.281251	−52.0	2.1	2725	2882	−0.97	2516	2.7
OCY31-2-21	2549	0.135140	0.002141	0.281555	0.000020	0.281451	−43.0	10.6	2447	2383	−0.94	2549	10.6
OCY31-2-23	2508	0.035919	0.000625	0.281337	0.000017	0.281307	−50.7	4.5	2646	2741	−0.98	2516	4.7
OCY31-2-25	2520	0.048431	0.000906	0.281338	0.000015	0.281295	−50.7	4.3	2663	2761	−0.97	2516	4.3
OCY31-2-26	2479	0.038736	0.000739	0.281334	0.000016	0.281299	−50.9	3.5	2658	2781	−0.98	2516	4.4
OCY31-2-27	2508	0.028798	0.000528	0.281328	0.000014	0.281302	−51.1	4.3	2652	2752	−0.98	2516	4.5
OCY31-2-29	2482	0.030840	0.000563	0.281321	0.000014	0.281294	−51.3	3.5	2663	2789	−0.98	2516	4.2
OCY31-2-31	2585	0.066327	0.001317	0.281370	0.000018	0.281305	−49.6	6.2	2649	2691	−0.96	2585	6.2
OCY31-2-32	2520	0.050168	0.000950	0.281279	0.000016	0.281234	−52.8	2.2	2747	2900	−0.97	2516	2.1
OCY33-1-2	2530	0.030904	0.000535	0.281287	0.000017	0.281262	−52.5	3.4	2707	2829	−0.98	2519	3.1
OCY33-1-3	2504	0.027933	0.000505	0.281266	0.000015	0.281242	−53.3	2.1	2734	2893	−0.98	2519	2.4

(continued)

Table 3.11 (continued)

Samples and analyzed spots	Apparent $^{207}Pb/^{206}Pb$ ages (t_1)	$^{176}Yb/^{177}Hf$	$^{176}Lu/^{177}Hf$	$^{176}Hf/^{177}Hf$	±2σ	$(^{176}Hf/^{177}Hf)_{t1}$	εHf (0)	εHf (t_1)	T_{DM}	T^C_{DM} (t_1)	$f_{Lu/Hf}$	Crystallization ages (t_2)	εHf (t_2)
OCY33-1-7	2446	0.028698	0.000581	0.281332	0.000014	0.281305	−50.9	3.0	2650	2790	−0.98	2519	4.7
OCY33-1-8	2448	0.020824	0.000431	0.281316	0.000015	0.281296	−51.5	2.7	2660	2808	−0.99	2519	4.4
OCY33-1-10	2519	0.022732	0.000427	0.281268	0.000015	0.281248	−53.2	2.6	2725	2869	−0.99	2519	2.6
OCY33-1-11	2441	0.024955	0.000510	0.281297	0.000015	0.281273	−52.2	1.7	2692	2866	−0.98	2519	3.5
OCY33-1-13	2497	0.019866	0.000380	0.281298	0.000016	0.281280	−52.1	3.3	2682	2811	−0.99	2519	3.8
OCY33-1-16	2518	0.026910	0.000502	0.281283	0.000013	0.281258	−52.7	3.0	2711	2845	−0.98	2519	3.0
OCY33-1-18	2456	0.022825	0.000409	0.281286	0.000016	0.281267	−52.6	1.9	2700	2870	−0.99	2519	3.3
OCY33-1-22	2427	0.030197	0.000513	0.281295	0.000017	0.281271	−52.2	1.3	2695	2881	−0.98	2519	3.4
OCY33-1-23	2502	0.022440	0.000395	0.281256	0.000019	0.281237	−53.6	1.9	2739	2905	−0.99	2519	2.3
OCY33-1-25	2512	0.043431	0.000711	0.281373	0.000021	0.281339	−49.5	5.7	2603	2666	−0.98	2519	5.9
OCY33-1-26	2440	0.021902	0.000430	0.281199	0.000019	0.281179	−55.6	−1.6	2818	3081	−0.99	2519	0.2
OCY33-1-27	2385	0.023589	0.000434	0.281265	0.000020	0.281245	−53.3	−0.5	2730	2969	−0.99	2519	2.5
OCY33-1-28	2460	0.031056	0.000626	0.281258	0.000017	0.281228	−53.6	0.6	2753	2954	−0.98	2519	1.9
OCY33-1-29	2463	0.028588	0.000476	0.281268	0.000019	0.281245	−53.2	1.3	2729	2913	−0.99	2519	2.5
OCY33-1-31	2498	0.017199	0.000356	0.281240	0.000018	0.281223	−54.2	1.3	2757	2938	−0.99	2519	1.8
OCY33-1-32	2443	0.031341	0.000602	0.281287	0.000016	0.281259	−52.5	1.3	2712	2897	−0.98	2519	3.0
OCY33-1-33	2449	0.044087	0.000784	0.281352	0.000015	0.281315	−50.2	3.4	2637	2765	−0.98	2519	5.0
OCY33-1-34	2503	0.031943	0.000541	0.281265	0.000016	0.281239	−53.3	2.0	2737	2899	−0.98	2519	2.3
OCY33-1-35	2436	0.045071	0.000786	0.281345	0.000016	0.281309	−50.4	2.9	2646	2788	−0.98	2519	4.8
OCY33-1-36	2470	0.042861	0.000883	0.281221	0.000021	0.281180	−54.8	−0.9	2821	3057	−0.97	2519	0.2
OCY33-1-37	2585	0.049065	0.000873	0.281402	0.000018	0.281359	−48.5	8.1	2575	2568	−0.97	2585	8.1
OCY33-1-38	2464	0.025634	0.000497	0.281251	0.000014	0.281227	−53.8	0.7	2753	2954	−0.99	2519	1.9

(continued)

Table 3.11 (continued)

Samples and analyzed spots	Apparent $^{207}Pb/^{206}Pb$ ages (t_1)	$^{176}Yb/^{177}Hf$	$^{176}Lu/^{177}Hf$	$^{176}Hf/^{177}Hf$	±2σ	$(^{176}Hf/^{177}Hf)_{t1}$	εHf (0)	εHf (t_1)	T_{DM}	T^{C}_{DM} (t_1)	$f_{Lu/Hf}$	Crystallization ages (t_2)	εHf (t_2)
CY31-2-1	2540	0.008860	0.000336	0.281316	0.000023	0.281299	−51.5	5.0	2655	2736	−0.99	2513	4.4
CY31-2-2	2395	0.022739	0.000794	0.281347	0.000018	0.281311	−50.4	2.0	2644	2813	−0.98	2513	4.7
CY31-2-3	2478	0.011246	0.000412	0.281482	0.000023	0.281462	−45.6	9.3	2437	2408	−0.99	2513	10.1
CY31-2-4	2487	0.010069	0.000387	0.281396	0.000018	0.281377	−48.7	6.5	2551	2596	−0.99	2513	7.1
CY31-2-5	2415	0.011870	0.000471	0.281324	0.000023	0.281302	−51.2	2.2	2653	2818	−0.99	2513	4.4
CY31-2-6	2411	0.013092	0.000444	0.281435	0.000026	0.281415	−47.3	6.1	2502	2565	−0.99	2513	8.4
CY31-2-7	2540	0.007701	0.000258	0.281328	0.000032	0.281315	−51.1	5.5	2634	2700	−0.99	2513	4.9
CY31-2-8	2432	0.014499	0.000526	0.281373	0.000024	0.281349	−49.5	4.2	2590	2700	−0.98	2513	6.1
CY31-2-9	2538	0.029887	0.001010	0.281399	0.000023	0.281350	−48.6	6.7	2589	2623	−0.97	2513	6.1
CY31-2-10	2500	0.035380	0.001377	0.281406	0.000027	0.281340	−48.3	5.5	2604	2672	−0.96	2513	5.8
CY31-2-11	2420	0.013913	0.000598	0.281391	0.000014	0.281364	−48.8	4.5	2571	2674	−0.98	2513	6.6
CY31-2-12	2455	0.016185	0.000548	0.281355	0.000021	0.281329	−50.1	4.1	2616	2728	−0.98	2513	5.4
CY31-2-13	2522	0.026715	0.001010	0.281386	0.000021	0.281337	−49.0	5.9	2606	2662	−0.97	2513	5.7
CY31-2-14	2417	0.019701	0.000666	0.281381	0.000024	0.281350	−49.2	3.9	2589	2707	−0.98	2513	6.1
CY31-2-15	2480	0.008210	0.000305	0.281326	0.000026	0.281311	−51.1	4.0	2639	2751	−0.99	2513	4.8
CY31-2-16	2507	0.026669	0.000994	0.281345	0.000016	0.281298	−50.5	4.1	2660	2764	−0.97	2513	4.3
CY31-2-17	2479	0.011152	0.000422	0.281332	0.000019	0.281312	−50.9	4.0	2639	2751	−0.99	2513	4.8
CY31-2-18	2451	0.012791	0.000443	0.281383	0.000026	0.281362	−49.1	5.1	2572	2657	−0.99	2513	6.5
CY31-2-19	2443	0.014420	0.000610	0.281348	0.000022	0.281320	−50.3	3.5	2630	2758	−0.98	2513	5.0
CY31-2-20	2491	0.011811	0.000419	0.281357	0.000027	0.281337	−50.0	5.2	2605	2685	−0.99	2513	5.7
CY31-2-21	2425	0.008977	0.000324	0.281350	0.000020	0.281335	−50.3	3.6	2608	2736	−0.99	2513	5.6
CY31-2-22	2454	0.012520	0.000425	0.281383	0.000022	0.281363	−49.1	5.2	2571	2653	−0.99	2513	6.6

(continued)

Table 3.11 (continued)

Samples and analyzed spots	Apparent $^{207}Pb/^{206}Pb$ ages (t_1)	$^{176}Yb/^{177}Hf$	$^{176}Lu/^{177}Hf$	$^{176}Hf/^{177}Hf$	±2σ	$(^{176}Hf/^{177}Hf)_{t1}$	εHf (0)	εHf (t_1)	T_{DM}	T_{DM}^{C} (t_1)	$f_{Lu/Hf}$	Crystallization ages (t_2)	εHf (t_2)
CY31-2-23	2447	0.017604	0.000565	0.281386	0.000028	0.281360	−49.0	5.0	2575	2664	−0.98	2513	6.5
CY31-2-24	2450	0.010453	0.000408	0.281371	0.000030	0.281351	−49.6	4.7	2586	2681	−0.99	2513	6.2
CY31-2-25	2444	0.019258	0.000747	0.281394	0.000023	0.281359	−48.7	4.9	2578	2669	−0.98	2513	6.4
CY31-2-26	2525	0.039024	0.001330	0.281436	0.000025	0.281371	−47.3	7.2	2559	2582	−0.96	2513	6.9
CY31-2-27	2517	0.009233	0.000325	0.281407	0.000027	0.281391	−48.3	7.7	2532	2543	−0.99	2513	7.6
CY31-2-28	2420	0.012012	0.000476	0.281339	0.000031	0.281317	−50.7	2.8	2633	2781	−0.99	2513	4.9
CY31-2-29	2513	0.033366	0.001097	0.281409	0.000028	0.281356	−48.2	6.4	2580	2625	−0.97	2513	6.4
CY31-2-30	2522	0.025530	0.000943	0.281384	0.000024	0.281338	−49.1	5.9	2604	2660	−0.97	2513	5.7
CY31-2-31	2453	0.015866	0.000617	0.281318	0.000020	0.281289	−51.4	2.6	2671	2821	−0.98	2513	4.0
CY31-2-32	2513	0.043781	0.001591	0.281425	0.000026	0.281348	−47.6	6.1	2592	2643	−0.95	2513	6.1
CY31-2-33	2431	0.014950	0.000517	0.281403	0.000020	0.281379	−48.4	5.3	2550	2633	−0.98	2513	7.1
CY31-2-34	2477	0.020452	0.000787	0.281366	0.000029	0.281329	−49.7	4.6	2618	2713	−0.98	2513	5.4
CY46-1-1	2514	0.014832	0.000497	0.281368	0.000023	0.281344	−49.7	6.0	2596	2653	−0.99	2506	5.8
CY46-1-2	2481	0.012955	0.000453	0.281246	0.000016	0.281224	−54.0	0.9	2757	2949	−0.99	2506	1.5
CY46-1-3	2513	0.012039	0.000418	0.281299	0.000017	0.281279	−52.1	3.6	2683	2802	−0.99	2506	3.5
CY46-1-4	2522	0.008818	0.000303	0.281230	0.000016	0.281216	−54.5	1.6	2767	2939	−0.99	2506	1.2
CY46-1-5	2448	0.011304	0.000372	0.281314	0.000017	0.281296	−51.6	2.7	2660	2808	−0.99	2506	4.1
CY46-1-6	2446	0.014382	0.000506	0.281292	0.000018	0.281268	−52.3	1.7	2699	2874	−0.98	2506	3.0
CY46-1-7	2439	0.012775	0.000445	0.281290	0.000026	0.281270	−52.4	1.6	2696	2875	−0.99	2506	3.1
CY46-1-8	2457	0.021921	0.000653	0.281345	0.000021	0.281314	−50.5	3.6	2637	2761	−0.98	2506	4.7
CY46-1-9	2487	0.009131	0.000337	0.281319	0.000016	0.281303	−51.4	3.9	2650	2765	−0.99	2506	4.3
CY46-1-10	2481	0.016907	0.000557	0.281322	0.000021	0.281296	−51.3	3.5	2661	2786	−0.98	2506	4.1

(continued)

Table 3.11 (continued)

Samples and analyzed spots	Apparent $^{207}Pb/^{206}Pb$ ages (t_1)	$^{176}Yb/^{177}Hf$	$^{176}Lu/^{177}Hf$	$^{176}Hf/^{177}Hf$	±2σ	$(^{176}Hf/^{177}Hf)_{t1}$	εHf (0)	εHf (t_1)	T_{DM}	T^C_{DM} (t_1)	$f_{Lu/Hf}$	Crystallization ages (t_2)	εHf (t_2)
CY46-1-11	2520	0.011404	0.000323	0.281296	0.000020	0.281280	−52.2	3.8	2681	2794	−0.99	2506	3.5
CY46-1-12	2383	0.009130	0.000315	0.281259	0.000019	0.281244	−53.5	−0.6	2730	2971	−0.99	2506	2.2
CY46-1-13	1862	0.009806	0.000303	0.281330	0.000022	0.281319	−51.0	−9.9	2633	3156	−0.99	2506	4.8
CY46-1-14	2411	0.008322	0.000284	0.281318	0.000024	0.281305	−51.4	2.2	2649	2815	−0.99	2506	4.4
CY46-1-15	2516	0.008523	0.000292	0.281280	0.000018	0.281266	−52.8	3.2	2700	2829	−0.99	2506	3.0
CY46-1-16	2518	0.009535	0.000338	0.281305	0.000021	0.281288	−51.9	4.1	2670	2776	−0.99	2506	3.8
CY46-1-17	2561	0.030770	0.001109	0.281313	0.000020	0.281259	−51.6	4.0	2712	2813	−0.97	2561	4.0
CY46-1-18	2468	0.010527	0.000367	0.281270	0.000017	0.281252	−53.1	1.6	2719	2894	−0.99	2506	2.5
CY46-1-19	2509	0.028539	0.000975	0.281301	0.000021	0.281254	−52.0	2.7	2719	2860	−0.97	2506	2.6
CY46-1-20	2392	0.027671	0.000968	0.281297	0.000022	0.281253	−52.1	−0.1	2724	2946	−0.97	2506	2.5
CY46-1-21	2506	0.006694	0.000208	0.281318	0.000018	0.281308	−51.4	4.5	2644	2742	−0.99	2506	4.5
CY46-1-22	2469	0.013523	0.000471	0.281269	0.000025	0.281247	−53.1	1.5	2727	2905	−0.99	2506	2.3
CY46-1-23	2683	0.005714	0.000165	0.281233	0.000023	0.281225	−54.4	5.6	2753	2804	−1.00	2506	1.5
CY46-1-24	2503	0.010655	0.000386	0.281243	0.000026	0.281225	−54.1	1.5	2756	2932	−0.99	2506	1.5
CY46-1-25	2494	0.010205	0.000318	0.281299	0.000020	0.281284	−52.1	3.4	2675	2803	−0.99	2506	3.6
OCY37-1-3	2539	0.060061	0.001074	0.281391	0.000015	0.281339	−48.8	6.4	2603	2646	−0.97	2527	6.1
OCY37-1-4	2478	0.007627	0.000125	0.281334	0.000014	0.281328	−50.9	4.5	2617	2715	−1.00	2527	5.7
OCY37-1-10	2404	0.035961	0.000563	0.281309	0.000012	0.281284	−51.7	1.3	2679	2868	−0.98	2527	4.1
OCY37-1-11	2415	0.039947	0.000738	0.281331	0.000018	0.281297	−51.0	2.0	2662	2830	−0.98	2527	4.5
OCY37-1-12	2411	0.040637	0.000755	0.281331	0.000015	0.281296	−51.0	1.9	2663	2835	−0.98	2527	4.5
OCY37-1-13	2511	0.048297	0.000931	0.281312	0.000017	0.281268	−51.6	3.2	2701	2829	−0.97	2527	3.5
OCY37-1-14	2522	0.047195	0.000887	0.281306	0.000017	0.281263	−51.9	3.3	2707	2832	−0.97	2527	3.4

(continued)

Table 3.11 (continued)

Samples and analyzed spots	Apparent $^{207}Pb/^{206}Pb$ ages (t_1)	$^{176}Yb/^{177}Hf$	$^{176}Lu/^{177}Hf$	$^{176}Hf/^{177}Hf$	±2σ	$(^{176}Hf/^{177}Hf)_{t1}$	εHf (0)	εHf (t_1)	T_{DM}	T^C_{DM} (t_1)	$f_{Lu/Hf}$	Crystallization ages (t_2)	εHf (t_2)
OCY37-1-15	2524	0.032920	0.000713	0.281307	0.000018	0.281272	−51.8	3.6	2693	2809	−0.98	2527	3.7
OCY37-1-17	2543	0.053448	0.000883	0.281336	0.000020	0.281293	−50.8	4.8	2665	2748	−0.97	2527	4.4
OCY37-1-18	2588	0.069067	0.001234	0.281425	0.000018	0.281364	−47.6	8.4	2568	2554	−0.96	2588	8.4
OCY37-1-19	2599	0.063226	0.001339	0.281355	0.000023	0.281288	−50.1	5.9	2672	2720	−0.96	2599	5.9
OCY37-1-20	2523	0.053586	0.001001	0.281283	0.000018	0.281235	−52.7	2.3	2746	2895	−0.97	2527	2.4
OCY37-1-22	2591	0.034303	0.000631	0.281352	0.000016	0.281321	−50.2	6.9	2626	2650	−0.98	2590	6.9
OCY37-1-23	2590	0.055345	0.001051	0.281349	0.000016	0.281297	−50.3	6.1	2659	2705	−0.97	2591	6.1
OCY37-1-25	2518	0.059228	0.001232	0.281325	0.000016	0.281266	−51.2	3.3	2704	2828	−0.96	2527	3.5
OCY37-1-26	2551	0.046314	0.000965	0.281364	0.000017	0.281317	−49.8	5.8	2633	2688	−0.97	2527	5.3
OCY37-1-29	2501	0.045354	0.000854	0.281340	0.000018	0.281299	−50.6	4.1	2658	2764	−0.97	2527	4.6
OCY37-1-30	2457	0.055941	0.001025	0.281335	0.000022	0.281287	−50.8	2.6	2676	2823	−0.97	2527	4.2
OCY46-1-1	2555	0.052633	0.000873	0.281355	0.000017	0.281312	−50.1	5.8	2639	2696	−0.97	2532	5.3
OCY46-1-2	2526	0.042421	0.000734	0.281304	0.000018	0.281269	−51.9	3.5	2698	2816	−0.98	2532	3.7
OCY46-1-5	2528	0.025433	0.000429	0.281284	0.000019	0.281263	−52.6	3.4	2704	2827	−0.99	2532	3.5
OCY46-1-6	2478	0.053128	0.000892	0.281320	0.000023	0.281278	−51.3	2.8	2687	2829	−0.97	2532	4.0
OCY46-1-8	2533	0.028740	0.000497	0.281272	0.000019	0.281248	−53.0	3.0	2725	2858	−0.99	2532	2.9
OCY46-1-9	2514	0.030904	0.000544	0.281259	0.000018	0.281233	−53.5	2.0	2745	2906	−0.98	2532	2.4
OCY46-1-10	2535	0.033516	0.000606	0.281325	0.000019	0.281296	−51.2	4.7	2661	2748	−0.98	2532	4.7
OCY46-1-11	2536	0.036525	0.000677	0.281321	0.000019	0.281288	−51.3	4.5	2671	2764	−0.98	2532	4.4
OCY46-1-15	2535	0.021083	0.000406	0.281265	0.000017	0.281245	−53.3	2.9	2728	2863	−0.99	2532	2.9
OCY46-1-16	2526	0.037083	0.000709	0.281334	0.000017	0.281300	−50.9	4.7	2656	2745	−0.98	2532	4.8
OCY46-1-17	2539	0.030163	0.000561	0.281306	0.000019	0.281279	−51.8	4.2	2683	2784	−0.98	2532	4.1

(continued)

Table 3.11 (continued)

Samples and analyzed spots	Apparent $^{207}Pb/^{206}Pb$ ages (t_1)	$^{176}Yb/^{177}Hf$	$^{176}Lu/^{177}Hf$	$^{176}Hf/^{177}Hf$	±2σ	$(^{176}Hf/^{177}Hf)_{t1}$	εHf (0)	εHf (t_1)	T_{DM}	T^C_{DM} (t_1)	$f_{Lu/Hf}$	Crystallization ages (t_2)	εHf (t_2)
OCY46-1-19	2551	0.032926	0.000605	0.281337	0.000023	0.281307	−50.7	5.5	2645	2710	−0.98	2532	5.1
OCY46-1-20	2520	0.036249	0.000657	0.281262	0.000024	0.281230	−53.4	2.1	2749	2907	−0.98	2532	2.3
OCY46-1-23	2536	0.029389	0.000535	0.281269	0.000024	0.281243	−53.2	2.9	2731	2867	−0.98	2532	2.8
OCY46-1-25	2516	0.015666	0.000336	0.281271	0.000017	0.281255	−53.1	2.8	2715	2854	−0.99	2532	3.2
OCY46-1-26	2532	0.044339	0.000883	0.281299	0.000016	0.281256	−52.1	3.3	2715	2840	−0.97	2532	3.3
OCY46-1-28	2521	0.032522	0.000588	0.281285	0.000020	0.281257	−52.6	3.0	2713	2847	−0.98	2532	3.3
OCY46-1-29	2526	0.044032	0.000814	0.281279	0.000019	0.281240	−52.8	2.5	2738	2882	−0.98	2532	2.6

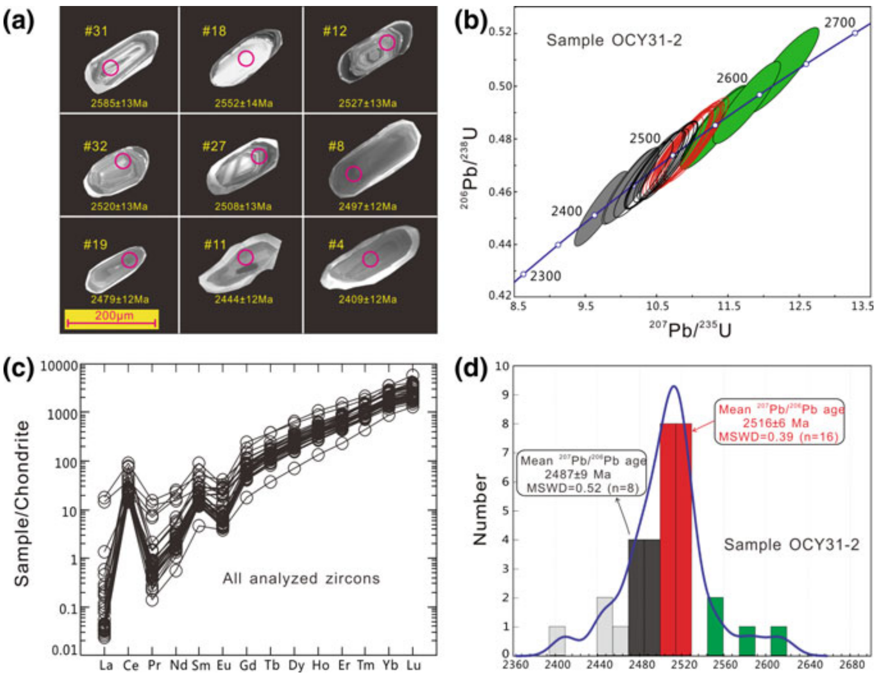

Fig. 3.28 Internal structures, age data, and rare earth element pattern of zircon grains from the tonalitic gneiss sample OCY31-2 (high magnesium group). **a** CL images of representative zircon grains showing internal structures and analyzed locations. Numbers are spot locations in Table 3.10. **b** Concordia diagram showing all analyzed spots. **c** Chondrite-normalized REE patterns for all the analyzed zircon spots. **d** Histogram of the apparent $^{207}Pb/^{206}Pb$ ages and calculated weighted mean ages of different zircon groups

concordia, yielding apparent $^{207}Pb/^{206}Pb$ ages ranging between 2614 ± 13 Ma and 2409 ± 12 Ma (Fig. 3.28b and Table 3.9). They show a wide range of Th (19–609 ppm) and U (40–984 ppm) contents, but the Th/U ratios are all higher than 0.20 (0.20–1.72). Rare earth elements of the analyzed zircon grains show consistent normalized patterns with positive Ce anomalies, moderately negative Eu anomalies and fractionated HREE patterns (Fig. 3.28c and Table 3.10). These suggest that the zircon grains were originally formed by magmatic crystallization [72]. On the probability density plot (Fig. 3.28d), these analyses define a major age peak with several minor peaks, and they are subdivided into four age groups as follows.

The oldest age group consists of four analyses on dark oscillatory zoned domains or bright structureless cores (e.g., spots #31 and #18). They have apparent $^{207}Pb/^{206}Pb$ ages from 2614 ± 13 Ma to 2549 ± 16 Ma, which are synchronous with the formation ages of supracrustal rock sequences in the JPGT (~2550–2555 Ma, and up to 2615 Ma) [43]. Considering the intrusive relationship between the tonalitic gneisses and supracrustal rocks (Fig. 3.19c), these old zircons could represent inherited/xenocrystic grains captured from either the source region or the wall-rocks during emplacement.

The major age peak is defined by sixteen analyses of euhedral cores with clear oscillatory zonings (e.g., spots #12, #32 and #27, Fig. 3.28a). They show a limited range of apparent $^{207}Pb/^{206}Pb$ ages between 2527 ± 13 Ma and 2520 ± 13 Ma, yielding a weighted mean age of 2516 ± 6 Ma (MSWD = 0.39; Fig. 3.28d). Considering the magmatic zircon-like oscillatory zonings and REE patterns as well as high Th/U ratios (0.20–1.34), the age of 2516 ± 6 Ma is proposed to be close to the crystallization age of the magmatic precursor.

The third age group is composed of eight analyses, which were conducted on dark cores that are blurred or lack magmatic zonings (e.g., spots #8 and #19, Fig. 3.28a). Integrated with the high Th/U ratios (0.24–1.72) and magmatic zircon-like REE patterns, zircon grains of this group might represent original magmatic zircons that underwent subsequent Pb loss [13]. They have apparent $^{207}Pb/^{206}Pb$ ages of 2497 ± 12 to 2475 ± 12 Ma, yielding a weighted mean age of 2487 ± 9 Ma (MSWD = 0.52). The fourth age group is defined by data from the dark cores with or without internal zoned structures (e.g., spots #4 and #11, Fig. 3.28a). These domains show the youngest apparent $^{207}Pb/^{206}Pb$ ages from 2465 ± 13 Ma to 2409 ± 12 Ma (Fig. 3.28d). These younger ages are within error of with the ~2485 Ma granulite facies metamorphism and ~2450–2401 Ma retrograde events in the JPGT [43].

Twenty Lu–Hf isotopic analyses were obtained from the spots where LA-ICPMS analyses were carried out (Table 3.11). When the data are calculated at the apparent $^{207}Pb/^{206}Pb$ ages (t_1), they show similar $^{176}Hf/^{177}Hf(t_1)$ ratios of 0.281234–0.281451. Except for the three analyses on inherited/xenocrystic zircon grains (#18, #21 and #31), the other analyses were calculated at the crystallization age of sample OCY31-2 (2516 Ma, t_2), yielding positive $\varepsilon Hf(t_2)$ values of +2.1 to +5.8 and $T_{DM}(Hf)$ ages of 2747–2603 Ma (Fig. 3.29a). When calculated at the apparent $^{207}Pb/^{206}Pb$ ages (t_1) (2552, 2549 and 2585 Ma), the three older zircon grains yield $\varepsilon Hf(t_1)$ values and $T_{DM}(Hf)$ ages from +6.0 to +10.6 and 2649–2447 Ma, respectively.

Sample OCY33-1 (HMG)

Most zircon grains from the sample OCY33-1 display stubby (e.g., spot #23) or oval (e.g., spot #2) shapes with lengths and length/width ratios ranging from 100 to 180 μm and 1:1 to 1.5:1, respectively (Fig. 3.30a). Minor zircon grains exhibit elongated shapes with lengths of 150–200 μm and length/width ratios of ~2:1 (e.g., spot #24). Cathodoluminescence images show core-rim structures. The cores are either dark oscillatory zoned (e.g., spots #16 and #3) or dark structureless (e.g., spots #13 and #24) domains, which are surrounded by bright thin rims. Some cores possess eroded to irregular shapes (e.g., spots #7 and #27), suggesting the effects of metamorphism or hydrothermal alteration. A total of thirty-eight analyses were carried out on thirty-four zircon grains. All of them plot on or close to the concordia, yielding apparent $^{207}Pb/^{206}Pb$ ages ranging between 2585 ± 15 Ma and

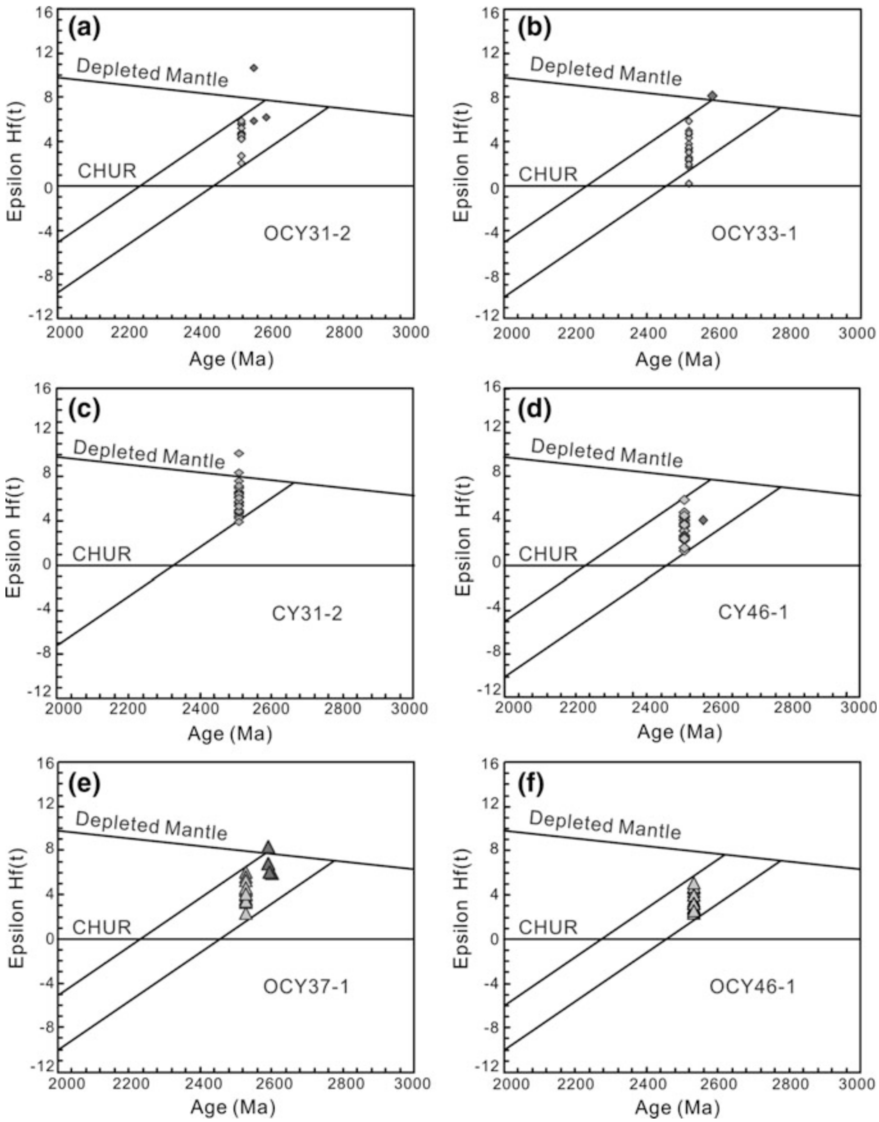

Fig. 3.29 Plots of zircon εHf(t) values versus formation ages for representative granitoid gneiss samples of the JPGT: **a**, **b**, **c** and **d** HMG tonalitic (OCY31-2, CY31-2 and CY46-1) and granodioritic (OCY33-1) gneisses; **e** and **f** LMG granodioritic (OCY37-1) and tonalitic (OCY46-1) gneisses. Note that the Lu–Hf isotopic data of inherited/xenocrystic zircon grains are calculated at their respective apparent $^{207}Pb/^{206}Pb$ ages, whereas those of the other analyzed spots are calculated at the magmatic crystallization age of each sample

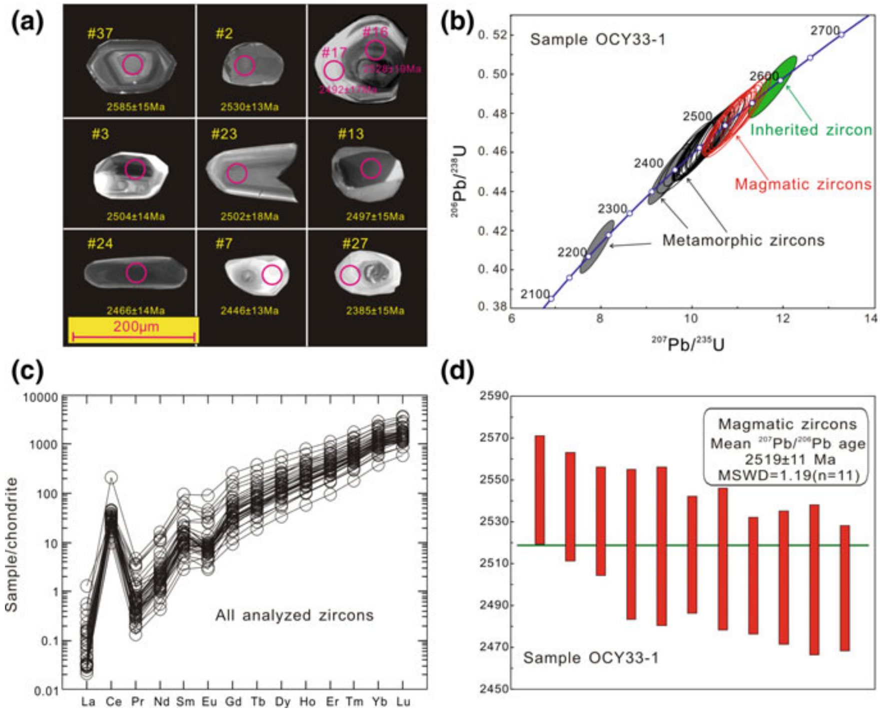

Fig. 3.30 Internal structures, age data, and the rare earth element pattern of zircon grains from the HMG granodioritic gneiss sample OCY33-1. **a** CL images of representative zircon grains showing internal structures and analyzed locations. Numbers are spot locations in Table 3.10. **b** Concordia diagram showing all analyzed spots. **c** Chondrite-normalized REE patterns for all the analyzed zircon spots. **d** Weighted average $^{207}Pb/^{206}Pb$ age for the eleven analyses of magmatic zircon grains

2224 ± 16 Ma (Fig. 3.30b and Table 3.9). The analyzed zircon grains show consistent chondrite-normalized REE patterns with positive Ce anomalies, moderately negative Eu anomalies and steep HREE patterns (Fig. 3.30c and Table 3.10), implying a magmatic origin [72]. Th and U contents vary widely from 10 to 965 ppm and 15 to 1434 ppm, respectively, yielding high Th/U values (mostly of 0.24–2.70, and only spot #28 shows a low ratio of 0.09). Spot #37 was analyzed on a dark oscillatory zoned domain, yielding the oldest apparent $^{207}Pb/^{206}Pb$ age of 2585 ± 15 Ma. This age deviates significantly from the age mode of the analyzed zircon grains, and is slightly older than the major formation ages of JPGT supracrustal rocks (2555–2550 Ma, and upper to ~2600 Ma, [43]. Given that the HMG samples show intrusive relationship with the supracrustal rocks (Fig. 3.19c), the age of ~2585 Ma is interpreted to represent the age of zircon grains captured either from the source region or trapped from the wall-rocks during magma ascent.

Based on the internal structures of zircon grains, the remaining thirty-seven analyses can be subdivided into three groups as follows. The first age group is defined by eleven analyses, which were obtained from oscillatory zoned domains (e.g., spots #16 and #23). They have apparent $^{207}Pb/^{206}Pb$ ages between 2545 ± 13 Ma and 2498 ± 15 Ma, which yield a weighted mean age of 2519 ± 11 Ma (MSWD = 1.19, Fig. 3.30d). Given the high Th/U ratios (0.36–2.06) and magmatic zircon-like REE patterns, the weighted mean age of 2519 ± 11 Ma is considered as the crystallization age of the magmatic precursor of sample OCY33-1, which is within error of that of the tonalitic gneiss sample OCY31-2 (2516 ± 6 Ma). The second age group is made up of twenty-three analyses on either dark structureless cores (e.g., spots #13 and #24) or bight thick rims (e.g., spots #7 and #17). They possess high Th/U ratios (mostly of 0.29–2.70, but 0.09 for spot #28) and chondrite-normalized REE patterns similar to those of magmatic zircons (Fig. 3.30c). Some of the oscillatory zoned cores (e.g., spot #16, 2528 ± 16 Ma) are enveloped by bright rims (e.g., spot #17, 2492 ± 19 Ma), suggesting that they were originally formed by magmatic crystallization, but subjected to metamictization (dark cores) or recrystallization (bright rims). They show apparent $^{207}Pb/^{206}Pb$ ages between 2497 ± 15 Ma and 2423 ± 20 Ma, which is nearly synchronous with the ~2485 Ma granulite facies metamorphism and the ~2450–2401 Ma retrograde events of the JPGT [43]. Three analyses on bright rims or dark cores without internal structures (e.g., spot #27) yield younger apparent $^{207}Pb/^{206}Pb$ ages of 2396 ± 13 Ma to 2224 ± 16 Ma. They have Th and U of 28–183 ppm and 29–749 ppm, respectively, with high Th/U ratios of 0.24–0.96. Regionally, metamorphism in the upper amphibolite facies and synchronous plutonism at ~2460–2350 Ma were recorded in the North Chaoyang area [42]. Similarly, multiple episodes of tectonothermal events between 2460 and 2043 Ma are recorded in the NCFY-GGB [89, 90]. Therefore, the younger ages could represent the effects of these Paleoproterozoic tectonothermal events.

A total of twenty-four Lu–Hf isotopic analyses were obtained from the domains where U–Pb isotopic chronological analyses were performed (Table 3.11). These zircon grains show similar $^{176}Hf/^{177}Hf$ (t_1) ratios between 0.281179 and 0.281359 when calculated at the apparent $^{207}Pb/^{206}Pb$ ages (t_1). Except for one analysis on the inherited/xenocrystic zircon grain (spot #37), the other isotopic data were calculated at the crystallization age of 2519 Ma (t_2). They yield positive εHf(t_2) values mostly of +1.8 to +5.9 and T_{DM}(Hf) ages of 2757–2603 Ma (Fig. 3.29b). Two spots (#26 and #36) show lower εHf(t_2) values of 0.2 with higher T_{DM}(Hf) of 2821–2818 Ma. The ancient zircon grain (spot #37), calculated at its apparent $^{207}Pb/^{206}Pb$ ages (t_1) (2585 Ma), shows εHf(t_1) value and T_{DM}(Hf) age of +8.1 and 2575 Ma, respectively.

Sample CY31-2 (HMG)

LA-ICPMS zircon U-Pb isotopic dating of the tonalitic gneiss sample CY31-2 yields a weighted mean $^{207}Pb/^{206}Pb$ age of 2513 ± 10 Ma (MSWD = 1.5), which was interpreted as the crystallization age [43]. Lu–Hf isotopic data were collected simultaneously by LA-MC-ICPMS for the dated thirty-four spots (Table 3.11). When calculated at the apparent $^{207}Pb/^{206}Pb$ ages (t_1), they show limited range of $^{176}Hf/^{177}Hf(t_1)$ values of 0.281289–0.281462. This implies that the Lu–Hf isotopic systematics were not significantly disturbed by later tectonothermal events, though intense Pb loss [43]. When calculated at the crystallization age (t_2, 2513 Ma), all the analyzed zircon spots yield positive εHf(t_2) values of +4.0 to +10.1 (mostly of +4.0 to +7.6) and T_{DM}(Hf) from 2671 to 2437 Ma (Fig. 3.29c).

Sample CY46-1 (HMG)

LA-ICPMS zircon U-Pb isotopic dating of the tonalitic gneiss sample CY46-1 yields an upper intercept age of 2506 ± 12 Ma (MSWD = 2.5), which was interpreted as its crystallization age [43]. All the dated twenty-five spots were synchronously analyzed for Lu–Hf isotopes (Table 3.11). When calculated at the apparent ^{207}Pb/^{206}Pb ages (t_1), they have ^{176}Hf/^{177}Hf(t_1) values ranging between 0.281216 and 0.281344. Spot #17 shows an older apparent ^{207}Pb/^{206}Pb age of 2561 ± 13 Ma, which was considered to be the age of inherited/xenocrystic zircons. It has εHf(t_1) value and T_{DM}(Hf) age of +4.0 and 2712 Ma, respectively (Fig. 3.29d). The other twenty-four analyses were calculated at the crystallization age of 2506 Ma (t_2), and they yield positive εHf(t_2) values from +1.2 to +5.8 and T_{DM}(Hf) of 2767–2596 Ma.

Sample OCY37-1 (LMG)

Zircon grains separated from the granodioritic gneiss sample OCY37-1 show either elongated or stubby shapes with lengths and length/width ratios of 80–150 μm and 1:1–2:1, respectively (Fig. 3.31a). Cathodoluminescence images reveal that most of the zircon grains possess core-rim structures, and some of them are bright structureless crystals. The cores are generally oscillatory zoned domains, though some are dark structureless. Thirty analyses were performed on thirty zircon domains, and most of them plot on or close to the concordia, except for three analyses (spots #7, #8 and #27) that deviate far from the concordia and are rejected during the age calculation. The other twenty-seven analyses yield apparent ^{207}Pb/^{206}Pb ages ranging between 2601 ± 23 Ma and 2394 ± 27 Ma (spot #5) (Table 3.9). They have Th and U contents of 17–321 ppm and 31–1400 ppm, respectively, with Th/U ratios mostly higher than 0.10 (0.10–2.97, except for spots #5 with a low ratio of 0.07). They define three age peaks on the probability density plot. Integrated with the internal structures of zircon grains, these analyses can be subdivided into three age groups as follows (Fig. 3.31a, b).

The oldest age group consists of six analyses on oscillatory zoned or blurred zoned cores (spots #5, #16, #18, #19, #22 and #23) (Fig. 3.31a–c). They have low Th of 17–141 ppm but high U of 58–518 ppm, with Th/U ratios mostly of 0.17–0.84 (with one exception of 0.07 for spot #5). They show apparent ^{207}Pb/^{206}Pb ages of 2601 ± 23 Ma to 2582 ± 28 Ma, yielding a weighted mean age of 2591 ± 21 Ma (MSWD = 0.075) and an upper intercept age of 2590 ± 24 Ma (MSWD = 0.051). This age, together with one older age of 2585 ± 15 Ma recorded by sample OCY33-1, define ages older than those of the main supracrustal rocks (2555–2550 Ma) [43]. Considering that the biotite plagioclase gneisses (LMG) show intrusive relationships with the supracrustal rocks (Fig. 3.19f), the age

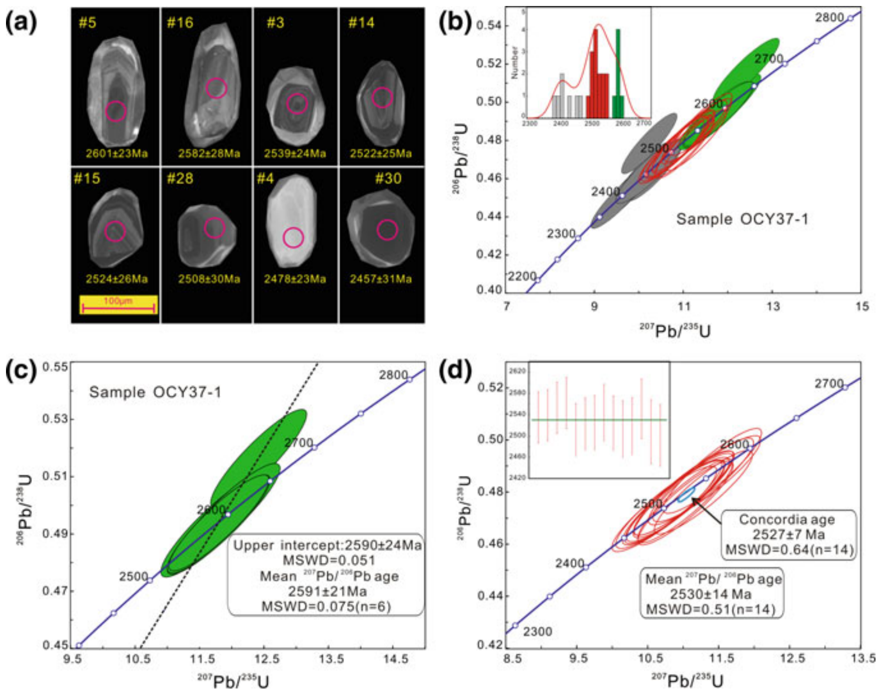

Fig. 3.31 Internal structures and age data of zircon grains from the LMG granodioritic gneiss sample OCY37-1. **a** CL images of representative zircon grains showing internal structures and analyzed locations. Numbers are spot locations in Table 3.10. **b** Concordia diagram showing all analyzed spots. The inset is a histogram of the apparent $^{207}Pb/^{206}Pb$ ages. **c** Concordia diagram of the six inherited zircon grains (filled with green color). **d** Concordia diagram for the fourteen magmatic zircon grains showing concordia and weighted average $^{207}Pb/^{206}Pb$ ages

of 2591 Ma might represent those of zircon grains entrained from the source region or trapped during magma ascent.

The second age group is defined by fourteen analyses of cores with clear oscillatory zonings (e.g., spots #3 and #28). They show apparent $^{207}Pb/^{206}Pb$ ages ranging between 2562 ± 24 Ma and 2501 ± 29 Ma, yielding a weighted mean age of 2530 ± 14 Ma (MSWD = 0.51) and a concordia age of 2527 ± 7 Ma (MSWD = 0.64) (Fig. 3.31d). These analyzed spots have Th and U from 62 to 321 ppm and from 77 to 325 ppm, respectively, with high Th/U ratios of 0.41–1.26. Considering the oscillatory zonings (Fig. 3.31a), the age of 2527 ± 7 Ma can be taken to be close to the crystallization age of the magmatic precursor.

Seven analyses constitute the third age group (spots #1, #4, #10, #11, #12, #24 and #30). These data were obtained from either bright or dark structureless domains (e.g., spots #4 and #30). Th and U contents range from 69 to 235 ppm and 31 to 1400 ppm, yielding generally high Th/U ratios (>0.10). They have apparent $^{207}Pb/^{206}Pb$ ages from 2478 ± 23 Ma to 2394 ± 27 Ma (Fig. 3.31b). These ages may register the effects of ~2485 Ma granulite facies metamorphism and ~2450–2401 Ma retrograde events of the JPGT [43].

Eighteen Lu–Hf isotopic analyses were obtained from the domains where U–Pb isotopic analyses were carried out (Table 3.11). When calculated at the respective apparent $^{207}Pb/^{206}Pb$ ages (t_1), they show similar $^{176}Hf/^{177}Hf(t_1)$ ratios between 0.281235 and 0.281364. Four analyses were performed on the inherited/xenocrystic zircon grains (spots #18, #19, #22 and #23), yielding εHf(t_1) values and T_{DM}(Hf) of +5.9 to +8.4 and 2672–2568 Ma, respectively. The other fourteen isotopic data were calculated at the crystallization age (2527 Ma, t_2), showing positive εHf(t_2) of +2.4 to +6.1 and T_{DM}(Hf) from 2746 Ma to 2603 Ma (Fig. 3.29e).

Sample OCY46-1 (LMG)

Most zircon grains from the tonalitic gneiss sample OCY46-1 display stubby or oval shapes, and have lengths and length/width ratios from 150 to 200 μm and 1:1 to 1.5:1 (Fig. 3.32a), though minor elongated grains (e.g., spot #22). Cathodoluminescence images reveal mostly magmatic zircon-like oscillatory

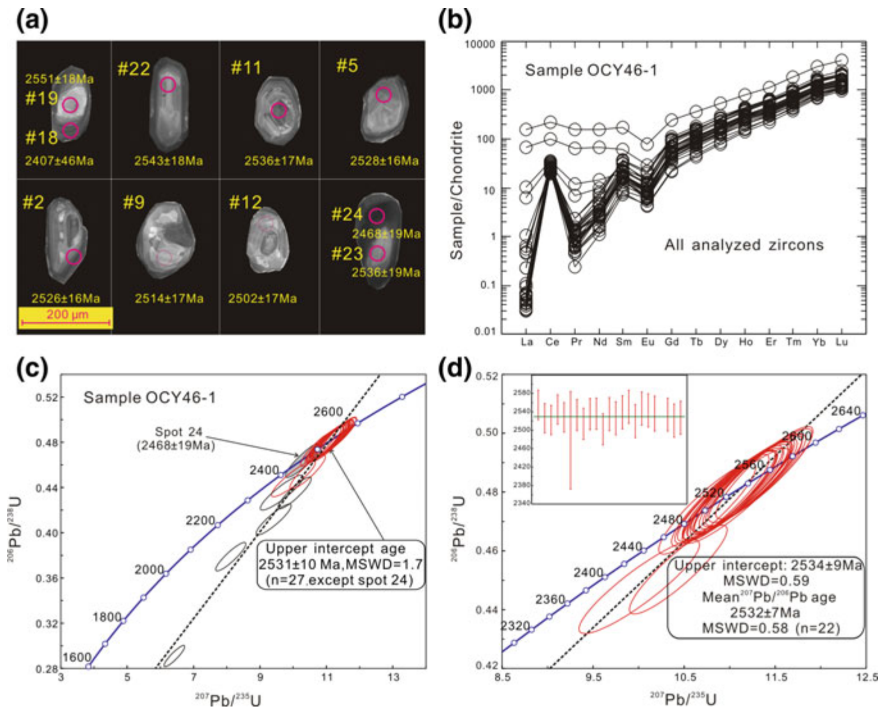

Fig. 3.32 Internal structures, rare earth element pattern, and age data of zircon grains from the LMG tonalitic gneiss sample OCY46-1. **a** CL images of representative zircon grains showing internal structures and analyzed locations. Numbers are spot locations in Table 3.10. **b** REE patterns for all analyzed spots. **c** Concordia diagram showing all analyzed spots. **d** Concordia diagram of the analyses (95–105% concordance level) used to determine the crystallization age of the tonalitic gneiss sample; the inset is the weighted average $^{207}Pb/^{206}Pb$ age diagram

zonings (e.g., spots #2 and #22). Some show blurred zoned cores that are enveloped by dark structureless rims (e.g., spots #19 and #23). A total of twenty-eight analyses were performed on twenty-four zircon grains, and the results yield apparent $^{207}Pb/^{206}Pb$ ages between 2555 ± 16 Ma and 2407 ± 46 Ma (Table 3). Th and U contents range from 47 to 376 ppm and from 62 to 339 ppm, respectively, with high Th/U ratios of 0.38–1.11. Most zircon domains show consistent chondrite-normalized REE patterns with positive Ce anomalies, negative Eu anomalies and fractionated HREE patterns (Fig. 3.32b and Table 3.10). Two analyses (spots #14 and #29) display high light rare earth element (LREE) contents, which can be ascribed to element mobility triggered by local recrystallization of the original magmatic zircon grains [96]. These suggest that all the zircon grains were originally formed by magmatic crystallization [72].

Twenty-seven analyses, except for spot #24, define a discordia with an upper intercept age of 2531 ± 10 Ma (Fig. 3.32c). Combined with the mostly oscillatory zoned structures, high Th/U ratios and magmatic zircon-like REE patterns, it is suggested that these zircon grains were crystallized during the same magmatic event, and that some of them were subjected to Pb loss. Twenty-two analyses plot on or close to the concordia, and yield an upper intercept age of 2534 ± 9 Ma (MSWD = 0.59) and a weighted mean $^{207}Pb/^{206}Pb$ age of 2532 ± 7 Ma (MSWD = 0.58) (Fig. 3.32d). Therefore, the age of 2532 Ma was considered as the crystallization age of the magmatic precursor of sample OCY46-1. Zircon spot #24 performed on a dark structureless rim, shows a concordant and young apparent $^{207}Pb/^{206}Pb$ age of 2468 ± 19 Ma (Fig. 3.32a, c). This age may record the effect of multiple Paleoproterozoic tectonothermal events in the JPGT [89, 90].

Eighteen Lu–Hf isotopic data were collected on the same dated locations (Table 3.11). When calculated at the apparent $^{207}Pb/^{206}Pb$ ages (t_1), these zircon grains show consistent $^{176}Hf/^{177}Hf$ (t_1) ratios of 0.281230–0.281313, further suggesting that they were formed during the same magmatic event. If the Lu–Hf isotopic data were calculated at the crystallization age of 2532 Ma (t_2), they yield positive εHf(t_2) values from +2.3 to +5.3 and T_{DM}(Hf) modal ages between 2749 and 2638 Ma (Fig. 3.29f).

3.2.4 Petrogenesis

3.2.4.1 Information from the Inherited/Xenocrystic Zircon Grains and Lu–Hf Isotopes

The above dating data reveal that the dated samples contain some inherited/xenocrystic zircon grains (Figs. 3.24, 3.26, 3.28, 3.30 and 3.31). Cathodoluminescence images reveal that most zircon grains display clear oscillatory or banded zonings, and some of them are enveloped by oscillatory zoned domains which grew during magmatic crystallization (Figs. 3.26a, 3.28a and 3.30a). A total of thirty-eight inherited/xenocrystic zircon grains were detected mainly from the LMG samples (Tables 3.6 and 3.9), and they show apparent $^{207}Pb/^{206}Pb$ ages and T_{DM}(Hf) ages ranging of 2668–2549 Ma and 2712–2548 Ma, respectively. Whereas two hundred and eighty-three magmatic zircons yield T_{DM}(Hf) ages mostly of 2767–2518 Ma, roughly comparable with those of the inherited or xenocrystic zircon grains.

On the zircon εHf(t) values versus age diagrams, the majority of analyses from inherited/xenocrystic zircon domains plot close to the coeval depleted mantle values (Fig. 3.29). The apparent $^{207}Pb/^{206}Pb$ ages (2668–2549 Ma) are almost equal to the T_{DM}(Hf) model ages (2712–2548 Ma), indicating an important episode of crustal growth during ~2670–2550 Ma. The marked overlap between the T_{DM}(Hf) model ages of the inherited/xenocrystic zircons (2712–2548 Ma) and those of the magmatic zircons (2767–2518 Ma) implies that these granitoid gneisses could have partially originated from the ~2670–2550 Ma juvenile crustal rocks (e.g., regional metavolcanic rocks with formation ages up to 2640 Ma) [93]. Moreover, the oldest age of the granitoid gneisses (2532 ± 7 Ma of sample OCY46-1) is consistent with the youngest T_{DM}(Hf) model age (2518 Ma) of the magmatic zircons, suggesting that mantle-derived or juvenile crustal materials could have been involved in their source region. In summary, both ~2670–2550 Ma crustal materials and mantle-derived or juvenile crustal materials could have contributed to the generation of the late Neoarchean granitoid gneisses in the Western Liaoning Province.

3.2.4.2 Information from Whole-Rock Geochemistry

Granitoid gneisses of WLP experienced amphibolite to granulite facies metamorphism (Figs. 3.17 and 3.20). In this case, the large ion lithophile elements (LILEs), including Cs, Rb, Ba and K, could have been mobilized. In the primitive mantle-normalized spider diagrams (Fig. 3.23), the Rb, Ba and Th generally show large variations, further implying their mobility. However, the well-defined positive correlations between Zr and other trace elements (rare earth elements (REEs, e.g. La, Ce and Yb), high field strength elements (HFSEs, e.g. Nb, Hf), Sc and V), suggest that the original contents of these elements are largely preserved (not shown, [61, 90]). Therefore, emphasis will be placed on Al, Ti, Mg, REEs and HFSEs during the following genetic discussion, which are considered to be less susceptible to medium to high grade metamorphism [31].

The petrographic and geochemical characteristics allow the classification of the granitoid gneisses of WLP into a high-magnesium group and a low-magnesium group. The two granitoid groups may be genetically linked by shallow-level fractional crystallization (e.g., hornblende). It is suggested that MREEs have the highest partition coefficients in hornblende compared to LREEs and HREEs, and hornblende fractionation will result in the increase of silica and decrease of Dy/Yb in the magmatic system [70]. Nonetheless, almost all the dioritic to TTG gneisses in the WLP show comparable Dy/Yb ratios (1.32–2.34), but without linear correlations with SiO_2 and total REE contents, precluding the involvement of hornblende fractionation (Fig. 3.33a, b). Fractionation of plagioclase and apatite is also unlikely

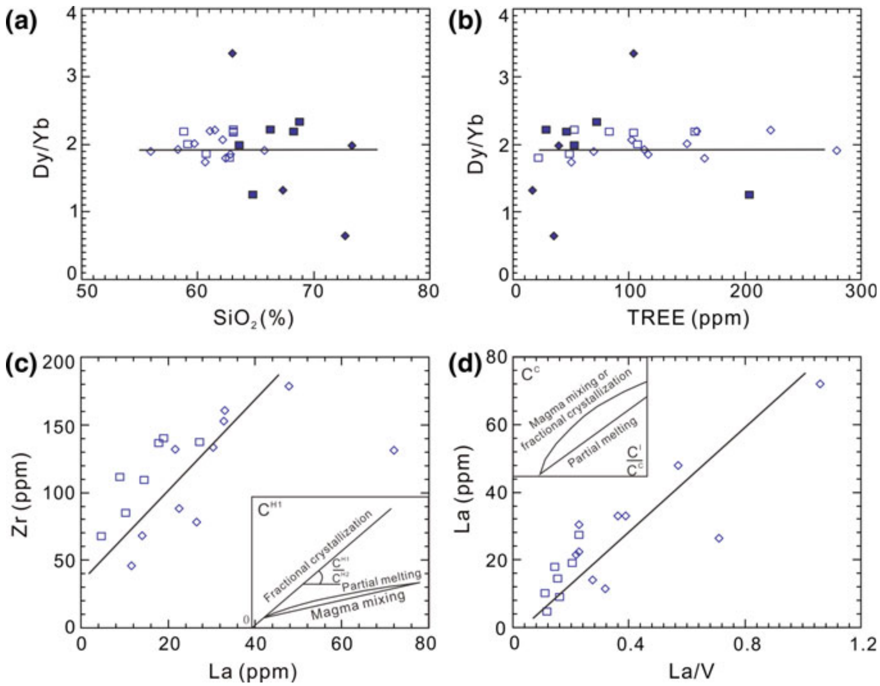

Fig. 3.33 Petrogenetic diagrams of the late Neoarchean granitoid gneisses in the Western Liaoning Province, showing that the geochemical features of HMG and LMG samples are controlled by separate partial melting processes. **a** Dy/Yb versus SiO_2 diagram; **b** Dy/Yb versus total rare earth element (TREE) diagram; **c** Zr versus La diagram for the HMG samples. The inset is a schematic C^{H1} versus C^{H2} diagram (H1 and H2 being two highly incompatible elements) with curves showing calculated melt compositions produced by fractional crystallization, partial melting and magma mixing processes. **d** La versus La/V diagram for the HMG samples. The inset is a schematic C^{I} versus C^{I}/C^{C} diagram (I and C being incompatible and compatible elements, respectively) with curves showing magmatic trends produced by magma mixing, fractional crystallization and partial melting processes (after Schiano et al. [74]). Symbols are the same as Fig. 3.21

since the lack of significant anomalies of Eu, Sr, and P in the normalized REE and multi-element plots (Figs. 3.22 and 3.23). Accordingly, granitoid gneisses of the two groups could record diverse genetic processes.

Granitoid gneisses of the HMG

The HMG samples are characterized by high MgO and Mg#, high Sr and low Y and Yb contents, with high $(La/Yb)_N$ and Sr/Y ratios, and these features resemble those of Phanerozoic adakites or adakitic rocks (Table 3.5) [50]. Despite low Mg# values (44.16–45.44) of samples OYX07-5, OYX07-11, and OCY31-2, they have low SiO_2 (59.65–62.72 wt%) and high MgO (2.46–3.12 wt%), clearly distinct from those of crustal-derived melts [54].

Several genetic models have been proposed for the adakitic rocks, including (1) partial melting of subducted oceanic slabs, with the melts contaminated by the mantle wedge materials [14]; (2) partial melting of thickened crust at the root area of arcs or oceanic plateaus [11]; (3) fractional crystallization of basaltic to andesitic rocks [9]; and (4) mixing between mafic and felsic magmas [77]. Previous experimental studies reveal that the partial melts derived from metabasaltic rocks show generally high SiO_2 (68.94 ± 3.82 wt%) but low MgO (0.84 ± 0.44 wt%) [68, 99]. Similarly, adakitic rocks (C-type adakites) derived from the partial melting of lower continental crustal materials display high SiO_2 (>66 wt%), low MgO (<1.5 wt%) but high K_2O contents (generally $K_2O > Na_2O$) [87]. The HMG samples in the WLP have MgO contents higher than those of experimental melts derived from the partial melting of basaltic rocks, and plot into the HSA (high silica adakites) field in the MgO versus SiO_2 diagram (Fig. 3.21b) [24, 50]. Therefore, these HMG samples cannot be derived solely from crustal materials. On the Zr versus La and La versus La/V diagrams (Fig. 3.33c, d), the HMG samples define a curved line and a positive correlation line, respectively, implying that the compositional variations are mainly controlled by the partial melting process but without the involvement of magma mixing or fractional crystallization [74]. Furthermore, the dated HMG samples (CY26-1, CY31-2, OCY31-2, OCY33-1 and CY46-1) display high zircon $\varepsilon Hf(t_2)$ values that are close to the depleted mantle value (Figs. 3.27 and 3.29). Accordingly, the HMG samples likely have been derived from the partial melting of subducted oceanic slabs with the melts contaminated by the mantle wedge materials during the ascent [50]. In the AFM versus CFM diagram (Fig. 3.34), they show low AFM and CFM values of 0.86–1.28 and 0.22–0.41, respectively, suggesting that they were mainly derived from the partial melting of metabasaltic rocks but not subducted sediments. The strongly fractionated REE patterns with high $(La/Yb)_N$ and Sr/Y ratios, low Yb and Y contents and mostly positive Eu anomalies, and negative Nb, Ta and Ti anomalies, are consistent with a source of plagioclase-free eclogites or garnet amphibolites (Figs. 3.22a, c and 3.23a, c; and Table 3.5). The absence of

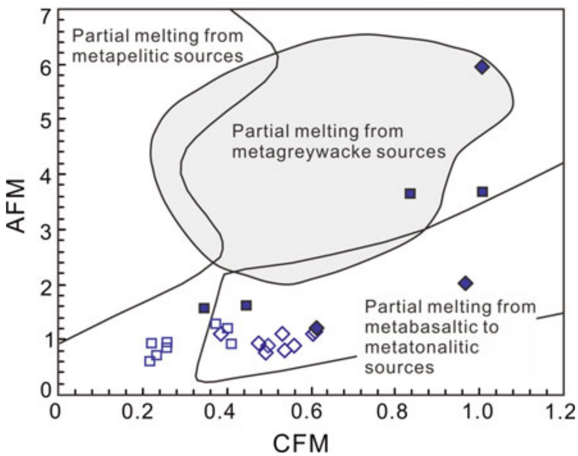

Fig. 3.34 Molar Al_2O_3/($MgO + FeO_T$) (AFM) versus molar CaO/($MgO + FeO_T$) (CFM) diagram showing source compositions of late Neoarchean granitoid gneisses in the Western Liaoning Province (after Altherr et al. [1]). Symbols are the same as Fig. 3.21

concave-upward REE patterns suggests that amphibole was 3.23not involved in the residue, and the descending oceanic slabs could have been converted to eclogites before partial melting [70]. Notably, minor inherited or xenocrystic zircon grains were detected in the HMG samples (Figs. 3.28 and 3.30). Their ages (2668–2549 Ma) are within error of regional metavolcanic rocks (up to ~2640 Ma), suggesting that these zircon grains could have been captured during the ascent of the slab melts through the crustal profile.

Granitoid gneisses of the LMG

Similar to the HMG samples, granitoid gneisses of the LMG have high Sr (241–744 ppm, and mostly of >400 ppm) and low Y (0.75–8.48 ppm) and Yb (0.07–1.05 ppm) contents, showing adakitic signatures with high $(La/Yb)_N$ (16.04–86) and Sr/Y (49–837) ratios (Table 3.5). However, the LMG samples are featured by low MgO, high Na_2O (3.70–6.13 wt%), and low K_2O/Na_2O (0.19–0.83, and mostly of <0.5). Al_2O_3 contents are generally high (15.30–19.51 wt%). These chemical characteristics are comparable with those of Archean high-Al TTG gneisses [5, 50]. High SiO_2 (63.02–73.29 wt%) and low MgO (0.40–2.10 wt%) and Mg# (mostly of 33.15–44.32) indicate that they were dominantly derived from a crustal source. On the AFM (molar Al_2O_3/(MgO + FeOT)] versus CFM (molar CaO/(MgO + FeOT)) diagram [1], Fig. 3.34), the LMG samples display generally high CFM (0.35–1.01) but low AFM (1.20–3.68) values, though minor higher AFM values (e.g., 5.92 of sample OFX11-2). These suggest the derivation of the magmatic precursors dominantly from metabasaltic rocks with some involvement of metagreywackes, which is consistent with the variable A/CNK values of 0.91–1.13. Recently, Moyen [53] pointed out that Archean TTGs are a composite group, which can be classified into low, medium and high pressure types, corresponding to the generation from partial melting of plagioclase-rich garnet-amphibolites, garnet-rich and plagioclase-poor amphibolites and rutile-bearing eclogites, respectively. For the LMG samples in this study, the combination of concave upward normalized REE patterns, high $(La/Yb)_N$ and Sr/Y ratios, low Yb and Y contents, slightly to strongly positive Eu anomalies and negative Nb, Ta and Ti anomalies, suggest that they could have been derived from the partial melting of garnet-rich but plagioclase-poor amphibolites (e.g., garnet amphibolites) at a medium pressure (15–20 °C/km) [53]. Sample FX01-1 has a fractionated normalized REE pattern without Eu anomaly ($Eu_N/Eu_N^* = 1.05$), together with high Sr (631 ppm) and Sr/Y (112.28), suggesting the involvement of garnet but not amphibole and plagioclase in the residue (Fig. 3.22b and Table 3.5). It could belong to the high pressure TTG type [53, 70].

3.2.5 Tectonic Implications

The petrogenetic studies reveal that granitoid gneisses of the HMG could have been derived from the partial melting of subducted oceanic slabs, with the ascending melts contaminated by the mantle wedge materials [49, 50]. Considering that early metavolcanic rocks show chemical features analogous to those of MORBs, island arc tholeiitic to calc-alkaline basalts, adakite-like rocks, and high magnesium andesites, it is suggested that these granitoid rocks could have been emplaced under a subduction-accretion-related arc setting. Recently, Archean adakite-like metavolcanic rocks have been identified in Superior, Dharwar, and Karelian cratons around the world, which are commonly considered to be formed at a convergent arc setting [23, 47, 76, 89, 90].

As typical Archean high-Al TTGs, the LMG granitoid gneisses were generated by the partial melting of mainly garnet amphibolites but without the involvement of mantle materials [5]. There are hot debates surrounding the geodynamic setting of Archean high-Al TTGs, including partial melting of flat-subducted oceanic slabs or hydrous mafic rocks at the thickened arc root, or alternatively under a mantle plume setting [50, 75]. If the TTGs were generated by mantle plume magmatism, the wall rocks should comprise ultramafic to mafic rocks including komatiites, continental flood basalts, and deep plumbing system of dyke swarms and layered mafic-ultramafic complex [15]. In addition, lithological assemblages formed by mantle plume magmatism are generally bimodal in composition with the felsic end-member showing peralkaline features [98, 105]. However, supracrustal metavolcanic rocks of WLP show chemical compositions ranging from mafic to felsic without apparent compositional gap, and both the felsic volcanic rocks and the plutonic granitoid gneisses show calc-alkaline affinities [43]. Moreover, ~2.5 Ga komatiites are absent in the study area. These lines of evidence imply that a mantle plume model is hard to account for the generation of the LMG granitoids. Considering that the formation of adakitic rocks, calc-alkaline metabasaltic rocks, and high magnesium andesites require a deep subduction angle of the oceanic slabs, a flat subduction model is also invalid. In summary, the high-Al TTGs of the LMG were likely generated by the partial melting of garnet amphibolites at the root zones of a thickened arc setting [90].

Accordingly, the Western Liaoning Province could have been evolved under an Archean convergent arc setting, recording tectonic evolution processes from mid-ocean ridge spreading (MORB-like rocks of Group MB-1), through initiation and maturation of an intra-oceanic arc system (tholeiitic to calc-alkaline basaltic to andesitic rocks, as well as voluminous dioritic to TTG gneisses) [93].

3.3 Late Neoarchean Potassium-Rich Granitoid Gneisses

Late Archean potassium-rich granitoid gneisses are increasingly identified in global ancient cratons with a proportion up to ~20% [34, 95]. The potassium-rich granitoid gneisses can be subdivided into two major lithological units: (1) K- and Mg-rich sanukitoid series, including dioritic, monzodioritic, and granodioritic gneisses, that are widely considered to have been derived from an enriched lithospheric mantle source metasomatized by slab-derived materials; and (2) K-rich and Mg-poor granodioritic, monzogranitic, and syenogranitic gneisses, with a dominantly crustal source. These granitoid gneisses generally occur during the late-tectonic to post-tectonic stages, marking the final cratonization of continental crust [55, 86]. Field geological, petrological, zircon U–Pb and Lu–Hf isotopic, and whole-rock geochemical studies were conducted on the Neoarchean potassium-rich granitoid gneisses of WLP, aiming to constrain the lithological assemblages, chronological framework, petrogenesis, and geodynamic setting.

3.3.1 Geological and Petrographic Features

Archean potassium-rich granitoid gneisses are developed mainly in the Waziyu (YX05-1, OYX02-1, and OYX11-1), Xiguanying (CY12-2), and Zhuluke areas (CY36-1 and CY39-1; Figs. 3.16 and 3.18). They show weakly gneissic to massive structures, and the magmatic precursors are granodioritic and monzogranitic in composition. Field studies reveal that they intrude both the supracrustal metavolcanic rocks (e.g., hornblende plagioclase gneisses; Fig. 3.35a, c) and the strongly deformed tonalitic gneisses (Fig. 3.35b, d), representing the latest tectono-magmatic events at the terminal Archean.

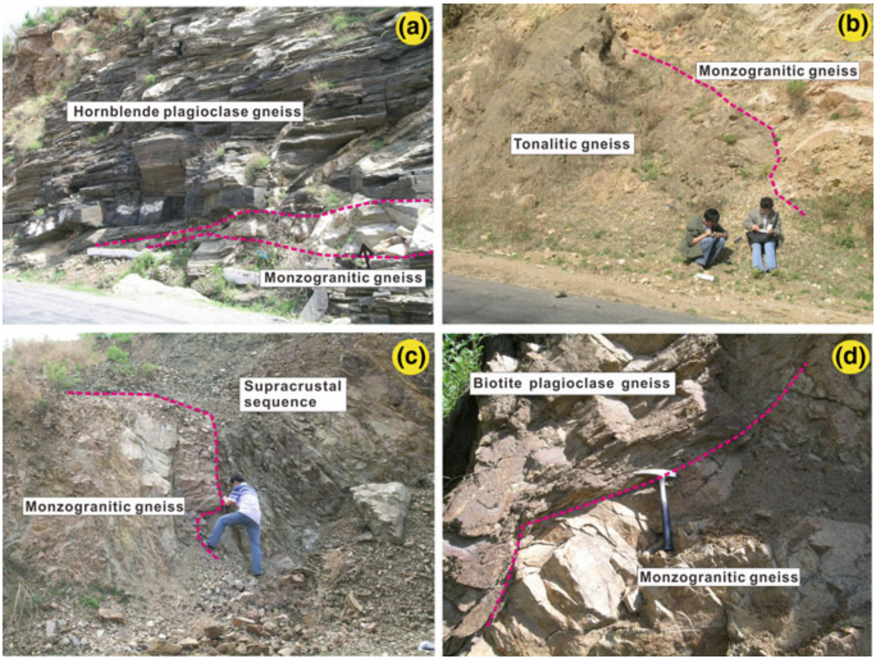

Fig. 3.35 Field geological characteristics of the potassium-rich granitoid gneisses in the Western Liaoning Province: **a/b** monzogranitic gneisses of the NCFY-GGB; **c/d** monzogranitic gneisses of the JPGT

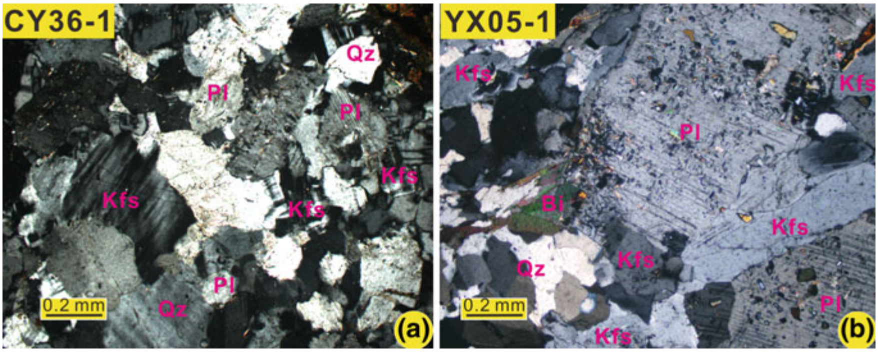

Fig. 3.36 Petrographic features of representative potassium-rich granitoid gneisses from the Western Liaoning Province: **a** monzogranitic gneiss sample CY36-1 of the JPGT; **b** granodioritic gneiss sample YX05-1 of the NCFY-GGB

The monzogranitic gneiss samples CY12-2, OYX11-1, CY36-1, and CY39-1 show mineral assemblages of plagioclase (35–38%), K-feldspar (28–30%), quartz (28–32%), and minor biotite, with accessory zircon, apatite, and epidote (Fig. 3.36a). They display a fine-grained texture and a weakly gneissic to massive structure. In comparison, the granodioritic gneiss samples YX05-1 and OYX02-1 have different mineral assemblages, i.e., plagioclase (46–52%), K-feldspar (18–22%), quartz (24–26%), and minor biotite. Zircon and apatite are the accessory minerals (Fig. 3.36b). These granodioritic gneisses show medium- to fine-grained texture and weakly gneissic to massive structure.

3.3.2 Geochemical Features

Six potassium-rich granitoid gneisses were analyzed for whole-rock geochemical data, which are listed in Table 3.12 and plotted in Figs. 3.37 and 3.38.

These rocks are characterized by high SiO_2 (65.38–73.69 wt%), and low MgO (0.30–1.81 wt%) and Mg# (14.24–49.27). In the An-Ab-Or diagram (Fig. 3.37a) [5], samples YX05-1 and OYX02-1 fall in the granodioritic field, whereas samples CY12-2, OYX11-1, CY36-1, and CY39-1 plot in the field of granites sensu stricto. In the MgO versus SiO_2 plot, they all plot in the field of experimentally-derived melts from metabasaltic rocks [50]. Distinct from the early TTG gneisses, the potassium-rich granitoid gneisses have higher K_2O (3.89–5.97 wt%) and K_2O/Na_2O (mostly of 0.99–1.32, but 0.77 for sample CY36-1). They all belong to the high-K calc-alkaline to shoshonitic rock series (Fig. 3.37c). The granodioritic gneiss samples YX05-1 and OYX02-1 and monzogranitic gneiss samples CY36-1

Table 3.12 Analyzed results of major (wt%) and trace elements (ppm) for the potassium-rich granitoid gneisses from the Western Liaoning Province

Samples	NCFY-GGB				JPGT	
	YX05-1	0YX02-1	CY12-2	OYX11-1	CY36-1	CY39-1
Lithology	GRD	GRD	MG	MG	MG	MG
SiO_2	65.38	66.89	71.96	73.69	67.69	67.86
TiO_2	0.29	0.35	0.12	0.14	0.50	0.43
Al_2O_3	16.74	15.29	14.87	13.92	15.16	16.24
FeO_T	3.39	3.45	0.69	1.31	4.17	1.93
MnO	0.04	0.05	0.01	0.01	0.06	0.05
MgO	1.64	1.88	0.30	0.57	0.65	0.18
CaO	3.47	3.32	0.76	1.07	1.79	0.93
Na_2O	3.43	4.03	3.08	3.52	5.04	5.22
K_2O	4.17	3.98	5.97	4.66	3.89	5.77
P_2O_5	0.21	0.19	<0.05	<0.05	<0.05	0.08
LOI	0.67	0.64	1.31	0.71	0.65	1.24
Total	99.44	100.07	99.08	99.60	99.60	99.92
Mg#	46.30	49.27	43.92	43.64	21.79	14.24
K_2O/Na_2O	1.21	0.99	1.94	1.32	0.77	1.11
A/CNK	1.02	0.90	1.15	1.09	0.96	0.98
Sc	2.43	3.90	0.230	0.260	3.04	2.91
V	47	44	7.00	16.6	42	6.94
Rb	57	96	52	96	53	52
Sr	277	472	216	296	415	58
Y	9.03	3.48	0.400	1.270	2.94	9.34
Nb	4.48	4.00	0.780	1.940	1.970	4.64
Cs	0.198	0.320	0.158	0.630	0.150	0.710
Ba	640	1335	441	1512	727	289
La	24	22	3.86	6.41	3.70	29
Ce	48	41	4.16	10.8	6.32	73
Pr	5.42	3.78	0.300	1.060	0.670	6.18
Nd	19.5	13.1	0.860	3.50	2.68	26
Sm	2.71	1.690	0.080	0.470	0.550	3.82
Eu	0.660	1.890	0.470	1.440	0.300	0.630
Gd	2.35	2.03	0.040	0.560	0.520	2.83
Tb	0.310	0.190	0.010	0.050	0.100	0.410
Dy	1.740	0.810	0.050	0.230	0.570	1.830
Ho	0.300	0.160	0.010	0.040	0.110	0.320
Er	0.930	0.460	0.030	0.140	0.330	1.050
Tm	0.140	0.060	0.010	0.020	0.050	0.160
Yb	0.830	0.470	0.050	0.150	0.350	1.040

(continued)

Table 3.12 (continued)

Samples	NCFY-GGB				JPGT	
	YX05-1	0YX02-1	CY12-2	OYX11-1	CY36-1	CY39-1
Lithology	GRD	GRD	MG	MG	MG	MG
Lu	0.130	0.070	0.010	0.020	0.060	0.150
Ta	0.120	0.240	0.110	0.100	0.100	0.180
Th	1.160	1.230	0.180	7.84	0.030	3.13
U	0.150	0.310	0.070	0.330	0.050	0.640
Zr	95	69	7.82	33	31	391
Hf	3.66	3.10	0.840	2.53	0.800	7.51
Eu_N/Eu_N^*	0.80	3.13	25.39	8.64	1.70	0.58
$(La/Yb)_N$	21	34	52	31	7.67	20
TREE	107	88	9.92	25	16.3	147
Sr/Y	31	136	536	232	141	6.23

Note LOI, loss on ignition; A/CNK = molar $Al_2O_3/(CaO + Na_2O + K_2O)$; TREE, total rare earth elements
Mg# = 100 $Mg/(Mg + Fe_{total})$ in atomic ratio, $Eu_N/Eu_N^* = Eu_N/SQRT(Sm_N \times Gd_N)$, subscript N-chondrite normalized value
<0.05 wt% for P_2O_5 means values below the detection limit
GRD—granodioritic gneiss; MG—monzogranitic gneiss

and CY39-1 are metaluminous to weakly peraluminous with low A/CNK values (0.90–1.02), whereas the monzogranitic gneiss samples CY12-1 and OYX11-1 have A/CNK values of 1.09–1.15, being strongly peraluminous (Fig. 3.37d).

All the potassium-rich granitoid gneisses are characterized by low total REE contents (TREE = 9.92–147 ppm), and strongly fractionated REE patterns, with $(La/Yb)_N$ ratios mostly in the range of 20–52, except for sample CY36-1 with a lower value of 7.67 (Fig. 3.38a, c). In detail, the granodioritic gneiss samples YX05-1 and OYX02-1 (NCFY-GGB) and the monzogranitic gneiss samples CY36-1 and CY39-1 (JPGT) have less fractionated REE patterns ($(La/Yb)_N$ ratios of 7.67–34.11) with weakly negative to moderately positive Eu anomalies (Eu_N/Eu_N^* = 0.58–3.13). In comparison, the monzogranitic gneisses CY12-2 and OYX11-1 (NCFY-GGB) display concave-upward REE patterns ($(La/Yb)_N$ ratios of 30.99 and 52.24, respectively), with strongly positive Eu anomalies (Eu_N/Eu_N^* = 8.64–25) (Fig. 3.38a).

In the primitive mantle-normalized multi-element plot (Fig. 3.38b, d), these granitoid gneisses are enriched in large ion lithophile elements (LILEs; e.g., Ba, Rb, and K), but depleted in Th, Nb, and Ta, with different degrees of Zr–Hf enrichment. Samples CY12-2, OYX11-1, and CY36-1 display positive Sr anomalies, and sample CY39-1 show negative Sr and P anomalies. However, samples YX05-1 and OYX02-1 don't have Sr and P anomalies. They have high Sr (mostly of 216–472 ppm) and low Y (0.400–9.34 ppm) and Yb (mostly of 0.050–1.040 ppm), yielding high Sr/Y ratios mostly in the range of 31–536 (Table 3.12).

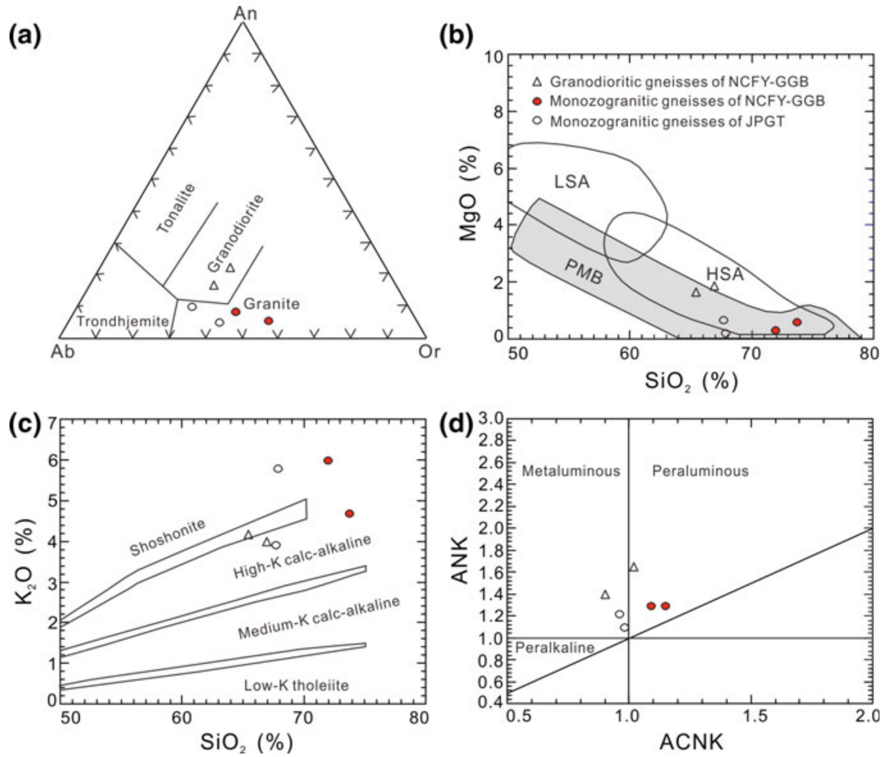

Fig. 3.37 Major element compositions of the potassium-rich granitoid gneisses from the WLP. **a** An-Ab-Or diagram [5]; **b** MgO versus SiO_2 plot (PMB: experimental partial melts from basalts or amphibolites; LSA: low silica adakite; HSA: high silica adakite, after Martin et al. [50]); **c** K_2O versus SiO_2 classification diagram (after Rollinson [70]); **d** ANK [molar Al_2O_3/(Na_2O + K_2O)] versus ACNK [molar Al_2O_3/(CaO + Na_2O + K_2O)] (after Maniar and Piccoli [45]). Symbols: open triangles—granodioritic gneisses of the NCFY-GGB; solid cycles—monzogranitic gneisses of the NCFY-GGB; open cycles—monzogranitic gneisses of the JPGT

3.3.3 Zircon U–Pb and Lu–Hf Isotopes

Sample YX05-1

Zircon grains from the granodioritic gneiss sample YX05-1 have prismatic shapes with lengths from 100 and 200 μm and length/width ratios of 2:1–4:1. Most of the zircon grains exhibit dark oscillatory zoned or structureless cores surrounded by bright oscillatory zoned rims (Fig. 3.39a). Some zircon grains display euhedral cores with weak oscillatory zonings enveloped by bright structureless rims (spots #29 and #35). Thirty-six spots were analyzed on thirty-five zircon grains, yielding apparent $^{207}Pb/^{206}Pb$ ages ranging from 2524 to 2394 Ma (Table 3.13). They have

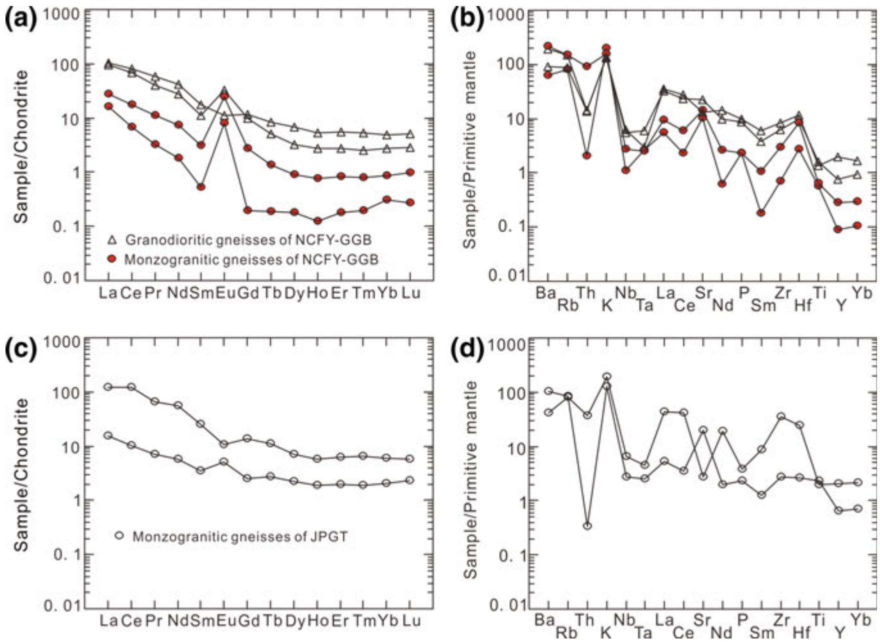

Fig. 3.38 Chondrite-normalized REE patterns and primitive mantle-normalized multi-element spider diagrams for **a** and **b** the granodioritic and monzogranitic gneisses from the NCFY-GGB, and **c** and **d** the monzogranitic gneisses from the JPGT. Symbols are the same as Fig. 3.37, and the chondrite and primitive mantle values are after Sun and McDonough [78]

Th and U contents of 58–244 ppm and 76–1641 ppm, respectively, and most of them have Th/U ratios between 0.10 and 0.82. Four analyses of dark zones (spots #6, #15 and #36) and bright recrystallized cores (spot #8) have low Th/U ratios of 0.06–0.08. However, all the analyzed spots show consistent chondrite-normalized REE patterns with positive Ce anomalies, moderately negative Eu anomalies and fractionated HREE patterns (Fig. 3.39b), indicating their primary origin from magmatic crystallization [72]; Table 3.14. On the concordia diagram (Fig. 3.39c), they define a discondia and yield an upper intercept age of 2498 ± 11 Ma with a large MSWD value of 9.3. Twelve analyses mainly on the oscillatory zoned rims and cores plot on or close to the concordia, and they yield a weighted mean $^{207}Pb/^{206}Pb$ age of 2494 ± 8 Ma (MSWD = 1.9) (Fig. 3.39d). This latter age is interpreted to be the best estimate of the crystallization age for the magmatic precursor of sample YX05-1. The discordance of the other isotopic ratios could be the result of recent Pb loss.

Lu–Hf isotopic analyses were synchronously obtained on the above thirty-six spots. These analyses show similar $^{176}Hf/^{177}Hf(t_1)$ ratios from 0.281216 to 0.281315, further implying that they were crystallized from the same magmatic

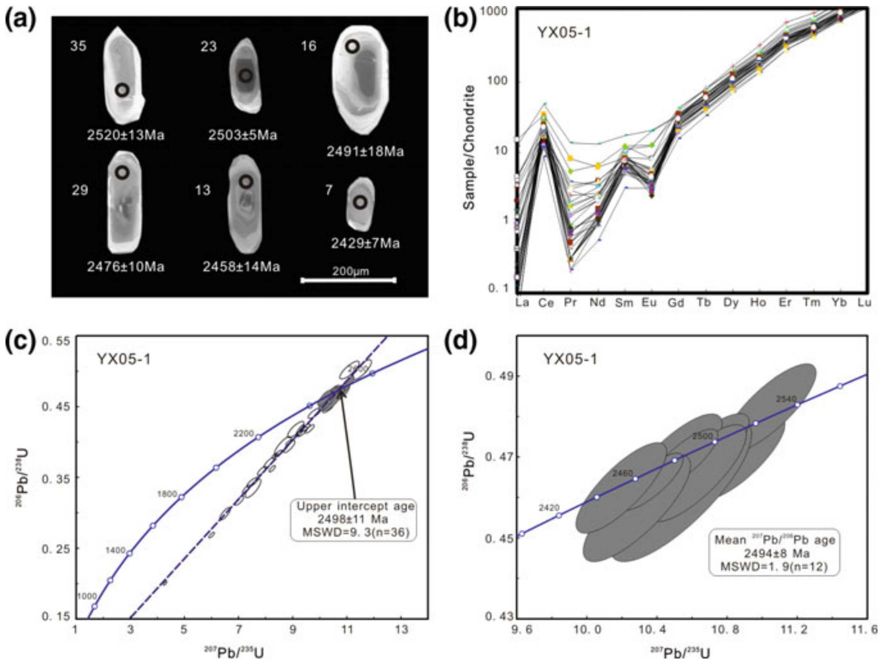

Fig. 3.39 Internal structures, rare earth element pattern, and age data of zircon grains from the granodioritic gneiss sample YX05-1: **a** CL images of representative zircon grains showing internal structures and analyzed locations. Numbers are spot locations in Table 3.14; **b** zircon REE patterns for all the analyses; **c** concordia diagram for all the analyzed spots; and **d** concordia diagram for analyses (with 95–105% concordance level) used to determine the weighted mean $^{207}Pb/^{206}Pb$ age. The chondrite normalized values are cited from Sun and McDonough [78]

events but subjected to different degrees of Pb loss (Table 3.15). Calculated at the crystallization age of 2494 Ma, these analyses give positive $\varepsilon Hf(t_2)$ values from +0.9 to +4.5 with depleted mantle model ages of 2634–2768 Ma (Fig. 3.40a).

Sample CY36-1

Zircon grains from the monzogranitic gneiss sample CY36-1 display stubby or oval shapes, and they have lengths and length/width ratios of 80–150 μm and 1:1–2:1, respectively (Fig. 3.41a). Cathodoluminescence images show that some grains represent fragments of dark oscillatory zoned grains (e.g., spots #9 and #14), whereas others show core-rim structures with weakly oscillatory zoned or dark structureless cores surrounded by thin bright rims (e.g., spots #6 and #21). A total of forty-one analyses were performed on forty-one zircon grains (Table 3.13), and most of them plot on or close to the concordia (Fig. 3.41b). Four analyses (spots #7, #30, #35 and #36) of dark structureless cores deviate far from the concordia, which are rejected from the age calculation. The remaining thirty-seven analyses have apparent $^{207}Pb/^{206}Pb$ ages ranging between 2644 ± 13 Ma and 2352 ± 22 Ma.

Table 3.13 LA-ICPMS zircon U-Pb isotopic dating data of potassium-rich granitoid gneiss samples YX05-1 and CY36-1 from the Western Liaoning Province

Samples and analyzed spots	Th (ppm)	U (ppm)	Th/U	Isotopic ratios						Apparent ages (Ma)					
				$^{207}Pb/^{206}Pb$	±1σ	$^{207}Pb/^{235}U$	±1σ	$^{206}Pb/^{238}U$	±1σ	$^{207}Pb/^{206}Pb$	±1σ	$^{207}Pb/^{235}U$	±1σ	$^{206}Pb/^{238}U$	±1σ
YX05-1-1	88	161	0.55	0.1640	0.0009	10.6658	0.1062	0.4706	0.0041	2497	9	2494	9	2486	18
YX05-1-2	100	242	0.41	0.1618	0.0011	9.2753	0.0623	0.4161	0.0034	2474	12	2366	6	2243	15
YX05-1-3	123	1289	0.10	0.1602	0.0005	7.0275	0.0664	0.3171	0.0027	2458	5	2115	8	1776	13
YX05-1-4	58	187	0.31	0.1586	0.0007	8.1165	0.0732	0.3703	0.0029	2443	8	2244	8	2031	14
YX05-1-5	69	128	0.54	0.1593	0.0017	8.6368	0.1283	0.3942	0.0055	2448	17	2300	14	2142	25
YX05-1-6	68	1025	0.07	0.1582	0.0007	7.8504	0.0634	0.3591	0.0026	2436	7	2214	7	1978	12
YX05-1-7	67	553	0.12	0.1575	0.0007	6.4992	0.0818	0.2986	0.0037	2429	7	2046	11	1684	18
YX05-1-8	58	1052	0.06	0.1582	0.0005	8.3334	0.0426	0.3809	0.0014	2436	6	2268	5	2080	6
YX05-1-9	64	232	0.27	0.1586	0.0021	9.1124	0.1259	0.4176	0.0047	2440	22	2349	13	2249	22
YX05-1-10	244	1329	0.18	0.1583	0.0012	7.5120	0.0853	0.3430	0.0028	2439	13	2174	10	1901	13
YX05-1-11	97	433	0.22	0.1607	0.0007	8.8587	0.0488	0.3991	0.0016	2463	7	2324	5	2165	7
YX05-1-12	102	1058	0.10	0.1582	0.0005	7.2813	0.0579	0.3331	0.0025	2437	6	2147	7	1853	12
YX05-1-13	165	240	0.69	0.1602	0.0013	10.1971	0.1055	0.4623	0.0046	2458	14	2453	10	2450	20
YX05-1-14	70	162	0.43	0.1612	0.0011	9.8109	0.0993	0.4407	0.003	2469	12	2417	9	2354	14
YX05-1-15	66	917	0.07	0.1600	0.0006	8.4746	0.0580	0.3837	0.002	2457	6	2283	6	2093	9
YX05-1-16	112	167	0.67	0.1634	0.0017	10.4774	0.1206	0.4678	0.0052	2491	18	2478	11	2474	23
YX05-1-17	65	307	0.21	0.1628	0.0010	9.4445	0.0798	0.4197	0.0023	2485	9	2382	8	2259	10
YX05-1-18	179	1118	0.16	0.1629	0.0005	8.8708	0.0859	0.3935	0.0035	2487	5	2325	9	2139	16
YX05-1-19	172	1641	0.10	0.1615	0.0006	6.0013	0.0428	0.2685	0.0017	2472	6	1976	6	1533	9
YX05-1-20	73	250	0.29	0.1642	0.0022	7.5350	0.1182	0.3344	0.0054	2500	24	2177	14	1860	26
YX05-1-21	115	170	0.68	0.1659	0.0009	10.3107	0.0867	0.4481	0.0028	2517	9	2463	8	2387	12
YX05-1-22	112	262	0.43	0.1660	0.0010	9.6264	0.0678	0.4185	0.0024	2518	9	2400	6	2254	11

(continued)

Table 3.13 (continued)

Samples and analyzed spots	Th (ppm)	U (ppm)	Th/U	Isotopic ratios						Apparent ages (Ma)					
				$^{207}Pb/^{206}Pb$	±1σ	$^{207}Pb/^{235}U$	±1σ	$^{206}Pb/^{238}U$	±1σ	$^{207}Pb/^{206}Pb$	±1σ	$^{207}Pb/^{235}U$	±1σ	$^{206}Pb/^{238}U$	±1σ
YX05-1-23	76	445	0.17	0.1645	0.0006	10.5356	0.1653	0.4616	0.0071	2503	5	2483	15	2447	31
YX05-1-24	83	170	0.49	0.1665	0.0011	10.8519	0.1152	0.4712	0.0047	2524	45	2511	10	2489	21
YX05-1-25	108	186	0.58	0.1662	0.0013	11.5573	0.1434	0.5021	0.0058	2520	13	2569	12	2623	25
YX05-1-26	155	1048	0.15	0.1542	0.0007	4.2865	0.0266	0.2007	0.0013	2394	206	1691	5	1179	7
YX05-1-27	115	141	0.82	0.1624	0.0012	10.5527	0.0797	0.4694	0.003	2481	13	2485	7	2481	13
YX05-1-28	65	234	0.28	0.1631	0.0010	9.3486	0.0775	0.4143	0.0028	2488	9	2373	8	2234	13
YX05-1-29	140	205	0.68	0.1618	0.0010	10.3677	0.0745	0.4639	0.0029	2476	10	2468	7	2457	13
YX05-1-30	62	76	0.82	0.1602	0.0018	11.0972	0.1477	0.5015	0.0052	2458	19	2531	12	2620	22
YX05-1-31	65	189	0.34	0.1624	0.0015	10.2863	0.1252	0.4573	0.0054	2481	15	2461	11	2428	24
YX05-1-32	86	150	0.57	0.1650	0.0014	11.0416	0.1089	0.4820	0.0045	2509	13	2527	9	2536	19
YX05-1-33	109	226	0.48	0.1638	0.0008	10.4933	0.0741	0.4600	0.0026	2496	8	2479	7	2439	12
YX05-1-34	131	934	0.14	0.1633	0.0005	8.2400	0.0476	0.3621	0.0018	2500	6	2258	5	1992	9
YX05-1-35	106	195	0.54	0.1662	0.0013	10.8824	0.1016	0.4698	0.0042	2520	13	2513	9	2483	18
YX05-1-36	68	863	0.08	0.1632	0.0006	10.6313	0.1144	0.4660	0.0049	2489	6	2491	10	2466	22
CY36-1-1	56	126	0.45	0.1557	0.0024	9.9102	0.2141	0.4600	0.0073	2410	26	2426	20	2440	32
CY36-1-2	171	225	0.76	0.1568	0.0018	10.0168	0.1888	0.4619	0.0069	2421	19	2436	17	2448	30
CY36-1-3	162	272	0.59	0.1566	0.0011	10.0137	0.1145	0.4628	0.0044	2420	12	2436	11	2452	19
CY36-1-4	84	153	0.55	0.1581	0.0017	10.1174	0.1278	0.4633	0.0034	2435	18	2446	12	2454	15
CY36-1-5	67	190	0.35	0.1591	0.0012	10.6330	0.1073	0.4830	0.0033	2446	12	2492	9	2540	14
CY36-1-6	126	211	0.60	0.1593	0.0011	10.5191	0.1519	0.4779	0.0066	2448	13	2482	13	2518	29
CY36-1-7	79	127	0.62	0.1220	0.0020	6.2499	0.1306	0.3695	0.0044	1987	25	2011	18	2027	21
CY36-1-8	36	81	0.44	0.1621	0.0018	10.7920	0.1813	0.4809	0.0063	2477	20	2505	16	2531	28
CY36-1-9	51	106	0.48	0.1661	0.0018	10.9460	0.1991	0.4742	0.0065	2520	18	2519	17	2502	28

(continued)

Table 3.13 (continued)

Samples and analyzed spots	Th (ppm)	U (ppm)	Th/U	Isotopic ratios						Apparent ages (Ma)					
				$^{207}Pb/^{206}Pb$	±1σ	$^{207}Pb/^{235}U$	±1σ	$^{206}Pb/^{238}U$	±1σ	$^{207}Pb/^{206}Pb$	±1σ	$^{207}Pb/^{235}U$	±1σ	$^{206}Pb/^{238}U$	±1σ
CY36-1-10	61	118	0.52	0.1609	0.0014	10.6111	0.1012	0.4755	0.0035	2465	15	2490	9	2508	15
CY36-1-11	78	432	0.18	0.1597	0.0007	10.5670	0.0702	0.4767	0.0025	2454	2	2486	6	2513	11
CY36-1-12	295	1295	0.23	0.1638	0.0006	10.9692	0.0966	0.4820	0.0038	2495	6	2521	8	2536	17
CY36-1-13	123	572	0.22	0.1634	0.0007	10.8989	0.0693	0.4800	0.0022	2491	7	2515	6	2527	10
CY36-1-14	45	90	0.50	0.1606	0.0014	11.0426	0.1075	0.4955	0.0032	2462	14	2527	9	2594	14
CY36-1-15	133	190	0.70	0.1668	0.0011	11.3372	0.0858	0.4892	0.0023	2528	10	2551	7	2567	10
CY36-1-16	117	182	0.64	0.1725	0.0015	11.5336	0.1662	0.4815	0.0045	2583	15	2567	13	2534	20
CY36-1-17	99	171	0.58	0.1721	0.0013	11.4788	0.1608	0.4813	0.0057	2589	12	2563	13	2533	25
CY36-1-18	60	132	0.45	0.1789	0.0018	11.8129	0.1250	0.4778	0.0034	2643	16	2590	10	2518	15
CY36-1-19	223	887	0.25	0.1736	0.0005	11.8395	0.0595	0.4934	0.0016	2592	5	2592	5	2585	7
CY36-1-20	58	100	0.58	0.1791	0.0015	12.5263	0.1382	0.5055	0.0047	2644	13	2645	10	2637	20
CY36-1-21	105	149	0.70	0.1694	0.0017	11.7749	0.1377	0.5041	0.0048	2554	16	2587	11	2631	20
CY36-1-22	43	93	0.46	0.1746	0.0018	11.9980	0.1365	0.4985	0.0041	2602	18	2604	11	2607	18
CY36-1-23	70	118	0.59	0.1693	0.0013	11.5007	0.1165	0.4922	0.0040	2550	12	2565	9	2580	17
CY36-1-24	66	106	0.62	0.1673	0.0024	11.4880	0.2185	0.4979	0.0074	2531	24	2564	18	2605	32
CY36-1-25	310	1305	0.24	0.1676	0.0006	11.7213	0.1073	0.5058	0.0043	2600	6	2582	9	2638	18
CY36-1-26	91	118	0.77	0.1630	0.0012	11.2868	0.1326	0.5011	0.0045	2487	11	2547	11	2619	19
CY36-1-27	301	1200	0.25	0.1644	0.0007	11.4327	0.1393	0.5033	0.0062	2501	8	2559	11	2628	26
CY36-1-28	55	111	0.50	0.1653	0.0016	11.6197	0.1243	0.5101	0.004	2511	17	2574	10	2657	17
CY36-1-29	48	81	0.60	0.1601	0.0020	10.9298	0.2977	0.4934	0.0113	2457	22	2517	25	2585	49
CY36-1-30	40	97	0.41	0.1551	0.0013	10.9754	0.1172	0.5122	0.0035	2403	14	2521	10	2666	15
CY36-1-31	167	274	0.61	0.1526	0.0011	10.1195	0.1237	0.4794	0.0046	2376	12	2446	11	2525	20
CY36-1-32	138	151	0.91	0.1550	0.0021	10.2913	0.1994	0.4805	0.0070	2402	18	2461	18	2530	30

(continued)

Table 3.13 (continued)

Samples and analyzed spots	Th (ppm)	U (ppm)	Th/U	Isotopic ratios						Apparent ages (Ma)					
				$^{207}Pb/^{206}Pb$	±1σ	$^{207}Pb/^{235}U$	±1σ	$^{206}Pb/^{238}U$	±1σ	$^{207}Pb/^{206}Pb$	±1σ	$^{207}Pb/^{235}U$	±1σ	$^{206}Pb/^{238}U$	±1σ
CY36-1-33	189	243	0.78	0.1571	0.0019	10.4824	0.2168	0.4831	0.0088	2424	25	2478	19	2541	38
CY36-1-34	145	537	0.27	0.1555	0.0011	10.2349	0.1535	0.4759	0.0062	2407	13	2456	14	2509	27
CY36-1-35	70	133	0.53	0.1547	0.0010	11.0190	0.0976	0.5153	0.0028	2399	11	2525	8	2679	12
CY36-1-36	47	112	0.42	0.1512	0.0013	10.5880	0.1107	0.5061	0.0033	2361	15	2488	10	2640	14
CY36-1-37	63	104	0.61	0.1505	0.0019	9.9052	0.1669	0.4773	0.0066	2352	22	2426	16	2516	29
CY36-1-38	7	24	0.29	0.1529	0.0058	9.6096	0.3978	0.4566	0.0102	2389	65	2398	38	2425	45
CY36-1-39	42	81	0.52	0.1509	0.0024	9.6580	0.2029	0.4619	0.0056	2367	27	2403	19	2448	25
CY36-1-40	11	37	0.30	0.1524	0.0051	9.7261	0.2921	0.4571	0.0104	2373	57	2409	28	2427	46
CY36-1-41	127	195	0.65	0.1520	0.0015	9.7982	0.1146	0.4665	0.0044	2369	18	2416	11	2468	19

Note ^{204}Pb has been corrected using the method of [2]

Table 3.14 Trace element data (ppm) for representative zircon domains from potassium-rich granitoid gneiss samples YX05-1 and CY36-1 of Western Lianong Province

Samples and analyzed spots	La	Ce	Pr	Nd	Sm	Eu	Gd	Tb	Dy	Ho	Er	Tm	Yb	Lu
YX05-1-1	0.02	13.0	0.03	0.48	0.84	0.17	4.99	1.90	26	10.5	58	14.0	148	34
YX05-1-2	0.04	12.5	0.05	0.54	0.98	0.19	4.93	1.74	23	9.66	54	13.3	140	33
YX05-1-3	0.30	10.7	0.17	1.19	1.10	0.32	5.43	1.98	27	11.4	65	16.4	183	43
YX05-1-4	0.35	18.3	0.16	1.17	1.50	0.22	6.56	2.50	33	13.3	70	16.3	166	37
YX05-1-5	0.04	18.2	0.05	0.60	1.15	0.19	6.59	2.31	31	12.5	66	15.4	158	34
YX05-1-6	0.48	8.11	0.29	1.87	1.27	0.48	5.68	2.07	28	11.7	67	16.3	182	42
YX05-1-7	0.18	8.11	0.12	1.01	1.23	0.32	5.75	2.04	27	11.6	66	16.4	180	43
YX05-1-8	0.03	5.40	0.02	0.26	0.47	0.18	3.16	1.24	18.0	7.83	47	12.1	137	33
YX05-1-9	0.04	18.1	0.03	0.62	1.13	0.18	6.49	2.34	32	12.9	69	15.1	153	32
YX05-1-10	0.18	12.5	0.13	1.10	1.87	0.47	8.59	3.04	39	15.7	89	21	231	53
YX05-1-11	0.02	11.2	0.03	0.44	0.82	0.23	4.77	1.83	25	10.4	62	14.9	162	38
YX05-1-12	0.84	11.3	0.32	1.82	1.26	0.35	4.31	1.50	19.3	8.01	48	11.6	131	33
YX05-1-13	0.01	19.4	0.07	0.74	1.30	0.34	6.43	2.17	29	11.5	65	14.1	149	33
YX05-1-14	0.02	13.0	0.02	0.47	0.78	0.19	4.96	1.80	24	10.1	58	13.2	140	32
YX05-1-15	0.23	7.53	0.12	0.96	0.82	0.20	3.91	1.52	21	9.16	57	13.9	159	37
YX05-1-16	0.02	13.3	0.04	0.51	1.36	0.25	6.76	2.57	35	14.9	86	19.1	202	45
YX05-1-17	1.12	11.0	0.36	1.61	1.02	0.22	4.42	1.59	22	9.33	59	14.1	159	37.2
YX05-1-18	0.36	13.3	0.19	1.50	1.46	1.15	6.95	2.53	34	13.8	83	18.6	201	47
YX05-1-19	0.97	17.2	0.51	3.10	1.90	0.75	7.45	2.53	33	13.4	81	18.4	206	47
YX05-1-20	3.53	21	0.76	2.84	1.30	0.27	4.38	1.56	21	8.77	55	12.5	140	31
YX05-1-21	0.02	12.7	0.03	0.55	1.18	0.24	6.23	2.26	30	12.4	75	16.1	171	40
YX05-1-22	0.01	12.5	0.03	0.58	1.06	0.22	6.30	2.16	29	12.3	74	15.9	169	39
YX05-1-23	0.06	9.80	0.07	0.69	1.09	0.24	5.24	1.73	23	10.1	65	14.6	167	41

(continued)

Table 3.14 (continued)

Samples and analyzed spots	La	Ce	Pr	Nd	Sm	Eu	Gd	Tb	Dy	Ho	Er	Tm	Yb	Lu
YX05-1-24	0.20	11.1	0.06	0.44	0.85	0.22	4.85	1.83	25	10.2	63	13.8	147	34
YX05-1-25	0	12.9	0.03	0.50	1.14	0.19	6.03	2.05	27	11.6	70	15.2	160	36
YX05-1-26	2.94	30	1.28	6.12	2.61	1.18	7.08	2.21	28	10.7	65	14.0	151	35
YX05-1-27	0.02	13.8	0	0.54	1.16	0	6.59	2.23	31	12.4	76	16.1	169	38
YX05-1-28	0.04	15.2	0.08	0.54	1.09	0.14	6.57	2.33	30	11.7	68	13.6	134	29
YX05-1-29	0.10	14.8	0.05	0.73	1.23	0.28	7.11	2.47	32	12.5	76	15.9	170	38
YX05-1-30	0.02	19.8	0.07	0.69	1.25	0.17	6.86	2.44	31	12.7	73	14.7	143	30
YX05-1-31	0.03	12.8	0.03	0.45	0.98	0.19	5.29	1.84	24	9.84	59	12.3	128	29
YX05-1-32	0.05	14.7	0.03	0.47	1.01	0.20	5.54	1.96	26	10.5	64	13.4	144	31
YX05-1-33	1.07	13.7	0.28	1.01	1.18	0.26	6.21	2.22	28	11.7	71	15.2	162	37
YX05-1-34	0.74	9.71	0.23	1.21	1.19	0.20	7.89	3.07	43	18.6	116	24	252	56
YX05-1-35	0.03	18.5	0.09	1.04	1.67	0.72	8.66	2.96	37	15.6	99	22	242	58
YX05-1-36	0.10	7.31	0.07	0.67	0.89	0.22	4.53	1.74	26	11.3	75	17.3	194	47
CY36-1-1	0	15.0	0.01	0.36	0.71	0.19	4.52	2.25	35	15.4	96	23	232	48
CY36-1-2	0.01	12.5	0.03	0.48	0.82	0.51	7.13	3.02	38	16.8	96	20	217	46
CY36-1-3	0.01	12.1	0.01	0.33	0.74	0.25	4.72	1.66	25	10.5	65	13.8	147	32
CY36-1-4	0.01	9.60	0.01	0.22	0.57	0.17	3.59	1.36	19.2	8.38	51	11.3	120	26
CY36-1-5	0.04	10.3	0.03	0.23	0.54	0.15	2.93	1.15	17.2	7.73	49	10.8	119	25
CY36-1-6	0.01	21	0.92	1.77	3.65	0.78	19.7	6.71	85	33	194	40	396	77
CY36-1-7	0.04	22	0.01	0.27	0.60	0.23	6.90	2.81	46	21	133	30	304	63
CY36-1-8	0.01	12.5	0.04	0.27	0.51	0.26	4.03	1.61	25	10.5	67	15.1	163	34
CY36-1-9	0	16.7	0.03	0.39	0.85	0.29	7.14	2.77	39	16.9	106	23	236	48
CY36-1-10	0.01	16.6	0.03	0.44	1.13	0.38	8.13	3.25	47	20	123	26	270	54
CY36-1-11	0.01	11.2	0.02	0.32	0.92	0.33	7.04	3.03	44	19.3	119	25	253	51

(continued)

Table 3.14 (continued)

Samples and analyzed spots	La	Ce	Pr	Nd	Sm	Eu	Gd	Tb	Dy	Ho	Er	Tm	Yb	Lu
CY36-1-12	0.09	26	0.09	0.73	1.35	0.39	7.96	3.32	49	22	142	31	327	64
CY36-1-13	0.13	15.0	0.05	0.42	0.71	0.21	4.21	1.69	25	11.4	73	16.2	169	34
CY36-1-14	0.19	12.9	0.03	0.50	0.71	0.18	5.48	2.15	30	13.4	84	17.6	184	38
CY36-1-15	0.02	9.89	0.02	0.25	0.60	0.31	4.37	1.80	27	11.8	72	14.9	157	35
CY36-1-16	0	9.97	0.01	0.22	0.56	0.23	4.78	1.98	27	11.9	74	15.5	165	36
CY36-1-17	0.01	17.9	0.03	0.78	1.57	0.30	9.35	3.31	46	20	123	25	266	54
CY36-1-18	0	15.8	0.02	0.32	0.90	0.21	5.91	2.23	32	13.8	86	18.6	193	40
CY36-1-19	0.11	26	0.07	0.70	1.09	0.37	6.35	2.61	39	17.6	115	24	248	50
CY36-1-20	0	12.7	0.02	0.29	0.69	0.19	4.31	1.73	26	11.1	72	15.0	162	35
CY36-1-21	0	19.7	0.07	1.13	2.76	0.70	17.4	6.65	86	35	202	39	381	76
CY36-1-22	0.13	16.2	0.22	0.42	0.87	0.25	7.03	2.85	43	18.6	120	25	256	54
CY36-1-23	0.01	16.5	0.04	0.42	1.17	0.30	8.88	3.65	54	23	144	29	292	61
CY36-1-24	0	16.1	0.02	0.45	0.76	0.26	6.99	3.03	47	21	141	29	300	64
CY36-1-25	0.09	25	0.08	0.67	1.29	0.52	8.45	3.37	50	23	151	33	326	67
CY36-1-26	0.02	15.3	0.03	0.41	0.94	0.30	7.33	3.04	44	18.7	116	24	243	52
CY36-1-27	0.02	24	0.02	0.50	1.24	0.49	9.33	3.93	62	27	183	38	396	81
CY36-1-28	0.01	14.3	0.05	0.34	0.73	0.14	4.07	1.82	25	11.4	74	15.5	162	35
CY36-1-29	0.03	13.7	0.03	0.37	0.87	0.27	6.53	2.65	38	16.7	107	22	229	48
CY36-1-30	0.01	14.0	0.06	0.53	0.79	0.24	4.96	1.93	27	12.1	77	16.1	167	36
CY36-1-31	0.03	11.7	0.02	0.21	0.60	0.25	4.55	1.73	26	11.2	70	14.1	154	34
CY36-1-32	0.01	15.0	0.03	0.43	1.20	0.33	8.23	3.20	47	20	110	25	254	55
CY36-1-33	0.03	11.8	0.02	0.45	1.08	0.47	7.08	2.73	38	16.3	89	20	214	47
CY36-1-34	0	18.4	0.02	0.31	0.72	0.20	5.07	2.12	33	14.7	86	21	217	43
CY36-1-35	0.01	14.0	0.01	0.32	0.80	0.23	4.85	1.85	27	11.8	65	16.1	166	36

(continued)

Table 3.14 (continued)

Samples and analyzed spots	La	Ce	Pr	Nd	Sm	Eu	Gd	Tb	Dy	Ho	Er	Tm	Yb	Lu
CY36-1-36	0	15.9	0.01	0.35	0.72	0.23	5.17	2.03	30	13.0	71	17.3	180	38
CY36-1-37	0	12.8	0.01	0.32	0.67	0.24	4.92	1.93	29	12.9	71	17.0	179	38
CY36-1-38	0	9.33	0.01	0.22	0.61	0.18	3.31	1.41	21	8.82	50	12.2	128	28
CY36-1-39	0	12.9	0.05	0.43	0.92	0.23	7.04	2.95	43	19.2	104	25	253	54
CY36-1-40	0.01	8.48	0.03	0.19	0.37	0.10	2.06	0.90	13.3	5.75	33	8.34	87	19.0
CY36-1-41	0.02	19.9	0.05	1.25	2.02	0.62	15.2	5.58	73	30	157	36	352	69

Table 3.15 Zircon Lu–Hf isotopic data of the potassium-rich granitoid gneiss samples YX05-1 and CY36-1 from the Western Liaoning Province

Samples and analyzed spots	Apparent $^{207}Pb/^{206}Pb$ ages (t_1)	$^{176}Yb/^{177}Hf$	$^{176}Lu/^{177}Hf$	$^{176}Hf/^{177}Hf$	±2σ	$(^{176}Hf/^{177}Hf)_{t1}$	εHf (0)	εHf (t_1)	T_{DM}	$f_{Lu/Hf}$	Crystallization ages (t_2)	εHf (t_2)
YX05-1-01	2497	0.012223	0.000407	0.281335	0.000014	0.281315	−50.8	4.5	2634	−0.99	2494	4.5
YX05-1-02	2474	0.011966	0.000403	0.281282	0.000015	0.281263	−52.7	2.1	2705	−0.99	2494	2.6
YX05-1-03	2458	0.014616	0.000501	0.281334	0.000013	0.281311	−50.8	3.5	2641	−0.98	2494	4.3
YX05-1-04	2443	0.013842	0.000435	0.281283	0.000013	0.281263	−52.7	1.4	2706	−0.99	2494	2.6
YX05-1-05	2448	0.013115	0.000399	0.281333	0.000019	0.281314	−50.9	3.4	2636	−0.99	2494	4.4
YX05-1-06	2436	0.015352	0.000515	0.281240	0.000018	0.281216	−54.2	−0.4	2768	−0.98	2494	0.9
YX05-1-07	2429	0.014741	0.000505	0.281305	0.000015	0.281282	−51.9	1.8	2680	−0.98	2494	3.3
YX05-1-08	2436	0.012092	0.000418	0.281295	0.000016	0.281275	−52.2	1.7	2689	−0.99	2494	3.0
YX05-1-09	2440	0.012856	0.000395	0.281276	0.000015	0.281258	−52.9	1.2	2712	−0.99	2494	2.4
YX05-1-10	2439	0.018357	0.000616	0.281289	0.000018	0.281260	−52.5	1.2	2710	−0.98	2494	2.5
YX05-1-11	2463	0.014915	0.000511	0.281285	0.000015	0.281261	−52.6	1.8	2708	−0.98	2494	2.5
YX05-1-12	2437	0.015634	0.000531	0.281262	0.000014	0.281237	−53.4	0.4	2741	−0.98	2494	1.7
YX05-1-13	2458	0.014338	0.000463	0.281306	0.000013	0.281284	−51.8	2.5	2677	−0.99	2494	3.4
YX05-1-14	2469	0.013848	0.000455	0.281300	0.000013	0.281279	−52.0	2.6	2684	−0.99	2494	3.2
YX05-1-15	2457	0.014028	0.000477	0.281286	0.000019	0.281264	−52.5	1.8	2704	−0.99	2494	2.6
YX05-1-16	2491	0.018646	0.000598	0.281320	0.000017	0.281291	−51.4	3.6	2667	−0.98	2494	3.6
YX05-1-17	2485	0.015589	0.000517	0.281263	0.000018	0.281238	−53.4	1.5	2738	−0.98	2494	1.7
YX05-1-18	2487	0.019626	0.000647	0.281284	0.000017	0.281253	−52.6	2.1	2720	−0.98	2494	2.2
YX05-1-19	2472	0.018477	0.000618	0.281326	0.000014	0.281297	−51.1	3.3	2660	−0.98	2494	3.8
YX05-1-20	2500	0.013446	0.000449	0.281283	0.000017	0.281262	−52.6	2.7	2706	−0.99	2494	2.6
YX05-1-21	2517	0.016804	0.000551	0.281281	0.000015	0.281254	−52.7	2.8	2717	−0.98	2494	2.3
YX05-1-22	2518	0.016018	0.000519	0.281278	0.000016	0.281253	−52.8	2.8	2718	−0.98	2494	2.3

(continued)

Table 3.15 (continued)

Samples and analyzed spots	Apparent $^{207}Pb/^{206}Pb$ ages (t_1)	$^{176}Yb/^{177}Hf$	$^{176}Lu/^{177}Hf$	$^{176}Hf/^{177}Hf$	±2σ	$(^{176}Hf/^{177}Hf)_{t1}$	εHf (0)	εHf (t_1)	T_{DM}	$f_{Lu/Hf}$	Crystallization ages (t_2)	εHf (t_2)
YX05-1-23	2503	0.017024	0.000599	0.281305	0.000017	0.281276	−51.9	3.3	2688	−0.98	2494	3.1
YX05-1-24	2524	0.015054	0.000494	0.281301	0.000016	0.281277	−52.0	3.8	2686	−0.99	2494	3.1
YX05-1-25	2520	0.014262	0.000465	0.281275	0.000015	0.281252	−53.0	2.8	2719	−0.99	2494	2.2
YX05-1-26	2394	0.015315	0.000486	0.281287	0.000016	0.281265	−52.5	0.4	2704	−0.99	2494	2.6
YX05-1-27	2481	0.016424	0.000532	0.281273	0.000020	0.281248	−53.0	1.8	2726	−0.98	2494	2.1
YX05-1-28	2488	0.012244	0.000381	0.281306	0.000017	0.281288	−51.8	3.4	2671	−0.99	2494	3.5
YX05-1-29	2476	0.016486	0.000540	0.281250	0.000016	0.281224	−53.8	0.8	2757	−0.98	2494	1.2
YX05-1-30	2458	0.013523	0.000403	0.281289	0.000020	0.281270	−52.4	2.0	2695	−0.99	2494	2.9
YX05-1-31	2481	0.011354	0.000366	0.281260	0.000035	0.281243	−53.5	1.6	2731	−0.99	2494	1.9
YX05-1-32	2509	0.011948	0.000379	0.281260	0.000026	0.281241	−53.5	2.2	2733	−0.99	2494	1.9
YX05-1-33	2496	0.014362	0.000474	0.281286	0.000021	0.281264	−52.5	2.7	2704	−0.99	2494	2.6
YX05-1-34	2500	0.021751	0.000709	0.281295	0.000018	0.281261	−52.2	2.7	2709	−0.98	2494	2.5
YX05-1-35	2520	0.023319	0.000815	0.281347	0.000028	0.281308	−50.4	4.8	2646	−0.98	2494	4.2
YX05-1-36	2489	0.017419	0.000592	0.281286	0.000017	0.281258	−52.5	2.3	2712	−0.98	2494	2.4
CY36-1-01	2410	0.019842	0.000517	0.281396	0.000024	0.281372	−48.7	4.6	2559	−0.98	2496	6.5
CY36-1-02	2421	0.020159	0.000557	0.281406	0.000019	0.281381	−48.3	5.1	2548	−0.98	2496	6.8
CY36-1-03	2420	0.018176	0.000502	0.281298	0.000021	0.281274	−52.1	1.3	2691	−0.98	2496	3.0
CY36-1-04	2435	0.018674	0.000510	0.281363	0.000019	0.281339	−49.8	4.0	2603	−0.98	2496	5.3
CY36-1-05	2446	0.014715	0.000390	0.281358	0.000016	0.281340	−50.0	4.2	2601	−0.99	2496	5.4
CY36-1-06	2448	0.033716	0.000876	0.281397	0.000017	0.281356	−48.6	4.9	2581	−0.97	2496	6.0
CY36-1-08	2477	0.014907	0.000396	0.281346	0.000016	0.281327	−50.4	4.5	2618	−0.99	2496	4.9
CY36-1-09	2520	0.027055	0.000708	0.281359	0.000021	0.281325	−50.0	5.4	2621	−0.98	2496	4.9

(continued)

Table 3.15 (continued)

Samples and analyzed spots	Apparent $^{207}Pb/^{206}Pb$ ages (t_1)	$^{176}Yb/^{177}Hf$	$^{176}Lu/^{177}Hf$	$^{176}Hf/^{177}Hf$	±2σ	$(^{176}Hf/^{177}Hf)_{t1}$	εHf (0)	εHf (t_1)	T_{DM}	$f_{Lu/Hf}$	Crystallization ages (t_2)	εHf (t_2)
CY36-1-10	2465	0.030025	0.000748	0.281364	0.000018	0.281329	−49.8	4.3	2617	−0.98	2496	5.0
CY36-1-11	2454	0.029234	0.000719	0.281387	0.000020	0.281353	−49.0	4.9	2585	−0.98	2496	5.9
CY36-1-12	2495	0.036158	0.000874	0.281410	0.000017	0.281369	−48.2	6.4	2564	−0.97	2496	6.4
CY36-1-13	2491	0.017957	0.000449	0.281363	0.000016	0.281341	−49.8	5.3	2600	−0.99	2496	5.4
CY36-1-14	2462	0.023337	0.000598	0.281361	0.000018	0.281333	−49.9	4.4	2612	−0.98	2496	5.1
CY36-1-15	2528	0.020520	0.000567	0.281319	0.000019	0.281292	−51.4	4.4	2666	−0.98	2496	3.7
CY36-1-16	2583	0.019583	0.000541	0.281368	0.000019	0.281341	−49.7	7.5	2599	−0.98	2583	7.5
CY36-1-17	2589	0.029724	0.000743	0.281373	0.000018	0.281337	−49.5	7.4	2605	−0.98	2589	7.4
CY36-1-18	2643	0.020852	0.000527	0.281378	0.000016	0.281351	−49.3	9.2	2584	−0.98	2643	9.2
CY36-1-19	2592	0.026507	0.000651	0.281411	0.000019	0.281379	−48.1	9.0	2548	−0.98	2592	9.0
CY36-1-20	2644	0.016593	0.000446	0.281327	0.000016	0.281305	−51.1	7.6	2647	−0.99	2644	7.6
CY36-1-21	2554	0.037669	0.000926	0.281375	0.000016	0.281330	−49.4	6.4	2615	−0.97	2554	6.4
CY36-1-22	2602	0.027965	0.000705	0.281379	0.000018	0.281344	−49.3	8.0	2595	−0.98	2602	8.0
CY36-1-23	2550	0.035065	0.000880	0.281398	0.000017	0.281355	−48.6	7.2	2581	−0.97	2550	7.2
CY36-1-24	2531	0.023995	0.000634	0.281373	0.000016	0.281342	−49.5	6.3	2598	−0.98	2496	5.5
CY36-1-25	2600	0.030085	0.000738	0.281341	0.000015	0.281304	−50.6	6.5	2648	−0.98	2600	6.5
CY36-1-26	2487	0.022433	0.000604	0.281368	0.000017	0.281340	−49.6	5.2	2602	−0.98	2496	5.4
CY36-1-27	2501	0.041908	0.001037	0.281372	0.000018	0.281323	−49.5	4.9	2626	−0.97	2496	4.8
CY36-1-28	2511	0.017276	0.000446	0.281333	0.000016	0.281311	−50.9	4.7	2640	−0.99	2496	4.4
CY36-1-29	2457	0.034234	0.000998	0.281348	0.000021	0.281301	−50.3	3.1	2656	−0.97	2496	4.0
CY36-1-31	2376	0.019488	0.000531	0.281374	0.000017	0.281350	−49.4	3.0	2589	−0.98	2496	5.7
CY36-1-32	2402	0.032556	0.000840	0.281348	0.000019	0.281309	−50.4	2.1	2646	−0.97	2496	4.2

(continued)

Table 3.15 (continued)

Samples and analyzed spots	Apparent $^{207}Pb/^{206}Pb$ ages (t_1)	$^{176}Yb/^{177}Hf$	$^{176}Lu/^{177}Hf$	$^{176}Hf/^{177}Hf$	±2σ	$(^{176}Hf/^{177}Hf)_{t1}$	εHf (0)	εHf (t_1)	T_{DM}	$f_{Lu/Hf}$	Crystallization ages (t_2)	εHf (t_2)
CY36-1-33	2424	0.022669	0.000623	0.281316	0.000020	0.281287	−51.5	1.9	2674	−0.98	2496	3.5
CY36-1-34	2407	0.018046	0.000475	0.281364	0.000018	0.281342	−49.8	3.4	2600	−0.99	2496	5.4
CY36-1-37	2352	0.020590	0.000535	0.281412	0.000021	0.281388	−48.1	3.8	2539	−0.98	2496	7.0
CY36-1-38	2389	0.015507	0.000412	0.281373	0.000021	0.281355	−49.5	3.4	2583	−0.99	2496	5.9
CY36-1-39	2367	0.030944	0.000815	0.281441	0.000019	0.281404	−47.1	4.7	2518	−0.98	2496	7.6
CY36-1-40	2373	0.010161	0.000276	0.281301	0.000016	0.281289	−52.0	0.7	2670	−0.99	2496	3.5
CY36-1-41	2369	0.039841	0.000982	0.281448	0.000016	0.281403	−46.8	4.7	2520	−0.97	2496	7.6

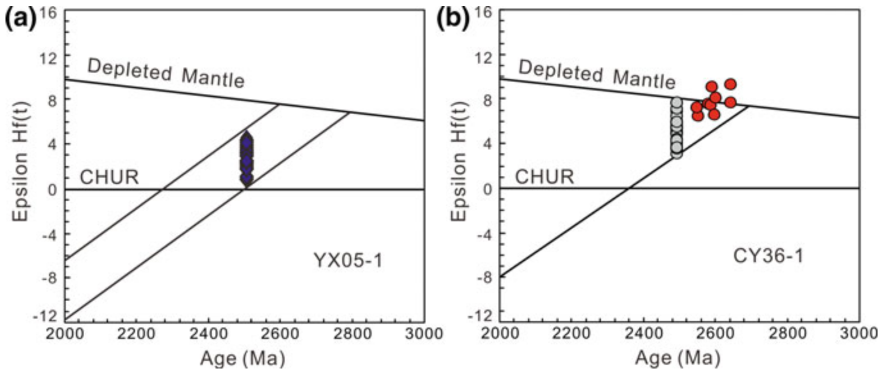

Fig. 3.40 Plots of zircon εHf(t) values versus formation age for representative potassium-rich granodioritic gneiss sample YX05-1 (**a**) and monzogranitic gneiss sample CY36-1. (**b**) Note that the Lu–Hf isotopic data of the analyzed spots are calculated at the magmatic crystallization ages

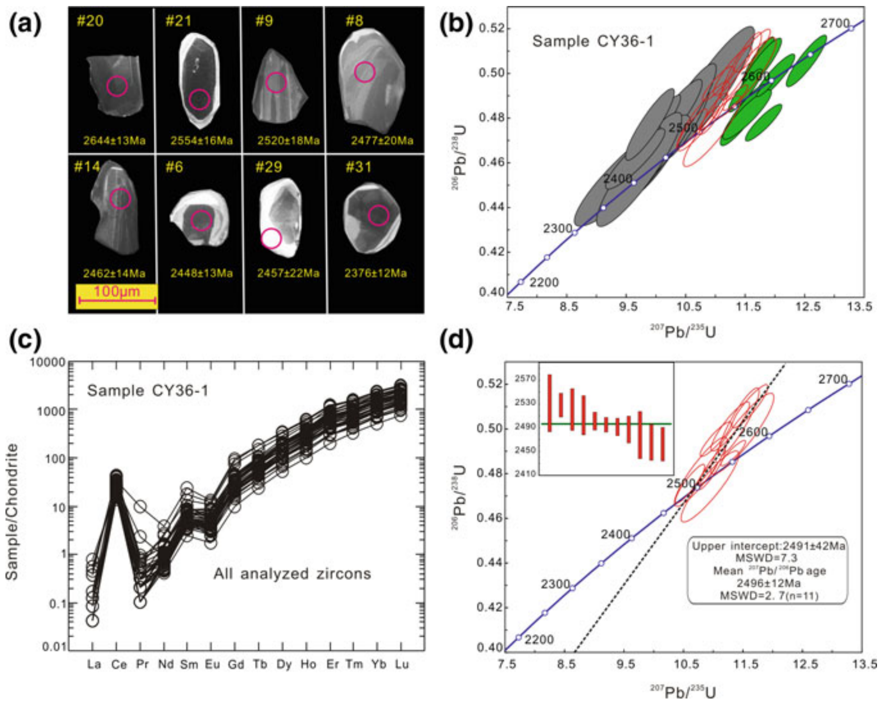

Fig. 3.41 Internal structures, age data, and chondrite-normalized rare earth element pattern of zircon grains from monzogranitic gneiss sample CY36-1. **a** CL images of representative zircon grains showing internal structures and analyzed locations. Numbers are spot locations in Table 3.14. **b** Concordia diagram showing all the analyzed spots. **c** REE patterns for all the analyzed spots. **d** Concordia diagram for the magmatic zircon grains showing the upper intercept and weighted mean $^{207}Pb/^{206}Pb$ ages. The chondrite normalized values are cited from Sun and McDonough [78]

They display Th and U contents of 7–310 ppm and 24–1305 ppm, respectively, yielding generally high Th/U ratios of 0.18–0.91. Most zircon domains show consistent chondrite-normalized REE patterns with positive Ce anomalies, negative Eu anomalies and steep HREE patterns (Fig. 3.41c and Table 3.14). Based on the age distribution and internal structures of zircons, the thirty-seven analyses can be subdivided into three groups as follows.

The first age group is defined by nine analyses of mostly dark structureless domains (e.g., spots #20 and #21, Fig. 3.41a), and they show apparent $^{207}Pb/^{206}Pb$ ages of 2644 ± 13 Ma to 2550 ± 12 Ma. These ages are consistent with those of supracrustal metavolcanic rocks in the JPGT (~2555–2550 Ma, and up to 2615 Ma). Accordingly, these older ages could represent those of inherited/xenocrystic zircon grains captured from the source region or trapped during magma ascent.

Eleven analyses on dark oscillatory zoned domains constitute the second age group (e.g., spots #8, #9 and #14), which show apparent $^{207}Pb/^{206}Pb$ ages of 2531 ± 24 Ma to 2462 ± 14 Ma. They define a discordia, yielding an upper intercept age of 2491 ± 42 Ma (MSWD = 7.3) and a weighted mean age of 2496 ± 12 Ma (MSWD = 2.7) (Fig. 3.41d). Given the magmatic zircon-like oscillatory zonings and REE patterns as well as high Th/U ratios, the age of 2496 Ma is taken as the crystallization age of the magmatic precursor.

The last age group is made up of seventeen analyses on either dark cores or bright rims without internal structures (e.g., spots #6, #29 and #31). The high Th/U ratios and magmatic zircon-like REE patterns imply that they were originally formed during magmatic crystallization, but were subjected to Pb loss during subsequent tectonothermal events [72]. They show young apparent $^{207}Pb/^{206}Pb$ ages of 2457 ± 22 Ma to 2352 ± 22 Ma, reflecting the effects of multiple Paleoproterozoic tectonothermal events in the WLP [42, 43].

All the dated zircon domains, except for the four rejected analyses, were synchronously analyzed for Lu–Hf isotopes (Table 3.15). When calculated at the apparent $^{207}Pb/^{206}Pb$ ages, they yield nearly consistent $^{176}Hf/^{177}Hf(t_1)$ ratios of 0.281274–0.281404. Nine zircon domains of the first age group, considered to be inherited/xenocrystic zircon grains, show $\varepsilon Hf(t_1)$ values of +6.4 to +9.2 with $T_{DM}(Hf)$ of 2648–2548 Ma, with the latter ages comparable with their apparent $^{207}Pb/^{206}Pb$ ages (2550 ± 12 to 2644 ± 13 Ma) (Fig. 3.40b). The other twenty-eight analyses were calculated on the crystallization age (t_2, 2496 Ma), and they yield $\varepsilon Hf(t_2)$ and $T_{DM}(Hf)$ values from +3.0 to +7.6 and 2518 and 2691 Ma, respectively (Fig. 3.40b).

3.3.4 Petrogenesis

Compared to the strongly gneissic TTGs, the weakly gneissic to massive potassium-rich granitoid gneisses are characterized by relative higher K_2O and K_2O/Na_2O, belonging to the high-K calc-alkaline or shoshonite rock series

(Fig. 3.37c and Table 3.12). Neoarchean syenogranitic gneisses were also documented in other terranes of North China Craton [86].

The monzogranitic gneiss samples CY12-2 and OYX11-1 show chemical affinities to the leucogranites, i.e., high SiO_2 (71.96–73.69 wt%) and K_2O (4.66–5.97 wt%), and low MgO (0.30–0.57 wt%) [4, 27]. They are strongly peraluminous with high A/CNK values of 1.09–1.15 (Fig. 3.37d). In the AFM-CFM diagram (Fig. 3.42), these monzogranitic gneisses fall into the partial melting field of metagreywackes [1]. All the data indicate that they could have been produced by the partial melting of metasedimentary rocks. The strongly fractionated concave-upward REE patterns with positive Eu anomalies suggest that garnet and amphibole are the major residue phases (Fig. 3.38a) [70]. In comparison, the granodioritic gneiss samples OYX02-1 and YX05-1 display low SiO_2 (65.38–66.89 wt %) and K_2O (3.98–4.17 wt%) but high MgO (1.64–1.88) and Mg# (49.30–49.27). The AFM and CFM values range from 1.59–1.87 and 0.63–0.70, respectively, together with the low A/CNK values of 0.90–1.02, suggesting that their parental magmas could have been derived from the partial melting of metatonalitic rocks (Fig. 3.42) [1, 94]. The dated sample YX05-1 has moderately positive zircon εHf (t_2) values of +0.9 to +4.5 with depleted mantle model ages of ~2.77–2.63 Ga. These largely overlap the T_{DM}(Hf) modal ages of early metavolcanic rocks and TTG gneisses, suggesting their derivation dominantly from juvenile crustal sources (Fig. 3.40). The fractionated normalized REE patterns with high $(La/Yb)_N$ (20.82–34.11) and Sr/Y (30.68–135.57) ratios as well as evidently positive Eu anomalies (Eu_N/Eu_N^* = 0.80–3.13), suggest the presence of garnet but not plagioclase and hornblende in the residue.

The monzogranitic gneiss samples CY36-1 and CY39-1 have SiO_2 and MgO contents of 67.69–67.86 wt% and 0.18–0.65 wt%, respectively. The AFM-CFM plot reveal that they may be generated by the partial melting of metapelites (Fig. 3.42). However, they are metaluminous with relatively low A/CNK values of

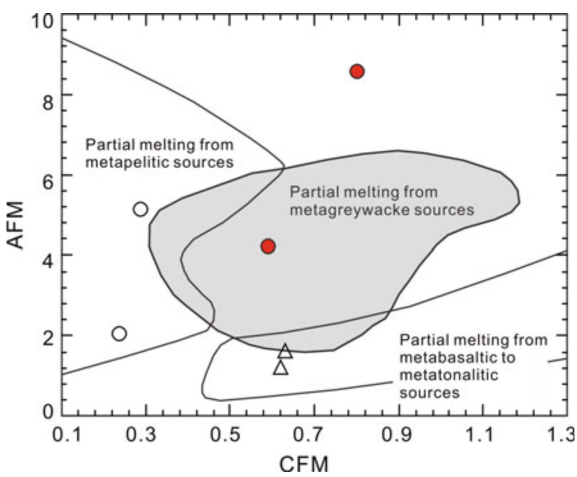

Fig. 3.42 Molar Al_2O_3/($MgO + FeO_T$) (AFM) versus molar $CaO/(MgO + FeO_T)$ (CFM) diagram showing the source compositions of the potassium-rich granitoid gneisses from the Western Liaoning Province (modified from Altherr et al. [1]). Sample symbols: triangles—granodioritic gneisses of NCFY-GGB; solid cycles—monzogranitic gneisses of NCFY-GGB; open cycles—monzogranitic gneisses of JPGT

0.96–0.98 (Fig. 3.37d). Considering the relatively higher CaO/Na_2O (0.18–0.36) and $FeO_T + MgO + TiO_2$ (2.54–5.32 wt%), some metabasaltic rocks may have been involved in the source region [79]. Sample CY36-1 show relatively lower $(La/Yb)_N$, less fractionated HREE patterns, and weakly positive Eu and Sr anomalies, implying that garnet and hornblende are the major residual phases with minor plagioclase. In comparison, the concave-upward REE patterns and weakly negative Eu and Sr anomalies of sample CY39-1 suggest plagioclase and hornblende in the residue (Fig. 3.38c, d).

3.3.5 Tectonic Setting

As discussed above, the supracrustal metavolcanic rocks and dioritic to TTG gneisses in the WLP could have been formed in a convergent arc setting [89–91]. The weakly gneissic to massive potassium-rich granitoid gneisses (~2495 Ma) formed later than the gneissic dioritic and TTG rocks (2532–2506 Ma). They were derived mainly from the partial melting of metatonalitic to metasedimentary rocks, and are nearly coeval with regional peak granulite facies metamorphism (~2485 Ma). It is indicated that the late Neoarchean mafic granulites record anti-clockwise P-T-t paths [36]. Considering the weakly gneissic to massive structures of these granitoid gneisses, we propose that they could have been generated under an extensional setting, possibly related to post-collisional stage following the accretion and stabilization of the arc system onto the northern continental margin of the Eastern Block [93].

3.4 Neoarchean Crustal Evolution and Crust-Mantle Geodynamics of the Western Liaoning Province

3.4.1 Neoarchean Sequences of Geological Events and Crustal Evolution

Though the NCFY-GGB and JPGT of Western Liaoning Province have different lithological assemblages and metamorphic grades, they could have experienced similar early Precambrian geological evolution as summarized below (Table 3.16) [42, 43, 89–91, 93]:

(1) ***~2640–2520 Ma***: Representative metavolcanic rocks in the Fuxin-Yixian greenstone belt (NCFY-GGB) yield formation ages of 2640 ± 9 Ma (12FX18-2), 2603 ± 19 Ma (OFX08-5), 2549 ± 19 Ma (12FX25-6), 2540 ± 17 Ma (12FX28-3), and 2534 ± 16 Ma (FX09-1) (Figs. 3.4, 3.5, 3.6, 3.7 and 3.8). This suggests that the volcano-sedimentary sequences in the NCFY-GGB were generated during 2640–2534 Ma. Mafic volcanism in the

Table 3.16 Summary of chronological data of the late Archean to early Paleoproterozoic basement rocks of the Western Liaoning Province

Sample	Lithology	Crystallization age	Age of inherited or xenocrystic zircon	Metamorphic age
Jianping gneissic terrane (JPGT)				
Supracrustal metavolcanic rocks				
CY32-3(2)	Hornblende plagioclase gneiss	2555 ± 7 Ma	2699 ± 35 Ma	2512 ± 12/2449 ± 12/ 2385 ± 12 Ma
CY55-3(2)	Biotite plagioclase gneiss	2550 ± 4 Ma	2581 ± 6 Ma	2471 ± 7/2435 ± 27/ 2406 ± 28 Ma
Early granitoid gneisses of high magnesium group with gneissic structures				
CY31-2(2)	Hornblende plagioclase gneiss	2513 ± 10 Ma		2476 ± 13/2449 ± 5/ 2410 ± 5 Ma
OCY31-2	Biotite two pyroxene granulite	2516 ± 6 Ma	2614 ± 13 to 2549 ± 16 Ma	2487 ± 9/2465 ± 13– 2409 ± 12 Ma
OCY33-1	Biotite two pyroxene granulite	2519 ± 11 Ma	2585 ± 15 Ma	2497 ± 15–2423 ± 20/ 2396 ± 13– 2224 ± 16 Ma
CY46-1(2)	Biotite plagioclase gneiss	2506 ± 12 Ma	2561 ± 13 Ma	2458 ± 12/2396 ± 30/ 1862 ± 30 Ma
Early granitoid gneisses of low magnesium group with gneissic structures				
OCY37-1	Hornblende biotite plagioclase gneiss	2527 ± 7 Ma	2591 ± 21 Ma	2478 ± 23– 2394 ± 27 Ma
OCY46-1	Two pyroxene plagiocase gneiss	2532 ± 7 Ma		2468 ± 19 Ma
Late potassium-rich granitoid gneisses with weakly gneissic to massive structures				
CY36-1	Monzogranitic gneiss	2496 ± 12 Ma	2644 ± 13 to 2550 ± 12 Ma	2457 ± 22– 2352 ± 22 Ma
North Chaoyang-Fuxin-Yixian granite-greenstone belt (NCFY-GGB)				
Supracrustal metavolcanic rocks				
FX09-1	Hornblende plagioclase gneiss	2534 ± 16 Ma	2633 ± 35 Ma	2498 ± 12/2432 ± 12– 2043 ± 22 Ma
OFX08-5	Garnet clinopyroxene plagiocase gneiss	2603 ± 19 Ma		1736 ± 29 Ma
12FX18-2	Garnet clinopyroxene amphibolite	2640 ± 19 Ma		2521 ± 14/2437 ± 20/ 2276 ± 24– 1725 ± 49 Ma
12FX25-6	Amphibolite	2546 ± 19 Ma		
12FX28-3	Clinopyroxene amphibolite	2540 ± 17 Ma		2470 ± 14/2343 ± 24/ 2381 ± 25 Ma
Early granitoid gneisses of high magnesium group with gneissic structures				
CY26-1(2)	Dioritic gneiss	2512 ± 15 Ma	2572 ± 20 Ma	2478 ± 9/ 2428 ± 10 Ma
OCY10-1	Tonalitic gneiss	2511 ± 7 Ma	2570 ± 17 Ma	2475 ± 15–2401 ± 12/ 2269 ± 15 Ma

(continued)

Table 3.16 (continued)

Sample	Lithology	Crystallization age	Age of inherited or xenocrystic zircon	Metamorphic age
OYX01-4	Granodioritic gneiss	2521 ± 9 Ma		2278 ± 46 Ma
Early granitoid gneisses of low magnesium group with gneissic structures				
OFX11-2	Trondhjemitic gneiss	2517 ± 13 Ma	2668 ± 12 to 2630 ± 11/ 2580 ± 8 Ma	2442 ± 11–2362 ± 16 Ma
Late potassium-rich granitoid gneisses with weakly gneissic to massive structures				
YX05-1	Granodioritic gneiss	2494 ± 8 Ma		
CY12-2(1)	Monzograntiic gneiss	2496 ± 7 Ma		

Note Chronological data marked by (1) and (2) are cited from Liu et al. [42, 43], respectively. Early chronological data obtained by single zircon evaporation method were not included in this summary

neighbouring Chaoyang Complex occurred between 2568 and 2520 Ma [42]. Supracrustal rock sequences of the JPGT were formed mainly during 2555–2550 Ma, and possibly up to 2615 Ma [43]. All the above data indicate that >2520 Ma volcanism occurred coevally within different segments of the WLP. Metavolcanic rocks in the NCFY-GGB show geochemical affinities to MORBs, arc tholeiitic to calc-alkaline basalts, adakitic rocks, and high magnesium andesites, respectively, and the volcanic rock assemblages could have been formed under late Neoarchean subduction-accretion processes. The metamorphosed mafic to felsic volcanic rocks with interlayered BIFs and quartzites in the JPGT were also suggested to have been formed under a convergent arc setting [43].

(2) ***~2532–2506 Ma***: Volumes of dioritic to TTG gneisses with strongly gneissic structures are pervasively developed in the WLP, and they intruded into early metamorphosed supracrustal rocks (Figs. 3.17 and 3.19). The parental magmas of TTG gneisses in the NCFY-GGB were crystallized during 2521–2511 Ma, which are roughly coeval with those of dioritic to TTG gneisses in the JPGT (2532–2506 Ma; Figs. 3.28, 3.29, 3.30, 3.31 and 3.32). According to the petrological, geochemical, and genetic features, these granitoid gneisses are subdivided into two different groups: (a) a high magnesium group (HMG), with adakite-like chemical features and high MgO contents, which could have been generated by the partial melting of subducted slabs, with the melts contaminated by the mantle wedge materials; and (b) a low magnesium group (LMG), showing chemical features typical of Archean high-Al TTG gneisses, which were considered to have been produced by the partial melting of garnet amphibolites at the arc root.

(3) ***~2495 Ma***: Small volume of potassium-rich granitoid gneisses were developed in the WLP, including the monzogranitic gneisses of JPGT and granodioritic

and monzogranitic gneisses in the NCFY-GGB (Figs. 3.35 and 3.36). They are characterized by weakly gneissic to massive structures, and were dominantly derived from the partial melting of metamorphosed felsic or sedimentary rocks. These granitoid gneisses formed coevally with regional granulite facies morphism (~2485 Ma), which together with the anti-clockwise P-T-t paths recorded by the mafic granulites [36], suggesting that they could have been evolved under an extensional setting.

(4) Zircon U-Pb isotopic dating data reveal that the JPGT experienced ~2485 Ma granulite facies and ~2450–2401 Ma retrograde metamorphism (Table 3.16). Whereas basement rocks of the NCFY-GGB record multiple episodes of metamorphic imprints at ~2521, ~2490–2470, ~2440, ~2350, ~2040, and ~1700 Ma. The first three episodes of metamorphism are consistent with regional ~2520–2495 Ma granitoid magmatism, ~2485 Ma peak granulite facies and ~2450–2401 Ma retrograde metamorphism [32, 43, 90]. ~1700 Ma metamorphic event may be triggered by the voluminous late Paleoproterozoic magmatism, e.g., ~1740 Ma Damiao anorthosite complex and ~1721–1696 Ma Jianping diorite-monzonite-syenite suite [92, 102]. ~2350–2040 Ma metamorphic events were also recorded in the nearby Eastern Hebei, possibly reflecting multiple episodes of middle Paleoproterozoic tectonothermal events [21, 90, 91, 93].

3.4.2 Late Neoarchean (~2.6–2.5 Ga) Crustal Growth

The formation and evolution of early continental crust is one of the major issues of Precambrian research. Early studies revealed three major episodes of crustal growth, i.e., ~2.7, ~1.9, and ~1.2 Ga, which were suggested to be linked to superplume events and supercontinental cycles [10]. Chronological data and Sm–Nd isotopes of global granitoid rocks as well as ages of detrital zircons were recently compiled, and it is indicated that ~2.6–2.5 Ga tectonothermal events are widely developed in East Asia, Africa, India, North Australia, and Antarctica. Importantly, both ~2.7 and ~2.5 Ga tectonothermal events could record significant crustal growth [12].

The parental magmas of metabasaltic to metaandesitic rocks in the NCFY-GGB of WLP formed between 2.64 and 2.53 Ga, and they show depleted zircon $\varepsilon Hf(t_2)$ values (+9.7 to +2.7; Figs. 3.4, 3.5, 3.6, 3.7 and 3.8). This indicates that the volcanic rocks were mainly derived from the partial melting of depleted mantle sources, recording evident late Neoarchean crustal growth (~2.6–2.5 Ga). The six dated granitoid gneisses of JPGT show T_{DM}(Hf) model ages ranging mostly of 2.77–2.52 Ga (Tables 3.8 and 3.11), and the two dated granitoid gneisses of NCFY-GGB give comparable model ages of 2.77–2.58 Ga (Tables 3.8 and 3.15). The model ages of these granitoid gneisses are largely coeval with those of metavolcanic rocks (2.79–2.51 Ga). The younger model ages of 2.58–2.52 Ga is close to the magmatic crystallization ages of these granitoid gneisses. Mantle materials could have been involved in the genesis of dioritic and TTG gneisses of the HMG, which show chemical features of adakites. Accordingly, granitoid gneisses in the WLP also record major episode of crustal growth during ~2.6–2.5 Ga.

For the whole NCC, ~2.6–2.5 Ga mafic to ultramafic volcanic rocks are widely preserved in Eastern Hebei, Western Liaoning, Northern Liaoning, Western Shandong of the Eastern Block, Guyang-Wuchuan areas of Western Block, as well as Wutai complex in the Trans-North China Orogen. They were directly generated from the mantle sources, signifying evident net crustal growth. Accordingly, the NCC record probably significant crustal growth during late Neoarchean (~2.6–2.5 Ga).

3.4.3 Late Neoarchean Crust-Mantle Geodynamics

The late Neoarchean tectonic setting of the Eastern Block, North China Craton remains hotly debated, with mantle plume and plate tectonic processes been proposed [18, 21, 37, 38, 43, 57, 85, 88–91, 93, 103, 104, 106]. According to the lithological assemblage, petrogenesis, and crustal evolution history of the WLP, the late Neoarchean crust-mantle geodynamic processes are summarized below:

(1) ~2640–2534 Ma: Intense volcanism occurred in the Western Liaoning Province, forming the magmatic precursors of supracrustal metavolcanic rocks [42, 43, 89, 93]. The Fuxin area is one of the major exposure region of supracrustal metavolcanic rocks, and they show chemical affinities to MORBs, arc tholeiitic to calc-alkaline basalts, adakites, and high magnesium andesites. They record crust-mantle geodynamic processes as follows (Fig. 3.43a–c): (I) Adiabatic decompression melting of the asthenospheric mantle under a mid-ocean ridge generated N-MORBs and E-MORBs of Group MB-1, yielding depleted to slightly enriched juvenile oceanic lithospheric mantle sources; (II) during the initiation stage of intra-oceanic subduction, the juvenile oceanic lithospheric mantle sources were metasomatized by small volume of fluids released from the subducted slabs, forming the island arc tholeiites of Group MB-2; (III) with gradual maturation of the island arc system, the sub-arc lithospheric mantle sources were increasingly metasomatized by the slab fluids/ melts and enriched in large ion lithophile elements (LILEs) and LREEs, the partial melting of which yield the calc-alkaline basalts of Group MB-3; (V) with the descending of oceanic slabs, partial melting of slab basalts occurred, with the ascending melts contaminated by the mantle wedge materials, forming adakite-like rocks of Group MA-1; and (IV) subsequent partial melting of the oceanic lithospheric mantle metasomatized by slab melts generated the high magnesium andesites of Group MA-2. Accordingly, the WLP experienced typical intra-oceanic arc subduction processes during ~2640–2534 Ma showing a southward subduction polarity, with probable accretion of MORB-type oceanic crust [93]. Notably, metavolcanic rocks in the WLP exhibit mostly depleted zircon εHf(t_2) values (Figs. 3.4, 3.5, 3.6, 3.7 and 3.8), whereas the E-MORBs of Group MB-1 may be derived from a slightly enriched

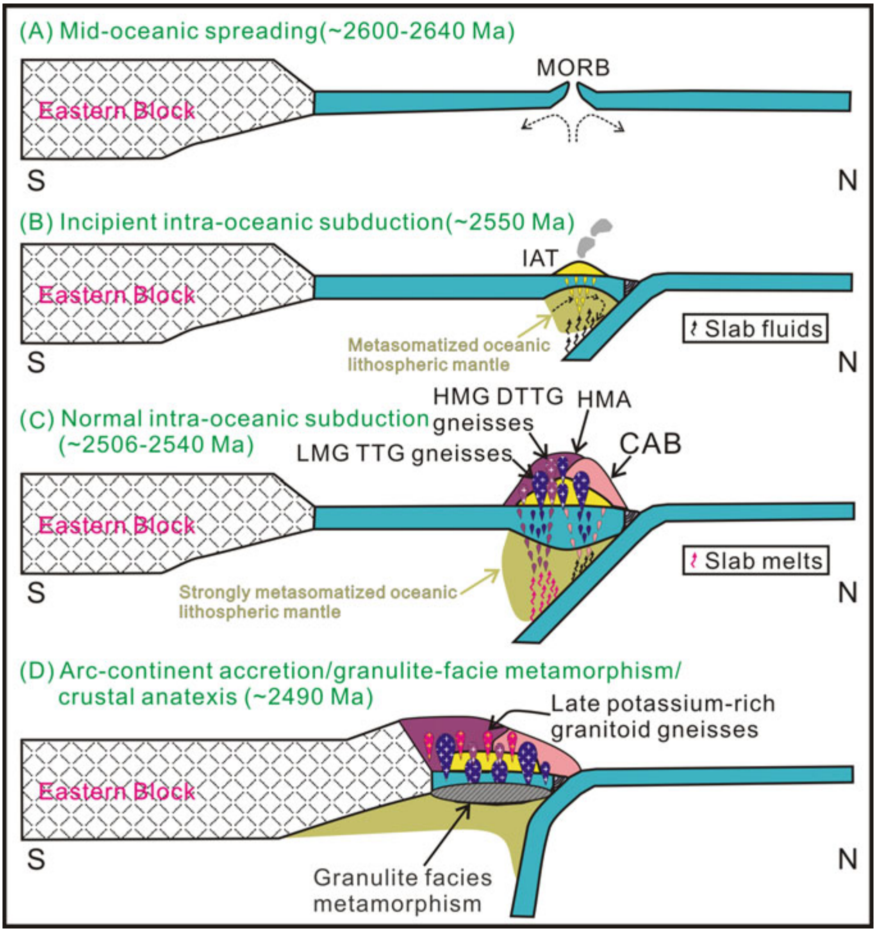

Fig. 3.43 Neoarchean to early Paleoproterozoic geodynamic evolution of the Western Liaoning Province showing the construction of an intra-oceanic arc system and its final accretion to the northern margin of the Eastern Block. **a** Mid-ocean ridge spreading and magmatism during ~2640–2600 Ma, with the formation of MORB-like metabasaltic rocks of Group MB-1. **b** Incipient subduction of oceanic slabs and intra-oceanic arc magmatism at ~2550 Ma, forming IAT-like metabasaltic rocks of Group MB-2. The depleted oceanic lithospheric mantle was weakly metasomatized and transformed to sub-arc lithospheric mantle. **c** With the development of the oceanic subduction system during ~2540–2506 Ma, the partial melting of strongly metasomatized (both slab-derived fluids and melts) lithospheric mantle sources, subducted slabs, and the arc root materials gave rise to the generation of CAB-like metabasaltic rocks of Group MB-3, adakite-like and HMA-like metaandesitic rocks of Groups MA-1 and MA-2, as well as HMG and LMG DTTG gneisses, respectively. **d** At ~2490 Ma, the accretion of this oceanic arc system onto the northern margin of Eastern Block triggered both granulite-facie metamorphism at the arc root and crustal anatexis, forming the potassium-rich granitoids

mantle source, suggesting late Neoarchean mantle heterogeneities along the northern margin of Eastern Block.

(2) During ~2532–2506 Ma, voluminous TTG and dioritic gneisses emplaced in the WLP, and they show strongly gneissic structure, which could have been formed in a compressional tectonic environment. These granitoid gneisses were derived from the partial melting of either subducted slab basalts or metabasaltic rocks at the arc root. They could record complex crust-mantle interaction processes related to the dehydration and partial melting of descending slabs as well as slab-mantle wedge interactions, with the underplating mantle-derived magmas triggered the partial melting of metabasaltic rocks at the root area [90, 91, 93] (Fig. 3.43c).

(3) Some granodioritic to monzogranitic gneisses occurred at ~2495 Ma. The weakly gneissic to massive structures as well as nearly coeval granulite facies metamorphism suggest that these granitoid magmatism could have been evolved at an extensional setting, i.e., the accretion of the above intra-oceanic arc onto the northern continental margin of Eastern Block triggered slab rollback or breakoff, and the high heat flux brought in by the upwelling asthenospheric mantle induced crustal anataxis, with the partial melting of accreted metamorphosed felsic and sedimentary rocks forming the potassium-rich granitoids (Fig. 3.43d).

Accordingly, basement rocks of the Western Liaoning Province could have been evolved in a late Neoarchean accretionary orogen, recording crust-mantle geodynamic processes from mid-oceanic ridge spreading, through initiation and maturation of an intra-oceanic arc system, to the final arc-continent accretion along the northern margin of Eastern Block (Fig. 3.43). Similarly, a subduction-related tectonic regime has been invoked to account for the late Neoarchean crustal formation and evolution in the Zunhua-Qinglong Block of Eastern Hebei, Northern Hebei, Western Shandong, Wutai and Fuping Complex in the Trans-North China Orogen [21, 37–41, 43, 57, 85, 88]. In summary, subduction-accretion processes may have been an important crust-mantle geodynamic regimes during the late Neoarchean continental growth of Eastern Block. Future geochemical and structural comparison of this Archean accretionary orogen with those of Phanerozoic ones will provide important insights into the prolonged thermodynamic evolution of the planetary Earth.

References

1. Altherr R, Holl A, Hegner E (2000) High-potassium, calc-alkaline I-type plutonism in the European Variscides: Northern Vosges (France) and northern Schwarzwald (Germany). Lithos 50:51–73
2. Anderson T (2002) Correlation of common lead in U–Pb analyses that do not report 204Pb. Chem Geol 192:59–79
3. Arzi AA (1978) Critical phenomena in the rheology of partially melted rocks. Tectonophysics 44:173–184
4. Ayres M, Harris N (1997) REE fractionation and Nd-isotope disequilibrium during crustal anatexis: constraints from Himalayan leucogranites. Chem Geol 139:249–269

5. Barker F (1979) Trondhjemite: definition, environment and hypotheses of origin. In: Barker F (ed) Trondhjemites, Dacites, and related rocks. Elsevier, Amsterdam, pp 1–12
6. Blichert-Toft J, Albarède F (1997) The Lu-Hf geochemistry of chondrites and the evolution of the mantle-crust system. Earth Planet Sci Lett 148:243–258
7. Cabanis B, Lecolle M (1989) Le diagramme La/10-Y/15-Nb/8: un outil pour la discrimination des series volcaniques et la mise en evidence des processus de melange et/ou de contamination crustale. C.R. Acad Sci Ser II 309:2023–2029
8. Castillo PR (2012) Adakite petrogenesis. Lithos 134–135:304–316
9. Castillo PR, Janney PE, Solidum RU (1999) Petrology and geochemistry of Camiguin Island, southern Philippines: insights to the source of adakites and other lavas in a complex arc setting. Contrib Mineral Petrol 134:33–51
10. Condie KC (1998) Episodic continental growth and supercontinents: a mantle avalanche connection? Earth Planet Sci Lett 163:97–108
11. Condie KC (2005) High field strength element ratios in Archean basalts: a window to evolving sources of mantle plumes? Lithos 79:491–504
12. Condie KC, O'Neill C, Aster RC (2009) Evidence and implications for a widespread magmatic shutdown for 250 My on Earth. Earth Planet Sci Lett 282:294–298
13. Corfu F, Hanchar JM, Hoskin PWO, Kinny P (2003) Atlas of zircon textures. In: Hanchar JM, Hoskin PWO (eds) Zircon, 53. Mineralogical Society of America Reviews in Mineralogy and Geochemistry, pp 469–500
14. Defant MJ, Drummond MS (1990) Derivation of some modern arc magmas by melting of young subducted lithosphere. Nature 347:662–665
15. Ernst RE, Wingate MTD, Buchan KL, Li ZX (2008) Global record of 1600–700 Ma Large Igneous Provinces (LIPs): implications for the reconstruction of the proposed Nuna (Columbia) and Rodinia supercontinents. Precambr Res 160:159–178
16. Foley S, Tiepolo M, Riccardo V (2002) Growth of early continental crust controlled by melting of amphibolite in subduction zones. Nature 417:837–840
17. Frey FA, Prinz M (1978) Ultramafic inclusions from San Carlos, Arizona: petrologic and geochemical data bearing on their petrogenesis. Earth Planet Sci Lett 38:129–176
18. Geng YS, Liu FL, Yang C (2006) Magmatic event at the end of the Archean in eastern Hebei Province and its geological implication. Acta Geol Sin (English version) 80:819–833
19. Grant ML, Wilde SA, Wu FY, Yang JH (2009) The application of zircon cathodoluminescence imaging, Th–U–Pb chemistry and U–Pb ages in interpreting discrete magmatic and high-grade metamorphic events in the North China Craton at the Archean/Proterozoic boundary. Chem Geol 261:155–171
20. Griffin WL, Pearson NJ, Belousova E, Jackson SE, van Achterbergh E, O'Reilly SY, Shee SR (2000) The Hf isotope composition of cratonic Mantle, LA-MC-ICPMS analysis of zircon megacrysts in kimberlites. Geochim Cosmochim Acta 64:133–147
21. Guo RR, Liu SW, Santosh M et al (2013) Geochemistry, zircon U-Pb geochronology and Lu-Hf isotopes of metavolcanics from eastern Hebei reveal Neoarchean subduction tectonics in the North China Craton. Gondwana Res 24:664–686
22. Hawkesworth CJ, Gallagher K, Hergt JM, McDetmott F (1993) Mantle and slab contributions in arc magmas. Annu Rev Earth Planet Sci 21:175–204
23. Heilimo E, Halla J, Hölttä P (2010) Discrimination and origin of the sanukitoid series: geochemical constraints from the Neoarchean western Karelian Province (Finland). Lithos 115:27–39
24. Huang XL, Xu YG, Lan JB, Yang QJ, Luo ZY (2009) Neoproterozoic adakitic rocks from Mopanshan in the western Yangtze Craton: partial melting of a thickened lower crust. Lithos 112:367–381
25. Jahn B, Glikson AY, Peucat JJ, Hickman AH (1981) REE geochemistry and isotopic data of Archaean silicic volcanics and granitoids from the Pilbara block, Western Australia: implications for early crustal evolution. Geochim Cosmochim Acta 45:1633–1652

26. Jourdan F, Bertrand H, Schärer U, Blichert-Toft J, Féraud G, Kampunzu AB (2007) Major and trace element and Sr, Nd, Hf, and Pb isotope compositions of the Karoo large igneous province, Botswana-Zimbabwe: lithospheric vs mantle plume contribution. J Petrol 48:1043–1077
27. Kalsbeek F, Jepsen HF, Jones KA (2001) Geochemistry and petrogenesis of S-type granites in the East Greenland Caledonides. Lithos 57:91–109
28. Katz O, Beyth M, Miller N, Stern R, Avigad D, Basu A, Anbar A (2004) A late Neoproterozic (630 Ma) high-magnesium andesite suite from southern Israel: implications for the consolidation of Gondwanaland. Earth Planet Sci Lett 218:475–490
29. Kelemen PB, Hanghoj K, Greene AR (2004) One view of the geochemistry of subduction-related magmatic arcs, with emphasis on primitive andesite and lower crust. In: Rudnick RL (ed) The crust, treatise on geochemistry, vol 3. Elsevier, Netherlands, pp 593–659
30. Kerrich R, Xie QL (2002) Compositional recycling structure of an Archean super-plume: Nb-Th-U-LREE systematics of Archean komatiites and basalts revised. Contrib Miner Petrol 142:476–484
31. Kerrich R, Wyman D, Fan J (1998) Boninite series: low Ti-tholeiite associations from the 2.7 Ga Abitibi greenstone belt. Earth Planet Sci Lett 164:303–316
32. Kröner A, Cui WY, Wang SQ, Wang CQ, Nemchin AA (1998) Single zircon ages from high-grade rocks of the Jianping Complex, Liaoning Province, NE China. J Asian Earth Sci 16:519–532
33. LaFlèche MR, Camire G, Jenner GA (1998) Geochemistry of post-Acadian, carboniferous continental intraplate basalts from the Maritimes basin, Magdalen islands, Quebec, Canada. Chem Geol 148:115–136
34. Laurent O, Martin H, Moyen JF, Doucelance R (2014) The diversity and evolution of late-Archean granitoids: evidence for the onset of "modern-style" plate tectonics between 3.0 and 2.5 Ga. Lithos 205:208–235
35. Li SG (1993) Ba-Nb-Th-La diagrams used to identify tectonic environments of ophiolite. Acta Petrol Sin 9:146–157 (in Chinese with English abstract)
36. Lin BQ, Cui WY, Wang SQ, Shen ES (1997) The Archean geology and gold deposits in Western Liaoning Province. Seismological Press, Beijing, pp 1–130 (in Chinese)
37. Liu SW, Pan YM, Li JH, Zhang J, Li QG (2002) Geological and isotopic geochemical constraints on the evolution of the Fuping complex, North China Craton. Precambr Res 117:41–56
38. Liu SW, Pan YM, Xie QL, Zhang J, Li QG (2004) Archean geodynamics in the Central Zone, North China craton: constraints from geochemistry of two contrasting series of granitoids in the Fuping and Wutaishan complexes. Precambr Res 130:229–249
39. Liu SW, Tian W, Lv YJ et al (2006) Geochemistry, Nd isotopic characteristics of metamorphic complexes in Northern Hebei: implications for crustal accretion. Acta Geol Sin (English version) 80:807–818
40. Liu SW, Lü YJ, Feng YG, Zhang C, Tian W, Yan QR, Liu XM (2007) Geology and zircon U-Pb isotopic chronology of Dantazi complex, Northern Hebei Province. Geol J China Univ 13:484–497 (in Chinese with English abstract)
41. Liu SW, Lü YJ, Feng YG, Liu XM, Yan QR, Zhang C, Tian W (2007) Zircon and monazite geochronology of the Hongqiyingzi complex, northern Hebei, China. Geol Bull China 26:1086–1100 (in Chinese with English abstract)
42. Liu SW, Wang W, Bai X, Zhang F (2010) Geological events of early Precambrian complex in North Chaoyang area, Liaoning Province. Acta Petrol Sin 26:1993–2004 (in Chinese with English abstract)
43. Liu SW, Santosh M, Wang W, Bai X, Yang PT (2011) Zircon U-Pb chronology of the Jianping Complex: implications for the Precambrian crustal evolution history of the northern margin of North China Craton. Gondwana Res 20:48–63
44. Liu SW, Zhang J, Li QG, Zhang LF, Wang W, Yang PT (2012) Geochemistry and U-Pb zircon ages of metamorphic volcanic rocks of the Paleoproterozoic Lüliang complex and

constraints on the evolution of the Trans-North China Orogen, North China Craton. Precambr Res 222–223:173–190
45. Maniar PD, Piccoli PM (1989) Tectonic discrimination of granitoids. Geol Soc Am Bull 101:635–643
46. Manikyamba C, Kerrich R (2011) Geochemistry of alkaline basalts and associated high-Mg basalts from the 2.7 Ga Penakacherla Terrane, Dharwar craton, India: an Archean depleted mantle-OIB array. Precambr Res 188:104–122
47. Manikyamba C, Kerrich R (2012) Eastern Dharwar Craton, India: continental lithosphere growth by accretion of diverse plume and arc terranes. Geosci Front 3:225–240
48. Manikyamba C, Ganguly S, Santosh M, Saha A, Chatterjee A, Khelen AC (2015) Neoarchean arc-juvenile back-arc magmatism in eastern Dharwar Craton, India: geochemical fingerprints from the basalts of Kadiri greenstone belt. Precambr Res 258:1–23
49. Martin H (1999) Adakitic magmas: modern analogues of Archean granitoids. Lithos 46:411–429
50. Martin H, Smithies RH, Moyen JF, Champion D (2005) An overview of adakite, tonalite-trondhjemite-granodiorite (TTG), and sanukitoid: relationships and some implications for crust evolution. Lithos 79:1–24
51. Martin H, Moyen JF, Rapp R (2010) The sanukitoid series: magmatism at the Archaean-Proterozoic transition. In: Sixth Hutton symposium on the origin of granites and related rocks: proceedings of a symposium held in Stellenbosch, South Africa, 2–6 July 2007. Cambridge University Press, p 15
52. Moyen JF (2009) High Sr/Y and La/Yb ratios, the meaning of the "adakitic signature". Lithos 112:556–574
53. Moyen JF (2011) The composite Archaean grey gneisses: petrological significance, and evidence for a non-unique tectonic setting for Archaean crustal growth. Lithos 123:21–36
54. Moyen JF, Martin H (2012) Forty years of TTG research. Lithos 148:312–336
55. Moyen JF, Martin H, Jayananda M, Auvray B (2003) Late Archean granites: a typology based on the Dharwar Craton (India). Precambr Res 127:103–123
56. Naqvi SM, Khan RMK, Manikyamba C et al (2006) Geochemistry of the Neoarchaean high-Mg basalts, boninites and adakites from the Kushtagi-Hungund greenstone belt of the Eastern Dharwar Craton (EDC): implications for the tectonic setting. J Asian Earth Sci 27:25–44
57. Nutman AP, Wan YS, Du LL, Friend CRL, Dong CY, Xie HQ, Wang W, Sun HY, Liu DY (2011) Multistage late Neoarchaean crustal evolution of the North China Craton, eastern Hebei. Precambr Res 189:43–65
58. Ordóñez-Calderón JC, Polat A, Fryer BJ et al (2009) Geochemistry and geodynamic origin of the Mesoarchean Ujarassuit and Ivisaartoq greenstone belts, SW Greenland. Lithos 113:133–157
59. Pearce JA (2008) Geochemical fingerprinting of oceanic basalts with applications to ophiolite classification and the search for Archean oceanic crust. Lithos 100:14–48
60. Pearce JA (2014) Geochemical Fingerprinting of the Earth's Oldest Rocks. Geology 42:175–176
61. Pearce JA, van der Laan S, Arculus RJ, Murton BJ, Ishii T, Peate DW (1992) Boninite and Harzburgite from Leg 125 (Bonin–Mariana Fore-arc): a case study of magma genesis during the initial stage of subduction. In: Fryer P, Pearce JA, Stokking LB (eds) Proceedings for the Ocean Drilling Program: Sci. Results vol 125, pp 623–659
62. Polat A (2013) Geochemical variations in Archean volcanic rocks, southwestern Greenland: traces of diverse tectonic settings in the early Earth. Geology 41:379–380
63. Polat A, Hofmann AW (2003) Alteration and geochemical patterns in the 3.7–3.8 Ga Isua greenstone belt, West Greenland. Precambr Res 126:197–218
64. Polat A, Kerrich R (2001) Magnesian andesites, Nb-enriched basalt-andesites, and adakites from late-Archean 2.7 Ga Wawa greenstone belts, Superior Province, Canada: implications for late Archean subduction zone petrogenetic processes. Contrib Miner Petrol 141:36–52

65. Polat A, Kerrich R (2002) Nd-isotope systematics of ~2.7 Ga adakites, magnesian andesites, and arc basalts, Superior Province: evidence for shallow crustal recycling at Archean subduction zones. Earth Planet Sci Lett 202:345–360
66. Polat A, Kerrich R, Wyman DA (1999) Geochemical diversity in oceanic komatiites and basalts from the late Archean Wawa greenstone belts, Superior Province, Canada: trace element and Nd isotope evidence for a heterogeneous mantle. Precambr Res 94:139–173
67. Polat A, Hofmann AW, Rosing MT (2002) Boninite-like volcanic rocks in the 3.7–3.8 Ga Isua greenstone belt, West Greenland: geochemical evidence for intra-oceanic subduction zone processes in the early Earth. Chem Geol 184:231–254
68. Rapp RP, Watson EB (1995) Dehydration melting of metabasalt at 8-32 kbar: implications for continental growth and crust-mantle recycling. J Petrol 36:891–931
69. Reagan MK, Stern RJ, Kelley KA et al (2010) Fore-arc basalts and subduction initiation in the Izu-Bonin-Marianan system. Geochem Geophys Geosystems 11, https://doi.org/10.1029/2009gc002871
70. Rollinson HR (1993) Using geochemical data: evaluation, presentation, interpretation. Pearson Education Limited, London
71. Ross PS, Bédard JH (2009) Magmatic affinity of modern and ancient subalkaline volcanic rocks determined from trace-element discriminant diagrams. Can J Earth Sci 46:823–839
72. Rubatto D (2002) Zircon trace element geochemistry: partitioning with garnet and the link between U-Pb ages and metamorphism. Chem Geol 184:123–138
73. Sajona FG, Maury RC, Bellon H et al (1996) High field strength element enrichment of Pliocene-Pleistocene island arc basalts, Zamboanga Peninsula, western Mindanao (Philippines). J Petrol 37:693–726
74. Schiano P, Monzier M, Eissen JP, Martin H, Koga KT (2010) Simple mixing as the major control of the evolution of volcanic suites in the Ecuadorian Andes. Contrib Miner Petrol 160:297–312
75. Smithies RH (2000) The Archean tonalite-trondhjemite-granodiorite (TTG) series is not an analogue of Cenozoic adakite. Earth Planet Sci Lett 182:115–125
76. Stevenson R, Henry P, Gariépy C (1999) Assimilation-fractional crystallization origin of Archean Sanukitoid suites: Western Superior Province, Canada. Precambr Res 96:83–99
77. Streck MJ, Leeman WP, Chesley J (2007) High-magnesian andesite from Mount Shasta: a product of magma mixing and contamination, not a primitive mantle melt. Geology 35:351–354
78. Sun SS, McDonough WF (1989) Chemical and isotopic systematics of oceanic basalts: implication for mantle composition and processes. In: Saunders AD, Norry MJ (eds) Magmatism in ocean basins. Geological Society of London, Special Publication 42, pp 313–345
79. Sylvester PJ (1998) Post-collisional strongly peraluminous granites. Lithos 45:29–44
80. Szilas K, Hoffmann JE, Munker C et al (2014) Eoarchean within-plate basalts from southwest Greenland. Geology 42:330
81. Taylor SR, McLennan SM (1985) The continental crust: its composition and evolution. Blackwell, Oxford
82. Teklay M (2006) Neoproterozoic arc-back-arc system analog to modern arc-back-arc systems: evidence from tholeiite-boninite association, serpentinite mudflows and across-arc geochemical trends in Eritrea, southern Arabian-Nubian shield. Precambr Res 145:81–92
83. Treuil M, Joron JM (1975) Utilization des elements hydromagmayophiles pour la simplification de la modelisation quantitative des processes magmatiques. Exeples de l'Afar et de da dorsale medioatlantique. Rend SMP 31:125–174
84. Turner S, Rushmer T, Reagan M, Moyen JF (2014) Heading down early on? Start of subduction on Earth. Geology 42:139–142
85. Wan YS, Liu DY, Wang SJ et al (2010) Juvenile magmatism and crustal recycling at the end of the Neoarchean in Western Shandong Province, North China Craton: evidence from SHRIMP zircon dating. Am J Sci 310:1503–1552

86. Wan YS, Dong CY, Liu DY, Kröner A, Yang CH, Wang W, Du LL, Xie HQ, Ma MZ (2012) Zircon ages and geochemistry of late Neoarchean syenogranites in the North China Craton: a review. Precambr Res 222–223:265–289
87. Wang Q, McDermott F, Xu JF, Bellon H, Zhu YT (2005) Cenozoic K-rich adakitic volcanic rocks in the Hohxil area, northern Tibet: lower-crustal melting in an intra- continental setting. Geology 33:465–468
88. Wang YJ, Zhang YZ, Zhao GC, Fan WM, Xia XP, Zhang FF, Zhang AM (2009) Zircon U-Pb geochronological and geochemical constaints on the petrogenesis of the Taishan sanukitoids (Shandong): implications for Neoarchean subduction in the Eastern Block, North China Craton. Precambr Res 174:273–286
89. Wang W, Liu SW, Bai X, Yang PT, Li QG, Zhang LF (2011) Geochemistry and zircon U-Pb-Hf isotopic systematics of the Neoarchean Yixian-Fuxin greenstone belt, northern margin of the North China Craton: implications for petrogenesis and tectonic setting. Gondwana Res 20:64–81
90. Wang W, Liu SW, Wilde SA, Li QG, Zhang J (2012) Petrogenesis and geochronology of Precambrian granitoid gneisses in Western Liaoning Province: constraints on Neoarchean to early paleoproterozoic crustal evolution of the North China Craton. Precambr Res 222–223:290–311
91. Wang W, Liu SW, Bai X et al (2013) Zircon U-Pb-Hf isotopes and whole-rock geochemistry of granitoid gneisses in the Jianping gneissic terrane, Western Liaoning Province: constraints on the Neoarchean crustal evolution of the North China Craton. Precambr Res 224:184–221
92. Wang W, Liu SW, Bai X, Li QG, Yang PT, Zhao Y, Zhang SH, Guo RR (2013) Geochemistry and zircon U-Pb-Hf isotopes of the late Paleoproterozoic Jianping diorite-monzonite-syenite suites of the North China Craton: implications for petrogenesis and geodynamic setting. Lithos 162–163:175–194
93. Wang W, Liu SW, Santosh M, Wang GH, Bai X, Guo RR (2015) Neoarchean intra-oceanic arc system in the Western Liaoning Province: implications for early Precambrian crustal evolution in the Eastern block of the North China Craton. Earth Sci Rev 150:329–364
94. Watkins JM, Clemens JD, Treloar PJ (2007) Archean TTGs as sources of younger granitic magmas: melting of sodic metatonalites at 0.6-1.2 GPa. Contrib Miner Petrol 154:91–110
95. Whalen JB, Percival JA, McNicoll VJ, Longstaffe FJ (2004) Geochemical and isotopic (Nd-O) evidence bearing on the origin of late- to post-orogenic high-K granitoid rocks in the Western Superior Province: implication for late Archean tectonomagmatic processes. Precambr Res 132:303–326
96. Whitehouse MJ, Kamber BS (2003) A rare earth element study of complex zircons from early Archaean Amîtsoq gneisses, Godthåbsfjord, south-west Greenland. Precambr Res 126:363–377
97. Winchester JA, Floyd PA (1976) Geochemical magma type discrimination: application to altered and metamorphosed basic igneous rocks. Earth Planet Sci Lett 28:459–469
98. Xu YG, Chuang SL, Jahn BM, Wu GY (2001) Petrologic and geochemical constraints on the peteogenesis of Permian-Triassic Emeishan flood basalts in southwestern China. Lithos 58:145–168
99. Zamora D (2000) Fusion de la croute oceanique subductee: approche experimentale et geochimique. Universite Thesis Universite Blaise Pascal, Clermont-Ferrand, p 314
100. Zeh A, Gerdes A, Barton JMJ (2009) Archean accretion and crustal evolution of the Kalahari Cratonçthe zircon age and Hf isotope record of granitic rocks from Barberton/Swaziland to the Francistown Arc. J Petrol 50:933–966
101. Zeh A, Gerdes A, Klemd R et al (2007) Archaean to Proterozoic crustal evolution in the central zone of the Limpopo Belt (South Africa-Botswana): constraints from Combined U-Pb and Lu-Hf isotope analyses of Zircon. J Petrol 48:1605–1639
102. Zhang SH, Liu SW, Zhao Y, Yang JH, Song B, Liu XM (2007) The 1.75-1.68 Ga anorthosite-mangerite-alkali granitoid-rapakivi granite suite from the northern North China Craton: magmatism related to a Paleoproterozoic orogen. Precambr Res 155:287–312

103. Zhao GC, Wilde SA, Cawood PA et al (1999) Thermal evolution of two types of mafic granulites from the North China Craton: implications for both mantle plume and collisional tectonics. Geol Mag 136:223–240
104. Zhao GC, Sun M, Wilde SA et al (2005) Late Archean to Proterozoic evolution of the North China Craton: key issues revisited. Precambr Res 136:177–202
105. Zhao GC, He YH, Sun M (2009) The Xiong'er volcanic belt at the southern margin of the North China Craton: petrographic and geochemical evidence for its outboard position in the Paleo-Mesoproterozoic Columbia supercontinent. Gondwana Res 16:170–181
106. Zhao GC, Cawood PA, Li SZ, Wilde SA, Sun M, Zhang J, He YH, Yin CQ (2012) Amalgamation of the North China Craton: key issues and discussions. Precambr Res 222–223:55–76

Chapter 4
Paleo- to Mesoproterozoic Magmatic Rock Assemblage and Crust-Mantle Geodynamic Processes

Abstract The late Paleoproterozoic to Mesoproterozoic crust-mantle geodynamic evolution of North China Craton remains hotly debated, which have largely hampered our further understanding of the Precambrian tectonic evolution of North China Craton as well as the reconstruction of this ancient craton within global Columbia supercontinent. In this chapter, whole-rock geochemical and zircon U–Pb and Lu–Hf isotopic studies are conducted on the late Paleoproterozoic magmatic rocks in the Western Liaoning-Northeastern Hebei Provinces, particularly the Jianping diorite-monzonite-syenite suite (JDMSS) and the Pinggu K-rich volcanic rocks within the Changcheng Group, as well as the newly discovered ~1.23 Ga mafic dykes. It is suggested that the JDMSS suite were emplaced during ~1721–1696 Ma, and they were generated by the partial melting of an amphibole-bearing enriched subcontinental lithospheric mantle, with the parental magmas subjected to different degrees of fractional crystallization. In comparison, the Pinggu K-rich volcanic rocks in the Tuanshanzi and Dahongyu Formations of Changcheng Group were erupted during ~1671–1625 Ma, and they were considered to have been derived dominantly from the partial melting of a depleted asthenospheric mantle, with the melts interacted with the lithospheric mantle components at diverse extents. These late Paleoproterozoic extension-related magmatism occurred later than the final amalgamation between the Eastern Block and Western Block (~1.85 Ga) along the Trans-North China Orogen, suggesting that they may have in turn evolved under post-collisional to post-orogenic settings. The newly discovered ~1.23 Ga mafic dykes occur widely in Western Liaoning, Eastern Hebei, and Northern Liaoning. Together with coeval mafic dykes identified in other areas of the North China Craton, these mafic dykes constitute a Mesoproterozoic large igneous province (LIP) covering an area of at least 0.6×10^6 km^2. It is suggested that they were generated by extensive asthenosphere-lithospheric mantle interaction processes, possibly linked to a mantle plume event that triggered the final breakup of global Columbia supercontinent. Importantly, the late Paleoproterozoic enriched lithospheric mantle beneath the North China Craton witnessed at least two major episodes of intense erosion and rejuvenation by the upwelling asthenospheric mantle during the Proterozoic time.

W. Wang, *Archean-Mesoproterozoic Crustal Evolution and Crust-Mantle Geodynamics of Western Liaoning-Northeastern Hebei Provinces, North China Craton*, Springer Theses, https://doi.org/10.1007/978-981-10-7922-1_4

Keywords Jianping diorite-monzonite-syenite suite · Pinggu K-rich volcanic rocks · Mesoproterozoic (~1.23 Ga) mafic dykes · Late Paleoproterozoic to Mesoproterozoic crust-mantle geodynamic evolution · North China Craton

4.1 Late Paleoproterozoic Jianping Diorite-Monzonite-Syenite Suite in the Western Liaoning Province

Following the final collision between the Eastern Block and Western Block, the united crystalline basement of North China Craton experienced extensive late Paleoproterozoic plutonic magmatism along its northern margin (Fig. 2.2). These include the Damiao anorthosite complex, Miyun rapakivi granites, and other alkaline granitic rocks [76, 91, 94]. While some researchers consider that the Damiao anorthosites were derived from either the EM-I type enriched mantle or the ancient lower continental crust materials [91, 94], others argue that there was no EM-I type enriched lithospheric mantle underneath the NCC during late Paleoproterozoic [31]. Coeval alkaline granitic rocks were also proposed to have been sourced either from an enriched mantle or from the lower continental crust materials [31, 86, 88, 91].

Recently, a late Paleoproterozoic diorite-monzonite-syenite suite (JDMSS) is identified in the Jianping area of Western Liaoning Province (Fig. 4.1). These rocks record important information about the lithospheric mantle evolution and crust-mantle interaction processes during the transition from Paleo- to Mesoproterozoic. In this study, we provide detailed studies of the field geology, petrology, whole-rock geochemistry, as well as zircon U–Pb and Lu–Hf isotopes for this late Paleoproterozoic plutonic suite, aiming to determine the lithological assemblages and emplacement timing, and discuss the nature of the mantle sources and petrogenesis.

4.1.1 Geological and Petrographic Characteristics

The late Paleoproterozoic plutons, located to the north of Jianping town (Fig. 4.1), include the Hatonggou, Xiaozhangzi, and Shinao plutons from north to south, with outcrop areas of ca. 5, 15, and 20 km^2, respectively. These plutons show intrusive relationships with the Archean basement rocks of Jianping gneissic terrane. Together with a small stock discovered to the east of Jianchanggou town (the Jianchanggou stock), these plutons constitute the Jianping diorite-monzonite-syenite suite (JDMSS). The JDMSS is mainly made up of magnetite diorite, clinopyroxene monzonite, and syenite (including quartz syenite), and these rocks were intruded by late Paleozoic to Jurassic granitoids and unconformably overlain by Mesozoic

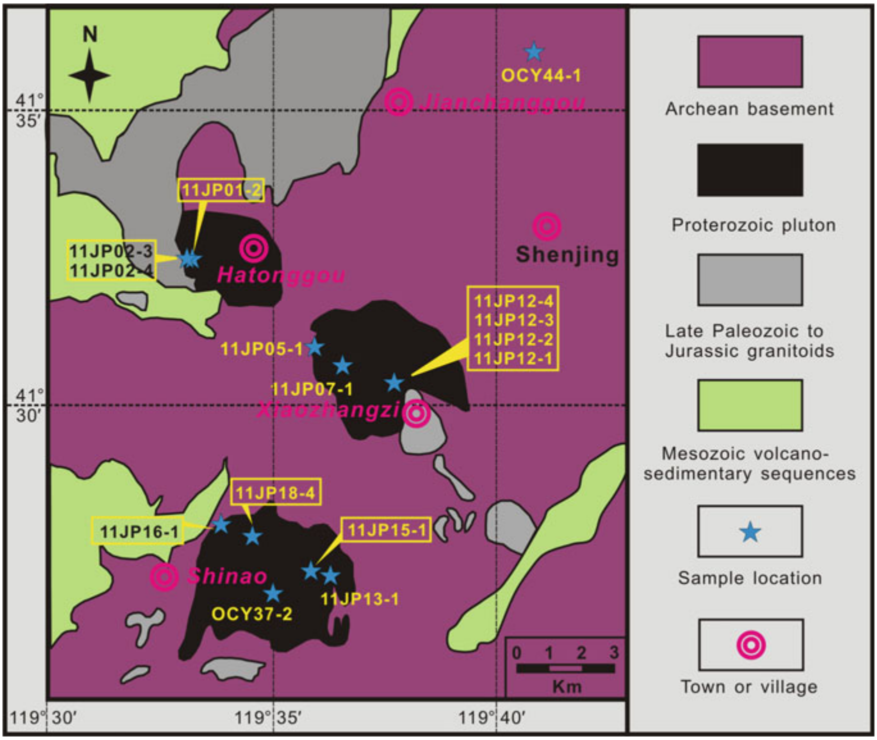

Fig. 4.1 Geological map of the late Paleoproterozoic Jianping diorite-monzonite-syenite suite (JDMSS), including Shinao, Xiaozhangzi, and Hatonggou plutons from south to north

volcano-sedimentary sequences (Fig. 4.1). Magnetite diorite is the main lithology in the Hatonggou pluton and Jianchanggou stock, and the diorites are intruded by ca. 260 Ma monzogranitic dykes (our unpublished data, Fig. 4.2a, b). In the Xiaozhangzi pluton, syenites intrude into the clinopyroxene monzonites (Fig. 4.2c, d). The southernmost Shinao pluton is dominated by syenites and quartz syenites, and they shows intrusive contacts with the Archean crystalline basement, as evidenced by the numerous xenoliths of amphibolites and TTG gneisses with lengths of several centimeters to tens of centimeters (Fig. 4.2e, f). Locally, syenite apophyses cut the gneissosity of Archean TTG gneisses (Fig. 4.2g). Moreover, all the intrusive rocks of the JDMSS are massive in structure (Fig. 4.2b, d, h, and i).

Fifteen representative samples, including four magnetite diorites, three clinopyroxene monzonites, six syenites, and two quartz syenites, were collected from the JDMSS (Table 4.1). The magnetite diorites have medium-grained textures and massive structures, and are composed mainly of plagioclase (45–48%), hornblende (14–36%), biotite (8–28%), and magnetite (5–6%). Accessory minerals include apatite, zircon, titanite, and epidote (Figs. 4.2b and 4.3a, b). The magnetite crystals are generally hypidiomorphic to euhedral, and some occur as inclusions

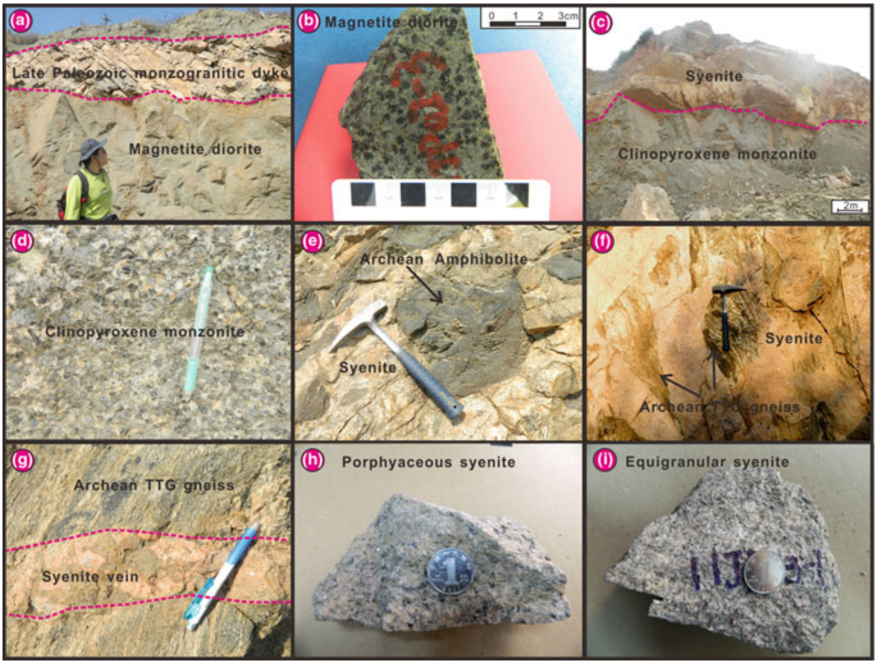

Fig. 4.2 Field geological features of the Jianping diorite-monzonite-syenite suite. **a** The outcrop feature of magnetite diorite, which is intruded by a late Paleozoic monzogranitic apophysis. **b** A hand specimen of magnetite diorite. **c** The occurrence of clinopyroxene monzonite, intruded by syenite dykes. **d** Textural features of the clinopyroxene monzonite; the pen is about 10 cm in length. **e** and **f** Numerous xenoliths of Archean amphibolites and TTG gneisses within the syenite, clearly indicating an intrusive relationship between the JDMSS suite and the Archean basement rocks; the hammer is 30 cm long. **g** A syenite vein cutting the Archean TTG gneisses of the JPGT; the pen is about 10 cm long. **h** and **i** Hand specimens of porphyaceous (**h**) and equigranular syenite (**i**); the coin is 1 cm in diameter

within hornblende or biotite crystals, representing an early crystallization mineral phase (Fig. 4.3c). Similarly, euhedral apatites with lengths of 0.1–0.5 mm are widely distributed within the plagioclase (Fig. 4.3d). The clinopyroxene monzonites display coarse-grained textures and massive structures. They contain K-feldspar (52–55%, including antiperthite and orthoclase), biotite (20–22%), plagioclase (12–16%), clinopyroxene (5–8%), and apatite ($\sim$2%), and most clinopyroxene and apatite are enveloped by biotite (Figs. 4.2d and 4.3e, f, and g). Accessory minerals include zircon, magnetite, and epidote. The syenites and quartz syenites have fine-grained porphyraceous or equigranular textures and massive structures, and consist of K-feldspar (58–72%, including perthite, microcline, and orthoclase), plagioclase (15–25%), biotite (3–10%), and quartz (2–8%), with minor zircon, titanite, magnetite, and epidote (Fig. 4.3h, i). In the porphyraceous syenites (Fig. 4.3h), K-feldspar (0.5–1.0 mm) is the main phenocryst phase, and the groundmass consists dominantly of K-feldspar, plagioclase, biotite, and quartz.

Table 4.1 Major (wt%) and trace element (ppm) compositions of representative samples from Jianping diorite-monzonite-syenite suite, Western Liaoning Province

Sample	11JP01-2	11JP02-3	11JP02-4	OCY44-1	11JP12-1	11JP12-2	11JP12-3	11JP07-1	11JP12-4	11JP13-1	11JP15-1	11JP16-1	11JP18-4	11JP05-1	OCY37-2
Lithology	Magnetite diorite				Clinopyroxene monzonite			Syenite						Quartz syenite	
SiO_2	50.86	46.28	48.31	52.58	53.03	54.77	53.77	58.62	60.99	63.35	61.75	63.63	60.85	64.85	64.68
Al_2O_3	18.58	21.26	18.84	17.30	18.63	18.88	18.58	17.40	16.82	17.39	17.14	17.16	17.41	16.50	15.92
Fe_2O_3T	10.35	13.01	11.00	8.29	7.62	6.57	7.75	7.15	5.51	3.87	4.38	3.62	5.49	3.71	3.84
MgO	4.09	3.01	4.14	2.53	2.88	2.51	2.44	1.41	1.20	0.53	0.85	0.78	1.30	0.71	0.61
CaO	7.15	8.17	7.95	6.60	5.33	4.83	5.29	2.24	1.78	0.82	1.78	0.96	2.13	1.11	1.54
Na_2O	3.97	4.00	3.91	4.51	4.71	4.81	4.79	4.74	5.18	5.54	5.27	5.50	5.44	4.66	4.70
K_2O	1.90	1.08	1.74	2.29	3.92	4.24	4.07	6.20	6.29	7.01	6.53	6.45	5.19	6.80	6.60
MnO	0.13	0.11	0.14	0.12	0.09	0.08	0.09	0.07	0.08	0.11	0.09	0.07	0.07	0.07	0.10
TiO_2	1.27	1.58	1.50	1.69	1.54	1.40	1.16	1.10	1.22	0.92	0.98	0.85	0.92	0.88	0.83
P_2O_5	0.56	0.52	0.95	1.04	1.14	0.79	0.88	0.32	0.33	0.07	0.14	0.17	0.29	0.12	0.06
LOI	1.13	0.97	1.49	1.50	0.53	0.55	0.61	0.66	0.51	0.29	0.99	0.81	0.81	0.58	0.70
Total	99.99	99.98	99.96	98.44	99.42	99.43	99.43	99.91	99.91	99.90	99.90	100.00	99.89	99.99	99.57
Mg#	43.91	31.43	42.71	37.64	42.81	43.08	38.41	28.09	30.14	21.28	27.77	29.94	31.93	27.60	23.80
K_2O/Na_2O	0.48	0.27	0.45	0.51	0.83	0.88	0.85	1.31	1.21	1.27	1.24	1.17	0.95	1.46	1.40
A/CNK	0.86	0.94	0.83	0.79	0.86	0.89	0.85	0.94	0.91	0.96	0.90	0.97	0.94	0.97	0.90
Sc	12.4	8.57	11.5	12.3	10.1	9.85	10.2	9.53	10.2	5.65	9.05	6.42	8.12	10.1	5.53
V	185	296	174	71	108	80	108	55	31	24	30	44	59	32	21
Cr	1.14	2.10	1.41	–	0.991	0.850	0.859	1.62	2.23	1.93	28	2.84	13.1	1.73	–
Co	31	43	23	–	13.1	10.6	11.6	4.50	1.95	1.30	2.07	3.16	6.09	2.11	–
Ni	9.56	23	7.25	–	5.49	4.45	4.69	3.11	2.91	1.30	2.39	1.65	11.40	1.49	–
Rb	41	15.2	27	56	61	68	46	110	178	169	159	198	185	155	205
Sr	1193	1635	1377	1946	2606	2793	3084	757	350	105	151	416	614	149	361
Y	27	17.2	27	29	32	28	28	45	104	106	61	58	72	90	75
Nb	8.23	5.34	8.82	14.9	8.42	9.85	5.97	27	75	83	44	66	68	53	86
Cs	0.543	0.135	0.314	0.550	0.333	0.603	0.338	0.276	1.66	0.480	0.828	1.92	2.07	0.183	0.501
Ba	1666	1132	1546	8173	7439	7082	7487	4537	1118	341	622	1037	1533	892	717

(continued)

Table 4.1 (continued)

Sample	11JP01-2	11JP02-3	11JP02-4	OCY44-1	11JP12-1	11JP12-2	11JP12-3	11JP07-1	11JP12-4	11JP13-1	11JP15-1	11JP16-1	11JP18-4	11JP05-1	OCY37-2
Lithology	Magnetite diorite				Clinopyroxene monzonite			Syenite						Quartz syenite	
La	34	26	29	130	128	115	138	187	460	487	721	306	286	633	515
Ce	75	55	69	266	258	225	266	383	974	961	1301	622	631	1162	999
Pr	9.66	7.35	9.57	33	33	27	32	48	121	118	157	74	67	138	108
Nd	43	35	45	134	142	118	143	189	464	422	556	273	239	501	361
Sm	8.52	6.32	7.44	19.8	21	16.2	21	28	58	57	57	36	35	61	45
Eu	3.89	2.89	4.09	12.4	13.1	12.6	14.6	10.7	10.9	6.44	7.67	5.92	6.11	9.22	5.21
Gd	7.37	5.41	7.82	18.05	18.3	16.2	15.8	19.3	41	41	43	25	25	42	36
Tb	1.13	0.792	1.07	1.81	1.82	1.51	1.67	2.49	4.99	5.26	4.10	2.88	3.13	5.19	3.44
Dy	5.49	3.92	5.58	7.03	6.96	6.38	6.82	9.75	24	24	16.6	13.7	14.1	21	15.0
Ho	1.03	0.632	1.03	1.19	1.21	0.918	1.06	1.66	3.85	4.03	2.50	2.08	2.52	3.34	2.67
Er	2.50	1.79	2.77	3.15	2.84	2.83	2.48	4.29	10.4	10.5	6.73	6.03	7.67	9.16	7.42
Tm	0.374	0.293	0.344	0.408	0.383	0.288	0.274	0.506	1.53	1.74	0.965	0.870	1.03	1.30	1.06
Yb	2.14	1.47	1.74	2.64	2.09	2.10	1.70	3.49	8.78	9.72	5.58	5.13	6.95	7.54	7.01
Lu	0.283	0.165	0.247	0.363	0.297	0.265	0.234	0.444	1.31	1.13	0.823	0.727	0.860	1.07	0.983
Ta	0.460	0.262	0.372	0.715	0.368	0.523	0.263	1.21	4.29	5.36	2.26	4.73	4.27	2.81	3.32
Th	1.38	0.263	0.349	1.02	1.27	2.39	1.46	4.98	16.0	15.1	18.2	12.8	18.5	18.6	26
U	0.685	0.082	0.171	0.225	0.325	0.488	0.334	0.556	2.04	1.21	1.21	1.63	2.41	0.974	2.07
Zr	26	27	15.2	84	87	126	116	72	241	211	76	121	340	230	1278
Hf	1.34	0.868	1.05	2.40	2.33	2.87	2.51	2.88	6.90	5.00	3.55	4.01	8.20	5.91	26
Eu_N/Eu_N^*	1.50	1.51	1.64	2.00	2.06	2.38	2.48	1.40	0.685	0.409	0.475	0.606	0.634	0.554	0.398
$(La/Yb)_N$	11.5	12.6	12.0	35	44	39	58	38	38	36	93	43	30	60	53
$(La/Sm)_N$	2.59	2.64	2.53	4.22	4.01	4.58	4.35	4.30	5.11	5.52	8.18	5.43	5.26	6.69	7.41
$(Gd/Yb)_N$	2.85	3.04	3.72	5.66	7.24	6.38	7.69	4.57	3.83	3.46	6.36	3.95	2.94	4.64	4.22
TREE	194	147	185	629	629	544	644	888	2183	2148	2880	1373	1325	2595	2106
Sr/Y	45	95	51	67	80	100	111	16.9	3.37	0.99	2.50	7.16	8.56	1.66	4.79
Rb/V	0.222	0.051	0.152	0.790	0.562	0.858	0.424	2.00	5.84	6.93	5.28	4.48	3.14	4.92	9.80
Rb/La	1.20	0.589	0.911	0.432	0.474	0.594	0.332	0.588	0.387	0.347	0.221	0.647	0.647	0.245	0.399

(continued)

Table 4.1 (continued)

Sample	11JP01-2	11JP02-3	11JP02-4	OCY44-1	11JP12-1	11JP12-2	11JP12-3	11JP07-1	11JP12-4	11JP13-1	11JP15-1	11JP16-1	11JP18-4	11JP05-1	OCY37-2
Lithology	Magnetite diorite				Clinopyroxene monzonite			Syenite						Quartz syenite	
Rb/Sr	0.034	0.009	0.019	0.029	0.023	0.024	0.015	0.145	0.509	1.61	1.05	0.476	0.301	1.04	0.568
Ba/Rb	41	74	58	146	123	104	163	41	6.28	2.02	3.91	5.24	8.29	5.75	3.50
Th/Ce	0.018	0.005	0.005	0.004	0.005	0.011	0.005	0.013	0.016	0.016	0.014	0.021	0.029	0.016	0.026
La/Nb	4.16	4.83	3.30	8.70	15.2	11.7	23	7.06	6.12	5.86	16.2	4.61	4.21	11.9	5.98
Nb*	0.350	0.368	0.532	0.208	0.117	0.141	0.077	0.225	0.246	0.263	0.099	0.313	0.301	0.130	0.228

Note LOI, loss on ignition; A/CNK = molar $Al_2O_3/(CaO + Na_2O + K_2O)$; TREE = total rare earth element; Mg# = 100 $Mg/(Mg + Fe_{total})$ in atomic ratio; $Eu_N/Eu_N^* = Eu_N/SQRT(Sm_N \times Gd_N)$. Subscript N—chondrite normalized value, subscript PM—primitive mantle normalized value, "–" represents data that are not analyzed

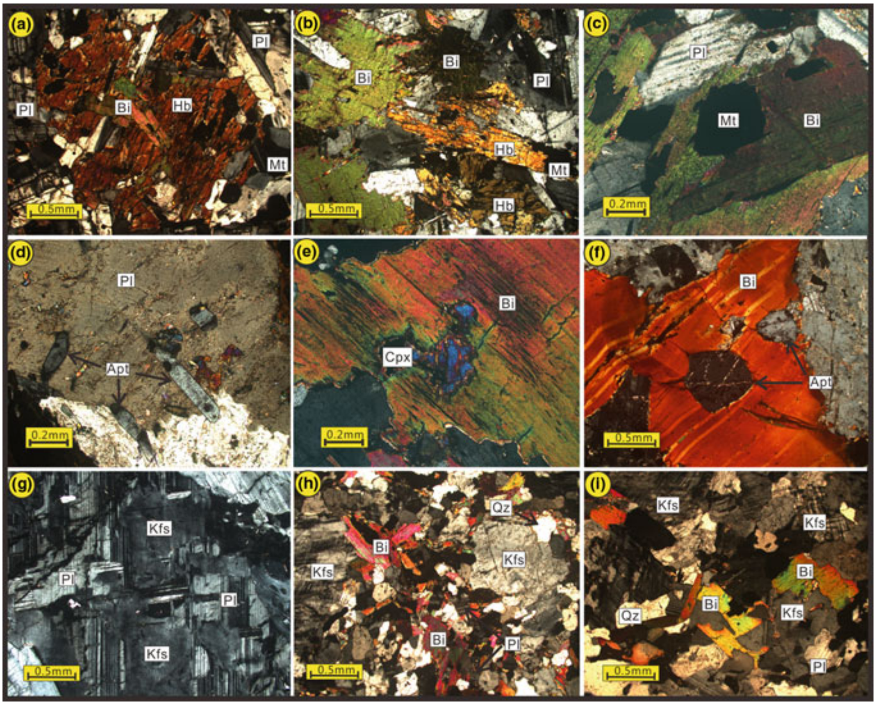

Fig. 4.3 Photomicrographs of representative samples from the JDMSS showing textures and mineral assemblages: **a** and **b** magnetite diorites with different proportions of amphibole and biotite; **c** and **d** hypidiomorphic to euhedral magnetite and apatite inclusions (early crystalline phases) within biotite and plagioclase, respectively, from the magnetite diorites; **e** and **f** clinopyroxene and apatite inclusions within biotite from the clinopyroxene monzonite; **g** antiperthitic crystals in the clinopyroxene monzonites; **h** porphyaceous syenite; and **i** equigranular quartz syenite. Mineral abbreviations: Hb—hornblende, Bi—biotite, Pl—plagioclase, Mt—magnetite, Cpx—clinopyroxene, Apt—apatite, Kfs—potassic feldspar, Qz—quartz

4.1.2 Geochemical Characteristics

4.1.2.1 Whole-Rock Geochemistry

Major and trace element data of the fifteen representative samples are listed in Table 4.1 and plotted in Figs. 4.4 and 4.5. They show low LOI (loss on ignition) values of 0.290–1.500 wt%, indicating insignificant post-magmatic alteration and the preservation of original geochemical features. This is consistent with the lack of secondary alteration in all the samples (Fig. 4.3).

Major element compositions

The JDMSS samples have SiO_2 contents ranging from 46.3 to 64.9 wt%, and all the samples plot in the alkaline field in the total alkalis-silica diagram (TAS diagram

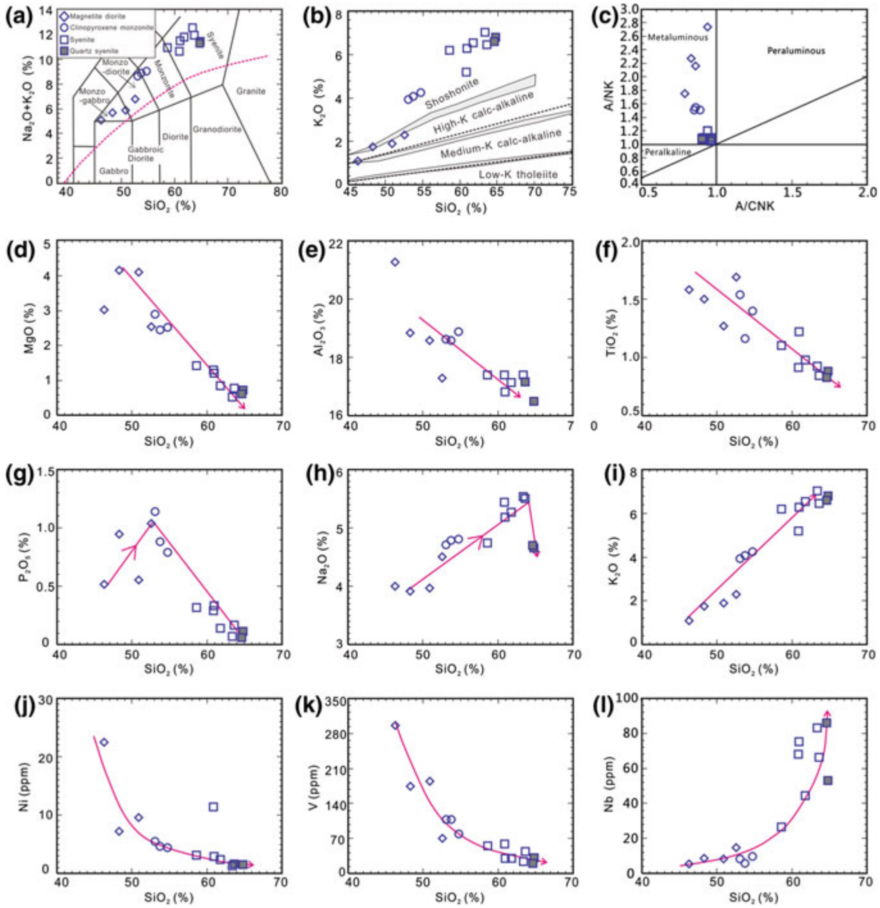

Fig. 4.4 Petrochemical classifications of the JDMSS samples, and their geochemical characteristics. **a** Total alkalis versus silica diagram (TAS, after [47]). **b** K_2O versus SiO_2 classification diagram after [60]. **c** ANK (molar $Al_2O_3/(Na_2O + K_2O)$) versus ACNK (molar $Al_2O_3/(CaO + Na_2O + K_2O)$) diagram after [42]. **d–l** Covariation diagrams of SiO_2 versus selected major oxides and trace elements (the red trajectories show the variation trends with increasing SiO_2 contents). Symbols: diamonds—magnetite diorites, circles—clinopyroxene monzonites, open squares—syenites, solid squares—quartz syenites

after Middlemost [47] Fig. 4.4a). The magnetite diorites plot in the monzogabbro-monzodiorite fields, and they have the lowest SiO_2 (46.3–52.6 wt%) and the highest MgO, Fe_2O_3T, and CaO contents (2.53–4.14 wt%, 8.29–13.01 wt%, and 6.60–8.17 wt%, respectively), and the Mg# values (100 Mg/(Mg + Fe_{total}) atomic ratio) range from 31.43 to 43.91. They have low K_2O contents (1.080–2.29 wt%) relative to Na_2O (3.91–4.51 wt%), yielding low K_2O/Na_2O ratios of 0.27–0.51, and these rocks belong to the high-K calc-alkaline series (Fig. 4.4b). In the A/NK (molecular $Al_2O_3/(Na_2O + K_2O)$) versus A/CNK (molecular

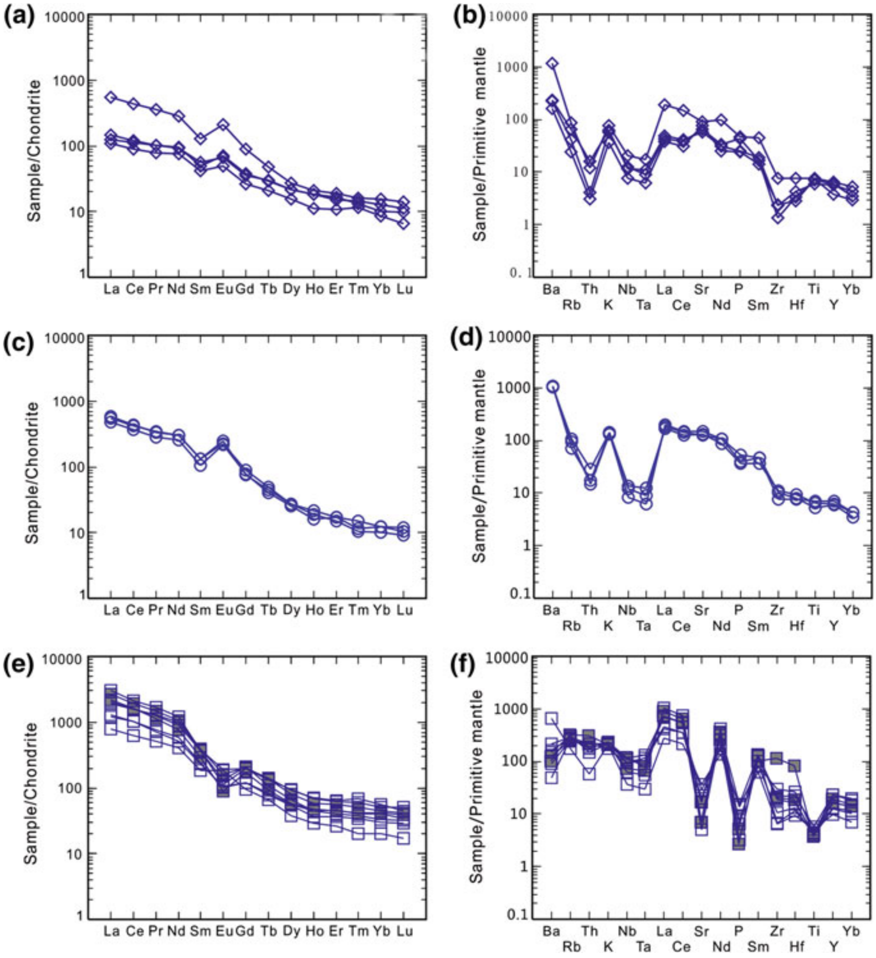

Fig. 4.5 Chondrite-normalized REE patterns and primitive mantle-normalized multi-element spider diagrams for magnetite diorites (**a** and **b**), clinopyroxene monzonites (**c** and **d**), and syenites and quartz syenites (**e** and **f**). Symbols are the same as Fig. 4.4. The chondrite and primitive mantle values are after Sun and McDonough [66]

Al_2O_3/(CaO + Na_2O + K_2O)) diagram [42], they display metaluminous features with moderate A/CNK values of 0.79–0.94 but the highest A/NK values of 1.75–2.74 (Fig. 4.4c).

The clinopyroxene monzonites plot at the boundary field between monzodiorite and monzonite in the TAS diagram (Fig. 4.4a). They are characterized by contents of SiO_2 (53.0–54.8 wt%), MgO (2.44–2.88 wt%), Fe_2O_3T (6.57–7.75 wt%), CaO (4.83–5.33 wt%), and K_2O (3.92–4.24 wt%) that range between those of magnetite diorites and syenites (including the quartz syenites). Mg# values range from 38.41 to 43.08, similar to those of the magnetite diorites. In the K_2O versus SiO_2 diagram

(Fig. 4.4b), they plot in the shoshonitic field with higher K_2O/Na_2O ratios of 0.83–0.88. They are metaluminous with A/CNK values of 0.85–0.89 and moderate A/NK values of 1.51–1.55 (Fig. 4.4c).

As the felsic end-members of the JDMSS, the syenites (including quartz syenites) fall into the syenite field in the TAS diagram (Fig. 4.4a). They have the highest SiO_2 (58.6–64.9 wt%) and K_2O (5.19–7.01 wt%) contents, and the lowest MgO (0.528–1.410 wt%), Fe_2O_3T (3.62–7.15 wt%), CaO (0.818–2.24 wt%), and Mg# (21.28–31.93). In the K_2O versus SiO_2 diagram (Fig. 4.4b), they belong to the shoshonitic series with the highest K_2O/Na_2O ratios of 0.95–1.46. They also show metaluminous features with A/CNK values of 0.90–0.97, but have the lowest A/NK values of 1.07–1.20, close to the peralkaline field (Fig. 4.4c).

On the Harker diagrams (Fig. 4.4d–i), there is a continuous decrease in MgO, Al_2O_3, and TiO_2 but an increase in K_2O with increasing SiO_2. The P_2O_5 contents increase from magnetite diorites to clinopyroxene monzonites, and then decrease rapidly in the syenites. Most samples show a positive correlation between Na_2O and SiO_2, except for the two quartz syenites (samples 11JP05-1 and OCY37-2), where there is a decrease in Na_2O with increasing SiO_2.

Trace element compositions

The JDMSS samples show negative correlations between compatible elements (e.g., Ni and V) and SiO_2, but positive correlations between incompatible elements (e.g., Nb) and SiO_2 (Fig. 4.4 j–l). Moreover, they all plot along hyperbolic lines from magnetite diorites through clinopyroxene monzonites to (quartz) syenites.

The magnetite diorites and clinopyroxene monzonites have nearly consistent chondrite-normalized REE patterns (Fig. 4.5a and c). The magnetite diorite samples 11JP01-2, 11JP02-3, and 11JP02-4 are characterized by the lowest total rare earth element (TREE) contents of 147.03–193.79 ppm, and moderately fractionated REE patterns with the lowest $(La/Sm)_N$, $(Gd/Yb)_N$, and $(La/Yb)_N$ ratios of 2.53–2.64, 2.85–3.72, and 11.46–12.59, respectively. In comparison, the clinopyroxene monzonites show higher TREE contents between 544.29 and 644.34 ppm, and more fractionated REE patterns with high $(La/Sm)_N$, $(Gd/Yb)_N$, and $(La/Yb)_N$ ratios from 4.01 to 4.58, 6.38 to 7.69, and 39.28 to 58.23, respectively. However, the REE fractionation degree of the magnetite diorite sample OCY44-1 lies between the other three magnetite diorites and the clinopyroxene monzonites, with TREE content, $(La/Sm)_N$, $(Gd/Yb)_N$, and $(La/Yb)_N$ of 629.15 ppm, 4.22, 5.66, and 35.20, respectively. Moreover, all the above seven samples show positive Eu anomalies with high Eu_N/Eu_N* values between 1.50 and 2.48. The syenites and quartz syenites have the highest TREE contents ranging from 887.93 to 2879.77 ppm. They are characterized by highly fractionated chondrite-normalized REE patterns with high $(La/Sm)_N$, $(Gd/Yb)_N$, and $(La/Yb)_N$ ratios of 4.30–8.18, 2.94–6.36, and 29.52–92.68, respectively (Fig. 4.5e). Nearly all the syenites and quartz syenites show negative Eu anomalies ($Eu_N/Eu_N* = 0.40–0.69$), except for sample 11JP07-1 (showing the lowest SiO_2 content of 58.62 wt%) with a positive Eu anomaly ($Eu_N/Eu_N* = 1.40$).

In the primitive mantle-normalized trace element patterns, the magnetite diorites and clinopyroxene monzonites are generally enriched in LILEs (large ion lithophile elements, e.g., Rb, Ba, and K), but depleted in HFSEs (high field strength elements, e.g., Th, Nb, Ta, Zr, and Hf) with weakly negative Ti anomalies (Fig. 4.5b and d). The magnetite diorite samples 11JP01-2, 11JP02-3, and 11JP02-4 display slightly positive P and strongly positive Sr anomalies, whereas slightly negative P and Sr anomalies are observed in sample OCY44-1 and the clinopyroxene monzonites. They have high Sr (1193–3084 ppm), Y (17.20–32.40 ppm), and Yb (1.47–2.64 ppm) contents, yielding high Sr/Y ratios between 45.02 and 111.34. Most syenites and quartz syenites are characterized by the enrichment in Rb, Ba, K, and Th, and depletion in Nb, Ta, Zr, Hf, and Ti (Fig. 4.5f). They are strongly depleted in Sr and P, distinct from those of magnetite diorites and clinopyroxene monzonites. In particular, the quartz syenite sample OCY37-2 shows some enrichment in Zr and Hf, possibly implying the aggregation of Zr–bearing minerals such as zircons. In addition, sample 11JP07-1 (with the lowest SiO_2 content amongst the syenites) is depleted in Th, similar to those of magnetite diorites and clinopyroxene monzonites. All the syenite and quartz syenite samples have relatively lower Sr (105–757 ppm) but higher Y (44.90–106.00 ppm) and Yb (3.49–9.72 ppm) contents, with lower Sr/Y ratios that range between 0.99 and 16.86.

4.1.2.2 Whole-Rock Rb–Sr Isotopes

Sample OCY44-1 was selected for whole-rock Rb–Sr isotopic analyses (Table 4.2). It has $^{87}Rb/^{86}Sr$ and $^{87}Sr/^{86}Sr$ ratios of 0.0763 and 0.705450, respectively, and a relatively low initial $^{87}Sr/^{86}Sr$ ratio of 0.703564 (calculated at 1721 Ma). In order to determine the nature of late Paleoproterozoic subcontinental lithospheric mantle beneath the northern margin of NCC, we compiled published whole-rock Rb–Sr isotopic data of three samples from the nearly coeval Damiao anorthosite complex (to the west of Western Liaoning Province), including one anorthosite and two mangerites (Table 4.2; [86]). They exhibit $^{87}Rb/^{86}Sr$ and $^{87}Sr/^{86}Sr$ ratios of 0.0127–0.3852 and 0.704327–0.713307, respectively. When calculated at the crystallization age of 1730 Ma, they show nearly homogeneous initial $^{87}Sr/^{86}Sr$ ratios that lie between 0.703372 and 0.704012.

4.1.3 Zircon U–Pb and Lu–Hf Isotopes

4.1.3.1 The Hatonggou Pluton and Jianchanggou Stock

Magnetite diorite is the main lithology of Hatonggou pluton and Jiangchanggou stock (Fig. 4.1). The representative sample OCY44-1, collected from the east of Jianchanggou town, has zircon grains that are generally stubby with lengths between 100 and 150 μm and length/width ratios of 1:1–2:1 (Fig. 4.6).

Table 4.2 Whole-rock Rb–Sr isotopic data for representative samples from the Jianping diorite–monzonite–syenite suite (JDMSS), Western Liaoning Province and the adjacent Damiao Anorthosite Complex along the northern margin of North China Craton

Sample	Lithology	Age (Ma)	Rb (ppm)	Sr (ppm)	$^{87}Rb/^{86}Sr$	$^{87}Sr/^{86}Sr$	$(^{87}Sr/^{86}Sr)_i$
OCY44-1	Magnetite diorite	1721	56	2118	0.0763	0.705450	0.703564
384-2[a]	Anorthosite	1730	5.12	1169	0.0127	0.704327	0.704012
431[a]	Mangerite	1730	44	359	0.3535	0.712144	0.703372
419[a]	Mangerite	1730	64	483	0.3852	0.713307	0.703749

Note The ^{87}Rb decay constant ($\lambda^{87}Rb$) of 1.42×10^{-11} $year^{-1}$ was used to calculate the initial Sr isotopic ratios (Steiger and Jager 1977)
Samples with [a]were cited from Xie [86]

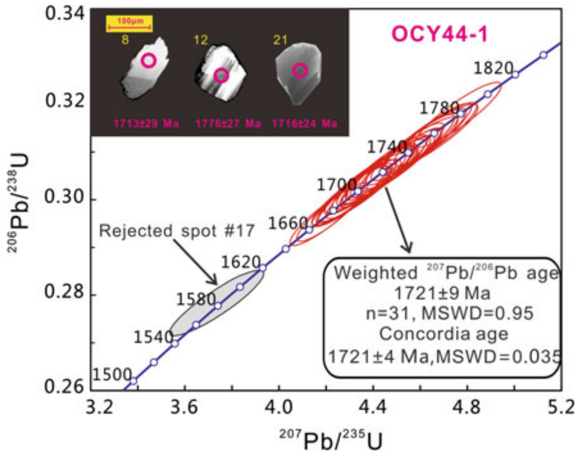

Fig. 4.6 Zircon U–Pb isotopic concordia diagram of sample OCY44-1 from the east of Jianchanggou town. The inset is the cathodoluminescence images showing zircon internal structures and analyzed locations

Cathodoluminescence (CL) images reveal that most of them have oscillatory (e.g., spots #12 and #21) or banded (e.g., spot #8) zonings, except for spot #17 that is bright and structureless. Thirty-two spots were analyzed on thirty-two zircon grains, and all the isotopic ratios are plotted on the concordia (Fig. 4.6). They have high Th/U ratios of 0.43–1.97, and most of them have apparent $^{207}Pb/^{206}Pb$ ages that range from 1776 ± 27 Ma to 1675 ± 25 Ma (Table 4.3). Spot #17 has a younger apparent $^{207}Pb/^{206}Pb$ age of 1574 ± 42 Ma, which plots far away from the age mode, and is thus rejected from the age calculation. The remaining thirty-one analyses yield a weighted mean $^{207}Pb/^{206}Pb$ age of 1721 ± 9 Ma (MSWD = 0.95) and a concordia age of 1721 ± 4 Ma (MSWD = 0.035). Considering the magmatic zircon-like CL images and high Th/U ratios, the age of 1721 ± 4 Ma is taken to be the crystallization age of sample OCY44-1.

A total of twenty-one dated spots were further analyzed for zircon Lu–Hf isotopes (Table 4.4). When calculated at the crystallization age of 1721 Ma (t), they show initial $^{176}Hf/^{177}Hf(t)$ and $\varepsilon_{Hf}(t)$ values of 0.281405–0.281679 and −10.0 to −0.3,

Table 4.3 Zircon U–Pb isotopic dating data for representative samples from the Jianping diorite–monzonite–syenite suite (JDMSS), Western Liaoning Province

Sample and analytical spot number	Th (ppm)	U (ppm)	Th/U	Isotopic ratios						Apparent ages (Ma)					
				$^{207}Pb/^{206}Pb$	±1σ	$^{207}Pb/^{235}U$	±1σ	$^{206}Pb/^{238}U$	±1σ	$^{207}Pb/^{206}Pb$	±1σ	$^{207}Pb/^{235}U$	±1σ	$^{206}Pb/^{238}U$	±1σ
OCY44-1-01	95	73	1.30	0.1069	0.0023	4.5908	0.1023	0.3115	0.0042	1747	22	1748	19	1748	21
OCY44-1-02	97	120	0.81	0.1044	0.0023	4.3503	0.0984	0.3022	0.0041	1704	23	1703	19	1702	20
OCY44-1-03	43	53	0.82	0.1070	0.0024	4.5998	0.1074	0.3117	0.0043	1749	23	1749	19	1749	21
OCY44-1-04	52	44	1.18	0.1063	0.0025	4.5356	0.1090	0.3096	0.0043	1736	25	1738	20	1739	21
OCY44-1-05	60	51	1.20	0.1076	0.0024	4.6535	0.1091	0.3137	0.0043	1759	24	1759	20	1759	21
OCY44-1-06	23	24	0.94	0.1076	0.0029	4.6472	0.1278	0.3134	0.0046	1758	29	1758	23	1757	22
OCY44-1-07	206	146	1.41	0.1039	0.0022	4.3067	0.0948	0.3007	0.0040	1694	22	1695	18	1695	20
OCY44-1-08	42	34	1.24	0.1049	0.0028	4.4080	0.1193	0.3047	0.0044	1713	29	1714	22	1715	22
OCY44-1-09	62	43	1.43	0.1072	0.0027	4.6169	0.1182	0.3124	0.0044	1752	27	1752	21	1753	22
OCY44-1-10	73	76	0.97	0.1050	0.0023	4.4111	0.1016	0.3047	0.0041	1714	23	1714	19	1714	20
OCY44-1-11	123	93	1.32	0.1031	0.0023	4.2259	0.0991	0.2974	0.0041	1680	24	1679	19	1678	20
OCY44-1-12	55	49	1.12	0.1086	0.0027	4.7593	0.1224	0.3178	0.0045	1776	27	1778	22	1779	22
OCY44-1-13	127	84	1.51	0.1028	0.0025	4.2025	0.1027	0.2966	0.0041	1675	25	1675	20	1674	20
OCY44-1-14	34	36	0.94	0.1054	0.0026	4.4626	0.1138	0.3070	0.0043	1722	27	1724	21	1726	21
OCY44-1-15	95	71	1.34	0.1051	0.0024	4.4261	0.1047	0.3055	0.0042	1716	24	1717	20	1718	21
OCY44-1-16	38	41	0.93	0.1076	0.0031	4.6397	0.1360	0.3129	0.0047	1758	32	1756	24	1755	23
OCY44-1-17	29	36	0.81	0.0973	0.0035	3.7355	0.1323	0.2784	0.0045	1574	42	1579	28	1583	23
OCY44-1-18	269	184	1.46	0.1051	0.0023	4.4191	0.1006	0.3051	0.0041	1715	23	1716	19	1716	20
OCY44-1-19	55	54	1.00	0.1062	0.0026	4.5153	0.1135	0.3083	0.0043	1736	26	1734	21	1732	21
OCY44-1-20	85	73	1.16	0.1043	0.0027	4.3435	0.1156	0.3020	0.0043	1703	28	1702	22	1701	21
OCY44-1-21	499	254	1.97	0.1051	0.0024	4.4240	0.1026	0.3053	0.0041	1716	24	1717	19	1717	20
OCY44-1-22	106	70	1.51	0.1039	0.0026	4.3069	0.1098	0.3007	0.0042	1695	27	1695	21	1695	21
OCY44-1-23	66	54	1.22	0.1049	0.0026	4.4123	0.1100	0.3051	0.0042	1713	26	1715	21	1716	21

(continued)

Table 4.3 (continued)

Sample and analytical spot number	Th (ppm)	U (ppm)	Th/U	Isotopic ratios						Apparent ages (Ma)					
				$^{207}Pb/^{206}Pb$	±1σ	$^{207}Pb/^{235}U$	±1σ	$^{206}Pb/^{238}U$	±1σ	$^{207}Pb/^{206}Pb$	±1σ	$^{207}Pb/^{235}U$	±1σ	$^{206}Pb/^{238}U$	±1σ
OCY44-1-24	28	46	0.60	0.1048	0.0031	4.3938	0.1304	0.3042	0.0046	1710	33	1711	25	1712	22
OCY44-1-25	87	65	1.35	0.1056	0.0028	4.4628	0.1194	0.3065	0.0044	1725	29	1724	22	1723	22
OCY44-1-26	56	65	0.86	0.1040	0.0025	4.3198	0.1069	0.3014	0.0041	1696	26	1697	20	1698	20
OCY44-1-27	32	34	0.94	0.1068	0.0028	4.5755	0.1219	0.3107	0.0044	1746	28	1745	22	1744	22
OCY44-1-28	37	85	0.43	0.1037	0.0025	4.3013	0.1073	0.3008	0.0041	1692	26	1694	21	1695	20
OCY44-1-29	94	112	0.83	0.1064	0.0025	4.5259	0.1112	0.3086	0.0042	1738	26	1736	20	1734	21
OCY44-1-30	71	82	0.86	0.1059	0.0027	4.4818	0.1183	0.3070	0.0043	1730	28	1728	22	1726	21
OCY44-1-31	50	63	0.79	0.1044	0.0027	4.3650	0.1142	0.3033	0.0042	1704	28	1706	22	1708	21
OCY44-1-32	137	103	1.33	0.1055	0.0026	4.4551	0.1119	0.3063	0.0042	1723	26	1723	21	1722	21
11JP12-1-01	25	104	0.24	0.1082	0.0034	4.7197	0.1287	0.3163	0.0048	1770	58	1771	23	1772	23
11JP12-1-02	27	147	0.19	0.1056	0.0022	4.4859	0.1006	0.3080	0.0045	1725	21	1728	19	1731	22
11JP12-1-03	58	166	0.35	0.1051	0.0022	4.3932	0.0991	0.3031	0.0045	1716	21	1711	19	1706	22
11JP12-1-04	174	154	1.13	0.1056	0.0023	4.4291	0.1005	0.3042	0.0045	1724	21	1718	19	1712	22
11JP12-1-05	2	86	0.03	0.1048	0.0025	4.3884	0.1085	0.3036	0.0046	1711	24	1710	20	1709	23
11JP12-1-06	34	112	0.31	0.1058	0.0024	4.4359	0.1060	0.3041	0.0046	1728	23	1719	20	1711	23
11JP12-1-07	42	140	0.30	0.1044	0.0023	4.3588	0.1003	0.3029	0.0045	1703	22	1705	19	1706	22
11JP12-1-08	10	79	0.12	0.1064	0.0026	4.4441	0.1107	0.3028	0.0046	1739	24	1721	21	1705	23
11JP12-1-09	32	77	0.41	0.1061	0.0025	4.4951	0.1089	0.3074	0.0047	1733	23	1730	20	1728	23
11JP12-1-10	9	56	0.16	0.1056	0.0029	4.4073	0.1230	0.3028	0.0048	1724	29	1714	23	1705	24
11JP12-1-11	66	207	0.32	0.1058	0.0034	4.3927	0.1267	0.3011	0.0045	1728	61	1711	24	1697	22
11JP12-1-12	18	166	0.11	0.1065	0.0024	4.5401	0.1057	0.3093	0.0046	1739	22	1738	19	1737	23
11JP12-1-13	50	111	0.45	0.1055	0.0025	4.4663	0.1083	0.3069	0.0046	1724	24	1725	20	1725	23
11JP12-1-14	48	124	0.39	0.1056	0.0024	4.4330	0.1066	0.3045	0.0046	1724	23	1719	20	1713	23
11JP12-1-15	2	26	0.08	0.1044	0.0043	4.4298	0.1822	0.3076	0.0055	1704	50	1718	34	1729	27

(continued)

Table 4.3 (continued)

Sample and analytical spot number	Th (ppm)	U (ppm)	Th/U	Isotopic ratios						Apparent ages (Ma)					
				$^{207}Pb/^{206}Pb$	±1σ	$^{207}Pb/^{235}U$	±1σ	$^{206}Pb/^{238}U$	±1σ	$^{207}Pb/^{206}Pb$	±1σ	$^{207}Pb/^{235}U$	±1σ	$^{206}Pb/^{238}U$	±1σ
11JP12-1-16	17	136	0.12	0.1069	0.0025	4.6868	0.1131	0.3178	0.0048	1748	23	1765	20	1779	23
11JP12-1-17	4	35	0.10	0.1062	0.0036	4.5139	0.1524	0.3082	0.0053	1735	37	1734	28	1732	26
11JP12-1-18	40	78	0.52	0.1061	0.0029	4.4587	0.1253	0.3049	0.0048	1733	29	1723	23	1715	24
11JP12-1-19	19	144	0.13	0.1047	0.0024	4.3969	0.1071	0.3046	0.0046	1709	24	1712	20	1714	23
11JP12-1-20	41	73	0.57	0.1059	0.0027	4.4306	0.1177	0.3035	0.0047	1729	27	1718	22	1709	23
11JP12-1-21	23	128	0.18	0.1046	0.0027	4.4509	0.1174	0.3087	0.0048	1707	27	1722	22	1734	23
11JP12-1-22	10	56	0.18	0.1054	0.0032	4.4608	0.1359	0.3070	0.0049	1720	33	1724	25	1726	24
11JP12-1-23	5	75	0.06	0.1053	0.0029	4.1919	0.1174	0.2887	0.0046	1720	29	1672	23	1635	23
11JP12-1-24	36	171	0.21	0.1057	0.0026	4.4064	0.1120	0.3022	0.0046	1727	25	1714	21	1702	23
11JP12-1-25	23	160	0.14	0.1059	0.0026	4.4371	0.1141	0.3038	0.0046	1730	26	1719	21	1710	23
11JP12-1-26	20	66	0.30	0.1058	0.0030	4.4904	0.1286	0.3078	0.0049	1728	30	1729	24	1730	24
11JP12-3-01	32	106	0.30	0.1044	0.0020	4.4521	0.0925	0.3092	0.0045	1704	19	1722	17	1737	22
11JP12-3-02	36	113	0.32	0.1026	0.0020	4.3659	0.0913	0.3087	0.0045	1671	19	1706	17	1734	22
11JP12-3-03	36	110	0.32	0.1057	0.0021	4.5195	0.0955	0.3102	0.0045	1726	19	1735	18	1742	22
11JP12-3-04	43	109	0.39	0.1063	0.0024	4.5227	0.1075	0.3086	0.0048	1737	22	1735	20	1734	24
11JP12-3-05	18	86	0.21	0.1043	0.0021	4.4156	0.0952	0.3071	0.0045	1702	20	1715	18	1726	22
11JP12-3-06	25	95	0.26	0.1044	0.0021	4.2319	0.0909	0.2939	0.0043	1704	20	1680	18	1661	21
11JP12-3-07	36	144	0.25	0.1058	0.0020	4.5065	0.0923	0.3089	0.0045	1728	18	1732	17	1735	22
11JP12-3-08	10	55	0.18	0.1061	0.0024	4.5679	0.1089	0.3122	0.0047	1734	23	1743	20	1751	23
11JP12-3-09	19	82	0.23	0.1070	0.0023	4.6071	0.1034	0.3122	0.0046	1749	21	1751	19	1751	23
11JP12-3-10	14	89	0.15	0.1043	0.0022	4.4461	0.0973	0.3091	0.0046	1702	20	1721	18	1736	22
11JP12-3-11	85	243	0.35	0.1048	0.0019	4.3863	0.0877	0.3037	0.0043	1710	18	1710	17	1709	21
11JP12-3-12	55	182	0.30	0.1055	0.0020	4.4707	0.0906	0.3073	0.0044	1723	18	1726	17	1727	22
11JP12-3-13	47	110	0.43	0.1049	0.0033	4.4093	0.1374	0.3049	0.0055	1712	32	1714	26	1716	27

(continued)

Table 4.3 (continued)

Sample and analytical spot number	Th (ppm)	U (ppm)	Th/U	Isotopic ratios						Apparent ages (Ma)					
				$^{207}Pb/^{206}Pb$	±1σ	$^{207}Pb/^{235}U$	±1σ	$^{206}Pb/^{238}U$	±1σ	$^{207}Pb/^{206}Pb$	±1σ	$^{207}Pb/^{235}U$	±1σ	$^{206}Pb/^{238}U$	±1σ
11JP12-3-14	35	104	0.33	0.1056	0.0022	4.4830	0.0970	0.3078	0.0045	1725	20	1728	18	1730	22
11JP12-3-15	22	78	0.29	0.1062	0.0024	4.5028	0.1054	0.3075	0.0046	1735	22	1731	19	1728	23
11JP12-3-16	32	97	0.33	0.1065	0.0022	4.4856	0.0978	0.3055	0.0045	1740	20	1728	18	1718	22
11JP12-3-17	22	69	0.32	0.1069	0.0025	4.4296	0.1075	0.3004	0.0045	1748	24	1718	20	1693	22
11JP12-3-18	33	98	0.34	0.1053	0.0023	4.4243	0.1013	0.3048	0.0045	1719	22	1717	19	1715	22
11JP12-3-19	29	248	0.12	0.1048	0.0020	4.4073	0.0910	0.3050	0.0044	1710	19	1714	17	1716	22
11JP12-3-20	88	285	0.31	0.1054	0.0020	4.4670	0.0912	0.3074	0.0044	1721	18	1725	17	1728	22
11JP12-3-21	11	111	0.10	0.1052	0.0021	4.4301	0.0955	0.3054	0.0045	1717	20	1718	18	1718	22
11JP12-3-22	88	277	0.32	0.1048	0.0020	4.3800	0.0916	0.3031	0.0044	1711	19	1709	17	1707	22
11JP12-3-23	20	104	0.20	0.1058	0.0024	4.4805	0.1051	0.3070	0.0046	1729	22	1727	19	1726	23
11JP12-3-24	30	57	0.53	0.1059	0.0030	4.4123	0.1269	0.3021	0.0051	1730	29	1715	24	1702	25
11JP12-3-25	29	145	0.20	0.1063	0.0022	4.4282	0.0962	0.3022	0.0044	1736	20	1718	18	1702	22
11JP12-3-26	23	133	0.17	0.1054	0.0023	4.4433	0.1006	0.3058	0.0046	1721	21	1720	19	1720	23
11JP12-3-27	32	108	0.30	0.1056	0.0023	4.4626	0.1026	0.3064	0.0046	1725	22	1724	19	1723	22
11JP05-1-01	93	99	0.94	0.1051	0.0021	4.4232	0.0925	0.3052	0.0044	1716	19	1717	17	1717	21
11JP05-1-02	97	114	0.85	0.1052	0.0022	4.4353	0.0972	0.3058	0.0044	1717	20	1719	18	1720	22
11JP05-1-03	46	55	0.84	0.1070	0.0026	4.4987	0.1114	0.3048	0.0045	1750	24	1731	21	1715	22
11JP05-1-04	236	151	1.57	0.1052	0.0020	4.4342	0.0904	0.3058	0.0043	1717	19	1719	17	1720	21
11JP05-1-05	44	44	0.99	0.1051	0.0025	4.4165	0.1079	0.3047	0.0046	1716	24	1715	20	1715	23
11JP05-1-06	111	128	0.87	0.1050	0.0021	4.4004	0.0933	0.3039	0.0043	1714	20	1712	18	1711	21
11JP05-1-07	27	67	0.39	0.1048	0.0023	4.3891	0.1005	0.3037	0.0045	1711	22	1710	19	1710	22
11JP05-1-08	40	48	0.84	0.1046	0.0026	4.3558	0.1084	0.3021	0.0046	1707	25	1704	21	1702	23
11JP05-1-09	134	105	1.27	0.1043	0.0022	4.3282	0.0939	0.3010	0.0043	1701	20	1699	18	1696	22
11JP05-1-10	38	48	0.78	0.1056	0.0026	4.4841	0.1124	0.3079	0.0046	1725	25	1728	21	1730	23

(continued)

Table 4.3 (continued)

Sample and analytical spot number	Th (ppm)	U (ppm)	Th/U	Isotopic ratios						Apparent ages (Ma)					
				$^{207}Pb/^{206}Pb$	±1σ	$^{207}Pb/^{235}U$	±1σ	$^{206}Pb/^{238}U$	±1σ	$^{207}Pb/^{206}Pb$	±1σ	$^{207}Pb/^{235}U$	±1σ	$^{206}Pb/^{238}U$	±1σ
11JP05-1-11	95	84	1.14	0.1051	0.0022	4.4171	0.0959	0.3047	0.0044	1717	20	1716	18	1714	22
11JP05-1-12	121	123	0.99	0.1053	0.0022	4.4485	0.0967	0.3065	0.0044	1719	20	1721	18	1724	22
11JP05-1-13	477	314	1.52	0.1046	0.0021	4.1348	0.0856	0.2868	0.0040	1707	19	1661	17	1625	20
11JP05-1-14	53	58	0.92	0.1310	0.0028	5.8657	0.1311	0.3246	0.0048	2112	20	1956	19	1812	23
11JP05-1-15	83	118	0.70	0.1053	0.0023	4.1953	0.0933	0.2889	0.0042	1720	21	1673	18	1636	21
11JP05-1-16	60	88	0.68	0.1064	0.0041	4.3185	0.1518	0.2943	0.0045	1739	72	1697	29	1663	23
11JP05-1-17	62	91	0.68	0.1060	0.0023	4.4213	0.0997	0.3024	0.0044	1732	21	1716	19	1703	22
11JP05-1-18	277	216	1.28	0.1044	0.0022	4.3876	0.0952	0.3047	0.0043	1704	20	1710	18	1715	21
11JP05-1-19	118	127	0.93	0.1054	0.0023	4.4242	0.0996	0.3045	0.0044	1720	21	1717	19	1714	22
11JP05-1-20	166	128	1.30	0.1090	0.0024	4.7592	0.1076	0.3166	0.0046	1783	21	1778	19	1773	22
11JP05-1-21	154	115	1.33	0.1051	0.0024	4.4031	0.1032	0.3038	0.0044	1716	23	1713	19	1710	22
11JP05-1-22	233	173	1.35	0.1058	0.0024	4.4950	0.1031	0.3082	0.0045	1728	22	1730	19	1732	22
11JP05-1-23	34	64	0.54	0.1049	0.0026	4.3995	0.1102	0.3042	0.0046	1712	25	1712	21	1712	23
11JP05-1-24	42	73	0.58	0.1055	0.0026	4.4097	0.1093	0.3032	0.0045	1723	25	1714	21	1707	22
11JP05-1-25	56	70	0.80	0.1048	0.0025	4.3841	0.1072	0.3034	0.0045	1711	24	1709	20	1708	22
11JP05-1-26	60	100	0.60	0.1048	0.0025	4.3899	0.1063	0.3038	0.0045	1710	24	1710	20	1710	22
11JP15-1-01	26	46	0.57	0.1039	0.0021	4.3354	0.0904	0.3026	0.0043	1695	19	1700	17	1704	21
11JP15-1-02	120	73	1.66	0.1046	0.0020	4.3642	0.0873	0.3026	0.0043	1707	18	1706	17	1704	21
11JP15-1-03	61	45	1.35	0.1018	0.0022	4.2582	0.0959	0.3033	0.0044	1657	22	1685	19	1708	22
11JP15-1-04	22	25	0.89	0.1046	0.0033	4.3579	0.1359	0.3022	0.0049	1706	34	1704	26	1702	24
11JP15-1-05	81	72	1.12	0.1050	0.0021	4.3979	0.0923	0.3038	0.0044	1714	19	1712	17	1710	22
11JP15-1-06	24	163	0.14	0.1042	0.0019	4.4092	0.0840	0.3067	0.0043	1701	17	1714	16	1724	21
11JP15-1-07	72	48	1.49	0.1045	0.0024	4.3701	0.1016	0.3033	0.0045	1705	22	1707	19	1708	22
11JP15-1-08	20	21	0.94	0.1044	0.0031	4.3615	0.1293	0.3028	0.0050	1704	31	1705	24	1705	25

(continued)

Table 4.3 (continued)

Sample and analytical spot number	Th (ppm)	U (ppm)	Th/U	Isotopic ratios						Apparent ages (Ma)					
				$^{207}Pb/^{206}Pb$	±1σ	$^{207}Pb/^{235}U$	±1σ	$^{206}Pb/^{238}U$	±1σ	$^{207}Pb/^{206}Pb$	±1σ	$^{207}Pb/^{235}U$	±1σ	$^{206}Pb/^{238}U$	±1σ
11JP15-1-09	27	34	0.79	0.1043	0.0026	4.3503	0.1088	0.3026	0.0046	1701	25	1703	21	1704	23
11JP15-1-10	22	21	1.07	0.1046	0.0035	4.3419	0.1432	0.3010	0.0050	1707	37	1701	27	1696	25
11JP15-1-11	17	90	0.19	0.1033	0.0020	4.2108	0.0863	0.2956	0.0042	1684	19	1676	17	1669	21
11JP15-1-12	91	74	1.23	0.1043	0.0022	4.3291	0.0937	0.3010	0.0044	1702	20	1699	18	1696	22
11JP15-1-13	32	33	0.96	0.1048	0.0024	4.3614	0.0998	0.3019	0.0045	1710	22	1705	19	1701	22
11JP15-1-14	18	86	0.21	0.1045	0.0020	4.3577	0.0876	0.3025	0.0043	1705	18	1704	17	1704	21
11JP15-1-15	21	25	0.82	0.1047	0.0031	4.3571	0.1293	0.3018	0.0048	1709	32	1704	25	1700	24
11JP15-1-16	38	34	1.10	0.1034	0.0026	4.2958	0.1087	0.3012	0.0045	1686	26	1693	21	1697	22
11JP15-1-17	26	26	0.99	0.1042	0.0033	4.3930	0.1381	0.3057	0.0053	1700	33	1711	26	1720	26
11JP15-1-18	33	37	0.89	0.1044	0.0024	4.3499	0.1020	0.3022	0.0045	1703	22	1703	19	1702	22
11JP15-1-19	67	50	1.35	0.1155	0.0077	5.1844	0.3328	0.3255	0.0063	1888	124	1850	55	1817	30
11JP15-1-20	53	47	1.12	0.1048	0.0022	4.3816	0.0961	0.3032	0.0045	1711	20	1709	18	1707	22
11JP15-1-21	50	32	1.53	0.1045	0.0025	4.3828	0.1078	0.3041	0.0047	1706	24	1709	20	1711	23
11JP15-1-22	23	24	0.96	0.1045	0.0031	4.3617	0.1281	0.3026	0.0049	1706	31	1705	24	1704	24
11JP15-1-23	42	31	1.38	0.1044	0.0026	4.3645	0.1099	0.3030	0.0047	1704	25	1706	21	1706	23
11JP15-1-24	15	18	0.84	0.1044	0.0030	4.3607	0.1259	0.3030	0.0048	1703	30	1705	24	1706	24
11JP15-1-25	40	29	1.39	0.1044	0.0027	4.3406	0.1140	0.3015	0.0047	1704	26	1701	22	1699	23
OCY37-2-01	34	34	1.00	0.1009	0.0035	4.0481	0.1402	0.2910	0.0045	1641	41	1644	28	1646	23
OCY37-2-02	43	85	0.51	0.1037	0.0032	4.2916	0.1323	0.3001	0.0044	1692	35	1692	25	1692	22
OCY37-2-03	38	64	0.59	0.1042	0.0032	4.3313	0.1322	0.3016	0.0044	1700	35	1699	25	1699	22
OCY37-2-04	423	307	1.38	0.1043	0.0030	4.3547	0.1281	0.3029	0.0043	1701	33	1704	24	1706	21
OCY37-2-05	54	245	0.22	0.1000	0.0030	3.9391	0.1194	0.2858	0.0041	1624	35	1622	25	1620	21
OCY37-2-06	69	201	0.34	0.1077	0.0031	4.6635	0.1380	0.3140	0.0045	1762	33	1761	25	1760	22
OCY37-2-07	171	248	0.69	0.1038	0.0031	4.3144	0.1306	0.3015	0.0043	1693	35	1696	25	1699	21

(continued)

Table 4.3 (continued)

Sample and analytical spot number	Th (ppm)	U (ppm)	Th/U	Isotopic ratios						Apparent ages (Ma)					
				$^{207}Pb/^{206}Pb$	±1σ	$^{207}Pb/^{235}U$	±1σ	$^{206}Pb/^{238}U$	±1σ	$^{207}Pb/^{206}Pb$	±1σ	$^{207}Pb/^{235}U$	±1σ	$^{206}Pb/^{238}U$	±1σ
OCY37-2-08	107	179	0.60	0.1026	0.0032	4.1718	0.1297	0.2950	0.0043	1671	36	1669	25	1667	21
OCY37-2-09	358	284	1.26	0.1041	0.0030	4.3097	0.1273	0.3003	0.0042	1699	34	1695	24	1693	21
OCY37-2-10	44	162	0.27	0.1066	0.0032	4.5398	0.1369	0.3091	0.0044	1741	34	1738	25	1736	22
OCY37-2-11	127	187	0.68	0.1044	0.0031	4.3650	0.1305	0.3032	0.0043	1704	34	1706	25	1707	21
OCY37-2-12	34	96	0.36	0.1045	0.0034	4.3677	0.1411	0.3033	0.0045	1705	38	1706	27	1708	22
OCY37-2-13	387	277	1.40	0.1028	0.0031	4.1936	0.1269	0.2958	0.0042	1676	35	1673	25	1670	21
OCY37-2-14	117	143	0.81	0.1057	0.0032	4.4675	0.1371	0.3066	0.0044	1726	35	1725	25	1724	22
OCY37-2-15	56	139	0.40	0.1046	0.0032	4.3640	0.1330	0.3025	0.0043	1708	35	1706	25	1704	21
OCY37-2-16	135	240	0.57	0.1038	0.0031	4.2934	0.1301	0.3000	0.0043	1693	35	1692	25	1691	21
OCY37-2-17	335	281	1.19	0.1033	0.0032	4.2509	0.1315	0.2984	0.0043	1684	36	1684	25	1684	21
OCY37-2-18	57	102	0.56	0.1043	0.0033	4.3598	0.1401	0.3033	0.0045	1701	38	1705	27	1708	22
OCY37-2-19	111	120	0.92	0.1036	0.0033	4.2704	0.1374	0.2991	0.0044	1689	38	1688	26	1687	22
OCY37-2-20	38	181	0.21	0.1033	0.0032	4.2337	0.1328	0.2974	0.0043	1683	37	1681	26	1679	21
OCY37-2-21	94	105	0.89	0.1055	0.0033	4.4515	0.1411	0.3062	0.0044	1722	37	1722	26	1722	22
OCY37-2-22	405	299	1.35	0.1030	0.0032	4.1999	0.1321	0.2957	0.0043	1679	37	1674	26	1670	21
OCY37-2-23	357	379	0.94	0.1039	0.0032	4.2991	0.1339	0.3001	0.0043	1695	36	1693	26	1692	21
OCY37-2-24	82	192	0.43	0.1045	0.0033	4.3759	0.1391	0.3036	0.0044	1706	37	1708	26	1709	22
OCY37-2-25	199	179	1.11	0.1051	0.0033	4.4240	0.1402	0.3053	0.0044	1716	37	1717	26	1717	22
OCY37-2-26	192	233	0.83	0.1054	0.0033	4.4398	0.1415	0.3056	0.0044	1721	37	1720	26	1719	22
OCY37-2-27	284	243	1.17	0.1027	0.0033	4.1952	0.1339	0.2964	0.0043	1673	38	1673	26	1673	21
OCY37-2-28	46	52	0.88	0.1053	0.0035	4.4552	0.1485	0.3068	0.0046	1720	39	1723	28	1725	22

Note ^{204}Pb has been corrected using the method of [1]

Table 4.4 Zircon Lu–Hf isotopic data of the dated samples from the Jianping diorite–monzonite–syenite suite (JDMSS), Western Liaoning Province

Sample and analytical spot number	Crystallization age (t, Ma)	$^{176}Yb/^{177}Hf$	$^{176}Lu/^{177}Hf$	$^{176}Hf/^{177}Hf$	±2σ	$(^{176}Hf/^{177}Hf)_t$	$\varepsilon_{Hf}(0)$	$\varepsilon_{Hf}(t)$	T_{DM}	$T^{C}_{DM}(t)$	$f_{Lu/Hf}$
OCY44-1-2	1722	0.067726	0.001289	0.281508	0.000020	0.281466	−44.7	−7.9	2457	2921	−0.96
OCY44-1-3	1722	0.020415	0.000388	0.281483	0.000017	0.281470	−45.6	−7.7	2434	2911	−0.99
OCY44-1-4	1722	0.061447	0.001201	0.281540	0.000021	0.281501	−43.6	−6.6	2407	2842	−0.96
OCY44-1-5	1722	0.115059	0.002218	0.281595	0.000022	0.281523	−41.6	−5.8	2395	2793	−0.93
OCY44-1-6	1722	0.038731	0.000811	0.281468	0.000024	0.281442	−46.1	−8.7	2480	2974	−0.98
OCY44-1-7	1722	0.148634	0.002622	0.281727	0.000020	0.281642	−36.9	−1.6	2232	2525	−0.92
OCY44-1-8	1722	0.053807	0.000963	0.281528	0.000021	0.281497	−44.0	−6.8	2408	2851	−0.97
OCY44-1-9	1722	0.045610	0.000836	0.281553	0.000021	0.281526	−43.1	−5.7	2366	2785	−0.97
OCY44-1-10	1722	0.040714	0.000751	0.281470	0.000020	0.281446	−46.0	−8.6	2474	2965	−0.98
OCY44-1-12	1722	0.046397	0.000875	0.281499	0.000022	0.281471	−45.0	−7.7	2442	2909	−0.97
OCY44-1-13	1722	0.090986	0.001548	0.281664	0.000021	0.281613	−39.2	−2.6	2257	2590	−0.95
OCY44-1-14	1722	0.063203	0.001154	0.281561	0.000027	0.281523	−42.8	−5.8	2375	2792	−0.97
OCY44-1-15	1722	0.067149	0.001175	0.281622	0.000022	0.281584	−40.7	−3.7	2293	2656	−0.96
OCY44-1-18	1722	0.128844	0.002242	0.281651	0.000023	0.281578	−39.6	−3.9	2317	2669	−0.93
OCY44-1-19	1722	0.047577	0.000907	0.281499	0.000024	0.281469	−45.0	−7.7	2445	2913	−0.97
OCY44-1-20	1722	0.050085	0.000903	0.281573	0.000019	0.281544	−42.4	−5.1	2343	2745	−0.97
OCY44-1-21	1722	0.144642	0.002413	0.281758	0.000028	0.281679	−35.9	−0.3	2176	2441	−0.93
OCY44-1-23	1722	0.055080	0.000950	0.281498	0.000022	0.281467	−45.1	−7.8	2449	2919	−0.97
OCY44-1-26	1722	0.037290	0.000619	0.281511	0.000018	0.281490	−44.6	−7.0	2411	2866	−0.98
OCY44-1-28	1722	0.048837	0.001143	0.281442	0.000031	0.281405	−47.0	−10.0	2538	3057	−0.97
OCY44-1-30	1722	0.032136	0.000566	0.281468	0.000021	0.281450	−46.1	−8.4	2464	2956	−0.98
11JP12-1-1	1770	0.026706	0.000590	0.281461	0.000029	0.281441	−46.4	−7.7	2477	2945	−0.98

(continued)

Table 4.4 (continued)

Sample and analytical spot number	Crystallization age (t, Ma)	$^{176}Yb/^{177}Hf$	$^{176}Lu/^{177}Hf$	$^{176}Hf/^{177}Hf$	±2σ	$(^{176}Hf/^{177}Hf)_t$	$\varepsilon_{Hf}(0)$	$\varepsilon_{Hf}(t)$	T_{DM}	$T^C_{DM}(t)$	$f_{Lu/Hf}$
11JP12-1-2	1719	0.034512	0.000733	0.281507	0.000022	0.281483	−44.7	−7.3	2422	2883	−0.98
11JP12-1-4	1719	0.044364	0.001524	0.281445	0.000049	0.281396	−46.9	−10.4	2559	3080	−0.95
11JP12-1-5	1719	0.026367	0.000589	0.281554	0.000025	0.281535	−43.1	−5.5	2350	2768	−0.98
11JP12-1-6	1719	0.040435	0.001551	0.281405	0.000055	0.281354	−48.3	−11.9	2617	3171	−0.95
11JP12-1-8	1719	0.011162	0.000433	0.281510	0.000023	0.281496	−44.6	−6.9	2400	2855	−0.99
11JP12-1-11	1719	0.024890	0.000688	0.281429	0.000030	0.281407	−47.5	−10.0	2526	3055	−0.98
11JP12-1-12	1719	0.124858	0.004432	0.281561	0.000026	0.281417	−42.8	−9.7	2599	3033	−0.87
11JP12-1-13	1719	0.032179	0.000838	0.281488	0.000029	0.281461	−45.4	−8.1	2455	2934	−0.97
11JP12-1-15	1719	0.030591	0.001100	0.281440	0.000089	0.281404	−47.1	−10.1	2538	3061	−0.97
11JP12-1-17	1719	0.018320	0.000721	0.281474	0.000032	0.281451	−45.9	−8.5	2467	2956	−0.98
11JP12-1-22	1719	0.022090	0.000858	0.281362	0.000049	0.281334	−49.9	−12.6	2628	3217	−0.97
11JP12-1-24	1719	0.054863	0.002061	0.281464	0.000038	0.281397	−46.3	−10.4	2570	3078	−0.94
11JP12-3-2	1720	0.026761	0.000817	0.281489	0.000039	0.281462	−45.4	−8.0	2453	2931	−0.98
11JP12-3-3	1720	0.020743	0.000739	0.281463	0.000036	0.281439	−46.3	−8.9	2483	2982	−0.98
11JP12-3-5	1720	0.013468	0.000270	0.281534	0.000025	0.281525	−43.8	−5.8	2358	2789	−0.99
11JP12-3-7	1720	0.019202	0.000413	0.281521	0.000026	0.281507	−44.3	−6.4	2384	2829	−0.99
11JP12-3-9	1720	0.024881	0.000738	0.281450	0.000027	0.281426	−46.7	−9.3	2500	3010	−0.98
11JP12-3-11	1720	0.041089	0.001258	0.281481	0.000030	0.281440	−45.6	−8.8	2491	2979	−0.96
11JP12-3-18	1720	0.013891	0.000533	0.281472	0.000031	0.281455	−46.0	−8.3	2457	2946	−0.98
11JP12-3-23	1720	0.032689	0.001256	0.281564	0.000052	0.281523	−42.7	−5.9	2377	2793	−0.96
11JP05-1-1	1715	0.091537	0.001840	0.281479	0.000027	0.281419	−45.7	−9.7	2534	3030	−0.94
11JP05-1-2	1715	0.065343	0.001954	0.281461	0.000022	0.281397	−46.4	−10.5	2567	3079	−0.94

(continued)

Table 4.4 (continued)

Sample and analytical spot number	Crystallization age (t, Ma)	$^{176}Yb/^{177}Hf$	$^{176}Lu/^{177}Hf$	$^{176}Hf/^{177}Hf$	±2σ	$(^{176}Hf/^{177}Hf)_t$	$\varepsilon_{Hf}(0)$	$\varepsilon_{Hf}(t)$	T_{DM}	$T^C_{DM}(t)$	$f_{Lu/Hf}$
11JP05-1-3	1715	0.052044	0.001044	0.281493	0.000023	0.281459	−45.2	−8.3	2462	2941	−0.97
11JP05-1-5	1715	0.066709	0.001371	0.281470	0.000022	0.281426	−46.0	−9.5	2515	3015	−0.96
11JP05-1-8	1715	0.061454	0.001353	0.281525	0.000021	0.281481	−44.1	−7.5	2438	2892	−0.96
11JP05-1-10	1715	0.060462	0.001270	0.281453	0.000024	0.281412	−46.6	−9.9	2531	3045	−0.96
11JP05-1-12	1715	0.075503	0.001626	0.281468	0.000023	0.281415	−46.1	−9.8	2535	3040	−0.95
11JP05-1-16	1783	0.045960	0.000961	0.281442	0.000035	0.281410	−47.0	−8.5	2525	3006	−0.97
11JP05-1-18	1715	0.083148	0.001627	0.281488	0.000033	0.281435	−45.4	−9.1	2508	2995	−0.95
11JP05-1-20	1783	0.094329	0.001810	0.281480	0.000029	0.281419	−45.7	−8.1	2530	2985	−0.95
11JP05-1-21	1715	0.086350	0.001663	0.281510	0.000031	0.281456	−44.6	−8.4	2479	2948	−0.95
11JP05-1-22	1715	0.057324	0.001075	0.281419	0.000029	0.281384	−47.8	−10.9	2565	3107	−0.97
11JP05-1-24	1715	0.046202	0.000865	0.281458	0.000032	0.281430	−46.5	−9.3	2497	3005	−0.97
11JP05-1-25	1715	0.059940	0.001166	0.281521	0.000027	0.281483	−44.3	−7.4	2432	2888	−0.96
11JP05-1-26	1715	0.049129	0.000967	0.281511	0.000026	0.281479	−44.6	−7.5	2433	2896	−0.97
11JP15-1-1	1702	0.015409	0.000409	0.281542	0.000021	0.281528	−43.5	−6.1	2356	2794	−0.99
11JP15-1-2	1702	0.063119	0.001262	0.281504	0.000026	0.281463	−44.8	−8.4	2461	2940	−0.96
11JP15-1-3	1702	0.042804	0.000897	0.281569	0.000028	0.281540	−42.5	−5.7	2348	2767	−0.97
11JP15-1-4	1702	0.020001	0.000427	0.281488	0.000031	0.281474	−45.4	−8.0	2429	2915	−0.99
11JP15-1-7	1702	0.049815	0.000991	0.281499	0.000030	0.281467	−45.0	−8.3	2450	2931	−0.97
11JP15-1-8	1702	0.021476	0.000445	0.281488	0.000028	0.281473	−45.4	−8.0	2431	2917	−0.99
11JP15-1-10	1702	0.032851	0.000649	0.281509	0.000031	0.281488	−44.7	−7.5	2415	2885	−0.98
11JP15-1-11	1702	0.014927	0.000392	0.281488	0.000021	0.281475	−45.4	−8.0	2428	2914	−0.99
11JP15-1-12	1702	0.068321	0.001319	0.281556	0.000030	0.281513	−43.0	−6.6	2393	2828	−0.96

(continued)

Table 4.4 (continued)

Sample and analytical spot number	Crystallization age (t, Ma)	$^{176}Yb/^{177}Hf$	$^{176}Lu/^{177}Hf$	$^{176}Hf/^{177}Hf$	±2σ	$(^{176}Hf/^{177}Hf)_t$	$\varepsilon_{Hf}(0)$	$\varepsilon_{Hf}(t)$	T_{DM}	$T^C_{DM}(t)$	$f_{Lu/Hf}$
11JP15-1-13	1702	0.015264	0.000313	0.281509	0.000028	0.281499	−44.7	−7.1	2394	2860	−0.99
11JP15-1-15	1702	0.013983	0.000303	0.281577	0.000027	0.281567	−42.3	−4.7	2302	2707	−0.99
11JP15-1-16	1702	0.022206	0.000454	0.281447	0.000027	0.281432	−46.9	−9.5	2486	3008	−0.99
11JP15-1-18	1702	0.024458	0.000485	0.281497	0.000028	0.281482	−45.1	−7.8	2420	2898	−0.99
11JP15-1-19	1888	0.057457	0.001060	0.281464	0.000031	0.281425	−46.3	−5.5	2503	2901	−0.97
11JP15-1-20	1702	0.043094	0.000798	0.281449	0.000034	0.281423	−46.8	−9.8	2506	3028	−0.98
11JP15-1-21	1702	0.051161	0.000961	0.281556	0.000027	0.281525	−43.0	−6.2	2370	2800	−0.97
11JP15-1-22	1702	0.021184	0.000409	0.281473	0.000029	0.281460	−45.9	−8.5	2448	2947	−0.99
11JP15-1-23	1702	0.046563	0.000891	0.281468	0.000023	0.281439	−46.1	−9.3	2487	2994	−0.97
11JP15-1-24	1702	0.010051	0.000245	0.281493	0.000020	0.281485	−45.2	−7.6	2411	2890	−0.99
11JP15-1-25	1702	0.038220	0.000751	0.281534	0.000023	0.281510	−43.8	−6.8	2387	2835	−0.98
OCY37-2-1	1696	0.067233	0.001058	0.281590	0.000022	0.281556	−41.8	−5.3	2330	2736	−0.97
OCY37-2-2	1696	0.050531	0.000847	0.281525	0.000019	0.281498	−44.1	−7.3	2405	2865	−0.97
OCY37-2-3	1696	0.036891	0.000622	0.281544	0.000020	0.281524	−43.4	−6.4	2366	2808	−0.98
OCY37-2-4	1696	0.161134	0.002682	0.281772	0.000027	0.281686	−35.3	−0.6	2171	2443	−0.92
OCY37-2-6	1696	0.050470	0.000986	0.281568	0.000022	0.281537	−42.6	−5.9	2355	2779	−0.97
OCY37-2-7	1696	0.108324	0.002032	0.281645	0.000020	0.281580	−39.8	−4.4	2313	2682	−0.94
OCY37-2-8	1696	0.054086	0.000936	0.281567	0.000019	0.281537	−42.6	−5.9	2353	2778	−0.97
OCY37-2-9	1696	0.140845	0.002421	0.281700	0.000023	0.281622	−37.9	−2.9	2259	2587	−0.93
OCY37-2-10	1696	0.022682	0.000440	0.281532	0.000017	0.281518	−43.9	−6.6	2371	2821	−0.99
OCY37-2-11	1696	0.069251	0.001240	0.281628	0.000024	0.281589	−40.4	−4.1	2288	2663	−0.96
OCY37-2-12	1696	0.072964	0.001289	0.281596	0.000020	0.281554	−41.6	−5.3	2336	2739	−0.96

(continued)

Table 4.4 (continued)

Sample and analytical spot number	Crystallization age (t, Ma)	$^{176}Yb/^{177}Hf$	$^{176}Lu/^{177}Hf$	$^{176}Hf/^{177}Hf$	±2σ	$(^{176}Hf/^{177}Hf)_t$	$\varepsilon_{Hf}(0)$	$\varepsilon_{Hf}(t)$	T_{DM}	$T^C_{DM}(t)$	$f_{Lu/Hf}$
OCY37-2-13	1696	0.126366	0.002151	0.281700	0.000024	0.281631	−37.9	−2.6	2242	2566	−0.94
OCY37-2-14	1696	0.054122	0.000983	0.281535	0.000022	0.281503	−43.7	−7.1	2400	2853	−0.97
OCY37-2-15	1696	0.055052	0.001031	0.281612	0.000019	0.281578	−41.0	−4.5	2298	2685	−0.97
OCY37-2-16	1696	0.103490	0.001915	0.281705	0.000025	0.281643	−37.7	−2.1	2221	2539	−0.94
OCY37-2-18	1696	0.049988	0.000988	0.281638	0.000018	0.281606	−40.1	−3.5	2259	2622	−0.97
OCY37-2-19	1696	0.132223	0.002482	0.281652	0.000023	0.281572	−39.6	−4.7	2331	2699	−0.93
OCY37-2-20	1696	0.032658	0.000704	0.281570	0.000019	0.281547	−42.5	−5.6	2335	2755	−0.98
OCY37-2-21	1696	0.126138	0.002186	0.281583	0.000023	0.281513	−42.0	−6.8	2410	2832	−0.93
OCY37-2-22	1696	0.111134	0.002094	0.281619	0.000022	0.281552	−40.8	−5.4	2354	2746	−0.94
OCY37-2-23	1696	0.045248	0.000926	0.281552	0.000019	0.281523	−43.1	−6.4	2373	2810	−0.97
OCY37-2-24	1696	0.022785	0.000466	0.281535	0.000018	0.281520	−43.8	−6.5	2369	2817	−0.99
OCY37-2-25	1696	0.098725	0.001742	0.281615	0.000022	0.281559	−40.9	−5.1	2337	2729	−0.95
OCY37-2-28	1696	0.071939	0.001426	0.281542	0.000027	0.281496	−43.5	−7.4	2419	2870	−0.96

Note The present $^{176}Hf/^{177}Hf$ and $^{176}Lu/^{177}Hf$ ratios of chondrite and depleted mantle are 0.282772 and 0.0332, and 0.28325 and 0.0384, respectively, Blichert-Toft and Albarède [5], Griffin et al. (2000). $\lambda = 1.867 \times 10^{-11}\ a^{-1}$, Soderlund et al. (2004)

$\varepsilon_{Hf}(t) = 10000\{[(^{176}Hf/^{177}Hf)_S - (^{176}Lu/^{177}Hf)_S \times (e^{\lambda t} - 1)]/[(^{176}Hf/^{177}Hf)_{CHUR,0} - (^{176}Lu/^{177}Hf)_{CHUR} \times (e^{\lambda t} - 1)] - 1\}$

$T_{DM} = 1/\lambda \times \ln\{1 + [(^{176}Hf/^{177}Hf)_S - (^{176}Hf/^{177}Hf)_{DM}]/[(^{176}Lu/^{177}Hf)_S - (^{176}Lu/^{177}Hf)_{DM}]\}$; $f_{Lu/Hf} = (^{176}Lu/^{177}Hf)_S/(^{176}Lu/^{177}Hf)_{CHUR}-1$

$T^C_{DM} = 1/\lambda \ln\{1 + [(^{176}Hf/^{177}Hf)_{s,t} - (^{176}Hf/^{177}Hf)_{DM,t}]/[(^{176}Lu/^{177}Hf)_c - (^{176}Lu/^{177}Hf)_{DM}]\} + t$

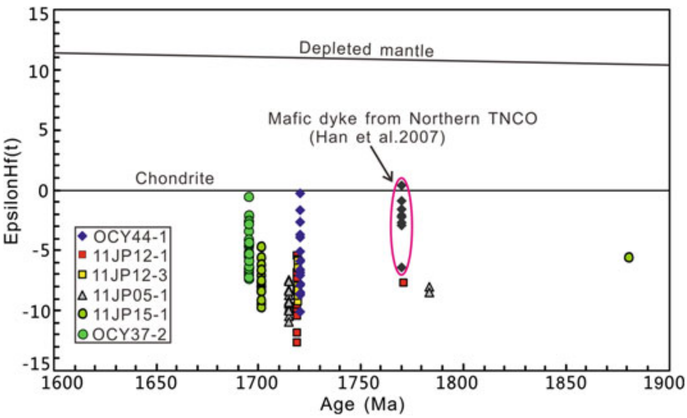

Fig. 4.7 Plots of zircon $\varepsilon_{Hf}(t)$ values versus crystallization ages for the six dated JDMSS samples (including $\varepsilon_{Hf}(t)$ values of the xenocrystic zircon grains calculated at the apparent $^{207}Pb/^{206}Pb$ ages). Zircon Lu–Hf isotopic data for a mafic dyke from Fengzhen, northern end of the Trans-North China Orogen, are plotted for comparison [26]. The $^{176}Lu/^{177}Hf$ isotopic ratios of the depleted mantle and chondrite are 0.0384 and 0.0332, respectively, after Blichert-Toft and Albarède [5] and Griffin et al. [21]

respectively, with Hf depleted mantle model ages (T_{DM}(Hf)) varying from 2538 to 2176 Ma (Fig. 4.7 and Table 4.4).

4.1.3.2 The Xiaozhangzi Pluton

Clinopyroxene monzonites and syenites (and quartz syenites) are the main lithologies in this pluton. Sample 11JP12-1 is a clinopyroxene monzonite, and the separated zircon grains are rounded (e.g., spot #1) or stubby crystals (e.g., spots #12 and #25), with lengths and length/width ratios of 80–120 μm and 1:1–1.5:1, respectively. Cathodoluminescence images of these zircon grains show oscillatory zonings, typical of magmatic zircons (Fig. 4.8a). A total of twenty-six spots were analyzed on twenty-six zircon grains, and they yield apparent $^{207}Pb/^{206}Pb$ ages that range from 1770 ± 58 Ma to 1703 ± 22 Ma (Table 4.3). Most of them have Th/U ratios of 0.10–1.13, except for three anomalous analyses of spots #5, #15, and #23, showing lower ratios of 0.03–0.08. In the concordia diagram, most analyses plot along the concordia, except for spot #23 that falls below (Fig. 4.8a). Nevertheless, spot #23 yields an apparent $^{207}Pb/^{206}Pb$ age of 1720 ± 29 Ma, which is within error of the age range of the other analyses. This implies some degree of Pb loss of spot #23, as evidenced by its low Th/U ratio of 0.06. Of the other 25 analyses, spots #1 and #16 yield older apparent $^{207}Pb/^{206}Pb$ ages of 1770 ± 58 Ma and 1748 ± 23 Ma, respectively, and the remaining twenty-three analyses give younger apparent $^{207}Pb/^{206}Pb$ ages that range between 1739 ± 22 Ma and 1703 ± 22 Ma, yielding a concordia age of 1719 ± 5 Ma (MSWD = 1.8) and a weighted mean age

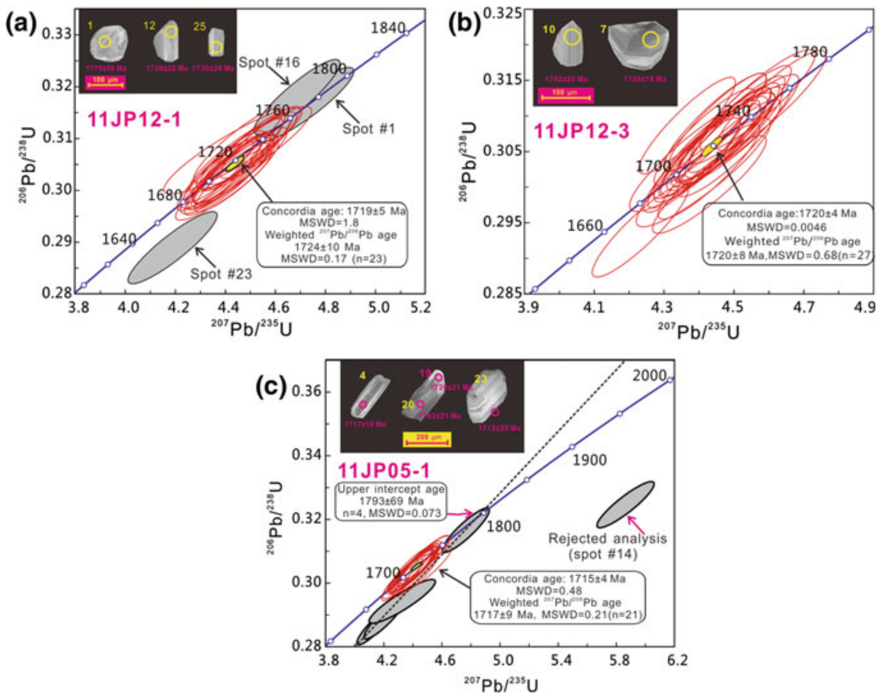

Fig. 4.8 Zircon U–Pb isotopic concordia diagrams for samples 11JP12-1 (**a**), 11JP12-3 (**b**), and 11JP05-1 (**c**) of the Xiaozhangzi pluton. The insets show zircon internal structures and analyzed locations on the cathodoluminescence images for each sample

of 1724 ± 10 Ma (MSWD = 0.17). Considering the magmatic features of most zircon grains, the two spots with older apparent ages (spots #1 and #16) are taken to be xenocrystic zircons, whereas the concordia age of 1719 ± 5 Ma is considered as the crystallization age of sample 11JP12-1. A total of thirteen dated spots were analyzed for Lu–Hf isotopes (Table 4.4). The inherited zircon grain (spot #1, calculated at 1770 Ma) shows initial $^{176}Hf/^{177}Hf(t)$, $\varepsilon_{Hf}(t)$, and $T_{DM}(Hf)$ values of 0.281441, −7.7, and 2477 Ma, respectively. When calculated at the crystallization age of 1719 Ma (t), the other twelve analyses yield initial $^{176}Hf/^{177}Hf(t)$ and $\varepsilon_{Hf}(t)$ values of 0.281334–0.281535 and −12.6 to −5.5, respectively, with $T_{DM}(Hf)$ ages of 2628–2350 Ma (Fig. 4.7).

The clinopyroxene monzonite sample 11JP12-3 has zircon grains that are rounded (e.g., spot #7) or stubby (e.g., spot #10) with lengths of 100–150 μm and length/width ratios of 1:1–2:1. On the cathodoluminescence images, all of them display oscillatory zonings, typical of magmatic zircons (Fig. 4.8b). Combined with the Th/U ratios of 0.10–0.53 (Table 4.3), the data indicate that these zircon grains formed from magma crystallization. Twenty-seven spots were analyzed on twenty-six zircon grains, and they yield apparent $^{207}Pb/^{206}Pb$ ages that range from 1749 ± 21 Ma to 1671 ± 19 Ma (Table 4.3). All the analyses plot on the concordia, and yield a concordia age of 1720 ± 4 Ma (MSWD = 0.0046) and a weighted mean $^{207}Pb/^{206}Pb$ age of 1720 ± 8 Ma (MSWD = 0.68, Fig. 4.8b). Therefore, the age of 1720 ± 4 Ma is considered to be the crystallization age of sample 11JP12-3, which is coeval with the formation ages of samples OCY44-1 and 11JP12-1 (Figs. 4.6 and 4.8a). Eight dated spots (spots #2, #3, #5, #7, #9, #11, #18, and #23) were further analyzed for zircon Lu–Hf isotopes (Table 4.4). When calculated at the crystallization age of 1720 Ma (t), they yield initial $^{176}Hf/^{177}Hf(t)$ and $\varepsilon_{Hf}(t)$ values of 0.281426–0.281525 and −9.3 to −5.8, respectively, with $T_{DM}(Hf)$ ages between 2500 and 2358 Ma (Fig. 4.7 and Table 4.4).

Zircon grains from the quartz syenite sample 11JP05-1 vary from stubby (e.g., spot #23) to long prismatic crystals (e.g., spot #4), with lengths and length/width ratios of 150–250 μm and 1.5:1–2:1, respectively. On the cathodoluminescence images (Fig. 4.8c), most of them show concentric oscillatory or banded zonings, whereas some grains have core-rim structures, with both the cores and rims showing oscillatory zonings (e.g., spots #19 and #20). A total of twenty-six spots were analyzed on twenty zircon grains, and most of them plot on or close to the concordia, except for spot #14 that plots far away from the concordia and is thus rejected from the age calculation (Fig. 4.8c). The remaining twenty-five analyses yield apparent $^{207}Pb/^{206}Pb$ ages that range between 1783 ± 21 and 1701 ± 20 Ma, and they have high Th/U ratios of 0.39–1.57. Four analyses (spots #13, #15, #16, and #20) of the oscillatory zoned cores define a discordia and yield an older upper intercept age of 1793 ± 69 Ma (MSWD = 0.073), which is consistent with the concordia analysis of spot #20 that shows an apparent $^{207}Pb/^{206}Pb$ age of 1783 ± 21 Ma. This age of 1783 ± 21 Ma is nearly coeval with ages (1770 ± 58 and 1748 ± 23 Ma) of the two xenocrystic zircon grains from sample 11JP12-1, which are taken as the crystallization age of xenocrystic zircons (Fig. 4.8a). The remaining twenty-one analyses have younger apparent $^{207}Pb/^{206}Pb$ ages of 1750 ± 24–1701 ± 20 Ma, yielding a weighted mean age of 1717 ± 9 Ma (MSWD = 0.21) and a concordia age of 1715 ± 4 Ma (MSWD = 0.48), respectively (Fig. 4.8c). Considering the oscillatory zoned internal structures and high Th/U ratios (Fig. 4.8c), the age of 1715 ± 4 Ma is taken as the crystallization age of sample 11JP05-1. A total of fifteen dated spots were further analyzed for zircon Lu–Hf isotopes (Table 4.4). The two analyses of xenocrystic zircon domains (spots #16 and #20, calculated at 1783 Ma) show initial $^{176}Hf/^{177}Hf(t)$ and $\varepsilon_{Hf}(t)$ values of 0.281410–0.281419 and −8.5 to −8.1, respectively, with $T_{DM}(Hf)$ values between 2530 and 2525 Ma. The other thirteen analyses, when calculated at the magmatic crystallization age of 1715 Ma (t), yield initial $^{176}Hf/^{177}Hf(t)$, $\varepsilon_{Hf}(t)$, and $T_{DM}(Hf)$ values of 0.281384–0.281483, −10.9 to −7.4, and 2567–2432 Ma, respectively (Fig. 4.7).

4.1.3.3 The Shinao Pluton

Syenites, including quartz syenites, are the main lithologies in the Shinao pluton. Zircon grain from the syenite sample 11JP15-1 show stubby shapes with lengths and length/width ratios from 150 to 250 μm and 1:1 to 1.5:1, respectively. On the cathodoluminescence images (Fig. 4.9a), most of them display bright and oscillatory zonings that are typical of magmatic zircons. A total of twenty-five spots were analyzed on twenty-two zircon grains. These analyses give high Th/U ratios between 0.14 and 1.66, and plot on the concordia (Fig. 4.9a). Most of them show apparent $^{207}Pb/^{206}Pb$ ages between 1714 ± 19 and 1657 ± 22 Ma, yielding a weighted mean age of 1701 ± 9 Ma (MSWD = 0.28) and a concordia age of 1702 ± 4 Ma (MSWD = 0.18) (Fig. 4.9a). Spot #19 has an older apparent $^{207}Pb/^{206}Pb$ age of 1888 ± 124 Ma (Table 4.3), possibly reflecting the age of xenocrystic zircon grain, whereas the concordia age of 1702 ± 4 Ma is taken to be the crystallization age of sample 11JP15-1. A total of twenty dated spots were analyzed for zircon Lu–Hf isotopes (Table 4.4). The xenocrystic zircon spot #19 is calculated at the apparent age of 1888 Ma, showing initial $^{176}Hf/^{177}Hf(t)$, $\varepsilon_{Hf}(t)$, and $T_{DM}(Hf)$ values of 0.281425, −5.5, and 2503 Ma, respectively. The remaining nineteen analyses, when calculated at the crystallization age of 1702 Ma (t), yield initial $^{176}Hf/^{177}Hf(t)$ and $\varepsilon_{Hf}(t)$ values that range from 0.281423 to 0.281567 and −9.8 to −4.7, respectively, with $T_{DM}(Hf)$ ages between 2505 and 2302 Ma (Fig. 4.7).

Sample OCY37-2 is a quartz syenite, and zircon grains from this sample are similar to those of sample 11JP05-1, with elongated shapes, lengths of 200 to 300 μm, and length/width ratios of 1.5:1–2:1. Cathodoluminescence images show clear oscillatory zonings, typical of magmatic zircons (Fig. 4.9b). A total of twenty-eight spots were analyzed on twenty-eight zircon grains, and they all plot on the concordia (Fig. 4.9b). They have apparent $^{207}Pb/^{206}Pb$ ages that range from 1762 ± 33 Ma to 1624 ± 35 Ma, yielding a concordia age of 1696 ± 4 Ma (MSWD = 0.014) and a weighted mean $^{207}Pb/^{206}Pb$ age of 1698 ± 13 Ma (MSWD = 0.6) (Fig. 4.9b). Given the high Th/U ratios of 0.21 to 1.40, the age of 1696 ± 4 Ma is taken as the crystallization age of sample OCY37-2. Twenty-four dated spots were further analyzed for zircon Lu–Hf isotopes (Fig. 4.7 and Table 4.4). All the isotopic ratios were calculated at the crystallization age of

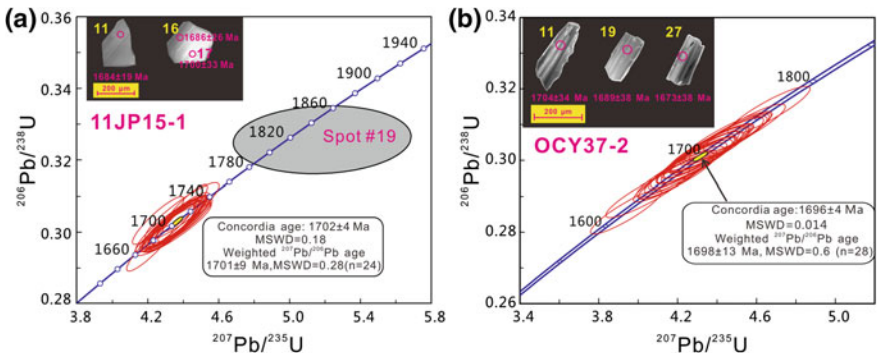

Fig. 4.9 Zircon U–Pb isotopic concordia diagrams for samples 11JP15-1 (**a**) and OCY37-2 (**b**) of the Shinao pluton. The insets show zircon internal structures and analyzed locations for each sample

1696 Ma (t), and these analyses show initial $^{176}Hf/^{177}Hf(t)$ and $\varepsilon_{Hf}(t)$ values of 0.281496–0.281686 and −7.4 to −0.6, respectively, with $T_{DM}(Hf)$ ages of 2419 and 2171 Ma (Fig. 4.7 and Table 4.4).

4.1.4 Petrogenesis

4.1.4.1 Genetic Links Among Different Lithologies

In the major and trace elements versus SiO_2 binary diagrams (Fig. 4.4d–l), the JDMSS rock samples show continuous compositional variation. Previous studies have demonstrated that trace element modeling is useful in discriminating different petrogenetic processes [39, 51, 62]. In the Rb versus Rb/V diagram (Fig. 4.10a), all the JDMSS samples plot along a hyperbolic curve, consistent with magma mixing

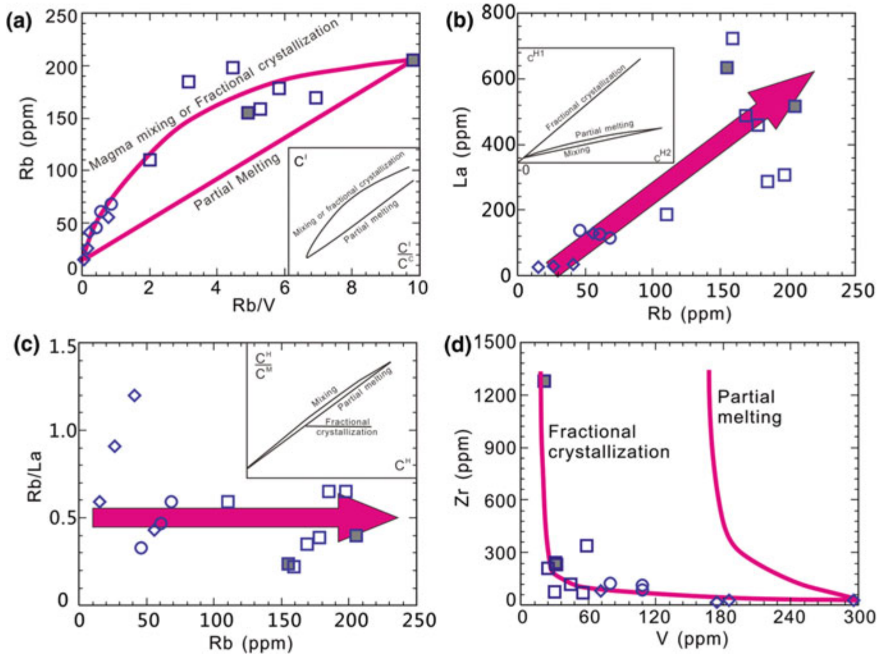

Fig. 4.10 Petrogenetic diagrams of the JDMSS samples **a** Rb versus Rb/V diagram. The inset is a schematic C^I versus C^I/C^C diagram (C^I, incompatible element concentration, and C^C, compatible element concentrations). **b** La versus Rb diagram. The inset is a schematic C^{H1} versus C^{H2} diagram (with H1 and H2 being two highly incompatible elements). **c** Rb/La versus Rb diagram. The inset is a schematic C^H/C^M versus C^H diagram (with H and M being respectively a highly incompatible and a moderately incompatible element). The curves in (**a**), (**b**), and (**c**) are calculated melt compositions produced by partial melting, magma mixing, and fractional crystallization processes [62]. (**d**) Zr versus V diagram showing distinct curves of partial melting and fractional crystallization processes [51]. Symbols are the same as Fig. 4.3

or fractional crystallization. However, they show positive correlation between La and Rb that nearly pass through the original point with a high slope (Fig. 4.10b), implying a fractional crystallization process [62]. In the Rb/La versus Rb diagram (with Rb and La as highly and moderately incompatible elements, respectively), all the samples define a horizontal line, further indicating that fractional crystallization played a key role during the generation of the JDMSS rocks (Fig. 4.10c). In addition, modeling based on Zr versus V indicates that a partial melting process is incompatible with the geochemical trend defined by the clinopyroxene diorites and syenites (including quartz syenites). Therefore, fractional crystallization processes from a common parental magma are favored for the compositional variations of the JDMSS rocks ([51]; Fig. 4.10d).

From a broad point of view, the anorthosite-mangerite-alkali granitoid-rapakivi granite (AMGRS) suite along the northern margin of NCC has compositions ranging from norites through anorthosites and mangerites to granitoids (including syenites, rapakivi granites, and other A-type granites; [91, 94]. Although these rocks have long been studied, the genetic relationships among different lithologies remain controversial [31, 88, 91, 94]. In order to resolve this problem, we compile the published geochemical data of seventy samples from the AMGRS [31, 86, 91, 94]. Similar to the JDMSS samples, the data define a horizontal line on the Rb/La versus Rb diagram, and a curved trend on the Zr versus V diagram, both following the trajectories of fractional crystallization (figures not shown). Therefore, a similar petrogenetic process involving fractional crystallization is favored for the AMGRS samples.

4.1.4.2 Nature of the Magma Sources

As mafic end-member of the Damiao anorthosite complex, the norites and anorthosites were previously thought to have been derived by high degree (>75%) partial melting of an ancient lower crust [94]. However, nearly half of them have high Mg# values of 47.33–61.68, arguing against a pure crustal source [86], although the other samples show lower Mg# values of 8.88–44.27 due to strong fractional crystallization. Similarly, magnetite diorites of the JDMSS may also have been generated by the partial melting of early Precambrian lower continental crust. Nonetheless, the magnetite diorite samples show low SiO_2 (46.3–52.6 wt%) but high MgO contents (2.53–4.14 wt%) and moderate Mg# values (31.43–43.91) (Table 4.1). On the other hand, LILEs are more incompatible than HFSEs during crustal anatexis, and partial melts from crustal rocks generally show comparable or increased LILE/HFSE ratios than the source rocks [51, 81]. The magnetite diorites have Rb/Nb, Rb/Ta, and La/Ta ratios that range from 2.85 to 4.98, 58.02 to 89.13, and 74.35 to 181.25, respectively, which are comparable with or lower than those of the Archean Jianping supracrustal rocks (metamorphosed basaltic and andesitic rocks, with Rb/Nb, Rb/Ta, and La/Ta ratios ranging mostly from 0.50–20.44, 14.18–424.67 to 11.53–241.11, respectively; unpublished data). Since a magma mixing process has been precluded by geochemical modeling (Fig. 4.10), it is proposed that the parental magma of the magnetite diorites could have been directly derived from a mantle source, and such a mantle source was also invoked for the Damiao norites and anorthosites [91].

In the Nb/Yb versus Th/Yb diagrams (Fig. 4.11a), most magnetite diorites plot close to the E-MORB field, indicating an enriched mantle source with an enrichment degree similar to those of E-MORBs. Notably, the magnetite diorites fall generally within the mantle array, implying little or no crustal contamination [50]. Sample OCY44-1 has zircon $\varepsilon_{Hf}(t)$ values between −10.0 and −0.3, further indicating an enriched mantle source (Fig. 4.7). It is noteworthy that the mantle source differs signficantly from those of E-MORBs, as the magnetite diorites show pronounced subduction-related features with depletion of HFSEs (e.g., Nb, Ta, Zr, and Hf) relative to the neighboring elements in the primitive mantle-normalized patterns (Fig. 4.5b). Given the lack of evident crustal contamination, the parental magmas of the JDMSS could have been produced by the partial melting of an enriched subcontinental lithospheric mantle (SCLM). In fact, an enriched mantle source was also proposed to explain the origin of widespread late Paleoproterozoic mafic dykes (in the Trans-North China Orogen), Xiong'er volcanic rocks, and mafic end-members of the AMGRS suite (Fig. 4.7; [26, 53, 73, 91]). Therefore, an enriched SCLM

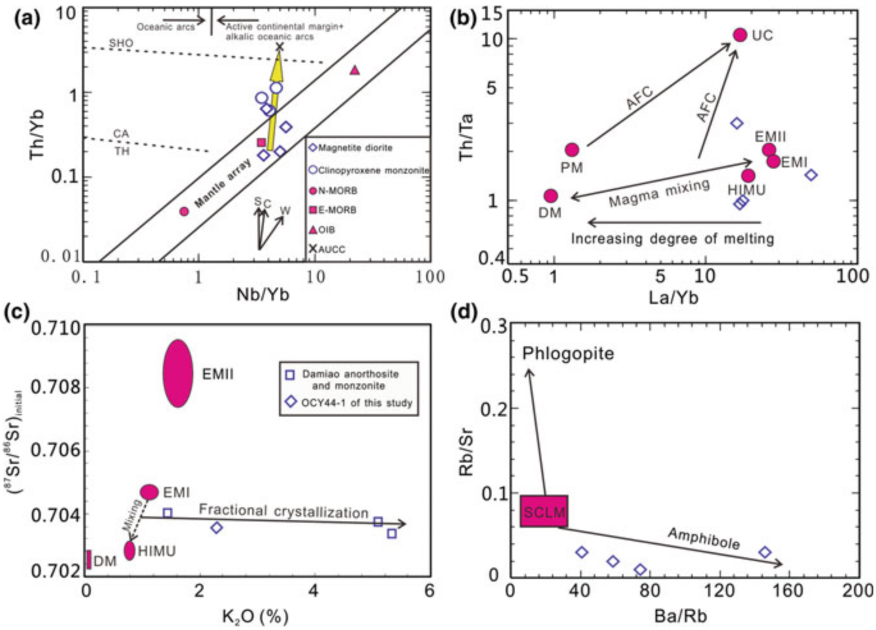

Fig. 4.11 Mantle source characteristics of the JDMSS samples. **a** Th/Yb versus Nb/Yb diagram [50]. The mantle array extends from normal-mid ocean ridge basalts (N-MORB) through enriched-mid ocean ridge basalts (E-MORB) to ocean island basalts (OIB). **b** Th/Ta versus La/Yb diagram [10]. **c** $(^{87}Sr/^{86}Sr)_{initial}$ versus K_2O diagram [30]. Data for the Damiao anorthosites and mangerites are cited from Xie [86]. **d** Rb/Sr versus Ba/Rb diagram showing an amphibole-bearing mantle source for the JDMSS samples (SCLM-subcontinental lithospheric mantle; [18]). Symbols are the same as Fig. 4.3

served as the major magma sources for the late Paleoproterozoic magmatism throughout the NCC (1.78–1.69 Ga).

In the Th/Ta versus La/Yb diagram, the magnetite diorites plot around the EMI, EMII, and HIMU fields, but far away from the field of depleted mantle (Fig. 4.11b). Sample OCY44-1 was analyzed for whole-rock Rb–Sr isotopes, which when combined with the data from the Damiao anorthosites and mangerites, suggesting homogeneous and low initial $^{87}Sr/^{86}Sr$ ratios between 0.703372 and 0.704012. Therefore, the involvement of an EMII-type mantle in their sources can be precluded [86, 98]. In the initial $^{87}Sr/^{86}Sr$ versus K_2O diagram [30], these rocks plot along a horizontal line between the EMI and HIMU mantle, suggesting a mixed origin from both HIMU and EMI mantle sources (Fig. 4.11c). The magnetite diorites have high K_2O contents (1.080–2.29 wt%), high Ba/Rb ratios (40.63–146.05), but low Rb/Sr (0.01–0.03) ratios (Table 4.1), implying the existence of amphibole in the mantle source (Fig. 4.11d; [18]). The supra-chondritic Nb/Ta ratios of 17.89–23.71 also suggest an amphibole-bearing enriched mantle ($D^{Nb}/D^{Ta} > 1$ for low-Mg# amphibole with a chondritic value of 17.6; [66; 68]). Phanerozoic-like plate tectonic processes are considered to have initiated in the EB since the late Neoarchean [25, 38, 74, 75, 77, 78], and they continued and played fundamental roles in the Paleoproterozoic evolution of the NCC, leading to ocean closure and final collision of the EB and WB along the TNCO [22–24, 36, 37, 39, 92, 93, 96]. These early subduction processes may have resulted in the addition of subducted materials into the mantle source and the formation of an enriched SCLM. Low Th/Ce ratios (0.004–0.018) and chondrite-normalized Hf/Sm and Ta/La ratios (0.17–0.23 and 0.09–0.23, respectively) imply that the mantle source was mainly metasomatized by slab fluids with minor involvement of melts from either subducted oceanic slabs or pelagic sediments (Table 4.1; [27, 35]). In summary, the parental magma of the JDMSS was derived from the partial melting of an amphibole-bearing SCLM (mixed EMI and HIMU mantle sources) previously metasomatized by slab fluids.

4.1.4.3 Assessment of Crustal Contamination and Fractional Crystallization

The magnetite diorites plot within the mantle array on the Th/Yb versus Nb/Yb diagram, and they show little or no contamination by the continental crust (Fig. 4.11a, b). However, compared with the primitive mantle magmas (Mg# = 63–72), they have relatively low MgO contents and Mg# values (2.53–4.14 wt% and 31.43–43.91, respectively), indicating that they are highly differentiated [17, 74]. Considering the low Cr, Co, and Ni contents (1.14–2.10, 22.50–43.10, and 7.25–22.50 ppm, respectively), large amounts of olivine and clinopyroxene could have been fractionated from the magma system [2]. The chondrite-normalized REE patterns of the three magnetite diorites (samples 11JP01-2, 11JP02-3, and 11JP02-4) show positive Eu anomalies, and together with the positive Sr and P anomalies on the primitive mantle-normalized trace element patterns, indicating some accumulation of plagioclase and apatite (Fig. 4.5a, b; [60]). The decreasing Fe_2O_3T, V, and Ti with increasing SiO_2 indicate fractionation of Fe–Ti oxides (e.g., magnetite) during the early stage of magma evolution. These are compatible with the high Al_2O_3 contents (18.58–21.3 wt%) and the presence of magnetite and apatite crystals (Table 4.1, and Fig. 4.3a, c and d). In comparison, sample OCY44-1 has the highest SiO_2 content among the magnetite diorites, and it has negative Sr and P anomalies (Fig. 4.5b), indicating that plagioclase and apatite fractionation began at least at 52.6 wt% SiO_2. However, it displays a positive Eu anomaly on the chondrite-normalized REE pattern (Fig. 4.5a). Considering the rapid decrease in V with increasing SiO_2 of the magnetite diorites (Fig. 4.4k), amphibole fractionation may also be involved (the partition coefficient (K_d) of Eu is much lower than the coefficients of Sm and Gd, and the K_d of V in amphibole is 3.40 within a basaltic magma system; [60]). This interpretation may well reconcile the positive Eu but negative Sr anomalies in sample OCY44-1.

Compared with the magnetite diorites ($\varepsilon_{Hf}(t)$ values of −10.0 to −0.3, with an average value of −6.2), the clinopyroxene monzonites have comparable or slightly lower zircon $\varepsilon_{Hf}(t)$ values of −12.6 to −5.5 and −9.3 to −5.8, respectively, with average values of −9.3 and −7.7, respectively (Fig. 4.7; Table 4.1). In the Th/Yb versus Nb/Yb diagram (Fig. 4.11a), the clinopyroxene monzonites have higher Th/Yb ratios (0.61–1.14), implying significant crustal contamination. In addition, they display positive correlations between La/Nb and SiO_2 but negative correlations between Nb/Nb* and Sm/Nd and SiO_2 (not shown; $Nb/Nb^* = 2Nb_{PM}/(Th_{PM} + La_{PM})$, with the subscript PM as primitive mantle-normalized values). All these lines of evidence indicate that crustal contamination could have been an important factor during the genesis of clinopyroxene monzonites. Notably, rare xenocrystic zircons were detected in the clinopyroxene monzonites (Fig. 4.8a). Since the parental mafic magma of JDMSS experienced prolonged evolution within the magma chamber, most xenocrystic zircons might have been dissolved [33, 84]. Similar to sample OCY44-1, clinopyroxene monzonite samples have positive Eu and slightly negative Sr and P anomalies on the normalized trace element patterns (Fig. 4.4c, d). Combined with the negative correlations of Fe_2O_3T, TiO_2, and V with SiO_2, the rapid decrease in P_2O_5 from sample 11JP12-1, and the occurrence of large apatite crystals, the major fractionation phases at this magmatic evolution stage could be a combination of amphibole, plagioclase, apatite, and Fe–Ti oxides (magnetite; Figs. 3.3f and 3.4f, g, and k). The clinopyroxene monzonites have little variation in Ni contents (4.45–5.49 ppm), suggesting only a limited fractionation of magnetite (K_d(Ni) in magnetite is 29; Rollinson [60]), and that hornblende fractionation contributes dominantly to the decrease in V.

The syenites (including quartz syenites) also show comparable or slightly lower zircon $\varepsilon_{Hf}(t)$ values of −9.8 to −4.9 (average of −7.6), −10.9 to −7.4 (average of −9.1), and −7.4 to −0.6 (average of −5.1), respectively (Fig. 4.7). The La/Nb (mostly of 4.21–7.06) and Nb/Nb* (mostly of 0.22–0.31) ratios are similar to those in the magnetite diorites, indicating insignificant crustal contamination (Table 4.1). In the normalized trace element patterns (Fig. 4.5e, f), the syenites show evidently negative Eu, Sr, P, and Ti anomalies. Given the absence of apatite and Fe–Ti oxides (e.g., magnetite; Fig. 4.3h–l), nearly all the apatite and Fe–Ti oxides, as well as significant volume of plagioclase, may have been fractionated when the parental magma evolved at the stage with SiO_2 contents of 54.8–58.6 wt%. The sharp decrease in Na_2O and the moderate decrease in P_2O_5 contents are consistent with plagioclase and some apatite fractionation during the final evolution stage of the magma system. Moreover, the homogeneous V contents (20.92–58.90 ppm) is compatible with the lack of amphibole and magnetite fractionation.

In summary, the parental magma of JDMSS experienced a prolonged evolution history that include early fractionation of olivine, clinopyroxene, hornblende, and magnetite, and the accumulation of plagioclase and apatite, a middle stage with fractionation of amphibole, plagioclase, apatite, and limited amount of magnetite, and a late stage with plagioclase and apatite fractionation. Crustal contamination was also involved, especially during the middle evolution stage of the magma system (forming clinopyroxene monzonites).

4.1.5 Summary

(1) The late Paleoproterozoic JDMSS suite consists mainly of magnetite diorites, clinopyroxene monzonites, syenites, and quartz syenites, and they show massive structures without involvement of any metamorphism or deformation. LA-ICPMS zircon U–Pb isotopic dating data reveal that they were crystallized during 1721–1696 Ma, which are coeval with the AMGRS suite (1750–1680 Ma) along the northern margin of the NCC.

(2) The entire compositional spectrum of the JDMSS could be generated by fractional crystallization from a common parental magma, with subordinate involvement of crustal contamination. The parental magma was derived from the partial melting of an amphibole-bearing enriched subcontinental lithospheric mantle (mixed EMI and HIMU mantle), and it experienced early fractionation of large amounts of olivine, clinopyroxene, hornblende, and magnetite, as well as the accumulation of plagioclase and apatite. A middle magmatic evolution stage involved fractionation of amphibole, plagioclase, apatite, and a small amount of magnetite, and late-stage fractionation includes mainly plagioclase and apatite. Crustal contamination was also involved, especially during the middle stage of magmatic evolution.

4.2 Late Paleoproterozoic Pinggu K-Rich Volcanic Rocks

Voluminous K-rich volcanic rocks were developed in the Yanliao rift along the northern part of North China Craton, representing the latest magmatic events during the late Paleoproterozoic (Figs. 2.2 and 4.12; [41]). Systematic geological, petrological, geochronological, and geochemical data are provided for these K-rich volcanic rocks, aiming to (1) determine the lithological assemblages and eruption timing; (2) analyze the nature of mantle sources and petrogenesis; and (3) decipher the nature and evolution of the late Paleoproterozoic subcontinental lithospheric mantle underneath the northern margin of North China Craton [79].

4.2.1 Geological and Petrographic Characteristics

The Yanliao rift is an E-W trending depression basin extending from Zhangjiakou to Fuxin along the northern margin of NCC, and it is bounded by deep extensional faults (Fig. 4.12; [90]). Accompanying formation and evolution of the Yanliao rift, thick sedimentary sequences were deposited [41]. Within the oldest Changcheng Group, the lowermost Changzhougou and Chuanlinggou Formations have no syn-depositional magmatic record. Unconformably overlying the Archean to Paleoproterozoic crystalline basement, the Changzhougou Formation is composed mainly of sandstones with minor conglomerates and pebble-bearing sandstones, and these rocks are in turn conformably overlain by shales of the Chuanlinggou Formation. The two formations have a total thickness of ~1740 m (860 m and 880 m, respectively).

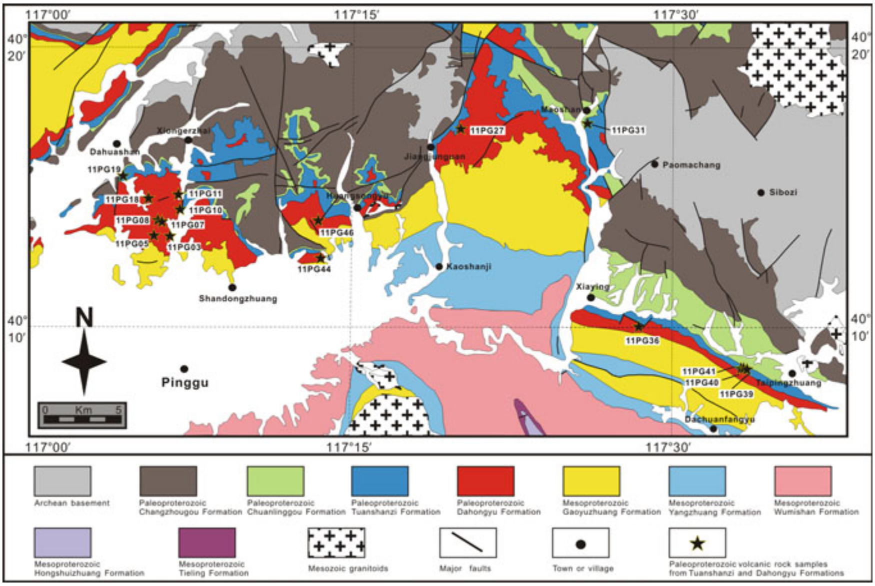

Fig. 4.12 Geological map of the late Paleoproterozoic K-rich volcanic rocks from the Tuanshanzi and Dahongyu Formations in the Changcheng Group, NCC, showing strata distribution, regional geological setting and sample locations

Conformably overlying the Chuanlinggou Formation, the Tuanshanzi Formation is dominated by thick dolostones with subordinate thin silty shales and minor sandstones (a total thickness of 520 m). The sedimentary rocks show ripple mark and mud crack (Fig. 4.13a, b). In the Dahuashan, Maoshan and Taipingzhuang areas, minor volcanic rocks were recognized in the upper sequence of this formation, with a compositional variation from trachybasalts to trachytes (Fig. 4.13). They are interlayered with the sedimentary sequences (shales and sandstones; Fig. 4.13c, d). The volcanic rocks display vesicular and amygdaloidal structures.

The Dahongyu Formation is the uppermost unit of the Changcheng Group with a thickness of ~410 m, which is well known for the preservation of voluminous K-rich volcanic rocks [40, 41]. Stratigraphically, three distinct units can be recognized within this formation from base upward, with the lower two members dominated by sandstones and intercalated shales, whereas dolostones with minor sandstones are the main lithologies in the upper unit (Figs. 4.14a and 4.15). In the Pinggu-Xiaying areas (Fig. 4.12), K-rich volcanic rocks are mainly developed at

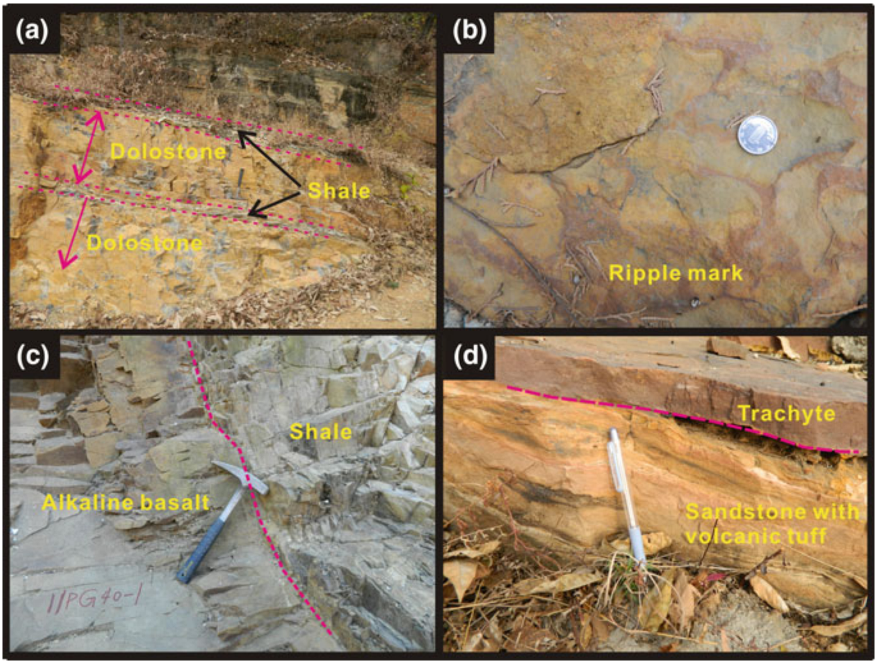

Fig. 4.13 Field geological characteristics of volcanic rocks in the Tuanshanzi Formation. **a** Sedimentary sequence dominated by dolostones with minor interlayered shales and sandstones. **b** Ripple mark structure in the sandstones. **c** Alkaline basalts with interlayered shales. **d** Trachytes with interlayered sandstones and volcanic tuffs. The hammer and pen are 30 and 10 cm in length, respectively, and the coin is 1 cm in diameter

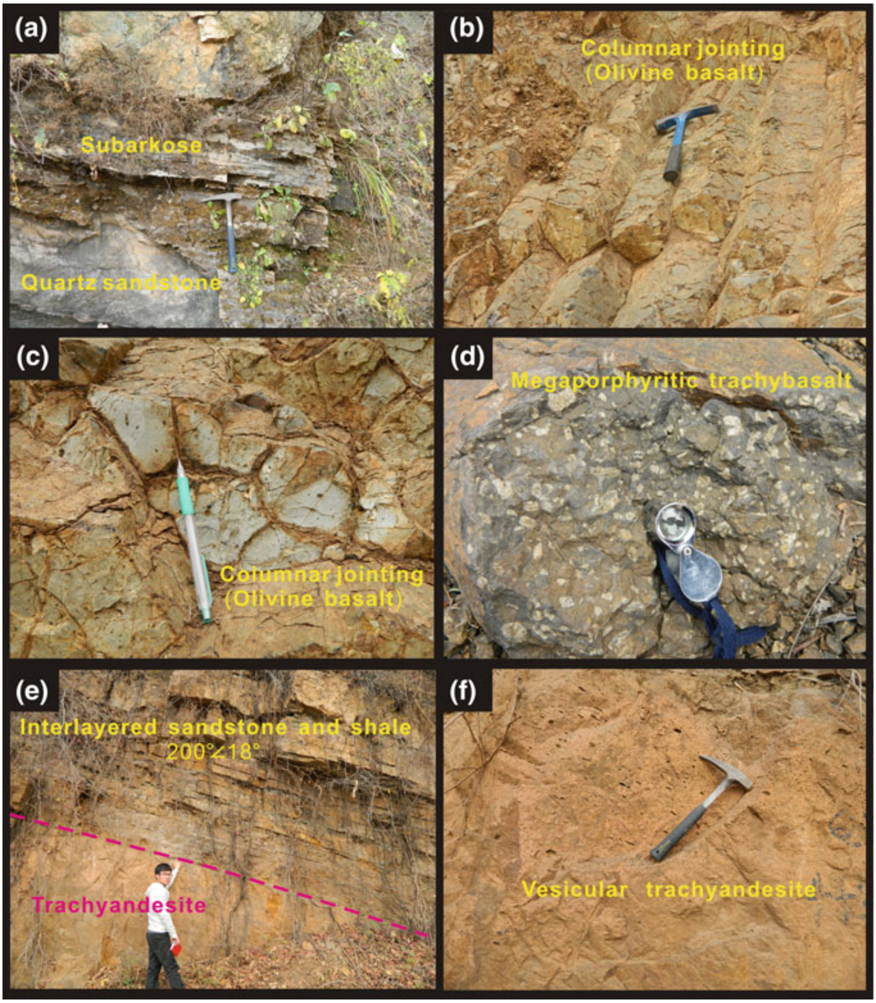

Fig. 4.14 Field geological characteristics of volcanic rocks in the Dahongyu Formation. **a** The major sedimentary sequence of sandstones (including quartz sandstones and arkoses). **b** and **c** Well-developed columnar jointing structure in the olivine basalts. **d** Megaporphyritic trachybasalt (the bright phenocrysts are mainly plagioclase and K-feldspar). **e** Trachyandesites with thin-layered sandstones and shales. **f** Vesicular structure preserved in the trachyandesites. The hammer, pen, and magnifier are 30, 10, and 5 cm in length, respectively

the middle to upper sequences of this formation with at least four eruption cycles: (1) olivine basalts with minor trachybasalts overlain by sandstones; (2) trachybasalts with minor trachyandesites overlain by sandstones; (3) trachyandesites intercalated with sandstones, but overlain by dolostones; and (4) trachytes and trachybasalts interlayered with dolostones (Fig. 4.15; [29, 90]). Minor sub-alkaline

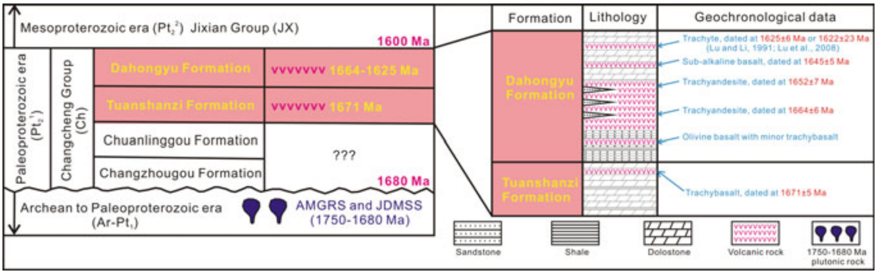

Fig. 4.15 Stratigraphic column and geochronological framework of the Changcheng Group in the standard Jianxian section modified from Gao et al. [19], showing the lower and upper boundary ages of the Changcheng Group at ~1680 and ~1600 Ma, respectively. The age data of the volcanic rocks from the Changcheng Group are mostly from the present study, except for those of a trachyte from the upper sequence of Dahongyu Formation cited from Lu and Li [40] and Lu et al. [41]. The age data of the AMGRS and JDMSS are cited from Zhang et al. [91] and Wang et al. [76], respectively

basalts were discovered in this study, and the interlayered relationship with dolostones suggests that they belong to the fourth eruption cycle. As illustrated in Fig. 4.15, volcanic rocks of the two older cycles erupted within the lower to middle sequences, and those of the two younger cycles within the upper sequence of the Dahongyu Formation. To the south of the Dahuashan town, olivine basalts display typical columnar jointing, and the diameter of the basalt columns ranges from 5 to 30 cm (Fig. 4.14b, c). Locally, trachybasalts with megaphenocryst of K-feldspar and plagioclase are present (Fig. 4.14d). In general, thick trachyandesites (several meters) are intercalated with thin-layered (~10 cm) sandstones and shales (dip and dip angle of 200° and 18°, respectively, Fig. 4.14e). The increasing development of vesicular structure from the base upwards imply that the stratigraphic successions were not overturned (Fig. 4.14f). To the south of the Xiaying town (Kuliyu village), a trachyte sample was dated using different isotopic methods, yielding a consistent age of ~1625 Ma [41]. This sample is intercalated with dolostones and minor sandstones [29, 40], together with some trachybasalts, representing the latest eruption cycle (Fig. 4.15).

A total of sixty-five samples were collected from the volcanic rocks of Changcheng Group. After detailed petrographic detection, samples with evident vesicular and amygdaloidal structures were excluded, and a suite of twenty-two representative samples, including seven samples from the Tuanshanzi Formation and fifteen samples from the Dahongyu Formation, were selected for whole-rock geochemical analyses. Samples from the Tuanshanzi Formation consist of six trachybasalts (11PG31-1, 11PG31-2, 11PG39-1, 11PG40-1, 11PG41-2 and 11PG41-3) and one trachyte (11PG19-2) (Table 4.5). Samples 11PG40-1, 11PG41-2, and 11PG41-3 display fine-grained doleritic texture and massive structure (with sporadic and local amygdaloidal structure), and are composed of clinopyroxene (~30–42%), plagioclase (~34–45%), K-feldspar (~15–18%),

Table 4.5 Zircon U–Pb isotopic dating data of representative volcanic rocks from the Tuanshanzi and Dahongyu Formations in the Changcheng Group, NCC

Sample and analyzed spot number	Th (ppm)	U (ppm)	Th/U	Isotopic ratios						Apparent ages (Ma)					
				$^{207}Pb/^{206}Pb$	±1σ	$^{207}Pb/^{235}U$	±1σ	$^{206}Pb/^{238}U$	±1σ	$^{207}Pb/^{206}Pb$	±1σ	$^{207}Pb/^{235}U$	±1σ	$^{206}Pb/^{238}U$	±1σ
11PG31-2-01	26	66	0.40	0.10372	0.00434	4.27769	0.17609	0.29925	0.00744	1692	41	1689	34	1688	37
11PG31-2-02	75	141	0.53	0.1016	0.00356	4.10177	0.14097	0.29291	0.00677	1654	32	1655	28	1656	34
11PG31-2-03	250	276	0.90	0.10187	0.00308	4.11488	0.12177	0.29309	0.00626	1658	26	1657	24	1657	31
11PG31-2-04	64	111	0.58	0.10297	0.00357	4.17888	0.14232	0.29445	0.00675	1678	32	1670	28	1664	34
11PG31-2-05	330	368	0.90	0.10087	0.00296	4.04468	0.11564	0.29094	0.00612	1640	25	1643	23	1646	31
11PG31-2-06	235	321	0.73	0.10258	0.0033	3.8815	0.12208	0.27456	0.00594	1671	29	1610	25	1564	30
11PG31-2-07	135	221	0.61	0.1026	0.00318	4.19229	0.12708	0.29647	0.00644	1672	27	1673	25	1674	32
11PG31-2-08	136	197	0.69	0.10314	0.00321	3.94476	0.11978	0.27752	0.00601	1681	27	1623	25	1579	30
11PG31-2-09	216	320	0.68	0.10245	0.0033	4.22623	0.13314	0.29931	0.00648	1669	29	1679	26	1688	32
11PG31-2-10	222	311	0.72	0.10295	0.00305	4.23628	0.1225	0.29856	0.0063	1678	26	1681	24	1684	31
11PG31-2-11	141	193	0.73	0.10356	0.0037	4.2359	0.14882	0.29679	0.00664	1689	34	1681	29	1675	33
11PG31-2-12	73	147	0.50	0.10285	0.00386	4.20094	0.15481	0.29636	0.00683	1676	36	1674	30	1673	34
11PG31-2-13	33	97	0.34	0.10349	0.00379	4.2782	0.15393	0.29993	0.00703	1688	34	1689	30	1691	35
11PG31-2-14	96	174	0.55	0.10275	0.00353	4.20448	0.14164	0.29689	0.00678	1674	31	1675	28	1676	34
11PG31-2-15	45	98	0.45	0.10281	0.00372	4.21959	0.14977	0.2978	0.00685	1675	34	1678	29	1680	34
11PG31-2-16	456	520	0.88	0.10246	0.0031	4.19285	0.1239	0.2969	0.00629	1669	26	1673	24	1676	31
11PG31-2-17	141	194	0.73	0.10279	0.0034	4.19755	0.13603	0.2963	0.00656	1675	30	1674	27	1673	33
11PG31-2-18	188	285	0.66	0.10342	0.00317	4.25478	0.1273	0.29851	0.00633	1686	27	1685	25	1684	31
11PG31-2-19	285	384	0.74	0.10294	0.00303	4.22144	0.12096	0.29754	0.0062	1678	25	1678	24	1679	31
11PG31-2-20	245	343	0.71	0.10218	0.00306	4.14938	0.12109	0.29465	0.00618	1664	26	1664	24	1665	31
11PG31-2-21	175	271	0.65	0.10291	0.00319	4.20209	0.12725	0.29627	0.00626	1677	28	1674	25	1673	31
11PG31-2-22	144	235	0.61	0.10297	0.00321	4.22955	0.12885	0.29803	0.00635	1678	28	1680	25	1682	32
11PG31-2-23	227	318	0.71	0.10188	0.00326	4.10454	0.12824	0.29231	0.00634	1659	29	1655	26	1653	32
11PG31-2-24	112	191	0.59	0.10162	0.00356	4.10226	0.14102	0.29291	0.00663	1654	32	1655	28	1656	33

(continued)

Table 4.5 (continued)

Sample and analyzed spot number	Th (ppm)	U (ppm)	Th/U	Isotopic ratios						Apparent ages (Ma)					
				$^{207}Pb/^{206}Pb$	±1σ	$^{207}Pb/^{235}U$	±1σ	$^{206}Pb/^{238}U$	±1σ	$^{207}Pb/^{206}Pb$	±1σ	$^{207}Pb/^{235}U$	±1σ	$^{206}Pb/^{238}U$	±1σ
11PG31-2-25	67	102	0.66	0.10322	0.00399	4.01811	0.15258	0.28244	0.0068	1683	37	1638	31	1604	34
11PG11-3-01	27	69	0.39	0.09928	0.00326	3.89344	0.12547	0.2845	0.00651	1611	29	1612	26	1614	33
11PG11-3-02	143	206	0.69	0.10067	0.0034	3.99918	0.13264	0.2882	0.0068	1636	30	1634	27	1633	34
11PG11-3-03	63	111	0.57	0.10095	0.00292	4.07518	0.1153	0.29286	0.00626	1642	25	1649	23	1656	31
11PG11-3-04	13	29	0.45	0.10138	0.00533	4.08376	0.21236	0.29223	0.00763	1650	58	1651	42	1653	38
11PG11-3-05	14	27	0.51	0.10035	0.00789	4.03412	0.31469	0.29164	0.00775	1631	106	1641	63	1650	39
11PG11-3-06	15	21	0.75	0.1017	0.00569	4.10167	0.22733	0.29261	0.00838	1655	61	1655	45	1655	42
11PG11-3-07	168	249	0.68	0.1011	0.00274	3.94974	0.10464	0.28342	0.00589	1644	23	1624	21	1609	30
11PG11-3-08	122	191	0.64	0.10102	0.00296	4.006	0.11514	0.2877	0.00628	1643	25	1635	23	1630	31
11PG11-3-09	122	188	0.65	0.10163	0.00277	4.16665	0.11102	0.29744	0.00629	1654	23	1667	22	1679	31
11PG11-3-10	20	56	0.35	0.1015	0.00354	4.06592	0.13949	0.29063	0.00678	1652	32	1647	28	1645	34
11PG11-3-11	79	134	0.59	0.10121	0.00312	4.06222	0.12309	0.29118	0.00626	1646	27	1647	25	1647	31
11PG11-3-12	40	94	0.43	0.10104	0.00306	4.00935	0.11897	0.28789	0.00638	1643	26	1636	24	1631	32
11PG11-3-13	197	295	0.67	0.10194	0.00266	4.1267	0.10528	0.2937	0.00603	1660	22	1660	21	1660	30
11PG11-3-14	8	18	0.45	0.10162	0.01156	4.0995	0.46008	0.29269	0.01082	1654	154	1654	92	1655	54
11PG11-3-15	160	231	0.69	0.10089	0.00267	4.02407	0.10405	0.28938	0.00602	1641	22	1639	21	1638	30
11PG11-3-16	57	117	0.49	0.10109	0.00292	4.03322	0.11402	0.28945	0.00613	1644	25	1641	23	1639	31
11PG11-3-17	19	57	0.33	0.10189	0.00503	4.09955	0.19984	0.2919	0.00836	1659	50	1654	40	1651	42
11PG11-3-18	151	224	0.68	0.10078	0.00259	4.024	0.10103	0.28968	0.00594	1639	21	1639	20	1640	30
11PG11-3-19	238	293	0.81	0.0999	0.00268	4.00157	0.10482	0.29062	0.00608	1622	22	1635	21	1645	30
11PG11-3-20	80	137	0.58	0.10293	0.00277	4.22064	0.11116	0.2975	0.00624	1678	22	1678	22	1679	31
11PG11-3-21	192	283	0.68	0.10074	0.00297	4.04498	0.11705	0.29131	0.00617	1638	26	1643	24	1648	31
11PG11-3-22	6	13	0.44	0.10143	0.01267	4.12927	0.51214	0.29537	0.01492	1650	156	1660	101	1668	74
11PG11-3-23	176	242	0.73	0.10104	0.00262	4.06777	0.10287	0.29209	0.00598	1643	21	1648	21	1652	30

(continued)

Table 4.5 (continued)

Sample and analyzed spot number	Th (ppm)	U (ppm)	Th/U	Isotopic ratios						Apparent ages (Ma)					
				$^{207}Pb/^{206}Pb$	±1σ	$^{207}Pb/^{235}U$	±1σ	$^{206}Pb/^{238}U$	±1σ	$^{207}Pb/^{206}Pb$	±1σ	$^{207}Pb/^{235}U$	±1σ	$^{206}Pb/^{238}U$	±1σ
11PG18-3-01	42	71	0.60	0.10033	0.00394	3.9885	0.154	0.28842	0.007	1630	38	1632	31	1634	35
11PG18-3-02	141	184	0.77	0.10151	0.00284	4.11557	0.11249	0.29414	0.00617	1652	24	1657	22	1662	31
11PG18-3-03	61	104	0.59	0.10219	0.0032	4.16463	0.12764	0.29568	0.00652	1664	27	1667	25	1670	32
11PG18-3-04	31	59	0.52	0.10271	0.00396	4.20671	0.15971	0.29717	0.00686	1674	38	1675	31	1677	34
11PG18-3-05	62	97	0.64	0.10322	0.00344	4.24833	0.13899	0.29863	0.00674	1683	30	1683	27	1685	33
11PG18-3-06	53	94	0.56	0.10259	0.00321	4.18525	0.12818	0.296	0.00652	1672	27	1671	25	1671	32
11PG18-3-07	56	85	0.66	0.10279	0.00375	4.20909	0.15112	0.2971	0.00672	1675	35	1676	29	1677	33
11PG18-3-08	496	395	1.26	0.10161	0.00365	2.30348	0.08021	0.16448	0.0038	1654	33	1213	25	982	21
11PG18-3-09	103	127	0.81	0.10164	0.00358	4.12265	0.14248	0.29429	0.00669	1654	33	1659	28	1663	33
11PG18-3-10	21	43	0.48	0.10248	0.00444	4.16441	0.17832	0.29483	0.00733	1670	44	1667	35	1666	36
11PG18-3-11	52	94	0.55	0.1028	0.00338	4.20096	0.13561	0.2965	0.00668	1675	29	1674	26	1674	33
11PG18-3-12	455	499	0.91	0.10123	0.00297	3.98732	0.11436	0.28578	0.0061	1647	25	1632	23	1620	31
11PG18-3-13	158	161	0.98	0.16437	0.00457	10.78829	0.29532	0.47622	0.01016	2501	21	2505	25	2511	44
11PG18-3-14	220	334	0.66	0.10398	0.00353	4.24339	0.14123	0.2961	0.00629	1696	32	1682	27	1672	31
11PG18-3-15	8	58	0.13	0.1026	0.00843	4.17185	0.34276	0.29501	0.00833	1672	110	1669	67	1667	41
11PG18-3-16	38	79	0.49	0.10186	0.00384	4.12943	0.15307	0.29414	0.00709	1658	35	1660	30	1662	35
11PG18-3-17	75	146	0.51	0.10273	0.00319	4.20613	0.12769	0.29705	0.00648	1674	27	1675	25	1677	32
11PG18-3-18	30	50	0.59	0.10267	0.0042	4.20448	0.16936	0.29713	0.0075	1673	39	1675	33	1677	37
11PG18-3-19	21	44	0.48	0.10111	0.00878	4.0704	0.35239	0.29207	0.009	1645	115	1648	71	1652	45
11PG18-3-20	43	82	0.52	0.10306	0.00384	4.19174	0.15375	0.29511	0.0068	1680	36	1672	30	1667	34
11PG18-3-21	77	130	0.60	0.10279	0.0038	4.16629	0.15184	0.29408	0.00651	1675	36	1667	30	1662	32
11PG18-3-22	70	145	0.49	0.10172	0.00324	4.12059	0.12848	0.2939	0.0064	1656	28	1658	25	1661	32
11PG18-3-23	129	176	0.73	0.10285	0.00344	4.20459	0.13781	0.29661	0.0067	1676	30	1675	27	1674	33
11PG18-3-24	63	110	0.57	0.10104	0.00343	4.07702	0.13554	0.29275	0.00647	1643	31	1650	27	1655	32

(continued)

Table 4.5 (continued)

Sample and analyzed spot number	Th (ppm)	U (ppm)	Th/U	Isotopic ratios						Apparent ages (Ma)					
				$^{207}Pb/^{206}Pb$	±1σ	$^{207}Pb/^{235}U$	±1σ	$^{206}Pb/^{238}U$	±1σ	$^{207}Pb/^{206}Pb$	±1σ	$^{207}Pb/^{235}U$	±1σ	$^{206}Pb/^{238}U$	±1σ
11PG18-3-25	31	57	0.55	0.10104	0.0041	4.04357	0.16164	0.29035	0.00729	1643	39	1643	33	1643	36
11PG44-1-01	17	36	0.48	0.10097	0.0041	4.06237	0.16271	0.2919	0.00717	1642	40	1647	33	1651	36
11PG44-1-02	44	65	0.67	0.10154	0.00349	4.09974	0.1386	0.29292	0.00682	1652	31	1654	28	1656	34
11PG44-1-03	19	38	0.51	0.10131	0.00494	4.09865	0.19743	0.29353	0.00793	1648	50	1654	39	1659	40
11PG44-1-04	76	99	0.76	0.10225	0.00392	4.14744	0.15684	0.29427	0.0074	1665	35	1664	31	1663	37
11PG44-1-05	32	44	0.73	0.10002	0.00615	3.96645	0.2412	0.28772	0.00921	1624	66	1627	49	1630	46
11PG44-1-06	69	116	0.60	0.10169	0.00427	4.06929	0.16869	0.29033	0.00705	1655	42	1648	34	1643	35
11PG44-1-07	12	30	0.40	0.10131	0.00787	4.04424	0.30985	0.28963	0.00978	1648	92	1643	62	1640	49
11PG44-1-08	40	66	0.61	0.10026	0.00427	3.97378	0.1668	0.28756	0.00758	1629	41	1629	34	1629	38
11PG44-1-09	51	64	0.79	0.10111	0.00379	4.05052	0.14952	0.29066	0.00683	1645	36	1644	30	1645	34
11PG44-1-10	68	109	0.63	0.10135	0.00377	4.08863	0.14928	0.29269	0.00703	1649	35	1652	30	1655	35
11PG44-1-11	23	52	0.45	0.09973	0.00387	4.07738	0.156	0.29662	0.00735	1619	37	1650	31	1675	37
11PG44-1-12	15	36	0.41	0.10164	0.00497	4.09119	0.19732	0.29205	0.00781	1654	51	1653	39	1652	39
11PG44-1-13	25	42	0.60	0.17534	0.00633	12.04162	0.44119	0.49826	0.0138	2609	29	2608	34	2606	59
11PG44-1-14	32	51	0.63	0.10247	0.00441	4.19339	0.17808	0.2969	0.00743	1669	43	1673	35	1676	37
11PG44-1-15	45	66	0.68	0.10223	0.00946	4.1935	0.38524	0.29762	0.0128	1665	107	1673	75	1679	64
11PG44-1-16	31	40	0.76	0.10215	0.00419	4.14805	0.16758	0.29462	0.0072	1664	40	1664	33	1665	36
11PG44-1-17	16	33	0.47	0.10271	0.00482	4.19658	0.1938	0.29645	0.00792	1674	47	1673	38	1674	39
11PG44-1-18	88	138	0.64	0.10116	0.00356	4.06602	0.14128	0.29161	0.00641	1646	34	1648	28	1650	32
11PG44-1-19	21	56	0.38	0.10102	0.0036	4.06304	0.14229	0.2918	0.0069	1643	33	1647	29	1651	34
11PG44-1-20	170	165	1.03	0.10093	0.00294	4.04959	0.11525	0.29109	0.0062	1641	25	1644	23	1647	31
11PG44-1-21	70	84	0.83	0.16831	0.00629	11.26813	0.4263	0.48574	0.01387	2541	30	2546	35	2552	60
11PG44-1-22	471	160	2.94	0.1652	0.0045	10.81922	0.29104	0.47517	0.01034	2510	21	2508	25	2506	45
11PG44-1-23	402	889	0.45	0.14837	0.00369	6.57001	0.15902	0.32127	0.00645	2327	19	2055	21	1796	31

Note ^{204}Pb has been corrected using the method of [1]

magnetite (~3–5%), and minor orthopyroxene. Accessory minerals include zircon, epidote, and apatite (Fig. 4.16a). The clinopyroxene crystals (including some magnetite) show hypidiomorphic to xenomorphic textures, with grain sizes in the range of 0.2–0.4 mm. The feldspar comprises euhedral plagioclase and K-feldspar (0.2–0.5 mm). In comparison, samples 11PG31-1, 11PG31-2, and 11PG39-1 show porphyritic texture and massive structure, and the phenocryst is generally hypidiomorphic plagioclase, with a grain size of ~1.0 mm (Fig. 4.16b). Euhedral plagioclase and K-feldspar microcrystals (<0.5 mm) display typical doleritic texture in the groundmass (Fig. 4.16c). The mafic minerals are chlorite, biotite, and magnetite, with the former two as secondary minerals altered from other mafic minerals (e.g., clinopyroxene). Sample 11PG19-2 is a trachyte, showing porphyritic texture and vesicular structure, and euhedral K-feldspar (0.5–1.0 mm) constitutes the phenocrysts with a proportion of ~8% (Figs. 4.13d and 4.16d). The groundmass is

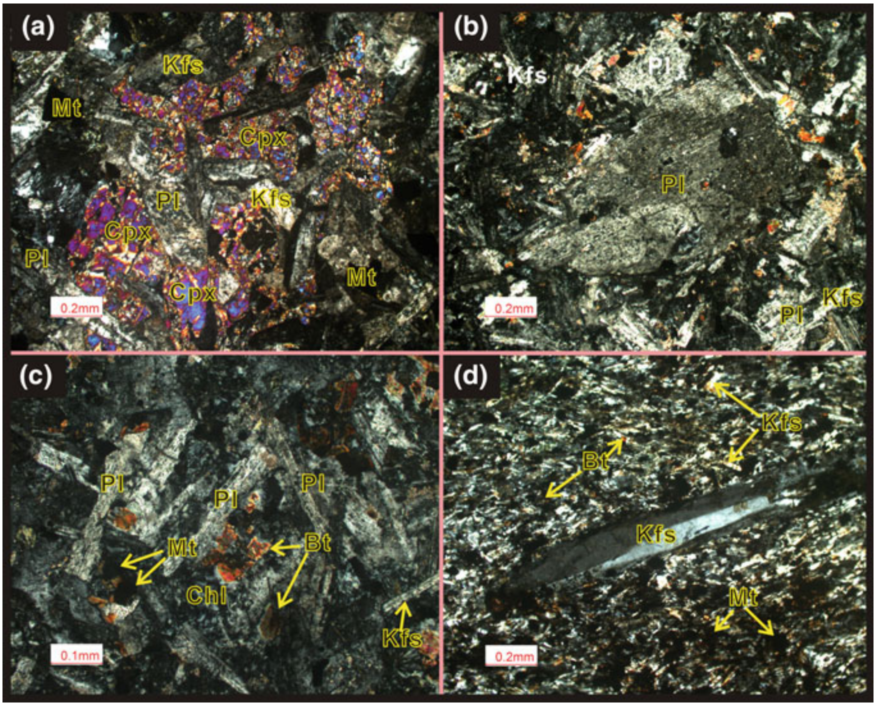

Fig. 4.16 Photomicrographs of representative volcanic rocks in the Tuanshanzi Formation. **a** Trachybasalts with a fine-grained doleritic texture. **b** Trachybasalts showing porphyritic texture (plagioclase as the phenocrysts). **c** Doleritic texture preserved in the groundmass of the porphyritic trachyandesites, with the mafic minerals altered to chlorite and biotite. **d** Trachytes with K-feldspar as the phenocrysts. Mineral abbreviations: Cpx—clinopyroxene; Mt—magnetite; Pl—plagioclase; Kfs—K-feldspar; Bi—biotite; Chl—chlorite

dominated by K-feldspar (<0.2 mm) with a typical trachytic texture, and biotite crystals in the groundmass were altered to chlorite.

In the Dahongyu Formation, fifteen samples were collected from different eruption cycles (Fig. 4.15), and these include: (1) olivine basalts (samples 11PG05-1 and 11PG05-2) of the first cycle; (2) interlayered trachybasalts (samples 11PG07-1, 11PG08-1, 11PG08-2, 11PG36-1 and 11PG46-1) and trachyandesites (samples 11PG03-1, 11PG03-2, 11PG10-1, 11PG10-2, 11PG18-3 and 11PG44-1) of the second and third cycles, that are intercalated with sandstones (Fig. 4.14e); and (3) two sub-alkaline basalts (samples 11PG11-3 and 11PG27-6, intercalated with dolostones) of the fourth cycle. Geochemical data of five trachybasalts and one trachyte of the fourth cycle were previously reported by Hu et al. [29]. In their study, only the trachyte sample (dhy-12) shows a low LOI value of 2.39 wt% (LOI values of the other samples are in the range of 4.60–10.35 wt%). Therefore, geochemical data of only sample dhy-12 are cited in this study. Among these, the olivine basalts show fine-grained porphyritic texture (Fig. 4.17a) and columnar jointing structure (Fig. 4.14b, c). Olivine and clinopyroxene are the main phenocrysts (~10%, and grain size in the range of <0.1–0.5 mm). The groundmass shows an intersertal texture, and consists of microcrystals of plagioclase, K-feldspar, magnetite, and other cryptocrystals. The trachybasalts display megaporphyritic texture and vesicular structure (Fig. 4.14d). Euhedral clinopyroxene, K-feldspar, and plagioclase constitute the megaphenocrysts, with grain sizes of 0.1–1.5 cm (mostly of >0.5 cm). In some samples, stubby clinopyroxene is the major phenocryst, whereas elongated K-feldspar and plagioclase dominate in other samples (Fig. 4.17b, c). The modal content of phenocrysts ranges from ~5 to ~30%. In the groundmass, plagioclase, K-feldspar, clinopyroxene, and magnetite (<0.2 mm) define typical intergranular texture. The trachyandesites exhibit fine-grained porphyritic texture and vesicular structure, and euhedral to hypidiomorphic K-feldspar and minor plagioclase serve as the major phenocrysts, with grain sizes of ~0.5–2.0 mm (Fig. 4.17d–e). Commonly, K-feldspar, plagioclase, magnetite and other mafic minerals in the groundmass constitute a pilotaxitic texture. The grain size of the groundmass minerals ranges from ~0.1–0.2 mm to <0.1 mm (Fig. 4.17d and e). Mafic minerals were almost altered to chlorite and biotite (Fig. 4.17d). The sub-alkaline basalts show porphyritic texture and vesicular structure (Fig. 4.17f). They show a mineral assemblage of plagioclase (~52%), hornblende (~35%), and magnetite (~5%) with accessory zircon, apatite, and epidote, distinct from the other volcanic rocks from the Tuanshanzi and Dahongyu Formations. Elongated and euhedral hornblende crystals with lengths of 0.5–2 mm occur as the major phenocrysts, whereas the intersertal groundmass consists mainly of euhedral plagioclase and hypidiomorphic hornblende (<0.5 mm, Fig. 4.17f). In general, chloritization of hornblende, and sericitization and kaolinization of plagioclase are common phenomena, especially in sample 11PG11-3 where the hornblende was completely altered to chlorite.

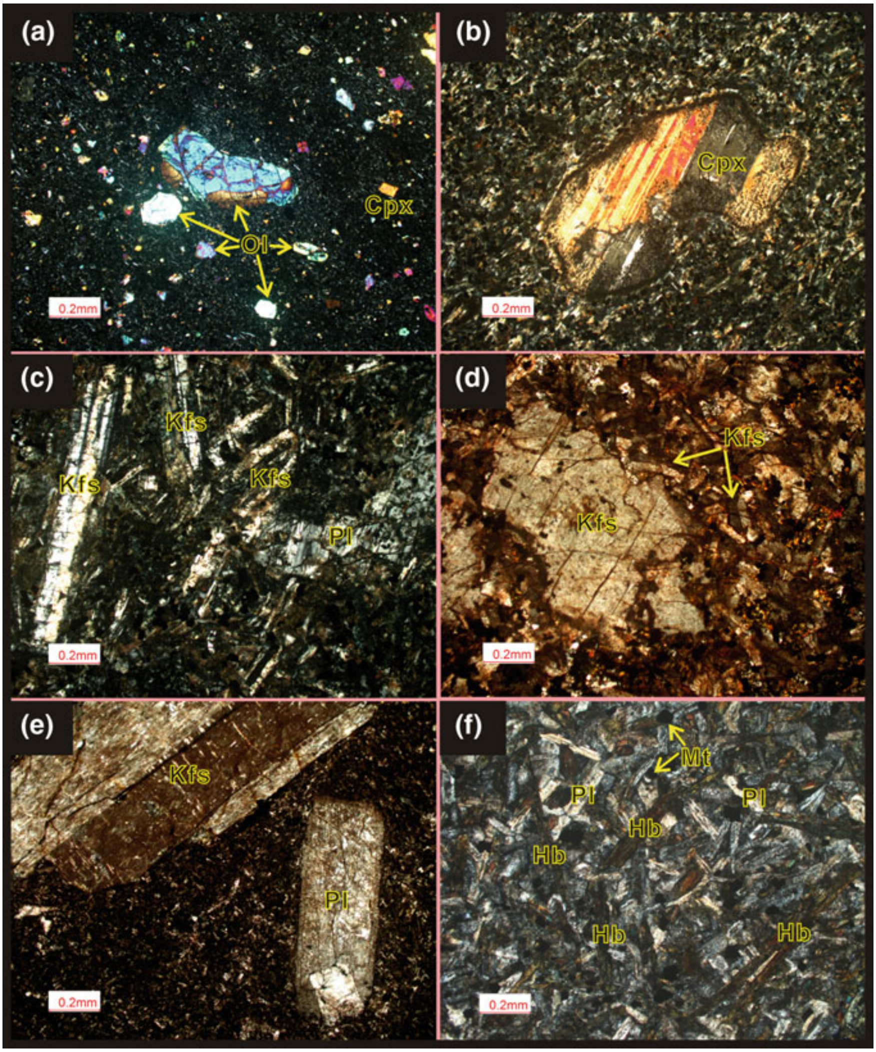

Fig. 4.17 Photomicrographs of representative volcanic rocks in the Dahongyu Formation: **a** olivine basalts; **b** trachybasalts with clinopyroxene as the phenocrysts; **c** trachybasalts with K-feldspar and plagioclase as the phenocrysts; **d** and **e** trachyandesites with the groundmass minerals displaying diverse grain sizes; and **f** porphyritic sub-alkaline basalts. Mineral abbreviations: Ol—olivine; Cpx—clinopyroxene; Hb—hornblende; Mt—magnetite; Pl—plagioclase; Kfs—K-feldspar

4.2.2 *Zircon U–Pb and Lu–Hf Isotopes*

4.2.2.1 The Tuanshanzi Formation

Trachybasalts are the dominant volcanic rocks of Tuanshanzi Formation, and a representative sample 11PG31-2, collected from the Maoshan town, was dated (Figs. 4.12 and 4.18a). Zircon grains separated from this sample are generally stubby in shape, with lengths and length/width ratios of 80–200 μm and 1:1–1.5:1, respectively (Fig. 4.18a). On the cathodoluminescence images, they show broad oscillatory (e.g., spot #16) or banded (e.g., spot #11) zonings, but without cores or overgrowth rims, typical of magmatic zircons [11]. Twenty-five spots were analyzed on twenty-five grains, and they yield apparent $^{207}Pb/^{206}Pb$ ages ranging from 1692 ± 41 Ma to 1640 ± 25 Ma, with high Th/U ratios of 0.34–0.90 (Table 4.5). On the concordia diagram (Fig. 4.18a), most analyses plot on or close to the concordia, except for three discordant analyses (spots #6, #8, and #25). Nonetheless, the twenty-five analyses yield a weighted mean $^{207}Pb/^{206}Pb$ age of

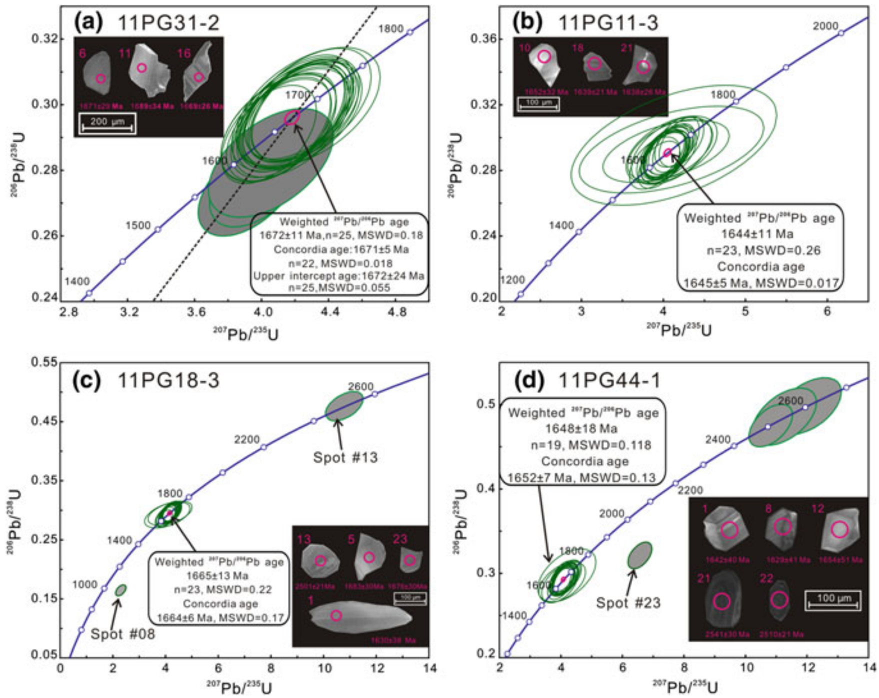

Fig. 4.18 Zircon U–Pb isotopic concordia diagrams for **a** the trachybasalt sample 11PG31-2 from the Tuanshanzi Formation, and **b** sub-alkaline basalt sample 11PG11-3 and **c** and **d** trachyandesite samples 11PG18-3 and 11PG44-1 from the Dahongyu Formation. The insets are cathodoluminescence images, analyzed spots of representative zircon grains and calculated ages for each sample

1672 ± 11 Ma (MSWD = 0.18), and an upper intercept age of 1672 ± 24 Ma (MSWD = 0.055), which are within error of each other. The twenty-two concordant analyses give a concordia age of 1671 ± 5 Ma (MSWD = 0.018). The three discordant analyses (spots #6, #8, and #25) give apparent $^{207}Pb/^{206}Pb$ ages that are nearly the same as the others (Table 4.5), and the discordance reflects possibly some Pb loss. Accordingly, the age of 1671 ± 5 Ma is considered as the crystallization age of sample 11PG31-2.

Twenty-five dated spots were further analyzed for in situ zircon Lu–Hf isotopes (Table 4.6). When calculated at the crystallization age of 1671 Ma (Fig. 4.19), they yield consistent initial $^{176}Hf/^{177}Hf(t)$ and $\varepsilon_{Hf}(t)$ values of 0.281723–0.281771 and +0.1 to +1.8, respectively, with Hf depleted mantle model ages (T_{DM}(Hf)) ranging between 2117 and 2039 Ma.

4.2.2.2 The Dahongyu Formation

Sample 11PG11-3 is a sub-alkaline basalt collected from the southern part of Xiong'erzhai town (Figs. 4.1 and 4.17f). Zircons from this sample show stubby or irregular shapes (Fig. 4.18b). Compared with those from sample 11PG31-2, zircon grains from sample 11PG11-3 are smaller (<100 μm), with length/width ratios of 1:1–1.5:1. On the cathodoluminescence images, they display banded or broad oscillatory zonings, suggesting a magmatic origin [11, 39]. A total of twenty-three analyses were performed on twenty-three grains, and they yield apparent $^{207}Pb/^{206}Pb$ ages ranging between 1678 ± 22 Ma and 1611 ± 29 Ma, with high Th/U ratios of 0.33–0.81 (Table 4.5). On the concordia diagram, the isotopic data plot on the concordia, yielding a weighted mean $^{207}Pb/^{206}Pb$ age of 1644 ± 11 Ma (MSWD = 0.26) and a concordia age of 1645 ± 5 Ma (MSWD = 0.017; Fig. 4.18b). Considering the magmatic feature of these zircon grains, the age of 1645 ± 5 Ma is interpreted as the crystallization age of sample 11PG11-3. Nineteen dated spots were further analyzed for in situ zircon Lu–Hf isotopes (Table 4.6). The isotopic ratios were calculated at 1645 Ma, and they yield initial $^{176}Hf/^{177}Hf(t)$, $\varepsilon_{Hf}(t)$, and T_{DM}(Hf) values of 0.281760–0.281857, +0.8 to +4.3, and 2072–1923 Ma, respectively (Fig. 4.19).

Sample 11PG18-3 is a trachyandesite collected to the south of Dahuashan (Figs. 4.1 and 4.17d). Most zircon grains from this sample exhibit stubby shapes (e.g., spots #5 and #23), with a minor population showing rounded (e.g., spot #13) or elongate (e.g., spot #1) shapes (Fig. 4.18c). They have lengths and length/width ratios of 50–300 μm (mostly of <100 μm) and 1:1–3:1 (mostly of 1:1–1.5:1), respectively. On the cathodoluminescence images, most of them show banded or broad oscillatory zonings, typical of magmatic zircons, except for spot #13 with a weak concentric oscillatory zoning. Twenty-five spots were analyzed on twenty-five grains, and except for spot #8, all the other isotopic data plot along the concordia (Fig. 4.18c). Most of them yield apparent $^{207}Pb/^{206}Pb$ ages between 1696 ± 32 Ma and 1630 ± 38 Ma with Th/U ratios of 0.13–1.25. However, spot #13 gives a much older apparent $^{207}Pb/^{206}Pb$ age of 2501 ± 21 Ma with a Th/U

Table 4.6 Zircon Lu–Hf isotopic data of the dated volcanic rocks from the Tuanshanzi and Dahongyu Formations in the Changcheng Group, NCC

Sample and analytical spot number	Crystallization age (t, Ma)	$^{176}Yb/^{177}Hf$	$^{176}Lu/^{177}Hf$	$^{176}Hf/^{177}Hf$	±2σ	$(^{176}Hf/^{177}Hf)_t$	$\varepsilon_{Hf}(0)$	$\varepsilon_{Hf}(t)$	T_{DM}	$T_{DM}^{C}(t)$	$f_{Lu/Hf}$
11PG31-2-01	1671	0.045821	0.001312	0.281800	0.000016	0.281759	−34.4	1.4	2054	2296	−0.96
11PG31-2-02	1671	0.057200	0.001587	0.281821	0.000017	0.281771	−33.6	1.8	2039	2267	−0.95
11PG31-2-03	1671	0.133206	0.003640	0.281877	0.000019	0.281762	−31.6	1.5	2075	2289	−0.89
11PG31-2-04	1671	0.044643	0.001299	0.281800	0.000017	0.281759	−34.4	1.4	2053	2295	−0.96
11PG31-2-05	1671	0.073084	0.001997	0.281801	0.000016	0.281738	−34.3	0.6	2090	2342	−0.94
11PG31-2-06	1671	0.070331	0.001981	0.281810	0.000016	0.281747	−34.0	1.0	2078	2322	−0.94
11PG31-2-07	1671	0.093816	0.002652	0.281809	0.000019	0.281725	−34.1	0.2	2117	2372	−0.92
11PG31-2-08	1671	0.055878	0.001521	0.281799	0.000015	0.281751	−34.4	1.1	2067	2313	−0.95
11PG31-2-09	1671	0.093140	0.002517	0.281840	0.000023	0.281760	−33.0	1.4	2065	2293	−0.92
11PG31-2-10	1671	0.078333	0.002138	0.281806	0.000016	0.281738	−34.2	0.7	2091	2341	−0.94
11PG31-2-11	1671	0.078336	0.002032	0.281805	0.000017	0.281741	−34.2	0.7	2087	2336	−0.94
11PG31-2-12	1671	0.047418	0.001260	0.281790	0.000016	0.281750	−34.7	1.1	2065	2314	−0.96
11PG31-2-13	1671	0.048672	0.001322	0.281778	0.000017	0.281736	−35.1	0.6	2085	2346	−0.96
11PG31-2-14	1671	0.055854	0.001427	0.281776	0.000015	0.281730	−35.2	0.4	2094	2359	−0.96
11PG31-2-15	1671	0.062264	0.001597	0.281781	0.000014	0.281731	−35.0	0.4	2096	2359	−0.95
11PG31-2-16	1671	0.136226	0.003167	0.281865	0.000020	0.281765	−32.1	1.6	2065	2281	−0.90
11PG31-2-17	1671	0.093468	0.002140	0.281790	0.000020	0.281723	−34.7	0.1	2114	2377	−0.94
11PG31-2-18	1671	0.088360	0.002172	0.281818	0.000016	0.281749	−33.7	1.0	2077	2318	−0.93
11PG31-2-19	1671	0.105612	0.002602	0.281822	0.000020	0.281740	−33.6	0.7	2095	2339	−0.92
11PG31-2-20	1671	0.084463	0.002078	0.281799	0.000020	0.281733	−34.4	0.5	2099	2354	−0.94
11PG31-2-21	1671	0.073743	0.001833	0.281789	0.000016	0.281731	−34.8	0.4	2099	2359	−0.94

(continued)

Table 4.6 (continued)

Sample and analytical spot number	Crystallization age (t, Ma)	$^{176}Yb/^{177}Hf$	$^{176}Lu/^{177}Hf$	$^{176}Hf/^{177}Hf$	±2σ	$(^{176}Hf/^{177}Hf)_t$	$\varepsilon_{Hf}(0)$	$\varepsilon_{Hf}(t)$	T_{DM}	$T^C_{DM}(t)$	$f_{Lu/Hf}$
11PG31-2-22	1671	0.071174	0.001777	0.281791	0.000017	0.281734	−34.7	0.5	2093	2351	−0.95
11PG31-2-23	1671	0.092693	0.002254	0.281836	0.000017	0.281764	−33.1	1.6	2055	2282	−0.93
11PG31-2-24	1671	0.051516	0.001289	0.281791	0.000018	0.281750	−34.7	1.1	2065	2314	−0.96
11PG31-2-25	1671	0.061347	0.001482	0.281800	0.000015	0.281753	−34.4	1.2	2063	2308	−0.96
11PG11-3-01	1645	0.036012	0.000868	0.281787	0.000025	0.281760	−34.8	0.8	2048	2311	−0.97
11PG11-3-02	1645	0.042096	0.000995	0.281796	0.000016	0.281765	−34.5	1.0	2042	2299	−0.97
11PG11-3-03	1645	0.097031	0.002210	0.281843	0.000015	0.281774	−32.9	1.3	2043	2279	−0.93
11PG11-3-04	1645	0.018743	0.000474	0.281776	0.000014	0.281762	−35.2	0.9	2042	2306	−0.99
11PG11-3-05	1645	0.066095	0.001564	0.281832	0.000018	0.281783	−33.2	1.7	2023	2257	−0.95
11PG11-3-06	1645	0.129727	0.002950	0.281857	0.000016	0.281765	−32.4	1.0	2065	2300	−0.91
11PG11-3-07	1645	0.132100	0.002993	0.281854	0.000027	0.281760	−32.5	0.8	2072	2309	−0.91
11PG11-3-08	1645	0.030389	0.000720	0.281816	0.000015	0.281794	−33.8	2.0	2000	2234	−0.98
11PG11-3-09	1645	0.056561	0.001304	0.281832	0.000019	0.281791	−33.2	1.9	2009	2239	−0.96
11PG11-3-10	1645	0.009356	0.000229	0.281783	0.000012	0.281776	−35.0	1.4	2020	2275	−0.99
11PG11-3-11	1645	0.113097	0.002569	0.281871	0.000020	0.281791	−31.9	1.9	2022	2239	−0.92
11PG11-3-12	1645	0.081988	0.001912	0.281916	0.000021	0.281857	−30.3	4.3	1923	2091	−0.94
11PG11-3-13	1645	0.091100	0.002169	0.281860	0.000022	0.281792	−32.3	2.0	2017	2237	−0.93
11PG11-3-14	1645	0.087305	0.001993	0.281860	0.000018	0.281798	−32.2	2.2	2007	2224	−0.94
11PG11-3-15	1645	0.058313	0.001360	0.281821	0.000014	0.281779	−33.6	1.5	2027	2267	−0.96
11PG11-3-16	1645	0.157416	0.003538	0.281922	0.000020	0.281811	−30.1	2.7	2003	2194	−0.89
11PG11-3-17	1645	0.095064	0.002201	0.281862	0.000015	0.281794	−32.2	2.0	2015	2234	−0.93

(continued)

Table 4.6 (continued)

Sample and analytical spot number	Crystallization age (t, Ma)	$^{176}Yb/^{177}Hf$	$^{176}Lu/^{177}Hf$	$^{176}Hf/^{177}Hf$	±2σ	$(^{176}Hf/^{177}Hf)_t$	$\varepsilon_{Hf}(0)$	$\varepsilon_{Hf}(t)$	T_{DM}	$T^{C}_{DM}(t)$	$f_{Lu/Hf}$
11PG11-3-18	1645	0.177526	0.003931	0.281939	0.000031	0.281817	−29.4	2.8	1999	2181	−0.88
11PG11-3-19	1645	0.184077	0.004206	0.281949	0.000025	0.281818	−29.1	2.9	1999	2178	−0.87
11PG18-3-01	1664	0.062301	0.001360	0.281756	0.000017	0.281713	−35.9	−0.4	2118	2404	−0.96
11PG18-3-02	1664	0.121299	0.002566	0.281810	0.000023	0.281729	−34.0	0.2	2110	2367	−0.92
11PG18-3-03	1664	0.043600	0.000972	0.281768	0.000015	0.281738	−35.5	0.5	2080	2348	−0.97
11PG18-3-04	1664	0.053759	0.001192	0.281752	0.000014	0.281714	−36.1	−0.4	2114	2400	−0.96
11PG18-3-05	1664	0.051017	0.001166	0.281797	0.000014	0.281761	−34.5	1.3	2050	2296	−0.96
11PG18-3-06	1664	0.086410	0.001907	0.281787	0.000019	0.281727	−34.8	0.1	2105	2372	−0.94
11PG18-3-07	1664	0.132590	0.002997	0.281846	0.000017	0.281751	−32.8	0.9	2084	2317	−0.91
11PG18-3-09	1664	0.040316	0.000926	0.281762	0.000017	0.281733	−35.7	0.3	2086	2359	−0.97
11PG18-3-10	1664	0.019746	0.000496	0.281733	0.000013	0.281717	−36.7	−0.3	2102	2394	−0.99
11PG18-3-11	1664	0.054161	0.001187	0.281764	0.000013	0.281727	−35.6	0.1	2097	2373	−0.96
11PG18-3-12	1664	0.097690	0.001934	0.281828	0.000039	0.281767	−33.4	1.5	2048	2281	−0.94
11PG18-3-14	1664	0.090657	0.001859	0.281807	0.000021	0.281748	−34.1	0.8	2075	2324	−0.94
11PG18-3-15	1664	0.010573	0.000233	0.281730	0.000010	0.281722	−36.9	−0.1	2092	2382	−0.99
11PG18-3-16	1664	0.045104	0.001053	0.281760	0.000022	0.281727	−35.8	0.1	2095	2372	−0.97
11PG18-3-17	1664	0.058073	0.001316	0.281786	0.000015	0.281744	−34.9	0.7	2074	2333	−0.96
11PG18-3-18	1664	0.108265	0.002388	0.281854	0.000019	0.281779	−32.5	1.9	2037	2255	−0.93
11PG18-3-19	1664	0.228375	0.004995	0.281924	0.000026	0.281766	−30.0	1.5	2085	2283	−0.85
11PG18-3-20	1664	0.023440	0.000627	0.281779	0.000028	0.281759	−35.1	1.2	2047	2300	−0.98
11PG44-1-01	1652	0.023953	0.000599	0.281750	0.000014	0.281731	−36.1	0.0	2084	2370	−0.98

(continued)

Table 4.6 (continued)

Sample and analytical spot number	Crystallization age (t, Ma)	$^{176}Yb/^{177}Hf$	$^{176}Lu/^{177}Hf$	$^{176}Hf/^{177}Hf$	±2σ	$(^{176}Hf/^{177}Hf)_t$	$\varepsilon_{Hf}(0)$	$\varepsilon_{Hf}(t)$	T_{DM}	$T^C_{DM}(t)$	$f_{Lu/Hf}$
11PG44-1-02	1652	0.084278	0.002072	0.281820	0.000020	0.281755	−33.7	0.8	2069	2317	−0.94
11PG44-1-03	1652	0.026509	0.000672	0.281763	0.000014	0.281742	−35.7	0.3	2071	2347	−0.98
11PG44-1-04	1652	0.068071	0.001673	0.281763	0.000015	0.281710	−35.7	−0.8	2126	2418	−0.95
11PG44-1-05	1652	0.057150	0.001380	0.281763	0.000014	0.281720	−35.7	−0.4	2109	2396	−0.96
11PG44-1-06	1652	0.035915	0.000876	0.281700	0.000015	0.281673	−37.9	−2.1	2168	2502	−0.97
11PG44-1-07	1652	0.019514	0.000496	0.281753	0.000013	0.281737	−36.0	0.2	2075	2357	−0.99
11PG44-1-08	1652	0.023661	0.000610	0.281770	0.000014	0.281751	−35.4	0.7	2058	2326	−0.98
11PG44-1-09	1652	0.070527	0.001705	0.281794	0.000015	0.281741	−34.6	0.3	2084	2348	−0.95
11PG44-1-10	1652	0.026261	0.000647	0.281722	0.000012	0.281702	−37.1	−1.1	2125	2437	−0.98
11PG44-1-11	1652	0.027385	0.000714	0.281764	0.000013	0.281741	−35.7	0.3	2072	2347	−0.98
11PG44-1-12	1652	0.022451	0.000564	0.281756	0.000015	0.281739	−35.9	0.2	2074	2354	−0.98
11PG44-1-14	1652	0.039771	0.000998	0.281783	0.000017	0.281752	−35.0	0.7	2060	2323	−0.97
11PG44-1-15	1652	0.054701	0.001297	0.281789	0.000018	0.281749	−34.7	0.6	2068	2331	−0.96
11PG44-1-16	1652	0.025378	0.000623	0.281771	0.000014	0.281752	−35.4	0.7	2057	2324	−0.98
11PG44-1-17	1652	0.054486	0.001247	0.281817	0.000019	0.281778	−33.8	1.6	2027	2265	−0.96

Note The present $^{176}Hf/^{177}Hf$ and $^{176}Lu/^{177}Hf$ ratios of chondrite and depleted mantle are 0.282772 and 0.0332, and 0.28325 and 0.0384, respectively, Blichert-Toft and Albarède [4], Griffin et al. (2000). $\lambda = 1.867 \times 10^{-11}\ a^{-1}$, Soderlund et al. (2004)

$\varepsilon_{Hf}(t) = 10000\{[(^{176}Hf/^{177}Hf)_S - (^{176}Lu/^{177}Hf)_S \times (e^{\lambda t} - 1)]/[(^{176}Hf/^{177}Hf)_{CHUR,0} - (^{176}Lu/^{177}Hf)_{CHUR} \times (e^{\lambda t} - 1)] - 1\}$

$T_{DM} = 1/\lambda \times \ln\{1 + [(^{176}Hf/^{177}Hf)_S - (^{176}Hf/^{177}Hf)_{DM}]/[(^{176}Lu/^{177}Hf)_S - (^{176}Lu/^{177}Hf)_{DM}]\}$; $f_{Lu/Hf} = (^{176}Lu/^{177}Hf)_S/(^{176}Lu/^{177}Hf)^{-1}_{CHUR}$

$T^C_{DM} = 1/\lambda \ln\{1 + [(^{176}Hf/^{177}Hf)_{s,t} - (^{176}Hf/^{177}Hf)_{DM,t}]/[(^{176}Lu/^{177}Hf)_c - (^{176}Lu/^{177}Hf)_{DM}]\} + t$

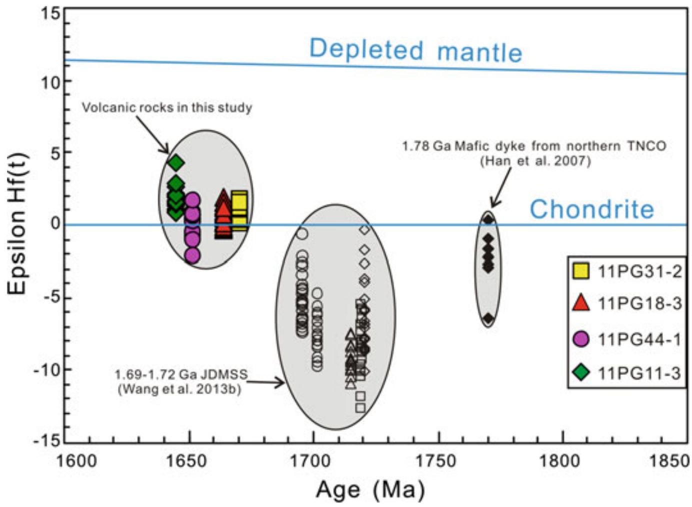

Fig. 4.19 Plots of zircon $\varepsilon_{Hf}(t)$ values versus crystallization ages for the dated volcanic rocks from both the Tuanshanzi and Dahongyu Formations. Also shown are zircon Lu–Hf isotopic data ($\varepsilon_{Hf}(t)$ values) and crystallization ages of a ~1.78 Ga mafic dyke [26] from the middle segment of the northern margin of the NCC and the Jianping diorite-monzonite-syenite suite in the Western Liaoning Province

ratio of 0.98, which may indicate an xenocrystic zircon grain captured from the wall rocks. Though spot #8 plots below the concordia, it gives an apparent $^{207}Pb/^{206}Pb$ age of 1654 ± 33 Ma, well within the age range of the other analyses (excluding spot #13). This implies probably some degree of Pb loss for spot #8. The remaining twenty-three analyses yield a weighted mean $^{207}Pb/^{206}Pb$ age of 1665 ± 13 Ma (MSWD = 0.22) and a concordia age of 1664 ± 6 Ma (MSWD = 0.17). Accordingly, the age of 1664 ± 6 Ma is considered as the crystallization age of sample 11PG18-3. A total of eighteen dated zircon spots (without the xenocrystic grain) are further analyzed for in situ Lu–Hf isotopes (Table 4.6). When the isotopic ratios were calculated at 1664 Ma (Fig. 4.19), they yield initial $^{176}Hf/^{177}Hf(t)$ and $\varepsilon_{Hf}(t)$ values varying from 0.281713 to 0.281779 and −0.4 to +1.9, respectively, with $T_{DM}(Hf)$ ages of 2118–2037 Ma.

Sample 11PG44-1 is a trachyandesite to the south of Huangsongyu (Figs. 4.1 and 4.17e). Zircon grains from this sample show stubby shapes, with lengths and length/width ratios of 80–120 μm and 1:1–1.5:1, respectively (Fig. 4.18d). On the cathodoluminescence images, two groups of zircon grains with distinct internal structures are recognized: group (1) with dark and weak oscillatory zonings (e.g., spots #21 and #22); and group (2) with bright oscillatory or banded zonings (e.g., spots #1, #8, and #12). A total of twenty-three analyses were performed on twenty-three grains, including four analyses on group (1) (spots #13, #21, #22, and #23) and nineteen analyses on group (2) zircon grains (Table 4.5). For group (1) analyses, three spots (#13, #21, and #22) plot on the concordia, and yield older apparent $^{207}Pb/^{206}Pb$ ages ranging from 2609 ± 29 Ma to 2510 ± 21 Ma with Th/U ratios of 0.60–2.94 (Fig. 4.18d). Spot #23 plots below the concordia, yielding a slightly younger apparent $^{207}Pb/^{206}Pb$ age of 2327 ± 19 Ma (a Th/U ratio of 0.45), implying some degree of Pb loss. Taken together, these four zircon grains are interpreted as those captured during ascent of the host magma. In comparison, the analyses of group (2) zircons plot on the concordia, and show apparent $^{207}Pb/^{206}Pb$ ages and Th/U ratios of 1674 ± 47 Ma to 1619 ± 37 Ma and 0.38 to 1.03, respectively (Fig. 4.18d and Table 4.5). They yield a weighted mean $^{207}Pb/^{206}Pb$ age of 1648 ± 18 Ma (MSWD = 0.118) and a concordia age of 1652 ± 7 Ma (MSWD = 0.13). Considering the internal structures and high Th/U ratios of group (2) zircon grains, the age of 1652 ± 7 Ma could represent the crystallization age of sample 11PG44-1. Sixteen dated spots of group (2) are analyzed for in situ zircon Lu–Hf isotopes (Table 4.6). The isotopic ratios are calculated at 1652 Ma (Fig. 4.19), and they yield initial $^{176}Hf/^{177}Hf(t)$ and $\varepsilon_{Hf}(t)$ values that vary from 0.281673 to 0.281778 and −2.1 to +1.6, respectively, with $T_{DM}(Hf)$ ages of 2168–2027 Ma.

4.2.3 *Whole-Rock Geochemical Data*

Petrochemical data and calculated parameters of twenty-three representative samples are listed in Table 4.7 and plotted in Figs. 4.20–4.21, including the trachyte sample dhy-12 in the fourth cycle of Dahongyu Formation cited from Hu et al. [29].

4.2.3.1 Major Element Compositions

Volcanic rocks of the Tuanshanzi Formation have SiO_2 contents ranging from 48.3 to 59.2 wt%, and they plot in the trachybasalt (samples 11PG31-1, 11PG31-2, 11PG39-1, 11PG40-1, and 11PG41-3), basaltic trachyandesite (sample 11PG41-2), and trachyte (sample 11PG19-2) fields in the total alkalis-silica diagram (TAS diagram after [47]; Fig. 4.20a). In the Zr/TiO_2*0.0001 versus Nb/Y diagram ([83]; Fig. 4.20b), the former six samples plot in the alkaline basalt field, whereas sample 11PG19-2 falls in the trachyte field. The alkaline basalts are characterized by low SiO_2 contents (48.3–51.5 wt%), and high MgO contents (mostly of 6.33–8.56 wt%) and Mg# (100 Mg/(Mg + Fe_{total}) atomic ratio) values (mostly of 53–59), except for sample 11PG41-2 with a slightly lower MgO content and Mg# value of 4.44 wt% and 48, respectively. They have Na_2O of 2.83–4.86 wt%, and slightly lower K_2O of 0.72–3.30 wt%, with K_2O/Na_2O ratios of 0.16–0.79. In comparison, the trachyte sample 11PG19-2 has higher SiO_2 (59.2 wt%), and lower MgO (0.86 wt%) and Mg# value (17). The moderate Na_2O (3.48 wt%) but high K_2O of 8.53 wt% lead to a high K_2O/Na_2O value of 2.45. The major element composition of sample 11PG19-2 resembles those of the ~1702 Ma syenites from the JDMSS suite of Western Liaoning Province [76].

Table 4.7 Analyzed results of major (wt%) and trace elements (ppm) of the K-rich volcanic rocks from the Tuanshanzi and Dahongyu Formations in the Changcheng Group, NCC

Sample	Tuanshanzi formation						
	11PG31-1	11PG31-2	11PG39-1	11PG40-1	11PG41-2	11PG41-3	11PG19-2
Latitude (N)	40°17.4′	40°17.4′	40°08.6′	40°08.6′	40°08.5′	40°08.5′	40°15.5′
Longitude (E)	117°26.0′	117°26.0′	117°33.7′	117°33.6′	117°33.6′	117°33.6′	117°04.5′
Lithology	Alkaline basalt						Trachyte
SiO_2	49.8	49.4	48.3	48.7	51.5	49.7	59.2
Al_2O_3	15.44	14.97	15.86	15.42	16.48	15.86	16.64
Fe_2O_3T	10.90	11.75	12.05	12.52	9.65	11.04	8.12
CaO	2.96	2.69	3.03	2.66	4.75	5.00	0.869
MgO	7.53	8.56	7.84	7.88	4.44	6.33	0.864
K_2O	1.489	0.717	1.061	2.14	3.30	1.523	8.53
Na_2O	4.86	4.52	4.35	2.83	4.20	4.43	3.48
MnO	0.238	0.117	0.142	0.193	0.175	0.195	0.100
TiO_2	1.349	1.493	1.717	1.733	1.530	1.496	0.576
P_2O_5	0.350	0.369	0.483	0.419	0.407	0.386	0.131
LOI	4.87	5.29	4.84	5.20	3.33	3.90	1.335
Total	99.8	99.9	99.7	99.7	99.7	99.8	99.8
Mg#	58	59	56	56	48	53	17
K_2O/Na_2O	0.31	0.16	0.24	0.76	0.79	0.34	2.45
Sc	13.8	16.2	17.0	21	15.9	16.1	7.58
V	87	101	108	140	108	111	0.724
Cr	213	230	168	279	151	281	17.5
Co	30	35	33	45	26	37	1.727
Ni	90	79	84	116	71	120	17.4
Rb	32	15.4	23	41	39	17.8	159
Sr	185	185	352	569	337	277	59
Y	20	17.2	19.8	19.5	19.0	16.5	53
Nb	52	42	49	55	52	46	95

(continued)

Table 4.7 (continued)

Sample	Tuanshanzi formation						
	11PG31-1	11PG31-2	11PG39-1	11PG40-1	11PG41-2	11PG41-3	11PG19-2
Latitude (N)	40°17.4′	40°17.4′	40°08.6′	40°08.6′	40°08.5′	40°08.5′	40°15.5′
Longitude (E)	117°26.0′	117°26.0′	117°33.7′	117°33.6′	117°33.6′	117°33.6′	117°04.5′
Lithology	Alkaline basalt						Trachyte
Cs	1.323	1.349	0.602	0.718	0.210	0.619	1.189
Ba	464	361	2188	1776	1436	603	638
La	36	29	35	40	38	35	79
Ce	68	59	71	79	76	69	170
Pr	7.82	7.02	8.78	9.27	8.72	8.03	21
Nd	29	27	34	35	33	31	82
Sm	5.25	5.02	6.03	6.17	5.93	5.29	14.6
Eu	1.812	1.707	2.28	2.47	2.29	1.888	2.84
Gd	5.21	4.89	5.69	5.89	5.83	5.00	14.0
Tb	0.736	0.691	0.783	0.791	0.773	0.671	2.10
Dy	3.84	3.52	4.01	4.03	3.82	3.35	11.1
Ho	0.771	0.678	0.777	0.770	0.725	0.643	2.20
Er	2.06	1.749	2.03	1.974	1.866	1.656	5.92
Tm	0.300	0.251	0.287	0.277	0.265	0.237	0.921
Yb	1.887	1.552	1.802	1.747	1.674	1.513	5.86
Lu	0.289	0.227	0.267	0.256	0.246	0.223	0.933
Ta	3.09	2.56	3.02	3.62	3.61	3.01	5.47
Th	3.78	2.43	2.99	3.46	3.88	3.42	8.44
U	0.879	0.608	0.725	0.817	0.905	0.842	1.677
Zr	194	133	152	142	173	157	586
Hf	4.96	3.51	4.15	3.95	4.42	4.05	14.6
Eu_N/Eu_N^*	1.06	1.05	1.19	1.25	1.19	1.12	0.61
$(La/Sm)_N$	4.45	3.71	3.71	4.23	4.14	4.31	3.48
$(Gd/Yb)_N$	2.28	2.61	2.61	2.79	2.88	2.74	1.97

(continued)

Table 4.7 (continued)

Sample	Tuanshanzi formation						
	11PG31-1	11PG31-2	11PG39-1	11PG40-1	11PG41-2	11PG41-3	11PG19-2
Latitude (N)	40°17.4′	40°17.4′	40°08.6′	40°08.6′	40°08.5′	40°08.5′	40°15.5′
Longitude (E)	117°26.0′	117°26.0′	117°33.7′	117°33.6′	117°33.6′	117°33.6′	117°04.5′
Lithology	Alkaline basalt						Trachyte
$(La/Yb)_N$	13.8	13.4	13.8	16.6	16.3	16.8	9.66
TREE	163	143	173	188	179	164	413
Nb/Y	3	2	2	3	3	3	2
Zr/Nb	4	3	3	3	3	3	6
Nb/U	59	69	67	67	58	54	56
Zr/Hf	39	39	37	36	39	39	40
$(Nb/La)_{PM}$	1.38	1.39	1.36	1.30	1.32	1.25	1.15
$(Nb/Th)_{PM}$	1.64	2.05	1.95	1.89	1.60	1.60	1.34

Sample	Dahongyu formation														
	11PG05-1	11PG05-2	11PG07-1	11PG08-1	11PG08-2	11PG36-1	11PG46-1	11PG03-1	11PG03-2	11PG18-3	11PG44-1	11PG10-1	11PG10-2	dhy-12	11PG11-3	11PG27-6
Latitude (N)	40°13.1′	40°13.1′	40°13.8′	40°06.8′	40°06.8′	40°10.0′	40°12.5′	11PG03-1	11PG03-2	11PG18-3	11PG44-1	11PG10-1	11PG10-2	dhy-12	11PG11-3	11PG27-6
Longitude (E)	117° 06.0′	117° 06.0′	117° 06.4′	117° 06.3′	117° 06.3′	117° 28.5′	117° 13.4′	117° 06.8′	117° 06.8′	117° 05.7′	117° 13.6′	117° 07.2′	117° 07.2′		117° 07.2′	117° 20.2′
Lithology	Alkaline basalt							Trachyandesite						Trachyte	Sub-alkaline basalt	
SiO_2	43.3	43.3	46.5	48.3	48.2	50.5	47.9	60.5	59.1	48.2	52.6	59.3	56.7	58.3	53.2	48.1
Al_2O_3	13.52	13.46	17.05	17.90	16.06	15.99	17.69	16.50	18.37	13.42	14.87	16.43	16.72	15.75	17.08	16.19
Fe_2O_3T	15.45	15.36	9.11	10.44	13.12	9.45	9.35	7.16	5.84	6.18	10.72	8.10	1.52	8.25	8.34	8.55
CaO	9.45	9.40	5.68	5.06	2.77	2.86	3.61	0.323	0.151	4.18	0.593	0.383	3.34	0.340	1.985	6.33
MgO	7.55	7.68	7.71	6.43	6.43	7.70	8.27	0.766	0.102	3.70	1.728	0.104	1.049	1.940	0.816	7.55
K_2O	1.314	1.363	2.53	1.914	3.10	4.33	3.36	11.66	12.71	14.90	15.69	12.32	14.81	9.45	11.50	2.58
Na_2O	4.49	4.47	2.70	2.99	3.01	2.08	2.39	0.088	0.229	0.011	0.011	0.152	0.240	3.47	0.219	4.13
MnO	0.261	0.258	0.121	0.114	0.089	0.050	0.040	0.096	0.083	0.155	0.063	0.137	0.040	0.030	0.026	0.144
TiO_2	2.55	2.53	1.614	1.956	2.70	1.598	2.022	0.650	0.843	1.371	1.321	0.771	0.775	0.470	2.725	1.094
P_2O_5	0.721	0.719	0.241	0.371	0.539	0.446	0.373	0.173	0.079	0.628	0.519	0.247	0.274	0.100	1.018	0.296

(continued)

Table 4.7 (continued)

Sample	Dahongyu formation															
	11PG05-1	11PG05-2	11PG07-1	11PG08-1	11PG08-2	11PG36-1	11PG46-1	11PG03-1	11PG03-2	11PG18-3	11PG44-1	11PG10-1	11PG10-2	dhy-12	11PG11-3	11PG27-6
Latitude (N)	40°13.1′	40°13.1′	40°13.8′	40°06.8′	40°06.8′	40°10.0′	40°12.5′	11PG03-1	11PG03-2	11PG18-3	11PG44-1	11PG10-1	11PG10-2	dhy-12	11PG11-3	11PG27-6
Longitude (E)	117° 06.0′	117° 06.0′	117° 06.4′	117° 06.3′	117° 06.3′	117° 28.5′	117° 13.4′	117° 06.8′	117° 06.8′	117° 05.7′	117° 13.6′	117° 07.2′	117° 07.2′		117° 07.2′	117° 20.2′
Lithology	Alkaline basalt							Trachyandesite						Trachyte	Sub-alkaline basalt	
LOI	1.074	1.113	6.54	4.28	3.81	4.69	4.79	1.934	2.34	7.14	1.720	1.888	4.36	2.39	2.89	4.77
Total	99.7	99.7	99.8	99.8	99.8	99.7	99.7	99.8	99.9	99.9	99.8	99.8	99.9	100.5	99.9	99.7
Mg#	49	50	63	55	49	62	64	17	3	54	24	2	58	32	16	64
K_2O/Na_2O	0.29	0.30	0.94	0.64	1.03	2.08	1.41	131.91	55.38	1382.28	1407.64	80.98	61.82	2.72	52.42	0.62
Sc	21	20	22	20	23	16.8	21	9.47	13.2	14.0	15.4	9.79	10.0	18.1	14.4	29
V	165	165	156	157	192	108	171	0.501	4.08	55	76	10.2	7.58	0.330	157	229
Cr	293	328	81	51	36	239	172	17.7	98			11.1	12.2		47	206
Co	46	46	39	29	40	32	40	1.400	4.41	12.2	15.5	1.740	7.82		9.34	29
Ni	164	175	54	42	28	83	91	11.1	31			13.1	17.9		24	75
Rb	40	44	43	38	53	77	54	137	152	110	149	167	150	160	119	53
Sr	989	1051	368	606	353	485	468	10.7	6.43	128	53	21	12.3	58	62	615
Y	34	34	19.4	23	31	18.4	18.2	45	71	48	40	40	53	71	37	17.7
Nb	109	109	27	36	52	47	27	76	101	58	55	73	63	109	3.55	3.35
Cs	1.150	1.259	0.944	0.648	0.870	2.66	1.099	0.445	1.528	0.138	0.217	0.860	0.469	1.220	1.320	1.346
Ba	972	939	650	882	892	1281	982	949	607	648	873	903	544	693	753	736
La	80	79	22	30	37	35	21	61	79	45	45	71	71	81	52	15.2
Ce	165	163	48	65	79	71	46	127	167	100	95	157	151	171	116	37
Pr	19.7	19.2	6.20	8.08	9.91	8.35	5.77	16.3	20	12.6	12.2	18.4	18.4	22	15.0	5.02
Nd	72	70	25	32	39	32	24	65	75	48	46	67	67	85	58	22
Sm	12.0	11.9	5.31	6.17	7.66	5.64	4.58	11.7	13.5	9.76	9.08	12.6	12.2	16.8	11.0	4.49
Eu	3.77	3.76	2.09	2.13	2.58	2.25	1.933	3.24	3.86	2.30	2.57	3.77	3.27	3.02	3.33	1.585
Gd	11.1	10.9	5.23	6.05	7.56	5.36	4.45	11.5	13.4	9.80	9.40	11.7	11.6	14.4	11.7	4.30
Tb	1.456	1.445	0.760	0.869	1.099	0.728	0.645	1.729	2.24	1.512	1.449	1.651	1.733	2.08	1.644	0.640

(continued)

Table 4.7 (continued)

Sample	Dahongyu formation															
	11PG05-1	11PG05-2	11PG07-1	11PG08-1	11PG08-2	11PG36-1	11PG46-1	11PG03-1	11PG03-2	11PG18-3	11PG44-1	11PG10-1	11PG10-2	dhy-12	11PG11-3	11PG27-6
Latitude (N)	40°13.1′	40°13.1′	40°13.8′	40°06.8′	40°06.8′	40°10.0′	40°12.5′	11PG03-1	11PG03-2	11PG18-3	11PG44-1	11PG10-1	11PG10-2	dhy-12	11PG11-3	11PG27-6
Longitude (E)	117° 06.0′	117° 06.0′	117° 06.4′	117° 06.3′	117° 06.3′	117° 28.5′	117° 13.4′	117° 06.8′	117° 06.8′	117° 05.7′	117° 13.6′	117° 07.2′	117° 07.2′		117° 07.2′	117° 20.2′
Lithology	Alkaline basalt							Trachyandesite						Trachyte	Sub-alkaline basalt	
Dy	7.15	7.12	3.91	4.59	5.90	3.70	3.54	9.19	13.4	8.38	7.72	8.50	9.71	12.1	7.89	3.43
Ho	1.362	1.348	0.763	0.903	1.201	0.716	0.711	1.839	2.82	1.734	1.527	1.658	2.01	2.40	1.409	0.698
Er	3.50	3.44	1.97	2.38	3.22	1.852	1.894	4.98	7.75	4.71	3.94	4.30	5.51	6.92	3.16	1.866
Tm	0.507	0.492	0.286	0.344	0.477	0.262	0.269	0.786	1.173	0.670	0.573	0.614	0.812	1.010	0.373	0.280
Yb	3.09	3.00	1.733	2.09	2.95	1.617	1.692	4.93	7.21	4.14	3.56	3.75	4.96	6.84	1.958	1.787
Lu	0.476	0.454	0.265	0.319	0.460	0.238	0.249	0.779	1.122	0.644	0.554	0.575	0.753	0.950	0.264	0.271
Ta	5.78	7.17	1.755	2.29	3.33	2.58	1.722	4.14	5.47	3.10	2.90	3.24	2.94		0.124	0.224
Th	9.09	8.84	1.981	2.77	3.99	3.13	1.947	7.28	11.1	6.03	5.44	7.42	7.81		4.10	1.227
U	2.38	2.30	0.472	0.702	1.048	0.711	0.435	2.09	2.52	1.118	1.354	1.398	3.51		0.949	0.412
Zr	389	381	139	180	257	145	147	455	732	487	414	521	469	690	213	104
Hf	9.26	9.13	3.82	4.82	6.76	3.96	3.86	12.1	18.1	10.6	9.45	13.0	11.2		6.13	2.87
Eu_N/Eu_N^*	1.00	1.01	1.21	1.06	1.04	1.25	1.31	0.86	0.88	0.72	0.85	0.95	0.84	0.59	0.90	1.10
$(La/Sm)_N$	4.35	4.31	2.67	3.18	3.12	4.06	2.98	3.38	3.80	2.99	3.20	3.64	3.75	3.10	3.06	2.18
$(Gd/Yb)_N$	2.96	3.01	2.50	2.40	2.12	2.74	2.17	1.93	1.54	1.96	2.19	2.59	1.93	1.74	4.93	1.99
$(La/Yb)_N$	18.7	19.0	9.11	10.5	9.01	15.7	8.95	8.86	7.89	7.84	9.08	13.6	10.3	8.45	19.1	6.10
TREE	381	375	124	161	198	169	117	320	408	250	238	363	360	425	283	98
Nb/Y	3	3	1	2	2	3	1	2	1	1	1	2	1	2	0.09	0.19
Zr/Nb	4	3	5	5	5	3	6	6	7	8	8	7	7	6	60	31
Nb/U	46	47	57	51	49	66	61	36	40	52	40	52	18		3.74	8.14
Zr/Hf	42	42	36	37	38	37	38	38	40	46	44	40	42		35	36
$(Nb/La)_{PM}$	1.30	1.33	1.18	1.15	1.35	1.28	1.22	1.20	1.23	1.23	1.17	0.99	0.85	1.30	0.07	0.21
$(Nb/Th)_{PM}$	1.42	1.47	1.62	1.56	1.54	1.80	1.64	1.24	1.09	1.14	1.20	1.18	0.96		0.10	0.33

Note LOI, loss on ignition; Mg# = 100 Mg/(Mg + Fe_{total}) in atomic ratio; TREE, total rare earth elements

Eu_N/Eu_N^* = Eu_N/SQRT(Sm_N*Gd_N); subscript N-chondrite normalized value; subscript PM-primitive mantle normalized value

The geochemical data of sample dhy-12 from the Dahongyu Formation are cited from Hu et al. [29], where the GPS coordinate is not presented

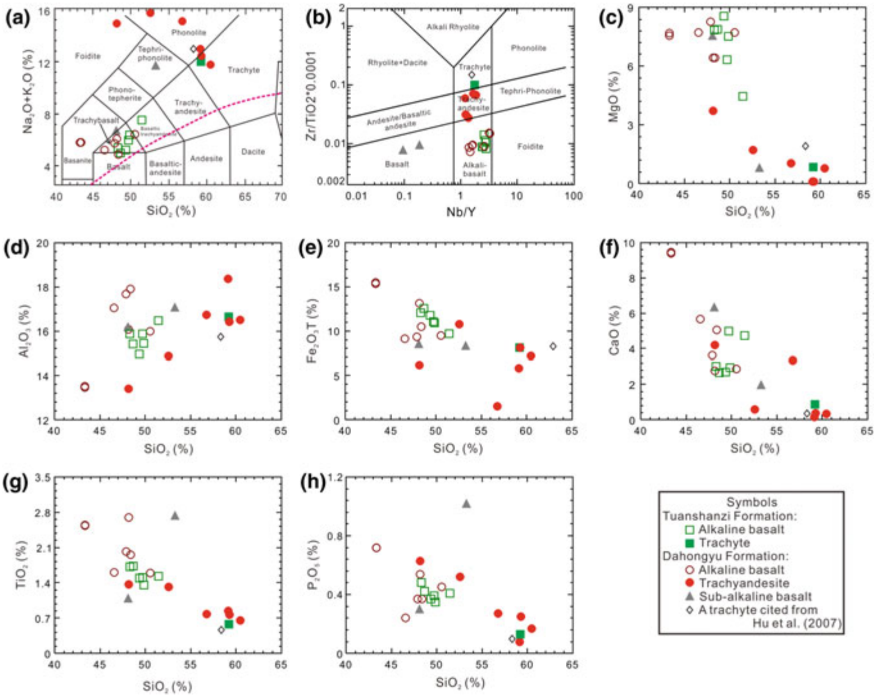

Fig. 4.20 Petrochemical classification and major element composition of the K-rich volcanic rocks in the Tuanshanzi and Dahongyu Formations. **a** Total alkalis versus SiO_2 diagram (TAS, after [47]. **b** Zr/TiO_2*0.0001 versus Nb/Y diagram [83]. **c**–**h** Binary diagram of SiO_2 versus selected whole-rock major oxides. Geochemical data of the trachyte sample dhy-12 in the upper section of Dahongyu Formation are cited from Hu et al. [29] for comparison. Symbols: Tuanshanzi Formation: open squares—alkaline basalts; solid square—trachyte; Dahongyu Formation: open cycles—alkaline basalts; solid cycles—trachyandesites; solid triangles—sub-alkaline basalts; open diamond—the trachyte sample dhy-12 from Hu et al. [29]

Compared to rocks of the Tuanshanzi Formation, the Dahongyu volcanic rock samples display a wider range of SiO_2 contents of 43.3–60.5 wt%. All the samples plot in the alkaline field, and show a wide scatter in the TAS diagram (Fig. 4.20a). In the Zr/TiO_2*0.0001 versus Nb/Y diagram (Fig. 4.20b), however, these data are distributed more regularly, with seven samples (11PG05-1, 11PG05-2, 11PG07-1, 11PG08-1, 11PG08-2, 11PG36-1, and 11PG46-1) plotting in the alkaline basalt field, seven samples in the trachyandesite (11PG03-1, 11PG03-2, 11PG10-1, 11PG10-2, 11PG18-3, and 11PG44-1) to trachyte (dhy-12) fields, and two samples (11PG11-3 and 11PG27-6) in the sub-alkaline basalt field. Among these, the alkaline basalts are characterized by low SiO_2 contents of 43.3–50.5 wt%, and high MgO contents and Mg# values of 6.43–8.27 wt% and 49–64, respectively. They display Na_2O and K_2O contents of 2.08–4.49 wt% and 1.31–4.33 wt%, respectively, yielding K_2O/Na_2O ratios of 0.29–2.08. The trachyandesites and trachyte show higher SiO_2 (48.2–60.5 wt%), lower MgO (0.10–3.70 wt%) and Mg# (2–58).

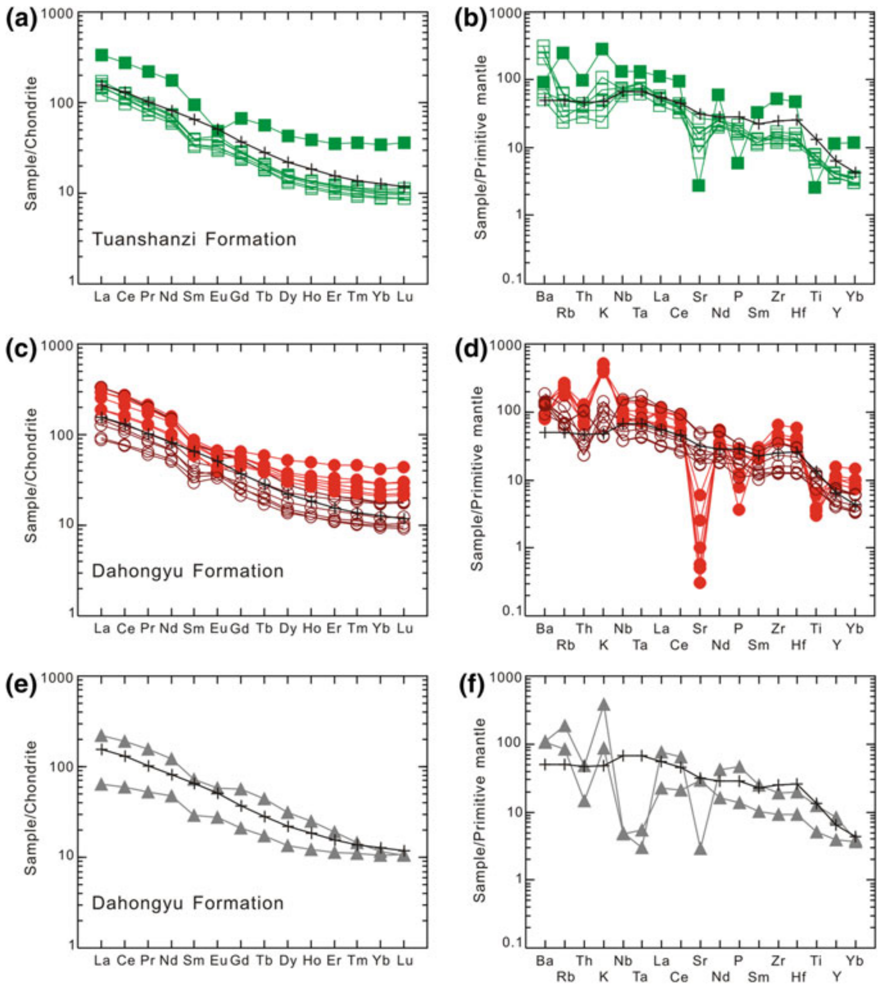

Fig. 4.21 Chondrite-normalized REE patterns and primitive mantle-normalized multi-element spider diagrams for **a** and **b** the Tuanshanzi volcanic rocks; **c** and **d** the Dahongyu alkaline volcanic rocks; and **e** and **f** the Dahongyu sub-alkaline volcanic rocks. Geochemical patterns of the ocean island basalts (OIBs) are also shown (with a black crossed symbol) for comparison. Symbols are the same as Fig. 4.20. The chondrite, primitive mantle, and OIB values are after Sun and McDonough [66]

They have high K_2O (9.45–15.69 wt%) but low Na_2O contents (0.011–3.47 wt%), yielding high K_2O/Na_2O ratios (2.72–1407.46). Samples 11PG11-3 and 11PG27-6 have contrasting major element compositions, with SiO_2 contents of 48.1 and 53.3 wt%, K_2O of 2.58 and 11.50 wt%, Na_2O of 0.219 and 4.13 wt%, respectively (with K_2O/Na_2O ratios of 0.62 and 52.42), MgO of 0.82 and 7.55 wt%, and Mg# of 16 and 64, respectively. Nevertheless, both of them display low Nb/Y ratios of 0.09

and 0.19, respectively, falling in the sub-alkaline basalt field in the $Zr/TiO_2*0.0001$ versus Nb/Y diagram.

In the Harker diagrams (Fig. 4.20c–h), the MgO, Fe_2O_3T, CaO, TiO_2, and P_2O_5 contents generally decrease, whereas the Al_2O_3 increases, with increasing SiO_2 contents for the twenty-three samples. Sample 11PG11-3 has high K_2O, TiO_2 and P_2O_5 contents, and deviates from the other samples, especially from the calc-alkaline basalt sample 11PG27-6.

4.2.3.2 Rare Earth Elements (REEs)

The six trachybasalts of Tuanshanzi Formation have nearly consistent chondrite-normalized REE patterns, and are characterized by strongly fractionated REE patterns with high $(La/Sm)_N$, $(Gd/Yb)_N$, and $(La/Yb)_N$ ratios of 3.71–4.45, 2.28–2.88, and 13.4–16.8, respectively (Fig. 4.21a). They show slightly positive Eu anomalies, and display Eu_N/Eu_N* values of 1.05–1.25. In comparison, the trachyte sample 11PG19-2 shows a less fractionated REE pattern ($(La/Sm)_N$, $(Gd/Yb)_N$, and $(La/Yb)_N$ ratios of 3.48, 1.97, and 9.66, respectively), and has a negative Eu anomaly with a low Eu_N/Eu_N* value of 0.61.

Seven alkaline basalts in the Dahongyu Formation (including two olivine basalts and five trachybasalts) are characterized by strongly fractionated REE patterns with high $(La/Sm)_N$, $(Gd/Yb)_N$, and $(La/Yb)_N$ ratios of 2.67–4.35, 2.12–3.01, and 9.01–19.0, respectively, and show no or positive Eu anomalies (Eu_N/Eu_N* values of 1.00–1.31, Fig. 4.21c). Similar to that of trachyte sample in the Tuanshanzi Formation (Fig. 4.21a), the six trachyandesites and one trachyte of the Dahongyu Formation display less fractionated REE patterns with negative Eu anomalies ($(La/Sm)_N$, $(Gd/Yb)_N$, $(La/Yb)_N$, and Eu_N/Eu_N* values of 2.99–3.80, 1.54–2.59, 7.84–13.6, and 0.59–0.95, respectively). The two sub-alkaline basalts (samples 11PG11-3 and 11PG27-6, Fig. 4.21e) possess fractionated REE patterns without apparent Eu anomalies ($(La/Sm)_N$, $(Gd/Yb)_N$, $(La/Yb)_N$, and Eu_N/Eu_N* values of 2.18–3.06, 1.99–4.93, 6.10–19.1, and 0.90–1.10, respectively).

Notably, chondrite-normalized REE patterns of alkaline basalts from both the Tuanshanzi and Dahongyu Formations resemble those of ocean island basalts (OIBs after [66] Fig. 4.21a and c).

4.2.3.3 Other Trace Elements

In the primitive mantle-normalized multi-element diagrams (Fig. 4.21b and d), alkaline basalts from the two formations display overall OIB-like geochemical features, and are characterized by the enrichment in LILEs (large ion lithophile elements, e.g., Ba, Rb, and K) and HFSEs (high field strength elements, e.g., Nb, Ta, Zr, and Hf) without Ti anomalies. Notably, negative Sr anomalies are detected from the alkaline basalts of Tuanshanzi Formation (Fig. 4.21b). In comparison, trachyandesites and trachytes of the two formations are enriched in Ba, Th, Nb, and

Ta, and especially in Rb, K, Zr and Hf, but depleted in Sr, P, and Ti. In contrast to the above samples, the two sub-alkaline basalts from the Dahongyu Formation (Fig. 4.21f) show negative Nb and Ta anomalies, and are enriched in Ba, Rb, and K, with slightly positive to strongly negative Sr anomalies.

In particular, the majority of samples show high $(Nb/La)_{PM}$ and $(Nb/Th)_{PM}$ ratios of 0.85–1.39 (mostly of 1.15–1.39) and 0.96–2.05, respectively, except for the two sub-alkaline basalts with low values of 0.07–0.21 and 0.10–0.33, respectively (Table 4.6).

4.2.4 Petrogenetic Discussion

4.2.4.1 Assessment of Element Mobility

As described in the petrographic section, some volcanic rock samples experienced intense secondary alteration, which is consistent with the moderate to high loss on ignition (LOI) values (mostly of 1.07–5.29 wt%, except for samples 11PG07-1 and 11PG18-3 with high values of 6.54–7.14 wt%). These samples show a large scatter in the TAS diagram, but are more regular in the discrimination diagram using less mobile HFSEs (Fig. 4.20a, b). In the normalized spider diagrams (Fig. 4.21), most elements show nearly consistent patterns, though large variations of Rb, Th, K, Sr, and P. Considering the lack of carbonate and silica enrichment and significant Ce anomalies, and the mostly <6 wt% LOI values [56], the following petrogenetic discussions will be focused on the alteration-insensitive oxides and elements (i.e., MgO, TiO_2, Al_2O_3, rare earth elements, high field strength elements, and transition group metals).

4.2.4.2 Genetic Relationships Among Different Lithologies

Volcanic rocks from both the Tuanshanzi and Dahongyu Formations have complex lithological assemblages, and the mafic endmember consists of trachybasalts with some olivine basalts and sub-alkaline basalts, whereas the intermediate endmember is dominated by trachyandesites and trachytes (Figs. 4.16–4.17). They show continuous geochemical trends on the major elements versus SiO_2 diagrams (Fig. 4.20). Considering the close spatial and temporal distribution, petrogenetic relationships among these lithologies are firstly discussed below.

The ratios of two incompatible elements with different partition coefficients (K_d) (e.g., La/Sm and Zr/Nb) are commonly applied for petrogenetic discrimination [39, 69, 73]. In the La/Sm versus La diagram (Fig. 4.22a), La/Sm ratios (3.38–6.89) of all the samples are nearly constant with increasing La contents. Similarly, all the alkaline samples show lower Zr/Nb ratios of 3–8, and plot along a horizontal line in the Zr/Nb versus Zr diagram, except for the two sub-alkaline basalts of Dahongyu Formation (samples 11PG11-3 and 11PG27-6) with higher Zr/Nb ratios (31–60;

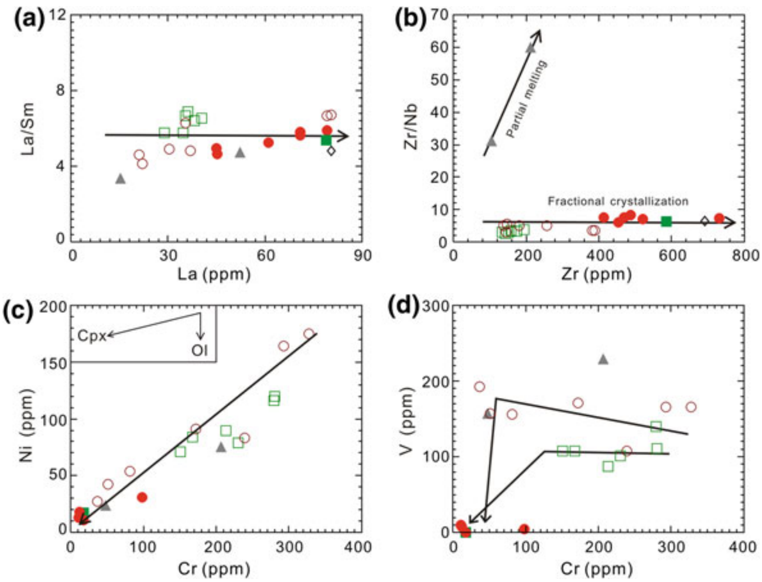

Fig. 4.22 Petrogenetic diagrams of K-rich volcanic rocks in the Tuanshanzi and Dahongyu Formations. Geochemical features of the alkaline volcanic rocks are controlled by fractional crystallization processes, whereas those of the sub-alkaline basalts are dominated by a partial melting process. **a** La/Sm versus La diagram (the arrow shows a fractional crystallization trend; [69]). **b** Zr/Nb versus Zr diagram (the arrows show partial melting and fractional crystallization trends, respectively; [73]. **c** Ni versus Cr diagram (the inset shows the fractional crystallization trends of olivine (Ol) and clinopyroxene (Cpx), respectively). **d** V versus Cr diagram, showing the effect of magnetite fractionation [60]. Symbols are the same as Fig. 4.20

Fig. 4.22b). Accordingly, the alkaline rocks from the two formations were fractionated from a common parental magma. The sub-alkaline basalts of Dahongyu Formation display contrasting normalized trace element patterns as compared with the other samples (e.g., "negative" vs. "positive" Nb–Ta anomalies; Fig. 4.21), implying a distinct petrogenetic process. Sample 11PG27-6 has high MgO content and Mg# value (7.55 wt% and 64), which are analogous to those of primitive mantle magmas without significant fractional crystallization (Mg# of 63–72, [17]). Sample 11PG11-3 shows intense post-magmatic alteration, and its low MgO (0.82 wt%), Mg# (16), and Sr (61.6 ppm), but high K_2O (11.50%) may therefore not represent the primary geochemical composition. Considering the similarity in the normalized trace element patterns and geochemical parameters (Fe_2O_3T, Al_2O_3, $(Nb/La)_{PM}$, and $(Nb/Th)_{PM}$) of the two calc-alkaline samples (Figs. 4.21e–f and 4.23), petrogenetic discussions will focus mainly on the REEs and HFSEs of sample 11PG27-6.

The alkaline basalts show positive correlations between Cr and Ni (Fig. 4.22c), suggesting fractional crystallization of both olivine and clinopyroxene from the parental magma [60]. On the chondrite-normalized REE patterns (Fig. 4.21a and c),

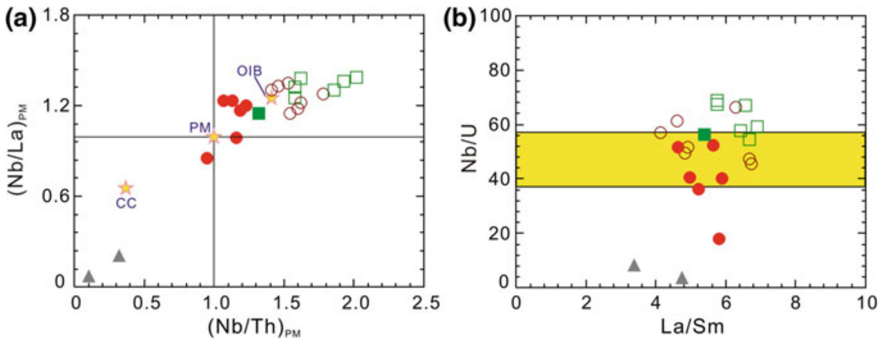

Fig. 4.23 **a** $(Nb/La)_{PM}$ versus $(Nb/Th)_{PM}$ diagram, with values of ocean island basalt (OIB), primitive mantle (PM), and bulk continental crust (CC) marked for comparison (PM and OIB values after Sun and McDonough [66]; and CC values after Taylor and McLennan [67]). **b** Nb/U versus La/Sm diagram (the yellow domain shows the nearly constant Nb/U ratios (47 ± 10) of OIB and MORB (mid-ocean ridge basalt); [66]. Symbols are the same as Fig. 4.20

they display weakly positive Eu anomalies (Eu_N/Eu_N^* values of 1.00–1.31), which could be ascribed to either plagioclase (Pl) accumulation or hornblende (Hb) fractional crystallization. Notably, hornblende fractionation could simultaneously result in the decrease in $(Gd/Yb)_N$, V, and TREE contents, since the partition coefficient (Kd) of V in Hb is high (3.40), and the Kd of Gd in Hb is higher than those of the other rare earth elements [60]. However, all the samples of alkaline rocks from the two formations display parallel chondrite-normalized REE patterns without positive correlations between V, TREE and $(Gd/Yb)_N$ (not shown). The accumulation of Pl may be a viable process to account for the positive Eu anomalies. The negative Sr anomalies in the primitive mantle-normalized multi-element spider diagrams (Fig. 4.21b and d) could be explained by post-magmatic alteration due to the large variations of Sr contents (185–1051 ppm) and the moderately high LOI values (mostly of 1.07–5.29 wt%). The slightly negative P anomalies indicate minor apatite fractionation (Fig. 4.21b and d). Moreover, V increases slightly with decreasing Cr of the Dahongyu alkaline basalts (Fig. 4.21d), indicating minor accumulation of Fe–Ti oxides. This is compatible with the presence of magnetite (Mt) crystals (Fig. 4.17).

The trachyandesites and trachytes show negative anomalies of Eu, P, Sr, and Ti in the normalized trace element patterns (Fig. 4.21a, b, c and d), suggesting fractional crystallization of Pl, apatite (Ap), and possibly Mt from the magma system. The strongly negative and varied Sr anomalies are incompatible with the moderately negative Eu anomalies, possibly reflecting the effects of post-magmatic alteration. On the other hand, the $(Gd/Yb)_N$ ratios are lower than those of alkaline basalts (Fig. 4.21a and c, Table 4.7). Considering the broadly positive correlation between $(Gd/Yb)_N$ and V (not shown), together with the sharp decrease in V contents during the transition from alkaline basalts to trachyandesites (Fig. 4.22d), both the fractionation of Hb and Mt could have been involved [60].

In summary, the alkaline samples from both the two formations are the products of fractional crystallization from a common parental magma. The magma system experienced Ol + Cpx fractionation and minor Pl + Mt accumulation in the early evolution stage, and Hb + Pl + Ap + Mt fractionation in the late evolution stage. In contrast, the sub-alkaline basalts of Dahongyu Formation could have been derived from a different mantle source, and were mainly controlled by a partial melting process.

4.2.4.3 Nature of the Mantle Source and Melting Conditions

As discussed above, alkaline samples from the two formations were generated by fractional crystallization from a common parental magma. In order to determine the nature of their mantle sources and melting conditions, only the most primitive alkaline basalt samples were used so as to minimize the effects of magma differentiation. On the chondrite-normalized REE and primitive mantle-normalized trace element patterns (Fig. 4.21a–d), these alkaline basalts show strongly fractionated REE patterns and positive Nb–Ta and Zr–Hf anomalies, resembling those of ocean island basalts (OIBs, [66]). This is further corroborated by the OIB-like high $(Nb/La)_{PM}$, $(Nb/Th)_{PM}$, and Nb/U ratios of 1.15–1.39, 1.41–2.05, and 46–69, respectively (Fig. 4.23; [28]). On the other hand, zircon Lu–Hf isotopic data of a dated trachybasalt (11PG31-2) show positive $\varepsilon_{Hf}(t)$ values of +0.1 to +1.8 (Fig. 4.19 and Table 4.6). Two alkaline basalts and one trachyte of the Dahongyu Formation were previously analyzed for whole-rock Sm–Nd isotopes, and they display positive $\varepsilon_{Nd}(t)$ values of +0.83 to + 2.25 (calculated at 1.65 Ga, Fig. 4.24a; [29]). These geochemical features are clearly different from the Basin and Range basalts, with lithospheric mantle components showing negative isotopic compositions ($\varepsilon_{Nd}(t)$ of ~ -9), negative Nb–Ta anomalies, and high and variable La/Nb ratios (>1) [14]. Despite the analytical error in isotopic values (±0.5), the positive isotopic compositions (+0.1 to +1.8) of alkaline basalts are evident. As shown by the empirical evolution trends [4], the ~1.65 Ga asthenospheric mantle has $\varepsilon_{Hf}(t)$ and $\varepsilon_{Nd}(t)$ of +10 and +5, respectively. However, it is suggested that the nature and evolution of the asthenospheric mantle is more complex, and mantle heterogeneity is inevitable as the effects of crustal recycling or interplay between the depleted asthenospheric mantle and the less depleted (or primitive) lower mantle [13]. Since significant crustal contamination has been precluded for the Pinggu volcanic rocks, we propose that the parental magmas of alkaline volcanic rocks in the two formations were produced by the partial melting of an OIB-like, depleted asthenospheric mantle source.

In the Th/Yb versus Nb/Yb diagram (Fig. 4.24b), alkaline basalts of the two formations fall within the mantle array, and cluster around the OIB field, showing no subduction imprints. The high $(Hf/Sm)_N$ and $(Ta/La)_N$ ratios (1.00–1.36 and 1.22–1.60, respectively) indicate that the mantle source was generally not metasomatized by subduction melts or fluids and carbonatite melts [35, 72, 76]. In the

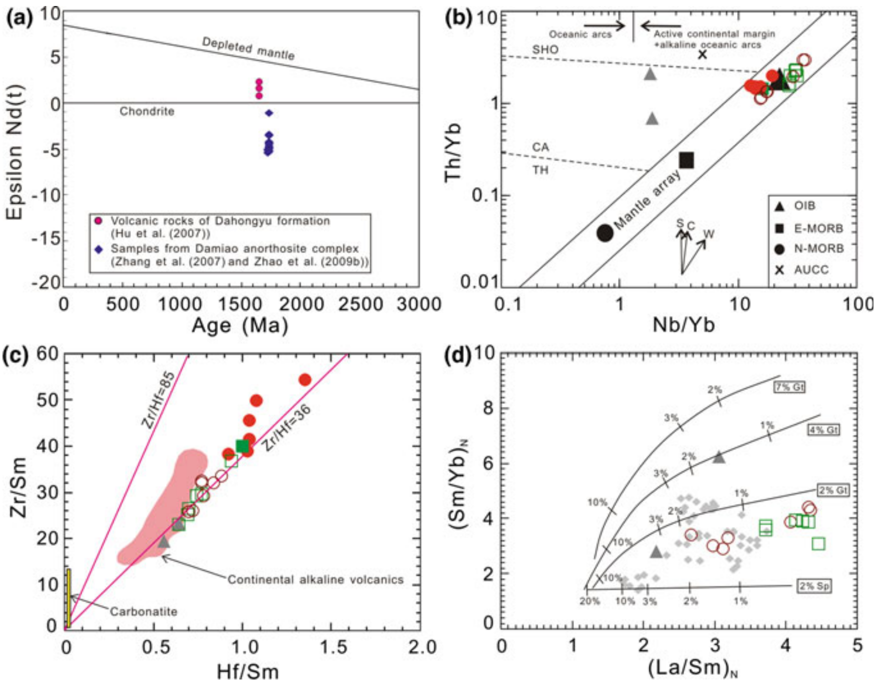

Fig. 4.24 Nature of the mantle sources for the K-rich volcanic rocks in the Tuanshanzi and Dahongyu Formations. **a** Whole-rock $\varepsilon_{Nd}(t)$ values versus formation ages of the ~1.65 Ga volcanic rocks in the Dahongyu Formation and the ~1.73 Ga Damiao anorthosite complex [29, 91, 94]. **b** Th/Yb versus Nb/Yb diagram [50]. **c** Zr/Sm versus Hf/Sm diagram [15]. **d** $(Sm/Yb)_N$ versus $(La/Sm)_N$ diagram ([30]; the shaded diamonds represent data of the ~1.78 Ga mafic dykes along the northern margin and the TNCO of the NCC; [53]). Values are chondrite-normalized after Sun and McDonough [66]. Symbols are the same as Fig. 4.20

Zr/Sm versus Hf/Sm diagram (Fig. 4.24c), they show Zr/Hf ratios of 36–42, which are close to the chondrite Zr/Hf value of 36 but are far from the carbonatite field [8, 15, 66]. Combined with the generally positive Zr and Hf anomalies in the primitive mantle-normalized trace element patterns (Fig. 4.21b and d), the involvement of carbonatite melts in the mantle source can be further precluded [12]. Melting conditions of the parental magma of the alkaline basalts can be modeled using trace element ratios, especially ratios of REEs. In the chondrite-normalized REE diagrams (Fig. 4.21a and c), the alkaline basalts display strongly fractionated patterns with generally high $(La/Yb)_N$ ratios of 8.95–19.0 (mostly of >10.5). Meanwhile, the $(Sm/Yb)_N$ versus $(La/Sm)_N$ diagram shows that these alkaline basalts can be modeled by low degree (<2%) partial melting of lherzolites with ~2% (or less) garnet, which is consistent with their high $(La/Yb)_N$ ratios and high Nb/Y and alkalis contents (though mobilized during post-magmatic alteration; [32]; Figs. 4.20a, b, and 4.21a and c).

Compared with the alkaline samples, the two sub-alkaline basalts show fractionated REE patterns and strongly negative Nb–Ta anomalies (Fig. 4.21e–f). These geochemical features may be ascribed to shallow-level crustal contamination or inherited from the mantle source. The representative sample 11PG27-6 has high MgO content and Mg# value, similar to the primitive mantle-derived magmas (Table 4.7), precluding the involvement of significant crustal contamination. The two sub-alkaline basalts have low $(Nb/La)_{PM}$ (0.07–0.21), $(Nb/Th)_{PM}$ (0.10–0.32), and Nb/U (3.74–8.14) ratios (Fig. 4.24 and Table 4.7). On the Th/Yb versus Nb/Y diagram (Fig. 4.24b), they plot above the mantle array with evident subduction imprints. These geochemical features are similar to those of earlier ~1721–1696 Ma JDMSS suite in the WLP, the parental magma of which is believed to have been produced by the partial melting of an enriched lithospheric mantle [76]. The sub-alkaline basalts in this study exhibit positive zircon $\varepsilon_{Hf}(t)$ values that range between +0.8 and +4.3, which is different from the JDMSS suite with negative $\varepsilon_{Hf}(t)$ values (Fig. 4.19). In this case, a depleted lithospheric mantle is invoked as the source of the sub-alkaline basalts. The moderate $(Hf/Sm)_N$ (0.80–0.92) but low $(Ta/La)_N$ (0.04–0.25) ratios imply that the mantle source was mainly metasomatized by slab-derived fluids but without addition of slab-derived melts or carbonatite melts [35, 72, 76]. In the $(Sm/Yb)_N$ versus $(La/Sm)_N$ diagram (Fig. 4.24d), they can be modeled by low degree (1–3%) partial melting of lherzolites with 2–4% garnet [32].

Accordingly, the parental magma of alkaline volcanic rocks in the two formations was derived from low degree partial melting of an OIB-like, depleted asthenospheric mantle, whereas the sub-alkaline basalts of Dahongyu Formation were generated by low degree partial melting of a depleted lithospheric mantle metasomatized by slab-derived fluids.

4.2.4.4 Lithosphere Signature Preserved in the Alkaline Volcanic Rocks

The alkaline rocks from both the Tuanshanzi and Dahongyu Formations display two geochemical characteristics: (1) high $(Nb/La)_{PM}$ ratios (mostly of 1.15–1.39); and (2) high Nb/U ratios (mostly of 36–69) (Fig. 4.24 and Table 4.7). These correlate well with OIB-like geochemical features (Fig. 4.21a–d; [64]), which are distinct from rocks that were derived from the partial melting of continental crustal materials or lithospheric mantle sources previously metasomatized by subduction-derived fluids or melts [59, 76]. However, the $(Nb/La)_{PM}$ and $(Nb/Th)_{PM}$ ratios of these alkaline volcanic rocks show a clear positive correlation, with the two parameters decreasing from alkaline basalts to trachyandesites and trachytes (Fig. 4.23a). A similarly decreasing trend was also observed in the Nb/U ratios (Fig. 4.23b). Zircon Lu–Hf isotopic data reveal that $\varepsilon_{Hf}(t)$ values of the two trachyandesites (−0.4 to +1.9 of 11PG18-3 and −2.1 to +1.6 of 11PG44-1) are lower than those of alkaline basalt (+0.1 to +1.8 of 11PG31-2) (Fig. 4.19 and Table 4.6). Notably, the $(Nb/La)_{PM}$ ratios of 1.39, 1.23, and 1.17 for samples 11PG31-2, 11PG18-3, and 11PG44-1, respectively, are positively correlated with the lowest $\varepsilon_{Hf}(t)$ values of each sample (from +0.1, through −0.4, to −2.1) (Table 4.6). All these lines of evidence suggest that a component with lower $(Nb/La)_{PM}$ and $(Nb/Th)_{PM}$ ratios and enriched isotopic composition was involved in the sources of trachyandesite and trachytes and some alkaline basalts (e.g., 11PG07-1, 11PG08-1, and 11PG41-3).

Previous studies suggest that the late Paleoproterozoic (~1.7 Ga) lithospheric mantle along the northern margin of North China Craton is generally enriched, as indicated by the mostly negative zircon $\varepsilon_{Hf}(t)$ values of the ~1721–1696 Ma JDMSS suite (WLP) and the ~1780 Ma mafic dykes in the Huai'an area (Fig. 2.2; [26, 76, 91]). Late Archean TTG gneisses with subordinate metamorphosed volcano-sedimentary rocks are exposed within the Yanliao rift zone (Fig. 2.2; [38, 74, 75, 77, 96]). When the isotopic data of these Archean crustal rocks were recalculated at ~1650 Ma, they also show negative $\varepsilon_{Hf}(t)$ values [91]. In this regard, there are two possible sources of the above low $(Nb/La)_{PM}$, $(Nb/Th)_{PM}$, and $\varepsilon_{Hf}(t)$ components: (1) contamination of the parental magma by Archean continental crust; or (2) mixing of magmas derived from enriched lithospheric mantle during the ascent of asthenospheric mantle-derived magmas. On the basis of the following lines of evidence, we propose that a lithospheric mantle component was involved:

(1) Though decrease in $(Nb/La)_{PM}$ ratios for some alkaline basalts, the MgO (6.33–7.71 wt%) and Mg# (53–63) are comparable to, or even higher than those of samples with high $(Nb/La)_{PM}$ ratios (MgO and Mg# of 4.44–8.56 wt% and 48–64, respectively) (Table 4.7). Pb is considered as one of the most sensitive trace elements to monitor crustal contamination in continental rift basalts [57]. However, some volcanic rocks in this study were subjected to intense alteration, and the original Pb contents could have been modified, and therefore cannot be used with confidence to evaluate crustal contamination. Similar to the OIBs, most alkaline volcanic rocks possess high LREEs, Nb, and Ta contents, much higher than those of the bulk continental crust [67]. These argue against the contamination by continental crustal materials, which will simultaneously result in the decrease in MgO, Mg#, LREEs and $(Nb/La)_{PM}$.

(2) For the three dated alkaline samples (11PG31-2, 11PG18-3, and 11PG44-1), only four captured zircons were detected, though a total of seventy-three zircon spots were analyzed (Fig. 4.18a–d). Therefore, significant crustal contamination can be better precluded for the parental magmas.

(3) Alkaline samples from the Tuanshanzi and Dahongyu Formations are generally enriched in K_2O, especially for the trachyandesites and trachytes (Table 4.7). Considering the variable LOI contents of 1.07–7.14 wt%, the high K_2O contents may be ascribed to post-magmatic alteration. However, the two trachyte samples (11PG19-2 and dhy-12) show lower LOI contents (1.34–2.39 wt%), and plot in the trachyte field (11PG19-2) or at the boundary field between

trachyte and phonolite (dhy-12) in the TAS and Zr/TiO_2*0.0001 versus Nb/Y diagrams (Fig. 4.21a, b), implying the general preservation of their primary geochemical compositions. These two samples also have high K_2O contents of 8.53–9.45 wt%, which are hardly explained by fractional crystallization from the alkaline basalt magma (with generally low K_2O content of 0.72–3.36 wt%). The widespread Archean TTG gneisses along the northern margin of NCC may represent a high K source, since it has been shown that partial melting of TTGs with some amounts of sedimentary rocks will produce high-K monzogranites or syenogranites (2.53–2.49 Ga; [70, 75]). Nonetheless, the K_2O contents of these late Archean monzogranites and syenogranites throughout the NCC are generally 3–6 wt%, much lower than those of the high-K trachytes (>8 wt%) in this study. In contrast, partial melting of an enriched lithospheric mantle with hydrous minerals (e.g., phlogopite) can produce melts with extremely high K_2O contents, which is commonly invoked to account for the genesis of some potassic and ultrapotassic rocks [49, 76]. The low partial melting degrees of the alkaline rocks in this study may further contribute to the enrichment of K (Fig. 4.24d).

Accordingly, parental magma of the alkaline samples in the Pinggu area was mainly derived from the partial melting of an OIB-like depleted asthenospheric mantle source, with no significant crustal contamination. Their geochemical diversity was ascribed to the involvement of some enriched lithospheric mantle components.

4.2.4.5 Late Paleoproterozoic Asthenospheric Mantle Upwelling

Distinct from the early ~1780–1680 Ma magmatic rocks, the ~1671–1625 Ma Pinggu volcanic rocks commonly show positive to chondrite-like zircon $\varepsilon_{Hf}(t)$ values (Fig. 4.19). They were mainly produced by the partial melting of a depleted asthenopheric mantle, and some calc-alkaline basalts may be sourced from a depleted lithospheric mantle source. In the $(Sm/Yb)_N$ versus $(La/Yb)_N$ diagram (Fig. 4.24d), the Pinggu alkaline volcanic rocks and most of the ~1780 Ma mafic dykes and JDMSS rocks were derived from low degree (<3%) partial melting of garnet Iherzolites with ~2% garnet, implying comparable melting pressures of magma sources. Given that the Pinggu volcanic rocks and ~1780–1680 Ma plutonic rocks show distinct mantle sources (i.e., asthenopheric mantle vs. lithospheric mantle), the origin of Pinggu volcanic rocks could be linked to an important upwelling event of the asthenospheric mantle. Minor calc-alkaline basalts and some late Paleoproterozoic high-Ti mafic dykes along the TNCO are characterized by depleted isotopic features and negative Nb–Ta anomalies, pointing to a depleted lithospheric mantle source [53, 54]. Accordingly, late Paleoproterozoic lithospheric mantle heterogeneities could have existed beneath the northern margin of North China Craton [79].

4.2.5 Summary

(1) In the lowermost Changcheng Group of Yanliao rift, volcanic rocks of the Tuanshanzi Formation are dominated by trachybasalts and trachytes, whereas those of the overlying Dahongyu Formation consist mainly of olivine basalts, trachybasalts, trachyandesites, trachytes, and minor sub-alkaline basalts. LA-ICP-MS zircon U–Pb isotopic dating data reveal that the Tuanshanzi and Dahongyu Formations formed at ~1670 and ~1664–1625 Ma, respectively.
(2) Alkaline volcanic rocks of the two formations were generated by fractional crystallization from a parental magma derived from low-degree partial melting of an OIB-like depleted asthenospheric mantle source, with some involvement of magmas sourced from the overlying enriched lithospheric mantle. In addition to the contribution from the low-degree partial melts of the enriched lithospheric mantle, the high K contents of these rocks possibly resulted from post-magmatic alteration. In contrast, the sub-alkaline basalts were produced by the partial melting of a depleted lithospheric mantle source previously metasomatized by subduction-derived fluids. The ancient lithospheric mantle along the northern margin of North China Craton witnessed an intense upwelling event of asthenospheric mantle during the late Paleoproterozoic.

4.3 Mesoproterozoic (~1.23 Ga) Mafic Dykes Along the Northern Margin of North China Craton

A suite of Mesoproterozoic (~1.23 Ga) mafic dykes with an inferred distribution area of ~0.6×10^6 km^2 is recently identified in the North China Craton [80]. Detailed zircon U–Pb and Lu–Hf isotopes and whole-rock geochemistry were analyzed in order to determine the emplacement timing, nature of the mantle sources, and petrogenetic processes of these Mesoproterzoic mafic dykes.

4.3.1 Geological and Petrographic Features

Mesoproterozoic mafic dykes are identified in three Precambrian terranes of NCC, i.e., the Western Liaoning Province (WLP), Eastern Hebei Province (EHP), and Northern Liaoning Province (NLP; Fig. 2.2). These dykes are 20–70 m in width, and trend northeast to east, and they intrude Archean tonalite-trondhjemite-granodiorite (TTG) gneisses or metamorphosed supracrustal rocks.

In the Jianping area of WLP, three mafic dykes (dip 128°; dip angle 64°) intrude both the ~2.52 Ga TTG gneisses and ~1.70 Ga JDMSS suite (Fig. 4.25; [76, 77]). These dykes outcrop near the Xiaozhangzi town, where the largest dyke is ~70 m in

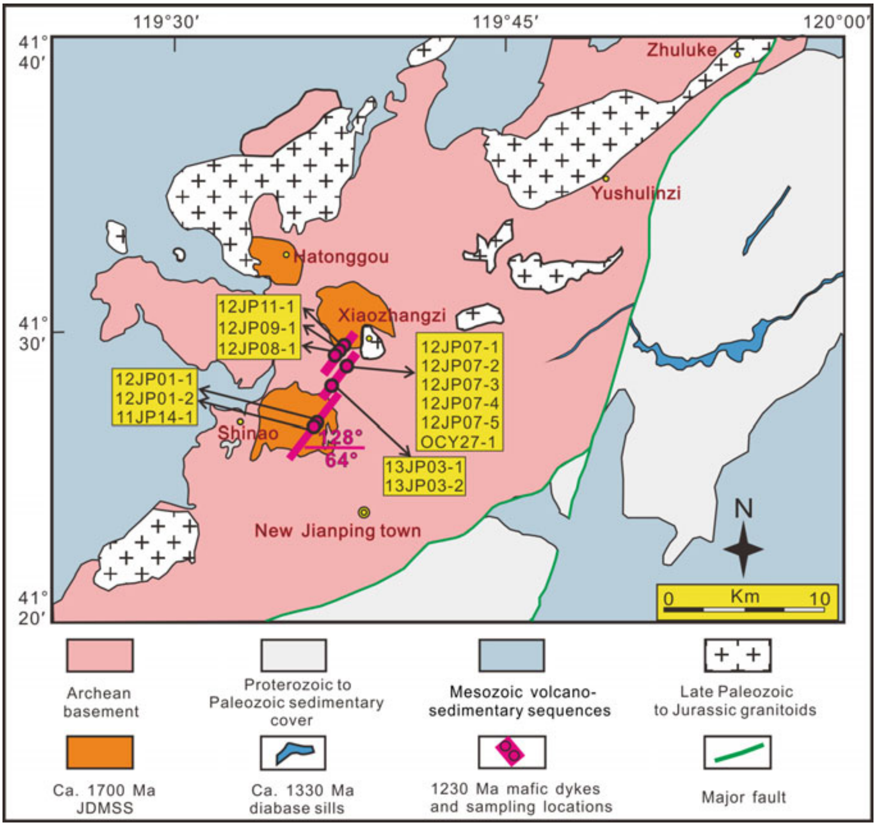

Fig. 4.25 Geological map of 1.23 Ga mafic dykes in the southwestern WLP (Western Liaoning Province)

width and extends for >5 km (Fig. 4.26a). Gabbro is the main lithology, and the rocks are massive and grade from medium- to coarse-grained at the center to fine-grained at the margins (Fig. 4.26b, c). The mineral assemblage is plagioclase and clinopyroxene, with subordinate amounts of orthopyroxene and hornblende, and traces of magnetite (Fig. 4.26d, e). In general, the mafic rocks are fresh, with only minor sericitization of plagioclase (Fig. 4.26d). A total of fourteen samples were selected from the mafic dykes in Jianping area (Fig. 4.25). Samples from both fine-grained margins (e.g., 12JP07-1, 12JP07-5, and 13JP03-1) and medium- to coarse-grained central domains (e.g., 12JP07-3 and 13JP03-2) were collected.

In the northeast part of EHP, a mafic dyke (dip 130°; dip angle 68°) was emplaced into the Archean tonalitic gneisses in the Qinglong area, east of the early Mesozoic Dushan granitoid pluton (Fig. 4.27). The dyke has a width of 30 m and a length of 3 km (Fig. 4.28a). The massive rocks show a fining trend from the center to the margins (Fig. 4.28b, c). In contrast to the Jianping mafic dykes, the Qinglong dyke is dominated by hornblende gabbros, with a mineral assemblage of

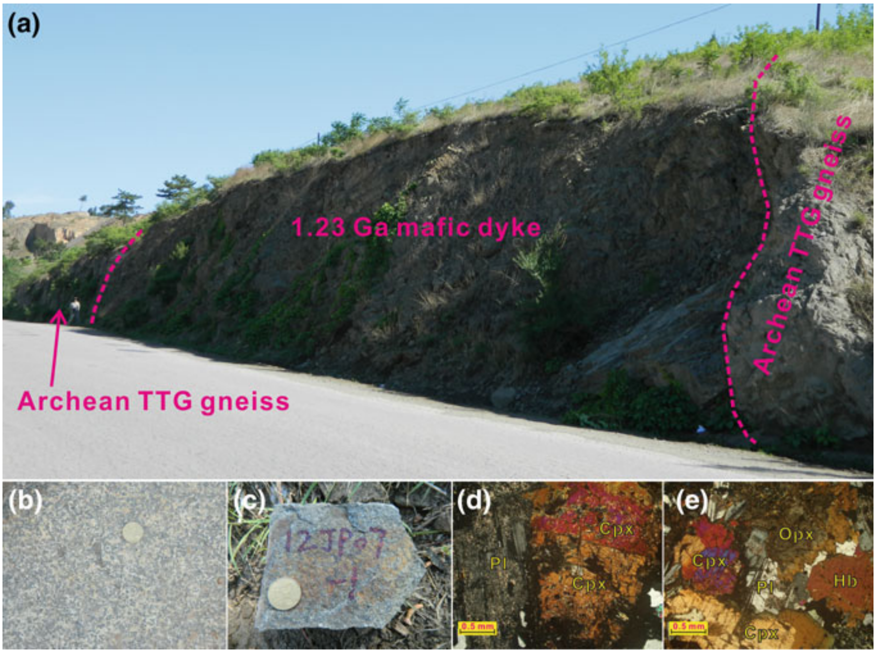

Fig. 4.26 Field geological features and photomicrographs of 1.23 Ga mafic dykes from the Jianping area of Western Liaoning Province

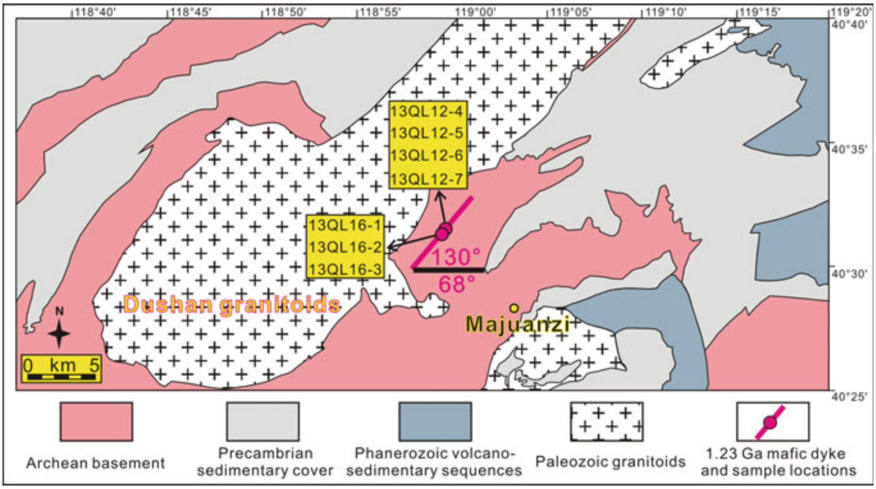

Fig. 4.27 Geological map of a 1.23 Ga mafic dyke in the Qinglong area of the Eastern Hebei Province

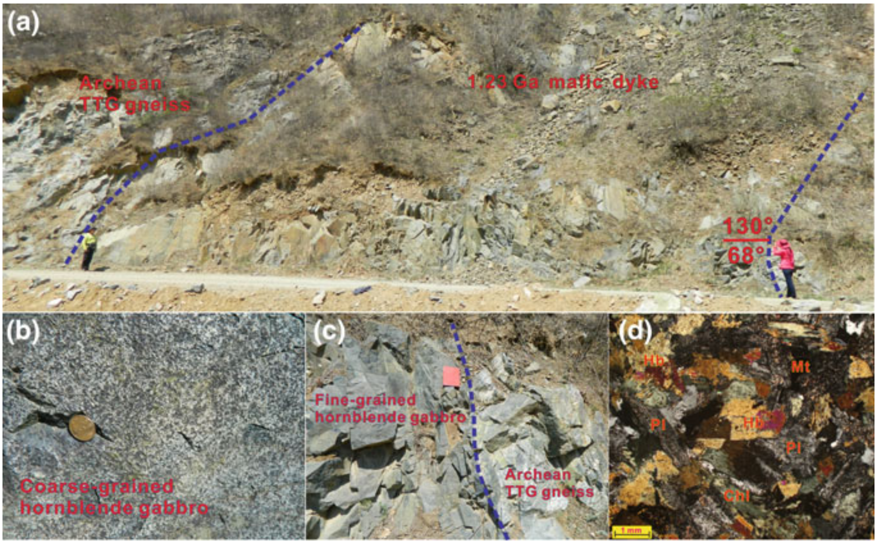

Fig. 4.28 Field geological features and photomicrographs of the 1.23 Ga mafic dyke from the Qinglong area of Eastern Hebei Province

plagioclase and hornblende, and minor clinopyroxene and magnetite (Fig. 4.28d). Notably, these rocks show intense alteration, with chloritization of hornblende and sericitization of plagioclase. A total of seven gabbroic samples from both the fine-grained margins and coarse-grained central domains are collected from this dyke (Fig. 4.27).

The Archean metamorphosed supracrustal rocks in the Qingyuan area of NLP were intruded by a mafic dyke (dip 0°; dip angle 34°) extending for >3 km with a width of ~20 m (Figs. 4.29 and 4.30a). The dyke cuts the gneissosity of Archean hornblende plagioclase gneisses (Fig. 4.30b). Similar to the Jianping dykes, the gabbros are composed of plagioclase and clinopyroxene, with subordinate amounts of orthopyroxene, hornblende, and magnetite (Fig. 4.30c). Sericitization of plagioclase and epidotization of clinopyroxene are common. One representative sample (12LN54-1) of this dyke was collected (Fig. 4.29).

4.3.2 *Zircon U–Pb and Lu–Hf Isotopes*

Three gabbroic rock samples (12JP01-1, OCY27-1, and 12JP07-3) from the Jianping mafic dykes were dated. On the cathodoluminescence images, the zircon grains are bright, and show either banded or broad zonings, typical of magmatic zircons from gabbro or diabase [11, 74, 76]. A total of seventy-three analyses were conducted on the three samples (Table 4.8). Except for several older analyses in samples 12JP01-1 (spots #02, #03, #05, #06, #08, and #10) and 12JP07-3 (spot #7)

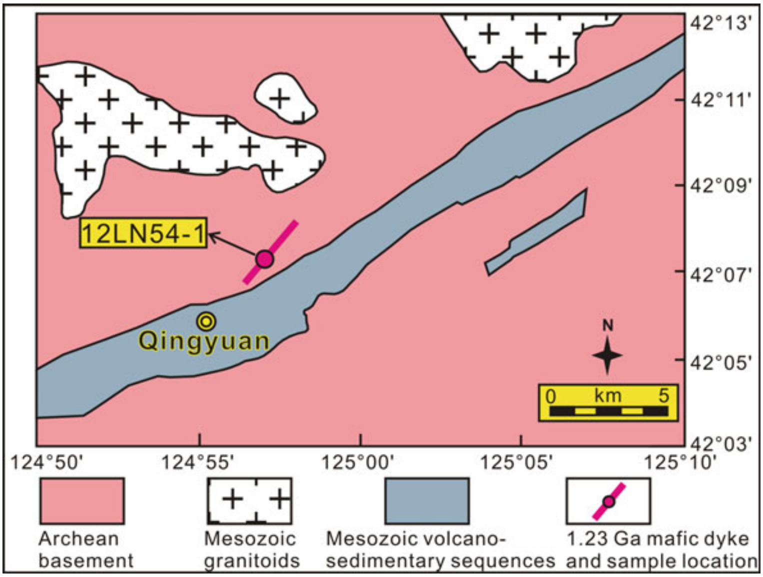

Fig. 4.29 Geological map of a 1.23 Ga mafic dyke in the Qingyuan area of the Northern Liaoning Province

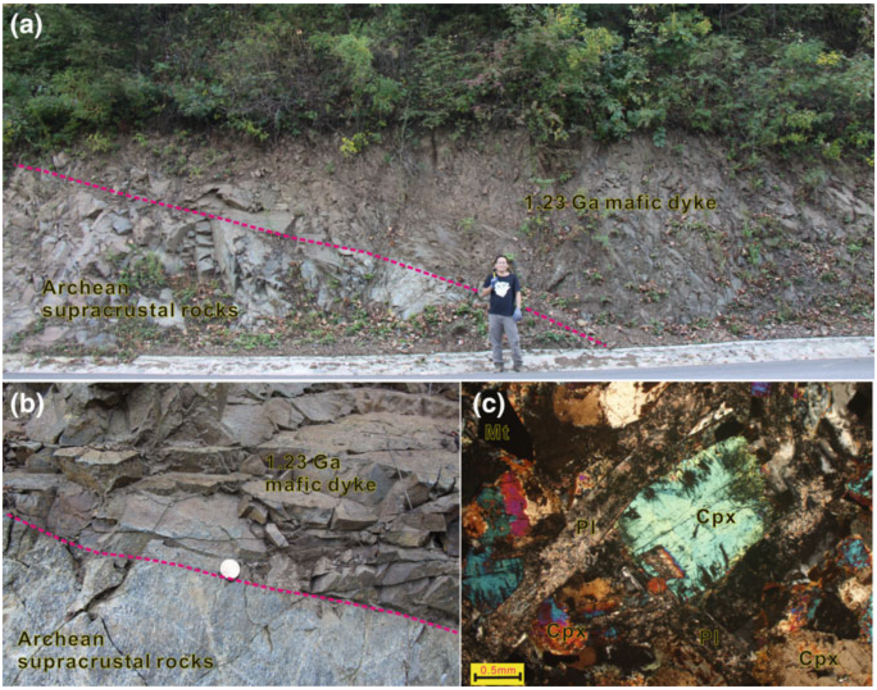

Fig. 4.30 Field geological features and photomicrographs of the 1.23 Ga mafic dyke from the Qinglong area in the Eastern Hebei Province

Table 4.8 LA-ICP-MS zircon U–Pb dating data of 1.23 Ga mafic dykes from the North China Craton (NCC)

Sample and analytical spot number	Th (ppm)	U (ppm)	Th/U	Isotopic ratios						Apparent ages (Ma)					
				$^{207}Pb/^{206}Pb$	±1σ	$^{207}Pb/^{235}U$	±1σ	$^{206}Pb/^{238}U$	±1σ	$^{207}Pb/^{206}Pb$	±1σ	$^{207}Pb/^{235}U$	±1σ	$^{206}Pb/^{238}U$	±1σ
12JP01-1-01 (WLP)	1213	881	1.38	0.0811	0.0020	2.3486	0.0554	0.2102	0.0042	1223	21	1227	17	1230	22
12JP01-1-02	99	279	0.36	0.0861	0.0025	2.7387	0.0761	0.2309	0.0048	1340	25	1339	21	1339	25
12JP01-1-03	183	262	0.70	0.0852	0.0030	2.6711	0.0918	0.2274	0.0051	1321	34	1320	25	1321	27
12JP01-1-04	572	497	1.15	0.0817	0.0023	2.3876	0.0651	0.2120	0.0044	1238	25	1239	20	1239	23
12JP01-1-05	148	281	0.53	0.0854	0.0028	2.6374	0.0843	0.2240	0.0049	1325	31	1311	24	1303	26
12JP01-1-06	195	294	0.66	0.0859	0.0027	2.7087	0.0840	0.2287	0.0050	1337	29	1331	23	1328	26
12JP01-1-07	409	430	0.95	0.0812	0.0022	2.3345	0.0608	0.2087	0.0043	1225	24	1223	19	1222	23
12JP01-1-08	225	301	0.75	0.0854	0.0026	2.6919	0.0800	0.2286	0.0049	1326	28	1326	22	1327	26
12JP01-1-09	828	643	1.29	0.0813	0.0022	2.3585	0.0605	0.2106	0.0043	1227	23	1230	18	1232	23
12JP01-1-10	1057	1061	1.00	0.0849	0.0022	2.6466	0.0646	0.2261	0.0045	1314	21	1314	18	1314	24
12JP01-1-11	313	530	0.59	0.0811	0.0026	2.3197	0.0719	0.2075	0.0045	1224	30	1218	22	1216	24
12JP01-1-12	1418	856	1.66	0.0811	0.0020	2.3345	0.0548	0.2088	0.0041	1224	21	1223	17	1222	22
12JP01-1-13	1006	744	1.35	0.0814	0.0022	2.1018	0.0543	0.1874	0.0038	1230	23	1149	18	1107	21
12JP01-1-14	1476	1006	1.47	0.0807	0.0020	2.2962	0.0560	0.2065	0.0041	1213	22	1211	17	1210	22
12JP01-1-15	1688	1185	1.42	0.0809	0.0022	2.3289	0.0622	0.2087	0.0043	1220	25	1221	19	1222	23
12JP01-1-16	645	900	0.72	0.0810	0.0036	2.3596	0.1026	0.2114	0.0049	1220	50	1230	31	1236	26
12JP01-1-17	1468	958	1.53	0.0823	0.0021	2.3872	0.0577	0.2104	0.0042	1253	21	1239	17	1231	22
12JP01-1-18	1542	992	1.55	0.0820	0.0021	2.3904	0.0595	0.2115	0.0042	1246	22	1240	18	1237	23
12JP01-1-19	978	832	1.18	0.0810	0.0021	2.3478	0.0573	0.2103	0.0042	1222	22	1227	17	1230	22
12JP01-1-20	2134	1192	1.79	0.0814	0.0020	2.3168	0.0538	0.2064	0.0041	1232	20	1217	16	1210	22
12JP01-1-21	2205	1277	1.73	0.0807	0.0019	2.3171	0.0535	0.2082	0.0041	1215	20	1218	16	1219	22

(continued)

Table 4.8 (continued)

Sample and analytical spot number	Th (ppm)	U (ppm)	Th/U	Isotopic ratios						Apparent ages (Ma)					
				$^{207}Pb/^{206}Pb$	±1σ	$^{207}Pb/^{235}U$	±1σ	$^{206}Pb/^{238}U$	±1σ	$^{207}Pb/^{206}Pb$	±1σ	$^{207}Pb/^{235}U$	±1σ	$^{206}Pb/^{238}U$	±1σ
12JP01-1-22	1920	1111	1.73	0.0811	0.0021	2.2972	0.0560	0.2055	0.0041	1224	22	1211	17	1205	22
12JP01-1-23	110	211	0.52	0.0813	0.0028	2.3322	0.0794	0.2081	0.0046	1229	35	1222	24	1219	24
12JP01-1-24	485	543	0.89	0.0820	0.0024	2.4107	0.0686	0.2134	0.0045	1245	27	1246	20	1247	24
12JP01-1-25	1202	948	1.27	0.0811	0.0020	2.3626	0.0568	0.2115	0.0042	1223	21	1231	17	1237	22
12JP01-1-26	694	662	1.05	0.0810	0.0021	2.2302	0.0543	0.1997	0.0040	1222	22	1191	17	1174	21
12JP01-1-27	1507	980	1.54	0.0814	0.0020	2.2087	0.0518	0.1969	0.0039	1231	21	1184	16	1159	21
12JP01-1-28	1117	973	1.15	0.0817	0.0021	2.4424	0.0590	0.2169	0.0043	1239	21	1255	17	1265	23
OCY27-1-01 (WLP)	1774	1048	1.69	0.0813	0.0013	2.5136	0.0363	0.2241	0.0022	1230	30	1276	10	1304	12
OCY27-1-02	959	708	1.35	0.0810	0.0013	2.3271	0.0350	0.2085	0.0021	1221	31	1221	11	1221	11
OCY27-1-03	80	106	0.75	0.1049	0.0019	3.8005	0.0639	0.2628	0.0028	1713	32	1593	14	1504	14
OCY27-1-04	850	689	1.23	0.0812	0.0013	2.3643	0.0350	0.2113	0.0021	1225	30	1232	11	1236	11
OCY27-1-05	761	632	1.20	0.0813	0.0013	2.3200	0.0366	0.2071	0.0021	1228	32	1218	11	1213	11
OCY27-1-06	1006	813	1.24	0.0812	0.0013	2.3084	0.0357	0.2061	0.0021	1227	31	1215	11	1208	11
OCY27-1-07	267	396	0.67	0.1313	0.0021	5.4266	0.0826	0.2997	0.0031	2116	27	1889	13	1690	15
OCY27-1-08	1524	918	1.66	0.0816	0.0014	2.1754	0.0347	0.1934	0.0020	1235	32	1173	11	1140	11
OCY27-1-09	1487	1077	1.38	0.0815	0.0014	2.3044	0.0377	0.2052	0.0022	1232	32	1214	12	1203	12
OCY27-1-10	89	132	0.67	0.1394	0.0025	5.7832	0.1003	0.3010	0.0034	2219	30	1944	15	1696	17
OCY27-1-11	1264	1108	1.14	0.0812	0.0014	2.3517	0.0389	0.2101	0.0022	1226	33	1228	12	1230	12
OCY27-1-12	731	562	1.30	0.0815	0.0015	2.4187	0.0438	0.2153	0.0024	1234	36	1248	13	1257	13
OCY27-1-13	124	964	0.13	0.0811	0.0015	2.3896	0.0435	0.2137	0.0024	1225	35	1240	13	1248	13
OCY27-1-14	304	580	0.52	0.0816	0.0016	2.1414	0.0413	0.1904	0.0022	1235	37	1162	13	1124	12

(continued)

Table 4.8 (continued)

Sample and analytical spot number	Th (ppm)	U (ppm)	Th/U	Isotopic ratios						Apparent ages (Ma)					
				$^{207}Pb/^{206}Pb$	±1σ	$^{207}Pb/^{235}U$	±1σ	$^{206}Pb/^{238}U$	±1σ	$^{207}Pb/^{206}Pb$	±1σ	$^{207}Pb/^{235}U$	±1σ	$^{206}Pb/^{238}U$	±1σ
OCY27-1-15	659	527	1.25	0.0813	0.0016	2.3166	0.0447	0.2067	0.0024	1229	37	1217	14	1211	13
OCY27-1-16	545	725	0.75	0.0822	0.0017	2.1855	0.0444	0.1930	0.0023	1249	39	1176	14	1138	12
OCY27-1-17	877	653	1.34	0.0816	0.0017	2.3922	0.0506	0.2126	0.0025	1237	40	1240	15	1243	13
OCY27-1-18	1000	966	1.04	0.0819	0.0017	1.6439	0.0348	0.1456	0.0017	1244	40	987	13	876	10
OCY27-1-19	659	620	1.06	0.0814	0.0018	2.1767	0.0484	0.1941	0.0024	1231	42	1174	15	1144	13
OCY27-1-20	750	638	1.17	0.0817	0.0017	2.4355	0.0530	0.2163	0.0026	1239	40	1253	16	1262	14
12JP07-3-01 (WLP)	1786	1027	1.74	0.0811	0.0020	2.3301	0.0543	0.2084	0.0041	1224	21	1222	17	1220	22
12JP07-3-02	548	508	1.08	0.0825	0.0021	2.4394	0.0592	0.2144	0.0043	1258	21	1254	17	1252	23
12JP07-3-03	1030	848	1.21	0.0820	0.0020	2.3141	0.0549	0.2048	0.0040	1245	21	1217	17	1201	22
12JP07-3-04	2571	5467	0.47	0.0816	0.0019	2.3642	0.0534	0.2102	0.0041	1236	20	1232	16	1230	22
12JP07-3-05	1863	1236	1.51	0.0813	0.0020	2.3749	0.0571	0.2121	0.0042	1227	21	1235	17	1240	22
12JP07-3-06	1290	918	1.41	0.0812	0.0021	2.3459	0.0588	0.2096	0.0042	1227	22	1226	18	1226	22
12JP07-3-07	296	717	0.41	0.0879	0.0022	2.9107	0.0690	0.2402	0.0048	1381	21	1385	18	1388	25
12JP07-3-08	935	908	1.03	0.0808	0.0023	2.3114	0.0643	0.2075	0.0043	1217	26	1216	20	1216	23
12JP07-3-09	1005	788	1.28	0.0808	0.0021	2.3046	0.0590	0.2070	0.0042	1216	23	1214	18	1213	22
12JP07-3-10	631	494	1.28	0.0824	0.0025	2.4419	0.0720	0.2151	0.0046	1254	28	1255	21	1256	24
12JP07-3-11	131	194	0.67	0.0824	0.0030	2.4086	0.0843	0.2122	0.0048	1254	35	1245	25	1241	26
12JP07-3-12	417	454	0.92	0.0816	0.0032	2.3957	0.0923	0.2129	0.0047	1237	42	1241	28	1244	25
12JP07-3-13	298	312	0.96	0.0823	0.0024	2.4123	0.0682	0.2127	0.0044	1253	26	1246	20	1243	23
12JP07-3-14	1349	953	1.42	0.0817	0.0021	2.4061	0.0603	0.2137	0.0043	1238	22	1244	18	1249	23
12JP07-3-15	1738	1005	1.73	0.0812	0.0022	2.3434	0.0608	0.2093	0.0042	1227	24	1226	18	1225	23

(continued)

Table 4.8 (continued)

Sample and analytical spot number	Th (ppm)	U (ppm)	Th/U	Isotopic ratios						Apparent ages (Ma)					
				$^{207}Pb/^{206}Pb$	±1σ	$^{207}Pb/^{235}U$	±1σ	$^{206}Pb/^{238}U$	±1σ	$^{207}Pb/^{206}Pb$	±1σ	$^{207}Pb/^{235}U$	±1σ	$^{206}Pb/^{238}U$	±1σ
12JP07-3-16	1240	880	1.41	0.0815	0.0020	2.3900	0.0575	0.2129	0.0042	1233	21	1240	17	1244	22
12JP07-3-17	662	643	1.03	0.0821	0.0022	2.3764	0.0606	0.2100	0.0042	1248	23	1236	18	1229	22
12JP07-3-18	1247	982	1.27	0.0807	0.0022	2.2850	0.0609	0.2056	0.0042	1213	25	1208	19	1205	22
12JP07-3-19	554	583	0.95	0.0805	0.0026	2.2901	0.0713	0.2064	0.0044	1210	30	1209	22	1209	24
12JP07-3-20	1789	1142	1.57	0.0818	0.0022	2.3797	0.0617	0.2112	0.0043	1240	23	1237	19	1235	23
12JP07-3-21	792	702	1.13	0.0810	0.0023	2.3890	0.0643	0.2139	0.0043	1222	25	1239	19	1250	23
12JP07-3-22	1124	837	1.34	0.0810	0.0021	2.3135	0.0562	0.2072	0.0041	1221	22	1216	17	1214	22
12JP07-3-23	525	483	1.09	0.0809	0.0023	2.3358	0.0627	0.2096	0.0043	1218	25	1223	19	1227	23
12JP07-3-24	709	643	1.10	0.0804	0.0021	2.3283	0.0578	0.2102	0.0042	1206	22	1221	18	1230	22
12JP07-3-25	583	674	0.86	0.0810	0.0022	2.3150	0.0598	0.2074	0.0042	1221	23	1217	18	1215	22
13QL12-4-01 (EHP)	1973	1735	1.14	0.0803	0.0013	1.3895	0.0216	0.1256	0.0013	1203	32	885	9	763	7
13QL12-4-02	2880	1357	2.12	0.0745	0.0012	0.7700	0.0119	0.0750	0.0008	1054	33	580	7	466	5
13QL12-4-03	1303	1370	0.95	0.0811	0.0013	1.5025	0.0226	0.1344	0.0014	1224	31	931	9	813	8
13QL12-4-04	66	231	0.29	0.1767	0.0026	10.1824	0.1412	0.4181	0.0045	2622	24	2452	13	2252	20
13QL12-4-05	1135	1781	0.64	0.0805	0.0011	2.1282	0.0266	0.1917	0.0018	1210	26	1158	9	1131	10
13QL12-4-06	2448	1662	1.47	0.0743	0.0011	0.9495	0.0127	0.0927	0.0009	1050	28	678	7	572	5
13QL12-4-07	1453	1236	1.17	0.0803	0.0011	2.1675	0.0273	0.1959	0.0019	1203	26	1171	9	1153	10
13QL12-4-08	7286	2689	2.71	0.0750	0.0010	1.3381	0.0163	0.1294	0.0012	1069	26	862	7	785	7
13QL12-4-09	923	1591	0.58	0.0803	0.0011	2.2526	0.0276	0.2035	0.0019	1204	26	1198	9	1194	10
13QL12-4-10	521	820	0.64	0.0505	0.0012	0.2396	0.0054	0.0344	0.0004	219	54	218	4	218	2
13QL12-4-11	382	269	1.42	0.1344	0.0018	5.4084	0.0687	0.2918	0.0029	2157	23	1886	11	1651	14

(continued)

Table 4.8 (continued)

Sample and analytical spot number	Th (ppm)	U (ppm)	Th/U	Isotopic ratios						Apparent ages (Ma)					
				$^{207}Pb/^{206}Pb$	±1σ	$^{207}Pb/^{235}U$	±1σ	$^{206}Pb/^{238}U$	±1σ	$^{207}Pb/^{206}Pb$	±1σ	$^{207}Pb/^{235}U$	±1σ	$^{206}Pb/^{238}U$	±1σ
12LN54-1-01 (NLP)	134	379	0.35	0.1137	0.0015	5.2362	0.0685	0.3342	0.0036	1860	24	1859	11	1859	17
12LN54-1-02	4684	2176	2.15	0.0809	0.0010	2.1798	0.0268	0.1957	0.0020	1218	24	1175	9	1152	11
12LN54-1-03	15335	2568	5.97	0.0811	0.0010	1.8155	0.0224	0.1624	0.0017	1225	24	1051	8	970	9
12LN54-1-04	1765	1298	1.36	0.0824	0.0012	2.4346	0.0344	0.2146	0.0023	1254	28	1253	10	1253	12
12LN54-1-05	1758	1948	0.90	0.0810	0.0010	2.3333	0.0281	0.2091	0.0021	1221	24	1223	9	1224	11
12LN54-1-06	5839	2273	2.57	0.0813	0.0010	2.0191	0.0255	0.1803	0.0019	1228	25	1122	9	1069	10
12LN54-1-07	18650	2108	8.85	0.0802	0.0010	1.8594	0.0237	0.1682	0.0018	1203	25	1067	8	1002	10
12LN54-1-08	6263	1999	3.13	0.0818	0.0010	2.3207	0.0288	0.2058	0.0021	1241	24	1219	9	1207	11
12LN54-1-09	4601	1626	2.83	0.0807	0.0010	2.2997	0.0285	0.2068	0.0021	1215	24	1212	9	1212	11
12LN54-1-10	17205	3531	4.87	0.0792	0.0010	1.7148	0.0211	0.1572	0.0016	1176	24	1014	8	941	9
12LN54-1-11	6366	2169	2.93	0.0826	0.0010	2.4070	0.0292	0.2115	0.0022	1259	24	1245	9	1237	12
12LN54-1-12	2374	1381	1.72	0.0814	0.0010	2.3866	0.0289	0.2128	0.0022	1231	24	1239	9	1244	12
12LN54-1-13	972	1700	0.57	0.0814	0.0010	2.3251	0.0278	0.2072	0.0021	1232	23	1220	8	1214	11
12LN54-1-14	1081	1854	0.58	0.0811	0.0010	2.3516	0.0283	0.2105	0.0022	1223	24	1228	9	1231	12
12LN54-1-15	6788	1416	4.79	0.0817	0.0011	2.3254	0.0310	0.2065	0.0022	1239	26	1220	9	1210	12
12LN54-1-16	9676	2506	3.86	0.0807	0.0010	2.1691	0.0263	0.1951	0.0020	1214	24	1171	8	1149	11
12LN54-1-17	3667	1708	2.15	0.0813	0.0011	2.3503	0.0305	0.2098	0.0022	1229	26	1228	9	1228	12
12LN54-1-18	11515	2407	4.78	0.0820	0.0010	2.0617	0.0253	0.1825	0.0019	1245	24	1136	8	1081	10
12LN54-1-19	6165	2558	2.41	0.0814	0.0010	2.3103	0.0275	0.2060	0.0021	1231	23	1215	8	1208	11
12LN54-1-20	5894	2431	2.42	0.0807	0.0011	1.8894	0.0246	0.1699	0.0018	1214	26	1077	9	1012	10

Note ^{204}Pb has been corrected using [1]; the abbreviative WLP (Western Liaoning Province), EHP (Eastern Hebei Province), and NLP (Northern Liaoning Province) represent the sample locations of the dated mafic dykes within the NCC

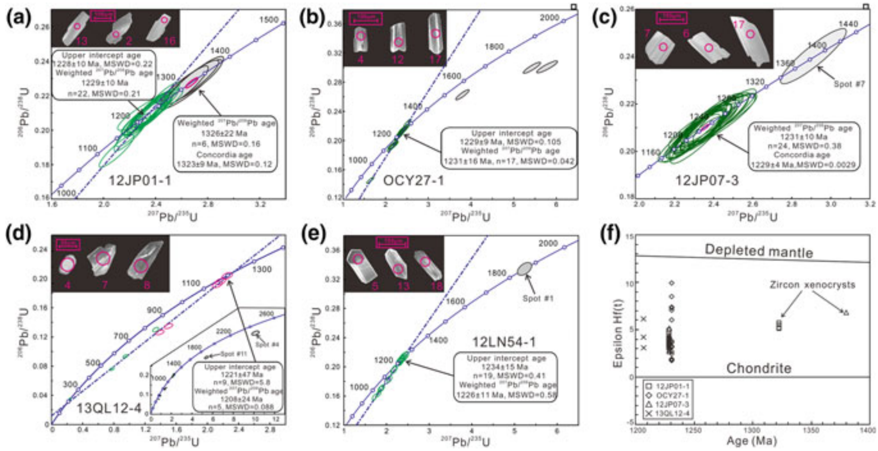

Fig. 4.31 Plots of zircon U–Pb concordia (**a**–**e**) and $\varepsilon_{Hf}(t)$ versus crystallization ages (**f**) for the 1.23 Ga mafic dykes from northern part of the North China Craton

and a few discordant analyses (spots #03, #07, and #10) in sample OCY27-1 (Fig. 4.31a–c), most data plot on or close to the concordia. Twenty-two analyses of sample 12JP01-1 yield apparent $^{207}Pb/^{206}Pb$ ages between 1253 ± 21 Ma and 1213 ± 22 Ma, with an upper intercept age of 1228 ± 10 Ma (MSWD = 0.22) and a weighted mean age of 1229 ± 10 Ma (Fig. 4.31a). Seventeen analyses of sample OCY27-1 show apparent $^{207}Pb/^{206}Pb$ ages ranging from 1249 ± 39 Ma to 1221 ± 31 Ma, yielding an upper intercept age of 1229 ± 9 Ma (MSWD = 0.105) and a weighted mean age of 1231 ± 16 Ma (MSWD = 0.042; Fig. 4.21b). Twenty-four analyses of sample 12JP07-3 yield apparent $^{207}Pb/^{206}Pb$ ages of 1258 ± 21 to 1206 ± 22 Ma, with a weighted mean age of 1231 ± 10 Ma (MSWD = 0.38) and a concordia age of 1229 ± 4 Ma (MSWD = 0.0029) (Fig. 4.31c). Accordingly, the ages of 1229 ± 10, 1231 ± 16, and 1229 ± 4 Ma are considered to be the crystallization ages of these samples.

Sample 13QL12-4 was collected from the Qinglong mafic dyke of EHP, and a total of eleven zircon spots were analyzed (Table 4.8). On the cathodoluminescence images, most zircon grains display bright banded zonings, except for two spots (#4 and #11) that show concentric oscillatory zonings (Fig. 4.31d). On the concordia diagram, spots #4 and #11 plot below the concordia, and give older apparent $^{207}Pb/^{206}Pb$ ages of 2622 ± 24 and 2157 ± 16 Ma, respectively. They could represent xenocrystic zircon grains captured during the ascent and emplacement of the host mafic magmas. The remaining nine analyses define a discordia with an upper intercept age of 1221 ± 47 Ma (MSWD = 5.8), indicating that these grains have experienced different degrees of Pb loss. Five analyses with comparable apparent $^{207}Pb/^{206}Pb$ ages (#1, #3, #5, #7, and #9) yield a weighted mean age of 1208 ± 24 Ma (MSWD = 0.088), which is within error of the upper intercept age.

Accordingly, the age of 1208 ± 24 Ma is considered to be the magmatic crystallization age of sample 13QL12-4, and thus emplacement age of the Qinglong mafic dyke.

A total of twenty zircon spots were analyzed for sample 12LN54-1 from the Qingyuan area of NLP (Table 4.8). On the cathodoluminescence (CL) images, all the zircon grains show banded or weakly broad zonings (Fig. 4.31e). On the concordia diagram, they plot on or close to the concordia. Except for spot #1 with an older apparent $^{207}Pb/^{206}Pb$ age (1860 ± 24 Ma), the remaining analyses yield ages of 1259 ± 24 to 1176 ± 24 Ma. A discordia defined by these isotopic data yields an upper intercept age of 1234 ± 15 Ma (MSWD = 0.41) and a weighted mean $^{207}Pb/^{206}Pb$ age of 1226 ± 11 Ma (MSWD = 0.58) (Fig. 4.31e). Therefore, the age of 1226 ± 11 Ma is considered to be close to the crystallization age of sample 12LN54-1.

The four dated samples (12JP01-1, OCY27-1, 12JP07-3, and 13QL12-4) from Jianping and Qinglong mafic dykes were analyzed for zircon Lu–Hf isotopes (Table 4.9). Excluding the captured zircon grains, the isotopic data from the other grains were calculated at the crystallization ages of the host rocks, and they show positive $\varepsilon_{Hf}(t)$ values of +3.0 to+ 5.0, +1.8 to + 10.0, +2.7 to + 5.2, and +3.1 to + 6.1, respectively (Fig. 4.31f).

All the isotopic data are calculated to the crystallization age of each sample, except for the captured zircons that are corrected to their respective apparent $^{207}Pb/^{206}Pb$ ages. In the main text, only the Lu–Hf isotopic data of magmatic zircons (except for the older captured zircons) are discussed.

Minor mafic dykes reported from other areas of NCC may be contemporaneous with those presented in this study. For example, a suite of NE-trending diabase dykes cutting Archean basement rocks in the Tonghua area of eastern NLP, yield LA-ICP-MS zircon U–Pb isotopic age of 1244 ± 28 Ma [52]. In the southeastern NCC, two NE-trending mafic dykes (massive and medium- to coarse-grained gabbros) in the Linyi area of Western Shandong give a SHRIMP U–Pb age of 1208 ± 20 Ma [55]. Farther northwest in the Yinshan Block, mafic dykes intruded the banded REE ore body and the overlying slates of the Bayan Obo Group. These dykes yield a Sm–Nd isochron age of 1227 ± 60 Ma, albeit with a large error [89].

4.3.3 Whole-Rock Geochemistry

Whole-rock major and trace element data of the ~1.23 Ga mafic dykes are listed in Supplementary Table 4.10, and plotted in Figs. 4.32 and 4.33. Geochemical data of mafic dykes from Tonghua and Yishui areas are compiled for comparison [52, 55]. All the ~1.23 Ga mafic rocks have low SiO_2 (mostly of 44.4–49.9 wt%), and high MgO (3.72–7.92 wt%) contents, with Mg# values (100 Mg/(Mg + Fe total) atomic ratio) of 32.20–56.62 (Table 4.10). In the Zr/TiO_2*0.0001 versus Nb/Y discrimination diagram (Winchester and Floyd [82]; Fig. 4.32a), the samples are classified

Table 4.9 In-situ Lu–Hf isotopes of the dated zircons from the 1.23 Ga mafic dykes in the North China Craton

Sample	Age (Ma)	$^{176}Yb/^{177}Hf$	$^{176}Lu/^{177}Hf$	$^{176}Hf/^{177}Hf$	2σ	$(^{176}Hf/^{177}Hf)_i$	$e_{Hf}(0)$	$e_{Hf}(t)$	T_{DM} (Ma)	$f_{Lu/Hf}$
12JP01-1-01	1229	0.082358	0.002387	0.282196	0.000022	0.282141	−20.4	5.0	1544	−0.93
12JP01-1-02	1323	0.049416	0.001484	0.282122	0.000017	0.282085	−23.0	5.1	1612	−0.96
12JP01-1-03	1229	0.110422	0.003175	0.282203	0.000015	0.282129	−20.1	4.5	1569	−0.90
12JP01-1-04	1323	0.097004	0.002753	0.282157	0.000022	0.282088	−21.8	5.2	1618	−0.92
12JP01-1-05	1323	0.029145	0.000969	0.282120	0.000023	0.282096	−23.1	5.5	1593	−0.97
12JP01-1-06	1229	0.072760	0.002102	0.282154	0.000015	0.282106	−21.8	3.7	1593	−0.94
12JP01-1-07	1323	0.086620	0.002481	0.282164	0.000022	0.282102	−21.5	5.7	1595	−0.93
12JP01-1-08	1229	0.081749	0.002441	0.282151	0.000018	0.282094	−22.0	3.3	1612	−0.93
12JP01-1-09	1229	0.087376	0.002502	0.282144	0.000024	0.282086	−22.2	3.0	1626	−0.92
12JP01-1-10	1229	0.072901	0.002076	0.282165	0.000030	0.282116	−21.5	4.1	1577	−0.94
12JP01-1-11	1229	0.069919	0.002017	0.282143	0.000016	0.282097	−22.2	3.4	1605	−0.94
12JP01-1-12	1229	0.059481	0.001768	0.282158	0.000019	0.282117	−21.7	4.1	1573	−0.95
12JP01-1-13	1229	0.076506	0.002195	0.282167	0.000019	0.282116	−21.4	4.1	1579	−0.93
12JP01-1-14	1229	0.078134	0.002309	0.282146	0.000014	0.282092	−22.1	3.2	1614	−0.93
12JP01-1-15	1229	0.053560	0.001351	0.282146	0.000018	0.282115	−22.1	4.0	1573	−0.96
12JP01-1-16	1229	0.095482	0.002674	0.282163	0.000018	0.282101	−21.5	3.5	1605	−0.92
12JP01-1-17	1229	0.080511	0.002301	0.282170	0.000020	0.282116	−21.3	4.1	1579	−0.93
12JP01-1-18	1229	0.068670	0.001932	0.282152	0.000018	0.282107	−21.9	3.8	1589	−0.94
12JP01-1-19	1229	0.085188	0.002485	0.282152	0.000020	0.282094	−21.9	3.3	1613	−0.93
12JP01-1-20	1229	0.076169	0.001832	0.282156	0.000013	0.282113	−21.8	4.0	1579	−0.94
12JP01-1-21	1229	0.069999	0.001988	0.282179	0.000015	0.282133	−21.0	4.7	1553	−0.94
OCY27-1-01	1231	0.028042	0.000719	0.282297	0.000015	0.282281	−16.8	10.0	1337	−0.98
OCY27-1-02	1231	0.075787	0.002512	0.282109	0.000022	0.282050	−23.5	1.8	1677	−0.92
OCY27-1-03	1231	0.027240	0.000693	0.282222	0.000013	0.282206	−19.4	7.3	1440	−0.98

(continued)

Table 4.9 (continued)

Sample	Age (Ma)	$^{176}Yb/^{177}Hf$	$^{176}Lu/^{177}Hf$	$^{176}Hf/^{177}Hf$	2σ	$(^{176}Hf/^{177}Hf)_i$	$e_{Hf}(0)$	$e_{Hf}(t)$	T_{DM} (Ma)	$f_{Lu/Hf}$
OCY27-1-04	1231	0.052555	0.001769	0.282092	0.000018	0.282051	−24.0	1.8	1667	−0.95
OCY27-1-05	1231	0.073642	0.002377	0.282144	0.000016	0.282089	−22.2	3.2	1619	−0.93
OCY27-1-06	1231	0.122249	0.003500	0.282152	0.000018	0.282071	−21.9	2.5	1659	−0.89
OCY27-1-07	1231	0.087268	0.002802	0.282157	0.000019	0.282092	−21.7	3.3	1619	−0.92
OCY27-1-08	1231	0.082515	0.002564	0.282162	0.000017	0.282102	−21.6	3.6	1602	−0.92
OCY27-1-09	1231	0.079684	0.002483	0.282111	0.000014	0.282054	−23.4	1.9	1672	−0.93
OCY27-1-10	1231	0.017059	0.000492	0.282119	0.000013	0.282108	−23.1	3.8	1574	−0.99
OCY27-1-11	1231	0.099616	0.002809	0.282155	0.000015	0.282090	−21.8	3.2	1622	−0.92
OCY27-1-12	1231	0.100328	0.003066	0.282148	0.000021	0.282077	−22.1	2.7	1645	−0.91
OCY27-1-13	1231	0.013224	0.000291	0.282215	0.000010	0.282208	−19.7	7.4	1435	−0.99
OCY27-1-14	1231	0.052685	0.001307	0.282270	0.000015	0.282240	−17.8	8.5	1397	−0.96
OCY27-1-15	1231	0.049671	0.001401	0.282202	0.000031	0.282169	−20.2	6.0	1496	−0.96
OCY27-1-16	1231	0.035468	0.000874	0.282219	0.000014	0.282199	−19.5	7.1	1451	−0.97
12JP07-3-01	1229	0.079203	0.002341	0.282165	0.000015	0.282111	−21.5	3.9	1588	−0.93
12JP07-3-02	1229	0.083339	0.002538	0.282183	0.000018	0.282124	−20.8	4.4	1570	−0.92
12JP07-3-03	1229	0.072245	0.002151	0.282197	0.000017	0.282147	−20.3	5.2	1534	−0.94
12JP07-3-04	1380	0.044531	0.001427	0.282136	0.000014	0.282099	−22.5	6.9	1590	−0.96
12JP07-3-05	1229	0.079696	0.002355	0.282166	0.000015	0.282112	−21.4	3.9	1587	−0.93
12JP07-3-06	1229	0.092828	0.002745	0.282141	0.000016	0.282077	−22.3	2.7	1640	−0.92
12JP07-3-07	1229	0.089051	0.002632	0.282156	0.000017	0.282095	−21.8	3.3	1614	−0.92
12JP07-3-08	1229	0.103624	0.003068	0.282181	0.000021	0.282110	−20.9	3.8	1597	−0.91
12JP07-3-09	1229	0.077586	0.002314	0.282161	0.000017	0.282107	−21.6	3.7	1593	−0.93
12JP07-3-10	1229	0.060767	0.001785	0.282149	0.000017	0.282107	−22.0	3.8	1587	−0.95
12JP07-3-11	1229	0.102149	0.002991	0.282157	0.000016	0.282088	−21.7	3.1	1628	−0.91

(continued)

Table 4.9 (continued)

Sample	Age (Ma)	$^{176}Yb/^{177}Hf$	$^{176}Lu/^{177}Hf$	$^{176}Hf/^{177}Hf$	2σ	$(^{176}Hf/^{177}Hf)_i$	$e_{Hf}(0)$	$e_{Hf}(t)$	T_{DM} (Ma)	$f_{Lu/Hf}$
12JP07-3-12	1229	0.106815	0.003166	0.282155	0.000031	0.282082	−21.8	2.9	1639	−0.90
12JP07-3-13	1229	0.073720	0.002162	0.282166	0.000014	0.282116	−21.4	4.1	1578	−0.93
12JP07-3-14	1229	0.042286	0.001325	0.282140	0.000017	0.282110	−22.3	3.8	1580	−0.96
12JP07-3-15	1229	0.074836	0.002195	0.282163	0.000019	0.282112	−21.5	3.9	1585	−0.93
12JP07-3-16	1229	0.077388	0.002326	0.282156	0.000015	0.282102	−21.8	3.6	1600	−0.93
12JP07-3-17	1229	0.061994	0.001941	0.282137	0.000016	0.282092	−22.5	3.2	1610	−0.94
12JP07-3-18	1229	0.044364	0.001343	0.282156	0.000019	0.282125	−21.8	4.4	1558	−0.96
12JP07-3-19	1229	0.072664	0.002171	0.282158	0.000020	0.282107	−21.7	3.8	1591	−0.93
13QL12-4-01	1206	0.258267	0.006248	0.282328	0.000028	0.282186	−15.7	6.0	1514	−0.81
13QL12-4-02	1206	0.112971	0.002617	0.282161	0.000024	0.282102	−21.6	3.0	1606	−0.92
13QL12-4-03	1206	0.198231	0.004356	0.282232	0.000029	0.282133	−19.1	4.2	1577	−0.87

Note The present $^{176}Hf/^{177}Hf$ and $^{176}Lu/^{177}Hf$ ratios of chondrite and depleted mantle are 0.282772 and 0.0332, and 0.28325 and 0.0384, respectively [5]; Griffin et al. [21]. $\lambda = 1.867 \times 10^{-11}\ a^{-1}$ (Söderlund et al. 2004)

$\varepsilon_{Hf}(t) = 10000\{[(^{176}Hf/^{177}Hf)_S - (^{176}Lu/^{177}Hf)_S \times (e^{\lambda t} - 1)]/[(^{176}Hf/^{177}Hf)_{CHUR,0} - (^{176}Lu/^{177}Hf)_{CHUR} \times (e^{\lambda t} - 1)] - 1\}$

$T_{DM} = 1/\lambda \times \ln\{1 + [(^{176}Hf/^{177}Hf)_S - (^{176}Hf/^{177}Hf)_{DM}]/[(^{176}Lu/^{177}Hf)_S - (^{176}Lu/^{177}Hf)_{DM}]\}$; $f_{Lu/Hf} = (^{176}Lu/^{177}Hf)_S/(^{176}Lu/^{177}Hf)_{CHUR}$-1

$T^C_{DM} = 1/\lambda \ln\{1 + [(^{176}Hf/^{177}Hf)_{s,t} - (^{176}Hf/^{177}Hf)_{DM,t}]/[(^{176}Lu/^{177}Hf)_c - (^{176}Lu/^{177}Hf)_{DM}]\} + t$

Table 4.10 Whole-rock major (wt%) and trace element (ppm) compositions of the 1.23 Ga mafic dykes from North China Craton

Sample	Jianping (WLP)													
	12JP01–1	12JP01–2	11JP14–1	12JP03–1	12JP04–1	12JP07–1	12JP07–2	12JP07–3	12JP07–4	12JP07–5	12JP08–1	12JP09–1	12JP11–1	OCY27–1
SiO_2	48.0	48.1	49.9	43.8	42.6	41.1	45.4	47.6	44.5	46.5	48.7	43.7	44.9	46.2
Al_2O_3	17.18	17.76	14.57	17.16	16.86	14.86	17.32	17.50	17.70	16.26	19.01	15.28	16.69	13.05
Fe_2O_3T	10.66	9.73	12.95	13.87	13.77	11.17	11.49	10.87	11.83	11.92	7.95	13.79	12.44	16.03
MgO	5.39	4.84	4.92	6.74	7.75	7.36	7.01	5.60	6.75	7.11	4.91	7.92	6.59	6.39
CaO	7.69	7.52	8.42	7.27	5.70	10.15	8.30	7.84	8.69	7.95	8.38	9.15	8.51	9.87
Na_2O	5.15	6.63	2.80	4.22	5.12	2.49	4.17	4.67	4.14	4.02	6.29	3.52	4.50	2.34
K_2O	0.982	0.884	1.040	1.630	0.690	1.250	0.780	0.959	0.758	1.130	0.547	0.450	0.805	0.660
MnO	0.144	0.128	0.188	0.175	0.261	0.149	0.142	0.146	0.136	0.154	0.103	0.157	0.161	0.210
TiO_2	2.16	1.840	2.67	2.71	2.66	2.38	2.82	2.31	3.22	2.63	1.090	3.56	3.08	3.56
P_2O_5	0.465	0.320	0.513	1.470	1.280	0.416	0.491	0.717	0.354	0.525	0.491	0.428	0.465	0.260
LOI	1.910	1.780	1.980	0.560	2.86	8.32	1.710	1.530	1.600	1.460	2.19	1.540	1.600	1.170
Total	99.7	99.6	100.0	99.6	99.6	99.7	99.6	99.7	99.7	99.6	99.7	99.5	99.7	99.7
Mg#	50.04	49.63	42.94	49.05	52.72	56.62	54.72	50.51	53.06	54.16	55.02	53.22	51.20	44.12
Sc	27	21	22	33	33	28	32	29	32	35	14.8	35	32	31
V	247	221	323	259	259	327	344	272	399	330	151	469	357	434
Cr	73	55	107	15	34	70	68	51	64	106	98	55	69	
Co	32	28	42	42	41	34	48	35	50	32	21	51	35	
Ni	36	31	50	40	52	49	50	35	55	53	17.0	86	43	
Rb	26	25	27	77	36	59	25	23	28	48	12.7	12.9	26	16.0
Sr	725	1052	651	550	627	595	705	672	689	670	775	673	705	469
Y	25	21	29	39	38	23	19.8	23	16.3	24	18.5	21	19.6	16.2
Zr	230	212	310	172	178	146	142	178	109	165	133	127	133	132
Nb	29	27	25	14.0	18.3	22	22	23	19.0	22	12.2	23	21	24
Cs	0.611	0.373	0.549	1.67	0.968	2.10	0.340	0.310	0.315	0.267	0.149	0.237	0.425	0.231

(continued)

Table 4.10 (continued)

Sample	Jianping (WLP)													
	12JP01–1	12JP01–2	11JP14–1	12JP03–1	12JP04–1	12JP07–1	12JP07–2	12JP07–3	12JP07–4	12JP07–5	12JP08–1	12JP09–1	12JP11–1	OCY27–1
Ba	424	362	552	1023	702	405	334	428	358	676	240	268	437	307
La	35	30	36	30	28	23	21	29	15.8	25	20	17.6	19.4	16.6
Ce	79	70	77	70	66	54	46	65	37	59	52	43	46	42
Pr	10.0	8.48	10.2	9.56	9.27	6.98	6.22	8.67	4.89	7.61	6.11	5.77	5.98	5.29
Nd	39	32	46	41	39	28	25	36	20	31	25	25	25	25
Sm	7.79	6.43	8.39	8.69	8.52	6.04	5.50	7.10	4.36	6.53	5.23	5.50	5.34	5.39
Eu	2.82	2.54	3.18	3.51	3.11	2.34	2.16	2.63	1.81	2.54	2.18	2.14	2.17	2.04
Gd	7.40	6.15	8.00	8.69	8.46	5.92	5.29	6.85	4.27	6.37	5.13	5.39	5.19	5.47
Tb	1.04	0.866	1.29	1.31	1.29	0.877	0.783	0.960	0.635	0.938	0.742	0.817	0.770	0.778
Dy	4.95	4.08	6.09	6.73	6.64	4.33	3.79	4.77	3.15	4.60	3.56	4.10	3.76	4.06
Ho	0.921	0.768	1.12	1.36	1.35	0.831	0.715	0.900	0.601	0.882	0.673	0.785	0.712	0.729
Er	2.28	1.91	2.74	3.56	3.55	2.09	1.77	2.19	1.49	2.20	1.66	1.96	1.75	1.95
Tm	0.304	0.256	0.429	0.494	0.487	0.273	0.236	0.310	0.204	0.297	0.224	0.265	0.233	0.248
Yb	1.83	1.55	2.66	3.07	3.02	1.63	1.41	1.76	1.21	1.78	1.32	1.59	1.39	1.58
Lu	0.265	0.228	0.338	0.472	0.463	0.242	0.206	0.260	0.177	0.262	0.195	0.234	0.202	0.220
Hf	5.34	4.88	8.58	4.01	4.14	3.61	3.34	4.79	2.70	3.94	3.12	3.17	3.17	3.68
Ta	2.39	1.95	1.79	1.61	1.69	1.57	1.63	1.45	1.50	1.76	0.994	1.79	1.64	1.07
Th	3.35	3.57	3.40	0.869	0.856	2.11	1.70	2.70	1.41	2.22	2.34	1.37	1.67	1.59
U	0.778	0.837	0.733	0.293	0.205	0.393	0.523	0.660	0.314	0.521	0.492	0.283	0.360	0.372
TREE	192	165	203	188	180	137	121	166	95	149	124	113	117	111
Eu*	1.13	1.24	1.19	1.24	1.12	1.20	1.22	1.15	1.28	1.20	1.28	1.20	1.26	1.15
$(La/Sm)_N$	2.89	3.04	2.77	2.21	2.14	2.50	2.42	2.66	2.34	2.52	2.52	2.07	2.35	1.98
$(Gd/Yb)_N$	3.34	3.29	2.49	2.35	2.32	3.01	3.11	3.22	2.93	2.97	3.21	2.81	3.10	2.87
$(La/Yb)_N$	13.68	14.03	9.71	6.95	6.73	10.29	10.53	11.90	9.36	10.28	11.09	7.97	10.05	7.54

(continued)

Table 4.10 (continued)

Sample	Jianping (WLP)													
	12JP01–1	12JP01–2	11JP14–1	12JP03–1	12JP04–1	12JP07–1	12JP07–2	12JP07–3	12JP07–4	12JP07–5	12JP08–1	12JP09–1	12JP11–1	OCY27–1
$(Nb/La)_{PM}$	0.81	0.85	0.66	0.45	0.62	0.89	1.03	0.77	1.16	0.84	0.58	1.26	1.03	1.37
$(Nb/Th)_{PM}$	1.04	0.89	0.87	1.92	2.54	1.22	1.54	1.03	1.61	1.20	0.62	2.00	1.48	1.78

Sample	Jianping (WLP)		Qingyuan (NLP)	Qinglong (EHP)							Tonghua (NLP)	
	13JP03-1	13JP03-2	12LN54-1	13QL12-4	13QL12-5	13QL12-6	13QL12-7	12QL16-1	13QL16-2	13QL16-3	CB16-2	CB16-3
SiO_2	52.9	47.7	47.9	48.8	49.9	47.8	48.6	49.3	47.1	47.3	49.3	49.5
Al_2O_3	10.96	14.55	12.19	15.42	13.91	14.34	14.13	15.22	13.97	14.19	13.10	13.20
Fe_2O_3T	12.41	15.82	14.11	13.76	15.52	13.51	12.95	13.02	14.36	13.04	14.10	13.60
MgO	6.88	4.56	6.86	5.18	3.72	6.51	6.81	6.05	5.90	5.73	4.69	4.59
CaO	9.36	7.79	10.27	8.60	7.22	9.14	8.80	9.47	9.77	9.64	7.81	7.92
Na_2O	3.81	2.30	2.14	2.73	3.58	3.39	3.82	1.88	3.68	5.34	3	2.76
K_2O	0.704	1.258	1.127	1.091	1.398	1.082	0.907	0.959	0.695	0.810	1.430	1.460
MnO	0.232	0.216	0.200	0.180	0.200	0.186	0.183	0.181	0.190	0.190	0.180	0.180
TiO_2	1.370	3.51	3.02	2.41	2.90	2.12	2.01	2.11	2.38	2.04	3.70	3.56
P_2O_5	0.356	0.424	0.456	0.256	0.415	0.213	0.207	0.212	0.197	0.176	0.350	0.350
LOI	0.820	1.630	1.520	1.360	1.060	1.600	1.450	1.480	1.560	1.340	2.2	2.62
Total	99.8	99.8	99.8	99.8	99.8	99.8	99.8	99.8	99.8	99.8	99.9	99.7
Mg#	52.36	36.35	49.06	42.70	32.20	48.83	51.02	47.92	44.85	46.56	39.72	40.07
Sc	42	28	31	33	27	39	38	36	38	37	26	26
V	206	408	281	384	345	365	353	329	439	348	354	364
Cr			201								74	65
Co			39								40	41
Ni			64								17.6	17.6
Rb	7.69	51	34	28	36	25	18.6	27	16.7	19.3	47	43

(continued)

Table 4.10 (continued)

Sample	Jianping (WLP)		Qingyuan (NLP)	Qinglong (EHP)							Tonghua (NLP)	
	13JP03-1	13JP03-2	12LN54-1	13QL12-4	13QL12-5	13QL12-6	13QL12-7	12QL16-1	13QL16-2	13QL16-3	CB16-2	CB16-3
Sr	445	720	626	455	435	412	400	450	444	429	725	679
Y	35	24	18.3	22	30	21	19.7	19.9	19.5	19.8	24	24
Zr	223	170	175	167	256	142	129	140	129	135	197	196
Nb	17.3	21	16.6	15.9	26	13.5	12.5	13.8	12.5	13.2	27	26
Cs	0.096	0.266	1.22	0.374	0.459	0.383	0.216	0.385	0.424	0.409	1.20	1.44
Ba	592	508	618	474	607	272	287	381	259	398	459	415
La	35	27	23	23	40	17.7	16.8	17.2	16.3	16.4	32	30
Ce	84	61	55	53	88	43	40	41	40	40	68	65
Pr	11.0	7.97	7.21	6.91	11.2	5.54	5.24	5.40	5.23	5.14	8.98	8.60
Nd	51	36	34	32	50	26	25	26	25	24	37	35
Sm	10.4	7.11	7.19	6.37	9.45	5.45	5.12	5.25	5.22	5.06	7.81	7.55
Eu	3.34	2.50	3.06	2.14	3.06	1.86	1.75	1.83	1.79	1.79	2.68	2.58
Gd	10.2	6.97	7.07	6.18	8.97	5.42	5.13	5.22	5.20	5.07	6.62	6.35
Tb	1.40	0.939	0.910	0.851	1.17	0.763	0.718	0.722	0.712	0.714	0.920	0.890
Dy	7.53	4.99	4.53	4.57	6.20	4.22	4.02	4.04	3.99	4.04	5.15	4.94
Ho	1.40	0.928	0.804	0.871	1.160	0.816	0.780	0.778	0.770	0.782	0.970	0.910
Er	3.60	2.36	2.20	2.27	3.03	2.22	2.07	2.06	2.07	2.10	2.22	2.12
Tm	0.504	0.333	0.264	0.334	0.437	0.319	0.300	0.307	0.301	0.313	0.320	0.290
Yb	3.09	2.04	1.69	2.07	2.71	2.02	1.89	1.94	1.90	1.98	1.77	1.77
Lu	0.428	0.282	0.238	0.291	0.373	0.281	0.261	0.260	0.254	0.265	0.270	0.260
Hf	6.58	4.81	4.56	4.70	7.19	4.05	3.79	4.08	3.81	3.94	5.11	5.02
Ta	1.16	1.37	1.06	1.03	1.59	0.916	0.768	0.816	0.749	0.785	1.79	1.76
Th	3.51	2.36	2.16	2.12	3.69	1.65	1.56	1.67	1.53	1.55	5.05	4.86
U	0.705	0.470	0.506	0.499	0.851	0.387	0.348	0.365	0.335	0.338	1.23	1.22

(continued)

Table 4.10 (continued)

Sample	Jianping (WLP)		Qingyuan (NLP)	Qinglong (EHP)							Tonghua (NLP)	
	13JP03-1	13JP03-2	12LN54-1	13QL12-4	13QL12-5	13QL12-6	13QL12-7	12QL16-1	13QL16-2	13QL16-3	CB16-2	CB16-3
TREE	222	161	147	141	226	116	109	112	109	108	174	167
Eu*	0.99	1.08	1.31	1.04	1.02	1.05	1.05	1.07	1.05	1.08	1.14	1.14
$(La/Sm)_N$	2.17	2.48	2.10	2.32	2.71	2.10	2.12	2.12	2.02	2.09	2.63	2.59
$(Gd/Yb)_N$	2.73	2.82	3.47	2.47	2.73	2.23	2.24	2.22	2.26	2.12	3.09	2.97
$(La/Yb)_N$	8.13	9.61	9.96	7.94	10.50	6.30	6.36	6.37	6.17	5.96	12.89	12.28
$(Nb/La)_{PM}$	0.48	0.75	0.68	0.67	0.62	0.74	0.72	0.77	0.74	0.78	0.80	0.84
$(Nb/Th)_{PM}$	0.59	1.08	0.91	0.90	0.83	0.98	0.95	0.99	0.97	1.02	0.63	0.65

Sample	Yishui (WSP)											
	08YS-61	08YS-62	08YS-63	08YS-65	08YS-67	08YS-68	08YS-69	08YS-71	08YS-123	08YS-124	08YS-125	08YS-126
SiO_2	46.4	46.3	46.2	46.7	45.6	46.7	46.1	46.3	45.3	44.4	45.6	45.4
Al_2O_3	12.64	12.47	12.62	12.87	11.90	13.10	12.43	13.14	15.55	14.16	15.01	14.87
Fe_2O_3T	16.72	16.83	16.63	16.38	18.07	16.23	17.02	16.26	15.82	17.22	15.56	16.02
MgO	6.19	6.25	6.13	6.16	6.45	5.97	6.22	5.56	4.85	5.32	5.12	4.78
CaO	9.99	10.04	9.98	9.99	9.87	9.94	9.99	9.83	6.74	7.24	6.89	6.81
Na_2O	2.34	2.28	2.68	2.32	2.17	2.37	2.36	2.39	3.21	3.08	3.30	3.14
K_2O	0.670	0.670	0.680	0.680	0.690	0.680	0.660	0.510	2.21	1.830	2.05	2.48
MnO	0.210	0.220	0.210	0.210	0.230	0.210	0.230	0.220	0.200	0.240	0.210	0.210
TiO_2	3.31	3.49	3.30	3.12	3.56	3.18	3.47	3.38	2.93	3.21	2.94	3.04
P_2O_5	0.410	0.410	0.390	0.400	0.390	0.400	0.390	0.450	0.670	0.700	0.690	0.760
LOI	0.620	0.620	0.710	0.710	0.630	0.800	0.630	1.510	2.12	2.18	2.19	2.05
Total	99.6	99.6	99.6	99.5	99.6	99.6	99.6	99.6	99.6	99.6	99.6	99.6
Mg#	42.31	42.38	42.20	42.69	41.42	42.15	41.99	40.38	37.78	37.96	39.46	37.15
Sc	36	36	36	35	38	35	38	34	21	25	22	23
V	364	353	361	349	413	353	383	348	290	304	270	266
Cr	142	137	234	133	140	144	150	110	71	84	77	82
Co	61	61	65	60	69	61	66	60	57	58	51	50

(continued)

Table 4.10 (continued)

Sample	Yishui (WSP)											
	08YS-61	08YS-62	08YS-63	08YS-65	08YS-67	08YS-68	08YS-69	08YS-71	08YS-123	08YS-124	08YS-125	08YS-126
Ni	71	69	107	65	83	69	78	60	79	85	71	75
Rb	18.0	18.0	19.0	18.0	19.0	19.0	19.0	14.0	70	56	64	73
Sr	524	511	530	526	493	553	535	539	487	453	464	464
Y	24	24	24	24	24	24	25	26	30	31	31	33
Zr	215	219	222	211	219	214	224	230	149	143	144	151
Nb	19.2	19.5	19.3	18.1	20	18.4	20	21	11.0	10.5	10.6	11.3
Cs												
Ba	380	379	388	387	384	393	393	337	926	911	926	1030
La	24	23	24	24	24	24	24	27	19.2	19.1	19.2	20
Ce	54	54	53	54	55	54	55	60	49	50	49	52
Pr	6.44	6.37	6.44	6.37	6.51	6.44	6.70	7.11	6.44	6.46	6.40	6.74
Nd	31	31	30	30	31	30	32	33	30	30	30	32
Sm	6.04	5.97	5.78	5.97	6.15	5.87	6.21	6.50	6.92	7.11	6.84	7.59
Eu	2.34	2.31	2.33	2.27	2.34	2.39	2.44	2.50	2.54	2.58	2.54	2.71
Gd	4.95	4.89	4.97	4.76	4.77	4.96	4.94	5.11	6.02	6.27	6.08	6.58
Tb	0.810	0.800	0.800	0.790	0.820	0.800	0.830	0.840	1.06	1.13	1.08	1.16
Dy	4.69	4.56	4.52	4.52	4.78	4.52	4.73	4.75	5.74	6.22	5.88	6.33
Ho	0.870	0.850	0.850	0.830	0.870	0.850	0.880	0.900	1.24	1.29	1.29	1.36
Er	2.19	2.24	2.26	2.21	2.32	2.24	2.36	2.39	3.26	3.34	3.35	3.55
Tm	0.290	0.300	0.290	0.280	0.310	0.290	0.300	0.310	0.440	0.470	0.460	0.470
Yb	1.92	1.89	1.82	1.79	1.94	1.79	1.96	1.99	2.77	3.05	2.95	3.01
Lu	0.280	0.270	0.280	0.270	0.280	0.270	0.290	0.280	0.410	0.440	0.450	0.470
Hf	4.75	4.86	4.85	4.74	4.96	4.78	5.00	5.23	4.13	4.16	4.36	4.63
Ta	1.27	1.28	1.26	1.19	1.28	1.19	1.34	1.32	0.730	0.730	0.730	0.800

(continued)

Table 4.10 (continued)

Sample	Yishui (WSP)											
	08YS-61	08YS-62	08YS-63	08YS-65	08YS-67	08YS-68	08YS-69	08YS-71	08YS-123	08YS-124	08YS-125	08YS-126
Th	1.61	1.52	1.52	1.59	1.62	1.56	1.61	1.79	0.900	0.880	0.950	0.970
U	0.350	0.370	0.360	0.370	0.370	0.360	0.380	0.380	0.250	0.240	0.250	0.240
TREE	139	138	137	138	140	139	143	153	136	137	135	144
Eu*	1.31	1.31	1.33	1.30	1.32	1.35	1.35	1.33	1.20	1.18	1.20	1.17
$(La/Sm)_N$	2.52	2.52	2.64	2.60	2.49	2.63	2.54	2.64	1.79	1.73	1.81	1.71
$(Gd/Yb)_N$	2.13	2.14	2.26	2.20	2.03	2.29	2.09	2.12	1.80	1.70	1.70	1.81
$(La/Yb)_N$	8.82	8.84	9.30	9.62	8.76	9.58	8.93	9.59	4.97	4.49	4.67	4.79
$(Nb/La)_{PM}$	0.78	0.81	0.79	0.73	0.82	0.74	0.80	0.76	0.55	0.53	0.53	0.54
$(Nb/Th)_{PM}$	1.42	1.53	1.51	1.36	1.48	1.41	1.50	1.39	1.46	1.42	1.33	1.39

Note LOI, loss on ignition; Mg# = 100 Mg/(Mg + Fe_{total}) in atomic ratio; TREE, total rare earth elements
$Eu_N/Eu_N^* = Eu_N/SQRT(Sm_N*Gd_N)$; subscript N-chondrite normalized value; subscript PM-primitive mantle normalized value
The abbreviative WLP (Western Liaoning Province), EHP (Eastern Hebei Province), NLP (Northern Liaoning Province), and WSP (Western Shandong Province) represent the locations of analyzed mafic dykes within the NCC. Also shown are the cited data for Tonghua dykes of NLP and Yishui dykes of WSP [52, 55]. Element contents in the vacant positions were not analyzed

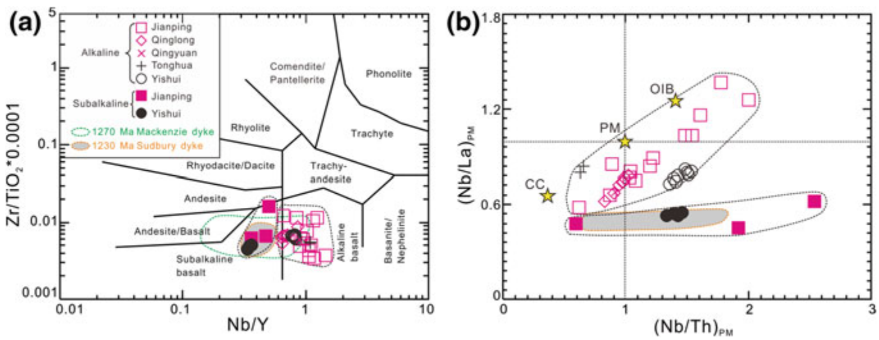

Fig. 4.32 Geochemical characteristics of the 1.23 Ga mafic dykes from the NCC. **a** Zr/TiO_2*0.0001 versus Nb/Y diagram [82], with the ∼1.23 Ga mafic dykes in the NCC subdivided into an alkaline gabbro group and a subalkaline gabbro group. **b** $(Nb/La)_{PM}$ versus $(Nb/Th)_{PM}$ diagram, showing that the alkaline and subalkaline samples defined two distinct variation trends. Also shown for comparison are the geochemical data of the 1.27 Ga Mackenzie (no data for element Th) and 1.23 Ga Sudbury mafic dykes from Laurentia, as well as average continental crust (CC), primitive mantle (PM), and ocean island basalt (OIB) [3, 63, 66, 67]

into alkaline and subalkaline groups. The alkaline rocks have higher $(Nb/La)_{PM}$ ratios of 0.58–1.37, and the $(Nb/La)_{PM}$ and $(Nb/Th)_{PM}$ values show a well-defined positive correlation, extending from OIB-like to CC (continental crust)-like values (Fig. 4.32b). In comparison, the subalkaline rocks exhibit consistently lower $(Nb/La)_{PM}$ values of 0.45–0.62 but a large extent of $(Nb/Th)_{PM}$ values (0.59–2.54). In the chondrite-normalized rare earth element (REE) diagrams (Fig. 4.33a and c), the alkaline rocks have strongly fractionated patterns, and show high $(La/Yb)_N$ and $(Gd/Yb)_N$ values of 5.96–14.03 and 1.70–3.34, respectively, with slightly positive Eu anomalies (Eu_N/Eu_N* = 1.02–1.35). The subalkaline rocks have less fractionated REE patterns, and show lower $(La/Yb)_N$ and $(Gd/Yb)_N$ values from 4.49 to 8.13 and from 1.70 to 2.73, respectively, with slightly negative to positive Eu anomalies (Eu_N/Eu_N* = 0.99–1.24). The REE fractionation degree of alkaline rocks is evidently higher than the ∼ 1.27 Ga Mackenzie mafic dykes from the Canadian Shield, whereas that of the subalkaline rocks overlaps or is slightly higher than the latter (Fig. 4.33a and c; [3]). The primitive mantle (PM)-normalized multi-element patterns of all the samples show enrichment in large ion lithophile elements (LILEs), and slightly positive to evidently negative Nb and Ta anomalies, with slightly positive to no Zr, Hf, and Ti anomalies (Fig. 4.33b and d). In the La/Sm versus La binary diagram (Fig. 4.33e), all the samples, including both alkaline and subalkaline rocks, have nearly consistent La/Sm ratios. However, samples of the two groups can be separated in the Th/Yb versus Nb/Yb diagram [50], i.e., most subalkaline rocks cluster around the E-MORB field, whereas the alkaline ones show close affinities to OIBs (Fig. 4.33f).

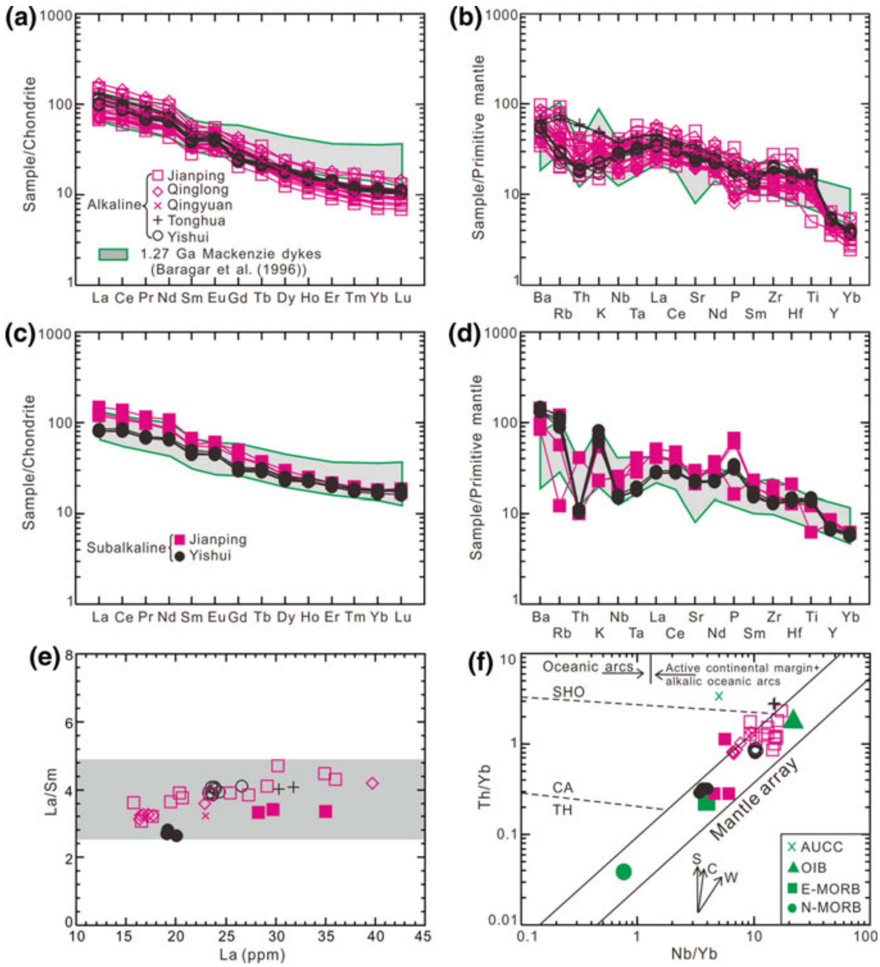

Fig. 4.33 Trace element geochemical features of the 1.23 Ga mafic dykes from the NCC. Chondrite-normalized REE patterns and primitive mantle-normalized multi-element patterns for the 1.23 Ga alkaline gabbros (**a** and **b**) and the subalkaline gabbros (**c** and **d**). The chondrite, primitive mantle, and OIB values are after Sun and McDonough [66]. Also shown for comparison are the trace element patterns of the 1.27 Ga Mackenzie mafic dykes from Laurentia [3]. **e** La/Sm versus La binary diagram. **f** Th/Yb versus Nb/Yb diagram [50]

4.3.4 Discussion

4.3.4.1 ~1.23 Ga Mafic Dykes Identified in the North China Craton

Our new zircon U–Pb geochronological data of mafic dykes from the WLP, EHP, and NLP of North China Craton show that they were emplaced at 1229 ± 10, 1231 ± 16, 1229 ± 4, 1208 ± 24, and 1226 ± 11 Ma, respectively. Minor mafic dykes from three other localities of NCC (Linyi, Tonghua, and Bayan Obo) yield a SHRIMP U–Pb age of 1208 ± 20 Ma, a LA-ICPMS U–Pb age of 1244 ± 28 Ma, and a Sm–Nd isochron age of 1227 ± 60 Ma [52, 55, 89] (the Sm–Nd isochron age needs further verification). These ages are within error consistent with each other. Combined with similar geochemical features and petrogenetic processes (as discussed below), as well as similar field occurrences, we propose that these mafic dykes were emplaced synchronously at ~1.23 Ga, and are widely distributed across the Eastern Block of NCC. It is generally difficult to assess the original volume of mafic magmatism due to intense erosion. Nonetheless, these mafic dykes of North China Craton represent a regionally extensive and short-lived magmatic event at ~1.23 Ga. They extend across the NCC for over 1600 km from Tonghua to Bayan Obo and ~800 km from Jianping to Linyi, with an inferred distribution area of $\sim 0.6 \times 10^6$ km^2 (Fig. 4.34). Therefore, these ~1.23 Ga mafic dykes might represent a Mesoproterozoic large igneous province (LIP) triggered possibly by a mantle plume, similar to other LIPs elsewhere in the world (e.g., Mackenzie magmatic event; Bryan and Ernst 2006).

Three major geometric types of mafic dyke swarms (fanning, linear, and arcuate) have been previously recognized, and are largely controlled by the distance from the plume center as well as the stress condition of the distal plate boundary [16]. It is common to see the transition from proximal radiating mafic dykes (near the plume center) to distal subparallel portions, such as the ~1.27 Ga Mackenzie mafic

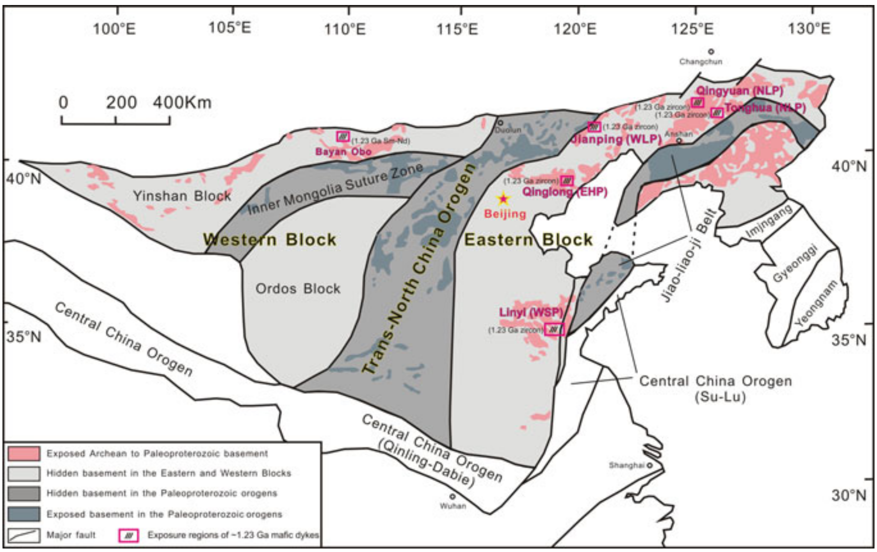

Fig. 4.34 Tectonic subdivision of the crystalline basement of the NCC and the distribution of ~1.23 Ga mafic dykes throughout the NCC (mafic dykes from Linyi, Tonghua, and Bayan Obo are cited from Peng et al. [52, 55], and Yang et al. 2013, respectively.)

dyke swarms, where the subparallel portions extend for thousands of kilometers [7]. With respect to the ~1.23 Ga mafic dykes of NCC, it is currently difficult to reconstruct the specific location of the plume center due to their discontinuous distribution patterns and the absence of coeval layered intrusions and flood basalts. However, on the basis of the large area extent (craton-scale) and almost subparallel patterns (broadly NE-SW trend), it is inferred that the plume center for these ~1.23 Ga mafic dykes might have been located outboard of the NCC, with the NCC dyke swarms acting as the distal portions of a larger dyke swarms. This model needs to be further improved when more contemporaneous mafic dykes are recognized across the NCC and in other ancient cratons.

4.3.4.2 Nature of the Mantle Sources and Petrogenesis

The mafic rocks in this study have low SiO_2 contents and high MgO, with Mg# values (100 Mg/(Mg + Fetotal) atomic ratio) of 56.62–32.20 (Table 4.10). The moderate to low Mg# values indicate that these rocks are the products of fractionation from a primitive mantle magma [17], although a small amount of older xenocrystic zircons points to minor crustal contamination (Fig. 4.31).

The alkaline mafic rocks have generally OIB-like trace element patterns, with $(Nb/La)_{PM}$ ratios ranging between 0.58 and 1.37 (Figs. 4.32, 4.33). The $(Nb/La)_{PM}$ and $(Nb/Th)_{PM}$ values of these samples show a well-defined positive correlation, extending from OIB-like to CC-like values (Fig. 4.32b). Considering the positive zircon $\varepsilon_{Hf}(t)$ values (dated samples are all alkaline samples), the high $(Nb/La)_{PM}$ (>1) samples may be derived from a depleted asthenospheric mantle source [4, 76]. On the other hand, the alkaline samples with lower $(Nb/La)_{PM}$ (<1) values could be ascribed to either crustal contamination or the involvement of a lithospheric mantle component. Considering the mafic compositions (low SiO_2 and high MgO contents), as well as high LREEs (light REEs) and LILE contents, the low $(Nb/La)_{PM}$ alkaline samples were most likely produced by mixing of magmas derived from both asthenospheric and lithospheric mantle sources [14, 67]. The subalkaline samples have comparable geochemical features with ~1.23 Ga Sudbury mafic dykes along the southern Canadian Shield, and they exhibit consistently lower $(Nb/La)_{PM}$ values of 0.62–0.45, defining a horizontal trend ([63], Fig. 4.32b). Though La/Sm ratios similar to the alkaline equivalents, most subalkaline rocks cluster around the E-MORB field, whereas the alkaline rocks show close affinities to OIBs in the Th/Yb versus Nb/Yb diagram (Fig. 4.33e–f), implying that rocks of two groups were derived from distinct mantle sources. As indicated by the negative $\varepsilon_{Nd}(t)$ values (−6.3 to −5.7) of the Yishui subalkaline gabbros [55], mafic compositions, negative Nb and Ta anomalies and less fractionated trace element patterns, the subalkaline rocks could have been produced by the partial melting of a subduction-modified enriched lithospheric mantle source [14].

Samples of the ~1.23 Ga mafic dykes in this study show more fractionated chondrite-normalized REE patterns than the giant ~1.27 Ga Mackenzie mafic dykes from the Canadian Shield (Fig. 4.33a and c), suggesting their derivation from a deeper mantle source [3]. In the $(Sm/Yb)_N$ versus $(La/Sm)_N$ diagram (not shown), both the alkaline and subalkaline samples can be modeled by the partial melting of a mantle source with ~2% garnet [32]. However, the degree of partial melting in the former case (1–3%) is lower than that of the latter (3–10%), implying that the partial melting of both the asthenospheric and lithospheric mantle sources occurred at a similar mantle depth. In this case, a strong upwelling event of the asthenospheric mantle beneath the NCC is implied at ~1.23 Ga. Combined with our recent studies of the ~1.67–1.62 Ga Pinggu volcanic rocks, we propose that the ancient lithospheric mantle of NCC witnessed at least two episodes of intense erosion by the upwelling asthenospheric mantle during Paleo- to Mesoproterozoic eras.

4.3.5 Summary

(1) New LA-ICPMS zircon U–Pb isotopic chronological data reveal a suite of ~1.23 Ga mafic dykes in Western Liaoning, Eastern Hebei, and North Liaoning of the North China Craton. Integrated with minor coeval mafic dykes in other parts of the NCC, we propose that a regionally extensive and short-lived magmatic event occurred at ~1.23 Ga within the NCC, covering an area of $\sim 0.6 \times 10^6$ km^2, representing a Mesoproterozoic large igneous province possibly triggered by a mantle plume.

(2) Samples of the 1.23 Ga mafic dykes can be geochemically classified into both alkaline and subalkaline groups. The parental magma of the alkaline group may have been derived from low degree partial melting of a depleted asthenospheric mantle, with limited involvement of a lithospheric mantle component, whereas the subalkaline group can be modeled by slightly higher degrees of partial melting of a subduction-modified enriched lithospheric mantle.

4.4 Paleo- to Mesoproterozoic Sequence of Geological Events and Crust-Mantle Geodynamics

4.4.1 Paleo- to Mesoproterozoic Geological Events of Western Liaoning-Northeastern Hebei Provinces

LA-ICPMS zircon U–Pb isotopic dating data reveal that the Jianping diorite-monzonite-syenite suite (JDMSS) of Western Liaoning formed during 1721–1696 Ma (Figs. 4.6 and 4.8, 4.9). The magnetite diorites and clinopyroxene monzonites represent early magmatic episode (~1720 Ma), whereas syenites and quartz syenites emplaced later at ~1715–1696 Ma. To the east of JDMSS suite, a ~1753–1680 Ma anorthosite-mangerite-alkali granitoid-rapakivi granite suite (AMGRS) was developed [91]. This magmatic suite includes the Wenquan A-type granites, Lanying-Changshaoying-Gubeikou anorthosite-alkali granitoid plutons, mafic dykes, Miyun rapakivi granites, and Damiao anorthosite complex (Fig. 1.2; [31, 54, 88, 91, 94]). The JDMSS and the AMGRS suite constitute a huge ~500 km late Paleoproterozoic (~1750–1680 Ma) magmatic belt along the middle to east segments of the northern margin of North China Craton. This magmatic belt is slightly younger than the late Paleoproterozoic post-collisional magmatic events along the Trans-North China Orogen, i.e., the ~1800 Ma Luyashan charnockites, Yunzhongshan and Dacaoping granites, and ~1780 Ma mafic dykes and Xiong'er volcanic rocks [26, 53, 73, 95]. Within the Yanliao rift, some ~1671–1625 Ma K-rich volcanic rocks occur interlayered with sedimentary rocks of the Tuanshanzi and Dahongyu Formations [79]. Then, the North China Craton experienced a prolonged period of tectonic quiescence [39]. However, intense ~1230 Ma mafic dykes were emplaced across the North China Craton, especially in the Eastern Block, with an inferred exposure region of ~0.6×10^6 km^2. These mafic dykes represent the most important Mesoproterozoic teconothermal events in the North China Craton, which could be ascribed to the final breakoff of Paleo- to Mesoproterozoic Columbia supercontinent [80].

4.4.2 *Late Paleoproterozoic Geodynamic Settings*

Alkaline igneous rocks worldwide are volumetrically minor, but they occur within a variety of geodynamic settings including continental rifts [51], intra-oceanic or continental intraplate settings related to mantle plumes [43, 44], back-arc extension [45], and post-collisional or post-orogenic settings [71]. The JDMSS samples are massive in structure (Figs. 4.2, 4.3), and they have relatively high values of alkalis in the TAS and K_2O versus SiO_2 classification diagrams (Fig. 4.4a, b), which were unlikely formed under a continental margin arc setting. The following lines of evidence indicate that they could have been generated within a post-collisional setting:

(1) The JDMSS samples show a continuous geochemical variation, and lack apparent silica gap, which are incompatible with a continental rift setting. Furthermore, there are no contemporaneous volcanic rock series or sedimentary sequences that indicate a rift environment along the northwestern margin of the Eastern Block.
(2) The subduction-related geochemical features (i.e., negative Nb, Ta, and Ti anomalies) and overall subchondritic zircon $\varepsilon_{Hf}(t)$ values (Figs. 4.4 and 4.7) are consistent with a derivation from the partial melting of an enriched SCLM. There are no records of mantle plume-related magmatic events, e.g., continental flood basalts, mafic dyke swarms (with OIB-like geochemical features), and high magnesium basalts [58, 85, 97].
(3) In a post-orogenic setting, the strong upwelling of asthenospheric mantle may lead to the partial melting of overlying lithospheric components as well as the

asthenospheric mantle itself [6]. All the JDMSS samples have negative zircon $\varepsilon_{Hf}(t)$ values, arguing against the involvement of a depleted asthenospheric mantle component. Therefore, it is impossible to link the genesis of the JDMSS to a post-orogenic setting.

As discussed by Bonin [6], medium-K to high-K magmatic rocks (including shoshonitic to ultrapotassic series) are commonly generated in a post-collisional setting, where they form as a result of partial melting of a phlogopite or amphibole-bearing lithospheric mantle. Similarly, the parental magma of the JDMSS, with ages of ~1721–1696 Ma, was derived from the partial melting of an amphibole-bearing subcontinental lithospheric mantle, which was later than the proposed collision between the Eastern Block and Western Block that formed the N-S trending TNCO (~1.85 Ga; [22, 23, 39, 92, 96]), or the E-W trending Inner Mongolia-Northern Hebei Orogen along the northern margin of the NCC (~1.90–1.85 Ga, [34]). Accordingly, the JDMSS emplaced probably in a post-collisional setting following the final amalgamation of the North China Craton.

With respect to the K-rich volcanic rocks in the Tuanshanzi and Dahongyu Formations, they were mainly derived from an OIB-like depleted asthenospheric mantle, and a strong upwelling event of the asthenospheric mantle is indicated. Based mostly on the OIB-like trace element patterns, Hu et al. [29] proposed a mantle plume setting for the generation of these volcanic rocks and formation of the Yanliao rift. In general, crustal doming and intense volcanism (e.g., continental flood basalts, picrites, and mafic-ultramafic complexes) occur during the early evolution stage of a plume-induced continental rift, and the graben formation and sedimentation occur at a later stage [9, 46, 87]. In addition, continental flood basalts are commonly tholeiitic in composition with less proportion of alkaline basalts [65, 85, 87]. Volcanic rocks of the Changcheng Group are mostly alkaline rocks with depleted isotopic features, and high MgO rocks (i.e., picrites or high-Mg basalts) characteristic of derivation from a mantle plume are absent (Figs. 4.19 and 4.20b). On the other hand, these volcanic rocks erupted later than the initiation of Yanliao rift, with thick sedimentary sequences in the underlying Changzhougou and Chuanlinggou Formations. Furthermore, the parental magma of these volcanic rocks were produced by the partial melting of lherzolites with <4% garnet, corresponding to a shallow melting depth (Fig. 4.24d). The above arguments, when combined with the limited eruption scale (Fig. 4.12), indicate that a mantle plume model cannot account for the generation of the Yanliao rift and eruption of the K-rich volcanic rocks. The preservation of huge sedimentary sequences in the absence of any major deformation in the Changcheng Group also argues against an arc setting. Alternatively, the temporal continuity of the ~1671–1625 Ma Pinggu volcanic rocks and early ~1780–1680 Ma plutonic rocks in the NCC suggest that they could belong to the same orogenic system. Considering the rapid transition of magma sources from an enriched lithospheric mantle (~1780–1680 Ma) to a depleted asthenospheric mantle (~1671–1625 Ma), a post-orogenic setting driven by the delamination of continental lithosphere is proposed for the initiation of Yanliao rift and generation of the Pinggu K-rich volcanic rocks.

Accordingly, the North China Craton experienced intense extension-related magmatism following the final amalgamation of basement blocks, and the voluminous ∼1780–1680 Ma plutonic rocks and ∼1671–1625 Ma Pinggu volcanic rocks are suggested to have been generated under a post-collisional and a post-orogenic setting, respectively.

4.4.3 Mesoproterozoic Geodynamic Setting

Following the prolonged tectonic quiescence period during the early to middle Mesoproterozoic, the NCC witnessed voluminous emplacement of mafic dykes at ∼1.23 Ga [80]. Apart from the newly-identified ∼1.23 Ga mafic dykes in the NCC, the Sudbury dyke swarm in southern Laurentia represents another major 1.23 Ga dyke swarm, although on a relatively smaller scale (∼0.03×10^6 km^2, [63]). The northwest-trending Sudbury dykes are 30–90 m in width, and display a typical gabbro-diabase texture. They show low Nb/Y (<0.52) and $(Nb/La)_{PM}$ (<0.54), as well as moderate $(La/Yb)_N$ (>5.4) values, and a lithospheric mantle source was proposed (Fig. 4.32; [63]). Although no available isotopic data for the Sudbury dykes, the field occurrence, geochemical feature, and age correlate well with the subalkaline equivalents in the NCC, which may also include the Seal Lake younger gabbros (1224 Ma) in the southeast Laurentia [61].

Globally, ∼1.27–1.21 Ga mafic-ultramafic magmatism is well documented in Laurentia, Baltica, and São Francisco, and now the NCC. These can be grouped into three episodes at ∼1.27–1.26, ∼1.25, and ∼1.23–1.21 Ga (Fig. 4.35a). The oldest phase is mainly distributed across the Canadian Shield, with minor occurrence in southern Greenland and southwestern Baltica [3, 64]. In the northern to central Laurentia, the Mackenzie radiating dyke swarm, Coppermine River flood basalts, and Muskox layered intrusion show a large exposure region and eruption volume, radial flow pattern, and short eruption duration, implying a mantle plume origin [3]. The ∼1.25 Ga magmatic episode is poorly developed, and is mainly distributed in the southeastern Canadian Shield, as represented by the older phase of Seal Lake gabbros, Mealy dykes, and possibly the Strange Lake complex (∼1.24 Ga), and minor dykes in Baltica [20, 48, 61, 64]. ∼1.23–1.21 Ga magmatic units are widely distributed, and include the Sudbury dykes and the younger phase of Seal Lake gabbros of southern Laurentia, mafic dykes in the NCC, Protogine Zone dolerites of Baltica, Marnda Moorn dyke swarm of Australia, and the upper Niquelandia layered complex of São Francisco (Fig. 4.35b). A back-arc tectonic setting was previously assigned to the 1.23 Ga Sudbury dykes [63]. However, there is no contemporaneous arc magmatism or ophiolite fragments. The massive structure and the lack of metamorphism in the exposure region of these mafic dykes argue against the opening and subsequent orogeny of the Elzevir back-arc basin. Alternatively, the ∼1.23 Ga Sudbury dykes and the younger phase of Seal Lake gabbros might represent the missing links to the large-scale ∼1.23 Ga

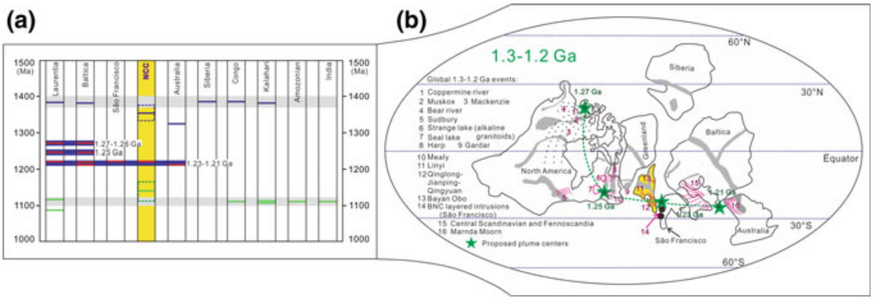

Fig. 4.35 Spatial and temporal distribution of global ~1.38–1.10 Ga mafic dykes and Columbia reconstruction: distribution of ~1.38–1.10 Ga mafic dykes in ancient cratons (**a**), showing that worldwide 1.27–1.21 Ga mafic dykes and intrusions can be grouped into three major episodes of 1.27–1.26 Ga, 1.25 Ga, and 1.23–1.21 Ga. **b** Reconstruction of Columbia supercontinent at 1.3–1.2 Ga based on the temporal and spatial distribution of mafic-ultramafic rocks of the three magmatic episodes and the defined Mesoproterozoic (1.27–1.21 Ga) hotspot track (marked by green stars and dotted line). The numbers correspond to the magmatic events listed at left. See the text for detailed description of the model [80]

mafic dykes across North China Craton. Together with the São Francisco layered intrusions, they may represent magmatic products of the same ~1.23 Ga mantle plume event.

References

1. Anderson T (2002) Correlation of common lead in U–Pb analyses that do not report 204Pb. Chem Geol 192: 59–79
2. Arth JG (1976) Behavior of trace-elements during magmatic processes-summary of theoretical models and their applications. J Res US Geological Survey 4:41–47
3. Baragar WRA, Ernst RE, Hulbert L, Peterson T (1996) Longitudinal petrochemical variation in the Mackenzie dyke swarm, northwestern Canadian Shield. J Petrol 37:317–359
4. Bennett VC (2003) Compositional Evolution of the Mantle. Treatise on Geochemistry, Volume 2. Editor: Richard W. Carlson. Executive Editors: Holland HD, Turekian KK, pp 568. ISBN 0-08-043751-6. Elsevier, p 493–519
5. Blichert-Toft J, Albarède F (1997) The Lu–Hf geochemistry of chondrites and the evolution of the mantle-crust system. Earth Planet Sci Lett 148:243–258
6. Bonin B (2004) Do coeval mafic and felsic magmas in post-collisional to within-plate regimes necessarily imply two contrasting, mantle and crustal, sources? A review. Lithos 78:1–24
7. Bryan SE, Ernst RE (2008) Revised definition of large igneous provinces (LIPs). Earth Sci Rev 86:175–202
8. Chakrabarti R, Basu AR, Santo AP, Tedesco D, Vaselli O (2009) Isotopic and geochemical evidence for a heterogeneous mantle plume origin of the Virunga volcanics, Western rift, East Africa Rift system. Chem Geol 259:273–289
9. Chung SL, Jahn BM (1995) Plume-lithosphere interaction in generation of the Emeishan flood basalts at the Permian-Triassic boundary. Geology 23:889–892
10. Condie KC (2001) Mantle plumes and their record in Earth history. Cambridge University Press, Cambridge, p 305

11. Corfu F, Hanchar JM, Hoskin PWO, Kinny P (2003) Atlas of zircon textures. In: Hanchar JM, Hoskin PWO (eds) Zircon, 53. Mineralogical Society of America Reviews in Mineralogy and Geochemistry, pp 469–500
12. Dasgupta R, Hirschmann MM, Smith ND (2007) Partial melting experiments of peridotite $+CO_2$ at 3GPa and genesis of alkaline ocean island basalts. J Petrol 48:2093–2124
13. Davies GF (1995) Punctuated tectonic evolution of the earth. Earth Planet Sci Lett 136:363–379
14. Depaolo DJ, Daley EE (2000) Neodymium isotopes in basalts of the southwest basin and range and lithospheric thinning during continental extension. Chem Geol 169:157–185
15. Dupuy C, Liotard JM, Dostal J (1992) Zr/Hf fractionation in intraplate basaltic rocks: carbonate metasomatism in the mantle source. Geochim Cosmochim Acta 6:2417–2423
16. Ernst RE, Buchan KL (2001) The use of mafic dyke swarms in identifying and locating mantle plumes. In: Ernst RE, Buchan KL (eds) Mantle plumes: their identifying through time. Boulder, Colorado, Geological Society of America Special Paper, 352, pp 247–265
17. Frey FA, Prinz M (1978) Ultramafic inclusions from San Carlos, Arizona: petrologic and geochemical data bearing on their petrogenesis. Earth Planet Sci Lett 38:129–176
18. Furman T, Graham D (1999) Erosion of lithospheric mantle beneath the East African Rift system: geochemical evidence from the Kivu volcanic province. Lithos 48:237–262
19. Gao LZ, Ding XZ, Pang WH, Zhang CH (2011) New geologic time scale of Meso- and Neoproterozoic of China and geochronologic constraint by SHRIMP zircon U–Pb dating. J Stratigraphy 35:1–7
20. Gower CF, Krogh TE (2002) A U–Pb geochronological review of the Proterozoic history of the eastern Grenville Province. Can J Earth Sci 39:795–829
21. Griffin WL, Pearson NJ, Belousova E, Jackson SE, van Achterbergh E, O'Reilly SY, Shee SR (2000) The Hf isotope composition of cratonic Mantle, LA-MC-ICPMS analysis of zircon megacrysts in kimberlites. Geochim Cosmochim Acta 64:133–147
22. Guo JH, O'Brien PJ, Zhai MG (2002) High-pressure granulites in the Sanggan area, North China craton: metamorphic evolution, P-T paths and geotectonic significance. J Metamorph Geol 20:741–756
23. Guo JH, Sun M, Chen FK, Zhai MG (2005) Sm–Nd and SHRIMP U–Pb zircon geochronology of high-pressure granulites in the Sanggan area, North China Craton: timing of Paleoproterozoic continental collision. J Asian Earth Sci 24:629–642
24. Guo JH, Peng P, Chen Y et al (2012) UHT sapphirine granulite metamorphism at 1.93–1.92 Ga caused by gabbronorite intrusions: Implications for tectonic evolution of the northern margin of the North China Craton. Precambr Res 222–223:124–142
25. Guo RR, Liu SW, Santosh M et al (2013) Geochemistry, zircon U–Pb geochronology and Lu–Hf isotopes of metavolcanics from eastern Hebei reveal Neoarchean subduction tectonics in the North China Craton. Gondwana Res 24:664–686
26. Han BF, Zhang L, Wang YM, Song B (2007) Enriched mantle source for Paleoproterozoic high Mg and low Ti-P mafic dykes in central part of the North China Craton: constraints from zircon Hf isotopic compositions. Acta Petrologica Sinica 23:277–284 (in Chinese with English abstract)
27. Hawkesworth CJ, Turner SP, McDermott F, Peate DW, van Calsteren P (1997) U–Th isotopes in arc magmas: implications for element transfer from the subducted crust. Science 276:551–555
28. Hofmann AW, Jochum KP, Seufert M, White WM (1986) Nb and Pb in oceanic basalts: new constraints on mantle evolution. Earth Planet sci lett 79:33–45
29. Hu JL, Zhao TP, Xu YH, Chen W (2007) Geochemistry and petrogenesis of the high-K volcanic rocks in the Dahongyu Formation, North China Craton. J Mineral Petrol 27:70–77 (in Chinese with English abstract)
30. Jackson MG, Dasgupta R (2008) Compositions of HIMU, EM1 and EM2 from global trends between radiogenic isotopes and major elements in ocean island basalts. Earth Planet Sci Lett 276:175–186

31. Jiang N, Guo JH, Zhai MG (2011) Nature and origin of the Wenquan granite: Implications for the provenance of Proterozoic A-type granites in the North China Craton. J Asian Earth Sci 42:76–82
32. Jourdan F, Bertrand H, Schärer U, Blichert-Toft J, Féraud G, Kampunzu AB (2007) Major and trace element and Sr, Nd, Hf, and Pb isotope compositions of the Karoo large igneous province, Botswana-Zimbabwe: lithospheric vs mantle plume contribution. J Petrol 48:1043–1077
33. Keay S, Steele D, Compston W (1999) Identifying granite sources by SHRIMP U–Pb zircon geochronology: an application to the Lachlan foldbelt. Contrib Mineral Petrol 137:323–341
34. Kusky TM, Li JH (2003) Paleoproterozoic tectonic evolution of the North China Craton. J Asian Earth Sci 22:383–397
35. LaFlèche MR, Camire G, Jenner GA (1998) Geochemistry of post-Acadian, Carboniferous continental intraplate basalts from the Maritimes basin, Magdalen islands, Quebec, Canada. Chem Geol 148:115–136
36. Liu SW, Pan YM, Xie QL, Zhang J, Li QG (2004) Archean geodynamics in the Central Zone, North China craton: constraints from geochemistry of two contrasting series of granitoids in the Fuping and Wutaishan complexes. Precambr Res 130:229–249
37. Liu SW, Pan YM, Xie QL, Zhang J, Li QG (2005) Geochemistry of the Paleoproterozoic Nanying granitic gneisses in the Fuping complex: implications for the tectonic evolution of the Central zone, North China Craton. J Asian Earth Sci 24:643–658
38. Liu SW, Santosh M, Wang W, Bai X, Yang PT (2011) Zircon U–Pb chronology of the Jianping Complex: implications for the Precambrian crustal evolution history of the northern margin of North China Craton. Gondwana Res 20:48–63
39. Liu SW, Zhang J, Li QG, Zhang LF, Wang W, Yang PT (2012) Geochemistry and U–Pb zircon ages of metamorphic volcanic rocks of the Paleoproterozoic Lüliang Complex and constraints on the evolution of the Trans-North China Orogen, North China Craton. Precambr Res 222–223:173–190
40. Lu SN, Li HM (1991) A precise U–Pb single zircon age determination for the volcanics of the Dahongyu Formation, Changcheng System in Jinxian. Bulletin of the Chinese Academy of Geological Sciences 22:137–145 (in Chinese with English abstract)
41. Lu SN, Zhao GC, Wang HC, Hao GJ (2008) Precambrian metamorphic basement and sedimentary cover of the North China Craton: a review. Precambr Res 160:77–93
42. Maniar PD, Piccoli PM (1989) Tectonic discrimination of granitoids. Geological Society of American Bulletin 101:635–643
43. Manikyamba C, Kerrich R (2011) Geochemistry of alkaline basalts and associated high-Mg basalts from the 2.7 Ga Penakacherla Terrane, Dharwar craton, India: An Archean depleted mantle-OIB array. Precambr Res 188:104–122
44. Manikyamba C, Kerrich R (2012) Eastern Dharwar Craton, India: Continental lithosphere growth by accretion of diverse plume and arc terranes. Geosci Front 3:225–240
45. Manikyamba C, Kerrich R, Polat A, Raju K, Satyanarayanan M, Krishna AK (2012) Arc picrite-potassic adakitic-shoshonitic volcanic association of the Neoarchean Sigegudda greenstone terrane, Western Dharwar Craton: transition from Arc wedge to lithosphere melting. Precambr Res 212–213:207–224
46. Merle O (2011) A simple continental rift classification. Tectonophysics 513:88–95
47. Middlemost EAK (1994) Naming materials in magma/igneous rock system. Earth Sci Rev 37:215–224
48. Miller RR, Heaman LM, Birkett TC (1997) U–Pb zircon age of the Strange Lake peralkaline complex: implications for Mesoproterozoic peralkaline magmatism in north-central Labrador. Precambr Res 81:67–82
49. Miller C, Schuster R, Klotzli U (1999) Post-collisional potassic and ultrapotassic magmatism in SW Tibet: geochemical and Sr–Nd–Pb–O isotopic constraints for mantle source characteristics and petrogenesis. J Petrol 40:1399–1424
50. Pearce JA (2008) Geochemical fingerprinting of oceanic basalts with applications to ophiolite classification and the search for Archean oceanic crust. Lithos 100:14–48

51. Peccerillo A, Barberio MR, Yirgu G, Ayalew D, Barbieri M, Wu TW (2003) Relationship between mafic and peralkaline felsic magmatism in continental rift settings: a petrological, geochemical and isotopic study of the Gedemsa Volcano, Central Ethiopian Rift. J Petrol 44:2003–2032
52. Pei FP, Ye YF, Wang F, Cao HH, Lu SM, Yang DB (2013) Discovery of Mesoproterozoic diabase dyke in Tonghua region, Jilin Province and its tectonic implications. Journal of Jilin University (Earth Science Edition) 43:110–118 (in Chinese with English Abstract)
53. Peng P, Zhai MG, Ernst RE, Guo JH, Liu F, Hu B (2008) A 1.78 Ga large igneous province in the North China craton: the Xiong'er Volcanic Province and the North China dyke swarm. Lithos 101:260–280
54. Peng P, Liu F, Zhai MG, Guo JH (2011) Age of the Miyun dyke swarm: constraints on the maximum depositional age of the Changcheng System. Chin Sci Bull 57:105–110 (in Chinese with English abstract)
55. Peng TP, Wilde SA, Fan WM, Peng BX, Mao YS (2013) Mesoproterozoic high Fe–Ti mafic magmatism in western Shandong, North China Craton: Petrogenesis and implications for the final breakup of the Columbia supercontinent. Precambr Res 235:190–207
56. Polat A, Hofmann AW (2003) Alteration and geochemical patterns in the 3.7–3.8 Ga Isua greenstone belt. West Greenland. Precambrian Research 126:197–218
57. Polat A, Kerrich R, Casey JF (1997) Geochemistry of Quaternary basalts erupted along the east Anatolian and Dead Sea fault zones of southern Turkey: implications for mantle sources. Precambr Res 40:55–68
58. Puffer JH (2001) Contrasting high field strength element contents of continental flood basalts from plume versus reactivated-arc sources. Geology 29:675–678
59. Rapp RP, Watson EB (1995) Dehydration melting of metabasalt at 8–32 kbar: Implications for continental growth and crust-mantle recycling. J Petrol 36:891–931
60. Rollinson HR (1993) Using geochemical data: evaluation, presentation, interpretation. Pearson Education Limited, London
61. Romer RL, Schärer U, Wardle RJ, Wilton DHC (1995) U–Pb age of the Seal Lake Group, Labrador: relationship to Mesoproterozoic extension-related magmatism of Laurasia. Can J Earth Sci 32:1401–1410
62. Schiano P, Monzier M, Eissen JP, Martin H, Koga KT (2010) Simple mixing as the major control of the evolution of volcanic suites in the Ecuadorian Andes. Contrib Miner Petrol 160:297–312
63. Shellnutt JG, MacRae ND (2012) Petrogenesis of the Mesoproterozoic (1.23 Ga) Sudbury dyke swarm and its questionable relationship to plate separation. Int J Earth Sci 101:3–23
64. Söderlund U, Isachsen CE, Bylund G, Heaman LM, Patchett PJ, Vervoort JD, Andersson UB (2005) U–Pb baddeleyite ages and Hf, Nd isotope chemistry constraining repeated mafic magmatism in the Fennoscandian Shield from 1.6 to 0.9 Ga. Contrib Miner Petrol 150:174–194
65. Song XY, Qi HW, Robinson PT, Zhou MF, Cao ZM, Chen LM (2008) Melting of the subcontinental lithospheric mantle by the Emeishan mantle plume; evidence from the basal alkaline basalts in Dongchuan, Yunnan, Southwestern China. Lithos 100:93–111
66. Sun, S.S., McDonough, W.F., 1989. Chemical and isotopic systematics of oceanic basalts: implication for mantle composition and processes. In: Saunders AD, Norry MJ (eds) Magmatism in Ocean Basins. Geological Society of London, Special Publication 42, pp 313–345
67. Taylor SR, McLennan SM (1985) The continental crust: its composition and evolution. Blackwell, Oxford
68. Tiepolo M, Vannucci R, Oberti R, Foley S, Bottazzi P, Zanetti A (2000) Nb and Ta incorporation and fractionation in titanian pargasite and kaersutite: crystal-chemical constraints and implications for natural systems. Earth Planet Sci Lett 176:185–201
69. Treuil M, Joron JM (1975) Utilization des elements hydromagmayophiles pour la simplification de la modelisation quantitative des processes magmatiques. Exeples de l'Afar et de da dorsale medioatlantique. Rend. SMP 31:125–174

70. Wan YS, Dong CY, Liu DY, Kröner A, Yang CH, Wang W, Du LL, Xie HQ, Ma MZ (2012) Zircon ages and geochemistry of late Neoarchean syenogranites in the North China Craton: a review. Precambr Res 222–223:265–289
71. Wang XL, Zhou JC, Qiu JS, Jiang SY, Shi YR (2008) Geochronology and geochemistry of Neoproterozoic mafic rocks from western Hunan, South China: implications for petrogenesis and post-orogenic extension. Geol Mag 2008:215–233
72. Wang YJ, Zhang YZ, Zhao GC, Fan WM, Xia XP, Zhang FF, Zhang AM (2009) Zircon U–Pb geochronological and geochemical constaints on the petrogenesis of the Taishan sanukitoids (Shandong): Implications for Neoarchean subduction in the Eastern Block, North China Craton. Precambr Res 174:273–286
73. Wang XL, Jiang SY, Dai BZ (2010) Melting of enriched Archean subcontinental lithospheric mantle: evidence from the ca. 1760 Ma volcanic rocks of the Xiong'er Group, southern margin of the North China Craton. Precambr Res 182:204–216
74. Wang W, Liu SW, Bai X, Yang PT, Li QG, Zhang LF (2011) Geochemistry and zircon U–Pb–Hf isotopic systematics of the Neoarchean Yixian-Fuxin greenstone belt, northern margin of the North China Craton: implications for petrogenesis and tectonic setting. Gondwana Res 20:64–81
75. Wang W, Liu SW, Wilde SA, Li QG, Zhang J (2012) Petrogenesis and geochronology of Precambrian granitoid gneisses in Western Liaoning Province: constraints on Neoarchean to early Paleoproterozoic crustal evolution of the North China Craton. Precambr Res 222–223:290–311
76. Wang W, Liu SW, Bai X, Li QG, Yang PT, Zhao Y, Zhang SH, Guo RR (2013) Geochemistry and zircon U–Pb–Hf isotopes of the late Paleoproterozoic Jianping diorite-monzonite-syenite suites of the North China Craton: implications for petrogenesis and geodynamic setting. Lithos 162–163:175–194
77. Wang W, Liu SW, Bai X et al (2013) Zircon U–Pb–Hf isotopes and whole-rock geochemistry of granitoid gneisses in the Jianping gneissic terrane, Western Liaoning Province: constraints on the Neoarchean crustal evolution of the North China Craton. Precambr Res 224:184–221
78. Wang W, Liu SW, Santosh M, Wang GH, Bai X, Guo RR (2015) Neoarchean intra-oceanic arc system in the Western Liaoning Province: Implications for Early Precambrian crustal evolution in the Eastern Block of the North China Craton. Earth Sci Rev 150:329–364
79. Wang W, Liu SW, Santosh M et al (2015) Late Paleoproterozoic geodynamics of the north China Craton: Geochemical and zircon U–Pb–Hf records from a volcanic suite in the Yanliao rift. Gondwana Res 27:300–325
80. Wang W, Liu SW, Santosh M, Zhang LF, Bai X, Zhao Y, Zhang SH, Guo RR (2015) 1.23 Ga mafic dykes in the North China Craton reconstruct the Columbia supercontinent. Gondwana Res 27:1407–1418
81. Watt GR, Harley SH (1993) Accessory phase controls on the geochemistry of crustal melts and restites produced during water undersaturated partial melting. Contrib Miner Petrol 201:220–231
82. Winchester JA, Floyd PA (1976) Geochemical magma type discrimination: application to altered and metamorphosed basic igneous rocks. Earth Planet Sci Lett 28:459–469
83. Winchester JA, Floyd PA (1977) Geochemical discrimination of different magma series and their differentiation products. Chem Geol 20:325–343
84. Wu FY, Zhang YB, Yang JH, Xie LW, Yang YH (2009) Are there any 3.8 Ga rock at Anshan in the North China Craton? Reply to comments on "Zircon U–Pb and Hf isotopic constraints on the Early Archean crustal evolution in Anshan of the North China Craton" by Nutman et al. Precambrian Research 172:361–363
85. Xiao L, Xu YG, Mei HJ, Zheng YF, He B, Pirajno F (2004) Distinct mantle sources of low-Ti and high-Ti basalts from the western Emeishan large igneous province, SW China: implications for plume-lithosphere interaction. Earth Planet Sci Lett 228:525–546
86. Xie GH (2005) Petrology and Geochemistry of the Damiao Anorthosite and the Miyun Rapakivi Granite. Science Press, Beijing, pp 1–195 (in Chinese)

87. Xu YG, Chuang SL, Jahn BM, Wu GY (2001) Petrologic and geochemical constraints on the peteogenesis of Permian-Triassic Emeishan flood basalts in southwestern China. Lithos 58:145–168
88. Yang JH, Wu FY, Liu XM, Xie LW (2005) Zircon U–Pb ages and Hf isotopes and their geological significance of the Miyun rapakivi granites from Beijing, China. Acta Petrologica Sinica 21:1633–1644 (in Chinese with English abstract)
89. Yang KF, Fan HR, Santosh M, Hu RZ, Wang KY (2011) Mesoproterozoic mafic and carbonatitic dykes from the northern margin of the North China Craton: Implications for the final breakup of Columbia supercontinent. Tectonophysics 498:1–10
90. Yu JH, Fu HQ, Zhang FL, Wan FX (1994) Petrogenesis of potassic alkaline volcanism and plutonism in a Proterozoic rift trough near Beijing. Regional Geology of China 2:115–122 (in Chinese with English abstract)
91. Zhang SH, Liu SW, Zhao Y, Yang JH, Song B, Liu XM (2007) The 1.75–1.68 Ga anorthosite-mangerite-alkali granitoid-rapakivi granite suite from the northern North China Craton: magmatism related to a Paleoproterozoic orogen. Precambr Res 155:287–312
92. Zhao GC, Wilde SA, Cawood PA et al (1999) Thermal evolution of two types of mafic granulites from the North China Craton: implications for both mantle plume and collisional tectonics. Geol Mag 136:223–240
93. Zhao GC, Sun M, Wilde SA et al (2005) Late Archean to Proterozoic evolution of the North China Craton: key issues revisited. Precambr Res 136:177–202
94. Zhao TP, Chen W, Zhou MF (2009) Geochemical and Nd-Hf isotopic constraints on the origin of the 1.74 Ga Damiao anorthosite complex. North China Craton. Lithos 113:673–690
95. Zhao GC, He YH, Sun M (2009) The Xiong'er volcanic belt at the southern margin of the North China Craton: petrographic and geochemical evidence for its outboard position in the Paleo-Mesoproterozoic Columbia Supercontinent. Gondwana Res 16:170–181
96. Zhao GC, Cawood PA, Li SZ, Wilde SA, Sun M, Zhang J, He YH, Yin CQ (2012) Amalgamation of the North China Craton: key issues and discussions. Precambr Res 222–223:55–76
97. Zhou MF, Zhao JH, Jiang CY, Gao JF, Wang W, Yang SH (2009) OIB-like, heterogeneous mantle sources of Permian basaltic magmatism in the western Tarim Basin, NW China: implications for a possible Permian large igneous province. Lithos 113:583–594
98. Zindler A, Hart S (1986) Chemical geodynamics. Annu Rev Earth Planet Sci 14:493–571

Chapter 5
Precambrian Crustal Evolution, Lithospheric Mantle Evolution and Crust-Mantle Geodynamics of Western Liaoning-Northeastern Hebei Provinces

Abstract How the Precambrian lithospheric mantle formed as well as related crust-mantle geodynamic regimes remain hotly debated, which eventually controlled the Precambrian crustal formation and evolution processes. Based on the studies of Archean to Mesoproterozoic geological events in the Western Liaoning-Northeastern Hebei Provinces, the prolonged evolution history of the lithospheric mantle and crust-mantle geodynamic processes are summarized and discussed in this chapter. The Precambrian lithospheric mantle evolution history of the study area is established as follows: (1) the juvenile depleted Neoarchean lithospheric mantle was generated by "lateral" subduction accretion processes along the northern margin of North China Craton, which was gradually evolved to an enriched mantle during Paleoproterozoic; (2) this enriched mantle was further metasomatized by slab-derived materials during late Paleoproterozoic eastward subduction processes of Trans-North China Orogen, resulting in the formation of a potassic and enriched lithospheric mantle; and (3) at ~1671–1625 Ma and ~1230 Ma, this enriched lithospheric mantle witnessed two episodes of "vertical" accretion processes, which were ascribed to asthenospheric mantle upwelling processes triggered by lithosphere delamination and a mantle plume activity, respectively. The Western Liaoning-Northeastern Hebei Provinces experienced prolonged Precambrian crust-mantle geodynamic evolution history: (1) at ~2640–2506 Ma, the depleted lithospheric mantle was initially generated by mid-ocean ridge spreading, yielding mid-ocean ridge basalts (MORBs). This juvenile lithospheric mantle was continuously metasomatized by subduction-related fluids and melts, the partial melting of which generated the island arc tholeiites and calc-alkaline basalts, adakite-like and high magnesium andesites, as well as HMG granitoid gneisses in the Western Liaoning Province. Meanwhile, the underplating of mantle-derived materials triggered partial melting of the metabasaltic rocks at the arc-root, resulting in the formation of LMG TTG gneisses; (2) at ~2495 Ma, partial melting of the metamorphosed felsic and sedimentary rocks was induced by the mantle upwelling in an extensional setting following arc-continent accretion, leading to regional granulite-facies metamorphism and the emplacement of potassium-rich granitoid gneisses; (3) during the Paleoproterozoic, the metasomatized Archean lithospheric mantle was gradually

W. Wang, *Archean-Mesoproterozoic Crustal Evolution and Crust-Mantle Geodynamics of Western Liaoning-Northeastern Hebei Provinces, North China Craton*, Springer Theses, https://doi.org/10.1007/978-981-10-7922-1_5

evolved to an enriched mantle source through close-system isotopic evolution, which was further metasomatized by slab-derived fluids or melts during the late Paleoproterozoic Trans-North China Orogen, resulting in the formation of a potassic and enriched lithospheric mantle. At ~1780–1680 Ma, the partial melting of this enriched mantle occurred in response to slab breakoff, yielding voluminous igneous rocks such as JDMSS, AMGRS, and mafic dykes; (4) later at ~1670–1625 Ma, the asthenospheric mantle upwelled and melted following the lithosphere delamination, resulting in the eruption of Pinggu volcanic rocks in the Yanliao rift; and (5) during the early to middle Mesoproterozoic, long-term tectonic quiescence dominated the NCC. However, ~1230 Ma mantle plume triggered the partial melting of asthenospheric mantle with intense asthenosphere-lithospheric mantle interaction, yielding voluminous mafic dykes throughout the NCC.

Keywords Neoarchean to Mesoproterozoic crustal evolution · Precambrian evolution of lithospheric mantle · Crust-mantle geodynamic processes Western Liaoning-Northeastern Hebei provinces · North china craton

Crustal evolution and geodynamic processes are essentially controlled by mantle convection and crust-mantle interactions, and deciphering the nature and evolution of lithospheric mantle is one of the major frontier issues in solid earth sciences [7, 9, 63]. It is suggested that typical Archean lithospheric mantle is refractory, and consists mainly of dunites, harzburgites, and minor Iherzolites, with a thickness of >200 km, whereas Proterozoic to Phanerozoic lithospheric mantle was gradually thinned and enriched by multiple episodes of metasomatism [7, 9, 32, 34]. The Western Liaoning-Northeastern Hebei Provinces experienced prolonged Precambrian crustal evolution history, which also lie in the overlapping field of the Paleozoic Central Asian orogenic belt to the north and the Mesozoic to Cenozoic Pacific tectonic domain in Eastern China (Fig. 2.2; [1, 34, 37–39, 47]). Accordingly, it is ideal to study the complex formation and evolution processes of the lithospheric mantle.

In this Chapter, the Precambrian crustal evolution history of Western Liaoning-Northeastern Hebei Provinces is summarized. Based on compilation of isotopic data of mafic rocks and petrogenetic studies of represent lithological assemblages at different Precambrian episodes (~2.6–1.2 Ga), the formation regime of Archean lithospheric mantle and its subsequent evolution as well as crust-mantle geodynamic evolution processes are discussed.

5.1 Precambiran Crustal Evolution History in Western Liaoning-Northeastern Hebei

The Western Liaoning-Northeastern Hebei Provinces are important exposure regions of Archean basement terranes along the northern margin of North China Craton, which record prolonged crustal evolution history as follows.

(1) **~3860–3135 Ma**: The oldest crustal materials are the ~3860–3135 Ma detrital zircons preserved in the metasedimentary rocks (fuchsite quartzites, hornblende gneisses, and garnet-biotite gneisses) of Caozhuang-Huangbaiyu complex, Eastern Hebei, with minor occurrence of ~3.4 and ~2.9 Ga plutonic rocks [17, 27, 35, 36, 46]. Comprehensive zircon U–Pb–Hf–O isotopic studies indicate crust-mantle differentiation possibly at ~4.0 Ga, as well as multiple episodes of juvenile crustal addition and recycling of older crustal rocks at ~4.0–3.5 Ga, with potential occurrence of Hadean crust [17, 21, 46, 62]. This is consistent with the occurrence of a ~4.17 Ga zircon xenocryst in the Neoarchean amphibolites of Anshan-Benxi areas [4].

(2) **~2640–2520 Ma**: The Western Liaoning Province experienced extensive volcanism during the late Neoarchean, forming voluminous tholeiitic basalts and calc-alkaline basaltic-andesitic-rhyolitic rocks (Figs. 3.2 and 3.9; [19, 43]). These rocks were metamorphosed under amphibolite to granulite facies, which are interlayered with banded iron formations (BIFs) and other metasedimentary rocks, constituting the supracrustal rock units. Supracrustal metavolcanic rocks in the Fuxin area show geochemical affinities to MORBs, island arc tholeiitic basalts, island arc calc-alkaline basalts, adakite-like and high magnesium andesites, respectively (Figs. 3.9, 3.10 and 3.11). They are suggested to have been derived from adiabatic decompression melting of asthenospheric mantle under an oceanic spreading ridge as well as complex interactions between the subducted slabs and mantle wedge materials, respectively (Fig. 5.1a). Zircon Lu–Hf isotopes reveal that all these metavolcanic rocks have depleted εHf(t) values (+2.7 to +9.7; Figs. 3.4, 3.5, 3.6, 3.7 and 3.8). Similarly in the Saheqiao area of Eastern Hebei, tholeiitic to calc-alkaline volcanic rocks were erupted during ~2614–2518 Ma [10]. They show almost depleted zircon εHf(t) values (−1.4 to +9.0), which were considered to have been generated by the interactions between subducted slabs and mantle wedge materials. Accordingly, the majority of late Neoarchean metavolcanic rocks in the study area were derived from depleted mantle materials, marking a major episode of crustal growth during ~2.6–2.5 Ga [37].

(3) **~2532–2506 Ma**: Voluminous TTG gneisses including minor dioritic gneisses were developed during this period, which are characterized by strong gneissosity (Figs. 3.17, 3.18 and 3.19). They show intrusive relationships with the supracrustal rock sequences, as further evidenced by the presence of xenoliths of supracrustal rocks. Petrogenetic studies reveal that dioritic and TTG gneisses of the high magnesium group (HMG) were derived from the partial melting of subducted slabs with the slab melts contaminated by the mantle wedge materials. In comparison, TTG gneisses of the low magnesium group (LMG) could have been mainly generated by the partial melting of metabasaltic rocks at the arc root (Fig. 5.1a). Collectively, this episode of granitoid gneisses likely have been formed at a compressional setting related to the evolution of a convergent arc. Zircon Lu–Hf isotopes indicate that T_{DM}(Hf) model ages of the granitoid gneisses (~2.77–2.52 Ga) overlap largely with those of metavolcanic rocks (~2.79–2.51 Ga; Wang et al. [37, 40]). These data suggest that the granitoid

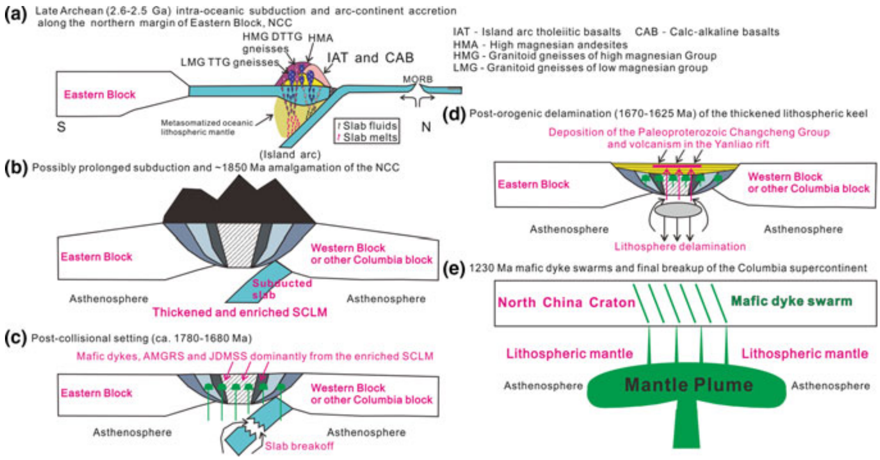

Fig. 5.1 Precambrian crust-mantle interaction and geodynamic evolution scenario of the Western Liaoning-Northeastern Hebei Provinces, North China Craton (see Parts 5.1 and 5.2 in the main text for details)

gneisses were mainly sourced from juvenile crustal materials (either subducted slab basalts or metabasaltic rocks at the arc root), with some involvement of mantle materials (especially granitoid gneisses of the HMG). Accordingly, a major episode of crustal growth at late Neoarchean is further implicated by these granitoid gneisses.

(4) **~2495 Ma**: Minor potassium-rich granitoid gneisses were developed in the Western Liaoning Province. They show weakly gneissic to massive structures, and intruded into early strongly gneissic dioritic to TTG rocks as well as metamorphosed supracrustal rocks (Fig. 3.35). It is suggested that these granitoid gneisses were derived from the partial melting of metamorphosed felsic rocks and sedimentary rocks (Fig. 3.42). Notably, they were nearly coeval with regional granulite facies metamorphism (~2485 Ma), implying a transition period from early convergent arc to late extensional setting possibly related to the post-collisional stage following accretion of the arc terrane onto the northern continental margin of Eastern Block [37]. Both the basement rocks in Western Liaoning and Eastern Hebei Provinces were subjected to the effects of ~2450–2400 Ma retrograde metamorphism and possibly ~2370–2040 Ma multi-episode tectonothermal events, with local emplacement of ~2400 Ma mafic rocks [20]. Notably, the study area experienced a tectonic quiescence period during ~2400–1850 Ma without intense tectono-magmatic events.

(5) **~1870–1680 Ma**: The Western Liaoning-Northeastern Hebei Provinces witnessed two major episodes of tectono-magmatic events during the late Paleoproterozoic: (I) ~1876–1810 Ma mafic dykes and granitoid gneisses emplaced in the Northern Hebei Province, accompanied by ~1800 Ma granulite facies metamorphism [22, 23]. These tectonothermal events may be

related to the collision between the Eastern Block and Western Block or the subduction-collision events along the northern margin of North China Craton [15, 59]; (II) intense plutonic magmatism was developed during ~1750–1680 Ma, including the Damiao anorthosite complex, Miyun rapakivi granites, Jianping diorite-monzonite-syenite suite and Miyun mafic dykes (Fig. 5.1c; [41]). These magmatic rocks extend ~500 km with an E-W trending, and show massive structures, which were emplaced later than the ~1780 Ma mafic dykes along the Trans-North China Orogen and the Xiong'er volcanic rocks [31]. Petrogenetic studies reveal that they were mainly sourced from an EM-I type lithospheric mantle, with the parental magmas subjected to subsequent crustal contamination and fractional crystallization [41].

(6) **~1671–1625 Ma**: Within the Yanliao rift, late Paleoproterozoic K-rich volcanic rocks are widely developed in the Tuanshanzi and Dahongyu Formations of the upper sections of Changcheng Group around the Pinggu-Jixian areas (Figs. 2.2 and 4.12). Representative lithological assemblages are olivine basalts, trachy-basalts, trachyandesites, and trachytes, with subordinate calc-alkaline hornblende-bearing basalts (Figs. 4.13 and 4.14; [38]). It is suggested that these volcanic rocks were erupted during ~1671–1625 Ma, and they were generated through complex interactions between the asthenospheric and lithospheric mantle [38]. This volcanic episode represents the latest regional late Paleoproterozoic tectono-magmatic events, which are accompanied by the onset of Yanliao rifting and deposition of thick sedimentary covers.

(7) **~1625–1330 Ma**: Following the eruption of Pinggu volcanic rocks, the North China Craton entered a prolonged tectonic quiescence period, with rare magmatic events reported [28, 53]. Recent paleomagnetic studies indicate that the North China Craton lies in the central part of the global Columbia supercontinent during ~1.8–1.3 Ga, which drifted as a stable craton [3, 6, 39].

(8) **~1330–1230 Ma**: Recently, a series of ~1330 Ma mafic sills, including minor granitic rocks, was identified in the Proterozoic sedimentary covers along the northern margin of North China Craton [53, 54]. They distribute as a ~600 km E–W trending belt from Chaoyang in Western Liaoning to Huade of Inner Mongolia, which were considered to have been formed by the interactions between the asthenospheric mantle-derived magmas and the ancient crustal materials. Comparatively, ~1230 Ma mafic dykes distributed much wider than the ~1330 Ma mafic sills (Fig. 4.34; [39]). In this study, a series of ~1230 Ma mafic dykes were discovered in the Qinglong (Eastern Hebei)-Jianping (Western Liaoning)-Qingyuan (Northern Liaoning) areas, and they all intruded into the Archean basement rocks (TTG gneisses or supracrustal metavolcanic rocks; Figs. 4.25, 4.26, 4.27, 4.28, 4.29 and 4.30; [39]). Combined with minor coeval mafic dykes in Linyi (Western Shandong), Tonghua (Southern Jilin), and Bayan Obo (Western Block), the short-lived ~1230 Ma mafic dykes may have a facial distribution pattern in the North China Craton with an exposure area of $\sim 0.6 \times 10^6$ km^2. Petrogenetic studies

suggest that the parental magmas of these mafic dykes could have been derived from complex interaction between the asthenospheric and lithospheric mantle (Fig. 5.1e; [39]). The ~1230 Ma mafic dykes of North China Craton could have been intimately linked to the ~1270 Ma Mackenzie mafic dykes and ~1230 Ma Sudbury mafic dykes in North America. They could represent the magmatic products of a mantle plume, probably contributing to the final breakup of Columbia supercontinent [2, 5, 33, 39].

5.2 Precambiran Lithospheric Mantle Evolution and Crust-Mantle Geodynamic Processes of the Western Liaoning-Northeastern Hebei Provinces

5.2.1 Formation Regime of Late Archean Lithospheric Mantle and Crust-Mantle Geodynamics

There are two major formation regimes of Archean lithospheric mantle [32]. Based on the strongly refractory nature of Archean lithospheric mantle as well as high Fo values (>92.5) of olivine crystals, it is suggested by some researchers that they could represent residues after high degree partial melting of a primitive mantle under a mantle plume setting. Whereas others argue that thick Archean lithospheric mantle was originally oceanic lithospheric mantle formed by low degree partial melting of shallow mantle sources. Subsequently, lateral accretion and thickening of the oceanic lithospheric mantle under a convergent arc setting resulted in the final generation of typical Archean sub-continental lithospheric mantle.

In the Western Liaoning Province, the widespread metavolcanic rocks and granitoid gneisses record complex crust-mantle interaction processes as follows (Figs. 3.43 and 5.1a): (1) the partial melting of depleted to slightly enriched asthenospheric mantle beneath a mid-ocean spreading ridge generated ~2640–2600 Ma MORB-like rocks (Group MB-1), giving rise to juvenile oceanic lithospheric mantle; (2) Subsequently at ~2550 Ma, this juvenile mantle was initially metasomatized by minor subduction-derived fluids, the partial melting of which yielded the island arc tholeiite (IAT)-like basaltic rocks of Group MB-2; (3) With continuous subduction, the mantle wedge materials were increasingly enriched in large ion lithophile elements and light rare earth elements, and the partial melting of this metasomatized lithospheric mantle formed the calc-alkaline basalts of Group MB-3; (4) The subducted slab started to melt at depths below the stability field of plagioclase, with the ascending partial melts contaminated by the mantle wedge materials, forming adakite-like andesitic rocks (Group MA-1) as well as TTG and dioritic rocks of the high magnesium group (HMG); whereas partial melting of the mantle wedge materials metasomatized by slab-derived melts yielded the high magnesium andesites (HMA) of Group MA-2. Meanwhile, continuous magma underplating further triggered partial melting of the arc-root materials, leading to the generation of TTGs of the low magnesium group; and (5) Finally at an extensional setting, lithospheric thinning as well as upwelling of the asthenospheric mantle resulted in granulite facies metamorphism and anatexis of metamorphosed felsic rocks and sedimentary rocks, forming the protoliths of weakly gneissic to massive granodioritic to monzogranitic gneisses. Accordingly, the late Neoarchean lithospheric mantle in Western Liaoning likely have been generated by lateral subduction-accretion processes along the northern margin of North China Craton.

The late Neoarchean metabasaltic rocks of Western Liaoning Province are largely tholeiitic in composition, with eruption ages of ~2640–2550 Ma (Figs. 3.4, 3.5, 3.6, 3.7 and 3.8). The protoliths of metabasaltic rocks with N-MORB-like geochemical features (OFX08-5 and 12FX18-2) formed earlier during ~2640–2600 Ma. They show zircon εHf(t) values of +2.8 to +9.7 close to the coeval model depleted mantle value, which could have been derived from adiabatic decompression melting of upwelling asthenospheric mantle beneath a mid-ocean spreading ridge. The metabasaltic rocks with IAT-like geochemical features formed later at ~2550 Ma, but also exhibit depleted zircon εHf(t) values of +4.5 to +7.5. Although minor tholeiitic metabasaltic rocks show chemical features analogous to those of E-MORBs (Fig. 3.13), late Neoarchean mafic volcanic rocks from both the Western Liaoning and Northern Hebei have depleted zircon εHf(t) values, suggesting derivation from depleted lithospheric mantle sources (Fig. 5.2; [10, 43, 48]). Accordingly, these tholeiitic metabasaltic rocks could have been generated under crust-mantle geodynamic processes from early mid-ocean ridge spreading to late initiation of intra-oceanic subduction. In this case, the juvenile oceanic lithospheric mantle was transformed to sub-arc lithospheric mantle during subduction initiation, which was subjected to gradual metasomatism by slab-derived materials. Subsequently, this metasomatized lithospheric mantle served as the mantle sources for regional tholeiitic to calc-alkaline basaltic to andesitic rocks (Fig. 5.2; [10, 16, 40, 42, 43]). Similarly, metabasaltic rocks in the early Archean Isua, Innersuartuut, and Ivisaartoq-Ujarassuit greenstone belts of Southwest Greenland show geochemical features transitional between MORBs and IATs, further suggesting that the sub-arc lithospheric mantle was transformed from oceanic lithospheric mantle that was initially formed under a spreading ridge.

In the adjacent Northern Liaoning, Eastern Hebei, and Wutai areas, late Neoarchean metabasaltic rocks also exhibit geochemical affinities to MORBs or island arc basalts [10, 45]. They show dominantly positive whole-rock Nd isotopic compositions that lie between those of depleted mantle and chondrite (though minor below the chondrite evolution line), which are compatible with the zircon Lu–Hf isotopic signatures (Figs. 5.2 and 5.3; [48]). These data indicate that metabasaltic rocks in the adjacent areas of Western Liaoning were chiefly derived from the

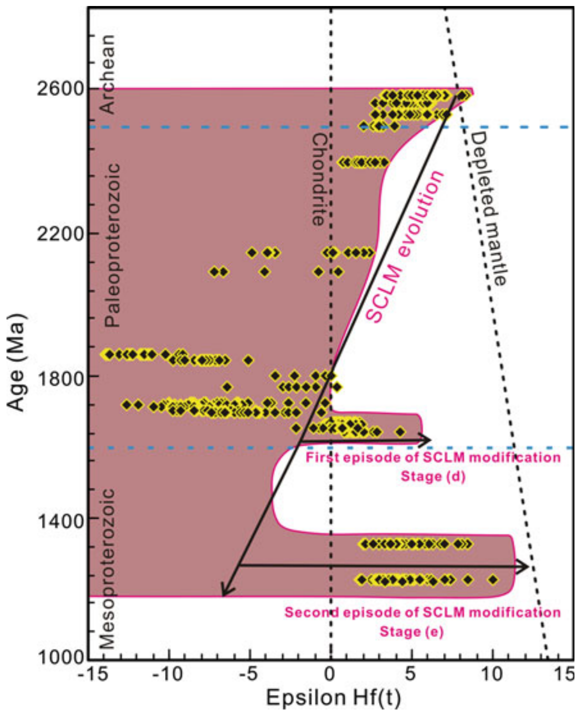

Fig. 5.2 Precambrian evolution (2600–1200 Ma) of the subcontinental lithospheric mantle beneath the North China Craton defined by zircon Lu–Hf isotopic compositions of mafic rocks with distinct formation ages

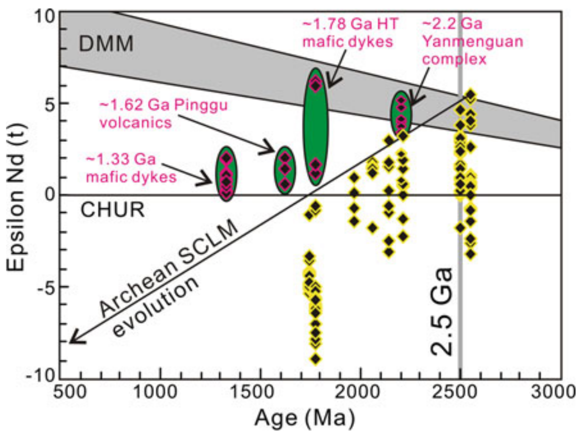

Fig. 5.3 Precambrian evolution (2600–1200 Ma) of the subcontinental lithospheric mantle beneath the North China Craton as defined by whole-rock Sm–Nd isotopic compositions of mafic rocks with distinct formation ages

partial melting of a juvenile lithospheric mantle that formed through subduction-accretion of oceanic lithospheric mantle. Accordingly, the northwestern margin of Eastern Block witnessed an important episode of lithospheric mantle growth during the late Neoarchean, which could be ascribed to lateral subduction-accretion processes [10, 29, 37, 45].

5.2.1.1 Formation of Late Paleoproterozoic Enriched Lithospheric Mantle and Crust-Mantle Geodynamic Processes

The late Paleoproterzoic plutonic rocks along the northern margin of North China Craton are featured by enriched isotopic compositions, including the ~1800 Ma mafic dykes in the Zunhua area of Eastern Hebei (zircon εHf(t) values of −3.5–0), ~1770 Ma mafic dykes (εHf(t) values of −6.4 to +0.4) in the Fengzhen area of Northern Hebei, norites from the ~1740 Ma Damiao anorthosite complex of Northern Hebei (zircon εHf(t) values of −8.3–−2.0), and magnetite diorites from the ~1721–1696 Ma JDMSS suites of Western Liaoning (zircon εHf(t) values of −10.0 to −0.3) [13, 41, 57]. These isotopic compositions are clearly distinct from those of late Neoarchean basement rocks (Fig. 5.2; [10, 16, 43]). Similarly, ~1780 Ma mafic dykes and Xiong'er volcanic rocks (zircon εHf(t) values of −14.1 to −10.1) within the Trans-North China Orogen as well as ~1855–1836 Ma metamorphosed mafic rocks (zircon εHf(t) values of −13.9 to −5.1) also show enriched isotopic compositions [38, 44]. These are further corroborated by the enriched whole-rock εNd(t) values (Fig. 5.3; [14, 31, 57]). Petrogenetic studies reveal that most late Paleoproterozoic lithologies were sourced from an enriched subcontinental lithospheric mantle, with the derivative melts subjected to different degrees of crustal contamination and fractional crystallization [13, 41, 44, 56]. Therefore, the subcontinental lithospheric mantle beneath the Eastern Block and the Trans-North China Orogen show dominantly enriched isotopic features during late Paleoproterozoic. Combined petrogenesis of these igneous rocks with regional geological background, it is suggested that the voluminous late Paleoproterozic (>1680 Ma) magmatism occurred later than the final amalgamation between the Eastern Block and Western Block, and they could have experienced the following crust-mantle geodynamic processes (Fig. 5.1b, c). Firstly, slab breakoff occurred following the collision of basement blocks of NCC, which brought about high heat flux that further triggered low degree partial melting of the overlying thick continental lithospheric mantle. The mantle-derived magmas were subjected to different degrees of crustal contamination and fractional crystallization processes during their ascent. During these processes, partial melting of lithospheric mantle formed the mafic dyke swarms, and the mafic endmemers of Xiong'er volcanic rocks, Damiao anorthosite complex and Jianping JDMSS alkaline suite (e.g., norites, anorthosites, and magnetite diorites). Whereas the felsic Xiong'er volcanic rocks, the Damiao mangerite-alkali granitoids, and the clinopyroxene monzonites and (quartz) syenites were dominantly generated by crustal contamination and fractional crystallization of the above mafic endmembers [41, 56]. Notably, materials from the underlying asthenospheric mantle or deeper mantle were not evidently sampled by these late Paleoproterozoic (>1680 Ma) magmatic rocks.

The formation regime of late Paleoproterozoic enriched lithospheric mantle in the NCC remains enigmatic. Whole-rock Nd isotopic compositions of mantle xenoliths trapped in the Phanerozoic basalts indicate that this enriched lithospheric mantle may be generated by the recycling of ancient Archean continental materials into the depleted lithospheric mantle [34]. Whereas others argued that late Paleoproterozoic enriched lithospheric mantle may be formed by metasomatism through mantle plume activities [31]. In order to resolve this issue, the isotopic data of late Archean to late Paleoproterozoic mafic rocks within the NCC were compiled (Figs. 5.2 and 5.3). Minor ~2400 Ma metamorphosed mafic dykes were documented in the Chaoyang area of Western Liaoning, which could have been derived from the partial melting of sub-arc lithospheric mantle but without evident involvement of crustal contamination [20] (our unreported data). These mafic dykes have depleted zircon εHf(t) values of +0.7 to +3.3, which are apparently lower than those of late Neoarchean metabasaltic rocks (Fig. 5.2). Some mafic dykes ranging in age between 2147 and 1973 Ma were developed in the Trans-North China Orogen, including the Hengling, Yixingzhai, and Xiwangshan dykes [30]. They were all suggested to have been produced by the partial melting of subcontinental lithospheric mantle. Notably, the depletion degree of lithospheric mantle during this period was further decreased, as suggested by the Hengling mafic dykes (~2147 Ma) with zircon εHf(t) values straddling the chondrite line (+2.3 to −4.9). Whole-rock εNd(t) isotopes of the three middle Paleoproterozoic mafic dykes ranging from −3.2 to +3.0, −1.7 to +1.8, and −1.4 to +1.0, respectively, suggesting that the subcontinental lithospheric mantle was further enriched during 2147–1973 Ma (Fig. 5.3). ~2087 Ma metabasaltic rocks in the Gantaohe Group of Zanhuang area show zircon εHf(t) values of −7.21 to +0.47 [51]. The low SiO_2 (48.80–49.22 wt%) and high MgO (6.35–6.13 wt%) contents suggest that they were not subjected to significant crustal contamination. Combined with zircon Lu–Hf isotopic composition of the ~2147 Ma Hengling mafic dykes (−4.9 to +2.3), it is suggested that the lithospheric mantle at ~2087 Ma was almost enriched with subchondritic isotopic values, implying that the depletion degree of the lithospheric mantle was further decreased during ~2147–2087 Ma (Fig. 5.2). This is supported by the whole-rock εNd(t) values of metabasaltic rocks from the ~2213–2210 Ma Lvliang and Yejishan Groups in the Lvliang complex (−2.3 to +3.2) and the ~2059 Ma Zhongtiao Group in the Zhongtiao area (+1.2 to +1.5) [58]. They were derived from a weakly depleted lithospheric mantle with decreasing degrees of depletion.

All the above isotopic data of Paleoproterozoic mafic rocks indicate that the late Neoarchean depleted lithospheric mantle was gradually enriched and transformed into the late Paleoproterozoic lithospheric mantle with almost subchondritic isotopic values (Figs. 5.2 and 5.3). Considering the late Neoarchean subduction-accretion processes along the northern and western margins of the Eastern Block, it is suggested the juvenile Neoarchean lithospheric mantle was metasomatized by subducted materials, and self-evolution of this metasomatized lithospheric mantle under a close system led to a gradually enriched lithospheric mantle [10, 25, 26, 37, 43, 45]. This gradually enriched lithospheric mantle served as the mantle sources for most Paleoproterozoic (>1680 Ma) magmatic rocks of the North China Craton.

From the viewpoint of trace elements, the parental magmas of late Paleoproterozoic JDMSS suite of Western Liaoning and other coeval mafic rocks in North China Craton are characterized by the enrichment of element K [31, 41, 44, 56]. These data imply the wide development of K-rich subcontinental lithospheric mantle beneath the North China Craton during late Paleoproterozoic. The enrichment of element K within lithospheric mantle may be ascribed to either lateral subduction recycling or vertical mantle metasomatism (linked to mantle convection or plume). ~1780–1680 Ma magmatic rocks throughout the North China Craton are mainly high-K calc-alkaline or alkaline in composition, and they were mainly sourced from an enriched lithospheric mantle, but without the involvement of asthenospheric mantle or deeper mantle materials. They are clearly distinct from the products of a mantle plume activity, which are characterized by a lithological assemblage of dominantly tholeiitic basalts with minor alkaline basalts and picrites, including some showing OIB-like geochemical features [50, 52]. Accordingly, vertical mantle metasomatism cannot account for the enrichment of K in the subcontinental lithospheric mantle. On the other hand, late Neoarchean metavolcanic rocks, TTG gneisses and subducted slabs are dominantly Na-riched with subordinate potassium-rich granitoids, and subduction recycling of these materials is also unlikely to supply enough K [10, 19, 40, 42, 43].

A series of high pressure granulites was developed in the Hengshan-Huai'an-Chengde areas. They show clockwise metamorphic P-T-t paths with near isothermal decompression (ITD) processes, indicating that the Trans-North China Orogen is a typical continent-continent collision belt [11, 12, 18, 49, 59, 61]. Detailed studies of the structural and deformation history of Hengshan complex reveal early northwest-trending asymmetric folds and late low-angle detachment faults, implying an eastward subduction polarity that led to the collision between the Eastern Block and Western Block [56]. During the late Paleoproterozoic subduction processes, the subcontinental lithospheric mantle could have been further enriched by the recycled slab or ancient continental materials, leading to the generation of a K-rich lithospheric mantle with subchondritic isotopic composition.

Accordingly, the late Neoarchean metasomatized depleted lithospheric mantle was gradually enriched through close-system isotopic evolution, which was further enriched during late Paleoproterozoic eastward subduction processes within the Trans-North China Orogen. During ~1780–1680 Ma, the above K-rich enriched lithospheric mantle was subjected to partial melting triggered possibly by slab breakoff following the collision between the Eastern Block and Western Block, forming the ~1721–1696 Ma Jianping diorite-monzonite-syenite suite as well as other coeval magmatic rocks.

Notably, ~2193 Ma mafic-ultramafic complex in the Yanlingguan area of Hengshan and minor ~1780 Ma high-Ti mafic dykes in the Trans-North China Orogen show depleted whole-rock Nd isotopes (εNd(t) values of +0.8 to +5.1 and +1.2 to +6.2, respectively). They could have been derived from the partial melting of juvenile late Paleoproterozoic lithospheric mantle formed by lateral subduction accretion between the Eastern and Western blocks (Fig. 5.3; [18, 24, 31, 59]).

5.2.2 Late Paleoproterozoic to Mesoproterozoic (~1670–1230 Ma) Lithospheric Mantle Evolution and Crust-Mantle Geodynamics

Early whole-rock Re–Os isotopic studies of Phanerozoic kimberlites and mantle xenoliths from alkaline basalts indicate coupling between Archean subcontinental lithospheric mantle and the overlying continental crust before Paleozoic, but the ancient lithospheric mantle was gradually rejuvenized by younger lithospheric mantle [8]. However, in situ Re–Os isotopic data of sulfides from mantle xenoliths suggest that the Re–Os isotopic system is susceptible to metasomatism, and multiple episodes of sulfides were identified within single mantle xenolith [54]. Continuous changes of Re–Os isotopes (i.e., T_{MA} and T_{RD}) from late Archean to Phanerozoic were recognized [34]. These suggest that the Archean depleted lithospheric mantle beneath Eastern Block could have been subjected to multiple episodes of metasomatism, probably linked to the late Paleoproterozoic subduction-collision processes between the Eastern and Western blocks as well as the Phanerozoic circum-craton subduction processes [34].

Late Paleoproterozoic to Mesoproterozoic magmatism provide further insights into the prolonged evolution of lithospheric mantle beneath the Eastern Block. Two major episodes of tectono-magmatic events were recognized in the North China Craton, and they record different crust-mantle geodynamic processes as follows. During ~1671–1625 Ma, lithosphere delamination following collision between the Eastern and Western blocks triggered intense upwelling of the asthenospheric mantle, and partial melting of both the upwelling asthenosphric mantle and overlying lithospheric mantle led to the generation of Pinggu K-rich volcanic rocks (Fig. 5.1d; [38]). Meanwhile, lithosphere extension resulted in the initiation of Yanliao rift with the deposition of thick sedimentary covers [28]. Afterwards, the North China Craton entered a prolonged period of tectonic quiescence, until the emplacement of ~1.33 Ga mafic sills along its northern continental margin and ~1.23 Ga mafic dykes throughout the whole craton [39, 53, 55]. Both of them display depleted whole-rock εNd(t) and zircon εHf(t) isotopic compositions, which were suggested to have been formed by intense interactions between the upwelling asthenospheric mantle and overlying lithospheric mantle. The ~1230 Ma mafic dykes are widely distributed in the Northern Liaoning, Western Liaoning, Eastern Hebei, Western Shandong, and possibly the Yinshan Block (Fig. 4.34). They cover possibly an area up to $\sim 0.6 \times 10^6$ km^2, representing the most important Mesoproterozoic tectono-magmatic event in North China Craton. Of which the alkaline gabbros show OIB-like geochemical features, suggesting the major derivation from a depleted asthenospheric mantle, with some involvement of lithospheric mantle materials (Fig. 4.32). Whereas the calc-alkaline gabbros were dominantly sourced from an enriched subcontinental lithospheric mantle [39].

The above crust-mantle geodynamic processes indicate that the North China Craton witnessed at least two major episodes of asthenospheric mantle upwelling at ~1671–1625 Ma and ~1230 Ma. During the two periods, the ancient enriched lithospheric mantle was subjected to intense vertical erosion and rejuvenization by the underlying depleted asthenospheric mantle probably related to (1) post-collision lithospheric delamination and (2) mantle plume event, respectively [38, 39, 41]. These late Paleoproterozic to Mesoproterozoic lithospheric mantle evolution could be the results of multiple episodes of breakup of the global Columbia supercontinent [39, 60].

References

1. Bai X, Liu SW, Wang W et al (2013) U-Pb geochronology and Lu-Hf isotopes of zircons from newly identified permian-early triassic plutons in western Liaoning province along the northern margin of the North China Craton: constraints on petrogenesis and tectonic setting. Int J Earth Sci 102:671–685
2. Baragar WRA, Ernst RE, Hulbert L, Peterson T (1996) Longitudinal petrochemical variation in the Mackenzie dyke swarm, Northwestern Canadian Shield. J Petrol 37:317–359
3. Chen LW, Huang BC, Yi ZY, Zhao J, Yan YG (2013) Paleomagnetism of ca. 1.35 Ga sills in northern North China Craton and implications for paleogeographic reconstruction of the Mesoproterozoic supercontinent. Precambr Res 228:36–47
4. Cui PL, Sun JF, Sha DM (2013) Oldest zircon xenocryst (4.17 Ga) from the North China Craton. Int Geol Rev 55:1902–1908
5. Ernst RE, Wingate MTD, Buchan KL, Li ZX (2008) Global record of 1600–700 Ma large igneous provinces (LIPs): implications for the reconstruction of the proposed Nuna (Columbia) and Rodinia supercontinents. Precambr Res 160:159–178
6. Evans DAD, Mitchell RN (2011) Assembly and breakup of the core of Paleoproterozoic-Mesoproterozoic supercontinent Nuna. Geology 39:443–446
7. Foley S (2008) Rejuvenation and erosion of the cratonic lithosphere. Nat Geosci 1:503–510
8. Gao S, Rudnick RL, Carlson RW (2002) Re-Os evidence for replacement of ancient mantle lithosphere benearth the North China Craton. Earth Planet Sci Lett 198:307–322
9. Griffin WL, O'Reilly SY, Afonso JC, Begg GC (2009) The composition and evolution of lithospheric mantle: a re-evaluation and its tectonic implications. J Petrol 50:1185–1204
10. Guo RR, Liu SW, Santosh M et al (2013) Geochemistry, zircon U-Pb geochronology and Lu–Hf isotopes of metavolcanics from eastern Hebei reveal Neoarchean subduction tectonics in the North China Craton. Gondwana Res 24:664–686
11. Guo JH, Sun M, Chen FK, Zhai MG (2005) Sm-Nd and SHRIMP U-Pb zircon geochronology of high-pressure granulites in the Sanggan area, North China Craton: timing of Paleoproterozoic continental collision. J Asian Earth Sci 24:629–642
12. Guo JH, O'Brien PJ, Zhai MG (2002) High-pressure granulites in the Sanggan area, North China craton: metamorphic evolution, P-T paths and geotectonic significance. J Metamorph Geol 20:741–756
13. Han BF, Zhang L, Wang YM, Song B (2007) Enriched mantle source for Paleoproterozoic high Mg and low Ti-P mafic dykes in central part of the North China Craton: constraints from zircon Hf isotopic compositions. Acta Petrologica Sinica 23:277–284 (in Chinese with English abstract)
14. Hu JL, Zhao TP, Xu YH, Chen W (2007) Geochemistry and petrogenesis of the high-K volcanic rocks in the Dahongyu Formation, North China Craton. J Mineral Petrol 27:70–77 (in Chinese with English abstract)
15. Kusky T, Li JH, Santosh M (2007) The Paleoproterozoic North China Orogen: North China Craton's collisional suture with the Columbia supercontinent. Gondwana Res 12:4–28

16. Li TS, Zhai MG, Peng P, Chen L, Guo JH (2010) Ca. 2.5 billion year old coeval ultramafic-mafic and syenitic dykes in Eastern Hebei: Implications for cratonization of the North China Craton. Precambr Res 180:143–155
17. Liu SJ, Wan YS, Sun HY et al (2013) Paleo- to Eoarchean crustal evolution in eastern Hebei, North China Craton: new evidence from SHRIMP U-Pb dating and in-situ Hf isotopic study of detrital zircons from paragneisses. J Asian Earth Sci 78:4–17
18. Liu SW, Zhang J, Li QG, Zhang LF, Wang W, Yang PT (2012) Geochemistry and U-Pb zircon ages of metamorphic volcanic rocks of the Paleoproterozoic Lüliang complex and constraints on the evolution of the Trans-North China Orogen. North China Craton Precambr Res 222–223:173–190
19. Liu SW, Santosh M, Wang W, Bai X, Yang PT (2011) Zircon U-Pb chronology of the Jianping complex: implications for the Precambrian crustal evolution history of the northern margin of North China Craton. Gondwana Res 20:48–63
20. Liu SW, Wang W, Bai X, Zhang F (2010) Geological events of early Precambrian complex in North Chaoyang area, Liaoning province. Acta Petrologica Sinica 26:1993–2004 (in Chinese with English abstract)
21. Liu DY, Wilde SA, Wan YS et al (2008) New U-Pb and Hf isotopic data confirm Anshan as the oldest preserved segment of the North China Craton. Am J Sci 308:200–231
22. Liu SW, Lü YJ, Feng YG, Zhang C, Tian W, Yan QR, Liu XM (2007) Geology and zircon U-Pb isotopic chronology of Dantazi complex, Northern Hebei province. Geol J China Univ 13:484–497 (in Chinese with English abstract)
23. Liu SW, Lü YJ, Feng YG, Liu XM, Yan QR, Zhang C, Tian W (2007) Zircon and monazite geochronology of the Hongqiyingzi complex, Northern Hebei, China. Geol Bull China 26:1086–1100 (in Chinese with English abstract)
24. Liu SW, Zhao GC, Wilde SA, Shu GM, Sun M, Li QG, Tian W, Zhang J (2006) Th-U-Pb monazite geochronology of the Lüliang and Wutai complexes: constraints on the tectonothermal evolution of the Trans-North China Orogen. Precambr Res 148:205–224
25. Liu SW, Pan YM, Xie QL, Zhang J, Li QG (2004) Archean geodynamics in the central zone, North China craton: constraints from geochemistry of two contrasting series of granitoids in the Fuping and Wutaishan complexes. Precambr Res 130:229–249
26. Liu SW, Pan YM, Li JH, Zhang J, Li QG (2002) Geological and isotopic geochemical constraints on the evolution of the Fuping complex, North China Craton. Precambr Res 117:41–56
27. Liu DY, Nutman AP, Compston W, Wu JS, Shen QH (1992) Remmants of ≥ 3800 Ma crust in the Chinese part of the Sino-Korean Craton. Geology 20:339–342
28. Lu SN, Zhao GC, Wang HC, Hao GJ (2008) Precambrian metamorphic basement and sedimentary cover of the North China Craton: a review. Precambr Res 160:77–93
29. Lv YJ, Liu SW, Zhao GC et al (2006) Geochemistry and Petrogenesis of Neoarchean metamorphic mafic rocks in the Wutai complex. Acta Geol Sin 80:899–911
30. Peng P, Guo JH, Zhai MG, Windley BF, Li TS, Liu F (2012) Genesis of the Hengling magmatic belt in the North China Craton: implications for Paleoproterozoic tectonics. Lithos 148:27–44
31. Peng P, Zhai MG, Ernst RE, Guo JH, Liu F, Hu B (2008) A 1.78 Ga large igneous province in the North China craton: the Xiong'er Volcanic province and the North China dyke swarm. Lithos 101:260–280
32. Rollinson H (2010) Coupled evolution of Archean continental crust and subcontinental lithospheric mantle. Geology 38:1083–1086
33. Shellnutt JG, MacRae ND (2012) Petrogenesis of the Mesoproterozoic (1.23 Ga) Sudbury dyke swarm and its questionable relationship to plate separation. Int J Earth Sci 101:3–23
34. Tang YJ, Zhang HF, Ying JF, Su BX (2013) Widespread refertilization of cratonic and circum-cratonic lithopheric mantle. Earth Sci Rev 118:45–68
35. Wan YS, Liu DY, Dong CY, Xie HQ, Kröner A, Ma MZ, Liu SJ, Xie SW, Ren P (2015) Formation and evolution of Archean continental crust of the North China Craton. In: Zhai MG (ed) Precambrian geology of China. Springer, pp 59–136

36. Wan YS, Liu DY, Dong CY, Nutman AP, Wilde SA, Wang W, Xie HQ, Yin XY, Zhou HY (2009) The oldest rocks and zircons in China. Acta Petrologica Sinica 25:1793–1807 (in Chinese with English abstract)
37. Wang W, Liu SW, Santosh M, Wang GH, Bai X, Guo RR (2015) Neoarchean intra-oceanic arc system in the Western Liaoning province: implications for Early Precambrian crustal evolution in the eastern block of the North China Craton. Earth Sci Rev 150:329–364
38. Wang W, Liu SW, Santosh M et al (2015) Late Paleoproterozoic geodynamics of the north China Craton: geochemical and zircon U-Pb-Hf records from a volcanic suite in the Yanliao rift. Gondwana Res 27:300–325
39. Wang W, Liu SW, Santosh M, Zhang LF, Bai X, Zhao Y, Zhang SH, Guo RR (2015) 1.23 Ga mafic dykes in the North China Craton reconstruct the Columbia supercontinent. Gondwana Res 27:1407–1418
40. Wang W, Liu SW, Bai X et al (2013) Zircon U-Pb-Hf isotopes and whole-rock geochemistry of granitoid gneisses in the Jianping gneissic terrane, Western Liaoning Province: constraints on the Neoarchean crustal evolution of the North China Craton. Precambr Res 224:184–221
41. Wang W, Liu SW, Bai X, Li QG, Yang PT, Zhao Y, Zhang SH, Guo RR (2013) Geochemistry and zircon U-Pb-Hf isotopes of the late Paleoproterozoic Jianping diorite-monzonite-syenite suites of the North China Craton: implications for petrogenesis and geodynamic setting. Lithos 162–163:175–194
42. Wang W, Liu SW, Wilde SA, Li QG, Zhang J (2012) Petrogenesis and geochronology of Precambrian granitoid gneisses in Western Liaoning province: constraints on Neoarchean to early Paleoproterozoic crustal evolution of the North China Craton. Precambr Res 222–223:290–311
43. Wang W, Liu SW, Bai X, Yang PT, Li QG, Zhang LF (2011) Geochemistry and zircon U-Pb-Hf isotopic systematics of the Neoarchean Yixian-Fuxin greenstone belt, northern margin of the North China Craton: implications for petrogenesis and tectonic setting. Gondwana Res 20:64–81
44. Wang XL, Jiang SY, Dai BZ (2010) Melting of enriched Archean subcontinental lithospheric mantle: evidence from the ca. 1760 Ma volcanic rocks of the Xiong'er group, southern margin of the North China Craton. Precambr Res 182:204–216
45. Wang ZH, Wilde SA, Wang KY et al (2004) A MORB-arc basalt-adakite association in the 2.5 Ga Wutai greenstone belt: late Archean magmatism and crustal growth in the North China Craton. Precambr Res 131:323–343
46. Wilde SA, Vallly JW, Kita NT et al (2008) SHRIMP U-Pb and CAMECA 1280 oxygen isotope results from ancient detrital zircons in the Caozhuang quartzite, Eastern Hebei, North China Craton: evidence for crustal reworking 3.8 Ga ago. Amercian J Sci 308:185–199
47. Wu FY, Walker RJ, Yang YH, Yuan HL, Yang JH (2006) The chemical-temporal evolution of lithospheric mantle underlying the North China Craton. Geochim Cosmochim Acta 70:5013–5034
48. Wu FY, Zhao GC, Wilde SA et al (2005) Nd isotopic constraints on crustal formation in the North China Craton. J Asian Earth Sci 24:523–545
49. Xiao LL, Wu CM, Zhao GC, Guo JH, Ren LD (2011) Metamorphic P-T paths of the Zanhuang amphibolites and metapelites: constraints on the tectonic evolution of the Paleoproterozoic Trans-North China Orogen. Int J Earth Sci 100:717–739
50. Xiao L, Xu YG, Mei HJ, Zheng YF, He B, Pirajno F (2004) Distinct mantle sources of low-Ti and high-Ti basalts from the western Emeishan large igneous province, SW China: implications for plume-lithosphere interaction. Earth and Planet Sci Lett 228:525–546
51. Xie HQ, Liu DY, Yin XY et al (2013) Formation age and tectonic environment of the Gantaohe Group, North China Craton: geology, geochemistry, SHRIMP zircon geochronology and Hf-Nd isotopic systematics. China Sci Bull 58:75–85 (in Chinese with English abstract)
52. Xu YG, Chuang SL, Jahn BM, Wu GY (2001) Petrologic and geochemical constraints on the peteogenesis of Permian-Triassic Emeishan flood basalts in southwestern China. Lithos 58:145–168

53. Zhang SH, Zhao Y, Santosh M (2012) Mid-Mesoproterozoic bimodal magmatic rocks in the northern North China Craton: implications for magmatism related to breakup of the Columbia supercontinent. Precambr Res 222–223:339–367
54. Zhang HF (2009) Peridotite-melt interaction: a key point for the destruction of cratonic lithospheric mantle. Chin Sci Bull 54:3417–3437 (in Chinese with English abstract)
55. Zhang SH, Zhao Y, Yang ZY, He ZF, Wu H (2009) The 1.35 Ga diabase sills from the northern North China Craton: implications for breakup of the Columbia (Nuna) supercontinent. Earth and Planet Sci Lett 288:588–600
56. Zhang SH, Liu SW, Zhao Y, Yang JH, Song B, Liu XM (2007) The 1.75-1.68 Ga anorthosite-mangerite-alkali granitoid-rapakivi granite suite from the northern North China Craton: magmatism related to a Paleoproterozoic orogen. Precambr Res 155:287–312
57. Zhao TP, Chen W, Zhou MF (2009) Geochemical and Nd-Hf isotopic constraints on the origin of the ~1.74 Ga Damiao anorthosite complex. North China Craton Lithos 113: 673–690
58. Zhao FQ (2006) Paleoproterozoic crustal evolution of the Zhongtiao Mountain, Shanxi province: constraints from geochronology and geochemistry. Ph.D. thesis of China University of Geosciences, Beijing
59. Zhao GC, Sun M, Wilde SA et al (2005) Late Archean to Proterozoic evolution of the North China Craton: key issues revisited. Precambr Res 136:177–202
60. Zhao GC, Sun M, Wilde SA, Li SZ (2004) A Paleo-Mesoproterozoic supercontinent: assembly, growth and breakup. Earth Sci Rev 67:91–123
61. Zhao GC, Wilde SA, Cawood PA et al (1999) Thermal evolution of two types of mafic granulites from the North China Craton: implications for both mantle plume and collisional tectonics. Geol Mag 136:223–240
62. Zheng JP, Griffin WL, O'Reilly SY (2004) 3.6 Ga lower crust in central China: new evidence on the assembly of the North China craton. Geology 32:229–232
63. Zhu RX, Xu YG, Zhu G et al (2012) Destruction of the North China Craton. Sci China Earth Sci 55:1565–1587

Chapter 6
Concluding Remarks

Abstract Based on detailed geochronological and geochemical studies of representative late Neoarchean to Mesoproterozoic (~2.6–1.2 Ga) lithological assemblages from the Western Liaoning-Northeastern Hebei Provinces, the nature of magma sources, genetic processes, and tectonic environment of each magmatic episode are summarized in this chapter. Accordingly, the prolonged Precambrian lithospheric mantle formation and evolution as well as the crust-mantle geodynamic processes of the Western Liaoning-Northeastern Hebei Provinces are established for the first time.

Keywords Precambrian lithospheric mantle formation and evolution
Crust-mantle geodynamic processes · Western Liaoning-Northeastern Hebei Provinces · North China Craton

1. Metavolcanic rocks in the Fuxin-Yixian greenstone belt of Western Liaoning Province consist mainly of amphibolites and hornblende plagioclase gneisses, and the basaltic to andesitic magmatic precursors were crystallized during ~2640–2534 Ma. Geochemical data indicate that they show geochemical affinities to MORB-type tholeiitic basalts, island arc tholeiitic to calc-alkaline basalts, adakites, and high magnesium andesites, respectively. Petrogenetic studies reveal that (a) the MORB-type metabasaltic rocks were generated by the partial melting of upwelling asthenospheric mantle beneath a mid-ocean spreading ridge; (b) the island arc tholeiitic to calc-alkaline metabasalts could have been formed by the partial melting of mantle wedge materials metasomatized by slab-derived fluids; and (c) the adakite-like and high magnesium metaandesites were produced by the partial melting of subducted slabs and complex slab melt-mantle wedge interaction processes. Considering that MORB-type metabasalts distribute mostly to the north of the island arc-related basaltic to andesitic rocks, it is suggested that the metavolcanic rocks of Fuxin-Yixian greenstone belt formed under a late Neoarchean subduction-accretion orogenic system with a southward subduction polarity, and they record intense ~2.6–2.5 Ga crustal growth.

W. Wang, *Archean-Mesoproterozoic Crustal Evolution and Crust-Mantle Geodynamics of Western Liaoning-Northeastern Hebei Provinces, North China Craton*, Springer Theses, https://doi.org/10.1007/978-981-10-7922-1_6

2. Voluminous TTG with subordinate dioritic gneisses were emplaced during ~2532–2506 Ma in the Western Liaoning Province. On the basis of petrographic and geochemical features, they are subdivided into two major groups, i.e., the high magnesium group (HMG) and the low magnesium group (LMG), which are considered to have been formed by the partial melting of subducted slabs and metabasaltic rocks at the arc root, respectively. Combined with the gneissic structures of these granitoid gneisses, they could have been evolved under a late Neoarchean subduction-related arc setting.

3. Some potassium-rich granodioritic to monzogranitic gneisses were formed at ~2495 Ma, showing weakly gneissic to massive structures. Petrogenetic studies suggest that they could have been generated by the partial melting of metamorphosed felsic rocks and sedimentary rocks. They are nearly coeval with regional peak granulite facies metamorphism, marking cratonization of the Eastern Block.

4. The ~1721–1696 Ma Jianping diorite-monzonite-syenite suite (JDMSS) is characterized by a lithological assemblage of magnetite diorites, clinopyroxene monzonites, and (quartz) syenites. Petrogenetic studies reveal that they were formed by fractional crystallization (including crustal contamination) from a common parental magma that was sourced from an enriched subcontinental lithospheric mantle. Combined with regional geological data, the JDMSS suite and the nearly coeval AMGRS suite along the northern margin of North China Craton are considered to have been evolved under a post-collisional setting following the collision between Eastern Block and Western Block. K-rich volcanic rocks in the Tuanshanzi and Dahongyu Formations were erupted during ~1671–1625 Ma, and they consist mainly of olivine basalts, trachybasalts, trachyandesites, trachytes, with minor hornblende basalts. It is suggested that they were evolved under a post-orogenic setting, which were chiefly generated by the partial melting of depleted asthenospheric mantle sources, with subsequent interactions with the overlying lithospheric mantle.

5. ~1230 Ma mafic dykes are widely developed in the study area, dominated by alkaline gabbros and subordinate sub-alkaline gabbros. The alkaline gabbros were mainly produced by the partial melting of depleted asthenospheric mantle, whereas the sub-alkaline gabbros were derived from an enriched lithospheric mantle source. They could represent the response of a mantle plume event that led to the final breakup of the Paleo- to Mesoproterozoic Columbia supercontinent.

6. The Western Liaoning-Northeastern Hebei Provinces record complex Precambrian lithospheric mantle evolution as follows: (a) late Neoarchean depleted lithospheric mantle was transformed from juvenile oceanic lithospheric mantle, which was metasomatized by slab-derived materials and became gradually enriched during the Paleoproterozoic; (b) this enriched lithospheric mantle was further modified by materials released from the subducted oceanic crust (and probably continental crust) during the late Paleoproterozoic subduction-collision between the Eestern and Western blocks, resulting in the formation of a K- and LILE-enriched subcontinental lithospheric mantle; and (c) the above lithospheric mantle witnessed at least two episodes of vertical accretion processes during late Paleoproterozoic to Mesoproterozoic, as evidenced by the intense upwelling of asthenospheric mantle during ~1671–1625 Ma and ~1230 Ma, which was triggered by lithospheric delamination and mantle plume event, respectively.

7. The Western Liaoning-Northeastern Hebei Provinces experienced complex Precambrian crust-mantle geodynamic processes as follows: (a) during ~2640–2506 Ma, adiabatic partial melting of upwelling asthenospheric mantle at a mid-ocean spreading ridge generated MORB-type tholeiitic basalts as well as depleted oceanic lithospheric mantle. This juvenile oceanic lithospheric mantle was gradually metasomatized by slab-derived fluids and melts, and the complex slab-mantle wedge interactions yielded island arc tholeiitic to calc-alkaline basalts, adakite-like and high magnesian andesites, as well as dioritic to TTG rocks of the high magnesium group (HMG). Partial melting of metabasaltic rocks at the arc-root triggered by the underplating of mantle- or slab-derived magmas formed TTG rocks of the low magnesium group (LMG); (b) following accretion of the above arc system onto the northern continental margin of Eastern Block, slab rollback or breakoff occurred, which induced regional granulite facies metamorphism and crustal anatexis, and the partial melting of regional metamorphosed felsic rocks (including sedimentary rocks) formed the potassium-rich granitoids; (c) the Archean depleted lithospheric mantle became gradually enriched due to modification by two major episodes of subduction processes at late Neoarchean and late Paleoproterozoic, respectively, and partial melting of this enriched lithospheric mantle due to post-collision slab breakoff at ~1780–1680 Ma led to the formation of voluminous alkaline plutonic rocks including the JDMSS and AMGRS suites; (d) during ~1671–1625 Ma, partial melting of the upwelling asthenospheric mantle occurred following lithospheric delamination, and interaction between the asthenosphere and lithospheric mantle-derived materials yielded K-rich volcanic rocks in the Yanliao rift; and (e) complex asthenosphere-lithosphere interactions during the ~1230 Ma mantle plume event led to the generation of mafic dyke swarms in the NCC, signifying possibly the final breakup of Columbia supercontinent.